

Chin-Hsing Kuo  
Pei-Chun Lin  
Terence Essomba  
Guan-Chen Chen *Editors*

# Robotics and Mechatronics

Proceedings of the 6th IFToMM  
International Symposium on Robotics  
and Mechatronics (ISRM 2019)



# **Mechanisms and Machine Science**

Volume 78

## **Series Editor**

Marco Ceccarelli, Department of Industrial Engineering, University of Rome  
Tor Vergata, Roma, Italy

## **Editorial Board Members**

Alfonso Hernandez, Mechanical Engineering, University of the Basque Country,  
Bilbao, Vizcaya, Spain

Tian Huang, Department of Mechatronical Engineering, Tianjin University,  
Tianjin, China

Yukio Takeda, Mechanical Engineering, Tokyo Institute of Technology, Tokyo,  
Japan

Burkhard Corves, Institute of Mechanism Theory, Machine Dynamics and  
Robotics, RWTH Aachen University, Aachen, Nordrhein-Westfalen, Germany

Sunil Agrawal, Department of Mechanical Engineering, Columbia University,  
New York, NY, USA



This book series establishes a well-defined forum for monographs, edited Books, and proceedings on mechanical engineering with particular emphasis on MMS (Mechanism and Machine Science). The final goal is the publication of research that shows the development of mechanical engineering and particularly MMS in all technical aspects, even in very recent assessments. Published works share an approach by which technical details and formulation are discussed, and discuss modern formalisms with the aim to circulate research and technical achievements for use in professional, research, academic, and teaching activities.

This technical approach is an essential characteristic of the series. By discussing technical details and formulations in terms of modern formalisms, the possibility is created not only to show technical developments but also to explain achievements for technical teaching and research activity today and for the future.

The book series is intended to collect technical views on developments of the broad field of MMS in a unique frame that can be seen in its totality as an Encyclopaedia of MMS but with the additional purpose of archiving and teaching MMS achievements. Therefore, the book series will be of use not only for researchers and teachers in Mechanical Engineering but also for professionals and students for their formation and future work.

The series is promoted under the auspices of International Federation for the Promotion of Mechanism and Machine Science (IFTToMM).

Prospective authors and editors can contact Mr. Pierpaolo Riva (publishing editor, Springer) at: [pierpaolo.riva@springer.com](mailto:pierpaolo.riva@springer.com)

Indexed by SCOPUS and Google Scholar.

More information about this series at <http://www.springer.com/series/8779>

Chin-Hsing Kuo · Pei-Chun Lin ·  
Terence Essomba · Guan-Chen Chen  
Editors

# Robotics and Mechatronics

Proceedings of the 6th IFToMM International  
Symposium on Robotics and Mechatronics  
(ISRM 2019)



 Springer

The Springer logo consists of a stylized black chess knight piece facing left, positioned to the left of the word 'Springer' in a black, serif font.

*Editors*

Chin-Hsing Kuo  
School of Mechanical, Materials,  
Mechatronic and Biomedical Engineering  
University of Wollongong  
Wollongong, NSW, Australia

Terence Essomba  
Department of Mechanical Engineering  
National Central University  
Taoyuan City, Taiwan

Pei-Chun Lin  
Department of Mechanical Engineering  
National Taiwan University  
Taipei, Taiwan

Guan-Chen Chen  
Department of Mechanical  
and Electro-Mechanical Engineering  
Tamkang University  
New Taipei City, Taiwan

ISSN 2211-0984

Mechanisms and Machine Science

ISBN 978-3-030-30035-7

<https://doi.org/10.1007/978-3-030-30036-4>

ISSN 2211-0992 (electronic)

ISBN 978-3-030-30036-4 (eBook)

© Springer Nature Switzerland AG 2020

This work is subject to copyright. All rights are reserved by the Publisher, whether the whole or part of the material is concerned, specifically the rights of translation, reprinting, reuse of illustrations, recitation, broadcasting, reproduction on microfilms or in any other physical way, and transmission or information storage and retrieval, electronic adaptation, computer software, or by similar or dissimilar methodology now known or hereafter developed.

The use of general descriptive names, registered names, trademarks, service marks, etc. in this publication does not imply, even in the absence of a specific statement, that such names are exempt from the relevant protective laws and regulations and therefore free for general use.

The publisher, the authors and the editors are safe to assume that the advice and information in this book are believed to be true and accurate at the date of publication. Neither the publisher nor the authors or the editors give a warranty, expressed or implied, with respect to the material contained herein or for any errors or omissions that may have been made. The publisher remains neutral with regard to jurisdictional claims in published maps and institutional affiliations.

This Springer imprint is published by the registered company Springer Nature Switzerland AG  
The registered company address is: Gewerbestrasse 11, 6330 Cham, Switzerland

# Preface

This book is edited as the Proceedings of *The 6th IFToMM International Symposium on Robotics and Mechatronics* (ISRM 2019), a biannual event organized by the Technical Committee for Robotics and Mechatronics under International Federation for the Promotion of Mechanism and Machine Science (IFTToMM).

The aim of ISRM is to promote timely scholarly exchange for the robotics and mechatronics R&D community. ISRM 2019 is the sixth edition of its series following the previous versions held in Hanoi (Vietnam) in 2009, Shanghai (China) in 2011, Singapore in 2013, Poitiers (France) in 2015, and Sydney (Australia) in 2017. The sixth ISRM comes to Taipei (Taiwan) hosted by National Taiwan University of Science and Technology during October 28–30, 2019.

Based on a peer-reviewed evaluation, the ISRM 2019 proceedings present state-of-the-art research findings in robotics and mechatronics in the 46 papers by the authors from 19 different countries throughout 5 continents. The contributed articles are categorized into 8 different technical sessions to be presented at the symposium, including mechanism synthesis, analysis, and design, kinematics and dynamics of multibody systems, modeling and simulation, sensors and actuators, novel robotic systems, industrial and service-related robotics and mechatronics, advances in medical robotics, and historical development in robotics and mechatronics.

Last, we thank the authors for their valuable contributions, as well as the anonymous and volunteer reviewers for having completed their work in a timely manner. We would also like to express our sincere gratitude to Professors Med Amine Laribi and Carl A. Nelson for their editorial work for the special session on advances in surgical robotics.

July 2019

Chin-Hsing Kuo  
Pei-Chun Lin  
Terence Essomba  
Guan-Chen Chen

# Organization

## Honorary Chair

Shuo-Hung Chang	National Taiwan University, Taiwan
-----------------	------------------------------------

## General Chair

Chin-Hsing Kuo	University of Wollongong, Australia
----------------	-------------------------------------

## General Co-chair

Pei-Chun Lin	National Taiwan University, Taiwan
--------------	------------------------------------

## Program Chair

Terence Essomba	National Central University, Taiwan
-----------------	-------------------------------------

## Program Co-chairs

Chao-Chien Lan	National Cheng Kung University, Taiwan
Po-Ting Lin	Taiwan Tech, Taiwan

## Special Session Co-chairs

Med Amine Laribi	University of Poitiers, France
Carl Nelson	University of Nebraska-Lincoln, USA

## Publication Chair

Guan-Chen Chen	Tamkang University, Taiwan
----------------	----------------------------

## Organized Sessions Chair

Meng-Kun Liu                      Taiwan Tech, Taiwan

## Publicity Chairs

Syuan-Yi Chen                      National Taiwan Normal University, Taiwan  
Win-Bin Shieh                      Ming Chi University of Technology, Taiwan

## Local Arrangement Chairs

I-Tsyuen Chang                      Taiwan Tech, Taiwan  
Hung-Lin Hsieh                      Taiwan Tech, Taiwan  
Tsrong-Yi Wen                      Taiwan Tech, Taiwan  
Pin-Chuan Chen                      Taiwan Tech, Taiwan  
Chen-Yang Lan                      Taiwan Tech, Taiwan  
Yu-Hsu Chen                      Taiwan Tech, Taiwan  
Chun-Hu Chung                      National Cheng Kung University, Taiwan  
Chi-Ying Lin                      Taiwan Tech, Taiwan

## Best Paper Awards Chair

Burkhard Corves                      RWTH Aachen University, Germany

## International Scientific Committee

Tobias Bruckmann                      University of Duisburg-Essen, Germany  
I-Ming Chen                      Nanyang Technological University, Singapore  
Nguyen Phong Dien                      Hanoi University of Science and Technology,  
   Vietnam  
Gu Fang                      Western Sydney University, Australia  
Feng Gao                      Shanghai Jiao Tong University, China  
Chin-Hsing Kuo                      University of Wollongong, Australia  
Lotfi Romdhane                      Université de Sousse, Tunisia  
Yukio Takeda                      Tokyo Institute of Technology, Japan  
Said Zeghloul                      University of Poitiers, France  
Teresa Zielinska                      Warsaw University of Technology, Poland

## Program Committee

Keisuke Arikawa                      Kanagawa Institute of Technology, Japan  
Guimin Chen                      Xi'an Jiaotong University, China  
Gökhan Kiper                      Izmir Institute of Technology, Turkey  
Philip Voglewede                      Marquette University, USA



## **Best Paper Awards Committee**

Tobias Bruckmann	University of Duisburg-Essen, Germany
Eduardo Castillo Castaneda	Instituto Politecnico Nacional (CICATA), Mexico
Clément Gosselin	Université Laval, Canada
Muthuswamy Sreekumar	IIITDM Kancheepuram, India
Yukio Takeda	Tokyo Institute of Technology, Japan

## **Webmaster**

Ebrahim Shahabi	Taiwan Tech, Taiwan
-----------------	---------------------

# Contents

## Mechanism Synthesis, Analysis, and Design

<b>Stiffness Analysis of a Semi-symmetrical Three-Translation Delta-CU Parallel Robot</b> . . . . .	3
Huiping Shen, Yixi Wang, Guanglei Wu, and Qingmei Meng	

<b>Review on Powered Mobility and Meal Preparing Assistive Devices for Physically Disabled Persons</b> . . . . .	16
Salman Masroor, Hasan Bulut, Bahrudin, and Chyi-Yeu Lin	

<b>Performance Evaluation of a Class of Gravity-Compensated Gear-Spring Planar Articulated Manipulators</b> . . . . .	29
Nguyen Vu Linh and Chin-Hsing Kuo	

<b>Design and Analysis of a Mechanism for Spherical Surface Processing</b> . . . . .	39
Alexey Fomin, Wsevolod Ivanov, and Victor Glazunov	

<b>A Short Note on Equivalent Four-Bar Linkages of Direct-Contact Mechanisms</b> . . . . .	51
Wen-Tung Chang and Dung-Yan Yang	

<b>Dynamic Analysis and Motion Simulation of the 3 DOFs Waist Mechanism for Humanoid Robots</b> . . . . .	63
Marko Penčić, Boris Brkić, Maja Čavić, and Milan Rackov	

## Kinematics and Dynamics of Multibody Systems

<b>On Kinetostatics and Workspace Analysis of Multi-platform Cable-Driven Parallel Robots with Unlimited Rotation</b> . . . . .	79
Thomas Reichenbach, Philipp Tempel, Alexander Verl, and Andreas Pott	

<b>Kinematics of a Planar Parallel Robot via Screw Theory: Details not Mentioned</b> . . . . .	91
Albert L. Balmaceda-Santamaría and Mario A. García-Murillo	

<b>Dynamic Modeling for Spatial Revolute Joint with Clearances in Multibody Systems Based on HLCP</b> .....	103
Long Li, Shengnan Lyu, and Xilun Ding	
<b>Kinematic Analysis of (2-RRU)-URR Parallel Mechanism Performing 2R1T Output Motion</b> .....	114
Woo-hyeok Choi and Yukio Takeda	
<b>Development of an Innovative 2-DOF Continuous–Rotatable Mechanism</b> .....	125
Chun Liu, Ting-Hao Wang, and Pei-Chun Lin	
<b>Modelling and Simulation</b>	
<b>Dynamic Model of a Crank Press in the Process of Braking</b> .....	141
Assylbek Jomartov, Amandyk Tuleshov, and Moldir Kumatova	
<b>Workspace Modelling of a Parallel Robot with Relative Manipulation Mechanisms Based on Optimization Methods</b> .....	151
Dmitry Malyshev, Larisa Rybak, Laxmidhar Behera, and Santhakumar Mohan	
<b>Disk Cam Mechanisms with a Translating Follower Having Double Oblique Flat Faces</b> .....	164
Kuan-Lun Hsu and Yen-Nien Chen	
<b>Computationally Efficient Cable Force Calculation Outside the Wrench-Feasible Workspace</b> .....	177
Roland Boumann and Tobias Bruckmann	
<b>A 3-Dimensional Dynamic Model of the Aerotrains and the Horizontal Tail Effect on the Longitudinal Stability</b> .....	189
Quang Huan Luong, Jeremy Jong, Yusuke Sugahara, Daisuke Matsuura, and Yukio Takeda	
<b>Towards Grey Box Modeling in Modelica</b> .....	203
Frederic Bruder and Lars Mikelsons	
<b>Sensors and Actuators</b>	
<b>Development of an Interactive System for a Companion Robot Based on Telepresence Technology</b> .....	219
Siyu Chen, Ligang Yao, Yehliang Hsu, and Teddy Chen	
<b>Motion Experiment of Reducer-Integrated Motor Using Inscribed Planetary Gear Mechanism</b> .....	227
Tatsuro Terakawa, Masaharu Komori, Ryo Kataoka, Yuya Morita, and Shouta Tamura	

<b>Conductive Fabric Strain Sensor Design and Electromechanical Characterization</b> .....	235
Jun Liang Lau, Hwee Choo Liaw, and Gim Song Soh	
<b>Based on a Calibration Machine and Process to Develop a Six-Axis Force/Torque Sensor</b> .....	244
Yu-Jen Wang, Ching-Wei Hsu, Pei-Hua Huang, Li-Chi Wu, Chung-Yang Sue, and Chih-Che Lin	
<b>Novel Robotic Systems</b>	
<b>Parallel Mechanism Designs for Humanoid Robots</b> .....	255
Marco Ceccarelli and Matteo Russo	
<b>Development and Optimization of an Intelligent Parking Slot Allotter and Billing System Based on Machine Learning and OCR</b> .....	265
D. Bhanu Priya and Guan-Chen Chen	
<b>Design and Requirements for a Mobile Robot for Team Cooperation</b> .....	277
Luca Di Nunzio, Giancarlo Cardarilli, Marco Ceccarelli, and Rocco Fazzolari	
<b>Learning Emotion Recognition and Response Generation for a Service Robot</b> .....	286
Jhih-Yuan Huang, Wei-Po Lee, and Bu-Wei Dong	
<b>Design and Testing of 2-Degree-of-Freedom (DOF) Printable Pneumatic Soft Finger</b> .....	298
Ebrahim Shahabi, Yu-Ta Yao, Cheng-Hsiu Chuang, Po Ting Lin, and Chin-Hsing Kuo	
<b>Industrial and Service Related Robotics and Mechatronics</b>	
<b>Intelligent Automation Module-Based Gear Edge Grinding System</b> . . . .	311
C. K. Huang, Y. B. Guu, C. Y. Yang, Yi-Ying Lin, and C. H. Chen	
<b>Development of an Automated and Adaptive System for Robotic Hybrid-Wire Arc Additive Manufacturing (H-WAAM)</b> .....	323
Audelia Gumarus Dharmawan, Yi Xiong, Shaohui Foong, and Gim Song Soh	
<b>A Motion Control System to Use Robots at up to 100 Times the Earth's Gravity</b> .....	334
Victor M. Cedeno-Campos, Uriel Martinez-Hernandez, and Adrian Rubio Solis	
<b>Fault Signature Analysis of Industrial Machines</b> .....	346
Wei-Ting Hsu, Chen-Yang Lan, Meng-Kun Liu, and Shu-Tzu Chang	

**Robot-Assisted Double-Pulse Gas Metal Arc Welding for Wire and Arc Additive Manufacturing** ..... 360  
Jukkapun Greebmalai, Eakkachai Warinsiruk, and Yin-Tien Wang

**Development of a Close-Fitting Assistive Suit with Adjustable Structure for Arm and Back as Needed - e.z.UP®** ..... 371  
Yun-Ting Liao, Toshifumi Ishioka, Kazuko Mishima, Chiaki Kanda, Kenji Kodama, and Eiichiro Tanaka

**An Experimental Characterization of the BIT Astronaut Robot** ..... 380  
Zheng Tao, Ceccarelli Marco, Li Hui, and Mo Yang

**Advances in Medical Robotics**

**An Experimental Test Procedure for Validation of Stiffness Model: A Case Study for R-CUBE Parallel Mechanism** ..... 391  
İbrahimcan Görgülü, M. İ. Can Dede, and Giuseppe Carbone

**Multi-camera Vision-Guided Manipulation: Application to Acne and Wrinkles Treatment** ..... 403  
Ho-Yu Chuang and Jen-Yuan (James) Chang

**A Novel Three Degrees of Freedom Haptic Device for Rendering Texture, Stiffness, Shape, and Shear** ..... 412  
Vijay Kumar Pediredla, Karthik Chandrasekaran, Srikar Annamraju, and Asokan Thondiyath

**Real-Time Resolution of the Forward Kinematic Model for a New Spherical Parallel Manipulator** ..... 423  
Houssem Saafi, Med Amine Laribi, and Said Zeghloul

**Kinematic Design of a Double Pantographic Mechanism for the Intracranial Echography on Incubated Newborns** ..... 432  
Terence Essomba and Jia-Yu Hsieh

**Kinematic Design of a Six-Degrees of Freedom 3-RRPS Parallel Mechanism for Bone Reduction Surgery** ..... 444  
Sinh Nguyen Phu and Terence Essomba

**Multi-objective Optimization of a Reconfigurable Spherical Parallel Mechanism for Tele-Operated Craniotomy** ..... 454  
Terence Essomba, Juan Sandoval, Med Amine Laribi, and Said Zeghloul

**Autonomous Robot-Assistant Camera Holder for Minimally Invasive Surgery** ..... 465  
Juan Sandoval, Med Amine Laribi, and Saïd Zeghloul

**A Low-Cost 6-DoF Master Device for Robotic Teleoperation** ..... 473  
Juan Sandoval, Med Amine Laribi, and Said Zeghloul

**Historical Development in Robotics and Mechatronics**

**The Exhibit of Industrial Robots Based on Concepts of Technology Education: Take “Smart Manufacturing Experience Zone” at National Science and Technology Museum as an Example** ..... 483  
Jian-Liang Lin and Chieh-Ya Lin

**Ancient Chinese Puzzle Locks** ..... 494  
K. H. Hsiao, Y. Zhang, K. Shi, Y. H. Chen, and H. An

**A Historical Study of Rope Applications in Mechanical Devices in Three Eastern Countries** ..... 502  
Yu-Hsun Chen

**Current Research Topics in Robotics at IGMR** ..... 510  
Burkhard Corves, Mathias Huesing, Nils Mandischer, Markus Schmitz, Amirreza Shahidi, Michael Lorenz, and Sami Charaf Eddine



# **Mechanism Synthesis, Analysis, and Design**



# Stiffness Analysis of a Semi-symmetrical Three-Translation Delta-CU Parallel Robot

Huiping Shen<sup>1</sup>, Yixi Wang<sup>1</sup>, Guanglei Wu<sup>2(✉)</sup>, and Qingmei Meng<sup>1</sup>

<sup>1</sup> Modern Institutional Research Center,  
Changzhou University, Changzhou 213016, China

<sup>2</sup> School of Mechanical Engineering,  
Dalian University of Technology, Dalian 116024, China  
gwwu@dlut.edu.cn

**Abstract.** The Delta-CU parallel mechanism is a semi-symmetrical 3-DOF translational parallel mechanism designed by the author based on the topological structure design theory of POC equation. Compared with the Delta mechanism, the structure is more simple, and the kinematics performance is consistent. The stiffness modeling and characteristics of Delta-CU mechanism are studied in this paper. First, the stiffness model of the limb is established by using the virtual spring method, and the equilibrium equation of the limb is given. Then, the differential mapping from the deflection of the virtual joint to the end-effector is obtained by the Screw theory, and the Cartesian stiffness matrix of the mechanism is obtained by the equilibrium equation; Finally, through the Virtual Work based stiffness index, the Delta-CU mechanism under given parameters is analyzed and compared with the Delta mechanism.

**Keywords:** Three-translation parallel mechanism · Stiffness analysis · Virtual spring method · Virtual Work stiffness index

## 1 Introduction

Existing stiffness analysis methods can be divided into: finite element analysis (FEA), matrix structure analysis (MSA) and virtual joint method (VJM). The obvious advantage of FEA is its high precision but is only limited by the discrete steps for being re-meshed and analysis of a parallel robot at different position. The modeling of the links and joints has accurate physical models [1, 2], but is difficult to analyze in real time due to recalculation and repeated meshing. FEA could be applied to the final design stage in practical applications [3], and often used as a comparative analysis in the study of other stiffness modeling methods [4]; MSA mainly combines the method of finite element analysis [5], considering the links and joints as units, and compared with the FEA method, the computational complexity is obviously reduced, but the Cartesian stiffness matrix (size of  $6 \times 6$ ) cannot be directly obtained, and it must be transformed from a high-dimensional matrix (size of  $n \times n$ ) to a low-dimensional matrix (size of  $6 \times 6$ ) [6, 7].

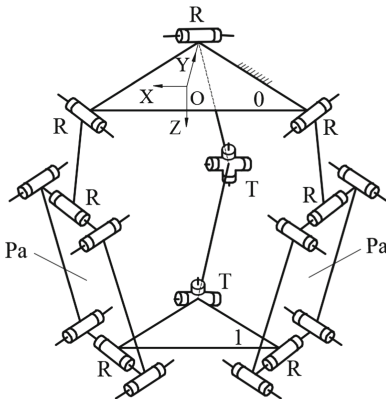
For the stiffness modeling of parallel mechanisms (PMs), the most widely used method is the VJM. This method is an extension of the traditional rigid body model in

which the link is considered a rigid body, but a flexible joint is created (in order to accumulate all types of compliance of the link or joint), geometrically, this is equivalent to adding a virtual joint (VJ) which is embedded next to the joint, apparently the lumped performance of compliance greatly simplifies the modeling. The main idea of the class of the VJM is proposed early [8], and only considering the compliance of active joints as the main source of the compliance of the PM. Thereafter, the VJM was applied to different PMs through different assumptions and numerical methods [9–16].

Different from other methods, the virtual spring method (VSM) of stiffness modeling proposed in [11] can be convenient and fast to analyze the stiffness performance of different PMs for optimization. In the process of stiffness modeling, the limbs of the PMs can be modeled separately. Therefore, after material and cross-section parameters of the links have been known, the stiffness can be calculated from just the inverse kinematics of the PMs, and also derived when the PMs are in a singular configuration. On the basis of this, the author simplifies the computational process of motion mapping by using Screw Theory [12], which improves practicability of the VSM.

This paper first introduces the composition of the semi-symmetric three-translation parallel mechanism Delta-CU. From the appearance, it is similar to Delta but the structure is simplified [17]. Based on the completion of kinematic analysis [18], the stiffness analysis of Delta-CU is carried out. Firstly, based on the VSM, the compliance model of the limb is established, and the Cartesian stiffness matrix (CSM) of Delta-CU is obtained by using Screw Theory. To solve the problem of unit inconsistency of the CSM, the stiffness characteristics of Delta-CU are analyzed by virtual work (VW) index. The stiffness difference between Delta and Delta-CU has been compared and analyzed.

## 2 Delta-CU Structure



(a) Delta-CU mechanism



(b) Experimental prototype

**Fig. 1.** Delta-CU manipulator

The Delta-CU designed according to the theory of parallel mechanism topology design based on Position and Orientation Characteristics (POC) equation is shown in Fig. 1.

It consists of a base platform (BP) 0, a mobile platform (MP) 1, and two identical  $\underline{R}$ -RPaR hybrid limbs and a  $\underline{R}$ -TT simple limb, each of which consists of an active link and a parallelogram (includes four revolute joints) which is written as Pa. The active link and the parallelogram are connected by a revolute joint, and are connected to the mobile platform 1 through a revolute joint (written as  $\underline{R}$ -RPaR); the two links of the  $\underline{R}$ -TT limb are connected by a universal joint T, the limb and the base platform 0 is connected by a revolute joint, another revolute joint connects the limb to the mobile platform 1. The lengths of the three active links connected to the base platform 0 in the three limbs are equal; the length of the link connected to the movable platform 1 in the  $\underline{R}$ -TT limb is equal to that of the parallelogram in the hybrid limb.

### 3 Stiffness Modeling

Each limb of the Delta-CU can be regarded as consisting of an active link and a passive link, which can be uniformly represented as a compliance model containing the virtual springs (VSs), and modeling of the  $\underline{R}$ -TT limb in the Delta-CU, as shown in the Fig. 2.

- 1-dof spring, indicates the servo stiffness of the actuator.
- 6-dof spring, corresponding to rotational and translational deflections of the link in the Cartesian coordinate.
- 2-dof, indicates that the passive universal joint T which is subjected to an external force to generate a passive motion.

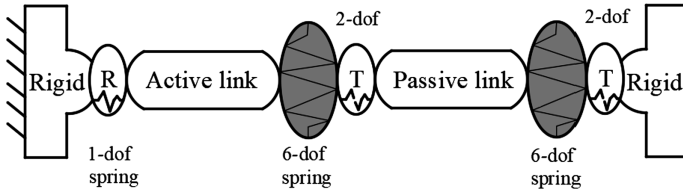


Fig. 2. Compliance model of the  $\underline{R}$ -TT limb

Similarly, Compliance model of the  $\underline{R}$ -RPaR has been established in Fig. 3

- 1-dof spring, between Active link and Parallelogram, indicates passive joint from the parallelogram.
- 5-dof spring, corresponding to rotational and translational deflections of the parallelogram in the Cartesian coordinate which will be explained below.
- 1-dof, at the end of the limb, represents that the passive joint R at the MP.

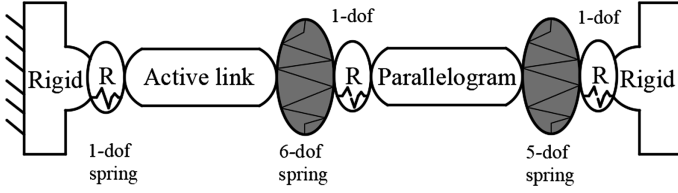


Fig. 3. Compliance model of the R-RPaR limb

### 3.1 Motion Equation of the Limb

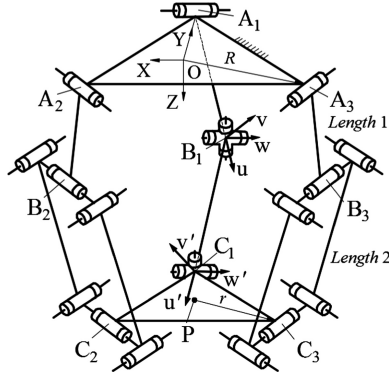


Fig. 4. Symbol of Delta-CU mechanism

As shown in Fig. 4,  $A_i, B_i, C_i$  ( $i = 1, 2, 3$ ) are the center of joints, the origin of Cartesian coordinate frame  $O$ -XYZ is at the center of the BP which is equilateral triangle, and  $A_1$  is on the Y axis of global coordinate frame  $O$ -XYZ.

From the compliance model of Figs. 2 and 3, a general equation of motion from deflections of the VSs and passive motion to deflection of the MP in the limb can be given

$$\Delta \mathbf{t} = \mathbf{J}_\theta^i \Delta \boldsymbol{\theta}_i + \mathbf{J}_\psi^i \Delta \boldsymbol{\psi}_i \quad (i = 1, 2, 3) \quad (1)$$

Wherein,  $\Delta \mathbf{t}$  representing the deflection of the MP in the Cartesian coordinate system, which consists of rotational deflections and translational deflections;  $\Delta \boldsymbol{\theta}_i$  is the deflection of the VS at the actuator and the end of links in the  $i$ -th limb;  $\Delta \boldsymbol{\psi}_i$  describes the passive motion of the passive joints in the  $i$ -th limb;  $\mathbf{J}_\theta^i$  and  $\mathbf{J}_\psi^i$  are the Jacobian matrices corresponding to the deflections  $\Delta \boldsymbol{\theta}_i$  and passive motion  $\Delta \boldsymbol{\psi}_i$ .

For example, the local Cartesian coordinate systems  $B_1$ -uvw and  $C_1$ -u'v'w' as shown in Fig. 4 are established, and the u-axis and the u'-axis are respectively along the axis directions of the links  $A_1B_1$  and  $B_1C_1$ ; the w-axis and w'-axis are along the axis of actuator; the v-axis and the v'-axis are perpendicular to the plane formed by the u-axis

and the w-axis, the u-axis and the w' axis, respectively. So  $\mathbf{J}_\theta^i$  and  $\mathbf{J}_\psi^i$  in  $\underline{R}$ -TT limb can be expressed as  $\mathbf{J}_\theta^1 = [\mathbf{J}_{\theta ac}^1 \quad \mathbf{J}_{\theta rd1}^1 \quad \mathbf{J}_{\theta rd2}^1]$  and  $\mathbf{J}_\psi^1$ , then

$$\mathbf{J}_{\theta ac}^1 = [\hat{\$}_{\theta ac}^1]; \quad \mathbf{J}_{\theta rd1}^1 = [\hat{\$}_{\theta 01}^1 \quad \hat{\$}_{\theta 02}^1 \quad \hat{\$}_{\theta 03}^1 \quad \hat{\$}_{\theta 04}^1 \quad \hat{\$}_{\theta 05}^1 \quad \hat{\$}_{\theta 06}^1];$$

$$\mathbf{J}_{\theta rd2}^1 = [\hat{\$}_{\theta 07}^1 \quad \hat{\$}_{\theta 08}^1 \quad \hat{\$}_{\theta 09}^1 \quad \hat{\$}_{\theta 010}^1 \quad \hat{\$}_{\theta 011}^1 \quad \hat{\$}_{\theta 012}^1]; \quad \mathbf{J}_\psi^1 = [\hat{\$}_{\psi 1}^1 \quad \hat{\$}_{\psi 1}^1 \quad \hat{\$}_{\psi 1}^1 \quad \hat{\$}_{\psi 1}^1]$$

where

$$\hat{\$}_{\theta ac}^1 = \begin{bmatrix} \mathbf{w} \\ (\mathbf{a} - \mathbf{p}) \times \mathbf{w} \end{bmatrix}$$

$$\hat{\$}_{\theta 01}^1 = \begin{bmatrix} \mathbf{u} \\ (\mathbf{b} - \mathbf{p}) \times \mathbf{u} \end{bmatrix}; \quad \hat{\$}_{\theta 02}^1 = \begin{bmatrix} \mathbf{v} \\ (\mathbf{b} - \mathbf{p}) \times \mathbf{v} \end{bmatrix}; \quad \hat{\$}_{\theta 03}^1 = \begin{bmatrix} \mathbf{w} \\ (\mathbf{b} - \mathbf{p}) \times \mathbf{w} \end{bmatrix}; \quad \hat{\$}_{\theta 04}^1 = \begin{bmatrix} \mathbf{0} \\ \mathbf{u} \end{bmatrix}; \quad \hat{\$}_{\theta 05}^1 = \begin{bmatrix} \mathbf{0} \\ \mathbf{v} \end{bmatrix}; \quad \hat{\$}_{\theta 06}^1 = \begin{bmatrix} \mathbf{0} \\ \mathbf{w} \end{bmatrix}$$

$$\hat{\$}_{\theta 07}^1 = \begin{bmatrix} \mathbf{u}' \\ (\mathbf{c} - \mathbf{p}) \times \mathbf{u}' \end{bmatrix}; \quad \hat{\$}_{\theta 08}^1 = \begin{bmatrix} \mathbf{v}' \\ (\mathbf{c} - \mathbf{p}) \times \mathbf{v}' \end{bmatrix}; \quad \hat{\$}_{\theta 09}^1 = \begin{bmatrix} \mathbf{w}' \\ (\mathbf{c} - \mathbf{p}) \times \mathbf{w}' \end{bmatrix}; \quad \hat{\$}_{\theta 010}^1 = \begin{bmatrix} \mathbf{0} \\ \mathbf{u}' \end{bmatrix}; \quad \hat{\$}_{\theta 011}^1 = \begin{bmatrix} \mathbf{0} \\ \mathbf{v}' \end{bmatrix}; \quad \hat{\$}_{\theta 012}^1 = \begin{bmatrix} \mathbf{0} \\ \mathbf{w}' \end{bmatrix}$$

$$\hat{\$}_{\psi 1}^1 = \begin{bmatrix} \mathbf{w} \\ (\mathbf{b} - \mathbf{p}) \times \mathbf{u} \end{bmatrix}; \quad \hat{\$}_{\psi 2}^1 = \begin{bmatrix} \mathbf{v}' \\ (\mathbf{b} - \mathbf{p}) \times \mathbf{v}' \end{bmatrix}; \quad \hat{\$}_{\psi 3}^1 = \begin{bmatrix} \mathbf{w} \\ (\mathbf{c} - \mathbf{p}) \times \mathbf{w} \end{bmatrix}; \quad \hat{\$}_{\psi 4}^1 = \begin{bmatrix} \mathbf{v}' \\ (\mathbf{c} - \mathbf{p}) \times \mathbf{v}' \end{bmatrix}$$

Wherein,  $\mathbf{u}, \mathbf{v}, \mathbf{w}, \mathbf{u}', \mathbf{v}', \mathbf{w}'$ : respectively represents a direction vector of the coordinate system of the local coordinate system in the state coordinate system;

$\mathbf{a}_i, \mathbf{b}_i, \mathbf{c}_i, \mathbf{p}$ : The position vectors of points A, B, C, and P are respectively denoted in the coordinate system O-XYZ.

### 3.2 Equilibrium Equation

Assuming that the force/torque of the VSs at the joints in the limb is  $\tau_\theta^i$ , then  $\tau_\theta^i = \mathbf{K}_\theta^i \Delta \theta^i$ , Wherein,  $\mathbf{K}_\theta^i$  represents stiffness of the VSs at the actuator or end of the link in the limb.

It is assumed that there are infinitesimal deflections of the VSs ( $\delta \theta_i$ ) and passive motion ( $\delta \psi_i$ ) when the limb is subjected to an external force/torque  $\mathbf{f}_i$  from the MP, then  $\delta \mathbf{t}_i = \mathbf{J}_\theta^i \delta \theta_i + \mathbf{J}_\psi^i \delta \psi_i$ .

The virtual work done by the constraint force in the limb is  $-\tau_\theta^i \delta \theta_i$  (opposite to force of the VSs), according to the principle of virtual work

$$\mathbf{f}_i^T \delta \mathbf{t}_i - \tau_\theta^i \delta \theta_i = 0 \quad (i = 1, 2, 3) \quad (2)$$

Only the VS is forced to work,  $\delta \theta_i$  and  $\delta \psi_i$  can be eliminated:

$$\mathbf{J}_\theta^{iT} \mathbf{f}_i = \tau_\theta^i \quad (i = 1, 2, 3) \quad (3)$$

$$\mathbf{J}_\psi^{iT} \mathbf{f}_i = 0 \quad (i = 1, 2, 3) \quad (4)$$

Equations (3) and (4) is the equilibrium equation of the limb. Due to the inverse matrix of the stiffness matrix is  $\mathbf{K}_\theta^{i-1}$  called the 'Flexibility matrix' because of  $\mathbf{K}_\theta^i$  being always symmetric positive, Each rod is treated as a cantilever, for which the



$6 \times 6$  compliance matrix is denoted by  $\mathbf{K}_{\text{rod}}^{-1} = [k_{ij}]$ , the nonzero elements calculated upon the Euler-Bernoulli beam theory taking the following form:

$$k_{11} = \frac{L}{GI_x}; k_{22} = \frac{L}{EI_y}; k_{33} = \frac{L}{EI_z}; k_{44} = \frac{L}{EA}; k_{55} = \frac{L^3}{3EI_y}; k_{66} = \frac{L^3}{3EI_z}; k_{35} = k_{53} = \frac{L^2}{2EI_z}$$

$$k_{26} = k_{62} = -\frac{L^2}{2EI_y}$$

Wherein,  $L$  is the length of the link;  $A$  is the cross-section area of the link;  $I_x$  is polar moment of inertia of the link;  $I_y$  and  $I_z$  is the moment of inertia of the section;  $E$  is the modulus of elasticity of the material,  $G$  is the shear modulus of the material.

Then, substitute  $\mathbf{K}_0^{i-1} \boldsymbol{\tau}_0^i = \Delta \boldsymbol{\theta}_i$  into the Eq. (1) together with Eq. (3) and simplified, the matrix form of equilibrium equation of the limb can be obtained.

$$\begin{bmatrix} \mathbf{S}_0^i & \mathbf{J}_\psi^i \\ \mathbf{J}_\psi^{i\text{T}} & 0 \end{bmatrix} \cdot \begin{bmatrix} \mathbf{f}_i \\ \Delta \boldsymbol{\psi}_i \end{bmatrix} = \begin{bmatrix} \Delta \mathbf{t} \\ 0 \end{bmatrix} \quad (5)$$

among them,  $\mathbf{S}_0^i = \mathbf{J}_0^i \mathbf{K}_0^{i-1} \mathbf{J}_0^{i\text{T}}$

### 3.3 Cartesian Stiffness Matrix

Because  $\mathbf{f}_i = \mathbf{K}_i \Delta \mathbf{t}$  ( $\mathbf{K}_i$  represents the stiffness matrix of the limb), the Eq. (5) is expressed as

$$\begin{bmatrix} \mathbf{K}_i & * \\ * & * \end{bmatrix} \cdot \begin{bmatrix} \Delta \mathbf{t} \\ 0 \end{bmatrix} = \begin{bmatrix} \mathbf{S}_0^i & \mathbf{J}_\psi^i \\ \mathbf{J}_\psi^{i\text{T}} & 0 \end{bmatrix}^{-1} \cdot \begin{bmatrix} \Delta \mathbf{t} \\ 0 \end{bmatrix} \quad (6)$$

The external force/torque  $\mathbf{f}$  at the center of the MP can be decomposed into the forces/torques  $\mathbf{f}_i$  of the limbs, resulting in:

$$\mathbf{f} = \sum_{i=1}^n \mathbf{f}_i \quad (7)$$

Because  $\mathbf{K} \Delta \mathbf{t} = \sum_{i=1}^n \mathbf{K}_i \Delta \mathbf{t}$  ( $\mathbf{K}$  represents the stiffness matrix of the PM), and eliminating the variable  $\Delta \mathbf{t}$  to obtain the Cartesian stiffness matrix of the PM in the global coordinate frame:

$$\mathbf{K} = \sum_{i=1}^n \mathbf{K}_i \quad (8)$$

However, for a complex  $\underline{R}$ -RPaR limb containing a parallelogram structure, the parallelogram structure must first be modeled as a separate structure. For this, a local coordinate frame as shown in Fig. 5 is established.

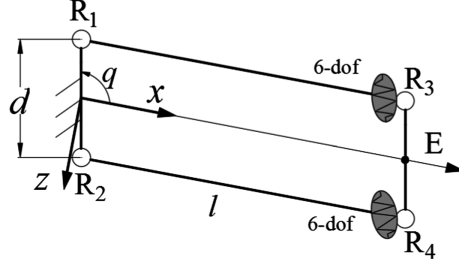


Fig. 5. Parallelogram modeling

The short bar in the parallelogram structure is regarded as a rigid link, and the stiffness of the parallelogram structure is modeled by the above calculation method, and the stiffness matrix  $\mathbf{K}_{\text{Par}}$  of the structure at the reference point E is calculated as

$$\mathbf{K}_{\text{Par}} = \begin{bmatrix} \frac{2}{k_{11}} + \frac{k_{33}d^2S_q^2}{2(k_{33}k_{55}-k_{35}^2)} & 0 & \frac{k_{33}d^2S_{2q}}{4(k_{33}k_{55}-k_{35}^2)} & 0 & 0 & 0 \\ 0 & \frac{d^2S_q^2}{2k_{44}} & 0 & 0 & 0 & 0 \\ \frac{k_{33}d^2S_{2q}}{4(k_{33}k_{55}-k_{35}^2)} & 0 & \frac{4k_{55}+d^2Cq^2}{2(k_{33}k_{55}-k_{35}^2)} & 0 & \frac{2k_{35}}{k_{35}^2-k_{33}k_{55}} & 0 \\ 0 & 0 & 0 & \frac{2}{k_{44}} & 0 & 0 \\ 0 & 0 & \frac{2k_{35}}{k_{35}^2-k_{33}k_{55}} & 0 & -\frac{2k_{33}}{k_{35}^2-k_{33}k_{55}} & 0 \\ 0 & 0 & 0 & 0 & 0 & 0 \end{bmatrix} \quad (9)$$

Where,  $C(\cdot)$ ,  $S(\cdot)$  represents  $\cos(\cdot)$ ,  $\sin(\cdot)$ ;  $[k]$  represents the element in the compliance matrix of the long link.

It can be seen that in the stiffness matrix  $\mathbf{K}_{\text{Par}}$ , the elements of the sixth row and the sixth column disappear due to the force of the reference point E in the direction of the passive R1, R3 and the passive R2, R4. To avoid the matrix singularity, the  $\mathbf{K}_{\text{Par}}$  must be a stiffness matrix of  $5 \times 5$ , so the parallelogram structure could be regarded as a passive link with a R-joint at the head and a 5-dof VS at the end.

## 4 Numerical Analysis

### 4.1 Structural Parameters

Referring to the design parameters of a certain type of Delta, the dimensional parameters of Delta-CU are as follows. As shown in Fig. 1, the length of the active link is Length 1, the length of the passive link is Length 2, and the radii of the circumscribed circle of the state and mobile platform are R and r respectively, as shown in Table 1.

**Table 1.** Design parameters of Delta-CU

$R$ (mm)	$r$ (mm)	$Length1$ (mm)	$Length2$ (mm)
108.5	60	223	442

The Sectional parameters and material parameters of the link are shown in Table 2, wherein the hollow link has an outer diameter  $D$  and an inner diameter  $d$ , and there are two long links in a parallelogram.

**Table 2.** Sectional parameters and material parameters

	Active link $D \times d$ (mm)	Passive link $D \times d$ (mm)	$E$ (GPa)
<u>R-RPaR</u>	$30 \times 26$	$16 \times 12 (\times 2)$	210
<u>R-TT</u>		$30 \times 26$	Poisson 0.3

## 4.2 Delta-CU Mechanism Stiffness Analysis

From the scale parameters shown in Table 1, according to the kinematics analysis of Delta-CU [17], a cylindrical working space with a diameter of 400 mm and a height range [250, 550] (mm) in the state coordinate system can be obtained. The position of the mechanism corresponding to [0, 0, 520] (mm) is substituted into Eqs. (1)–(8), the stiffness matrix  $K$  can be obtained by MATLAB:

$$\begin{bmatrix} 0.255 & 0 & 0 & 0 & 0.574 & 0 \\ 0 & 0.090 & -0.113 & -0.162 & 0 & 0 \\ 0 & -0.113 & 0.158 & 0.275 & 0 & 0 \\ 0 & -0.162 & 0.275 & 0.888 & 0 & 0 \\ 0.574 & 0 & 0 & 0 & 1.909 & 0 \\ 0 & 0 & 0 & 0 & 0 & 3.169 \end{bmatrix} \cdot 10^6$$

The above Cartesian stiffness matrix is divided into two  $6 \times 3$  matrices along the broken line, and the element units in the two matrices are N/rad and N/m respectively. Because the dimension of the matrix elements in the stiffness matrix is inconsistent and the coupling of translation and rotation exists, in order to analyze the stiffness characteristics of Delta-CU at different positions, this paper uses the virtual work (VW) stiffness index [13] for evaluation.

Assuming that a unit external force  $\mathbf{f}_{\text{unit}}$  is applied at the center of the MP which deflection is denoted by  $\delta \mathbf{t}$ , the virtual work of external force is

$$\mathbf{W} = \mathbf{f}_{\text{unit}}^T \cdot \delta \mathbf{t} \quad (10)$$

Therefore  $\delta \mathbf{t} = \mathbf{K}^{-1} \mathbf{f}_{\text{unit}}$ , the definition of the virtual work  $\mathbf{W} = \mathbf{f}_{\text{unit}}^T \mathbf{K}^{-1} \mathbf{f}_{\text{unit}}$ , VW stiffness index is:

$$\text{VW} = \frac{1}{\mathbf{f}_{\text{unit}}^T \mathbf{K}^{-1} \mathbf{f}_{\text{unit}}} \quad (11)$$

Under the external force of the same unit, the smaller external work, the smaller deflection, so the larger VW index, the better stiffness performance of the mechanism. The VW index based on the principle of virtual work is to evaluate the ability of the mechanism to resist deflection under a given external force or external torque by a single value. Therefore, the concept of virtual work is used to make the index more physical.

In most cases, the stiffness characteristics of the gravity direction are particularly important for the performance of the mechanism. Therefore, in order to analyze the resistance of Delta-CU in the working space, it is assumed that the external force and the unit external torque along the direction of gravity are applied to the end as  $\mathbf{f}_{\text{unit}} = [0 \ 0 \ 0 \ 0 \ 1]^T$  and  $\mathbf{f}_{\text{unit}} = [0 \ 0 \ 1 \ 0 \ 0]^T$ , using the above calculation method of the VW stiffness index, the variation diagram of the VW stiffness index in the workspace shown in Fig. 6 is obtained.

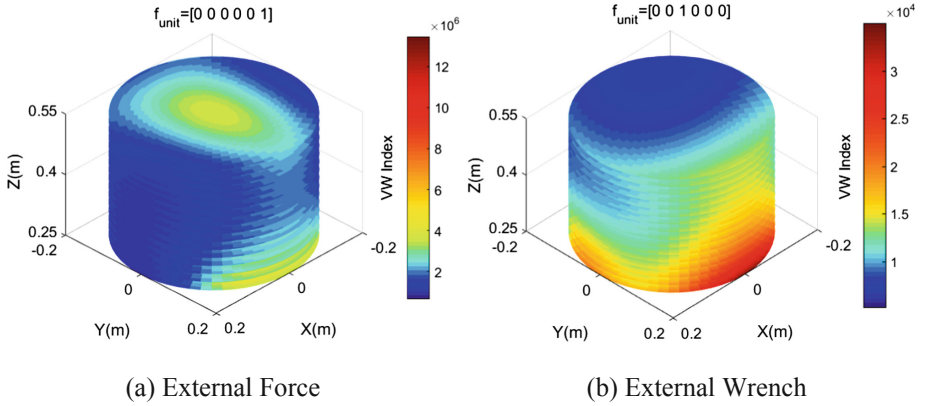


**Fig. 6.** VW index in workspace

It can be seen from Fig. 6 that at different working heights, the closer to working center, the better Delta-CU's ability to resist tensile deflection and the worse torsional resistance; however, whether torsional resistance or tensile resistance, the change in stiffness performance is more gradual at working height of  $z = 550$  (mm).

In actual working conditions, the deflection resistance of the mechanism is determined by the weakest working area. As can be seen from Fig. 6, although the maximum values are significantly different, the minimum values in the working area are relatively close, so the conclusion is obtained; the higher the working height, the more

stable the stiffness performance, and this working characteristic meets the requirements of the actual working conditions.

### 4.3 Stiffness Comparison of Delta-CU and Delta

It can be seen from the literature [17] that under the same design parameters, Delta-CU has the same kinematics performance as Delta, so according to the relevant parameters of Tables 1 and 2, Cartesian stiffness matrix of Delta has been also obtained at [0, 0, 520] (mm):

$$\begin{bmatrix} 0.255 & 0 & 0 & 0 & 0.574 & 0 \\ 0 & 0.255 & 0 & -0.574 & 0 & 0 \\ 0 & 0 & 0.228 & 0 & 0 & 0 \\ 0 & -0.574 & 0 & 1.908 & 0 & 0 \\ 0.574 & 0 & 0 & 0 & 1.908 & 0 \\ 0 & 0 & 0 & 0 & 0 & 3.165 \end{bmatrix} \cdot 10^6$$

From the above stiffness matrix, the stiffness of Delta still has coupling characteristics. The VW index is used to compare Delta-CU with Delta. In the Cartesian stiffness system, the distribution of stiffness characteristic is not only related to the external force, but also the action position of external force, so it is assumed that a unit force or a unit torque in a direction other than a single coordinate axis is applied at the same point, that is, the stiffness characteristics in a plurality of directions are considered for comparison.

It is assumed that the unit force  $\mathbf{f}_{\text{unit}} = [0 \ 0 \ 0 \ \sqrt{3}/3 \ \sqrt{3}/3 \ \sqrt{3}/3]^T$  (N) and the unit torque  $\mathbf{f}_{\text{unit}} = [\sqrt{3}/3 \ \sqrt{3}/3 \ \sqrt{3}/3 \ 0 \ 0 \ 0]^T$  (N·m) are sequentially applied. Because the structure of Delta-CU is similar to that of Delta, only the VW stiffness index value distribution on the working plane at  $z = 400$  (mm) is compared, as shown in Figs. 7 and 8.

It can be seen from the overall characteristics shown in Fig. 7 that although the index values are somewhat different, in general, the Delta-CU mechanism exhibits a similar stiffness characteristic to that of Delta on the working plane, so when resisting tensile deflection is taken into consideration, both have basically the same resistance to deflection.

It can be seen from Fig. 8 that Delta-CU and Delta exhibit different stiffness characteristics in anti-torsion deflection. The optimum position of Delta against torsional deflection is opposite to that of Delta-CU. The ability to anti-torsion is weaker than Delta. Due to Delta-CU used for grabbing and placing motion, the components are mainly subjected to tensile loads, and less torsional loads. Therefore, Delta-CU can meet the same working requirements as Delta.

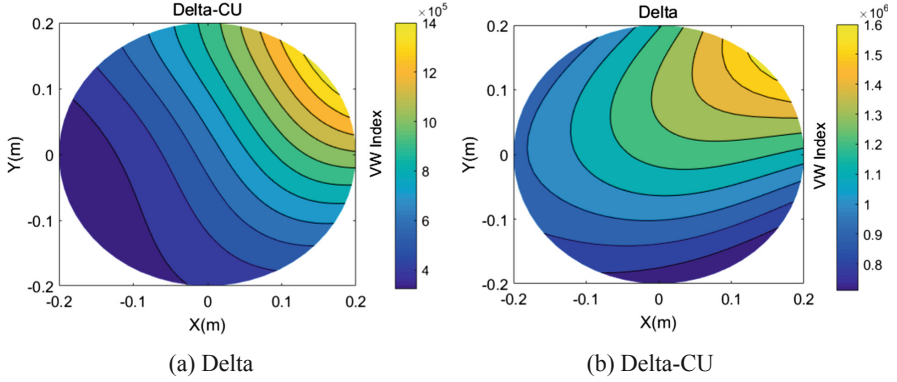


**Fig. 7.** Resistance against force

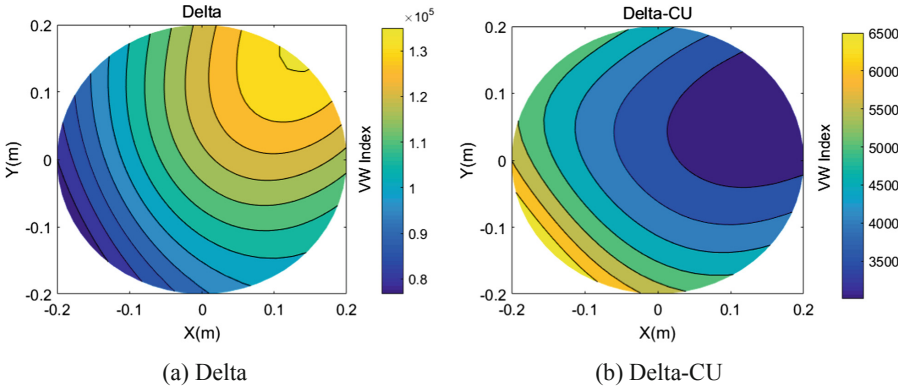


**Fig. 8.** Resistance against wrench

## 5 Conclusion

- (1) The stiffness of Delta-CU is modeled by VSM, and the stiffness matrix of Cartesian space has been obtained.
- (2) Using the VW index, the stiffness characteristics of Delta-CU in different working planes are analyzed. The results show that the higher working height, the more stable stiffness performance; the linear stiffness and torsional stiffness index values work differently. The lowest value of the VW index is close to the corresponding value of Delta, that is, the worst working conditions of two mechanisms at any working height are close.
- (3) The Delta-CU mechanism uses a structure of  $\underline{R}$ -TT, the complicated  $\underline{R}$ -RPaR is avoided, which reduces the difficulty of processing and assembly; the required active torque is smaller; it has the same tensile rigidity as Delta.



The kinematics and dynamics of Delta-CU have been completed by the authors, as well as the results of the stiffness research in this paper, show that Delta-CU is more simple in structure, the kinematics, tensile stiffness properties are basically the same, which can replace Delta mechanism for the application of pick-and-place operation.

**Acknowledgments.** NSFC No. 51375062 and No. 51475050 is greatly appreciated.

## References

1. Corradini, C., Fauroux, J.C., Krut, S. and Company, O.: Evaluation of a 4-degree of freedom parallel manipulator stiffness. In: Proceedings of the 11th World Congress in Mechanism and Machine Science, IFTOMM, Tianjin, China (2004)
2. Fernández-Bustos, I., Agirrebeitia, J., Ajuria, G., Angulo, C.: A new finite element to represent prismatic joint constraints in mechanisms. *Finite Elements Anal. Des.* **43**(1), 36–50 (2006)
3. Long, C.S., Snyman, J.A., Groenwold, A.A.: Optimal structural design of a planar parallel platform for machining. *Appl. Math. Model.* **27**(8), 581–609 (2003)
4. Wu, G., Zou, P.: Stiffness analysis and comparison of a Biglide parallel grinder with alternative spatial modular parallelograms. *Robotica* **35**(6), 1310–1326 (2017)
5. Martin, H.C.: Introduction to Matrix Methods of Structural Analysis. McGraw-Hill Book Company, Montreal (1966)
6. Deblaise, D., Hernot, X., Maurine, P.: A systematic analytical method for PKM stiffness matrix calculation. In: Proceedings of the 2006 IEEE International Conference on Robotics and Automation, Orlando, America, pp. 4213–4219 (2006)
7. Ecorchard, G., Neugebauer, R., Maurine, P.: Elasto-geometrical modeling and calibration of redundantly actuated PKMs Original Research Article. *Mech. Mach. Theory* **45**(5), 795–810 (2010)
8. Gosselin, C.M.: Stiffness mapping for parallel manipulators. *IEEE Trans. Robot. Autom.* **6**(3), 377–382 (1990)
9. Majou, F., Gosselin, C., Wenger, P., Chablat, D.: Parametric stiffness analysis of the Orthoglide. *Mech. Mach. Theory* **42**(3), 296–311 (2007)
10. Quennouelle, C., Gosselin, C.M.: Stiffness matrix of compliant parallel mechanisms. In: Lenarčič, J., Wenger, P. (eds.) *Advances in Robot Kinematics: Analysis and Design*, pp. 331–341. Springer, Dordrecht (2008)
11. Pashkevich, A., Chablat, D., Wenger, P.: Stiffness analysis of overconstrained parallel manipulators. *Mech. Mach. Theory* **44**, 966–982 (2010)
12. Wu, G., Bai, S., Kepler, J.: Mobile platform center shift in spherical parallel manipulators with flexible limbs. *Mech. Mach. Theory* **75**, 12–26 (2014)
13. Yan, S.J., Ong, S.K., Nee, A.Y.C.: Stiffness analysis of parallelogram-type parallel manipulators using a strain energy method. *Robot. Comput. Integr. Manuf.* **37**, 13–22 (2016)
14. Wu, G., Bai, S., Preben, H.: On the stiffness of three/four degree-of-freedom parallel pick-and-place robots with four identical limbs. In: *IEEE International Conference on Robotics and Automation*, Stockholm, Sweden, pp. 861–866 (2016)
15. Vu, L.N., Kuo, C.H.: An analytical stiffness method for spring-articulated planar serial or quasiseriial manipulators under gravity and an arbitrary load. *Mech. Mach. Theory* **137**, 108–126 (2019)

16. Yang, K., Yang, W., Cheng, G., Lu, B.: A new methodology for joint stiffness identification of heavy duty industrial robots with the counterbalancing system. *Robot. Comput. Integr. Manuf.* **53**, 58–71 (2018)
17. Li, J.Y., Shen, H.P., Meng, Q.M., Deng, J.M.: A Delta-CU – kinematic analysis and dimension design. In: *International Conference on Intelligent Robotics and Applications*, pp. 371–382. Springer, Heidelberg (2017)
18. Li, J.Y., Shen, H.P., Meng, Q.M., Deng, J.M., Zhang, Z.: A Delta deflection mechanism and its scale design based on workspace analysis. *Mech. Des.* **35**(07), 92–98 (2018)



# Review on Powered Mobility and Meal Preparing Assistive Devices for Physically Disabled Persons

Salman Masroor<sup>(✉)</sup>, Hasan Bulut, Bahrudin, and Chyi-Yeu Lin

National Taiwan University of Science and Technology,  
Taipei 10607, Taiwan (R.O.C.)  
D10603826@mail.ntust.edu.tw

**Abstract.** Over the past decade, disability and aging have become serious global problems. The rapid growth of disabled and aging people in the society necessitates the employment of caregivers to assist them in performing everyday activities. However, caregiving is highly expensive with high injury rates. To transfer the people who cannot help themselves, a transfer aide becomes essential equipment. Mobility assistive devices can increase the mobility and reduce the risk of injury for both disabled and caregiver, particularly in bedroom, bathroom and kitchen. Although many smart devices were invented, they all required some degree of manual operations and assistance but assistive devices with a fully autonomous operation capability is never achieved. The paper presents a brief review of powered mobility assistive and meal preparing devices for physically disabled used in homes.

**Keywords:** Assistive devices · Meal preparing · Physically disabled persons

## 1 Introduction

Disability and aging have become serious global issues over the past decade. It has been estimated that 15% of the world's population lives with some form of disability [1] whereas about 13% of world population is aged 60 or more, which is growing at the rate of 3% per year and is expected to double by 2050. Moreover, global population aged 60 or over is growing faster than all younger age groups [2].

Asia has a population of 4.4 billion, about 60% of the global population, with two of the largest populations of more than a billion people each in China and India. Currently, China and India have disabled populations of around 24.12 million and 5.4 million with disability prevalence rates of 6.5 and 2.2%, respectively [3, 4]. During the last decade, Japan is facing super-aging issues with the percentage of elderly people in 2016 at 27.3%, and is projected to reach 37.7% by 2050 [5]. Whereas the physically disabled population is approximately 5.9% of the total disabled population [6]. For Taiwan, the elderly population has risen to 14.7% in 2018, which has rendered it an aging society [7]. It is projected to become an aged society by 2026 and a super-aging society by 2061 [8]. On the other hand, the disabled population in 2016 was recorded at more than 0.7 million [9]. Technological advancements in medical and health care

delivery have prolonged life expectancy and increased the size of the elderly population. To address this issue, long-term care project (LTCP) and LTCP 2.0 is initiated by government. After implementation of LTCP, government is now facing some serious challenges, such as continuously growing extended life expectancy, shortage of manpower and services for the long-term care of the elderly. The old-dependency ratio has dropped due to low birthrates [10]. This rapid increase in disabled and aged population in the society necessitates a higher level of healthcare and living support as compared to previous decades. Global aging and physical disability had led to the decline in functional status and reduced mobility for people. Therefore, both the industry and the scientific community are turning their attention to the rising demands for health care in the society and are devising strategies and technologies to bring a paradigm shift in the healthcare of the disabled and the elderly population.

The review paper is based on the following sequence. The challenges and issues faced by disabled while living independently in the home (see Sect. 2). Powered mobility devices along with transfer aides for disabled (see Sect. 3). The devices to assist these people in bathroom (see Sect. 4). Further, the devices that are used to prepare meals in the kitchen (see Sect. 5) and conclude with a discussion proposing the solution.

## 2 Challenges and Issues Faced by Disabled in Daily Living

Activities of daily living are performed by each and every individual, however, due to functional limitations of disabled people, these activities are not performed by them independently. Caregiver (family and professional) provides various forms of services to the disabled people. Studies show that, these people mostly need assistance in daily living activities such as, bathing, toileting, eating, and getting around inside the house [11–13]. Dong et al. showed that, absence of caregiving leads to inadequate nutrition and hydration, poor personal hygiene and nonfulfillment of basic personal needs of disabled person [14].

Aging and limb disability significantly declines the muscular strength, effects the daily life activities of a person and also raises ethical problems identified by Sharket et al. [15]. These people become completely dependent on the caregivers, with respect to eating, personal hygiene, dressing, toileting, ambulating and managing medical routines. Assistance to individuals in mobility, bathing and toilet use, places a considerable physical burden on both the caregiver and the individual being cared, especially when toilet use is frequent. These activities not only puts an emotional burden, but also loss of personal dignity and independence in the life of cared individual. Additionally, caregiving is highly expensive with high injury rates. Besides the obvious cost of the paid caregivers, there is an enormous unseen cost of informal caregiving, which is often supported by close friends and relatives. For example, this informal caregiving in the United States is predicted to a cost about USD 522 billion a year, which is measured by estimating the income lost by unpaid caregivers during the time that they spend on eldercare [16].

### 3 Powered Mobility Device

For people with limited mobility, moving from one place to another, becomes a challenging task for them and caregivers, due to the weight of the person. It will take a great effort to transfer a person who cannot move his/her body from the bed to the wheelchair, from wheelchair to toilet, from wheelchair to bathtub, and vice versa. It will create a serious problem if the person is confined to bed for an extended period of time and no caregiving is provided.

To transfer the people who cannot help themselves, powered mobility and transfer devices become essential equipment. These devices mainly transfer person from one place to another by using the motion capability of the wheeled device. Popular wheeled mobility devices with transfer aides are discussed as follows;

RIBA is world's first robot capable of lifting human from bed. Its arm has 7 degrees of freedom and gets input through voice. It has vast range of tactile sensor by which, it can modify the lifting trajectory and understand the caregiver information. Figure 1(a) shows RIBA transferring a person [17]. Although RIBA has a user-friendly interface, but it has some functional limitations. First the risk of slippage from the arms of RIBA makes it unfit for use independently. Secondly, it has electrical input so it is dangerous to use it in toilets or bathrooms.

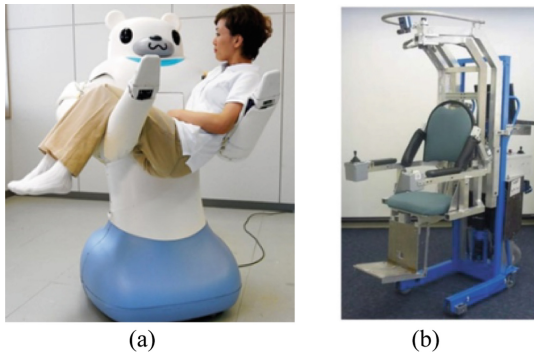


**Fig. 1.** (a) RIBA robot lifting a human [17] (b) HLPR chair [18].

Figure 1(b) shows, Home Lift, Position and Rehabilitation (HLPR) Chair. It is a multipurpose robotic chair that has focused on increasing mobility of a person, transfer to toilet, bed or rehabilitation [18]. Its design is based on a sturdy forklift. The fixed outer L-frame provides support to inner L-frame which carries a rotatable seat and is controlled by a joystick. This structure is mounted on four casters. Along with locomotion the chair can also be used as smart walker. HLPR chair is an attempt to resolve the issues of lifting, mobilizing, transferring and rehabilitation, but due to its bulky and complex structure, lack of maneuverability. The device cannot be used in home also, transferring the person to toilet through this chair is not possible.

Mori et al. developed a wheelchair that can perform mobility as well as transfer task together. Figure 2 shows functioning of wheelchair [19]. Lifting mechanism comprises

of lifting frame, a wearable toilet sling and electrically driven winch. During transfer, winch initially lifts the person and after lifting, seat is folded. Then the person is moved to the bed or commode from the rear side of the wheelchair. The wheelchair has a unique mechanism to solve the mobility and transfer problem, but the transfer through this system requires some infrastructural modifications. Moreover, in the absence of caregiver, approaching the toilet can be very dangerous.

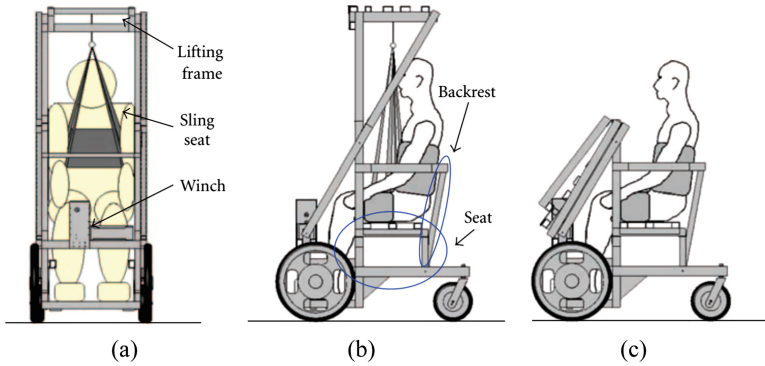


**Fig. 2.** Wheelchair with lifting function: (a) front view, (b) Side view (When transferring person), (c) Side view (after transfer) [19].

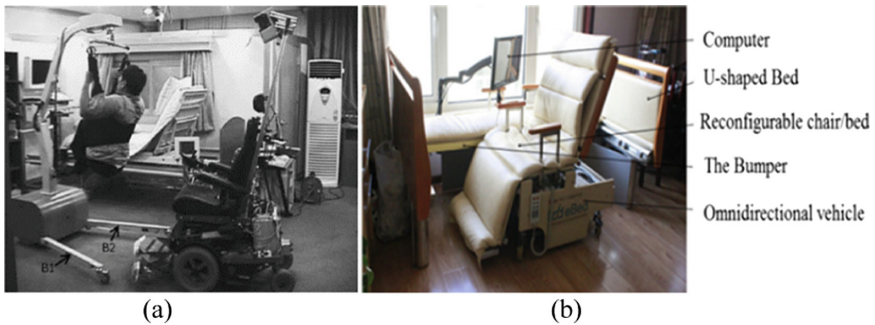


**Fig. 3.** (a) Intelligent sweet home [20] (b) The overview of the robotic chair/bed system [23].

Intelligent Sweet Home (ISH) [20–22] comprises of an intelligent bed with supporting manipulator, intelligent wheelchair and a robotic hoist. Figure 3(a) shows a view of an intelligent sweet home. All the devices are connected via communication modules and controlled by a central control unit. When the user wants to move out of the bed or to change the position, user provides the command through the voice input or a hand gesture to the system. Based on the received command, bed transforms accordingly. After the transformation, the robotic hoist lift move towards the bed, caregiver ties the hoist and user is lifted. At the same time, the intelligent wheelchair docks itself with the bed and the user is placed on it. Despite the fact that intelligent sweet home is fully automatic and all the devices are integrated with each other but it still requires the

involvement of a caregiver who can tie the sling over the body of the user. In addition to the involvement of the user, the lifting through robotic hoist is not safe.

Figure 3(b) [23] shows, a U-shaped bed with an integrated reconfigurable and omnidirectional wheelchair. It is designed for assisting bedridden people. The bed is also equipped with a mechanism for repositioning the people, to avoid bedsores. Additionally, the wheelchair is capable of automatic docking. Linear and lateral motion is accomplished by a two assemblies mounted on the chassis of the wheelchair. Robotic chair/bed has eliminated the need of an additional device for transferring the patient from wheelchair to bed. However the system is designed for lower extremity disabled people and it will need a continuous caregiver to help transferring the person from the wheelchair to the toilet commode. Furthermore, the lateral motion is achieved by the help of a separate assembly, which makes the operation of wheelchair complex.

For transferring the person to the bed the caregiver brings the person seated on the PTS wheelchair to a docking base located at the lower side of the bed as shown in Fig. 4 [24], in such a way that the rear wheels comes in contact with the docking base. After The docking process, caregiver provides command to the foot deck, through the remote control to rise up. So the foot deck rises up, with the help of linear actuator, to meet the back of the wheelchair. After this process the backside of the chair is lowered by the caregiver and the person's back comes in contact with the foot deck. Now the wheelchair seat and the conveyor belt rotates in anti-clockwise direction, simultaneously lowering the foot deck. The process takes 2–3 min in transferring the person from wheelchair to the bed and vice versa.

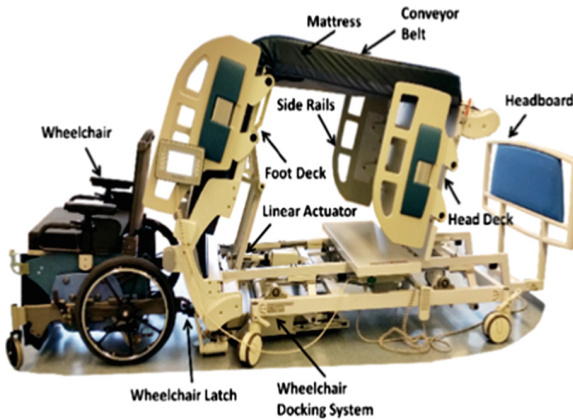


Fig. 4. AgileLife™ Patient Transfer System [24].



Fig. 5. Overview of Panasonic-Resyone showing transformation wheelchair to bed [26].

Panasonic-Resyone is a hybrid wheelchair/bed robot that combines an electric care bed and full reclining wheelchair as shown in Fig. 5 [26, 27].

A part of bed can be easily transformed into wheelchair and vice versa without performing tedious tasks. The caregiver can effortlessly transfer the care recipient from the bed to wheelchair without the change in posture of the care recipient. In this way the burden on the caregiver can be reduced and the quality of life of care recipient can be improved. The bed unit is equipped with three linear motion actuators for adjusting the support for backrest, leg rest, and height of the bed. On the other hand, the wheelchair unit has one linear actuator for reclining operation. In addition, the combination and separation operation of the bed unit and the wheelchair unit can be performed by the lateral movement operation (manual operation) of the wheelchair unit by the caregiver.

## 4 Transfer Aides for Bathroom and Toilet

Mobility assistive devices can increase independency for disabled people and reduce the risk of injury for caregiver, particularly in bathrooms and toilets [28]. An integration of automation technology and innovation in mechanical design would allow the limb disabled people to access the bathrooms and toilets with quality experience.

### 4.1 Transfer Aides for Bathroom

An electrical powered transfer mechanism developed by Hiwin Health Care for full limb disability is shown in Fig. 6(a) [29]. The idea is to allow a direct transfer to the bathtub using lifting device, and vice versa. The transfer mechanism is a separate structure from the bathtub. It reduces the dependency on assistant by providing controlled transfer mechanism using an electrical actuator.

Invacare designed a walk-in bathtub with a portable seat, shown in Fig. 6(b) [30]. The mobile structure is designed so that the seat can go into bathtub.



**Fig. 6.** (a) Hiwin Healthcare Living [29] (b) Invacare Bath lift [30] (c) Premier Care bathtub with transfer mechanism [31].



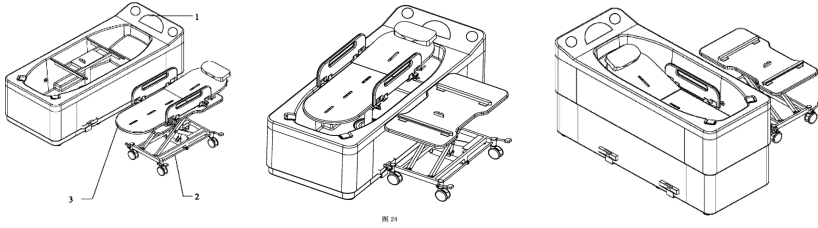


**Fig. 7.** Combination sliding and lifter mechanism on a shower [32].

Premier Care has an electric-powered transfer mechanism as shown in Fig. 6(c) [31].

The disabled would sit on the seat and straighten the legs, and the hydraulics will lift the seat and rotate to the position of the bath then take the seat down into the bathroom. However, to balance the weight of the person, the system requires a strong and heavy structure.

The CN204484581U Patent is a concept for transferring a person with complete limb disability from one area to shower using a combination of electric lifting and manual sliding mechanism as shown in Fig. 7 [32]. The lifting mechanism is connected to the bathroom and requires a hydraulic cylinder, pump station, and controller to operate electrically. However, use of electrical components may be dangerous in wet regions.

#### 4.2 Transfer Aides for Toilet

Lift Seats Company developed a product for people who has difficulty in standing up [33]. This product has a lift-and-tilt mechanism to support the body while the person changes position from standing to sitting position on a commode as shown in Fig. 8(a). OneCare Company designed a more reliable mechanism combining the commode and the lifter wheelchair powered by an electrical actuator to transfer the disabled person to the toilet as shown in Fig. 8(b) [34].



**Fig. 8.** (a) Lift seat [33] (b) Combination of wheelchair and commode [34].

Self-transfer aid systems has been developed by Takahashi et al. [35, 36], and also Toyota [37] to transfer people with lower limb disability to toilet as shown in Figs. 9 and 10(a) respectively. The platform shown in Fig. 9 can lift the person from the

wheelchair and rotate to the direction of the toilet and seat the person on the commode. Similarly, the patient transfer assist system from Toyota also has weight supporting arms to support the person as well as a wheeled platform that will transport the person from a place to another. For both of the systems, the transfer process risks the person's chest being congested and there is a possibility of slipping from the chest support.

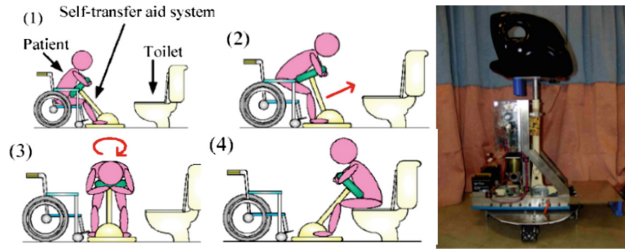


**Fig. 9.** Self-transfer aid system [35].

Figure 10(b) shows the self-undressing toilet, which was developed by Melvin to undress a person who has arm muscle disability by using an electrically powered gripping mechanism to pull out and turn down the pants and vice versa [38]. The controller is located on the end of the hand rest as a button. While the system can take off and put on pants, complicated procedure prevents it from being practical.

Due to mobility limitation, digestive and gastrointestinal disorder like colon cancer, hemorrhoids, anal fissures and constipation occur, which is solved by Krishan [39], who developed a squat mechanism for avoiding previous mentioned issues.



**Fig. 10.** (a) Toyota – Patient Transfer Assist [37] (b) Self-undressing toilet by Melvin [38].

## 5 Meal Preparing Assistive Devices

One of the problems faced by physically disabled people in home is access to food. They need help from the caregivers to provide meals. While an assistive feeding robot can be used to serve food and drink to the patient, the food and drinks have to be provided by human caregivers or service robots [40].

There are some solutions proposed to assist the users in meal preparation. Ficocelli and Nejat [41] proposed an interactive assistive kitchen with speech communication. In this system an automated cabinet system helps users to store and retrieve items and obtain recipes for meal preparation.

There are dishes that does not need cooking and just served in a plate, like a salad. As shown in Fig. 11, Sally the salad making robot is a vending machine that prepares a salad by getting orders from a touchscreen and dropping neat portions of refrigerated ingredients into a bowl [42]. It contains 22 ingredient canisters and serves 50–100 meals before replenishing.



**Fig. 11.** Sally the Salad Making Robot and inside view [42].

Ready-to-eat food may play a huge role in solving the problem of food access for disabled people since ready-to-eat food need little preparation process before serving. Ready-to-eat food can be food that does not need cooking or pre-cooked food. It can be served cold or heated One of the most widely consumed ready-to-eat food are instant noodles. In 2017, 100.1 billion servings of instant noodles were consumed in all around the world [43]. These noodles are ready to eat in a couple of minutes only by pouring boiling water to it. Most of the ready-to-eat meals only need to be microwaved before eaten. These foods should be stored in a refrigerated area and there are products that combine the refrigeration area and microwave into one machine.

Bicom Vending Machines is a company that specializes in producing vending machines for pre-cooked or frozen meals [44]. Their product serves the dish after the meal is chosen and heated. The model M300T can contain up to 100 different dishes at the same time and equipped with a microwave oven.

The kitchen for disabled people should also be able to store and serve different kinds of liquids like drinking water, beverages, beers, or sauces for food or salad. Traditional beverage dispensers have hygienic problems and they require regular professional cleaning. A Bag-in-Box or BiB is a type of container for the storage and transportation of liquids. It consists of a strong bladder seated inside a corrugated fiberboard box. The bag-in-box dispensers do not need any cleaning or professional sanitation since the bag-in-box container is for only one time use. The bag-in-box dispensers from the company Squell can store any kind of bag-in-box beverage and keeps the beverages fresh in a refrigerated environment up to 3 months after opening [45]. The bag-in-box dispensers from the company Gastro-Cool specializes in dispensing wine with different temperatures, also milk and juices [46].

Technology already started to replace the chefs in the kitchen. The companies Chef Automation [47] and Let's Pizza [48] offers products that can prepare and serve food autonomously. Based on the patent EP 2820978 A1 [49], the product from Chef Automation is an automatic noodle preparing and serving machine and the product from Let's Pizza is an automatic vending machine which prepares and cooks the pizza autonomously. As shown in Fig. 12, Spyce is a restaurant in Boston USA that has a robotic kitchen as its chef [50]. The robotic kitchen is designed to prepare food, cook it and clean up. The kitchen receives orders from an electronic kiosk and puts the ingredients into tumbling woks. The woks are heated with induction. The only human interference is to add the toppings and check the food.



Fig. 12. Robotic kitchen Spyce Restaurant [50].

## 6 Discussion

Continuously, growing disabled and aged population has become a global issue and the assistive technologies with intelligent features will be very effective to improve the quality of life for people with limited mobility [51]. The literature suggests that in the past, focus of research was on lower extremity disabled persons and caregivers are continuously required to assist these people. Users have to rely on the services of the caregivers, while using assistive technology products. However, none of the products can accommodate a fully disabled. Nevertheless, previously developed products involve some risk factor and limitations, due to which caregiver have to be continuously involved with these people. Therefore, the remedy of this problem is a smart home for disabled, where they can perform the activities of daily living independently.

In the smart home, these people can utilize smart bed integrated with wheeled mobility devices, smart toilet, and smart kitchen to live a normal life. Moving around the home with intelligent wheelchair, having toileting and bathing done without or limited requirement of caregiver. Smart bathroom and toilet will allow the people to perform bathing and toileting independently with safe transfer mechanism. In addition, the fully autonomous smart bathroom will be helpful in reducing the physical burden on the caregivers. The purpose of a smart kitchen for people with limb disabilities is to prepare, store, and serve the food. The smart kitchen will be a platform for preparing food by a robot, which can efficiently and effectively provide variety of meals.

## 7 Conclusion

The paper presents a brief review of mobility assistive and meal preparing devices for disabled used in home. Assistive technology is an area of research that is continuously advancing, engineers in collaboration with caregivers and physiotherapist are trying to develop the devices that can fulfill the needs of disabled. There are certain products developed, some are on research stage and some are commercialized to assist these people at home. However, they are unable to satisfy the end user needs because they involve some limitations. Complexity of operation, risk of falling, lack of maneuverability in tight spaces and cost are the factors that restricts the use of assistive technology. Although many smart assistive devices were invented, they all required some degree of manual operations and assistance. Although, devices with fully autonomous operation capability are never achieved. Until then, a person with partial to full limb mobility disability cannot perform activities of daily living without the involvement of a caregiver.

Thus, the ultimate goal of future research in mobility assistive technology, is to develop a human centered, safe, autonomous and smart device that can be used to facilitate the physically disabled at home. These features will not only decrease the anxiety and depression level but also increase the quality of life. A smart home is a comprehensive solution for achieving the functions above, where they can live with high self-esteem and improve their quality of life.

## References

1. World report on disability. [http://www.who.int/disabilities/world\\_report/2011/report/en/](http://www.who.int/disabilities/world_report/2011/report/en/). Accessed 24 Mar 2019
2. United Nations, Department of Economic and Social Affairs, Population Division: World Population Prospects: The 2017 Revision, Key Findings and Advance Tables. Working Paper No. ESA/P/WP/248 (2017)
3. Facts on People with Disabilities in China. [https://www.ilo.org/wcmsp5/groups/public/—asia/—ro-bangkok/—ilo-beijing/documents/publication/wcms\\_142315.pdf](https://www.ilo.org/wcmsp5/groups/public/—asia/—ro-bangkok/—ilo-beijing/documents/publication/wcms_142315.pdf). Accessed 29 Mar 2019
4. Disabled Population in India as per census 2011 (2016 updated). <https://enabled.in/wp/disabled-population-in-india-as-per-census-2011-2016-updated/>. Accessed 29 Mar 2019
5. Wakamats, C., Shinjuku, K.: Statistical Handbook of Japan 2017, Japan, p. 13 (2018)
6. Disability in Japan: Overview and Statistics. <https://www.disabled-world.com/news/asia/japan.php>. Accessed 24 Mar 2019
7. Ministry of Health and Welfare: Taiwan Health and welfare report 2017, Taiwan, p. 12 (2018)
8. National Development Council, Population Projections for the R.O.C. (Taiwan): 2018–2065. <https://www.ndc.gov.tw/en/cp.aspx?n=2E5DCB04C64512C>. Accessed 24 Mar 2019
9. Focus Taiwan. <http://focustaiwan.tw/news/asoc/201205270009.aspx>. Accessed 26 Mar 2019
10. Wang, H.H., Tsay, S.F.: Elderly and long-term care trends and policy in Taiwan: challenges and opportunities for health care professionals. *Kaohsiung J. Med. Sci.* **28**(9), 465–469 (2012)

11. Bass, D.M., et al.: Negative caregiving effects among caregivers of veterans with dementia. *Am. J. Geriatr. Psychiatry* **20**(3), 239–247 (2012)
12. San Antonio, P., et al.: Lessons from the Arkansas Cash and Counseling Program: How the experiences of diverse older consumers and their caregivers address family policy concerns. *J. Aging Soc. Policy* **22**(1), 1–17 (2010)
13. Charu, M., et al.: Awareness, availability, and accessibility of assistive technologies for the elderly in India. In: *Proceedings of ICoRD, Research Into Design for a Connected World*, vol. 2, pp. 537–544 (2019)
14. Dong, X., et al.: Decline in cognitive function and risk of elder self-neglect: finding from the Chicago Health Aging Project. *J. Am. Geriatr. Soc.* **58**(12), 2292–2299 (2010)
15. Sharkey, A., Sharkey, N.: Granny and the robots: ethical issues in robot care for the elderly. *Ethics Inf. Technol.* **14**(1), 27–40 (2012)
16. Chari, A.V., et al.: The opportunity costs of informal elder-care in the United States new estimates from the american time use survey. *Health Serv. Res.* **50**, 871–882 (2015)
17. Mukai, T., et al.: Realization and safety measures of patient transfer by nursing-care assistant robot RIBA with tactile sensor. *J. Robot. Mech.* **23**(3), 360–369 (2011)
18. Bostelman, R., Albus, J.: A multipurpose robotic wheelchair and rehabilitation device for the home. In: *2007 IEEE/RSJ International Conference on Intelligent Robots and Systems*, pp. 3348–3353, (2007)
19. Mori, Y., et al.: Development of a wheelchair with a lifting function. *Adv. Mech. Eng.* **4**, 1–9 (2012)
20. Jung, J.W., et al.: Advanced robotic residence for the elderly/the handicapped: realization and user evaluation. In: *IEEE International Conference on Rehabilitation Robotics*, Chicago, pp. 492–495 (2005)
21. Park, K., et al.: Robotic smart house to assist people with movement disabilities. *Auton. Robot. J.* **22**(2), 183–198 (2007)
22. Bien, Z.Z., et al.: Intelligent interaction for human friendly service robot in smart home environment. *Int. J. Comput. Intell. Syst.* **1**(1), 77–93 (2008)
23. Ning, M., et al.: Mechanism design of a robotic chair/ bed system for bedridden aged. *Adv. Mech. Eng.* **9**(3), 1–8 (2017)
24. Tanabe, S., et al.: Designing a robotic smart home for everyone, especially the elderly and people with disabilities. *Fujita Med. J.* **5**(2), 32–35 (2019)
25. Andrew, S., et al.: Evaluation of the agile life patient transfer and movement system (2009)
26. Kume, Y., Tsukada, S., Kawakami, H.: Development of safety technology for rise assisting robot. *Resyone Plus*, vol. 85, p. 18-00344 (2019). (In Japanese)
27. Panasonic Resyone. <https://news.panasonic.com/global/topics/2014/29420.html>. Accessed 24 Mar 2019
28. Bäckman, C., Bergkvist, L.: Welfare technology and user experience: a study of seniors' expectations on and first impressions of a robotic shower. In: *HICSS-52 2019*, Maui, pp. 4297–4306 (2019)
29. HIWIN Health Care. [https://www.hiwin.tw/download/tech\\_doc/me/Medical\\_Equipment\(E\).pdf](https://www.hiwin.tw/download/tech_doc/me/Medical_Equipment(E).pdf). Accessed 24 Mar 2019
30. Invacare. <http://store.allinonemobility-shop.com/bebasy.html>. Accessed 24 Mar 2019
31. Premier Care. <https://www.premierbathrooms.co.uk/>. Accessed 24 Mar 2019
32. Guan, T., et al.: Bathing device for disabled elder, CN204484581U, China (2015)
33. Lift Seat. <http://www.liftseat.com/>. Accessed 24 Mar 2019
34. On Care Medical. <https://www.oncaremedical.com/product/liftseat-powered-toilet-lift/>. Accessed 24 Mar 2019

35. Takahashi, Y., et al.: Psychological evaluation of simple self-transfer aid robotic system with horizontal movement system. In: IEEE International Symposium on Industrial Electronics, Bari, pp. 1925–1930 (2010)
36. Krishnan, R.H., Pugazhenthii, S.: Development of a self-transfer robotic facility for elderly and disabled. In: 2015 International Conference on Robotics, Automation, Control and Embedded Systems (RACE), pp. 1–4 (2015)
37. Toyota Patient Transfer Assist. <https://blog.toyota.co.uk/toyota-healthcare-robots-shown-in-japan/patient-transfer-assist>. Accessed 24 Mar 2019
38. Melvin. <http://www.en.mymelvin.com/>. Accessed 26 Mar 2019
39. Hari, K.R.: A review on squat-assist devices to aid elderly with lower limb difficulties in toileting to tackle constipation. *J. Eng. Med.* **233**(4), 464–475 (2019)
40. Alessandro, V., et al.: Robots in elderly care. *DigitCult Sci. J. Digit. Cult. ICT Neurodegener. Dis.* **2**(2), 37–50 (2018)
41. Ficocelli, M., Nejat, G.: The design of an interactive assistive kitchen system. *Assist. Technol.* **24**(4), 246–258 (2012)
42. Sally the Salad Making Robot. <http://www.chowbotics.com/sally/>. Accessed 24 Mar 2019
43. World Instant Noodles Association. <https://instantnoodles.org/en/noodles/report.html>. Accessed 24 Mar 2019
44. MIDA Vending Machine. <https://www.bicomvending.com/>. Accessed 24 Mar 2019
45. The Squell Bag-in-box Dispenser. <https://squell.com/>. Accessed 24 Mar 2019
46. Gastro Bag-in-box Dispenser Cooler. <https://gastro-cool.com/en/>. Accessed 24 Mar 2019
47. Automatic Noodle Serving Machine. <http://www.chef-automation.com.tw/>. Accessed 24 Mar 2019
48. Let's Pizza. <http://www.letspizza.it/index-en.html>. Accessed 24 Mar 2019
49. Lin, C.-Y.: Automatic Meal Serving System, Patent EP 2820978 A1 (2014)
50. Spyce Restaurant Boston USA. <https://www.spyce.com/>. Accessed 24 Mar 2019
51. Krishnan, R.H., et al.: Mobility assistive devices and self-transfer robotic systems for elderly, a review. *Intell. Serv. Robot.* **7**(1), 37–49 (2014)





# Performance Evaluation of a Class of Gravity-Compensated Gear-Spring Planar Articulated Manipulators

Nguyen Vu Linh<sup>1</sup> and Chin-Hsing Kuo<sup>2</sup>(✉)

<sup>1</sup> National Taiwan University of Science and Technology, Taipei 106, Taiwan

<sup>2</sup> University of Wollongong, Wollongong, NSW 2522, Australia  
chkuo@uow.edu.au

**Abstract.** This paper is devoted to evaluating the gravity compensation performance of a special class of planar articulated manipulators that are gravity balanced by using a series of gear-spring modules. First, the studied manipulators with one, two, and three DOFs are revisited. Then, the gravity compensation performance of these manipulators is determined via a peak-to-peak torque reduction criterion. As the manipulators were designed via two different approaches, i.e., the ideal balancing approximation and the realistic optimization, the gravity compensation performance of these two approaches is compared. It shows that the perfect balancing approximation can achieve a satisfied performance as nearly same as that of the optimization approach, while it, on the other hand, enjoys a significant reduction of the computational effort for gravity compensation design.

**Keywords:** Gravity compensation · Static balancing · Stiffness analysis

## 1 Introduction

Performance evaluation is a critical step in the design and analysis of robot manipulators [1]. Recently, attention on the effect of gravity, external forces, and elastic components in the robot structure has been intensively paid by researchers for improving the accuracy and reliability of the evaluation [2, 3].

In the literature, numerous indices and criteria were proposed for evaluating the performance of a robot manipulator with different approaches and specific targets. For instance, the stiffness index is widely employed to illustrate the stiffness state and structural compliance of the manipulator. It can be derived from the Cartesian stiffness matrix via different mathematical operators, such as eigenvalues, determinant, condition number, and Euclidean norm [3–5]. Kurazume and Hasegawa [6] introduced a performance index considering the dynamic manipulability and manipulating force ellipsoids of a serial-link manipulator. Han et al. [7] presented a performance index for evaluating the power input and output transmissibility of a parallel manipulator. Linh and Kuo [8] proposed the compliant uniformity index to assess the positioning errors in the spring-articulated manipulators under the effect of gravity and an arbitrary load. Nabavi et al. [9] introduced the kinetic energy index to measure the uniformity of



kinetic energy transferred to the payload carried by manipulators. Azad et al. [10] presented the effect of the weighting matrix on dynamic manipulability, which can be used to measure the physical capabilities of manipulators in different tasks. Chen et al. [11] proposed the normal stiffness performance index considering the robot posture and feed orientation in the robotic milling process. Bijlsma et al. [12] introduced the balancing quality criterion based on the work required in a gear system to evaluate the efficiency of static balance. Mori and Ishigami [13] presented the force-and-energy manipulability index to evaluate the manipulator configuration with low energy consumption in the soil sampling operation.

The work in this paper is dedicated to using a criterion, namely the peak-to-peak torque reduction, to evaluate the gravity compensation performance of a class of planar articulated manipulators that are gravity balanced by a series of gear-spring modules (GSMs) [14, 15]. The criterion can exhibit the efficiency of gravity compensation or peak torque reduction when the manipulator is integrated with the GSM as compared to that without it. In what follows, the designs of the 1-, 2-, and 3-degree-of-freedom (DOF) articulated manipulators with the GSM are presented in Sect. 2. Then, the performance evaluation of the manipulators is illustrated via some numerical examples in Sect. 3. Last, Sect. 4 draws the discussion and conclusions of the paper.

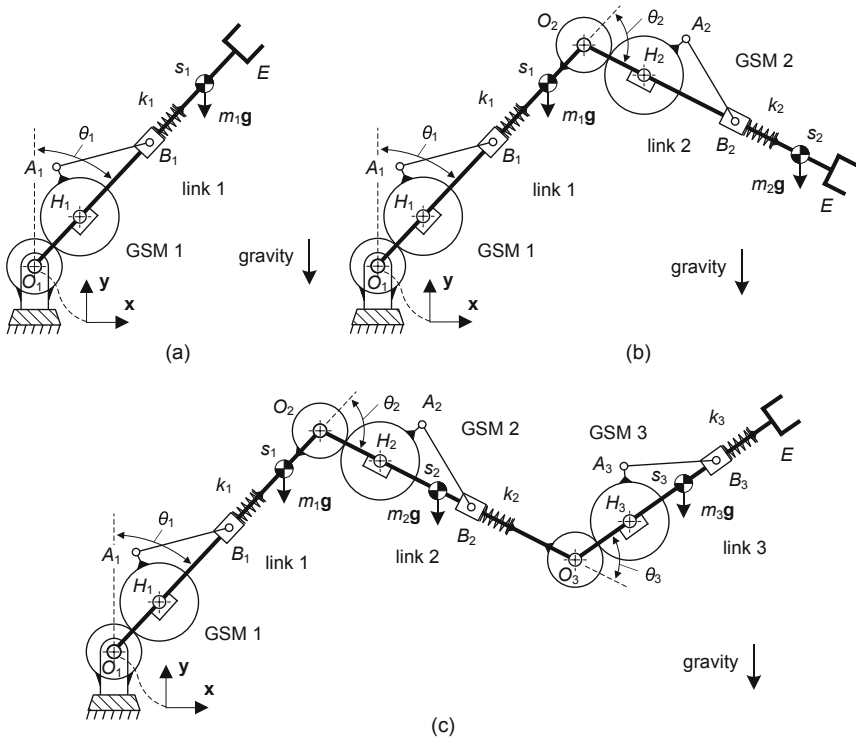


**Fig. 1.** The studied gear-spring articulated manipulators with (a) one DOF, (b) two DOFs, and (c) three DOFs.

## 2 The Studied Manipulators

The 1-, 2-, and 3-DOF gear-spring articulated manipulators in Ref. [15] are taken as examples for illustrating the performance of gravity compensation, as shown in Fig. 1 (a), (b), and (c), respectively. In these drawings,  $m_i$ ,  $s_i$ ,  $l_i$ , and  $\theta_i$  represent the equivalent mass, center of mass, length, and rotation angle of link  $i$  ( $i = 1, 2, \dots, n$ ) of the manipulator, respectively;  $d_{0i}$ ,  $d_{si}$ ,  $\psi_i$ ,  $n_{gi}$ , and  $k_i$  represent the spring compression at the initial position, slider displacement, assemblage angle between  $H_iA_i$  and the rotating link, gear ratio, and spring stiffness of GSM  $i$ , respectively;  $\varphi_{0i}$  and  $\varphi_{ci}$  represent the initial and instantaneous deflection angles of the connecting rod  $A_iB_i$  with respect to the rotating link  $O_iB_i$  of GSM  $i$ , respectively;  $r_{2ai} = H_iA_i$  and  $r_{3i} = A_iB_i$ .

Note that, in Ref. [15], the described gravity-compensated manipulators could be designed by two different approaches, i.e., the ideal balancing approximation and realistic optimization. The ideal balancing approximation is achieved by approximating the perfect balancing, which is derived from the zero-torque condition with some ideal assumptions, with logical design parameters of the manipulator. Oppositely, the realistic optimization aims at solving an optimization problem, wherein the objective is to minimize the driving torques of the manipulator.

## 3 Performance Evaluation

For each manipulator as mentioned above, the evaluation is performed for both design approaches. The criterion used for the evaluation is defined as follows:

$$\delta_{ti} = \left[ 1 - \frac{\max(|T_{m/si}(\theta_i)|)}{\max(|T_{mi}(\theta_i)|)} \right] \times 100\% \quad (1)$$

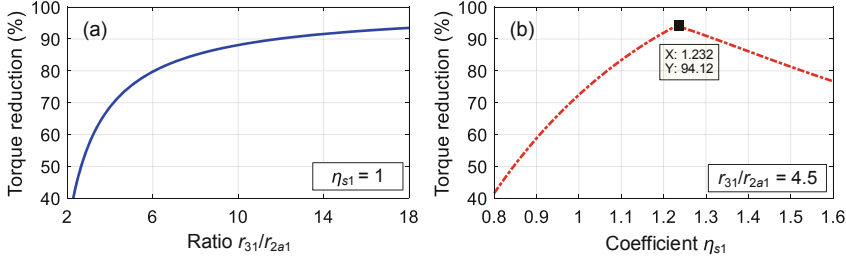
where  $T_{mi}$ ,  $T_{m/si}$ , and  $\delta_{ti}$  represent the motor torques of the manipulator without, with gravity compensation, and the peak-to-peak torque reduction at the joint  $O_i$  ( $i = 1, 2, 3$ ) of the manipulator, respectively.

### 3.1 The 1-DOF Articulated Manipulator

**Using the Ideal Balancing Approximation.** Assume that the design parameters of the 1-DOF articulated manipulator are given in Table 1. From these data, the influence of the ratio  $r_{31}/r_{2a1}$  to the peak-to-peak torque reduction  $\delta_{t1}$  can be illustrated in Fig. 2(a). As may be seen, increasing the ratio leads to improve the efficiency of torque reduction and  $\delta_{t1}$  can reach almost 100% when the ratio approaches infinity, as the ideal case. In order to obtain  $\delta_{t1} \geq 90\%$ , the ratio is expected to be greater than 12 or  $r_{31}$  0.48 m. However, this desirable parameter can make the connecting rod lengthy as compared to the radii of gears.

**Table 1.** Parameters of the 1-DOF gear-spring articulated manipulator.

$\psi_1$ ( $^\circ$ )	$n_{g1}$	$r_{11}$ (m)	$r_{21}$ (m)	$r_{2a1}$ (m)	$m_1$ (kg)	$s_1$ (m)
90	2	0.02	0.04	0.04	2.44	0.135

**Fig. 2.** Torque reduction of the 1-DOF gear-spring articulated manipulator versus (a) ratio  $r_{31}/r_{2a1}$  and (b) coefficient  $\eta_{s1}$ .

On the other hand, consider a case when the length of the connecting rod is prescribed, for example,  $r_{31} = 0.18$  m, whereas the coefficient  $\eta_{s1}$  is variable in the interval  $[0.8, 1.6]$ . Then, the peak-to-peak torque reduction  $\delta_{t1}$  can be computed versus the coefficient and the results are shown in Fig. 2(b). It can be seen that high torque reduction ( $\delta_{t1} \geq 90\%$ ) can be acquired whenever  $\eta_{s1}$  is selected from 1.2 to 1.3, even the ratio here  $r_{31}/r_{2a1} = 4.5$ . The highest value  $\delta_{t1} = 94.1\%$  is obtained when  $\eta_{s1} = 1.23$ . Compared to the previous case, it is clear that selecting an appropriate coefficient  $\eta_{s1} = [1.2, 1.3]$  is more convenient than using a long-length connecting rod ( $r_{31}/r_{2a1} = 12$ ) since both approaches could produce  $\delta_{t1} \geq 90\%$ . From the obtained parameters when  $\delta_{t1}$  is maximum, some other weights  $m_1$  were simulated and verified on MSC Adams; indeed, the results of  $\delta_{t1}$  remained relatively consistent in all these cases [14].

**Using the Realistic Optimization.** The optimization problem for minimizing the motor torque of the 1-DOF articulated manipulator was solved with the aid of *fmincon* solver in MATLAB. Here, the input parameters were given as:  $r_{2a1} = 0.04$  m,  $d_{01} = 0$ ,  $k_{s1} = [4000, 8000]$  N/m,  $r_{31}/r_{2a1} = [1, 5]$ ,  $\psi_1 = [0^\circ, 360^\circ]$ ,  $n_{g1} = [1, 3]$ , and  $\theta_1 = [0^\circ, 180^\circ]$ . The optimization was then performed and terminated within 35 iterations at  $\delta_{t1} = 96.1\%$ , whereas the optimal design parameters were also obtained as:  $k_{s1} = 6325$  N/m,  $r_{31}/r_{2a1} = 3.69$ ,  $\psi_1 = 91.42^\circ$ , and  $n_{g1} = 2.01$ .

Based on the above results, the motor torques of the manipulator by using the ideal balancing approximation  $T_{m/s1}$  (appro.) and the realistic optimization  $T_{m/s1}$  (opti.) can be illustrated in Fig. 3. Note that only the case with the highest value  $\delta_{t1}$  shown in Fig. 2(b) is taken in the representation for the approximation approach. The results show that  $T_{m/s1}$  (appro.) and  $T_{m/s1}$  (opti.) are much smaller than the motor torque without gravity compensation  $T_{m1}$  at almost rotation angle  $\theta_1$ . Besides,  $\delta_{t1}$  can be slightly improved from 94.1% (by the approximation) to 96.1% when the optimal design parameters are used. For reducing the computational effort, it is therefore preferable adopting the approximation approach for designing the 1-DOF articulated manipulator.

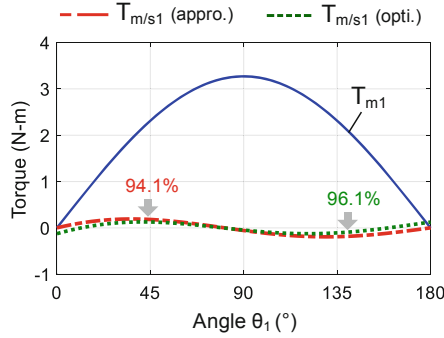


**Fig. 3.** Motor torques of the 1-DOF gear-spring articulated manipulator.

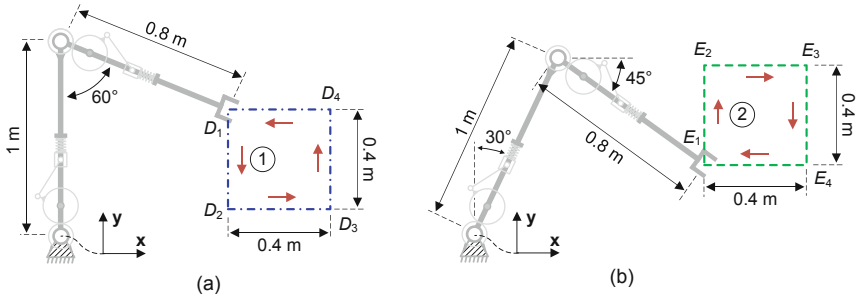


**Fig. 4.** Trajectory examples of the 2-DOF gear-spring articulated manipulator.

### 3.2 The 2-DOF Articulated Manipulator

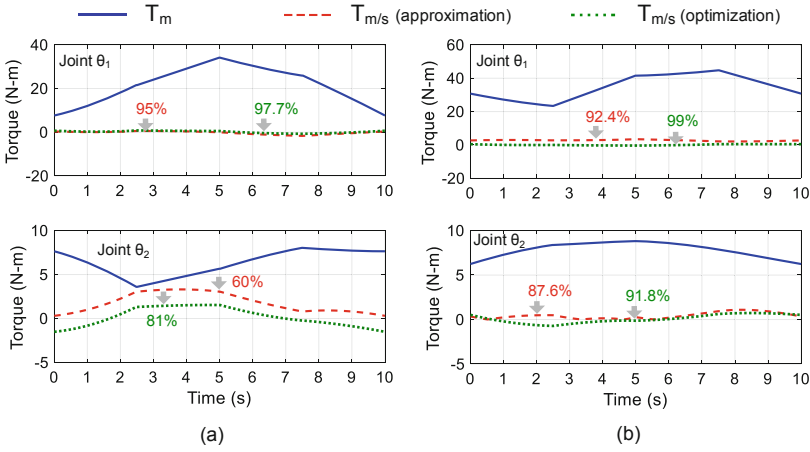
Similar to the previous section, a numerical example of the 2-DOF articulated manipulator integrated with two GSMs for gravity compensation is illustrated in this section. The performance evaluation of the manipulator via two described design approaches is also presented. Assume that the design parameters of the manipulator and GSMs used in the approximation are given in Tables 2 and 3, respectively. The manipulator is supposed to perform tasks on two predefined square trajectories  $D_1D_2D_3D_4$  and  $E_1E_2E_3E_4$  with the side length of 0.4 m and constant speed of 0.16 m/s (the total time is 10 s), as shown in Fig. 4(a) and (b), respectively. Note that trajectory 1 is with link 1 of the manipulator in the vertical direction, while trajectory 2 with an inclined angle  $30^\circ$  at the initial position. On the other hand, the optimal design parameters of the manipulator for the two trajectories were also derived, as listed in Table 3.

**Table 2.** Parameters of the 2-DOF gear-spring articulated manipulator.

$m_1$ (kg)	$m_2$ (kg)	$s_1$ (m)	$s_2$ (m)	$l_1$ (m)	$l_2$ (m)
5	3	0.4	0.3	1	0.8

**Table 3.** Parameters of the GSMs used in the 2-DOF gear-spring articulated manipulator (The parameters listed in Tables 3 and 5 are obtained from Ref. [15].).

Approach	GSM $i$	$\psi_i$ ( $^\circ$ )	$n_{gi}$	$r_{1i}$ (m)	$r_{2ai}$ (m)	$r_{3i}$ (m)	$k_i$ (N/m)
Approximation	$i = 1$	90	2	0.05	0.1	0.5	$1.595 \times 10^4$
	$i = 2$	105	2	0.04	0.08	0.4	$4.486 \times 10^3$
Optimization	Trajectory 1 - $D_1D_2D_3D_4$						
	$i = 1$	91.7	2	0.05	0.1	0.32	$1.442 \times 10^4$
	$i = 2$	117.6	2.9	0.04	0.08	0.36	$6.199 \times 10^3$
	Trajectory 2 - $E_1E_2E_3E_4$						
	$i = 1$	92.4	1.9	0.05	0.1	0.33	$1.413 \times 10^4$
	$i = 2$	119.8	2.9	0.04	0.08	0.33	$6.059 \times 10^3$

**Fig. 5.** Motor torques of the 2-DOF gear-spring articulated manipulator versus (a) trajectory  $D_1D_2D_3D_4$  and (b) trajectory  $E_1E_2E_3E_4$ .

The motor torques of the 2-DOF articulated manipulator on the two prescribed trajectories can be illustrated in Fig. 5(a) and (b), respectively. As can be seen, the motor torques at the joints ( $\theta_1$ ,  $\theta_2$ ) are significantly reduced when using either the approximation or optimization. It is interesting to observe that the peak-to-peak torque reduction at the two joints  $\delta_{ti}$  ( $i = 1, 2$ ) can be improved when the optimal design parameters are used. On the first trajectory,  $\delta_{t1}$  is slightly improved from 95% to 97.7% at the first joint while an increase of  $\delta_{t2}$  by 21% can be seen at the second joint. On the other hand, the improvement is little on the second trajectory, being 6.6% and 4.2% at the first and second joints, respectively.

### 3.3 The 3-DOF Articulated Manipulator

Similarly, the performance evaluation of the 3-DOF articulated manipulator integrated with three GSMs is presented in this section. Assume that the design parameters of the manipulator and GSMs used in the manipulator are listed in Tables 4 and 5, respectively. The manipulator is assumed to perform tasks on two predefined square trajectories  $F_1F_2F_3F_4$  and  $G_1G_2G_3G_4$  with the side length of 0.4 m and constant speed of 0.16 m/s, as shown in Fig. 6(a) and (b), respectively. Besides, the manipulator is also assumed to maintain link 3 in the horizontal direction during the first trajectory while an orientation  $45^\circ$  from the vertical direction during the second trajectory.

The motor torques of the 3-DOF articulated manipulator on the two prescribed trajectories are illustrated in Fig. 7(a) and (b), respectively. As compared to the case without gravity compensation, the motor torques at the first two joints ( $\theta_1$ ,  $\theta_2$ ) are significantly reduced by using the approximation, and that decreased almost half at the third joint ( $\theta_3$ ). The peak-to-peak torque reduction  $\delta_{ti}$  ( $i = 1, 2, 3$ ) can be improved when the optimal design parameters are used. On the first trajectory, the torque reduction by using the optimization is slightly improved by 7% and 2.8% at the first and second joints, respectively. The similar results at the first two joints of the manipulator can also be observed on the second trajectory. In contrast, there is a significant improvement observed at the third joint, being 46.6% and 57.4% on the first and second trajectories, respectively.

**Table 4.** Parameters of the 3-DOF gear-spring articulated manipulator.

$m_1$ (kg)	$m_2$ (kg)	$m_3$ (kg)	$s_1$ (m)	$s_2$ (m)	$s_3$ (m)	$l_1$ (m)	$l_2$ (m)	$l_3$ (m)
5	3	1.5	0.4	0.3	0.2	1	0.8	0.5

**Table 5.** Parameters of the GSMs used in the 3-DOF gear-spring articulated manipulator.

Approach	GSM $i$	$\psi_i$ ( $^\circ$ )	$n_{gi}$	$r_{1i}$ (m)	$r_{2ai}$ (m)	$r_{3i}$ (m)	$k_i$ (N/m)
Approximation	$i = 1$	90	2	0.05	0.1	0.5	$2.074 \times 10^4$
	$i = 2$	105	2	0.04	0.08	0.4	$1.196 \times 10^4$
	$i = 3$	157.5	2	0.03	0.06	0.35	$2.659 \times 10^3$
Optimization	Trajectory 1 - $F_1F_2F_3F_4$						
	$i = 1$	93.3	2.1	0.05	0.1	0.34	$2.126 \times 10^4$
	$i = 2$	115.8	2.5	0.04	0.08	0.16	$9.068 \times 10^3$
	$i = 3$	82.5	1.5	0.03	0.06	0.29	$3.213 \times 10^3$
	Trajectory 2 - $G_1G_2G_3G_4$						
	$i = 1$	100.8	2.5	0.05	0.1	0.32	$2.153 \times 10^4$
	$i = 2$	125.6	2.7	0.04	0.08	0.15	$9.625 \times 10^3$
	$i = 3$	49.5	3	0.03	0.06	0.14	$2.263 \times 10^3$

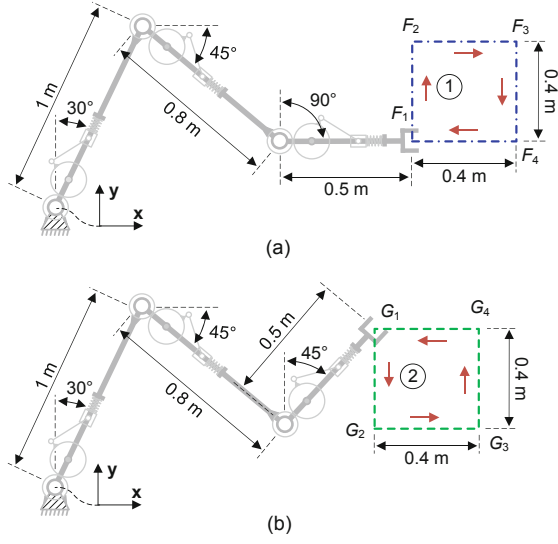


**Fig. 6.** Trajectory examples of the 3-DOF gear-spring articulated manipulator.

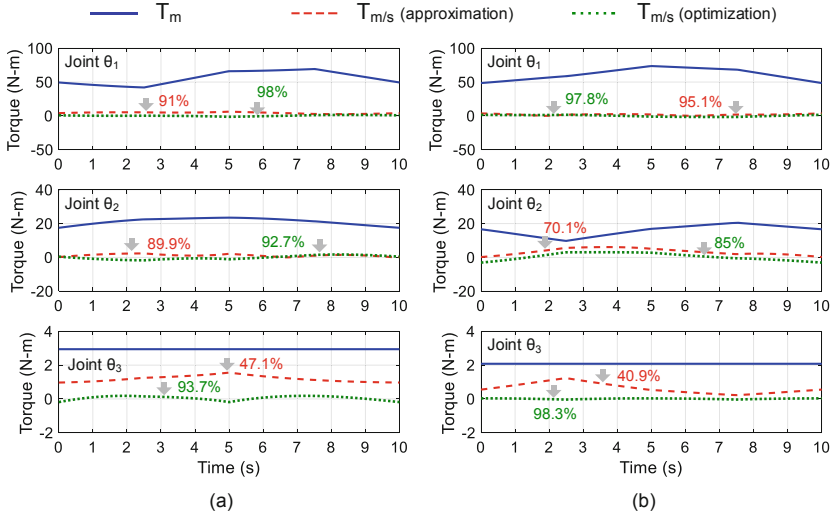


**Fig. 7.** Motor torques of the 3-DOF gear-spring articulated manipulator versus (a) trajectory  $F_1F_2F_3F_4$  and (b) trajectory  $G_1G_2G_3G_4$ .

## 4 Discussion and Conclusions

In this paper, we have presented the performance evaluation of the 1-, 2-, and 3-DOF gear-spring planar articulated manipulators via the peak-to-peak torque reduction criterion. Two design approaches for the gravity-compensated manipulators, i.e., the ideal

balancing approximation and the realistic optimization, were numerically evaluated and compared. The results showed that the motor torques of the manipulator at the first and second joints were significantly reduced by using the approximation, being up to 95.1% and 89.9%, respectively; whereas that almost half at the third joint. The torque reduction at all the joints was improved when the optimization is adopted. The average improvement at the first two joints was little, being 4.2% and 10.7%, respectively; oppositely, it was significant at the third joint 52%.

It should be noticed that the peak torque at the third joint without gravity compensation is much smaller than that at the first and second joints, approximately 25 and 10 times, respectively. Even the optimization could greatly improve the percentage of torque reduction at the third joint. However, it contributes less significant to the total amount of torque reduced in the overall manipulator as compared to that at the first two joints. It can be concluded that, in general, the approximation approach can produce a satisfied result of torque reduction, as nearly the same result of using the optimization approach. Therefore, the approximation approach is still valid for use in designing such gravity-compensated articulated manipulators while reducing the computational effort.

## References

1. Patel, S., Sobh, T.: Manipulator performance measures-a comprehensive literature survey. *J. Intell. Robot. Syst.* **77**(3–4), 547–570 (2015)
2. Raoofian, A., Taghvaeipour, A., Kamali, A.: On the stiffness analysis of robotic manipulators and calculation of stiffness indices. *Mech. Mach. Theory* **130**, 382–402 (2018)
3. Carbone, G., Ceccarelli, M.: Comparison of indices for stiffness performance evaluation. *Front. Mech. Eng. China* **5**(3), 270–278 (2010)
4. Wang, H., Zhang, L., Chen, G., Huang, S.: Parameter optimization of heavy-load parallel manipulator by introducing stiffness distribution evaluation index. *Mech. Mach. Theory* **108**, 244–259 (2017)
5. Bu, Y., Liao, W., Tian, W., Zhang, J., Zhang, L.: Stiffness analysis and optimization in robotic drilling application. *Precis. Eng.* **49**, 388–400 (2017)
6. Kurazume, R., Hasegawa, T.: A new index of serial-link manipulator performance combining dynamic manipulability and manipulating force ellipsoids. *IEEE Trans. Robot.* **22**(5), 1022–1028 (2006)
7. Han, G., Xie, F., Liu, X.-J.: Evaluation of the power consumption of a high-speed parallel robot. *Front. Mech. Eng.* **13**(2), 167–178 (2018)
8. Linh, N.V., Kuo, C.-H.: An analytical stiffness method for spring-articulated planar serial or quasi-serial manipulators under gravity and an arbitrary load. *Mech. Mach. Theory* **137**, 108–126 (2019)
9. Nabavi, S.N., Akbarzadeh, A., Enferadi, J., Kardan, I.: A homogeneous payload specific performance index for robot manipulators based on the kinetic energy. *Mech. Mach. Theory* **130**, 330–345 (2018)
10. Azad, M., Babič, J., Mistry, M.: Effects of the weighting matrix on dynamic manipulability of robots. *Auton. Robot.* **43**, 1867–1879 (2019)
11. Chen, C., Peng, F., Yan, R., Li, Y., Wei, D., Fan, Z., Tang, X., Zhu, Z.: Stiffness performance index based posture and feed orientation optimization in robotic milling process. *Robot. Comput. Integr. Manuf.* **55**, 29–40 (2019)



12. Bijlsma, B.G., Radaelli, G., Herder, J.L.: Design of a compact gravity equilibrator with an unlimited range of motion. *ASME J. Mech. Robot.* **9**(6), 061003 (2017)
13. Mori, D., Ishigami, G.: Generalized Force-and-Energy Manipulability for design and control of redundant robotic arm. In: *IEEE/RSJ International Conference on Intelligent Robots and Systems (IROS)*, pp. 1131–1136 (2015)
14. Linh, N.V., Kuo, C.-H.: A gear-slider gravity compensation mechanism: design and experimental study. In: *International Design Engineering Technical Conferences and Computers and Information in Engineering Conference (IDETC-CIE)*, Anaheim, CA, USA, 18–21 August 2019, p. IDETC2019-97602 (2019)
15. Linh, N.V., Kuo, C.-H.: Gravity compensation design of planar articulated robotic arms using the gear-spring modules. *ASME J. Mech. Robot.* (submitted)



# Design and Analysis of a Mechanism for Spherical Surface Processing

Alexey Fomin<sup>1,2(✉)</sup>, Wsevolod Ivanov<sup>1</sup>, and Victor Glazunov<sup>2</sup>

<sup>1</sup> Siberian State Industrial University, Novokuznetsk 654007, Russia  
alexey-nvkz@mail.ru

<sup>2</sup> Mechanical Engineering Research Institute of the RAS,  
Moscow 101990, Russia

**Abstract.** The proposed study presents a new single-driven mechanism for processing (polishing) of spherical surfaces. The fixed link in this mechanism connects with three movable links: in addition to the driving link and the output rocker, this mechanism is equipped with an additional swinging arm set to increase the rigidity of the whole system. The developed mechanism allows reproducing screw curves lying on a spherical surface. Kinematic analysis of the developed mechanism has been carried out and the spatial trajectories of its end-effector have been identified. Certain links in the mechanism are made as sliding, i.e. with variable lengths. Such design allows getting different trajectories of the end-effector at a permanent structure of the entire mechanism.

**Keywords:** Mechanism · Degree-of-freedom · Design · Kinematic analysis · Spatial trajectory · Spherical surface

## 1 Introduction

To perform various technical operations associated with processing or polishing spatial surfaces, cutting, and also reproducing three-dimensional curves, an end-effector needs to be assigned a complex motion along a spatial trajectory. When using the minimum number of drives, particularly one, these tasks cannot be implemented using planar kinematic chains, for example, given in [1–4]. The application of planar chains for these operations is possible only with the use of several drives capable of actuating end-effectors in several planes.

In terms of the application of spatial single-driven mechanisms, for example, belonging to the class of screw mechanisms [5, 6], their limitation in solving of this problem is in impossibility to move end-effectors along with curvilinear trajectories since the axis of a screw joint is the straight line. The application of spatial mechanical systems having several kinematic chains with independent drives [7–9] is not advisable for tasks requiring cyclic movements of end-effectors. The most effective mechanical systems for such tasks are those which have single drive and prescribed movements of end-effectors, i.e. such mechanisms in which end-effectors move along closed spatial trajectories [10–12].

Thus, the proposed study aims at developing such a one-degree-of-freedom (DoF) mechanism in which a movement of the end-effector will be realized along a complex spatial trajectory.

## 2 Mechanism Design

According to the aim of the study, as well as in providing a condition by which the links of the mechanism do not intersect with the reproducible trajectory, a kinematic scheme shown in Fig. 1 has been proposed. The mechanism includes fixed link 1, crank 2, screw 3, nut 4 with rod 5 rigidly mounted on it, rocker 6, stem 7, end-effector 8 acting as swinging arm on which the element 9 reproducing spatial trajectories is rigidly mounted.

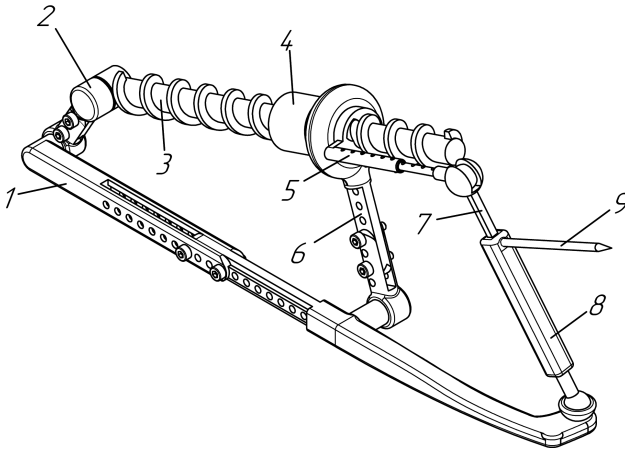


**Fig. 1.** The one-DoF mechanism for spherical surfaces processing.

Kinematic pairs 1–2, 2–3 and 6–1 are made rotational with parallel axes. Due to this, links 2, 3 and 6 are placed in parallel planes. Kinematic pair 4–6 is made rotational with the axis lying in a perpendicular plane to the axes of the remaining rotational kinematic pairs and coinciding with the axial axis of screw 3, which forms screw kinematic pair with nut 4. Kinematic pair 8–1 is spherical, pair 7–8 is prismatic, and pair 7–5 is two-DoF with two relative rotations.

In this mechanism, a spatial trajectory of element 9 does not intersect with any of its movable links. To obtain different trajectories of the end-effector, links 1, 2, 5, and 6 are made sliding with a possibility of changing their lengths. Element 9 moves along a spherical surface with a radius equal to the distance from the extreme point of element 9 to the center of spherical joint 1–8.

The developed mechanism works as follows. By setting the rotation of crank 2, link 3 will begin screwing into nut 4, thereby setting it in motion. In this case, the length between kinematic pairs 2–3 and 4–6 will vary. Rod 5, rigidly connected with nut 4,

will transmit a movement to stem 7 through kinematic pair 5–7, and then stem 7 will actuate end-effector 8 that guides element 9 along a given spatial trajectory.

### 3 Structural Analysis

Address a mobility analysis of the developed mechanism. As far as the mechanism includes two kinematic chains, particularly, chain 1–6 and chain 7–9, their mobilities are determined independently of each other. The total mobility of the whole mechanism is determined by the sum of these mobilities. For chain 1–6 the mobility is calculated by the following formulae

$$W_2 = 4n - 3p_5 - 2p_4 - p_3, \quad (1)$$

where  $W_2$  is mobility, defining number of DoF of spatial kinematic chain with two imposed constraints;  $n$  is number of movable links;  $p_5$ ,  $p_4$ , and  $p_3$  are numbers of one-, two- and three-DoF kinematic pairs. Kinematic chain 1–6 includes  $n = 4$ ,  $p_5 = 5$ ,  $p_4 = 0$ , and  $p_3 = 0$ , then in accordance with (1) its mobility is equal to  $W_2 = 1$ . On a related note links 3, 4 and 6 form three-bar group of zero-DoF with  $n = 3$  and  $p_5 = 4$ . By (1) the number of DoF of this group is zero ( $W_2 = 0$ ).

The mobility of chain 7–9 is defined as

$$W_0 = 6n - 5p_5 - 4p_4 - 3p_3 - 2p_2 - p_1, \quad (2)$$

where, in addition to the parameters indicated in (1), there is  $W_0$  that is mobility, defining number of DoF of a spatial kinematic chain without imposed constraints;  $p_2$  and  $p_1$  are numbers of kinematic pairs with four and five DoF. Thus, in accordance with (2), the mobility of kinematic chain 7–9 with  $n = 2$ ,  $p_5 = 1$ ,  $p_4 = 1$ ,  $p_3 = 1$ ,  $p_2 = 0$  and  $p_1 = 0$ , is equal to  $W_0 = 0$ , that indicates it as a zero-DoF group (Assur group).

Summing up the mobilities calculated by (1) and (2), it is determined that the total mobility of the investigated mechanism is equal to one, i.e.  $W = 1$ . Accordingly, to obtain a prescribed motion of all links, it is necessary to provide an input motion to a single link. In this case, it is given to crank 2.

### 4 Kinematic Analysis

Address to kinematic analysis of the developed mechanism in order to calculate rotational angles and displacements in kinematic pairs to determine a trajectory of element 9. Figure 2 shows a scheme of the mechanism, where spatial coordinate systems are connected with each link in the center of kinematic pairs. The given parameters are the lengths of all links, as well as angle  $\varphi_1$  that determines the rotation of crank 2 around axis  $O_1x_1$ .

Figure out two closed contours in this mechanism:  $O_1O_2O_3O_4O_6A_1O_1$  and  $A_1O_6O_4A_2O_7O_8A_1$ . For the considered case of kinematic analysis, the center of spherical joint 8–1 is located in the same plane with axis  $O_3y_3$  ( $O_4y_4$ ), so along with

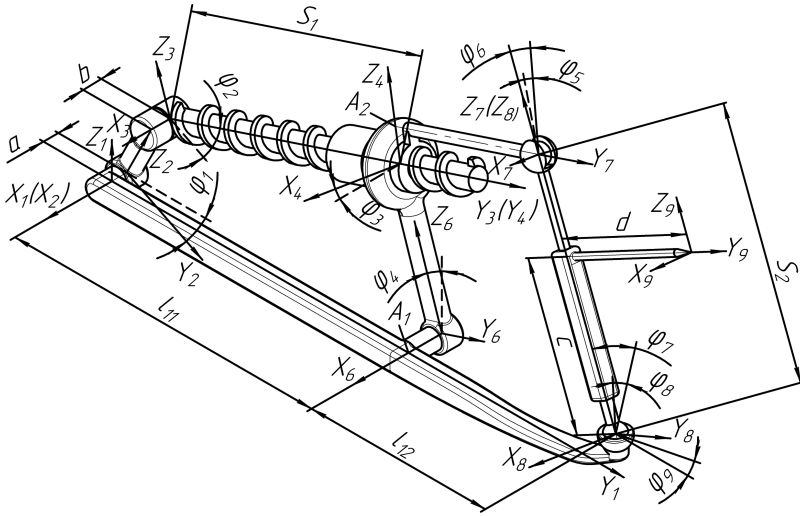


**Fig. 2.** Toward kinematic analysis of the mechanism for spherical surface processing.

axial axis of screw 3. In this case a trajectory of the end-effector is a symmetrical relative to axial axis of screw 3. To reach unsymmetrical trajectory of the end-effector, it needs to shift joint 8–1 left or right relative to axial axis of screw 3. Next address to the first contour of the mechanism and define variable rotational angles and displacements in kinematic pairs.

The origin of coordinate system  $O_1x_1y_1z_1$  is connected with fixed link 1, the origin of coordinate system  $O_2x_2y_2z_2$  is connected with crank 2. Both coordinate systems are located in rotational kinematic pair 1–2, so that axes  $O_1x_1$  and  $O_2x_2$  coincide. The matrix describing the position of coordinate system  $O_2x_2y_2z_2$  in  $O_1x_1y_1z_1$  is written as

$$M^{(2,1)} = \begin{pmatrix} 1 & 0 & 0 & 0 \\ -a & 1 & 0 & 0 \\ 0 & 0 & \cos(\varphi_1) & \sin(\varphi_1) \\ 0 & 0 & -\sin(\varphi_1) & \cos(\varphi_1) \end{pmatrix}, \quad (3)$$

where  $a$  is a given length, defining displacement of coordinate origin  $O_2x_2y_2z_2$  relative to  $O_1x_1y_1z_1$  along with axis  $O_1x_1$ ;  $\varphi_1$  is a given angle describing the rotation of crank 2 around fixed link 1.

Coordinate origin  $O_3x_3y_3z_3$  is connected with screw 3 and located in rotational joint 2–3. Axes  $O_2x_2$  and  $O_3x_3$  are parallel to each other. The matrix describing the position of coordinates  $O_3x_3y_3z_3$  in  $O_2x_2y_2z_2$  looks like

$$M^{(3,2)} = \begin{pmatrix} 1 & 0 & 0 & 0 \\ -b & 1 & 0 & 0 \\ 0 & 0 & \cos(\varphi_2) & -\sin(\varphi_2) \\ l_2 & 0 & \sin(\varphi_2) & \cos(\varphi_2) \end{pmatrix}, \quad (4)$$

where  $b$  is a given length defining displacement of coordinate origin  $O_3x_3y_3z_3$  relative to  $O_2x_2y_2z_2$  along with axis  $O_2x_2$ ;  $l_2$  is a given length of crank 2;  $\varphi_2$  is an unknown variable describing the rotation of screw 3 relative to crank 2.

Coordinate origin  $O_4x_4y_4z_4$  is connected with nut 4 and located in screw joint 3–4, where axes  $y_3$  and  $y_4$  are coincide. The position of coordinates  $O_4x_4y_4z_4$  in  $O_3x_3y_3z_3$  is described with the following matrix

$$M^{(4,3)} = \begin{pmatrix} 1 & 0 & 0 & 0 \\ 0 & \cos(\varphi_3) & 0 & -\sin(\varphi_3) \\ S_1 & 0 & 1 & 0 \\ 0 & \sin(\varphi_3) & 0 & \cos(\varphi_3) \end{pmatrix}, \quad (5)$$

where  $S_1$  is a variable length describing displacement of nut 4 relative to screw 3, i.e. defining displacement of coordinate origin  $O_4x_4y_4z_4$  relative to  $O_3x_3y_3z_3$ ;  $\varphi_3$  is an unknown angle describing rotation of nut 4 relative to screw 3.

Coordinate origin  $O_6x_6y_6z_6$  is connected with rocker 6 and located in rotational joint 6–1. The matrix describing the position of coordinates  $O_6x_6y_6z_6$  in  $O_4x_4y_4z_4$  looks like

$$M^{(6,4)} = \begin{pmatrix} 1 & 0 & 0 & 0 \\ -l_6 \sin(\varphi_3) & \cos(\varphi_3) & 0 & \sin(\varphi_3) \\ 0 & 0 & 1 & 0 \\ -l_6 \cos(\varphi_3) & -\sin(\varphi_3) & 0 & \cos(\varphi_3) \end{pmatrix}, \quad (6)$$

where  $l_6$  is a given length of rocker 6, defining displacement of coordinate origin  $O_6x_6y_6z_6$  relative to  $O_4x_4y_4z_4$ .

Next the matrix for transformation coordinates  $O_1x_1y_1z_1$  in  $O_6x_6y_6z_6$  is written in the following view

$$M^{(1,6)} = \begin{pmatrix} 1 & 0 & 0 & 0 \\ a+b & 1 & 0 & 0 \\ -l_{11} \cos(\varphi_4) & 0 & \cos(\varphi_4) & \sin(\varphi_4) \\ -l_{11} \sin(\varphi_4) & 0 & -\sin(\varphi_4) & \cos(\varphi_4) \end{pmatrix}, \quad (7)$$

where  $\varphi_4$  is an unknown angle describing rotation of rocker 6 around fixed link 1;  $l_{11}$  is a given length that is equal to  $A_1O_1$ .

The closedness equation for contour  $O_1O_2O_3O_4O_6A_1O_1$  is written as

$$M^{(2,1)}M^{(3,2)}M^{(4,3)}M^{(6,4)}M^{(1,6)} = E, \quad (8)$$

where  $E$  is identity matrix.

After multiplying matrix  $M^{(2,1)}$ ,  $M^{(3,2)}$ ,  $M^{(4,3)}$ ,  $M^{(6,4)}$  and  $M^{(1,6)}$ , described by (3)–(7) and indicated motions in kinematic pairs, the obtained equations have been numerically solved. The following numerical parameters have been introduced:  $l_{11} = 160$  mm;  $l_2 = 30$  mm;  $l_6 = 71.5$  mm;  $a = 8$  mm;  $b = 10$  mm. Table 1 shows the numerical values of unknown parameters  $\varphi_2$ ,  $\varphi_3$ ,  $\varphi_4$  and  $S_1$  depending on rotational angle  $\varphi_1$ .

**Table 1.** Numerical values of variables ( $\varphi_2$ ,  $\varphi_3$ ,  $\varphi_4$  and  $S_1$ ) for contour  $O_1O_2O_3O_4O_6A_1O_1$  of the mechanism depending on angle  $\varphi_1$ .

$\varphi_1, \text{deg}$	$\varphi_2, \text{deg}$	$\varphi_3, \text{deg}$	$\varphi_4, \text{deg}$	$S_1, \text{mm}$
0	15.43	4.33	15.43	146.25
30	48.88	414.71	18.88	128.79
60	85.63	761.51	25.63	114.34
90	123.37	899.99	33.37	108.57
120	158.40	761.51	38.40	114.34
150	170.80	414.71	39.20	128.79
180	216.67	-4.33	36.67	146.25
210	242.28	-378.25	32.28	161.83
240	267.14	-630.49	27.14	172.34
270	292.11	-719.05	22.11	176.03
300	317.92	-630.49	17.92	172.34
330	345.39	-378.25	15.39	161.83

Next, address to the investigation of contour  $O_4A_2O_7O_8O_1A_1O_6O_4$  to find out remaining unknown variables. Discuss two-DoF joint 5–7 with two independent rotations at angles  $\varphi_5$  and  $\varphi_6$ , indicated in Fig. 3.

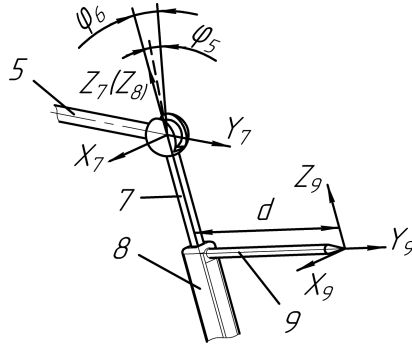


**Fig. 3.** Two-DoF joint 5–7 with two independent rotations at angles  $\varphi_5$  and  $\varphi_6$ .

Coordinate origin  $O_7x_7y_7z_7$  is connected with stem 7 and located in joint 5–7 to the effect that axis  $O_7z_7$  directs along with axial axis of stem 7. The position of coordinates  $O_7x_7y_7z_7$  in  $O_4x_4y_4z_4$  is defined as

$$M^{(7,4)} = M_{O_7x_7}^{(7,4)} M_{O_7y_7}^{(7,4)} M_S^{(7,4)}, \quad (9)$$

where  $M_{O_7x_7}^{(7,4)}$  is a matrix describes rotation around axis  $O_7x_7$  at angle  $\varphi_6$ ;  $M_{O_7y_7}^{(7,4)}$  is a matrix describing rotation around axis  $O_7y_7$  at angle  $\varphi_5$ ;  $M_S^{(7,4)}$  is a matrix describing linear displacements between coordinates  $O_7x_7y_7z_7$  and  $O_4x_4y_4z_4$ . These matrixes are shown below

$$M_{O_7x_7}^{(7,4)} = \begin{pmatrix} 1 & 0 & 0 & 0 \\ 0 & 1 & 0 & 0 \\ 0 & 0 & \cos(\varphi_5) & -\sin(\varphi_5) \\ 0 & 0 & \sin(\varphi_5) & \cos(\varphi_5) \end{pmatrix}, M_{O_7y_7}^{(7,4)} = \begin{pmatrix} 1 & 0 & 0 & 0 \\ 0 & \cos(\varphi_6) & 0 & \sin(\varphi_6) \\ 0 & 0 & 1 & 0 \\ 0 & -\sin(\varphi_6) & 0 & \cos(\varphi_6) \end{pmatrix},$$

$$M_S^{(7,4)} = \begin{pmatrix} 1 & 0 & 0 & 0 \\ 0 & 1 & 0 & 0 \\ l_5 & 0 & 1 & 0 \\ e & 0 & 0 & 1 \end{pmatrix}, \quad (10)$$

where  $l_5$  is a given length of rod 5 that is equal to  $A_2O_7$ ;  $e$  is a given parameter defining length  $O_4A_2$ .

Coordinate origin  $O_8x_8y_8z_8$  is connected with link 8 in the center of spherical joint 8–1, where axis  $O_8x_8$  is parallel to  $O_7x_7$ , axis  $O_8y_8$  is parallel to  $O_7y_7$ , axis  $O_8z_8$  coincides with axis  $O_7z_7$ . The position of coordinates  $O_8x_8y_8z_8$  in  $O_7x_7y_7z_7$  is described as

$$M^{(8,7)} = \begin{pmatrix} 1 & 0 & 0 & 0 \\ 0 & 1 & 0 & 0 \\ 0 & 0 & 1 & 0 \\ S_2 & 0 & 0 & 1 \end{pmatrix}, \quad (11)$$

where  $S_2$  is a variable length, defining displacement of coordinate origin  $O_8x_8y_8z_8$  relative to  $O_7x_7y_7z_7$ .

The position of coordinates  $O_1x_1y_1z_1$  in  $O_8x_8y_8z_8$  is described by the multiplication of the following matrixes

$$M^{(1,8)} = M_{O_1x_1}^{(1,8)} M_{O_1y_1}^{(1,8)} M_{O_1z_1}^{(1,8)} M_S^{(1,8)} = M_R^{(1,8)} M_S^{(1,8)}, \quad (12)$$

where  $M_{O_1x_1}^{(1,8)}$  is a matrix describing rotation around axis  $O_1x_1$  at angle  $\varphi_7$ ;  $M_{O_1y_1}^{(1,8)}$  is a matrix describing rotation around axis  $O_1y_1$  at angle  $\varphi_8$ ;  $M_{O_1z_1}^{(1,8)}$  is a matrix describing rotation around axis  $O_1z_1$  at angle  $\varphi_9$ ;  $M_R^{(1,8)}$  and  $M_S^{(1,8)}$  are matrixes describing rotations and linear displacements between coordinates  $O_1x_1y_1z_1$  and  $O_8x_8y_8z_8$ . These matrixes are shown below

$$M_{O_1x_1}^{(1,8)} = \begin{pmatrix} 1 & 0 & 0 & 0 \\ 0 & 1 & 0 & 0 \\ 0 & 0 & \cos(\varphi_7) & -\sin(\varphi_7) \\ 0 & 0 & \sin(\varphi_7) & \cos(\varphi_7) \end{pmatrix}, M_{O_1y_1}^{(1,8)} = \begin{pmatrix} 1 & 0 & 0 & 0 \\ 0 & \cos(\varphi_8) & 0 & \sin(\varphi_8) \\ 0 & 0 & 1 & 0 \\ 0 & -\sin(\varphi_8) & 0 & \cos(\varphi_8) \end{pmatrix},$$

$$M_{O_1z_1}^{(1,8)} = \begin{pmatrix} 1 & 0 & 0 & 0 \\ 0 & \cos(\varphi_9) & -\sin(\varphi_9) & 0 \\ 0 & \sin(\varphi_9) & \cos(\varphi_9) & 0 \\ 0 & 0 & 0 & 1 \end{pmatrix}, \quad (13)$$



$$\begin{aligned}
M_R^{(1,8)} &= M_{O_1x_1}^{(1,8)} M_{O_1y_1}^{(1,8)} M_{O_1z_1}^{(1,8)} \\
&= \begin{pmatrix} \cos(\varphi_8) \cos(\varphi_9) & \cos(\varphi_8) \sin(\varphi_9) & \sin(\varphi_8) \\ -\sin(\varphi_7) \sin(\varphi_8) \cos(\varphi_9) - \cos(\varphi_7) \sin(\varphi_9) & -\sin(\varphi_7) \sin(\varphi_8) \sin(\varphi_9) + \cos(\varphi_7) \cos(\varphi_9) & \sin(\varphi_7) \cos(\varphi_8) \\ -\cos(\varphi_7) \sin(\varphi_8) \cos(\varphi_9) + \sin(\varphi_7) \sin(\varphi_9) & -\cos(\varphi_7) \sin(\varphi_8) \sin(\varphi_9) - \sin(\varphi_7) \cos(\varphi_9) & \cos(\varphi_7) \cos(\varphi_8) \end{pmatrix}, \\
M_S^{(1,8)} &= \begin{pmatrix} 1 & 0 & 0 & 0 \\ l_{SX} & 1 & 0 & 0 \\ l_{SY} & 0 & 1 & 0 \\ l_{SZ} & 0 & 0 & 1 \end{pmatrix}, \tag{14}
\end{aligned}$$

where  $l_{SX}$ ,  $l_{SY}$ , and  $l_{SZ}$  are variable lengths, defining the position of coordinate origin  $O_1x_1y_1z_1$  in  $O_8x_8y_8z_8$  based on given lengths  $l_{11}$ ,  $l_{12}$ ,  $a$ ,  $b$  and variable angles  $\varphi_7$ ,  $\varphi_8$ ,  $\varphi_9$ .

The position of coordinates  $O_6x_6y_6z_6$  in  $O_1x_1y_1z_1$  is described by the matrix

$$M^{(6,1)} = \begin{pmatrix} 1 & 0 & 0 & 0 \\ -(a+b) & 1 & 0 & 0 \\ l_{11} & 0 & \cos(\varphi_4) & -\sin(\varphi_4) \\ 0 & 0 & \sin(\varphi_4) & \cos(\varphi_4) \end{pmatrix}, \tag{15}$$

The position of coordinates  $O_4x_4y_4z_4$  in  $O_6x_6y_6z_6$  is described by the matrix

$$M^{(4,6)} = \begin{pmatrix} 1 & 0 & 0 & 0 \\ 0 & \cos(\varphi_3) & 0 & -\sin(\varphi_3) \\ 0 & 0 & 1 & 0 \\ l_6 & \sin(\varphi_3) & 0 & \cos(\varphi_3) \end{pmatrix}, \tag{16}$$

The closedness equation for contour  $O_4A_2O_7O_8O_1A_1O_6O_4$  is written as

$$M^{(7,4)} M^{(8,7)} M^{(1,8)} M^{(6,1)} M^{(4,6)} = E, \tag{17}$$

where  $E$  is an identity matrix.

After multiplying matrix  $M^{(7,4)}$ ,  $M^{(8,7)}$ ,  $M^{(1,8)}$ ,  $M^{(6,1)}$  and  $M^{(4,6)}$  described by (9)–(16) and indicated motions in kinematic pairs, the obtained equations have been numerically solved. The following numerical parameters have been introduced:  $l_{12} = 98.7$  mm;  $l_5 = 74.3$  mm;  $e = 15$  mm. Table 2 shows the numerical values of unknown parameters  $\varphi_5$ ,  $\varphi_6$ ,  $\varphi_7$ ,  $\varphi_8$ ,  $\varphi_9$  and  $S_2$  depending on rotational angle  $\varphi_1$ .

The position of point  $B$  of the end-effector in base coordinates  $O_1x_1y_1z_1$  is defined as

$$\begin{pmatrix} 1 \\ X_{B1} \\ Y_{B1} \\ Z_{B1} \end{pmatrix} = M^{(2,1)} M^{(3,2)} M^{(4,3)} M^{(7,4)} M^{(8,7)} \begin{pmatrix} 1 \\ 0 \\ d \\ c \end{pmatrix},$$

**Table 2.** Numerical values of variables ( $\varphi_5$ ,  $\varphi_6$ ,  $\varphi_7$ ,  $\varphi_8$ ,  $\varphi_9$  and  $S_2$ ) for contour  $O_4A_2O_7O_8O_1A_1O_6O_4$  of the mechanism depending on angle  $\varphi_1$ .

$\varphi_1, \text{deg}$	$\varphi_5, \text{deg}$	$\varphi_6, \text{deg}$	$\varphi_7, \text{deg}$	$\varphi_8, \text{deg}$	$\varphi_9, \text{deg}$	$S_2, \text{mm}$
0	5.03	16.97	32.41	0.84	0.23	106.55
30	406.31	16.16	35.16	6.29	2.16	107.69
60	755.16	12.64	38.35	4.19	2.01	121.50
90	898.03	11.16	44.52	0.20	0.13	107.89
120	755.92	6.51	44.98	3.05	2.42	142.40
150	408.27	6.23	45.53	3.80	3.1	141.31
180	4.03	7.19	43.86	0.38	0.29	142.74
210	-375.91	9.29	41.58	1.68	1.06	135.03
240	-622.05	13.05	40.41	6.94	3.58	113.47
270	-721.12	13.95	36.05	0.16	0.06	118.43
300	620.58	18.04	36.19	8.82	2.88	97.92
330	375.28	17.08	32.49	2.51	0.69	105.95

where  $X_{B1}$ ,  $Y_{B1}$ , and  $Z_{B1}$  are the coordinates of point  $B$  in system  $O_1x_1y_1z_1$ ;  $c$  and  $d$  are given parameters, defining the length of element 9, rigidly mounted on link 8 ( $c = 71.33$  mm,  $d = 73.37$  mm). Table 3 shows the numerical values of coordinates  $X_{B1}$ ,  $Y_{B1}$ , and  $Z_{B1}$  relative to axes  $O_1x_1$ ,  $O_1y_1$ , and  $O_1z_1$ , as well as radius-vector  $R_1$ , defining the distance between point  $B$  and coordinate origin  $O_1x_1y_1z_1$  depending on angle  $\varphi_1$ . Figure 4 shows orientation of these parameters in system  $O_1x_1y_1z_1$ .

Then address the definition of trajectories of point  $B$  belonging to element 9. Figure 5 shows the trajectories obtained by numerical calculations, when the center of spherical joint 1–8 is equidistantly placed relative to the axial axis of screw to the left and right sides at a distance of  $(a + b) = 18$  mm.

Trajectories of the end-effector presented in Fig. 5 are asymmetrical. This is due to the displacement of the center of spherical joint 1–8 relative to the axial axis of screw. The symmetrical trajectory can be obtained only when the center of the spherical joint is located in the same plane with the axial axis of screw. Figure 6 shows a symmetrical path of the end-effector.

Radius  $R$  of the spherical surface along which point  $B$  moves in all three cases shown in Figs. 5 and 6 is equal to  $R = 102$  mm. A change in this radius can be achieved by varying the size of the end-effector, defined by parameters  $c$  and  $d$  indicated in Fig. 2.

**Table 3.** Numerical values of coordinates  $X_{B1}$ ,  $Y_{B1}$ ,  $Z_{B1}$  and radius-vector  $R_1$  defining the position of point  $B$  in base coordinates  $O_1x_1y_1z_1$  depending on angle  $\varphi_1$ .

$\varphi_1, \text{deg}$	$X_{B1}, \text{mm}$	$Y_{B1}, \text{mm}$	$Z_{B1}, \text{mm}$	$R_1, \text{mm}$
0	-5.48	297.53	99.00	313.62
30	-14.95	293.85	99.10	310.47
60	-11.03	286.52	102.17	304.39
90	-6.20	277.19	104.94	296.45
120	-8.18	272.80	105.45	292.59
150	-9.38	272.12	105.40	291.97
180	-2.91	274.23	105.70	293.91
210	-1.51	278.86	104.95	297.96
240	-15.50	284.76	101.91	302.84
270	-5.63	290.16	101.70	307.52
300	-19.30	294.26	98.00	310.75
330	-3.24	297.41	99.23	313.54

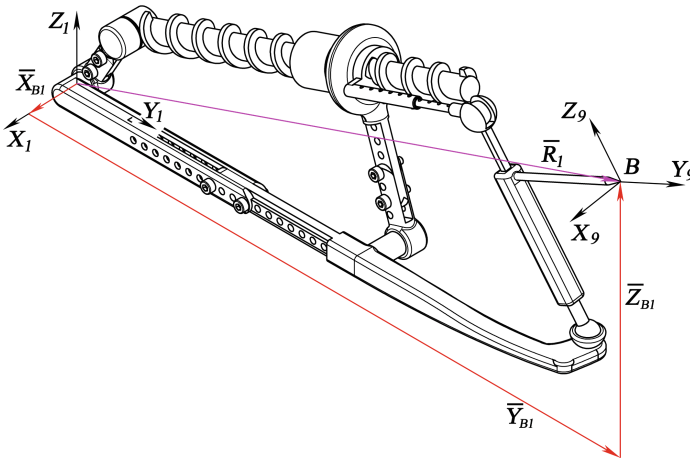


**Fig. 4.** Orientation of point  $B$  in base coordinates  $O_1x_1y_1z_1$ .

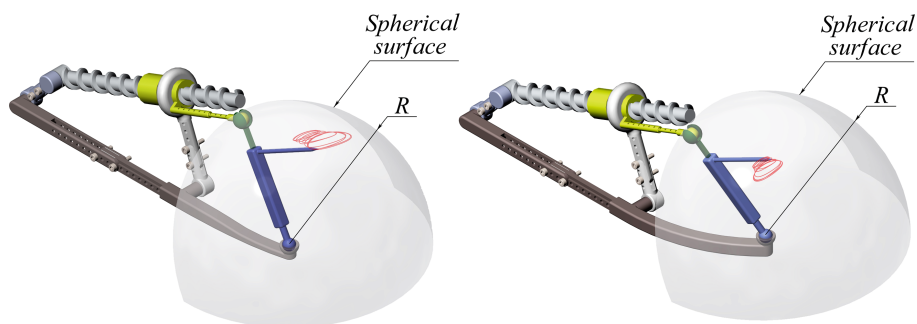


**Fig. 5.** The trajectories of the end-effector when spherical joint 1–8 is displaced left and right relative to the axial axis of screw.

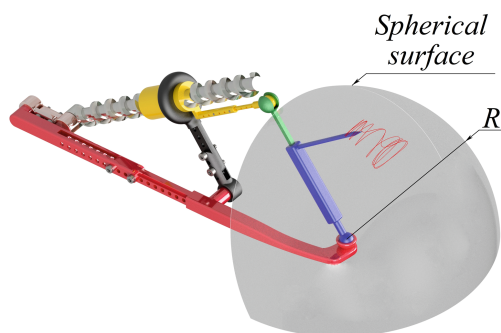


**Fig. 6.** The trajectory of the end-effector when the center of spherical joint 1–8 coplanar with the axial axis of screw.

## 5 Conclusions

The carried study provides a novel single-driven mechanism for spherical surface processing. The mechanism involves two kinematic chains forming two closed contours. The proposed mechanism allows reproducing helical trajectories placed on a spherical surface. The design of this mechanism has been developed with extending links. It allows reproducing various trajectories while having unchanged structure. The study provides structural analysis with mobility calculation and kinematic analysis with definition of variable rotational angles and displacements in all kinematic pairs. Based on the kinematic analysis the end-effector's trajectory has been numerically defined. It has been varied in terms of its symmetry.

**Acknowledgments.** The reported study was funded by *RFBR* according to the research project № 18-31-00440.

## References

1. Pennock, G.R., Kassner, D.J.: The workspace of a general geometry planar three degree of freedom platform manipulator. *J. Mech. Des.* **115**(2), 269–276 (1993)
2. Gosselin, C., Angeles, J.: The optimum kinematic design of a planar three-degree-of-freedom parallel manipulator. *J. Mech. Transm. Autom. Des.* **110**(1), 35–41 (1988)
3. Briot, S., Glazunov, V., Arakelian, V.: Investigation on the effort transmission in planar parallel manipulators. *J. Mech. Robot.* **5**(1) (2013). JMR-12-1148
4. Kuo, C.-H., Chen, Y.-C., Pan, T.-Y.: Continuum kinematics of a planar dual-backbone robot based on pseudo-rigid-body model: formulation, accuracy, and efficiency. In: ASME 2017 International Design Engineering Technical Conferences and Computers and Information in Engineering Conference, p. V05AT08A015 (2017)
5. Jones, M.H., Velinsky, S.A.: Kinematics of roller migration in the planetary roller screw mechanism. *J. Mech. Des.* **134**(6), 061006 (2012)
6. Wei, C.C., Lin, J.F.: Kinematic analysis of the ball screw mechanism considering variable contact angles and elastic deformations. *J. Mech. Des.* **125**(4), 717–733 (2004)
7. Glazunov, V., Nosova, N., Ceccarelli, M.: Kinematics of a 6 DOFs manipulator with interchangeable translation and rotation motions. In: Proceedings of Recent Advances in Mechanism Design for Robotics. Mechanisms and Machine Science, vol. 33. Springer (2015)
8. Pierrot, F., Reynaud, C., Fournier, A.: DELTA: a simple and efficient parallel robot. *Robotica* **8**(2), 105–109 (1990)
9. Alagheband, A., Mahmoodi, M., Mills, J.K., Benhabib, B.: Comparative analysis of a redundant pentapod parallel kinematic machine. *J. Mech. Robot.* **7**(3) (2015). Paper No: JMR-14-1112
10. Fomin, A.: The second genus machines and the methods of their structural synthesis. In: The Proceedings of the IFOST 2008. Third International Forum on Strategic Technologies, pp. 409–410 (2008)
11. Gileta, V., Choosovitin, N.: Parametric analysis of device for the mixing with the equal angles overlap and pressure. In: The Proceedings of the IFOST 2008. Third International Forum on Strategic Technologies, pp. 414–416 (2008)
12. Fomin, A., Ivanov, W., Paik, J.: Design of five-bar screw-lever manipulator and optimization of its output link path of motion. *Procedia Eng.* **206**, 1703–1708 (2017)



# A Short Note on Equivalent Four-Bar Linkages of Direct-Contact Mechanisms

Wen-Tung Chang<sup>(✉)</sup> and Dung-Yan Yang

Department of Mechanical and Mechatronic Engineering,  
National Taiwan Ocean University, Keelung 20224, Taiwan  
wtchang@mail.ntou.edu.tw

**Abstract.** In this paper, kinematic analysis for two types of classical direct-contact mechanisms, planar gear mechanisms with a pair of involute spur gears and disk cam mechanisms with a circular-arc cam and an oscillating roller follower, are presented in order to discuss the inequivalence of the direct-contact mechanisms and their equivalent four-bar linkages in jerk analysis. For the discussed gear mechanisms, it is found that the equivalent four-bar linkage is not able to give a correct value of jerk, unless the angular velocity ratio between the two mating gears is exactly negative one. For the discussed cam mechanisms, as the circular-arc cam is in contact with its follower at a point of tangency of two adjacent circular arcs, the two equivalent four-bar linkages simultaneously existing at that instant are both not able to correctly reflect an infinite jerk of the follower, because the suddenly changed curvature of the cam profile is not considered in sudden link-length variations of the equivalent linkages. The two presented case studies can give demonstrations for understanding the inequivalence of the direct-contact mechanisms and their equivalent four-bar linkages in the aspect of jerk analysis.

**Keywords:** Direct-contact mechanisms · Planar gear mechanisms · Involute spur gears · Disk cam mechanisms · Circular-arc cams · Equivalent four-bar linkage · Kinematic analysis

## 1 Introduction

Direct-contact mechanisms, such as gear and cam mechanisms, are mechanisms with higher pairs. The simplest direct-contact mechanism consists of a frame, a driving link and a driven link, in which the driving and driven links are in contact with each other to transmit motion and force. Kinematic analysis for such a three-link direct-contact mechanism can sometimes be replaced by its equivalent four-bar linkage to calculate the velocity and acceleration at a particular instant [1–5]. Although there may be an infinite number of equivalent four-bar linkages for a three-link direct-contact mechanism, the one with its coupler connecting the centers of curvature of the driving and driven links is referred to as the ‘representative equivalent four-bar linkage’ [2]. A proof is given in Martin’s textbook [5] to show that the equivalent four-bar linkage can give correct values of velocity and acceleration. However, the equivalent four-bar linkage cannot give a correct value of the time rate of change of acceleration, called the jerk or pulse.

Such a situation is described in most textbooks for kinematics of machinery but without giving proofs or demonstrations. In this paper, kinematic analysis for two types of classical direct-contact mechanisms, planar gear mechanisms with a pair of involute spur gears and disk cam mechanisms with a circular-arc cam and an oscillating roller follower, are presented in order to discuss the inequivalence of the direct-contact mechanisms and their equivalent four-bar linkages in the aspect of jerk analysis.

## 2 Equivalent Four-Bar Linkage of a Three-Link Direct-Contact Mechanism

A typical three-link direct-contact mechanism, consisting of a frame (link 1), a driving link (link 2) and a driven link (link 3), is shown in Fig. 1(a). The driving and driven links are pivoted to the frame on points  $O_2$  and  $O_3$ , respectively. Points  $K_2$  and  $K_3$  are the centers of curvature of the driving and driven links in contact at point A, respectively. The common normal at the contact point A must always pass through points  $K_2$ ,  $K_3$  and the instant velocity center  $I_{23}$ . The equivalent linkage of this direct-contact mechanism is the four-bar linkage  $O_2K_2K_3O_3$  shown in Fig. 1(b), in which the coupler (link 4) of the linkage connects the centers of curvatures of the driving link,  $K_2$ , and of the driven link,  $K_3$ . The instantaneous velocity and acceleration of links  $O_2K_2$  and  $O_3K_3$  [i.e. links 2 and 3 shown in Fig. 1(b)] are identical to those of the driving and driven links, respectively.

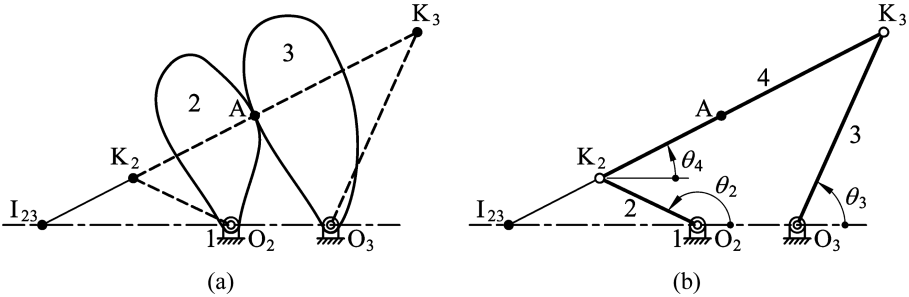


**Fig. 1.** Illustration of a three-link direct-contact mechanism and its equivalent four-bar linkage.

For the four-bar linkage shown in Fig. 1(b), its link lengths are  $r_1 = O_2O_3$ ,  $r_2 = O_2K_2$ ,  $r_3 = O_3K_3$ , and  $r_4 = K_2K_3$ , and the angular positions of links,  $\theta_2$ ,  $\theta_3$  and  $\theta_4$ , are measured counterclockwise from line  $O_2O_3$ . By using vector loop method to solve the velocity equations simultaneously, the analytical expressions of the angular velocities of link 3 ( $\omega_3$ ) and link 4 ( $\omega_4$ ) can be derived as [6]

$$\omega_3 = \dot{\theta}_3 = \frac{r_2 \sin(\theta_2 - \theta_4)}{r_3 \sin(\theta_3 - \theta_4)} \omega_2 \quad (1)$$

$$\omega_4 = \dot{\theta}_4 = \frac{r_2 \sin(\theta_2 - \theta_3)}{r_4 \sin(\theta_3 - \theta_4)} \omega_2 \quad (2)$$

in which,  $\omega_2 = \dot{\theta}_2$  is the known angular velocity of link 2. Then, by using vector loop method to solve the acceleration equations simultaneously, the analytical expressions of the angular accelerations of link 3 ( $\alpha_3$ ) and link 4 ( $\alpha_4$ ) can be derived as [6]

$$\alpha_3 = \ddot{\theta}_3 = \frac{r_2[\alpha_2 \sin(\theta_2 - \theta_4) + \omega_2^2 \cos(\theta_2 - \theta_4)] - r_3 \omega_3^2 \cos(\theta_3 - \theta_4) + r_4 \omega_4^2}{r_3 \sin(\theta_3 - \theta_4)} \quad (3)$$

$$\alpha_4 = \ddot{\theta}_4 = \frac{r_2[\alpha_2 \sin(\theta_2 - \theta_3) + \omega_2^2 \cos(\theta_2 - \theta_3)] + r_4 \omega_4^2 \cos(\theta_3 - \theta_4) - r_3 \omega_3^2}{r_4 \sin(\theta_3 - \theta_4)} \quad (4)$$

in which,  $\alpha_2 = \ddot{\theta}_2$  is the known angular acceleration of link 2. Furthermore, by using vector loop method to solve the jerk equations simultaneously, the analytical expressions of the angular jerks of link 3 ( $\zeta_3$ ) and link 4 ( $\zeta_4$ ) can be derived as

$$\begin{aligned} \zeta_3 &= \ddot{\theta}_3 \\ &= \{r_2[(\zeta_2 - \omega_2^3) \sin(\theta_2 - \theta_4) + 3\omega_2 \alpha_2 \cos(\theta_2 - \theta_4)] \\ &\quad + r_3[\omega_3^3 \sin(\theta_3 - \theta_4) - 3\omega_3 \alpha_3 \cos(\theta_3 - \theta_4)] + 3r_4 \omega_4 \alpha_4\} / [r_3 \sin(\theta_3 - \theta_4)] \end{aligned} \quad (5)$$

$$\begin{aligned} \zeta_4 &= \ddot{\theta}_4 \\ &= \{r_2[(\zeta_2 - \omega_2^3) \sin(\theta_2 - \theta_3) + 3\omega_2 \alpha_2 \cos(\theta_2 - \theta_3)] \\ &\quad + r_4[\omega_4^3 \sin(\theta_3 - \theta_4) + 3\omega_4 \alpha_4 \cos(\theta_3 - \theta_4)] - 3r_3 \omega_3 \alpha_3\} / [r_4 \sin(\theta_3 - \theta_4)] \end{aligned} \quad (6)$$

in which,  $\zeta_2 = \ddot{\theta}_2$  is the known angular jerk of link 2. The derived analytical expressions can be used to evaluate the kinematic characteristics of the equivalent four-bar linkage obtained from a direct-contact mechanism.

### 3 Kinematic Analysis for Planar Gear Mechanisms with Involute Spur Gears

A planar gear mechanism, consisting of a frame (link 1), a driving gear (link 2) and a driven gear (link 3), is illustrated in Fig. 2(a). The driving and driven gears are pivoted to the frame on points  $O_2$  and  $O_3$ , respectively, while the center distance is  $f$ . Both the driving and driven gears are typically involute spur gears that have involute tooth profiles generated from their base circles with radii of  $r_{b2}$  and  $r_{b3}$ , respectively. A constant angular velocity ratio between the two mating gears can thus be determined through the radii of their pitch circles  $r_{p2}$  and  $r_{p3}$ . Points  $K_2$  and  $K_3$  are the centers of curvature of a pair of involute tooth profiles in contact at point A, respectively. The common normal at the contact point A (i.e. the line of action) must always pass through points  $K_2$ ,  $K_3$  and also the pitch point P. It is known that the line of action must always



be the interior common tangent of the base circles of the two mating gears, while points  $K_2$  and  $K_3$  must always be coincident to the two points of tangency regardless of any positional change of the contact point A. Also, lines  $O_2K_2$  and  $O_3K_3$  are always parallel to each other, and the subtending acute angle between each of them and line  $O_2O_3$  is always equal to the pressure angle  $\phi$  of the gear mechanism. As a result, the equivalent linkage of this planar gear mechanism is the four-bar linkage  $O_2K_2K_3O_3$  shown in Fig. 2(b), in which the coupler (link 4) of the linkage connects the centers of curvature of a pair of involute tooth profiles. According to the geometric characteristics of involute tooth profiles, the configuration of the equivalent four-bar linkage  $O_2K_2K_3O_3$  shown in Fig. 2(b) is a permanently invariant crossed quadrilateral at all instants.

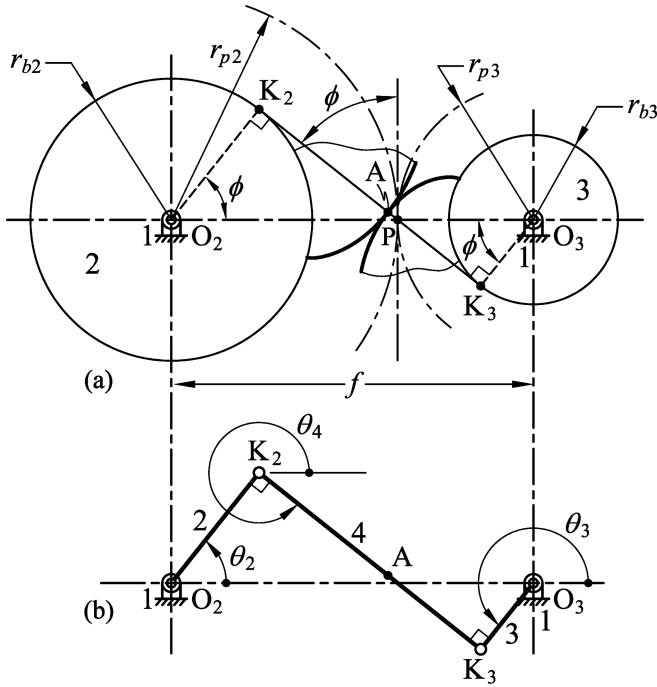


**Fig. 2.** Illustration of a planar gear mechanism with a pair of involute spur gears and its equivalent four-bar linkage.

For the four-bar linkage shown in Fig. 2(b), its link lengths are  $r_1 = O_2O_3 = f$ ,  $r_2 = O_2K_2 = r_{b2} = r_{p2}\cos\phi$ ,  $r_3 = O_3K_3 = r_{b3} = r_{p3}\cos\phi$ , and  $r_4 = K_2K_3 = f\sin\phi$ , and the angular positions of links,  $\theta_2$ ,  $\theta_3$  and  $\theta_4$ , are measured counterclockwise from line  $O_2O_3$ . Since the equivalent four-bar linkage is a permanently invariant crossed quadrilateral at all instants, thus the angular positions are invariantly  $\theta_2 = \phi$ ,  $\theta_3 = \phi + 180^\circ$  and  $\theta_4 = \phi + 270^\circ$ . By substituting the values of  $\theta_2$ ,  $\theta_3$  and  $\theta_4$  into Eqs. (1) and (2), the angular velocities of links 3 and 4 of the equivalent linkage can be expressed as

$$\omega_3 = \frac{r_2 \sin(-270^\circ)}{r_3 \sin(-90^\circ)} \omega_2 = -\frac{r_2}{r_3} \omega_2 \quad (7)$$

$$\omega_4 = \frac{r_2 \sin(-180^\circ)}{r_4 \sin(-90^\circ)} \omega_2 = -\frac{0}{r_4} \omega_2 = 0 \quad (8)$$

Equation (8) shows that the angular velocity of the coupler (link 4) is zero. Then, by substituting the values of  $\theta_2$ ,  $\theta_3$  and  $\theta_4$  and also  $\omega_4 = 0$  into Eqs. (3) and (4), the angular accelerations of links 3 and 4 of the equivalent linkage can be expressed as

$$\alpha_3 = \frac{r_2[\alpha_2 \sin(-270^\circ) + \omega_2^2 \cos(-270^\circ)] - r_3 \omega_3^2 \cos(-90^\circ) + r_4 \omega_4^2}{r_3 \sin(-90^\circ)} = -\frac{r_2}{r_3} \alpha_2 \quad (9)$$

$$\alpha_4 = \frac{r_2[\alpha_2 \sin(-180^\circ) + \omega_2^2 \cos(-180^\circ)] + r_4 \omega_4^2 \cos(-90^\circ) - r_3 \omega_3^2}{r_4 \sin(-90^\circ)} = \frac{r_2 \omega_2^2 + r_3 \omega_3^2}{r_4} \quad (10)$$

Furthermore, by substituting the values of  $\theta_2$ ,  $\theta_3$  and  $\theta_4$  and also  $\omega_4 = 0$  into Eqs. (5) and (6), the angular jerks of links 3 and 4 of the equivalent linkage can be expressed as

$$\begin{aligned} \zeta_3 &= \{r_2[(\zeta_2 - \omega_2^3) \sin(-270^\circ) + 3\omega_2 \alpha_2 \cos(-270^\circ)] \\ &\quad + r_3[\omega_3^3 \sin(-90^\circ) - 3\omega_3 \alpha_3 \cos(-90^\circ)] + 3r_4 \omega_4 \alpha_4\} / [r_3 \sin(-90^\circ)] \\ &= -\frac{r_2(\zeta_2 - \omega_2^3) - r_3 \omega_3^3}{r_3} \end{aligned} \quad (11)$$

$$\begin{aligned} \zeta_4 &= \{r_2[(\zeta_2 - \omega_2^3) \sin(-180^\circ) + 3\omega_2 \alpha_2 \cos(-180^\circ)] \\ &\quad + r_4[\omega_4^3 \sin(-90^\circ) + 3\omega_4 \alpha_4 \cos(-90^\circ)] - 3r_3 \omega_3 \alpha_3\} / [r_4 \sin(-90^\circ)] \\ &= \frac{3(r_2 \omega_2 \alpha_2 + r_3 \omega_3 \alpha_3)}{r_4} \end{aligned} \quad (12)$$

When considering that the driving gear rotates at a constant angular velocity  $\omega_2$ , its angular acceleration and jerk are  $\alpha_2 = 0$  and  $\zeta_2 = 0$ , respectively. The driven gear will also rotate at a constant angular velocity  $\omega_3$ , and its angular acceleration and jerk should be  $\alpha_3 = 0$  and  $\zeta_3 = 0$ , respectively. From Eq. (7), it is found that

$$\frac{\omega_3}{\omega_2} = -\frac{r_2}{r_3} = -\frac{r_{p2}}{r_{p3}} = -\frac{r_{b2}}{r_{b3}} \quad (13)$$

Equation (13) undoubtedly agrees with the fundamental law of gearing [6], that is, the angular velocity ratio between links 2 and 3 of the equivalent linkage is equal to that between the mating driving and driven gears. Hence, the equivalent four-bar linkage of the planar gear mechanism can give a correct value of angular velocity. Then, by substituting  $\alpha_2 = 0$  into Eq. (9), the angular acceleration of link 3 of the equivalent linkage is

$$\alpha_3 = -\frac{0}{r_3} = 0 \quad (14)$$

It shows that the angular acceleration of link 3 of the equivalent linkage is zero, which is equal to that of the driven gear. Hence, the equivalent four-bar linkage of the planar gear mechanism can give a correct value of angular acceleration. Furthermore, by substituting  $\alpha_2 = 0$ ,  $\alpha_3 = 0$ , and  $\zeta_2 = 0$  into Eqs. (11) and (12), the angular jerks of links 3 and 4 of the equivalent linkage are

$$\zeta_3 = \frac{r_2\omega_2^3 + r_3\omega_3^3}{r_3} = \frac{r_2}{r_3}\omega_2^3 + \omega_3^3 \quad (15)$$

$$\zeta_4 = \frac{0}{r_4} = 0 \quad (16)$$

From Eqs. (7) and (15), the angular jerk of link 3 of the equivalent linkage can be further expressed as

$$\zeta_3 = \frac{r_2}{r_3}\omega_2^3 + \left(-\frac{r_2}{r_3}\omega_2\right)^3 = \left[\frac{r_2}{r_3} - \left(\frac{r_2}{r_3}\right)^3\right]\omega_2^3 \quad (17)$$

From Eq. (17), it can be found that

$$\begin{cases} \zeta_3 = 0 & \text{for } \frac{r_2}{r_3} = 1 \\ \zeta_3 < 0 & \text{for } \frac{r_2}{r_3} > 1 \\ \zeta_3 > 0 & \text{for } \frac{r_2}{r_3} < 1 \end{cases} \quad (18)$$

It shows that the angular jerk of link 3 of the equivalent linkage is zero if and only if  $r_2 = r_3$ . In other words, the angular jerk of link 3 of the equivalent linkage is equal to that of the driven gear if and only if  $r_{p2} = r_{p3}$ . Hence, only when the angular velocity ratio between the two mating gears ( $\omega_3/\omega_2$ ) is exactly negative one ( $-1$ ), the equivalent four-bar linkage of the planar gear mechanism can give correct values of angular velocity, acceleration and jerk. Otherwise, the equivalent four-bar linkage of the planar gear mechanism can only give correct values of angular velocity and acceleration.

In this case study, it is found that the equivalent four-bar linkage of a planar gear mechanism with a pair of involute spur gears is not able to give a correct value of jerk, unless the angular velocity ratio between the two mating gears is exactly negative one ( $-1$ ).

#### 4 Kinematic Analysis for Disk Cam Mechanisms with a Circular-Arc Cam and an Oscillating Roller Follower

A disk cam mechanism, consisting of a frame (link 1), a circular-arc cam (link 2) and an oscillating roller follower (link 3), is illustrated in Fig. 3(a). The cam and the follower are pivoted to the frame on points  $O_2$  and  $O_3$ , respectively, while the center distance is  $f$ . The profile of the circular-arc cam is essentially composed of four circular arcs with three radii  $R_1$ ,  $R_2$  and  $R_3$ , respectively. Points  $K_1$ ,  $K_2$ ,  $K_3$  and  $K_4$  are the circular centers (also the centers of curvature) of the four circular arcs, respectively. Points  $A_{12}$ ,  $A_{23}$ ,  $A_{34}$  and  $A_{14}$  on the cam profile are the points of tangency of each two adjacent circular arcs, respectively. The circular arc between points  $A_{12}$  and  $A_{14}$  has a radius of  $R_1$  and a circular-arc angle of  $\gamma_1$ , the circular arc between points  $A_{12}$  and  $A_{23}$  or between points  $A_{14}$  and  $A_{34}$  has a radius of  $R_2$  and a circular-arc angle of  $\gamma_2$ , and the circular arc between points  $A_{23}$  and  $A_{34}$  has a radius of  $R_3$  and a circular-arc angle of  $\gamma_3$ . In this case, points  $O_2$ ,  $K_1$  and  $K_3$  are collinear, while the distance between points  $O_2$  and  $K_1$  is  $e$ , and that between points  $K_1$  and  $K_3$  is  $c$ . The follower has an arm length of  $l$  and a roller radius of  $r_f$ . The cam rotation angle  $\theta$  is measured counterclockwise from line  $O_2O_3$  to line  $O_2K_1$ , while the angular position of the follower  $\xi$  is measured clockwise from line  $O_2O_3$  to line  $O_3C$  for point  $C$  being the roller center. When the values of  $R_1$ ,  $R_2$ ,  $R_3$  and  $c$  are given, then from  $\triangle K_1K_2K_3$  (or  $\triangle K_1K_3K_4$ ) and the cosine law, the circular-arc angles  $\gamma_1$ ,  $\gamma_2$  and  $\gamma_3$  can be determined by

$$\gamma_1 = 2 \cos^{-1} \left[ \frac{c^2 + (R_2 - R_1)^2 - (R_2 - R_3)^2}{2c(R_2 - R_1)} \right] \quad (19)$$

$$\gamma_2 = \cos^{-1} \left[ \frac{(R_2 - R_1)^2 + (R_2 - R_3)^2 - c^2}{2(R_2 - R_1)(R_2 - R_3)} \right] \quad (20)$$

$$\gamma_3 = 2 \cos^{-1} \left[ \frac{c^2 + (R_2 - R_3)^2 - (R_2 - R_1)^2}{2c(R_2 - R_3)} \right] \quad (21)$$

It should be noted that the geometric relation of  $\gamma_1 + 2\gamma_2 + \gamma_3 = 360^\circ$  must be satisfied.

The equivalent linkage of this disk cam mechanism is a four-bar linkage whose coupler connects the circular center of one of the four circular-arc profiles and the roller center. The equivalent linkage corresponding to each circular-arc profile is an invariant one (i.e. its link lengths are invariant). The disk cam mechanism can thus be successively replaced by four invariant equivalent linkages (with different constant link lengths) as the circular-arc cam rotates a complete cycle. However, when considering a special situation that the contact point between the cam and the follower is point  $A_{23}$  (or one of the remaining three points of tangency), the equivalent four-bar linkages at that instant are shown in Fig. 3(b). It can be observed that two equivalent four-bar linkages  $O_2K_2CO_3$  and  $O_2K_3CO_3$  simultaneously exist at that instant. For clarity of illustration, the four-bar linkage  $O_2K_2CO_3$  consists of links 1,  $2a$ ,  $3a$  and  $4a$ , and the

four-bar linkage  $O_2K_3CO_3$  consists of links 1, 2b, 3b and 4b. The links 3a and 3b overlap with each other. The couplers 4a and 4b, also overlapping with each other, are collinear with the common normal at the contact point  $A_{23}$  that passes through points  $K_2$ ,  $K_3$  and C at that instant.

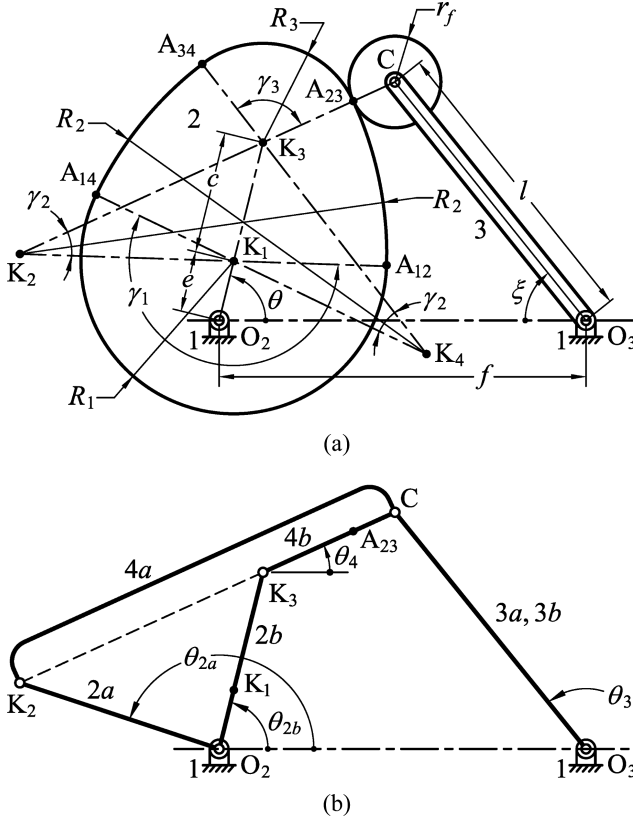


**Fig. 3.** Illustration of a disk cam mechanism with a circular-arc cam and an oscillating roller follower and its equivalent four-bar linkages.

For the four-bar linkages shown in Fig. 3(b), their link lengths are  $r_1 = O_2O_3 = f$ ,  $r_{2a} = O_2K_2$ ,  $r_{2b} = O_2K_3 = e + c$ ,  $r_{3a} = r_{3b} = O_3C = l$ ,  $r_{4a} = K_2C = R_2 + r_f$  and  $r_{4b} = K_3C = R_3 + r_f$ . The angular positions of links,  $\theta_{2a}$ ,  $\theta_{2b}$ ,  $\theta_3$ , and  $\theta_4$ , are measured counterclockwise from line  $O_2O_3$ . From  $\triangle O_2K_2K_3$  and the cosine law, the link length of  $r_{2a}$  can be further determined by

$$r_{2a} = O_2K_2 = \sqrt{(e+c)^2 + (R_2 - R_3)^2 - 2(e+c)(R_2 - R_3)\cos\left(\frac{\gamma_3}{2}\right)} \quad (22)$$

From  $\triangle O_2K_3C$  and the cosine law, the distance  $O_2C$  at that instant can be determined by

$$O_2C = \sqrt{(e+c)^2 + (R_3 + r_f)^2 + 2(e+c)(R_3 + r_f) \cos\left(\frac{\gamma_3}{2}\right)} \quad (23)$$

Hence, from  $\triangle O_2K_3C$ ,  $\triangle O_2O_3C$  and the cosine law, the values of the cam rotation angle  $\theta$  and the angular position of the follower  $\xi$  at that instant can be determined by

$$\theta = \cos^{-1} \left[ \frac{(e+c)^2 + (O_2C)^2 - (R_3 + r_f)^2}{2(e+c)(O_2C)} \right] + \cos^{-1} \left[ \frac{f^2 + (O_2C)^2 - l^2}{2f(O_2C)} \right] \quad (24)$$

$$\xi = \cos^{-1} \left[ \frac{f^2 + l^2 - (O_2C)^2}{2fl} \right] \quad (25)$$

Then, the values of  $\theta_{2a}$  and  $\theta_{2b}$  at that instant can be determined by

$$\begin{cases} \theta_{2a} = \theta + \cos^{-1} \left[ \frac{(e+c)^2 + r_{2a}^2 - (R_2 - R_3)^2}{2(e+c)r_{2a}} \right] \\ \theta_{2b} = \theta \end{cases} \quad (26)$$

Also, the values of  $\theta_3$  and  $\theta_4$  at that instant can be determined by

$$\theta_3 = 180^\circ - \xi \quad (27)$$

$$\theta_4 = \theta - \frac{\gamma_3}{2} \quad (28)$$

It is known that when the circular-arc cam rotates a complete cycle, the follower will instantaneously undergo non-continuous accelerations and infinite jerks as the circular-arc cam is in contact with the follower at one of the four points of tangency (i.e. points  $A_{12}$ ,  $A_{14}$ ,  $A_{34}$ , and  $A_{23}$ ) successively, although the velocity of the follower can be continuous at those instants. A practical example is given to evaluate such phenomena. A circular-arc cam with  $R_1 = 50$  mm,  $R_2 = 120$  mm,  $R_3 = 32.5$  mm,  $c = 40$  mm and  $e = 20$  mm is designed to drive an oscillating roller follower with  $l = 100$  mm and  $r_f = 15$  mm, while the center distance is  $f = 120$  mm. From Eqs. (19)–(21), the circular-arc angles are  $\gamma_1 = 203.832^\circ$ ,  $\gamma_2 = 26.570^\circ$  and  $\gamma_3 = 103.028^\circ$ . Such a disk cam mechanism is proportionally shown in Fig. 3(a). The circular-arc cam is specified to rotate counterclockwise with  $\omega_2 = 1$  rad/s,  $\alpha_2 = 0$  and  $\zeta_2 = 0$ . The angular position of the follower,  $\xi$ , in a complete cam rotation cycle is shown in Fig. 4(a), while its corresponding angular velocity  $\dot{\xi}$ , acceleration  $\ddot{\xi}$  and jerk  $\dddot{\xi}$  obtained through numerical differentiation, are shown in Figs. 4(b)–(d). The follower obviously undergoes non-continuous accelerations and infinite jerks when  $\theta = 31.076^\circ$ ,  $76.168^\circ$ ,  $118.6^\circ$  and  $354.043^\circ$ . When the contact point between the cam and the follower is point  $A_{23}$  as shown in Fig. 3(a), link lengths of the equivalent four-bar linkages shown in Fig. 3(b) are  $r_1 = f = 120$  mm,  $r_{2a} = O_2K_2 = 68.716$  mm [from Eq. (22)],  $r_{2b} = O_2K_3 = e + c = 60$  mm,  $r_{3a} = r_{3b} = O_3C = l = 100$  mm,  $r_{4a} = K_2C = R_2 + r_f = 135$  mm and  $r_{4b} = K_3C = R_3 + r_f = 47.5$  mm. At that instant, from Eqs. (24)–(28),  $\theta = 76.168^\circ$ ,  $\xi = 51.328^\circ$ ,  $\theta_{2a} = 161.538^\circ$ ,  $\theta_{2b} = 71.168^\circ$ ,  $\theta_3 = 128.672^\circ$  and  $\theta_4 = 24.654^\circ$  can be obtained. For the equivalent four-bar linkage  $O_2K_2CO_3$  (consisting of links 1, 2a, 3a and 4a), its angular velocities, accelerations and jerks at that instant, calculated by using Eqs. (1)–(6), are

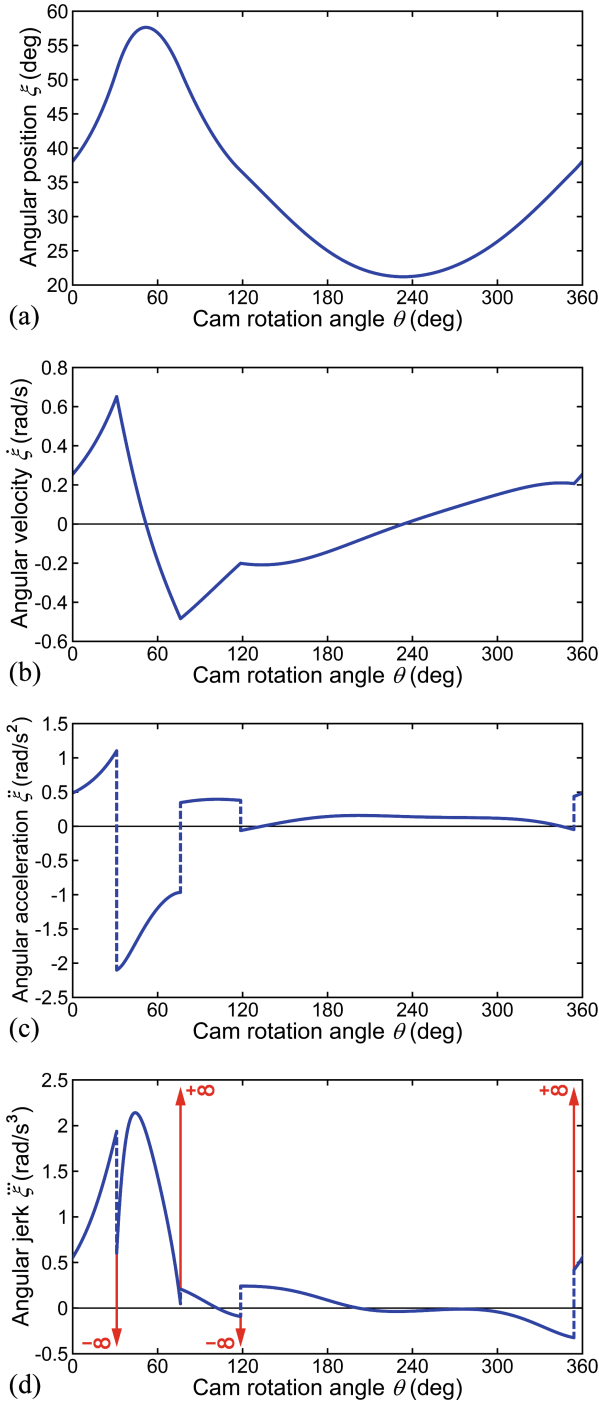


**Fig. 4.** Follower position, velocity, acceleration and jerk for a practical example.

$$\begin{cases} \omega_{3a} = 0.484 \text{ rad/s}, & \omega_{4a} = 0.285 \text{ rad/s} \\ \alpha_{3a} = -0.346 \text{ rad/s}^2, & \alpha_{4a} = 0.242 \text{ rad/s}^2 \\ \zeta_{3a} = -0.209 \text{ rad/s}^3, & \zeta_{4a} = 0.070 \text{ rad/s}^3 \end{cases} \quad (29)$$

For the equivalent four-bar linkage  $O_2K_3CO_3$  (consisting of links 1, 2b, 3b and 4b), its angular velocities, accelerations and jerks at that instant, calculated by using Eqs. (1)–(6), are

$$\begin{cases} \omega_{3b} = 0.484 \text{ rad/s}, & \omega_{4b} = -1.033 \text{ rad/s} \\ \alpha_{3b} = 0.966 \text{ rad/s}^2, & \alpha_{4b} = 0.018 \text{ rad/s}^2 \\ \zeta_{3b} = -0.047 \text{ rad/s}^3, & \zeta_{4b} = -3.099 \text{ rad/s}^3 \end{cases} \quad (30)$$

It is found that  $\omega_{3a} = \omega_{3b} = 0.484 \text{ rad/s}$  and  $\alpha_{3a} \neq \alpha_{3b}$ , which agree with the situations shown in Figs. 4(b) and (c) that the follower undergoes a non-continuous acceleration, although its velocity can be continuous at that instant. However, it is also found that  $\zeta_{3a} = -0.209 \text{ rad/s}^3$  and  $\zeta_{3b} = -0.047 \text{ rad/s}^3$  are finite values, which cannot correctly reflect an instantaneously infinite follower jerk as that shown in Fig. 4(d).

In addition, if a special case of  $R_1 = R_2 = R_3$  and  $c = 0$  is given, the circular-arc cam will degenerate to an eccentric circular cam while points  $K_1$ ,  $K_2$ ,  $K_3$  and  $K_4$  will coincide with the circular center of the eccentric circular cam. It is known that an eccentric circular cam mechanism has an invariant equivalent linkage that can completely duplicate the motion transmission between the cam and the follower [3]. Such an invariant equivalent linkage can give correct values of angular velocity, acceleration and jerk for all instants. As compared with the eccentric circular cam profile having constant curvature, the curvature of the circular-arc cam is suddenly changed at the points of tangency of each two adjacent circular arcs. As the circular-arc cam and its follower are in contact at such a point of tangency, the suddenly changed curvature of the cam profile is not considered in sudden link-length variations of the equivalent linkages. Thus, the two equivalent four-bar linkages simultaneously existing at that instant are both not able to correctly reflect an infinite jerk of the follower. For an ordinary disk cam profile with continuously varying curvature, the equivalent linkages corresponding to two infinitesimally closed profile points in contact with the follower cannot exactly have identical link lengths. Therefore, for most disk cam mechanisms, it can be deduced that their equivalent four-bar linkages should not be able to give a correct value of jerk because the continuously varying curvature of the cam profiles is not considered in continuous link-length variations of the equivalent linkages.

## 5 Conclusions

Kinematic analysis for two types of classical direct-contact mechanisms has been presented in this paper. For the discussed planar gear mechanism with a pair of involute spur gears, the configuration of its equivalent four-bar linkage is a permanently invariant crossed quadrilateral at all instants. It is found that the equivalent four-bar linkage for the planar gear mechanism is not able to give a correct value of jerk, unless



the angular velocity ratio between the two mating gears is exactly negative one. For the discussed disk cam mechanism with a circular-arc cam and an oscillating roller follower, it can be successively replaced by four invariant equivalent linkages (with different constant link lengths) as the circular-arc cam rotates a complete cycle. When the circular-arc cam is in contact with its follower at a point of tangency of two adjacent circular arcs, the two equivalent four-bar linkages simultaneously existing at that instant are both not able to correctly reflect an infinite jerk of the follower, because the suddenly changed curvature of the cam profile is not considered in sudden link-length variations of the equivalent linkages. The two presented case studies can give demonstrations for understanding the inequivalence of the direct-contact mechanisms and their equivalent four-bar linkages in the aspect of jerk analysis. Therefore, the results presented in this paper should verify that for most three-link direct-contact mechanisms, their ‘representative equivalent four-bar linkages’ (with a coupler connecting the centers of curvature of the driving and driven links) cannot be used to perform the jerk analysis.





**Acknowledgement.** The authors are grateful to the Ministry of Science and Technology of Taiwan for supporting this research under Grant No. MOST-107-2221-E-019-031.

## References

1. McPhate, A.J., Daniel Jr., L.R.: A kinematic analysis of four-bar equivalent mechanism for plane-motion direct-contact mechanisms. In: *Proceedings of the Seventh Conference on Mechanisms*, pp. 61–65. Purdue University, West Lafayette (1962)
2. Hall Jr., A.S.: *Kinematics and Linkage Design*. Waveland Press, Prospect Heights (1961)
3. Hartenberg, R.S., Denavit, J.: *Kinematic Synthesis of Linkages*. McGraw-Hill, New York (1964)
4. Grosjean, J.: *Kinematics and Dynamics of Mechanisms*, pp. 75–78, 82–83, 111–121, 267–285. McGraw-Hill, New York (1991)
5. Martin, G.H.: *Kinematics and Dynamics of Machines*, 2nd edn. McGraw-Hill, New York (1982)
6. Yan, H.S.: *Mechanisms—Theory and Applications*. McGraw-Hill, New York (2016)



# Dynamic Analysis and Motion Simulation of the 3 DOFs Waist Mechanism for Humanoid Robots

Marko Penčić<sup>(✉)</sup> , Boris Brkić , Maja Čavić ,  
and Milan Rackov 

Faculty of Technical Sciences, University of Novi Sad,  
Trg Dositeja Obradovića 6, 21000 Novi Sad, Serbia  
mpencic@uns.ac.rs

**Abstract.** The paper presents the dynamic analysis and motion simulation of the waist mechanism meant for humanoids. The proposed waist mechanism has a total of 3 DOFs, allowing movements of the robot's upper trunk around the pitch, roll and yaw axes. Within the dynamic analysis, the decomposition of the waist mechanism is performed and for each link of the mechanism, motion equations are formed. Reactions in the mechanism links are determined by using D'Alembert's principle and based on those, the equations for calculating of the driving forces are defined. Finally, the dynamic model of the waist mechanism was formed and a motion simulation for several scenarios was performed. Based on the analysis of the results, it was concluded that the waist mechanism requires small driving torques and therefore less and cheaper actuators, which is an important advantage of this solution.

**Keywords:** Humanoid robot · Waist mechanism · Dynamic analysis · Motion simulation

## 1 Introduction

Today there is an increasing number of humanoid robots that have at least one joint in the trunk region. Accordingly, bipedal walking robots with 1 DOF trunks for movements left-right, require significantly less energy for walking than robots with rigid trunk [1]. In addition, the movable abdomen allows the upper body to move without moving the pelvis, wherefore such robots have a larger assortment of movements and a larger workspace for manipulation of objects. Also, the motion of a robot with a multi-joint trunk is more natural and human-like. However, all of this gets even more important if one takes into account the practical application of robots in an unstructured environment. Therefore, special attention was paid to the development of a multi-joint waist mechanism.

---

Waist mechanism presented in this paper is patent pending.

The paper presents the dynamic analysis of a 3 DOFs waist mechanism that represents a new solution used in the redesign of existing 6 DOFs lumbar structure [2] of the SARA robot – Fig. 1 and Table 1. Some advanced features of the robot are shown in [3–5]. The goal of the redesign is to extend the assortment of movements and the range of motion of the robot trunk.

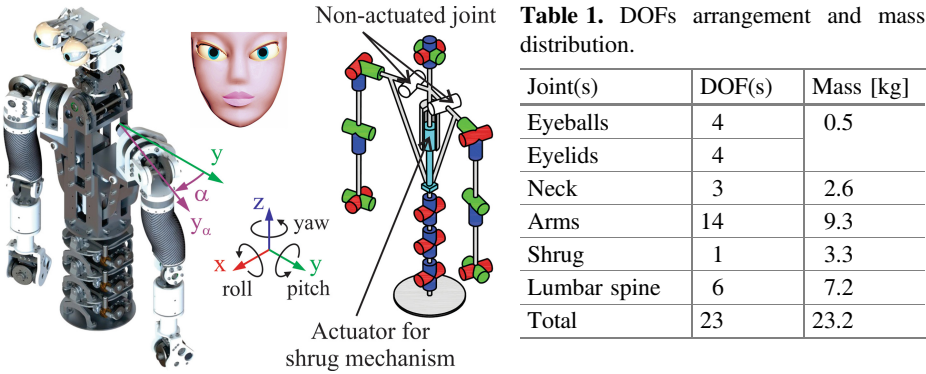


**Fig. 1.** The social humanoid robotic platform SARA and its kinematic structure.

### 1.1 The Human Trunk

According to [6], the human trunk consists of three segments – Fig. 2(a): the upper trunk representing the region of the chest part of the body along the thoracic vertebrae T1–T12, the middle trunk or the abdomen representing the lumbar region of the body along the lumbar vertebrae L1–L5 and lower trunk representing the pelvis region along the sacrum S1–S5. It should be noted that in humanoid robotics, the term “middle trunk”, refers to a robot waist that represents a moving platform/structure with one or more joints whose axes of rotation intersect in one point – the so-called waist joint, allowing the robot to move the upper trunk without moving the lower trunk.

The initial movements of the trunk are: flexion and extension or trunk bending forward and backward, respectively – Fig. 2(b), left and right lateral flexion or side bending of the trunk – Fig. 2(c) and left and right axial rotation of the trunk – Fig. 2(d). The biological aspects of the spine, the ranges of motion and the angular velocities of the lumbar spine region for adult persons aged 20 to 29 years are discussed in [7].

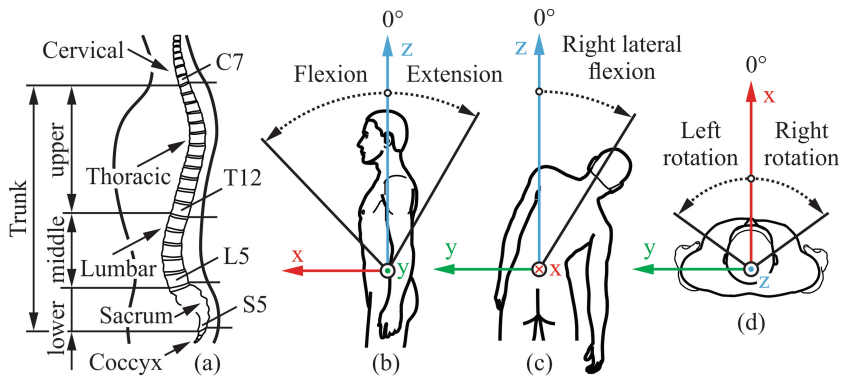


**Fig. 2.** The human trunk (a) and initial movements: (b) flexion and extension, (c) left and right lateral flexion and (d) left and right axial rotation.

## 2 State of the Art

By analyzing available literature, we found that waist joint/mechanisms usually have 1–3 DOFs allowing the robot to move the upper trunk around the pitch, roll and yaw axes, respectively. Therefore, robots that are able to move the thorax without moving the lower trunk – pelvis, by activating the middle trunk – waist joint/mechanism, are: Arash – social robot with total of 15 DOFs designed to support and encourage children with cancer in hospital environment, actuated by DC, linear and servo motors via gear mechanisms [8], ASIMO – versatile autonomous machine with total of 57 DOFs designed to cooperate with people in an unstructured environment, actuated by custom made motors integrated with a ballscrew [9], COMAN – Compliant huMANoid robot with total of 25 DOFs, actuated by passive compliance actuators based on the serial elastic actuation – SEA [10], DYROS-JET – humanoid robot with total of 32 DOFs developed for general tasks in the industry [11] by upgrading the robotic platform THORMANG, actuated by Robotis Dynamixel PRO actuators [12], Hydra – humanoid robot with total of 40 DOFs, actuated by electro-hydrostatic actuators – EHA [13], HRP-5P – electrically actuated humanoid with total of 37 DOFs, with high-power and wide-range joints [14], Hubo KHR-4 – humanoid robot with total of 41 DOFs, actuated by Maxon brushless DC motors through high-power harmonic drive gearboxes [15], LOLA – full-size humanoid with total of 25 DOFs, designed for the research and realization of human-like walking, actuated by high-performance permanent magnet synchronous motors – PMSM, through harmonic drive gears and planetary roller screws, respectively [16], MAHRU-Z – robotic platform with total of 35 DOFs, actuated by DC servo motors via harmonic drive gears [17], Reem-B – research platform with total of 40 DOFs, actuated by brushless DC motors through harmonic drives [18], SURALP – full-body humanoid robot with total of 29 DOFs for bipedal locomotion research, actuated by the DC motors via belt drives and harmonic drive gears, respectively [19], TORO – TORque-controlled humanoid ROBot with total of 27 DOFs for evaluating torque based control approaches, actuated by RoboDrive brushless DC motors through harmonic drive gears [20], WALK-MAN – the humanoid

platform with 29 DOFs excluding hands and neck, developed for physical interaction and manipulation with objects in an unstructured environment, actuated by SEA drives [21], YiRen – experimental robotic platform with total of 23 DOFs for research on intelligent robotics, whereby the waist is actuated by AC motors via differential mechanisms, linkage mechanisms, cable and compliant elements, respectively [22].

By analyzing these robots and based on available data from [14, 16, 20], we concluded that driving torques for actuation of waist joint/mechanisms have high values, namely:  $100 \div 211$  Nm for yaw rotation,  $147 \div 450$  Nm for roll rotation and up to 450 Nm for pitch rotation. Therefore, the power transmission from the actuator – motor with integrated gearhead, to the output link of the waist joint/mechanism is performed through an additional high-power gear reducer with a high reduction ratio, such as multi-stage epicyclic gearboxes, planetary roller screws and high-power harmonic drives. In addition to the high load capacity, the advantage of these mechanisms is high efficiency, compact design and low backlash ensuring high positioning accuracy and repeatability of the robot movement, which is of great importance for motion control [23].

Based on all this, we propose a waist mechanism of a special kinematic design that requires small actuators, has low backlash, high efficiency, small dimensions and lower price than the currently available low backlash mechanisms.

### 3 Dynamic Analysis

Figure 3(a) shows the kinematic scheme of a 3 DOFs waist mechanism consisting of three interconnected cylindrical segments: the bottom disc – immovable link 1, middle and upper discs – movable links 6 and 8, respectively. On link 8, the body of a robot is fixed – link 11. Links 1, 6, 8 are coupled with three 4-bar linkage mechanisms of which two are spatial linkage mechanisms for pitch and roll rotations, while the third is a planar linkage mechanism for yaw rotation. Considering the links configuration – see Fig. 3(a), spatial linkage mechanisms can work separately or both together. The rotation of link 6 relative to link 1 around the axis defined by the points R-S and P-Q is allowed by spatial linkage mechanisms 1c, 4, 5, 6 and 1a, 2, 3, 6 respectively, while the rotation of link 8 relative to link 6 around the axis defined by the points  $O_1$ - $O_2$  is allowed by the planar linkage mechanism 6a, 9, 10, 8. The kinematic structure of the waist mechanism has been thoroughly analysed in [7].

The goal of dynamic analysis is to determine driving forces for actuating input links 2, 4, 9 respectively. Figure 3(b) shows the forces acting on waist mechanism links. D'Alembert's principle is used to determine the reactions in the links of the mechanism, while the forces analysis is performed by the decomposition method. Based on principal dynamic laws, equations of motion are formed for each link of the mechanism, after which they are projected onto the axes of the fixed coordinate system Oxyz. In addition, the masses and moments of the inertia for all the links of the mechanism are negligible in relation to the mass and moments of the robots body inertia – link 11.

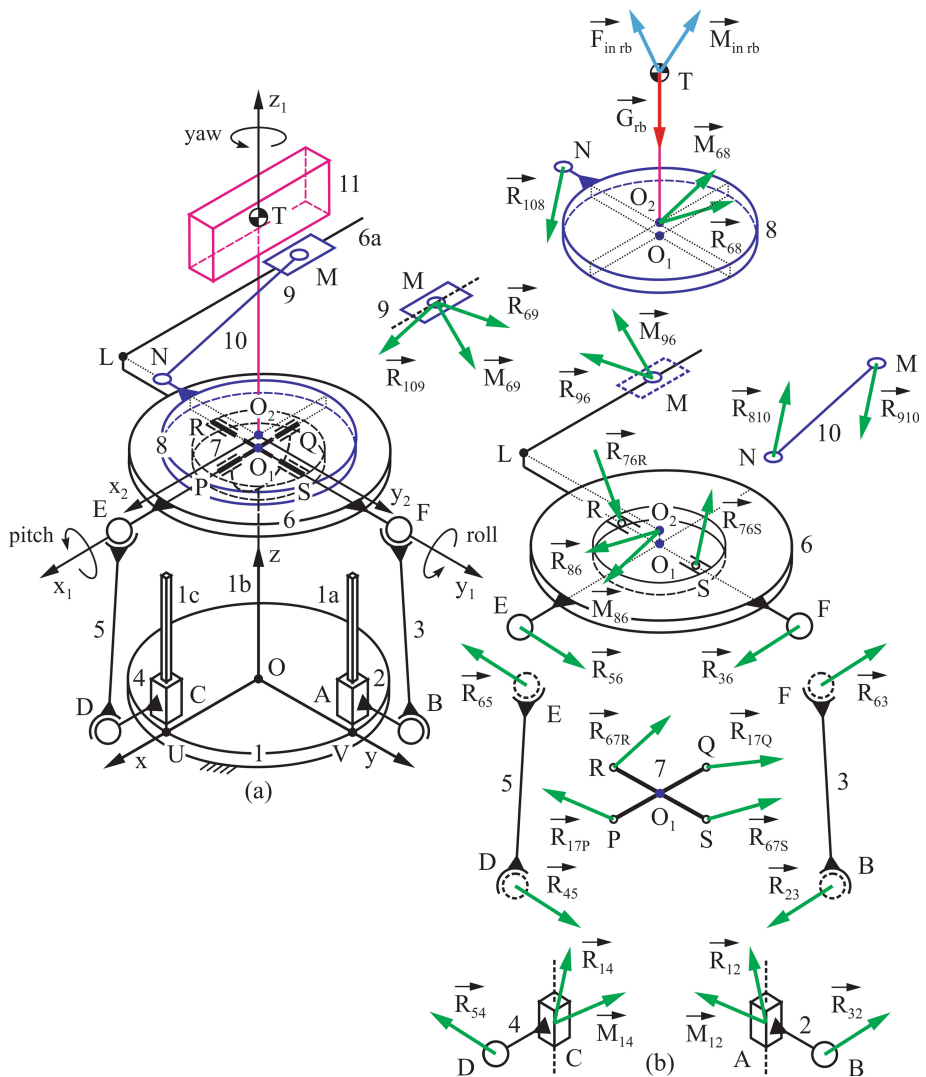


**Fig. 3.** The 3 DOFs waist mechanism: (a) initial position and (b) forces acting on mechanism links.

The following approach to mark the reaction forces is used:

$$\vec{R}_{ij} = \begin{bmatrix} X_{ij} \\ Y_{ij} \\ Z_{ij} \end{bmatrix} \quad (1)$$

where:  $\vec{R}$  represents a reaction force in joint whose components are  $\vec{X}_{ij}$ ,  $\vec{Y}_{ij}$ ,  $\vec{Z}_{ij}$  by which the indices  $ij$  indicate that a link  $i$  acts upon the link  $j$  by force  $\vec{R}$ . Also,  $\vec{R}_{ij} = -\vec{R}_{ji}$ .

If the force  $\vec{R}_{ij}$  acts in point L and forms the moment for point K, the following marking is used:

$$\vec{M}(\vec{R}_{ij}, K) = \vec{r}_L^K \times \vec{R}_{ij} = \begin{bmatrix} Z_{ij}(y_L - y_K) - Y_{ij}(z_L - z_K) \\ X_{ij}(z_L - z_K) - Z_{ij}(y_L - y_K) \\ Y_{ij}(x_L - x_K) - X_{ij}(y_L - y_K) \end{bmatrix} \quad (2)$$

where:  $\vec{M}(\vec{R}_{ij}, K)$  represents the moment of force  $\vec{R}_{ij}$  for point K, and  $\vec{r}_L^K$  is the position vector of point L relative to point K.

If a torque exists as a joint reaction, the following marking is used:

$$\vec{M}_{ij} = \begin{bmatrix} M_{xij} \\ M_{yij} \\ M_{zij} \end{bmatrix} \quad (3)$$

where:  $\vec{M}$  represents reaction torque in the joint whose components are  $\vec{M}_{xij}, \vec{M}_{yij}, \vec{M}_{zij}$  by which the indices  $ij$  indicate that a link  $i$  acts on the link  $j$  by torque  $\vec{M}$ . Also,  $\vec{M}_{ij} = -\vec{M}_{ji}$ .

After decomposition for each link of the mechanism, the vector equations are formed. First of all, for link 8:

$$\vec{R}_{108} + \vec{R}_{68} + \vec{G}_{rb} + \vec{F}_{inrb} = 0 \quad (4)$$

$$\vec{M}(\vec{R}_{108}, T) + \vec{M}_{68} + \vec{M}(\vec{R}_{68}, T) + \vec{M}_{inrb} = 0 \quad (5)$$

where:  $\vec{G}_{rb}$  represents the weight of the robot body – link 11,  $\vec{F}_{inrb}$  represents the inertial force of link 11, while  $\vec{M}_{inrb}$  represents the inertial moment of link 11, and T is the mass center of link 11.

For link 9:

$$\vec{R}_{109} + \vec{R}_{69} = 0 \quad (6)$$

$$\vec{M}_{69} = 0 \quad (7)$$

For link 10:

$$\vec{R}_{810} + \vec{R}_{910} = 0 \quad (8)$$

$$(\vec{R}_{910}, N) = 0 \quad (9)$$

For link 6:

$$\vec{R}_{56} + \vec{R}_{36} + \vec{R}_{86} + \vec{R}_{76R} + \vec{R}_{76S} + \vec{R}_{96} = 0 \quad (10)$$

$$(\vec{R}_{56}, O_2) + \vec{M}(\vec{R}_{36}, O_2) + \vec{M}(\vec{R}_{76R}, O_2) + \vec{M}(\vec{R}_{76S}, O_2) + \vec{M}(\vec{R}_{96}, O_2) + \vec{M}_{96} + \vec{M}_{86} = 0 \quad (11)$$

For link 7:

$$\vec{R}_{67R} + \vec{R}_{67S} + \vec{R}_{17P} + \vec{R}_{17Q} = 0 \quad (12)$$

$$(\vec{R}_{67R}, O_2) + \vec{M}(\vec{R}_{67S}, O_2) + \vec{M}(\vec{R}_{17P}, O_2) + \vec{M}(\vec{R}_{17Q}, O_2) = 0 \quad (13)$$

For link 5:

$$\vec{R}_{65} + \vec{R}_{45} = 0 \quad (14)$$

$$\vec{M}(\vec{R}_{45}, F) = 0 \quad (15)$$

For link 4:

$$\vec{R}_{54} + \vec{R}_{14} = 0 \quad (16)$$

$$\vec{M}(\vec{R}_{54}, D) + \vec{M}_{14} = 0 \quad (17)$$

For link 3:

$$\vec{R}_{63} + \vec{R}_{23} = 0 \quad (18)$$

$$\vec{M}(\vec{R}_{23}, C) = 0 \quad (19)$$

For link 2:

$$\vec{R}_{32} + \vec{R}_{12} = 0 \quad (20)$$

$$\vec{M}(\vec{R}_{32}, D) + \vec{M}_{12} = 0 \quad (21)$$

After projecting Eqs. (4)–(21) to the axes of the fixed coordinate system Oxyz, a system of algebraic equations is obtained, based on which the components of the link reactions are determined:

$$\vec{R}_{108}, \vec{R}_{68}, \vec{R}_{910}, \vec{R}_{69}, \vec{R}_{56}, \vec{R}_{36}, \vec{R}_{76R}, \vec{R}_{76S}, \vec{R}_{45}, \vec{R}_{23}, \vec{R}_{14}, \vec{R}_{12}, \vec{R}_{17P}, \vec{R}_{17Q}, \\ \vec{M}_{69}, \vec{M}_{12}, \vec{M}_{14}, \vec{M}_{68}$$

Finally, the intensities of the driving forces that act to input links 9, 4, 2 respectively, can be determined. First of all, for link 9:

$$F_{d9} = \vec{R}_{69} \vec{\kappa}_1 \quad (22)$$



$$\vec{\kappa}_1 = [R2] \begin{bmatrix} 1 \\ 0 \\ 0 \end{bmatrix} \quad (23)$$

$$[R2] = [R_{\varphi_2, x_1}] [R_{\psi_2, u_b}] = \begin{bmatrix} 1 & 0 & 0 \\ 0 & \cos \varphi_2 & -\sin \varphi_2 \\ 0 & \sin \varphi_2 & \cos \varphi_2 \end{bmatrix} \begin{bmatrix} \cos \psi_2 & 0 & -\sin \psi_2 \\ 0 & 1 & 0 \\ \sin \psi_2 & 0 & \cos \psi_2 \end{bmatrix} \quad (24)$$

where:  $\vec{\kappa}_1$  represents the unit vector in the direction of guide 6a, while  $\varphi_2$  and  $\psi_2$  represent the rotation angles of link 6 – see Fig. 2(b) from [7].

Driving force for link 4:

$$F_{d4} = \vec{R}_{14} \vec{k} \quad (25)$$

where:  $\vec{k} = (0, 0, 1)$  represents the unit vector in the direction of guide 1c.

Driving force for link 2:

$$F_{d2} = \vec{R}_{12} \vec{k} \quad (26)$$

where:  $\vec{k} = (0, 0, 1)$  represents the unit vector in the direction of guide 1a.

## 4 Motion Simulation and Results

Figure 4 shows the position of the center of mass T of the robot upper body – link 11, whose mass is  $m_{11} = 16$  kg without lumbar structure – see Table 1, depending on the pose of the robot arms: the right arm is extended laterally, and left arm in front of the robot body – Fig. 4(a), both arms in front of the body – Fig. 4(b), right arm above, and left arm in front of the body – Fig. 4(c) and both arms above the robot body – Fig. 4(d).

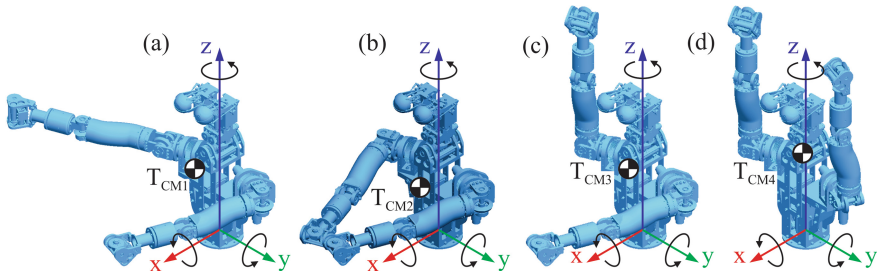


**Fig. 4.** Position of the mass center of the robot upper body depending on the arms pose: (a) the right arm is extended laterally, and left arm in front of the robot body:  $T_{CM1}(54.2; -47.8; 222.3)$  mm, (b) both arms in front of the body:  $T_{CM2} = (74.6; 0; 219.1)$  mm, (c) right arm above, and left arm in front of the body:  $T_{MC3}(41.6; -11.9; 260.4)$  mm and (d) both arms above the robot body:  $T_{MC4}(8.3; 0; 301.9)$  mm.

Based on the dynamic analysis of the waist mechanism, the dynamic model was formed. Simulation of waist mechanism for initial movements from Fig. 2(b-d), depending on the range of motion and pose of the robot arms – Fig. 4, was performed. The law of motion adopted for the driving links is a fifth-order polynomial, while for generating all of the movements the adopted time is 1 s. Considering the dimensions of the lumbar structure that is being reconstructed [2], the input geometric parameters are prescribed and given in Tables 2a and 2b). In addition, based on the prescribed range of initial movements from Fig. 5(a), by inverse kinematics the total stroke of the driving links 2, 4, 9 are determined, as shown in Fig. 5(b). Accordingly, for a flexion movement of  $40^\circ$ , the total stroke of the input link 4 is 46.48 mm, while for the movement of the extension of  $25^\circ$ , the total stroke of the input link 4 has a value of 31.97 mm. For the lateral flexion movement of  $30^\circ$ , the total stroke of the input link 2 is 36.9 mm, while for the movement of the axial rotation of  $20^\circ$ , the total stroke of the input link 9 amounts 18 mm. Finally, simulation of the waist mechanism was performed by using the MATLAB software.

**Table 2a.** The waist mechanism input geometric parameters.

$AB = CD$ [mm]	$BF = DE$ [mm]	$A_0V = C_0U$ [mm]	$MN$ [mm]	$M_0L$ [mm]	$OV = OU$ [mm]	$OO_1$ [mm]
15	90	100	40	40	60	190

**Table 2b.** The waist mechanism input geometric parameters.

$O_1O_2$ [mm]	$O_2L$ [mm]	$O_2N$ [mm]	$O_1F = O_1E$ [mm]	$O_1R = O_1S$ [mm]	$O_1P = O_1Q$ [mm]
10	60	50	75	25	25

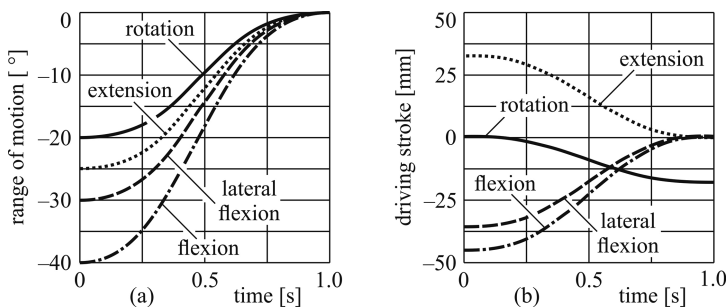


**Fig. 5.** The prescribed range of initial movements (a) and total stroke of the driving links (b).

Figures 6, 7, 8 and 9 show the results of the dynamic analysis, i.e., the time histories of the driving forces – to the left, and the reaction forces in the input links – to the right, for the initial movements of flexion, extension, lateral flexion and rotation depending on the robot arms pose – four cases from Fig. 4. In Table 3 are given the

maximum force values on the input links 2, 4, 9 respectively. Accordingly, the maximum value of the driving force on the input link 2 is 465.8 N, on the link 4 it is 792.4 N, while for link 9, the maximum value of the driving force is only 3.6 N. However, the reaction force on the link 9 is significantly higher, even 211.8 N, which is not the case for the other two links.

If the driving link 4 with guide 1c is realized as a ballscrew mechanism – see Fig. 3 (a), then link 4 represents a ballscrew nut, and guide 1c represents a ballscrew shaft. Accordingly, the driving torque for actuating the ballscrew mechanism is determined by:

$$T_4 = \frac{F_{d4} p_{bs}}{2\pi \eta_{bs}} \quad (27)$$

where:  $F_{d4}$  represents a force acting on a ballscrew, while  $p_{bs}$  is a thread pitch, and  $\eta_{bs}$  represents a ballscrew efficiency.

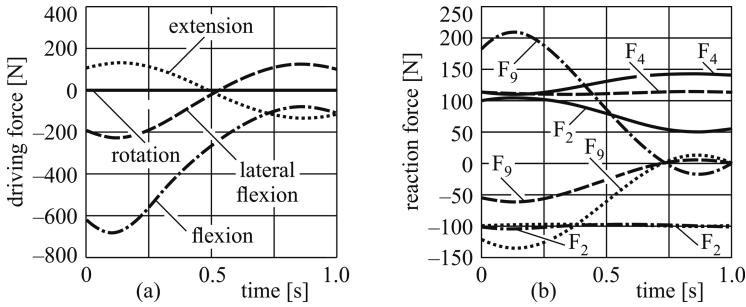


**Fig. 6.** The waist mechanism time histories for  $T_{MC1}$ : driving forces (a) and reaction forces (b).

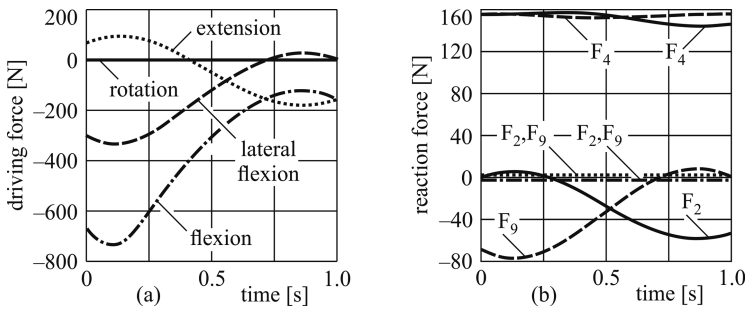


**Fig. 7.** The waist mechanism time histories for  $T_{MC2}$ : driving forces (a) and reaction forces (b).

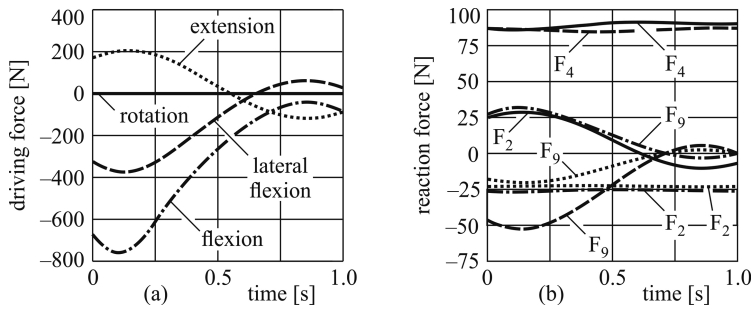


**Fig. 8.** The waist mechanism time histories for  $T_{MC3}$ : driving forces (a) and reaction forces (b).

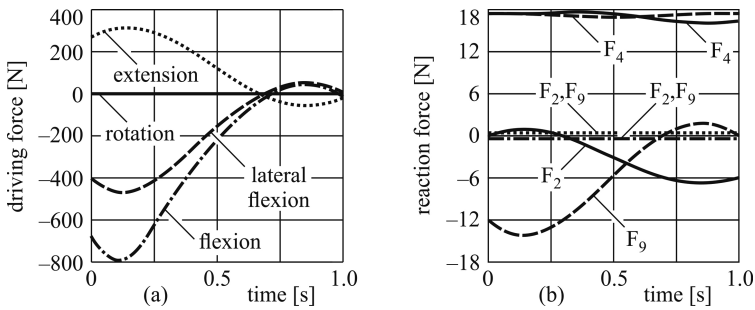


**Fig. 9.** The waist mechanism time histories for  $T_{MC4}$ : driving forces (a) and reaction forces (b).

**Table 3.** Maximal force values on the input links 2, 4, 9 for initial movements – Fig. 2(b–d), depending on the range of motion – Fig. 5(a) and the pose of the robot arms – Fig. 4; note: driving forces  $F$  [N] are marked with “\*”, while other forces represent reaction forces.

Type of movement	Case $T_{CM1}$			Case $T_{CM2}$			Case $T_{CM3}$			Case $T_{CM4}$		
	$F_2$	$F_4$	$F_9$	$F_2$	$F_4$	$F_9$	$F_2$	$F_4$	$F_9$	$F_2$	$F_4$	$F_9$
Flexion	102.8	688.5*	211.8	0	734.3*	0	25.4	759.3*	32	0	792.4*	0
Extension	101.2	135.9*	134.7	0	179.2*	0	25.1	204.3*	20.3	0	321.8*	0
Lateral flexion	228.2*	114.7	61.8	327.9*	156.1	75	368.9*	87.2	52.7	465.8*	17.3	14.1
Axial rotation	104.2	142.8	3.4*	58.5	157.1	3.6*	28.7	91.5	1.26*	6.7	17.5	0.13*

For example, for ballscrew R10-02.5T2-RSIT [24] with single thread whose shaft diameter is 9.9 mm, thread pitch and ballscrew efficiency are 2.5 mm and 96%, respectively, while dynamic load rating and axial play amounts 1.78 kN and 0.04 mm, respectively. By inserting the corresponding values in Eq. (27), taking into account the maximum value of the force on the input link 4, the driving torque for the actuation of link 4 is only 331.5 mNm, which allows the selection of small actuators.

## 5 Conclusion

In this paper, dynamic analysis of a 3 DOFs waist mechanism for humanoids is performed. The proposed waist mechanism consists of three cylindrical segments that are interconnected and coupled with three 4-bar linkage mechanisms. The first two are spatial linkage mechanisms for generating pitch and roll movements – separately and/or both together, while the last one is a planar linkage mechanism for yaw movements. Within the dynamic analysis, the decomposition of the waist mechanism is performed and for each link of the mechanism, the motion equations are formed. Reactions in the mechanism links are determined by using the D'Alembert's principle and the equations for determining driving forces are defined. Based on all of the above, the dynamic model is formed and motion simulation for several scenarios is performed, depending on the type of movement, the range of motion and the pose of the robot arms. By analysing the results, we concluded that the waist mechanism requires small driving torques and therefore less and cheaper actuators, which is a significant benefit to this solution. The future work will include multi-objective optimization of the waist mechanism, the goal being to enhance its efficiency and behavior, and the final aim being its practical realization, implementation and evaluation.

## References

1. Or, J.: Humanoids grow a spine: the effect of lateral spinal motion on the mechanical energy efficiency. *IEEE Robot. Autom. Mag.* **20**(2), 71–81 (2013)
2. Penčić, M.M., et al.: Development of the multi-segment lumbar spine for humanoid robots. *Therm. Sci.* **20**(suppl. 2), S581–S590 (2016)
3. Penčić, M., et al.: Drive system of the robot eyeballs and eyelids with 8 DOFs. In: Doroftei, I., Oprisan, C., Pisla, D., Lovasz, E.-C. (eds.) *New Advances in Mechanism and Machine Science: SYROM 2017. MMS*, vol. 57, pp. 47–56. Springer, Cham (2018)
4. Penčić, M., et al.: Social humanoid robot SARA: development and realization of the shrug mechanism. In: Gasparetto, A., Ceccarelli, M. (eds.) *Mechanism Design for Robotics: MEDER 2018. MMS*, vol. 66, pp. 369–377. Springer, Cham (2019)
5. Penčić, M., et al.: Social humanoid robot SARA: development of the wrist mechanism. *IOP Conf. Ser.: Mater. Sci. Eng.* **294**(1), 012079-1–012079-10 (2017)
6. Pearsall, D.J., et al.: Segmental inertial parameters of the human trunk as determined from computed tomography. *Ann. Biomed. Eng.* **24**(2), 198–210 (1996)
7. Penčić, M., et al.: A novel 3 DOFs waist mechanism for humanoid robots: kinematic analysis and motion simulation. In: Uhl, T. (ed.) *Advances in Mechanism and Machine Science: 15th IFToMM World Congress*. Springer (2019, accepted for publication)
8. Meghdari, A., et al.: Arash: a social robot buddy to support children with cancer in a hospital environment. *Proc. I. Mech. Eng. H.* **232**(6), 605–618 (2018)
9. Shigemi, S., et al.: Development of new ASIMO – realization of autonomous machine. *Honda R&D Tech. Rev.* **24**(1), 37–45 (2012)
10. Tsagarakis, N.G., et al.: Compliant humanoid COMAN: optimal joint stiffness tuning for modal frequency control. In: *Proceedings of the IEEE International Conference on Robotics and Automation, ICRA 2013*, pp. 673–678. IEEE Press (2013)

11. Kim, M., et al.: Disturbance observer based linear feedback controller for compliant motion of humanoid robot. In: Proceedings of the International Conference on Robotics and Automation, ICRA 2018, pp. 403–410. IEEE Press (2018)
12. Kim, M., et al.: Team SNU's control strategies for enhancing a robot's capability: lessons from the 2015 DARPA Robotics Challenge Finals. *J. Field. Robot.* **34**(2), 359–380 (2017)
13. Ko, T., et al.: Key design parameters of a few types of electro-hydrostatic actuators for humanoid robots. *Adv. Robot.* **32**(23), 1241–1252 (2018)
14. Kaneko, K., et al.: Humanoid robot HRP-5P: an electrically actuated humanoid robot with high-power and wide-range joints. *IEEE Robot. Autom. Lett.* **4**(2), 1431–1438 (2019)
15. Park, H.A., et al.: Closed-form inverse kinematic position solution for humanoid robots. *Int. J. Hum. Robot.* **9**(3), 1250022-1–1250022-28 (2012)
16. Lohmeier, S., et al.: System design and control of anthropomorphic walking robot LOLA. *IEEE-ASME Trans. Mech.* **16**(9), 658–666 (2009)
17. Kim, K.G., et al.: Providing services using network-based humanoids in a home environment. *IEEE Trans. Consum. Electr.* **57**(4), 1628–1636 (2011)
18. Tellez, R., et al.: Reem-B: an autonomous lightweight human-size humanoid robot. In: Proceedings of the 8th IEEE-RAS International Conference on Humanoid Robots, Humanoids 2008, pp. 462–468. IEEE Press (2009)
19. Erbacher, K., et al.: SURALP: a new full-body humanoid robot platform. In: Proceedings of the IEEE/RSJ International Conference on Intelligent Robots and Systems, IROS 2009, pp. 4949–4954. IEEE Press (2009)
20. Engelsberger, J., et al.: Overview of the torque-controlled humanoid robot TORO. In: Proceedings of the 14th IEEE-RAS International Conference on Humanoid Robots, Humanoids 2014, pp. 916–923. IEEE Press (2015)
21. Tsagarakis, N.G., et al.: WALK-MAN: A high-performance humanoid platform for realistic environments. *J. Field. Robot.* **34**(7), 1225–1259 (2017)
22. Tiejun, Z., et al.: The development of a mobile humanoid robot with varying joint stiffness waist. In: Proceedings of the IEEE International Conference Mechatronics and Automation, ICMA 2005, pp. 1402–1407. IEEE Press (2006)
23. Penčić, M., et al.: Development of the low backlash planetary gearbox for humanoid robots. *FME Trans.* **45**(1), 122–129 (2017)
24. HIWIM catalog: Motion Control & Systems – Ballscrews & Accessories, p. 38 (2019)

# **Kinematics and Dynamics of Multibody Systems**



# On Kinetostatics and Workspace Analysis of Multi-platform Cable-Driven Parallel Robots with Unlimited Rotation

Thomas Reichenbach<sup>✉</sup>, Philipp Tempel, Alexander Verl,  
and Andreas Pott

Institute of Control Engineering for Machine Tools and Manufacturing Units,  
University of Stuttgart, Seidenstrasse 36, 70174 Stuttgart, Germany  
thomas.reichenbach@isw.uni-stuttgart.de

**Abstract.** Cable-driven parallel robots are a special kind of parallel mechanism which use cables instead of rigid prismatic actuators to control a single platform. This paper presents a modeling approach to replace the single platform by multiple platforms. With this approach, it is possible to perform unlimited rotation with cable robots end-effector by relatively positioning these multiple platforms. We show how this class of cable robots can be modeled as multi-body system, where platforms are connected with linkages by using revolute joints. These linkages can be seen as coupling elements. For example, using a crankshaft as coupling element, cable robots can perform novel motions such as unlimited rotation. We find a generic approach describing such multi-platform cable robot systems, after which force distribution and workspace of a case study are analyzed. Finally, we find out that inclusion and total orientation workspace are nonempty, considering joint reaction forces and platform and linkage masses. Furthermore, our modeling approach can be used for spatial multi-platform cable robots with revolute joints.

**Keywords:** Cable-driven parallel robot · Unlimited rotation · Multi-platform · Workspace

## 1 Introduction

Cable-driven parallel robots (short: cable robots) can be described as lightweight form of parallel robots like the Gough-Stewart platform [17]. This structure of cable robot consists of a single platform which can be manipulated by varying the lengths of attached cables. Conventionally, a drum or winch attached to a fixed frame is used for winding. Because of using cables, only tensile forces can impinge on the platform. As result, a cable robot can be described as redundantly restrained parallel mechanism if  $m > n + 1$  is fulfilled, where  $m$  is the number of cables and  $n$  the number of controllable degrees of freedom (DOF) [9].

For single-platform cable robots, platform rotation capabilities are restricted. A conventional platform rotation angle about one axis maximizes to  $\pm 45^\circ$  for redundantly restrained cable robots. A higher rotation capability can be achieved by using special robot designs in suspended configurations, as described in [4], where



maximum rotation of  $105^\circ$  about one axis is feasible. For applications like handling, sorting, or inspection tasks, it is often necessary to fully rotate an object with the end-effector. Furthermore, a cable robot design with unlimited rotation can be used for space applications or to handle large-scaled objects [19].

Because of these rotation capabilities restriction, cable robots with multiple platforms performing unlimited rotation of end-effector are investigated by Pott and Miermeister [8, 11]. The authors replace the platform by a crankshaft geometry shown in Fig. 1a, with four cables attached to a common attachment point, respectively. During mechanical design, one common attachment point needs complex construction. Furthermore, the characteristics will change discontinuously if geometric conditions of common attachment points are not fulfilled. Instead, using conventional revolute joints for the mechanical construction, shown in Fig. 1b, will add additional DOFs to the system since each joint can be described as cable robot platform.

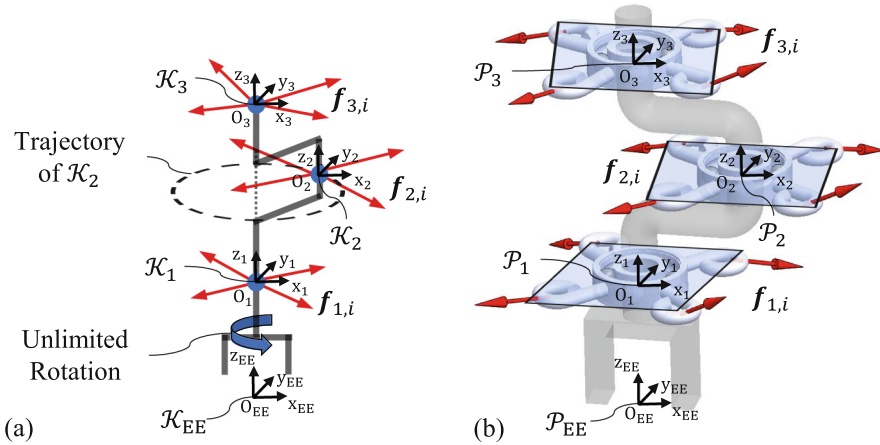


**Fig. 1.** Concept of a cable-driven parallel robot with crankshaft geometry with cable forces  $f_{j,i}$  with platform index  $j = 1, \dots, p$  and cable index  $i = 1, \dots, m_j$  of each platform: (a) Common attachment points for each anchor point of  $\mathcal{K}_j$ . (b) Ball bearings as example for revolute joints. Each ball bearing can be described as a single platform  $\mathcal{P}_j$  to perform unlimited rotation with end-effector  $\mathcal{P}_{EE}$ .

Lau et al. present arbitrary cable routing for multi-linked cable robots [6]. The authors show that all possible cable routings can be described in a single representation. Rezazadeh et al. present workspace calculations for multi-body cable robots using generalized forces and Lagrange's method [14]. Both contributions show that a single representation of each body within a multi-body cable robot system is possible.

Furthermore, in [13], a concept of a planar multi-platform robot is investigated for which a Jacobian matrix is described in explicit formulation depending on cable direction and twist. Also, workspace and force distribution analysis are performed. However, coupling forces between the two platforms caused by the linkage and its inertia force were neglected within the cable robot model.

In this paper, we present a multi-body formulation for modeling multi-platform cable robots performing unlimited rotation of its end-effector about one axis. Therefore, we describe a generic constraint formulation for each platform. Contrary to previous contributions where cables are attached to a common point, our formulation considers platform-side cable attachments as bodies including positions and orientations in kinetostatics and workspace analysis.

Section 2 recalls the kinetostatic fundamentals of single-platform cable robots and the structure matrix is described. In Sect. 3, a generic formulation is found with position and distance constraints. These constraints are used to derive the structure matrix and constraint matrix of multi-platform systems. Later, in Sect. 4, we calculate cable force distribution using the Improved Closed-Form method [12] on a case study. Also, total orientation, inclusion orientation, and maximum workspace of this example are analyzed. Section 5 concludes the paper and gives a short outlook on future work.

## 2 Kinetostatics of Single-Platform Cable Robots

Single-platform cable robots can be actuated in open-loop control. By calculating the scalar cable length  $l_i$  of the  $i$ -th cable ( $i = 1, \dots, m$ ) by means of the inverse kinematics for a given platform pose  $\mathbf{y} = (\mathbf{r}, \mathbf{R})$ , with Euclidean Norm  $\|\cdot\|_2$  one gets

$$l_i = \|\mathbf{l}_i\|_2 = \|\mathbf{a}_i - \mathbf{r} - \mathbf{R}\mathbf{b}_i\|_2. \quad (1)$$

Vector  $\mathbf{l}_i$  is the cable direction vector with respect to world coordinate system  $\mathcal{K}_0$ ,  $\mathbf{a}_i$  the position of cable outlet points on the frame,  $\mathbf{r}$  the end-effector position,  $\mathbf{R}$  the end-effector rotation matrix, and  $\mathbf{b}_i$  the platform anchor given in platform coordinates  $\mathcal{K}_j$ , see Fig. 2a. The so-called structure matrix  $\mathbf{A}^T$  consists of the cable direction unit vectors  $\|\mathbf{u}_i = \mathbf{l}_i/l_{i2}\|$  and twists  $\mathbf{b}_i^0 \times \mathbf{u}_i$  with respect to the world coordinate system described by Verhoeven [17] and Bruckmann et al. [1]. The structure matrix thus reads

$$\mathbf{A}^T = \begin{bmatrix} \mathbf{u}_1 & \dots & \mathbf{u}_m \\ \mathbf{b}_1^0 \times \mathbf{u}_1 & \dots & \mathbf{b}_m^0 \times \mathbf{u}_m \end{bmatrix}, \quad (2)$$

where vectors  $\mathbf{b}_i^0 = \mathbf{R}\mathbf{b}_i$  are described with respect to the world coordinate system. The static equilibrium at a given end-effector pose in Euclidian motion group ( $\mathbf{r} \in \mathbf{E}_3$ ,  $\mathbf{R} \in \mathbf{SO}_3$ ) can be calculated with

$$\mathbf{A}^T \mathbf{f} + \mathbf{w}_p = 0, \quad (3)$$

where  $\mathbf{f}$  contains the scalar force values of cables and  $\mathbf{w}_p$  the applied wrench on the platform with external forces [10].

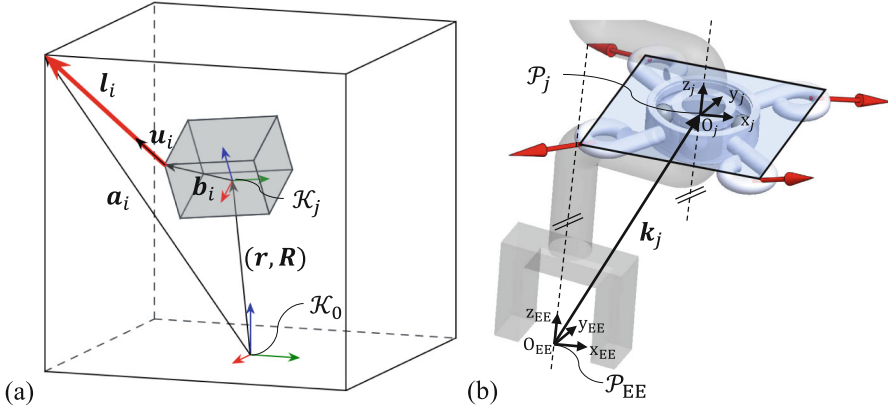


**Fig. 2.** (a) Single-platform cable robot geometry and kinematics. (b) Vector notation for constraint formulations  $g_{v,j}, g_{w,x,j}, g_{w,y,j}$ .

### 3 Multi-body Modeling of Cable Robots with Multiple Platforms

Consider a cable robot system consisting of multiple platforms  $\mathcal{P}_j$  with  $j = 1, \dots, p$ , each platform has  $m_j$  cables attached to it. The platforms are linked with a mechanical structure, for example a crankshaft or linkage, and uses joints for mechanical transmission. These joints transmit specific forces and torques depending on the joint valance to other platforms. For example, a ball bearing can be used to transmit three translational forces and torques about two different axes of each platform. For kinematic and kinetostatic modeling, dynamic effects are neglected. We assume revolute joints connect platform  $\mathcal{P}_j$  to the crankshaft, and cables as straight line between cable outlet point and platform anchor.

#### 3.1 Position Constraints of Platform and Linkage

Each platform of the cable robot system is redundantly constrained by the distance of attached cables. One can formulate the implicit holonomic position constraint (see [18]) for each platform in analogy to Eq. (1) as

$$g_{j,i} = \|l_{j,i}\|_2 - l_{j,i} = \|a_{j,i} - r_j - R_j b_{j,i}\|_2 - l_{j,i} = 0, \quad (4)$$

where  $r_j$  is position and  $R_j$  orientation of platform  $\mathcal{P}_j$  respectively, and  $l_{j,i}$  is the set point cable length. Because each platform is linked to another one, additional position and revolute joint constraints have to be added<sup>1</sup>, yielding

<sup>1</sup> Assuming that the linkage intersects with the origin of the platform coordinate system and each platform has single position constraints with the linkage.

$$g_{v,j} = \mathbf{r}_{EE} + \mathbf{R}_{EE}\mathbf{k}_j - \mathbf{r}_j = 0, \quad (5)$$

$$g_{wx,j} = \left(\mathbf{R}_j^x \mathbf{e}_j\right)^T (\mathbf{R}_{EE}^z \mathbf{e}_{EE}) = 0, \quad (6)$$

$$g_{wy,j} = \left(\mathbf{R}_j^y \mathbf{e}_j\right)^T (\mathbf{R}_{EE}^z \mathbf{e}_{EE}) = 0, \quad (7)$$

where  $\mathbf{k}_j$  is the vector pointing from end-effector coordinate system to intersection point of the revolute joint neutral axis with platform  $\mathcal{P}_j$ , see Fig. 2b. Vector  $\mathbf{r}_{EE}$  and rotation matrix  $\mathbf{R}_{EE}$  describe the end-effector pose. Additionally, further constraints of revolute joints must be considered (see Eqs. (6) and (7)), where  $^x\mathbf{e}_j$  and  $^y\mathbf{e}_j$  are unit-vectors of the platform  $\mathcal{P}_j$  which are orthogonal to the joint axis, and  $^z\mathbf{e}_{EE}$  is unit-vector of the rotation axis which is perpendicular to  $^x\mathbf{e}_j$  and  $^y\mathbf{e}_j$ .

We describe the constraint Jacobian matrix by deriving the implicit holonomic constraints  $g_{j,i}$ ,  $g_{v,j}$ ,  $g_{wx,j}$  and  $g_{wy,j}$  to obtain the directions of constraint forces. Derivates of  $g_{j,i}$  and  $g_{v,j}$  with respect to the generalized coordinates lead to

$$\frac{\partial g_{j,i}}{\partial \mathbf{q}} = \frac{\mathbf{l}_{j,i}^T}{\underbrace{\sqrt{\mathbf{l}_{j,i}^T \mathbf{l}_{j,i}}}_{\mathbf{u}_{j,i}^T}} \frac{\partial \mathbf{l}_{j,i}}{\partial \mathbf{q}}, \quad \frac{\partial g_{v,j}}{\partial \mathbf{q}} = \frac{\partial (\mathbf{r}_{EE} + \mathbf{R}_{EE}\mathbf{k}_j - \mathbf{r}_j)}{\partial \mathbf{q}}, \quad (8)$$

where  $\mathbf{l}_{j,i}$  is the cable direction vector of the  $i$ -th cable of the  $j$ -th platform and  $\mathbf{u}_{j,i}$  the unit vector of the cable direction, respectively. Vector  $\mathbf{q}$  contains generalized coordinates of each platform and end-effector. The derivates of Eqs. (6) and (7) are straight forward [18]. One can describe  $\frac{\partial g_{wx,j}}{\partial \mathbf{q}}$  and  $\frac{\partial g_{wy,j}}{\partial \mathbf{q}}$  as torsional force directions compensated by the revolute joint.

Following, constraint matrix  $\Phi$  can be described with the structure matrix  $\mathbf{A}_j^T$  of each platform  $j$ , constraints derivates of the linkage with platform generalized coordinates  $\mathbf{C}_j^T$  and linkage generalized coordinates  $\tilde{\mathbf{C}}_j^T$ .

$$\Phi^T = \begin{bmatrix} \mathbf{A}_1^T & 0 & 0 & -\mathbf{C}_1^T & 0 & 0 \\ 0 & \ddots & 0 & 0 & \ddots & 0 \\ 0 & 0 & \mathbf{A}_p^T & 0 & 0 & -\mathbf{C}_p^T \\ 0 & 0 & 0 & \tilde{\mathbf{C}}_1^T & \dots & \tilde{\mathbf{C}}_p^T \end{bmatrix}, \text{ with} \quad (9)$$

$$\mathbf{C}_j^T = \begin{bmatrix} \mathbf{I} & 0 & 0 \\ 0 & (\mathbf{R}_{EE}^z \mathbf{e}_{EE}) \times (\mathbf{R}_j^x \mathbf{e}_j) & (\mathbf{R}_{EE}^z \mathbf{e}_{EE}) \times (\mathbf{R}_j^y \mathbf{e}_j) \end{bmatrix},$$

$$\tilde{\mathbf{C}}_j^T = \begin{bmatrix} \mathbf{I} & 0 & 0 \\ [\mathbf{R}_{EE}\mathbf{k}_j]_{\times} & (\mathbf{R}_{EE}^z \mathbf{e}_{EE}) \times (\mathbf{R}_j^x \mathbf{e}_j) & (\mathbf{R}_{EE}^z \mathbf{e}_{EE}) \times (\mathbf{R}_j^y \mathbf{e}_j) \end{bmatrix},$$

identity matrix  $\mathbf{I}$  of size 3 and with skew symmetric matrix  $[\cdot]_{\times}$  by Lie-algebra satisfying  $\frac{\partial(\mathbf{R}_j(q)\mathbf{b}_{j,i})}{\partial q} = [\mathbf{R}_j\mathbf{b}_{j,i}]_{\times}$  and  $\frac{\partial(\mathbf{R}_{EE}(q)\mathbf{k}_j)}{\partial q} = [\mathbf{R}_{EE}\mathbf{k}_j]_{\times}$  [2, 16]. According to Featherstone [3], we can formulate constraint forces of the multi-platform cable robot system to

$$\boldsymbol{\tau}_C = \boldsymbol{\Phi}^T \boldsymbol{\lambda}, \quad (10)$$

where  $\boldsymbol{\lambda}$  is a vector containing unknown scalar forces of cables and linkage. However, we want to find a formulation similar to conventional single-platform cable robots with a single structure matrix and determined joint forces. Therefore, coupling forces of the linkage have to be expressed with respect to the cable forces.

### 3.2 Kinetostatics of Multi-platform Cable Robots

Assuming each platform's cable forces being projected onto revolute joint, static Newton equations can be described for each platform in explicit formulation. Furthermore, these reaction forces act in the opposite direction of the linkage, thus

$$\mathbf{C}_j^T \begin{bmatrix} \boldsymbol{\lambda}_{j,m+1} \\ \vdots \\ \boldsymbol{\lambda}_{j,m+5} \end{bmatrix} = \mathbf{A}_j^T \begin{bmatrix} \boldsymbol{\lambda}_{j,1} \\ \vdots \\ \boldsymbol{\lambda}_{j,m} \end{bmatrix}, \quad (11)$$

$$\tilde{\mathbf{C}}_1^T \begin{bmatrix} \boldsymbol{\lambda}_{1,m+1} \\ \vdots \\ \boldsymbol{\lambda}_{1,m+5} \end{bmatrix} + \dots + \tilde{\mathbf{C}}_p^T \begin{bmatrix} \boldsymbol{\lambda}_{p,m+1} \\ \vdots \\ \boldsymbol{\lambda}_{p,m+5} \end{bmatrix} = \mathbf{0}. \quad (12)$$

Equation (11) considers cable wrench and reaction wrench of the revolute joint, while Eq. (12) describes wrenches acting on the linkage. Hence, reaction forces of the revolute joints  $\boldsymbol{\lambda}_{j,m+1}$  through  $\boldsymbol{\lambda}_{j,m+5}$ , can be described by cable forces  $\boldsymbol{\lambda}_{j,1}$  through  $\boldsymbol{\lambda}_{j,m}$ . Thus, constraint Jacobian  $\boldsymbol{\Phi}$  (Eq. (9)) is converted to structure matrix  $\mathbf{J}^T$  and interchangeable projected wrenches of each platform  $\mathbf{V}^T$  with cable forces  $\mathbf{f}_c$ , denoted as structured constraint matrix (SCM), such that the static equilibrium of the multi-platform cable robot reads

$$\underbrace{(\mathbf{J}^T + \mathbf{V}^T)}_{\mathbf{G}^T} \mathbf{f}_c + \tilde{\mathbf{w}}_p = \mathbf{0}, \text{ with} \quad (13)$$

$$\mathbf{J}^T = \begin{bmatrix} \mathbf{A}_1^T & \mathbf{0} & \mathbf{0} \\ \mathbf{0} & \ddots & \mathbf{0} \\ \mathbf{0} & \mathbf{0} & \mathbf{A}_p^T \\ \mathbf{0} & \mathbf{0} & \mathbf{0} \end{bmatrix}, \quad \mathbf{V}^T = \begin{bmatrix} -\mathbf{C}_1^T \mathbf{C}_1^{-T} \mathbf{A}_1^T & \mathbf{0} & \mathbf{0} \\ \mathbf{0} & \ddots & \mathbf{0} \\ \mathbf{0} & \mathbf{0} & -\mathbf{C}_p^T \mathbf{C}_p^{-T} \mathbf{A}_p^T \\ \tilde{\mathbf{C}}_1^T \mathbf{C}_1^{-T} \mathbf{A}_1^T & \dots & \tilde{\mathbf{C}}_p^T \mathbf{C}_p^{-T} \mathbf{A}_p^T \end{bmatrix}$$

$$\tilde{\mathbf{w}}_p = \begin{bmatrix} \mathbf{w}_{p,1} \\ \vdots \\ \mathbf{w}_{p,p} \\ \mathbf{w}_{p,EE} \end{bmatrix}, \quad \text{and} \quad \mathbf{w}_{p,EE} = \begin{bmatrix} \mathbf{f}_{EE} \\ \boldsymbol{\tau}_{EE} \end{bmatrix}.$$

Here,  $\tilde{\mathbf{w}}_p$  consist of wrench vectors for each platform  $\mathbf{w}_{p,j}$  and wrench vector of the end-effector  $\mathbf{w}_{p,EE}$ . End-effector wrench  $\mathbf{w}_{p,EE}$  consist of external and process forces  $\mathbf{f}_{EE}$  and torques  $\tau_{EE}$ , respectively.

## 4 A Planar Case Study with Unlimited Rotation

In this section, the multi-platform structure matrix and SCM formulation for a planar case study are shown. This two-platform planar cable robot concept is schematically shown in Fig. 3a. Platform  $\mathcal{P}_1$  can be manipulated with the four cables drawn red with its vector of cable lengths  $\mathbf{l}_{1,i}$ , while platform  $\mathcal{P}_2$  uses cables drawn blue with its respective  $\mathbf{l}_{2,i}$ . These two platforms are linked by a symmetric coupling element with vectorial distance  $\mathbf{k}_1$  and a planar revolute joint within the center of each platform's coordinate system, respectively. The pose of each platform is given by the two-dimensional position vector  $\mathbf{r}_j$  and two-dimensional rotation matrix  $\mathbf{R}_j(\varphi_j)$ . Furthermore, the cable robot geometry is defined with the cable outlet positions  $\mathbf{a}_{j,i}$  and platform anchor points  $\mathbf{b}_{j,i}$ , given in Table 1. Platform  $\mathcal{P}_2$  can moved around platform  $\mathcal{P}_1$  along the dashed trajectory with angle  $\varphi_{EE}$ . The end-effector of this cable robot lies in the origin of the coordinate system of platform  $\mathcal{P}_1$ . For the planar case, cable-platform, cable-cable, and platform-platform collisions are neglected. In Fig. 3b, the multi-platform cable robot system is shown as a plotted model with MATLAB. This model is used for subsequent force distribution and workspace analysis.<sup>2</sup>

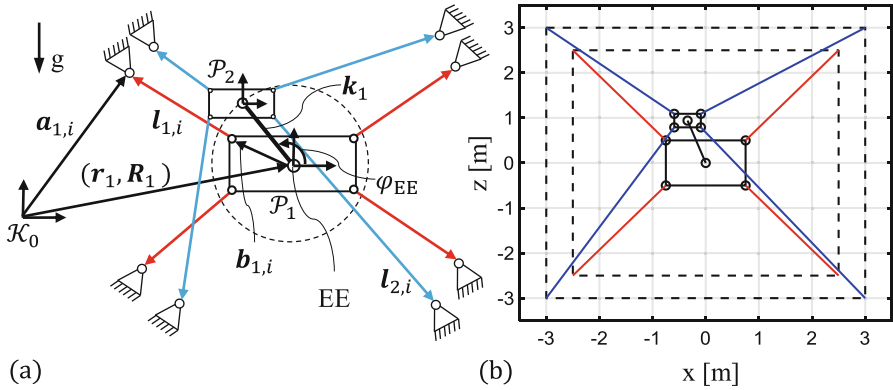


**Fig. 3.** Concept of a planar multi-platform cable robot with unlimited rotation: (a) Schematic drawing. (b) Graphical plot generated with cable robot geometry.

<sup>2</sup> Following force distribution and workspace analysis were performed with MATLAB Version 2018b.

With frame and geometry of the platforms, we can use Eqs. (4)–(13) to find a single structure matrix for this robot design, which is a straight forward task. It contains the conventional structure matrix for each platform such as a single platform cable robot. Applied wrenches, for example gravity forces or process forces  $\tilde{\mathbf{w}}_p$  can be calculated similarly. After simplification the SCM  $\mathbf{V}^T$  of this planar multi-platform cable robot consists of linkage direction  $\mathbf{v}_j$ . With Eqs. (11) and (12) we can calculate explicit forces to the linkage with respect to cable forces of each platform and collect  $\mathbf{V}^T$ .

$$\mathbf{V}^T = \frac{1}{2} \mathbf{v}_1 \begin{bmatrix} \mathbf{v}_1^T \mathbf{u}_{1,1} & \mathbf{v}_1^T \mathbf{u}_{1,2} & \mathbf{v}_1^T \mathbf{u}_{1,3} & \mathbf{v}_1^T \mathbf{u}_{1,4} & 0 & 0 & 0 & 0 \\ 0 & 0 & 0 & 0 & 0 & 0 & 0 & 0 \\ 0 & 0 & 0 & 0 & \mathbf{v}_1^T \mathbf{u}_{2,1} & \mathbf{v}_1^T \mathbf{u}_{2,2} & \mathbf{v}_1^T \mathbf{u}_{2,3} & \mathbf{v}_1^T \mathbf{u}_{2,4} \\ 0 & 0 & 0 & 0 & 0 & 0 & 0 & 0 \end{bmatrix} \quad (14)$$

The case study cable robot has 8 cables and 5 DOFs ( $\mathbf{r}_{EE}, \phi_1, \phi_2, \phi_{EE}$ ). Thus, in a non-singular pose, the null space dimension is at least 3. Each platform has a null space of dimension 1, and additional null space dimension resulting from the linkage. However, matrix  $\mathbf{G}^T$  has a null space of dimension 2, because of losing one null space dimension of applied forces to the end-effector by projecting these forces to each platform.

**Table 1.** Geometry of the planar case study.

Platform	Cable	$^x a_{j,i}/m$	$^z a_{j,i}/m$	$^x b_{j,i}/m$	$^z b_{j,i}/m$
1	1	-2.5	2.5	-0.75	0.5
	2	2.5	2.5	0.75	0.5
	3	2.5	-2.5	0.75	-0.5
	4	-2.5	-2.5	-0.75	-0.5
2	1	-3	3	-0.25	0.15
	2	3	3	0.25	0.15
	3	3	-3	0.25	-0.15
	4	-3	-3	-0.25	-0.15

#### 4.1 Force Distribution

Because Eq. (2) is underdetermined, the force distribution is not unique but yields infinitely many solutions. Feasible force distribution in solution space are computed using optimization algorithms, for example Dykstra method [5], Verhoeven Gradient method [17], or nonlinear programming [15], which use different criteria to choose a suitable solution. In this paper, possible force distributions of the planar multi-platform cable robot are found with the Improved Closed-Form method [10, 12].

Parameters for force distribution and workspace computation are shown in Table 2, mass of platform  $\mathcal{P}_1$  is  $M_1$  and mass of platform  $\mathcal{P}_2$  is  $M_2$ . Furthermore, minimum and maximum cable forces (depending on cable material parameters and drive system) must be considered for computation with the Improved Closed-Form method. Following the single-platform derivation in [12], it is possible to compute a force distribution for a given pose of the cable robot with

$$\mathbf{f}_v = \mathbf{f}_M - \mathbf{G}^{+T}(\tilde{\mathbf{w}}_p + \mathbf{G}^{+T}\mathbf{f}_M), \quad (15)$$

where  $\mathbf{f}_v$  is a column vector of cable forces of platforms,  $\mathbf{f}_M$  the mean feasible force vector with  $\mathbf{f}_M = (\mathbf{f}_{\min} + \mathbf{f}_{\max})/2$  and  $\mathbf{G}^{+T}$  the Moore-Penrose generalized matrix inverse of multi-platform cable robots structure matrix including SCM  $\mathbf{G}^T$ .

**Table 2.** Parameters of the planar study case.

Cable/load parameter	Value	Unit	Discretization parameter	Value	Unit
$f_{\min}$	20	N	$n_{\text{steps}}$	33	–
$f_{\max}$	500	N	$s$	5	–
$M_1$	20	kg	$^x\mathbf{r}_{EE}$	–2.4 to 2.4	m
$M_2$	10	kg	$^z\mathbf{r}_{EE}$	–2.4 to 2.4	m
$M_L$	2	kg	$\varphi_1$	–45 to 45	deg
			$\varphi_2$	–45 to 45	deg
			$\varphi_{EE}$	0 to 360	deg

The force distribution of the study case cable robot for a full rotation of platform  $\mathcal{P}_2$  about platform  $\mathcal{P}_1$  with angle  $\varphi_{EE}$  is shown in Fig. 4. To compute the force distribution, position and orientation of platform  $\mathcal{P}_1$  and orientation of platform  $\mathcal{P}_2$  are predefined. Thus, an unlimited rotation is performed manipulating the position of platform  $\mathcal{P}_2$ , therefore each position of platform  $\mathcal{P}_2$  was calculated with inverse kinematics and discretized with  $n_{\text{steps}}$ . For each position, we used the Improved Closed-Form Method to compute force distribution of all cables.

The graph shows an alternating cable force for cables of platform  $\mathcal{P}_1$ . The mean force values of upper cables ( $f_{1,1}, f_{1,2}$ ) are higher than bottom mean values, because the cables have to compensate for gravity of platform  $\mathcal{P}_1$ . In addition, alternating cable forces are not symmetric due to linkage mass  $M_L$ . Furthermore, the cable forces of platform  $\mathcal{P}_2$  are also alternating, because of its rotation about platform  $\mathcal{P}_1$ . As a result, unlimited rotation at this end-effector pose is feasible, because all cable forces of the two platforms are within the force limits.

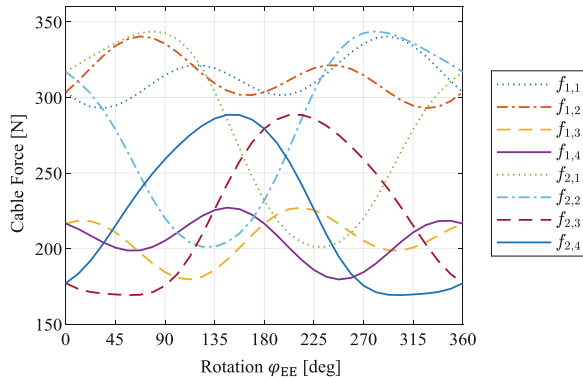


**Fig. 4.** Force Distribution for unlimited rotation of platform  $\mathcal{P}_2$  about platform  $\mathcal{P}_1$  with predefined positions and orientations  $\mathbf{r}_{EE} = [0, 0]^T$ ,  $\varphi_1 = 0^\circ$ , and  $\varphi_2 = 0^\circ$ .



## 4.2 Workspace Analysis

Definitions of workspaces for cable-driven parallel robots can be derived from conventional formulations of parallel mechanisms. Merlet gives an overview of workspace categories, which will be partly used to describe workspaces of the planar multi-platform cable robot [7]. For the case study, we use maximum workspace, inclusion orientation workspace, and total orientation workspace, see Fig. 5.

These workspaces are calculated using a pose list containing a regular grid size  $n_{\text{steps}}^s$  of discretized poses within the workspace limits of end-effector position in x- and z-direction  $\mathbf{r}_{EE}$  and orientations  $\varphi_{EE}$ ,  $\varphi_1$  and  $\varphi_2$ , see Table 2.

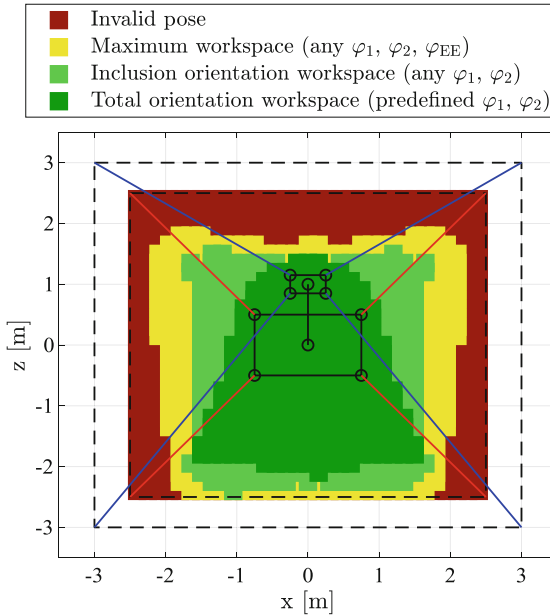


**Fig. 5.** Workspace with invalid poses (red), valid poses (yellow, green). Inclusion orientation workspace (bright green) can be reached with any platform orientation  $\varphi_1$  and  $\varphi_2$ , while total orientation workspace (dark green) is computed with predefined platform orientations  $\varphi_1 = 0^\circ$  and  $\varphi_2 = 0^\circ$  where any set of angles might be arbitrarily chosen.

Invalid poses (red) are those that cannot be reached with the given cable force limits. The maximum workspace (yellow) consists of all translational poses of the end-effector  $\mathbf{r}_{EE}$  at any orientation of platforms and end-effector. Furthermore, within the inclusion orientation workspace (bright green), unlimited rotation is possible given any platform orientations  $\varphi_1$  and  $\varphi_2$ . Total orientation workspace (dark green) can be reached by the end-effector for a predefined set of orientations of each platform. Poses of the planar cable robot in yellow, bright green, and dark green workspace can be assumed non-singular, because no cable forces become infinite or negative with Improved Closed-Form method. Singular poses are shown as invalid (red).

With the workspace graph in Fig. 5, inclusion orientation and total orientation workspace are not symmetric at the borders as could have been expected. A reason may lie in numerical instabilities due to computation of the Moore-Penrose pseudoinverse in Eq. (15). However, inclusion orientation and total orientation workspace are nonempty, considering platform masses, linkage mass, and force transmission between the platforms by the linkage and revolute joints.

## 5 Outlook and Conclusion

This paper presents a generic approach to calculate a single structure matrix by position constraint equations for multi-platform cable robots with unlimited rotation. With deriving these position constraints, a constraint matrix is built and explicit formulation of unknown forces of the system are formulated. Combining implicit holonomic constraints with explicit force formulation (referring to [3, 18]), one can describe a multi-platform cable robot system with structure matrix of each platform and SCM.

We presented a simplified planar study case to calculate the structure matrix and SCM for a multi-platform cable robot. With this work, a generic solution for this type of cable robots is found and it is possible to find formulations of structure matrix and SCM for a spatial type of multi-platform cable robot.

In the future, a spatial multi-platform cable-driven parallel robot with unlimited rotation will be designed and workspace and force distributions analyzed. Furthermore, the analyzed case study cable robot can be prototyped by using multiple construction levels to avoid collisions.

**Acknowledgments.** This work was supported by the German Research Foundation (DFG-project number: 358142701) at the University of Stuttgart.

## References

1. Bruckmann, T., Mikelsons, L., Brandt, T., et al.: Wire robots Part I: kinematics, analysis & design. In: Ryu, J.-H. (ed.) *Parallel Manipulators, New Developments*. I-Tech Education and Publishing, Vienna (2008)
2. Eade, E.: Lie Groups for 2D and 3D Transformations (2017). <http://ethaneade.com/>. Accessed 25 Mar 2019
3. Featherstone, R.: *Rigid Body Dynamics Algorithms*. Springer, New York (2008)
4. Gouttefarde, M., Merlet, J.-P., Daney, D.: Wrench-feasible workspace of parallel cable-driven mechanisms. In: *IEEE International Conference on Robotics and Automation*, Roma, Italy, pp. 1492–1497 (2007)
5. Hassan, M., Khajepour, A.: Minimum-norm solution for the actuator forces in cable-based parallel manipulators based on convex optimization. In: *IEEE International Conference on Robotics and Automation*, pp. 1498–1503 (2007)
6. Lau, D., Oetomo, D., Halgamuge, S.K.: Generalized modeling of multilink cable-driven manipulators with arbitrary routing using the cable-routing matrix. *IEEE Trans. Robot.* **29**, 1102–1113 (2013)

7. Merlet, J.-P.: *Parallel Robots. Solid Mechanics and its Applications*, vol. 74, 2nd edn. Kluwer Academic Publishers, Dordrecht (2006)
8. Miermeister, P., Pott, A.: Design of cable-driven parallel robots with multiple platforms and endless rotating axes. In: Kecskeméthy, A., Geu Flores, F. (eds.) *Interdisciplinary Applications of Kinematics*, pp. 21–29. Springer, Cham (2015)
9. Ming, A., Higuchi, T.: Study on multiple degree-of-freedom positioning mechanism using wires (Part 1) - concept, design and control. *Int. J. Jpn Soc. Precis. Eng.* **28**(2), 131–138 (1994)
10. Pott, A.: *Cable-Driven Parallel Robots: Theory and Application*, vol. 120. Springer, Cham (2018)
11. Pott, A., Miermeister, P.: Workspace and interference analysis of cable-driven parallel robots with an unlimited rotation axis. In: Lenarcic, J., Merlet, J.-P. (eds.) *Advances in Robot Kinematics 2016*, Grasse, France, vol. 4, pp. 341–350. Springer (2016)
12. Pott, A., Bruckmann, T., Mikelsons, L.: Closed-form force distribution for parallel wire robots. In: Kecskeméthy, A., Müller, A. (eds.) *Computational Kinematics*, pp. 25–34. Springer, Heidelberg (2009)
13. Reichenbach, T., Tempel, P., Verl, A., et al.: Static analysis of a two-platform planar cable-driven parallel robot with unlimited rotation. In: Pott, A., Bruckmann, T. (eds.) *Proceedings of the Fourth International Conference on Cable-Driven Parallel Robots*. Springer (2019, accepted for publication)
14. Rezazadeh, S., Behzadipour, S.: *Workspace analysis of multibody cable-driven mechanisms*, vol 3
15. Shiang, W.-J., Cannon, D.J., Gorman, J.: Optimal force distribution applied to a robotic crane with flexible cables. In: *IEEE International Conference on Robotics and Automation*, vol. 2, pp. 1948–1954 (2000)
16. Shiriaev, A.: *Control Methods for Robotics Applications*. Fall (2008). <http://www8.tfe.umu.se/courses/elektro/RobotControl/>. Accessed 31 Mar 2019
17. Verhoeven, R.: *Analysis of the workspace of tendon-based stewart platforms*. PhD thesis, Universität Duisburg-Essen (2004)
18. Woernle, C.: *Mehrkörpersysteme*. Springer, Heidelberg (2016)
19. Yao, R., Li, H., Zhang, X.: A modeling method of the cable driven parallel manipulator for FAST. In: Bruckmann, T., Pott, A. (eds.) *Cable-Driven Parallel Robots*, pp. 423–436. Springer, Heidelberg (2013)



# Kinematics of a Planar Parallel Robot via Screw Theory: Details not Mentioned

Albert L. Balmaceda-Santamaría<sup>1(✉)</sup> and Mario A. García-Murillo<sup>2</sup>

<sup>1</sup> Instituto de Estudios Superiores, Universidad Nacional de Ingeniería,  
Managua 5595, Nicaragua

albert.balmaceda@gmail.com

<sup>2</sup> Department of Mechanical Engineering, Universidad de Guanajuato,  
36885 Salamanca, Mexico

garcia.mario@ugto.mx

**Abstract.** In this work, the kinematic analysis of a parallel robot via screw theory is obtained step by step, with the aim to show details that no-one mentions since only a select group of researchers has the know-how of this mathematical tool. A 3-RRR parallel robot for obtaining the input-output equations of velocity and acceleration in screw form is used. A brief explanation of concepts used by applying screw theory in the kinematic analysis of parallel robots is provided. The Klein form, which is an important method for addressing the passive joints of the parallel manipulators, is applied to the velocity and acceleration equations of the robot. A numerical example in order to verify the kinematics formulation of the parallel manipulator based on screw theory is provided. With the details mentioned in this paper, to understand and apply this mathematical tool could be easier and simply than learning it by itself.

**Keywords:** Kinematics · Screw theory · Parallel robot

## 1 Introduction

The screw theory dates since year 1900, when Ball [1] defined the velocity of a rigid body as an infinitesimal twist of a screw. Since then, although in an intermittent way, the screw theory has been enriched by the contributions of many researchers. One of the most important contribution in this theory is in [2], where is defined the concept of acceleration motor, which led to the higher-order analysis was possible by means infinitesimal screw theory.

In 1985 Mohamed and Duffy [3] demonstrate that the twist, or velocity state, representing the instantaneous motion of the moving platform of a parallel robot can be expressed as the sum of the partial screws of the robots. Nevertheless, it was not until 1999 that the screw theory is presented in a systematic way for addressing kinematic analysis of open serial and closed chains [4]. Since then, over the years many researches on kinematic analysis of parallel robots via screw theory have been reported.

In Refs. [5, 6] the singularity analysis and Jacobian matrix of several parallel manipulators are presented, however the authors only show the velocity state equations

in screw form and then the input-output velocity equation of the manipulators, which is difficult to deduce for all those are non-skilled in the art.

Kong and Gosselin present several type syntheses of 3-DOF spherical, 3-DOF translational and 3T1R 4-DOF manipulators based on screw theory in [7–9], respectively. Nevertheless, the authors take advantage of the wrench system via screws to demonstrate their proposal, which means that the velocity and acceleration equations are not presented their works.

Using screw theory, kinematics and singularities of many types of parallel manipulators have been studied [10–12]. A parallel manipulator inspired by Gough-Stewart platform is presented in [13], where the velocity and acceleration equations are presented in screw form. Even generalized forces of a series-parallel manipulator are obtained via screw theory [14], which means a high level of applicability of this mathematical tool.

Kinematic and deformation analyses of a parallel robot for drilling task via screw theory is presented in [15], as well as the kinematics and dynamics analyses of pipe-bending mechanism is presented in [16] and [17]. Furthermore, the velocity and acceleration equations via screw theory of the well-known Delta-type parallel robot is presented in [18], including a reconfigurable Delta-type robot is addressed in [19].

Preliminary concepts about screw theory are provided in certain contributions [20–23], however the way to obtain step by step the velocity and acceleration input-output equations is not presented. In the case of a recent contribution in kinematic of parallel robots via screw theory [24], the author presents all the theoretical background of screw theory, which could be overwhelming to understand. Therefore, to obtain a simple way for applying this tool is not so evident, whether one wants to develop a numerical example.

In spite the fact screw theory is very useful, only a select group of researchers have the know-how of this mathematical tool applied to the kinematics of parallel robots. Accordingly, we provide the details for everyone can learn and apply the screw theory in kinematics of parallel robots.

In this work, a kinematic analysis with the aim to demonstrate how to obtain it by means screw theory with details that no-one presents is provided. A 3-RRR planar robot to obtain the velocity and acceleration equations in screw form step by step is presented. A numerical example of this mathematical tool is provided. Furthermore, the results are compared with the results obtained by a software CAD in order to validate the method.

## 2 Kinematics

### 2.1 Brief Mathematical Background

Firstly, it is necessary to define certain concepts before to know apply screw theory to the kinematic analysis of a robot. It is important to mention that in this work the concepts used in screw theory are explained in a practical and simple way, with the aim to understand them clearly. Therefore, if one wants to know thoroughly about such concepts can consult the references aforementioned.

**Plücker Coordinates.** Plücker coordinates are the coordinates of a line in 3-space  $\mathbf{E}^3$ , namely the coordinates of any point of a line as observed from a fixed reference frame of center  $\mathbf{O}$  (see Fig. 1).

The screw theory takes advantage of the Plücker coordinates in the concept of that any motion of a rigid body can be achieved as a rotation around a geometrical line  $l$  together with a pure translation along  $l$ . The line  $l$  is called the (screw) axis of the motion [25]. For a pure translation, the pitch  $h$  is at infinite. In other words, at any instant, the particle velocities of a rigid body can be represented by a screw motion, namely a rotation about an instantaneous axis combined with a velocity of translation along this axis [2].

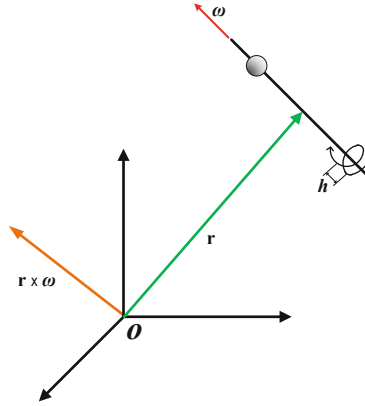


**Fig. 1.** Description of Plücker coordinates.

Hence, Plücker coordinates can be defined as a six-dimensional vector  $l = [\omega \ s_{\mathbf{O}}]^T$ , where the primal part  $\omega$  is the direction of the rotation axis and the dual part  $s_{\mathbf{O}} = \mathbf{r} \times \omega$  is the moment of  $\mathbf{r}$  about the center  $\mathbf{O}$ .

**Velocity State.** Let be the velocity state of any point of a rigid body B, as observed from another body or reference frame A defined as  ${}^A\mathbf{V}^B = [\omega \ v]^T$ , where  $\omega$  is vector of the angular velocity components and  $v$  is the vector of the linear velocity components. The velocity state  ${}^A\mathbf{V}^B$  is a six-dimensional vector, thus it may be expressed in screw form as follows

$${}^A\mathbf{V}^B = {}_A\omega_B {}^A\mathbb{S}^B \quad (1)$$

where,  ${}_A\omega_B$  is the joint-velocity rate of body B as observed from body A and  ${}^A\mathbb{S}^B$  is the infinitesimal screw computed by Plücker coordinates, which may be defined as

$${}^A\mathbb{S}^B = \begin{bmatrix} {}^A\hat{\omega}^B \\ {}^A\hat{\omega}^B \times -\mathbf{r} \end{bmatrix} \quad (2)$$

Note that, in Eq. (2) in the dual part the vector  $\mathbf{r}$  is negative, since  $\mathbf{r} \times {}^A\dot{\omega}^B$  does not produces linear velocity components.

**Acceleration State.** Let be the acceleration state of any point of a rigid body B, as observed from another body or reference frame A defined as  ${}^A\mathbf{A}^B = [\alpha \ a]^T$ , where  $\alpha$  is vector of the angular acceleration components and  $a$  is the vector of the acceleration components. The acceleration state  ${}^A\mathbf{A}^B$  is a six-dimensional vector [4], thus it may be expressed in screw form as follows

$${}^A\mathbf{A}^B = {}_A\dot{\omega}_B {}^A\$B \quad (3)$$

where,  ${}_A\dot{\omega}_B$  is the joint-acceleration rate of body B as observed from body A. The screw  ${}^A\$B$  is the same as in Eq. (2).

The acceleration state of multibody mechanical system composed of  $n, n+1, n+2, \dots, m-2, m-1, m$  serially connected bodies, may be written as

$${}^n\mathbf{A}^m = {}_n\dot{\omega}_{n+1} {}^n\$^{n+1} + {}_{n+1}\dot{\omega}_{n+2} {}^{n+1}\$^{n+2} + \dots + {}_{m-1}\dot{\omega}_m {}^{m-1}\$^m + {}^n\mathcal{L}^m \quad (4)$$

where

$$\begin{aligned} {}^n\mathcal{L}^m = & \left[ {}_n\omega_{n+1} {}^n\$^{n+1} \quad {}_{n+1}\omega_{n+2} {}^{n+1}\$^{n+2} + \dots + {}_{m-1}\omega_m {}^{m-1}\$^m \right] \\ & + \left[ {}_{n+1}\omega_{n+2} {}^{n+1}\$^{n+2} \quad {}_{n+2}\omega_{n+3} {}^{n+2}\$^{n+3} + \dots + {}_{m-1}\omega_m {}^{m-1}\$^m \right] \\ & + \dots + \left[ {}_{n+2}\omega_{n+3} {}^{n+2}\$^{n+3} \quad {}_{m-1}\omega_m {}^{m-1}\$^m \right] \end{aligned}$$

is the termed the Lie screw of acceleration of body  $m$  as observed from body  $n$ , which is represented by the form  $[\ast \ast]$ .

Let screws  $\$1 = [\omega_1 \ v_{o1}]$  and  $\$2 = [\omega_2 \ v_{o2}]$  be two infinitesimal screws, so that the Lie product of the Lie algebra  $se(3)$  of the Euclidean group  $SE(3)$  is defined as follows

$$\mathcal{L} = [\$1 \ \$2] = (\omega_1 \times \omega_2; \omega_1 \times v_{o2} - \omega_2 \times v_{o1}) \quad (5)$$

where  $\times$  represents the usual cross product of three-dimensional vectorial algebra.

**Klein Form.** The Klein form allows to simplify the velocity and acceleration analysis of parallel robot, since it is said that two screws  $\$1$  and  $\$2$  are reciprocal if the application of the Klein form between them yields  $\{\$1; \$2\} = 0$ . Thereby applying the Klein form between the screws yields

$$\{\$1; \$2\} = \omega_1 \bullet v_{o2} + \omega_2 \bullet v_{o1} \quad (6)$$

where the bullet ( $\bullet$ ) denotes the inner product of three-dimensional vectorial algebra.

## 2.2 Direct Position Analysis

Let  $X_o Y_o Z_o$  be the fixed reference frame coincident with the point  $A_1$  of the 3-RRR parallel manipulator (see Fig. 2). The coordinates of the points  $A_i = (Ax_i \ Ay_i \ Az_i)$  and  $B_i = (Bx_i \ By_i \ Bz_i)$  are obtained by projections as follows

$$\begin{aligned}
 A_2 &= [r \quad 0 \quad 0] \\
 A_3 &= [r/2 \quad r\sqrt{3}/2 \quad 0] \\
 B_i &= [Ax_i + a \cos(\theta_i) \quad Ay_i + a \sin(\theta_i) \quad 0]
 \end{aligned}$$

Unless otherwise, in remaining contribution  $i = 1, 2, 3$  kinematic chains. Furthermore, it is evident that  $A_1 = [0 \ 0 \ 0]$ .

The moving platform is an equilateral triangle  $C_1C_2C_3$  of side  $c$  and center  $P$ . It is established that  $C_1 = (X_1 \ Y_1 \ 0)$  and  $C_2 = (X_2 \ Y_2 \ 0)$ , thus the coordinates of the  $C_3$  can be computed according to

$$C_3 = \left[ \frac{(Y_1 - Y_2)\sqrt{3} + X_1 + X_2}{2} \quad \frac{(X_2 - X_1)\sqrt{3} + Y_1 + Y_2}{2} \quad 0 \right]$$

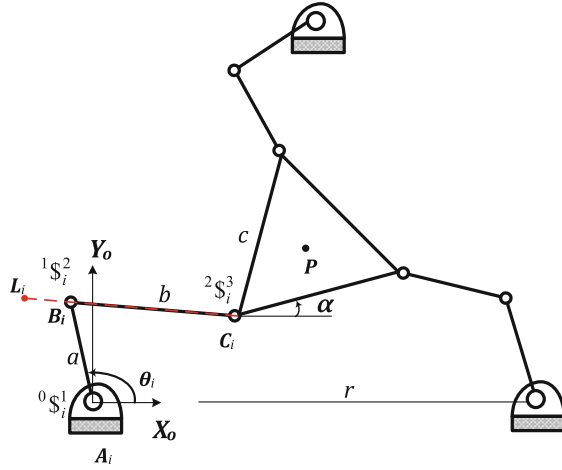


**Fig. 2.** Planar 3-RRR parallel robot parameters.

In order to calculate the coordinates of the center  $P$  and orientation angle  $\alpha$  of the moving platform of the robot, the following four closure equation are considered

$$\left. \begin{aligned}
 (C_i - B_i) \bullet (C_i - B_i) &= b^2 \\
 (C_2 - C_1) \bullet (C_2 - C_1) &= c^2
 \end{aligned} \right\} \quad (7)$$

The Jacobian matrix of the Eq. (7) is obtained with the aim to apply the Newton-Raphson method for computing the points  $C_i$ . Finally, the coordinates of point  $P$  are easily obtained as follows

$$P = \left( \frac{C_1 + C_2 + C_3}{3} \right) \quad (8)$$



The orientation angle  $\alpha$  of the moving platform is simply obtained calculating the angle between two points.

### 2.3 Velocity Analysis

Let  $\mathbf{V} = [\omega \ v]^T$  be the velocity state of the center  $\mathbf{P}$  of the moving platform, where the angular velocity vector is  $\omega = [0 \ 0 \ \omega_z]$  and the velocity vector is  $v = [v_x \ v_y \ 0]$ . The velocity state  $\mathbf{V}$  can be expressed in screw form through the limbs of the robot as follows

$$\mathbf{V} = \dot{\theta}_i {}^0\mathbb{S}_i^1 + {}_1\omega_2 {}^1\mathbb{S}_i^2 + {}_2\omega_3 {}^2\mathbb{S}_i^3 \quad (9)$$

where  $\dot{\theta}_i$  are the joint-velocity rates of the  $i$ th actuated revolute joint and each screw is calculated as

$${}^0\mathbb{S}_i^1 = \begin{bmatrix} \hat{\mathbf{u}}_i \\ \hat{\mathbf{u}}_i \times -\mathbf{A}_i \end{bmatrix} \quad {}^1\mathbb{S}_i^2 = \begin{bmatrix} \hat{\mathbf{v}}_i \\ \hat{\mathbf{v}}_i \times -\mathbf{B}_i \end{bmatrix} \quad {}^2\mathbb{S}_i^3 = \begin{bmatrix} \hat{\mathbf{w}}_i \\ \hat{\mathbf{w}}_i \times -\mathbf{C}_i \end{bmatrix}$$

and

$$\hat{\mathbf{u}}_i = \begin{bmatrix} Ax_i & Ay_i & 1 \\ \|Ax_i & Ay_i & 1\| \end{bmatrix} \quad \hat{\mathbf{v}}_i = \begin{bmatrix} Bx_i & By_i & 1 \\ \|Bx_i & By_i & 1\| \end{bmatrix} \quad \hat{\mathbf{w}}_i = \begin{bmatrix} Cx_i & Cy_i & 1 \\ \|Cx_i & Cy_i & 1\| \end{bmatrix}$$

Now, we consider that  $L_i = [lx_i \ ly_i \ 0 \ 0 \ 0 \ \hat{k}]^T$  is a line in Plücker coordinates that passes through the points  $B_i$  and  $C_i$  (see Fig. 2), and is reciprocal only to the associated screws at each passive joint in the same limb. The line  $L_i$  is given by

$$L_i = \begin{bmatrix} \frac{C_i - B_i}{\|C_i - B_i\|} \\ \frac{C_i - B_i}{\|C_i - B_i\|} \times -B_i \end{bmatrix} \quad (10)$$

Note that the dual part of Eq. (10) produces  $d_i = (ly_i Bx_i - lx_i By_i) \hat{k}$ .

In order to eliminate the passive velocity-joint rates from the Eq. (9), the Klein form to both sides of Eq. (9) is applied as follows

$$\{\mathbf{V}; L_i\} = \left\{ \dot{\theta}_i {}^0\mathbb{S}_i^1 + {}_1\omega_2 {}^1\mathbb{S}_i^2 + {}_2\omega_3 {}^2\mathbb{S}_i^3; L_i \right\}$$

note that

$$\{{}^1\mathbb{S}_i^2; L_i\} = \{{}^2\mathbb{S}_i^3; L_i\} = 0$$

hence

$$\{\mathbf{V}; L_i\} = \dot{\theta}_i \{{}^0\mathbb{S}_i^1; L_i\}$$

namely

$$\begin{aligned} (0 \ 0 \ \omega_z) \bullet (0 \ 0 \ d_i) + (l_x \ l_y \ 0) \bullet (v_x \ v_y \ 0) &= \dot{\theta}_i \{^0\mathbb{S}_i^1; L_i\} \\ \omega_z d_i + l_x v_x + l_y v_y &= \dot{\theta}_i \{^0\mathbb{S}_i^1; L_i\} \end{aligned} \quad (11)$$

Finally, from the Eq. (11) the input-output velocity equation of the robot can be obtained as follows

$$\mathbf{A} \mathbf{v} = \mathbf{B} \dot{\boldsymbol{\Theta}} \quad (12)$$

where

$\mathbf{A} = [d_i \ l_x \ l_y]^T$  is the active Jacobian matrix of the robot,

$\mathbf{v} = [\omega_z \ v_x \ v_y]$  is the vector of the angular and linear velocities, while

$\dot{\boldsymbol{\Theta}} = [\dot{\theta}_1 \ \dot{\theta}_2 \ \dot{\theta}_3]^T$  is the first-order generalized coordinates of the mechanism and

$\mathbf{B} = \text{diag}[\{^0\mathbb{S}_1^1; L_1\} \ \{^0\mathbb{S}_2^1; L_2\} \ \{^0\mathbb{S}_3^1; L_3\}]$  is the passive Jacobian matrix.

## 2.4 Acceleration Analysis

Let  $\mathbf{A} = [\alpha \ a]^T$  be the acceleration state of the center  $\mathbf{P}$  of the moving platform, where the angular acceleration vector is  $\alpha = [0 \ 0 \ \dot{\omega}_z]$  and the acceleration vector is  $a = [a_x \ a_y \ 0]$ . The acceleration state  $\mathbf{A}$  can be expressed in screw form through the limbs of the robot as follows

$$\mathbf{A} = \ddot{\theta}_i {}^0\mathbb{S}_i^1 + {}_1\dot{\omega}_2^1 {}^1\mathbb{S}_i^2 + {}_2\dot{\omega}_3^2 {}^2\mathbb{S}_i^3 + \mathcal{L}_i \quad (13)$$

where  $\ddot{\theta}_i$  are the joint-acceleration rates of the  $i$ th actuated revolute joint and  $\mathcal{L}_i$  is the Lie product or Lie screw of acceleration, which is given by

$$\mathcal{L}_i = [\dot{\theta}_i {}^0\mathbb{S}_i^1 \quad {}_1\dot{\omega}_2^1 {}^1\mathbb{S}_i^2 + {}_2\dot{\omega}_3^2 {}^2\mathbb{S}_i^3] + [{}_1\dot{\omega}_2^1 {}^1\mathbb{S}_i^2 \quad {}_2\dot{\omega}_3^2 {}^2\mathbb{S}_i^3]$$

Now, applying the Klein form to both sides of the Eq. (13) analogously to velocity analysis we have

$$\{\mathbf{A}; L_i\} = \ddot{\theta}_i \{^0\mathbb{S}_i^1; L_i\} + \{\mathcal{L}_i; L_i\}$$

namely

$$\dot{\omega}_z d_i + l_x a_x + l_y a_y = \ddot{\theta}_i \{^0\mathbb{S}_i^1; L_i\} + \mathbf{C} \quad (14)$$

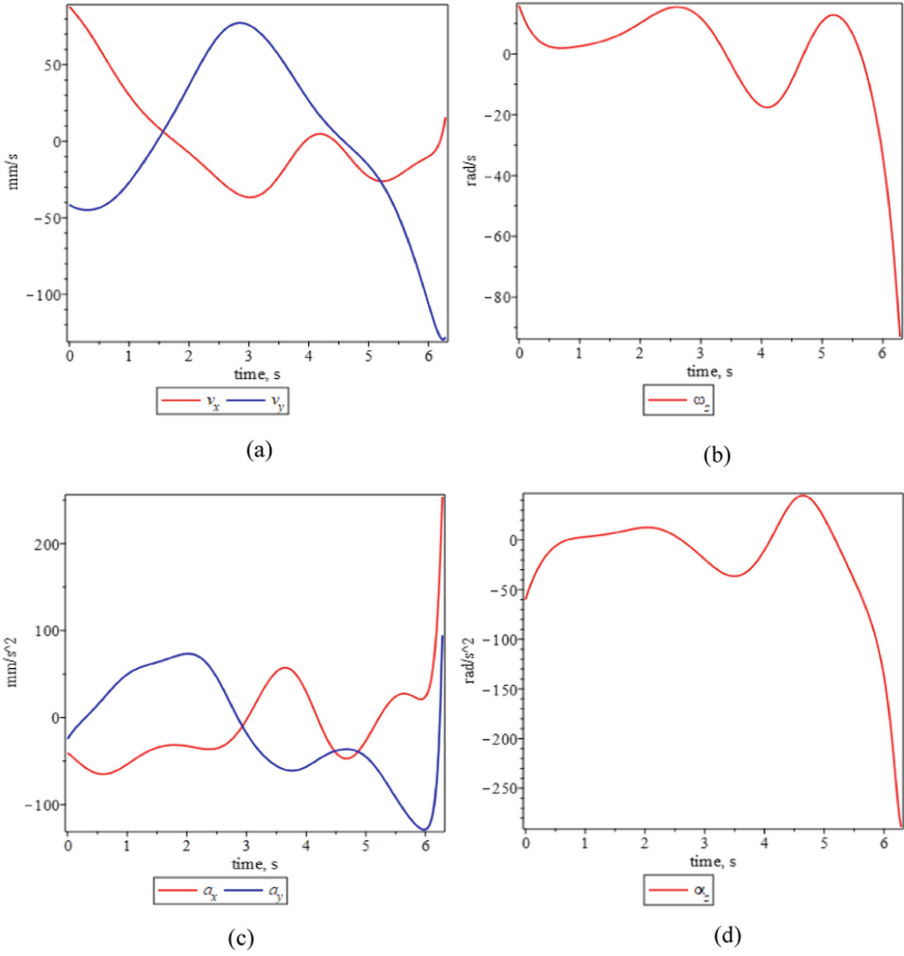


**Fig. 3.** Time history of the velocity and acceleration of the moving platform. (a) velocity components. (b) angular velocity component. (c) acceleration components. (d) angular acceleration component.

Finally, from de Eq. (14) the input-output acceleration equation of the robot can be obtained as follows

$$\mathbf{A}\mathbf{a} = \mathbf{B}\ddot{\mathbf{\Theta}} + \mathbf{C} \quad (15)$$

where

$\mathbf{a} = [\dot{\omega}_z \quad a_x \quad a_y]^T$  is the vector of the angular and linear acceleration, while

$\ddot{\mathbf{\Theta}} = [\ddot{\theta}_1 \quad \ddot{\theta}_2 \quad \ddot{\theta}_3]^T$  is the second-order generalized coordinates of the mechanism and

$\mathbf{C} = [\{\mathcal{L}_1; L_1\} \quad \{\mathcal{L}_2; L_2\} \quad \{\mathcal{L}_3; L_3\}]^T$  is the complementary matrix of acceleration.

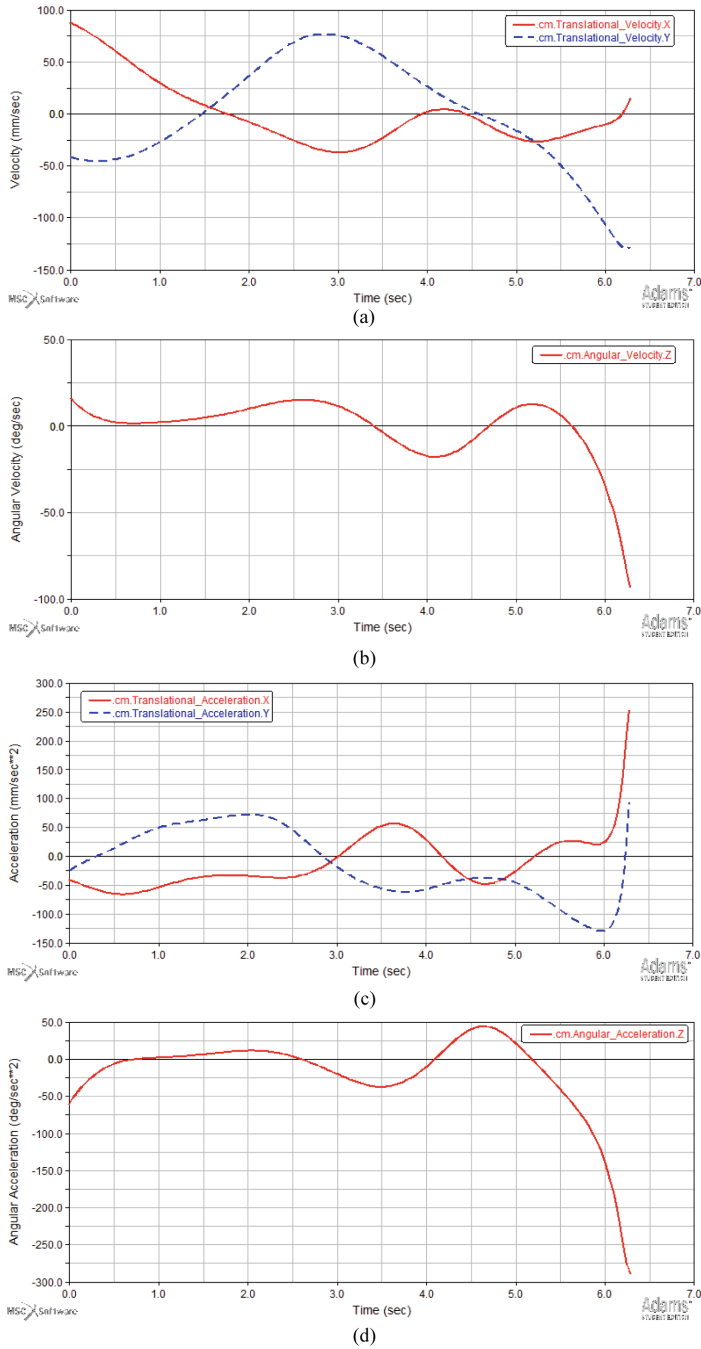


**Fig. 4.** Validation of velocity and acceleration components of the moving platform with ADAMS<sup>®</sup>. (a) velocity components. (b) angular velocity component. (c) acceleration components. (d) angular acceleration component.

### 3 Numerical Example

In this section a numerical example using SI units is solved. With the aim to obtain a temporal behavior of the moving platform of the manipulator the velocity and acceleration equations are used. The initial conditions as follows,  $\mathbf{P} = [175.86 \ 103.80 \ 0]$ ,  $\dot{\theta}_1 = 19^\circ t$ ,  $\dot{\theta}_2 = -49^\circ \sin(t)$ ,  $\dot{\theta}_3 = 45^\circ \sin(t)$ , where the interval for time  $t$  is  $0 \leq t \leq 2\pi$ . The link lengths are  $r = 350$  mm,  $a = 100$  mm,  $b = 150$  mm,  $c = 100$  mm.

The resulting temporal behavior of the moving platform of the robot is shown in Fig. 3. As observed in Fig. 3 the planar robot starts its motion at the time  $t = 0$  and  $2\pi$  s later finishes its trajectory in a final position.

In order to verify the kinematics formulation of the parallel manipulator based on screw theory, the velocity and acceleration components are obtained using a commercially available dynamic simulation software ADAMS<sup>®</sup>. The results obtained using the software CAD are shown in Fig. 4.

Finally, it is worthy to note that the results obtained via screw theory are the same as the results obtained by using ADAMS<sup>®</sup>.

### 4 Conclusions

In this work, the kinematic analysis of a 3-RRR parallel robot via screw theory is presented. A brief explanation of concepts used for applying screw theory in the kinematic analysis of parallel robots is provided.

The direct position analysis of the robot is presented in order to develop the velocity and acceleration analyses. Since, only a select group of researchers has the know-how of the screw theory, the input-output equations of velocity and acceleration are obtained step by step, with the aim to show details that no-one mentions in the kinematic analysis of a parallel robot via screw theory.

It is worthy to note that, the velocity and acceleration equations are obtained by resorting to reciprocal-screw by applying the Klein form, which is an important method for addressing the passive joints of the parallel manipulators.

In addition, a numerical example in order to verify the kinematics formulation of the parallel manipulator based on screw theory is provided. The temporal behavior of velocity and acceleration components are presented. The obtained results are evidently similar as the obtained results using a software CAD.

With the details mentioned in this paper, to understand and apply this mathematical tool could be easier and simply than learning it by itself.

## References

1. Ball, R.S.: *Treatise on the Theory of Screws*. Cambridge University Press, New York (1900). Reprint 1998
2. Brand, L.: *Vector and Tensor Analysis*. Wiley, New York (1947)
3. Mohamed, M.G., Duffy, J.: A direct determination of the instantaneous kinematics of fully parallel robot manipulators. *ASME J. Mech. Transm. Autom. Des.* **107**(2), 226–229 (1985)
4. Rico, J.M., Gallardo, J., Duffy, J.: Screw theory and higher order kinematic analysis of open serial and closed chains. *Mech. Mach. Theory* **34**, 559–586 (1999)
5. Bonev, L.A., Zlatanov, D., Gosselin, C.M.: Singularity analysis of a 3-DOF planar parallel mechanism via screw theory. *ASME J. Mech. Des.* **125**(3), 573–581 (2003)
6. Tsai, L.-W.: *Robot Analysis*. Wiley, New York (1999)
7. Kong, X., Gosselin, C.M.: Type synthesis of a 3-DOF spherical parallel manipulators based on screw theory. *ASME J. Mech. Des.* **126**(1), 101–108 (2004)
8. Kong, X., Gosselin, C.M.: Type synthesis of a 3-DOF translational parallel manipulators based on screw theory. *ASME J. Mech. Des.* **126**(1), 83–92 (2004)
9. Kong, X., Gosselin, C.M.: Type synthesis of a 3T1R 4-DOF parallel manipulators based on screw theory. *ASME J. Mech. Des.* **20**(2), 181–190 (2004)
10. Gallardo-Alvarado, J., Rico-Martínez, J., Alici, G.: Kinematics and singularity analyses of a 4-DOF parallel manipulator using screw theory. *Mech. Mach. Theory* **41**, 1048–1061 (2006)
11. Gallardo-Alvarado, J., et al.: Kinematics of a class of parallel manipulators which generates structures with three limbs. *Multibody Syst. Dyn.* **17**(1), 27–46 (2007)
12. Gallardo, J., Rodríguez, R., Caudillo, M., Rico, J.M.: A family of spherical parallel manipulators with two legs. *Mech. Mach. Theory* **43**(2), 201–216 (2008)
13. Gallardo-Alvarado, J., García-Murillo, M.A., Castillo-Castaneda, E.: A 2(3-RRPS) parallel manipulator inspired by Gough-Stewart platform. *Robotica* **31**(03), 381–388 (2012)
14. García-Murillo, M.A., Gallardo-Alvarado, J., Castillo-Castaneda, E.: Finding the generalized forces of a series-parallel manipulator. *Int. J. Adv. Robot. Syst.* **10**(4) (2013)
15. Maldonado-Echegoyen, R., Castillo-Castaneda, E., García-Murillo, M.A.: Kinematic and deformation analyses of a translational parallel robot for drilling task. *J. Mech. Sci. Technol.* **29**(10), 4437–4443 (2015)
16. García-Murillo, M.A., et al.: Kinematics and Dynamics of a 3-RPSR Parallel Robot Used as a Pipe-Bending Machine. In: Lenarčič, J., Khatib, O. (eds.) *Advances in Robot Kinematics*, pp. 307–316. Springer, Cham (2014)
17. Takeda, Y., et al.: Kinematic design of 3-RPSR parallel mechanism for movable-die drive mechanism of pipe bender. *Rom. J. Tech. Sci. Appl. Mech.* **58**(1–2), 71–96 (2013)
18. Gallardo-Alvarado, J., Balmaceda-Santamaría, A.L., Castillo-Castaneda, E.: An application of screw theory to the kinematic analysis of a Delta-type robot. *J. Mech. Sci. Technol.* **28**(9), 3785–3792 (2014)
19. Balmaceda-Santamaría, A.L., Castillo-Castaneda, E., Gallardo-Alvarado, J.: A novel reconfiguration strategy of a Delta-type parallel manipulator. *Int. J. Adv. Robot. Syst.* **13**(15), 11 pages (2016)
20. Gallardo-Alvarado, J.: Kinematics of a hybrid manipulator by means of screw theory. *Multibody Syst. Dyn.* **14**, 345–366 (2005)
21. Gallardo-Alvarado, J., Orozco, H., Rico, J.M.: Kinematics of 3-RPS parallel manipulators by means of screw theory. *Int. J. Adv. Manuf. Technol.* **36**, 598–605 (2008)
22. Gallardo-Alvarado, J., et al.: Kinematics and dynamics of 2(3-RPS) manipulators by means of screw theory and principle of virtual work. *Mech. Mach. Theory* **43**, 1281–1294 (2008)

23. Gallardo-Alvarado, J., Arroyo-Ramírez, B., Rojas-Garduño, H.: Kinematics of a five-degrees-of-freedom parallel manipulator using screw theory. *Int. J. Adv. Manuf. Technol.* **45**, 830–840 (2009)
24. Gallardo-Alvarado, J.: *Kinematic Analysis of Parallel Manipulators by Algebraic Screw Theory*, 1st edn. Springer, Cham (2016)
25. Chasles, M.: Notes on the general properties of a system of 2 identical bodies randomly located in space; and on the finite or infinitesimal motion of a free solid body. *Bulletin des Sciences Mathématiques, Astronomiques, Physiques et Chimiques* **14**, 321–326 (1830)



# Dynamic Modeling for Spatial Revolute Joint with Clearances in Multibody Systems Based on HLCP

Long Li, Shengnan Lyu<sup>(✉)</sup>, and Xilun Ding

Beihang University, Beijing 100191, China  
{bhlilong, shengnan\_lyu, xlding}@buaa.edu.cn

**Abstract.** This paper presents a modeling and simulation method for rigid multibody system (MBS) with clearance-affected spatial revolute joints (SRJ) under the assumption that the clearance is much less than the physical dimension of SRJ. The SRJ is treated as an assembly of a rigid journal undergoing no-impact fixed-point motion in a bearing. A simple formulation for solving non-smooth dynamics of MBS with spatial revolute joints with clearances (SRJC) is developed by employing the complementary condition of the normal contact force. The geometric constraints of the SRJ has been transformed into a set of orthogonal bilateral constraints. The contact state determined by the magnitude and orientation of normal constraint forces in cylindrical pairs is formulated as a horizontal linear complementarity problem (HLCP) which is solved by the first kind of Lagrange's equation and the Baumgarte stabilization method. A precession gyro is considered as a demonstrative application and the numerical results show some dynamical behaviors of MBS containing SRJC. Particularly, the proposed method can be equally applied to non-smooth dynamics of MBS considering the friction and impact.

**Keywords:** Spatial revolute joint · Clearance · Non-smooth dynamics · Linear complementarity problem

## 1 Introduction

The presence of joint clearance is non-negligible in realistic mechanisms. Dynamic analysis considering joint clearance is a complex and important issue in non-smooth MBS since the clearance affects the dynamic response of the system, which gains paramount importance due to the demand for proper design of real joints in engineering areas.

Over the last few years, many numerical methods for non-smooth multibody dynamics with joint clearance have been investigated [1–4]. Flores et al. presented and discussed an approach to model the planar rigid MBS with clearance joints based on the non-smooth dynamic method [5–7]. Zhuang and Wang presented a modeling and simulation method for the rigid MBS with frictional translational joints [8, 9].

Recently, extensive work has been performed to study the dynamic behavior of MBS with spatial joint clearance. Bauchau et al. developed the formulation of models for planar and spatial joints with clearance in flexible MBS within the framework of the finite element method [10]. Flores et al. developed a technique for dynamic analysis of



MBS based on a continuous contact force model, both the spatial revolute joints and spherical joints with clearance have been discussed [11, 12]. Tian et al. formulated the dynamics of spatial flexible MBS of lubricated spherical joints with clearance [13]. Liu et al. proposed a new four-point contact kinematic model of a natural coordinate formulation (NCF) for the rigid cylindrical joint with clearance, which has been applied to the dynamics in a spatial rigid-flexible MBS [14].

The linear complementary problem (LCP) based formulations can achieve good computational performance to detect non-smooth events of MBS [15, 16]. However, little research work has been developed to model SRJC based on LCP. Depending on the contacts is planar or spatial, the transitions of non-smooth events can be formulated as a linear complementarity problem (LCP) or nonlinear complementarity problem (NCP) [17]. Xu and Wang et al. transformed the state transition of two-dimensional Coulomb dry friction into an NCP and presented a numerical method for the MBS with two-dimensional Coulomb dry friction and non-holonomic constraints [18].

In this paper, we present a novel method to model the SRJC in non-smooth MBS based on the HLCP and Baumgarte stabilization technique. The attitude kinematics of the SRJC is described by a specific parameterization in  $SO(3)$ ; the orientation caused by clearance forms a 2-D Exp-submanifold of  $SO(3)$ . To illustrate the feasibility of the presented method, the non-smooth dynamic modeling has been validated by numerical simulation on a gyro with clearances.

This paper is organized as follows. The next section presents the kinematic model of spatial revolute joints with a small clearance. In Sect. 3, several different configurations of the SRJC are described as complementarity conditions. In Sect. 4, the dynamics of MBS with SRJC is formulated in Lie group setting, which is solved by event-driven method based on HLCP; the Baumgarte stabilization method is used to reduce the constraint drift. Numerical example is presented to show some non-smooth dynamical behaviors of the MBS with SRJC and validate the feasibility of the proposed method in Sect. 5.

## 2 Mathematical Model of SRJC

### 2.1 Contact State Description

The spatial revolute pair with clearance is composed of two rigid cylindrical bodies, i.e. journal and bearing. The journal is subjected to rigid motion with respect to the bearing. Figure 1 shows the schematic of SRJ with clearance, in which the geometric dimensioning is exaggerated for illustration. Four possible distributions of journal and bearing of an SRCJ are enumerated in Fig. 2 [19]:



Fig. 1. Schematic of spatial revolute joint with clearance

- (1) No contact exists between the two components of SRJC, i.e. the journal rotates inside the bearing without contacting. There is no reaction force in spatial revolute joints, as shown in Fig. 2(a).
- (2) Single point contact happens between the two components of SRJC. Only one normal force is acting at the contact point in spatial revolute joints, as shown in Fig. 2(b).
- (3) Two-points of contact happens between the two components of SRJC. Two reaction forces are acting at the two contact points in spatial revolute joints, as shown in Fig. 2(c).
- (4) Two components of SRJC performs line contact. The constraint forces are equivalently handled as the normal forces acting the two adjacent contact points, as shown in Fig. 2(d).

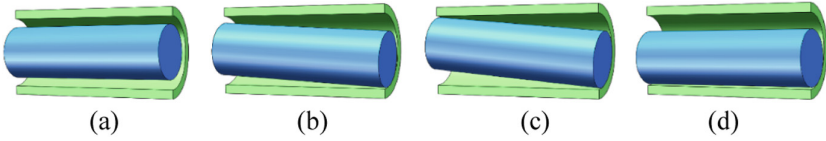


**Fig. 2.** Distribution possibilities of journal and bearing of an SRJC

## 2.2 Kinematic Description of SRJC

The coordinate frames of the SRJC are established as shown in Fig. 3.  $\Sigma_b$  denotes the bearing-fixed frame.  $\Sigma_j$  is the journal-fixed frame. The origins  $o_b$  and  $o_j$  are located at the center of mass of the bearing and the journal, respectively. The relative configuration between the bearing and the journal is described by the relative position and orientation. Thanks to the axial constraints of the SRJC in  $z_b$  direction, the vector  $o_j o_b$  is approximately located on the  $x_j y_j$  plane of  $\Sigma_b$ . The attitude is described by the rotation of the journal-fixed frame with respect to the bearing-fixed frame, which is represented by a rotation tensor  $R \in SO(3)$ . The special orthogonal group  $SO(3)$  can be represented as the  $3 \times 3$  orthogonal matrices group:

$$SO(3) = \{R \in GL(3, \mathbb{R}) \mid R^T R = I, \det R = 1\}.$$

The attitude of the journal with respect to the bearing can be characterized by tilt and torsion angles in a modified Euler angles parameterization [20, 21]. The tilt is a 2-D submanifold of  $SO(3)$  represented by the canonical coordinates of the first kind, which is named as *Exp-submanifold* in [22]. The torsion is a one-parameter subgroup  $\exp\{\theta \hat{z}\} \in SO(3)$ . We define the clearance motion as a tilt rotation, i.e.  $\exp\{\hat{x}_j, \hat{y}_j\}_{\text{span}}$ . So that, the composed finite rotation resulting from two successive rotations in  $\Sigma_j$  can be written as a mapping from  $S^3$  to  $SO(3)$ ,

$$(\alpha, \beta, \theta) \mapsto e^{2\hat{x}_j + \beta \hat{y}_j} e^{\theta \hat{z}_j} \in SO(3).$$

where the ‘hat’ operator is a map  $\wedge : \mathbb{R}^3 \rightarrow so(3)$ , where  $so(3)$  is the Lie algebra of  $SO(3)$ .

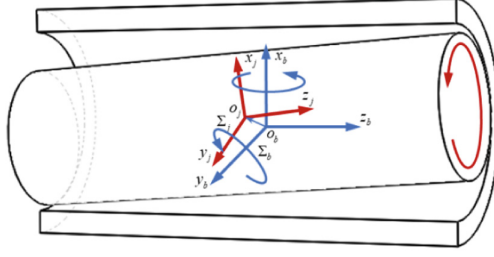


**Fig. 3.** The coordinate frames of SRJC

### 3 LCP Formulation

The normal contact forces between the journal and the bearing in SRJC are presented by means of complementary conditions in this section. The contact state can be formulated as a linear complementary problem (LCP). LCP is a set of linear equations subjected to the inequality complementarity conditions, which can be written in matrix form as [23]

$$\begin{cases} y = Ax + b \\ -y \in \text{Upr}(x) \end{cases} \quad (1)$$

where the function Upr applied to LCP is the unilateral primitive defined in (2). It is a maximal monotone set-valued map on  $\mathbb{R}_0^+$  which is illustrated in Fig. 4.

$$\text{Upr}(x) := \begin{cases} \{0\} & x > 0 \\ (-\infty, 0] & x = 0 \\ \emptyset & x < 0 \end{cases} \quad (2)$$

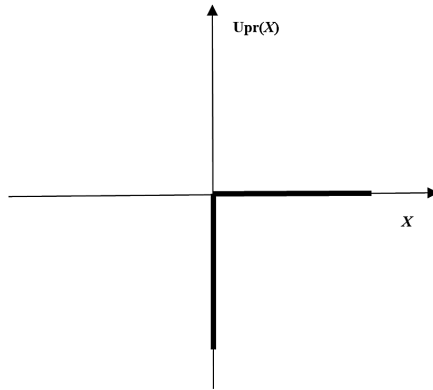


**Fig. 4.** The map:  $x \rightarrow \text{Upr}(x)$

To deal with the two-dimensional normal forces between the journal and the bearing, we cover the cylindrical inner surface of the bearing by using four open semi-cylinders, as shown in Fig. 5. For any configuration of the SRJC, the magnitude  $\lambda_j^i$  of components of the normal forces in the  $x$  and  $y$  direction are subject to the following complementarity conditions,

$$-\left[\lambda_a^{x-}, \lambda_a^{y-}, \lambda_b^{x-}, \lambda_b^{y-}\right]^T = \text{Upr}\left(\left[\lambda_a^{x+}, \lambda_a^{y+}, \lambda_b^{x+}, \lambda_b^{y+}\right]^T\right) \quad (3)$$

where the superscripts denote the semi-cylindrical covering surface  $x^-$ , surface  $x^+$ , surface  $y^-$ , surface  $y^+$ ; the subscripts  $a$  and  $b$  denote the two terminals of the SRJC in axial direction.

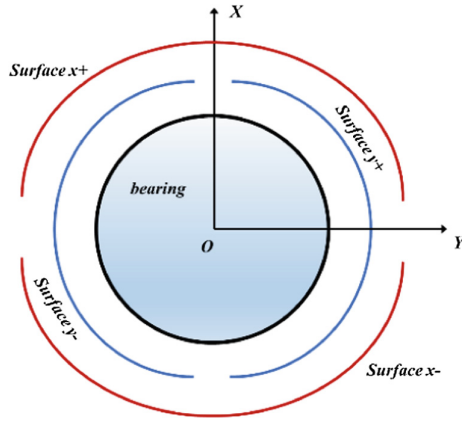


**Fig. 5.** The schematic of the bearing's semi-cylindrical covers

For an MBS consists of  $n$  SRJC, the complementarity conditions can be expressed as,

$$-\left[\lambda_x^-, \lambda_y^-\right]^T = \text{Upr}\left(\left[\lambda_x^+, \lambda_y^+\right]^T\right) \quad (4)$$

$$\text{where, } \begin{cases} \lambda_x^+ = [\lambda_{1a}^{x+}, \lambda_{1b}^{x+}, \dots, \lambda_{na}^{x+}, \lambda_{nb}^{x+}]^T \in \mathbb{R}^{2n} \\ \lambda_x^- = [\lambda_{1a}^{x-}, \lambda_{1b}^{x-}, \dots, \lambda_{na}^{x-}, \lambda_{nb}^{x-}]^T \in \mathbb{R}^{2n} \\ \lambda_y^+ = [\lambda_{1a}^{y+}, \lambda_{1b}^{y+}, \dots, \lambda_{na}^{y+}, \lambda_{nb}^{y+}]^T \in \mathbb{R}^{2n} \\ \lambda_y^- = [\lambda_{1a}^{y-}, \lambda_{1b}^{y-}, \dots, \lambda_{na}^{y-}, \lambda_{nb}^{y-}]^T \in \mathbb{R}^{2n} \end{cases}$$

The normal force  $F$  acting on the  $i$ th SRCJ can be split into two components  $F_x$  and  $F_y$  in  $x$  and  $y$  direction, and written in the matrix form as,

$$\begin{pmatrix} F_x \\ F_y \end{pmatrix} = \begin{pmatrix} G & H & 0_{2n \times 2n} & 0_{2n \times 2n} \\ 0_{2n \times 2n} & 0_{2n \times 2n} & G & H \end{pmatrix} \begin{pmatrix} \lambda_x^+ & \lambda_x^- & \lambda_y^+ & \lambda_y^- \end{pmatrix}^T \quad (5)$$

where  $F_x = [\lambda_1^{x+}, \lambda_1^{x-}, \dots, \lambda_n^{x+}, \lambda_n^{x-}]$ ,  $F_y = [\lambda_1^{y+}, \lambda_1^{y-}, \dots, \lambda_n^{y+}, \lambda_n^{y-}]$ ,  $G = \text{diag}[G_1, \dots, G_n]$ ,  $H = \text{diag}[H_1, \dots, H_n]$ ,  $G_i = \begin{bmatrix} 1 & 1 \\ 0 & 0 \end{bmatrix}$ ,  $H_i = \begin{bmatrix} 0 & 0 \\ 1 & 1 \end{bmatrix}$ ,  $(i = 1, \dots, n)$ .

#### 4 Dynamic Equations of MBS on Lie Group

The dynamic equations of an MBS comprising  $n$  rigid bodies with holonomic constraints form an index 3 system of differential-algebraic equations (DAEs) on the Lie group state space [24]

$$\begin{cases} \dot{M}(q)\dot{V} + \Phi_q^T \lambda = Q(q, V, t) \\ \dot{q} = qV \\ \Phi(q) = 0 \end{cases} \quad (6)$$

where  $q = (q_1, \dots, q_2) \in G$  describes the configuration of  $n$  rigid bodies,  $G = SE(3)^n$  is the  $6n$ -D Lie group, which represents the ambient space of an MBS consisting of  $n$  bodies,  $V = (V_1, \dots, V_n) \in g$  is the velocity of MBS expressed in the body-fixed frame,  $g = se(3)^n$  is the Lie algebra of  $G$ ,  $\lambda$  are Lagrange multipliers, and  $\Phi_q$  is the constraint Jacobian.

Using the Baumgarte stabilization method [25, 26], the constraint equations are rewritten on the acceleration level  $\ddot{\Phi} + 2\alpha\dot{\Phi} + \beta^2\Phi = 0$ , then the dynamic equations can be transformed to an index 1 system of DAEs in the matrix notation

$$\begin{pmatrix} M & \Phi_q^T \\ \Phi_q & 0 \end{pmatrix} \begin{pmatrix} \dot{V} \\ \lambda \end{pmatrix} = \begin{pmatrix} Q \\ h \end{pmatrix} \quad (7)$$

where  $h = -\dot{\Phi}_q\dot{q} - \dot{\Phi}_t - 2\alpha(\Phi_q\dot{q} + \Phi_t) - \beta^2\Phi$ ,  $\alpha$  and  $\beta$  represent the feedback control parameters.

The constraint equations of the MBS with  $k$  constraints can be expressed in the matrix form  $\Phi(q) = [\varphi_1^T, \dots, \varphi_k^T]^T = 0$ , which can be expanded into 4 items according to the complementarity conditions,

$$\Phi_q^T \lambda = [\Phi_x^T, \Phi_y^T][\lambda_x^T, \lambda_y^T]^T = V^+ \lambda_x^+ + V^- \lambda_x^- + H^+ \lambda_y^+ + H^- \lambda_y^- \quad (8)$$

where  $(V^+, V^-, H^+, H^-)$  is the constraint Jacobian matrix corresponding to  $(\lambda_x^+, \lambda_x^-, \lambda_y^+, \lambda_y^-)$ .

Substituting (8) into (7) can yields the following equations,

$$\begin{aligned} \begin{bmatrix} \Phi_q^x M^{-1} V^- & \Phi_q^x M^{-1} H^- \\ \Phi_q^y M^{-1} V^- & \Phi_q^y M^{-1} H^- \end{bmatrix} \begin{pmatrix} \lambda_x^- \\ \lambda_y^- \end{pmatrix} &= \begin{bmatrix} -\Phi_q^x M^{-1} V^+ & -\Phi_q^x M^{-1} H^+ \\ -\Phi_q^y M^{-1} V^+ & -\Phi_q^y M^{-1} H^+ \end{bmatrix} \begin{pmatrix} \lambda_x^+ \\ \lambda_y^+ \end{pmatrix} \\ &= \begin{pmatrix} -\Phi_q^x M^{-1} Q - \dot{\Phi}_q^x \dot{q} - \xi \Phi_q^x \dot{q} - \eta \Phi^x \\ -\Phi_q^y M^{-1} Q - \dot{\Phi}_q^y \dot{q} - \xi \Phi_q^y \dot{q} - \eta \Phi^y \end{pmatrix} \end{aligned} \quad (9)$$

(8) together with the complementarity conditions described by (3) form the HLCP for the dynamic analysis of MBS with SRJC.

## 5 Numerical Example

As a numerical illustration, the dynamics of a procession gyro with SRJC, as shown in Fig. 6, is analyzed in this section. Physical parameters of the system are:  $m = 12$  kg,  $J_e = 0.1$  kg · m<sup>2</sup>,  $L = 4$  m,  $a = 4$  m,  $b = 2$  m,  $\alpha = 50$ ,  $\beta = 50$ . The equations govern the MBS kinematics and dynamics are presented as follows.

The attitude kinematics described by the rotation tensor can be written by product of exponentials

$$R = \exp(\psi \hat{x}_b) \exp(\alpha \hat{x}_b + \beta \hat{y}_b) \exp(\theta \hat{z}_j) \quad (10)$$

The angular velocity expressed in the body-fixed frame can be given by

$$(\omega_x, \omega_y, \omega_z)^T = (R^{-1} \dot{R})^\vee = \left( Ad_{(\exp(\alpha \hat{x}_b + \beta \hat{y}_b) \exp(\theta \hat{z}_j))^{-1}} \dot{\psi} \hat{x}_b + Ad_{\exp^{-1}(\theta \hat{z}_j)} (\dot{\alpha} \hat{x}_b + \dot{\beta} \hat{y}_b) + \dot{\theta} \hat{z}_j \right)^\vee \quad (11)$$

where the ‘ $\vee$ ’ operator describes a map  $\vee : so(3) \rightarrow \mathbb{R}^3$ ,  $so(3)$  is the Lie algebra of  $SO(3)$ .

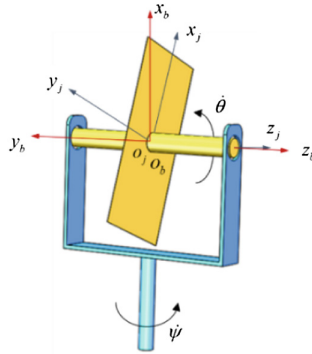


**Fig. 6.** A procession gyro with SRJC

By using the Lagrange multiplier, the constrained Newton-Euler equations can be written as

$$M\dot{v} - ad(v)^T Mv = Ad_g^{-T} \left( \Phi_q^T \lambda + Q \right), \quad (12)$$

where  $g = (\exp(\theta \hat{z}), \mathbf{0}_{3 \times 1})$ ,  $Q = (0, 0, mg, 0, 0, 0)^T$ ,  $\lambda = (\lambda_x^+, \lambda_x^-, \lambda_y^+, \lambda_y^-)^T$ .

The constraint equations of the system can be given by

$$\Phi_x(q) = \begin{bmatrix} x_c - m_a\beta \\ x_c + m_b\beta \end{bmatrix} = 0, \quad \Phi_y(q) = \begin{bmatrix} y_c + m_a\alpha \\ y_c - m_b\alpha \end{bmatrix} = 0. \quad (13)$$

Then, the constraint Jacobian matrix in (8) can be obtained

$$V^+ = \begin{pmatrix} 1 & 1 \\ 0 & 0 \\ 0 & 0 \\ 0 & 0 \\ -m_a & m_b \\ 0 & 0 \end{pmatrix}, \quad V^- = \begin{pmatrix} -1 & -1 \\ 0 & 0 \\ 0 & 0 \\ 0 & 0 \\ m_a & -m_b \\ 0 & 0 \end{pmatrix}, \quad H^+ = \begin{pmatrix} 0 & 0 \\ 1 & 1 \\ 0 & 0 \\ m_a & -m_b \\ 0 & 0 \\ 0 & 0 \end{pmatrix}, \quad H^- = \begin{pmatrix} 0 & 0 \\ -1 & -1 \\ 0 & 0 \\ -m_a & m_b \\ 0 & 0 \\ 0 & 0 \end{pmatrix} \quad (14)$$

According to the given physical parameters, the dynamic characteristics of the gyro have been calculated. The simulation results of the procession gyro are plotted in Figs. 7, 8 and 9. Due to the inertial centrifugal force generated by the precession angular velocity, when the  $x_j$  axis of the homogeneous thin plate is horizontal, i.e. the equilibrium position of the spin motion, the spin angular velocity reaches the maximum. The spin angular velocity and the moment of inertia in  $x_b$  direction reach the maximum synchronously. In addition, the system maintains the moment of momentum in  $x_b$  direction, hence the precession angular velocity reaches the minimum at this moment. It can be seen in Fig. 7 that the maximal spin angular velocity is corresponding to the minimal precession angular velocity. Figure 8 shows the history diagram of Lagrange multiplier, the constraint forces of the bearing  $a$  and  $b$  present the periodic change, balancing the gravity and gyro moment generated by the Coriolis force during the movement of the thin plate. Figure 9 depicts the mutation phenomena of constraint forces showing some non-smooth dynamical behaviors. In Fig. 10, the drift of position constraints  $(\|\alpha\|, \|\beta\|) \leq 1e-18$  and velocity constraints  $(\|\omega_a\|, \|\omega_\beta\|) \leq 1e-16$  obtaining from the Baumgarte's stabilization method are illustrated.

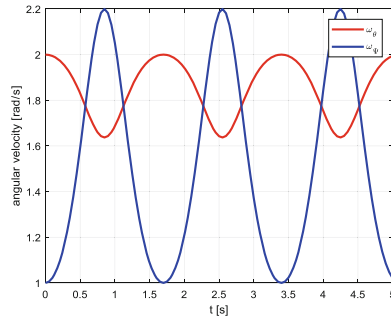


**Fig. 7.** Spin angular velocity  $\omega_\theta$  and procession angular velocity  $\omega_\psi$

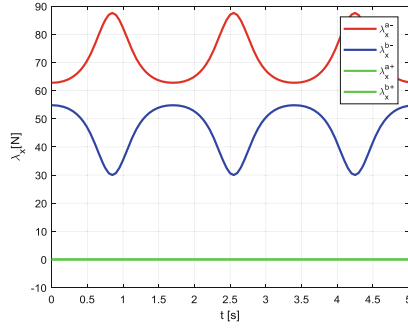


**Fig. 8.** Lagrange multipliers  $\lambda_x^a$  and  $\lambda_x^b$  corresponding to the constraining forces acting on the two terminals of SRJC in  $x$  direction

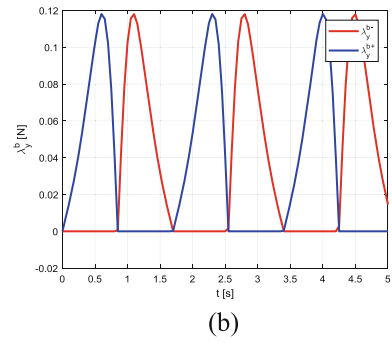
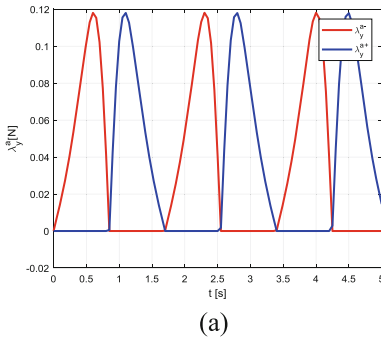
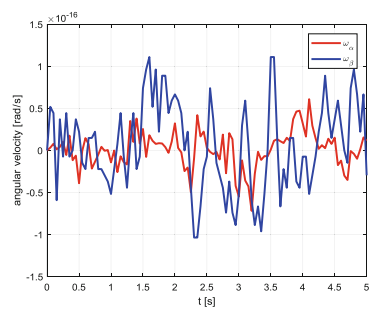
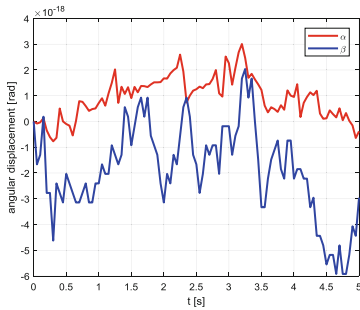


**Fig. 9.** Lagrange multipliers  $\lambda_y^a$  and  $\lambda_y^b$  corresponding to the constraining forces acting on the two terminals of SRJC in  $y$  direction



(a) position constraint

(b) velocity constraint

**Fig. 10.** The drift of constraint equations



## 6 Conclusions

The dynamics of rigid MBS with SRJC are investigated in this paper. HLCP has been adopted as the main methodology because of its simplicity and good performance in numerical calculation. The geometric constraints of SRJC are treated as two orthogonal bilateral constraints by covering the bearing in terms of 4 open semi-cylinder. So that the normal contact state of SRJC can be given by the complementarity conditions. The clearance motion is presented by Exp-submanifold of  $SO(3)$ . Based on the Lagrange multiplier method, the dynamic equations of non-smooth systems in Lie group setting have been obtained. The Baumgarte stabilization method is introduced to reduce the constraint drift of the constraint equations. Although the friction and impact are neglected in this paper, the method proposed can be straightforwardly extended to the non-smooth dynamics of MBS by taking the friction and impact into account.

**Acknowledgments.** This research has been supported by the National Natural Science Foundation of China under Grant 51635002(Key Program), 51605011, the Fundamental Research Funds for the Central Universities (YWF-19-BJ-J-336), and the State Key Laboratory of Robotics and System (HIT). The authors gratefully acknowledge the supporting agencies.

## References

1. Ebrahimi, S., Eberhard, P.: A linear complementarity formulation on position level for frictionless impact of planar deformable bodies. *ZAMM J. Appl. Math. Mech.* **86**(10), 807–817 (2010)
2. Muvengei, O., Kihui, J., Ikua, B.: Numerical study of parametric effects on the dynamic response of planar multi-body systems with differently located frictionless revolute clearance joints. *Mech. Mach. Theory* **53**(7), 30–49 (2012)
3. Erkaya, S., Uzmay, İ.: Modeling and simulation of joint clearance effects on mechanisms having rigid and flexible links. *J. Mech. Sci. Technol.* **28**(8), 2979–2986 (2014)
4. Flores, P., et al.: Translational joints with clearance in rigid multibody systems. *J. Comput. Nonlinear Dyn.* **3**(1), 112–113 (2008)
5. Flores, P., Leine, R., Glocker, C.: Modeling and analysis of planar rigid multibody systems with translational clearance joints based on the non-smooth dynamics approach. *Multibody Syst. Dyn.* **23**(2), 165–190 (2010)
6. Flores, P.: A parametric study on the dynamic response of planar multibody systems with multiple clearance joints. *Nonlinear Dyn.* **61**(61), 633–653 (2010)
7. Flores, P., Ambrósio, J.: Revolute joints with clearance in multibody systems. *Comput. Struct.* **82**(17–19), 1359–1369 (2004)
8. Zhuang, F., et al.: Modeling and simulation of the nonsmooth planar rigid multibody systems; with frictional translational joints. *Multibody Syst. Dyn.* **29**(4), 403–423 (2013)
9. Zhuang, F., Wang, Q.: Modeling and analysis of rigid multibody systems with driving constraints and frictional translation joints. *Acta. Mech. Sin.* **30**(3), 437–446 (2014)
10. Bauchau, O.A., Rodriguez, J.: Modeling of joints with clearance in flexible multibody systems. *Int. J. Solids Struct.* **39**(1), 41–63 (2002)
11. Flores, P., et al.: Spatial revolute joints with clearances for dynamic analysis of multi-body systems. *Proc. Inst. Mech. Eng. Part K J. Multi-Body Dyn.* **220**(4), 257–271 (2006)

12. Flores, P., et al.: Dynamics of multibody systems with spherical clearance joints. *J. Comput. Nonlinear Dyn.* **1**(3), 443–451 (2006)
13. Tian, Q., et al.: Dynamics of spatial flexible multibody systems with clearance and lubricated spherical joints. *Comput. Struct.* **87**(13–14), 913–929 (2009)
14. Liu, C., Tian, Q., Hu, H.: Dynamics and control of a spatial rigid-flexible multibody system with multiple cylindrical clearance joints. *Mech. Mach. Theory* **52**(52), 106–129 (2012)
15. Pfeiffer, F.: The idea of complementarity in multibody dynamics. *Arch. Appl. Mech.* **72**(11–12), 807–816 (2003)
16. Brogliato, B., et al.: Numerical simulation of finite dimensional multibody nonsmooth mechanical systems. *Appl. Mech. Rev.* **55**(2), 107 (2016)
17. Pfeiffer, F., Foerg, M., Ulbrich, H.: Numerical aspects of non-smooth multibody dynamics. *Comput. Methods Appl. Mech. Eng.* **195**(50–51), 6891–6908 (2006)
18. Xu, Z., Wang, Q., et al.: Numerical method for dynamics of multi-body systems with two-dimensional Coulomb dry friction and nonholonomic constraints. *Appl. Math. Mech. (Engl. Ed.)* **38**(12), 1733–1752 (2017)
19. Liu, Q., Lu, S., Ding, X.: An error equivalent model of revolute joints with clearances for antenna pointing mechanisms. *Chin. J. Mech. Eng.* **31**(02), 97–105 (2018)
20. Biesheuvel, C.J., et al.: Advantages of the nested case-control design in diagnostic research. *BMC Med. Res. Methodol.* **8**(1), 48 (2008)
21. Bonev, I.A., Ryu, J.: New approach to orientation workspace analysis of 6-DOF parallel manipulators. *Mech. Mach. Theory* **36**(1), 15–28 (2001)
22. Wu, Y., et al.: Exponential submanifolds: a new kinematic model for mechanism analysis and synthesis. In: *IEEE International Conference on Robotics and Automation*, pp. 4177–4182 (2013)
23. Pardalos, P.M.: *The Linear Complementarity Problem* (1994)
24. Terze, Z., Müller, A., Zlatar, D.: Lie-group integration method for constrained multibody systems in state space. *Multibody Syst. Dyn.* **34**(3), 275–305 (2014)
25. Baumgarte, J.: Stabilization of constraints and integrals of motion in dynamical systems. *Comput. Methods Appl. Mech. Eng.* **1**(1), 1–16 (1972)
26. Braun, D.J., Goldfarb, M.: Eliminating constraint drift in the numerical simulation of constrained dynamical systems. *Comput. Methods Appl. Mech. Eng.* **198**(37), 3151–3160 (2009)



# Kinematic Analysis of (2-RRU)-URR Parallel Mechanism Performing 2R1T Output Motion

Woo-hyeok Choi<sup>(✉)</sup> and Yukio Takeda<sup>id</sup>

Tokyo Institute of Technology, Meguro-ku, Tokyo 152-8552, Japan  
choi.w.ac@m.titech.ac.jp

**Abstract.** This paper describes the (2-RRU)-URR parallel mechanism, which performs rotational motion with two degrees of freedom (DOF) and translational motion with a single DOF. This mechanism consists of a base frame, moving platform, and three connecting chains. Since this mechanism is over-constrained, derivation of its DOF was done by considering the constraint condition of each connecting chain. One of the special structural features of this mechanism is the perpendicularity between the moving platform and URR chain, proving circular-like motion from the origin as the center. In addition, it has another rotational DOF of the moving platform. For a simple kinematic calculation, the mechanism was divided into two parts: the planar motion generator and the orientation generator, and equations for kinematic analysis were derived. In order to clarify the characteristics of the mechanism, workspace of the planar motion generator, rotational ability and sensitivity of the orientation generator were demonstrated by numerical examples and discussed.

**Keywords:** Mechanism design · Constraint analysis · Kinematic analysis · Over-constrained mechanism · Parallel mechanism

## 1 Introduction

Parallel robot is one kind of robots, in which the end-effector is connected to the base frame by various connecting chains arranged in parallel. In comparison with the serial robots, parallel robot have advantages in high stability, high stiffness, high position accuracy, low inertia, light weight, heavy load structure in the base frame. Due to these advantages, parallel robots are generally used for various industrial tasks such as industrial simulators, and force/torque sensors. Until then, numerous parallel robot structures have been proposed. Typical ones are Stewart-Gough platform with six degrees of freedom (DOF) [1], DELTA Robot performing spatial translational motion with three DOF [2], Agile Eye performing rotational motion with three DOF [3]. In these decades, lower-mobility parallel robots, which are ones having DOF less than six, have been paid much attention in the theoretical researches and industrial applications. One of the most well-known lower-mobility parallel robots is DELTA. It is generally used in the industrial field. As DELTA basically provides only three translational motions, its typical task in industrial field is the pick and place operation, for picking some objects and moving to another place. As for the spherical three DOF robot, which consist of the proximal link, distal link, three revolute actuators, and end-effector,

called Agile Eye, was investigated by Gosselin, C. M. [3]. The structural characteristics of this robot is that the axes of all pairs of adjacent joints are orthogonal and all links form a circular arc. Especially it is distinct from the general spherical parallel robot, the proximal link was designed as two circular arcs attached to each other and it affects to extend the range of the spherical motion. Lower-mobility spatial parallel robots performing coupled output motion (parasitic motion) were well discussed [4]. In these parallel robots, the connecting chains between the base and the end-effector usually have the same structure and dimensions, and are symmetrically located between the base and the end-effector.

On the other hand, parallel robots composed of multiple connecting chains of different structures were not popular though there is a possibility to realize a special type of output motion. A spatial parallel manipulator with one rotational and two translational DOFs was investigated by Liu, X. J. and Wang, J. [5, 6]. This robot consists of three non-identical chains, a movable platform, three prismatic joints. Furthermore, this robot has three advantages such as constructing by single-DOF joints, generating the combination motion by translational and rotational motions, and high rotational capability.

Another issue is the use of over-constrained mechanism. Though in such mechanisms, tolerance management should be carefully done, the robot structure can be made simple due to the less joints and links. Thanks to this feature of less number of joints and links, motion capability can be improved in over-constrained mechanisms.

Based on this background, in this paper, the (2-RRU)-URR lower-mobility parallel mechanism, which is composed of non-identical chains and an over-constrained mechanism, performing a spatial rotational mobility is proposed. This mechanism has three connecting chains. Thanks to the special arrangements of these connecting chains, it can provide two rotational mobility and one translational mobility. The structural characteristics and mobility of this proposed mechanism are revealed by a constraint analysis. In order to realize simple kinematic calculation, kinematic analysis is considered and equations are derived for two parts by dividing the mechanism into two parts: planar motion generator and orientation generator. Based on the derived kinematic equations, the kinematic capabilities of the proposed mechanism are demonstrated by its workspace of the planar motion generator, rotational ability and rotational sensitivity of the orientation generator. Finally, the results are discussed.

## 2 (2-RRU)-URR Mechanism and Its Mobility

The proposed mechanism is shown in Fig. 1. This mechanism is composed of three kinematic chains between the base and the output links. In the figure, links ABG and EFJ are base and output link, respectively. The chains 1 and 2 have the same kinematic structure, in which four revolute (R) joints are arranged from the base to the output link where the three successive three R joints are parallel and the fourth joint is perpendicular to the others so that the three and fourth R joints form a universal (U) joint. The fourth revolute joints in these chains are co-axial. The chain 3 is composed of four R joints. The second to fourth joints are parallel, and the first joint is perpendicular to the others, forming a U joint with the second one. Two coordinate systems. O-xyz on the base frame and P - x'y'z' on the output link are considered.

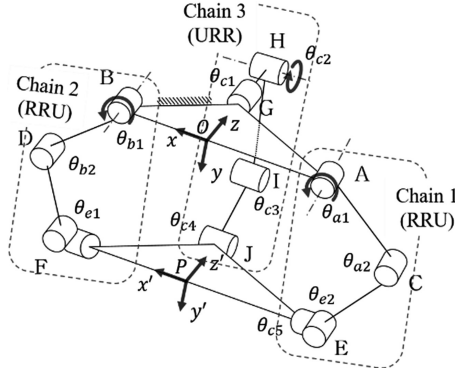


**Fig. 1.** Kinematic diagram of the proposed (2-RRU)-URR mechanism

Applying the mobility formula to this mechanism reveals that DOF of the proposed mechanism is zero as follows:

$$6(N - J - 1) + \sum_{i=1}^J f_i = 6(8 - 9 - 1) + (1 \times 6) + (2 \times 3) = 0 \quad (1)$$

where  $N$ ,  $J$ , and  $f_i$  are the number of links, the number of joints, and the DOF of joints respectively. However, this result is different from the real behavior of this mechanism, which was observed by the authors using a prototype. According to our observation, this mechanism is expected to have three DOF. That is rotational motion around  $z$  axis, translational motion in OP direction and rotational motion around  $x'$  axis. Let us consider the actual DOF of this mechanism taking into consideration the constraints imposed on the output link by each chain.

First, according to the structural and observed feature of this mechanism, let us consider the constraint by each chain with respect to the coordinate system  $P - x'y'z$ . According to the kinematic structure of the chain 1, rotational motion of the output link around  $y'$  axis is constrained and translational motion at P in  $z$  axis is constrained. The same constraints are imposed by the chain 2. As for the chain 3, rotational motion around  $y'$  axis is constrained and translational motion at O in  $x$  axis is constrained. If the screw theory is applied, the constraint wrenches corresponding to the chains 1 to 3 are described as follows:

$$W_{1,i} = \begin{bmatrix} 0 \\ 0 \\ 1 \\ 0 \\ 0 \\ 0 \end{bmatrix}, W_{2,i} = \begin{bmatrix} 0 \\ 0 \\ 0 \\ 0 \\ 1 \\ 0 \end{bmatrix} \quad (i = 1, 2), W_{1,3} = \begin{bmatrix} 1 \\ 0 \\ 0 \\ 0 \\ 0 \\ r \end{bmatrix}, W_{2,3} = \begin{bmatrix} 0 \\ 0 \\ 0 \\ 0 \\ 1 \\ 0 \end{bmatrix} \quad (2)$$

where  $r$  stands for the distance between O and P. From this result, it is confirmed that there exist three independent constraint wrenches in this mechanism since three of six

constraint wrenches in Eq. (2) are dependent and only three independent constraint wrenches exist even though there are six constraint wrenches. This fact agrees with the mobility analysis result in Eq. (1). Then, twist screws are obtained as follows:

$$T_1 = \begin{bmatrix} 1 \\ 0 \\ 0 \\ 0 \\ 0 \\ 0 \end{bmatrix}, T_2 = \begin{bmatrix} 0 \\ 0 \\ 1 \\ -r \\ 0 \\ 0 \end{bmatrix}, T_3 = \begin{bmatrix} 0 \\ 0 \\ 0 \\ 0 \\ 1 \\ 0 \end{bmatrix} \quad (3)$$

This means that the output link can perform rotational motion around  $x'$  axis, rotational motion around  $z$  axis and translational motion along  $y'$  axis. Therefore, the proposed mechanism is one of the 2R1T mechanisms where R and T stand for rotational and translational output motions. The result is summarized in Table 1.

According to the results, among the joints in the mechanism, joints A, B and H are considered as active joints while the others passive.

**Table 1.** Result of constraint analysis of the proposed mechanism (O: free, X: constrained)

Chains	Motions	$x'$ -axis	$y'$ -axis	$z$ -axis
1	Rotation	O	X	O
	Translation	O	O	X
2	Rotation	O	X	O
	Translation	O	O	X
3	Rotation	O	X	O
	Translation	X	O	O
Total	Rotation	O	X	O
	Translation	X	O	X

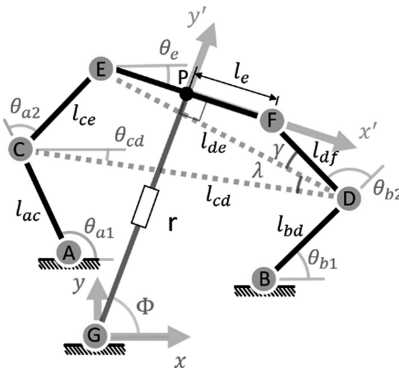


**Fig. 2.** Kinematic diagram of the planar motion generator model

### 3 Kinematic Analysis of the Proposed Mechanism

In order to derive the kinematic equations of the proposed mechanism, the mechanism is divided into two parts: planar motion generator and orientation generator and equations for them are derived.

#### 3.1 Forward Kinematics of Planar Motion Generator

The planar motion generator is shown in Fig. 2. The part GP in this generator is the projection of the chain 3 on the moving plane of linkage ACEFDB. Since the planar motion generator is considered to analyze the motion in the plane of the mechanism shown in Fig. 1. If the connecting relationship of  $r$  is not considered, this generator can be considered as 6-bar linkage, and this linkage requires three actuators in general. As it has only two actuators in joints A and B on the base, it is impossible to solve the forward kinematics in this condition (only these active joint angles are given). Assuming that one of C or D joints is actuated under a given set of joint angles of A and B, forward kinematics of planar motion generator can be calculated like a four-bar linkage as follows:

$$\mathbf{C} = \begin{bmatrix} c_x \\ c_y \end{bmatrix} = \begin{bmatrix} l_{ac} \cos \theta_{a1} \\ l_{ac} \sin \theta_{a1} \end{bmatrix}, \quad \mathbf{D} = \begin{bmatrix} d_x \\ d_y \end{bmatrix} = \begin{bmatrix} l_{bd} \cos \theta_{b1} \\ l_{bd} \sin \theta_{b1} \end{bmatrix} \quad (4)$$

$$l_{cd} = \|\mathbf{C} - \mathbf{D}\|, \quad \theta_{cd} = \text{atan2}(d_y - c_y, d_x - c_x) \quad (5)$$

where  $l_{cd}$ ,  $\theta_{cd}$ ,  $\theta_{a1}$  and  $\theta_{b1}$  are the link length of CD, the angle between  $l_{cd}$  and  $x$ -axis, the angle of joint A, and the angle of joint B, respectively.  $\theta_{a2}$ , which is the angle parameter of joint C, is assumed as the virtual active joint for analyzing the forward kinematics. In this assumption, the link length of DE is calculated using the law of cosine. As same method, the included angles (CDE and EDF) are obtained. Equations of these are shown in detail as follows:

$$l_{de} = \sqrt{l_{ce}^2 + l_{cd}^2 - 2l_{ce}l_{cd} \cos(\theta_{a1} + \theta_{a2} - \theta_{cd})} \quad (6)$$

$$\lambda = \cos^{-1} \left( \frac{l_{de}^2 + l_{cd}^2 - l_{ce}^2}{2l_{de}l_{cd}} \right) \quad (7)$$

$$\gamma = \cos^{-1} \left( \frac{l_{de}^2 + l_{df}^2 - (2l_e)^2}{2l_{de}l_{df}} \right) \quad (8)$$

where  $l_{cd}$ ,  $l_{ce}$ ,  $l_{de}$  and  $l_{df}$  are the link lengths of CD, CE, DE and DF, respectively and  $l_e$  is the half length of EF. Regarding the results of Eqs. (4)–(8),  $\theta_{b2}$  can be derived as following:

$$\theta_{b2} = \begin{cases} \pi - \lambda - \gamma & 0 \leq \theta_{a2} \leq \pi \\ \pi + \lambda - \gamma & -\pi \leq \theta_{a2} \leq 0 \end{cases} \quad (9)$$

From the results, the positions of E, F and P as the middle point of EF are calculated.

When the connecting condition between EF and GP is considered, EF should be perpendicular to GP. To find the solution of the assumed angle  $\theta_{a2}$ , the formed angle between EF and GP is calculated. Then, using the difference of this angle from  $90^\circ$ , the assumed angle  $\theta_{a2}$  is adjusted until this difference converges to zero. Then, the following values as well as the others are obtained as the solution of the forward kinematics of planar motion generator.

$$r = \|G - P\| \quad (10)$$

$$\Phi = \text{atan2}(p_y - g_y, p_x - g_x) \quad (11)$$

where  $r$  is the length of GP.

### 3.2 Inverse Kinematics of Planar Motion Generator

Using the perpendicular condition between EF and GP, when the end-point position of P is given, the positions of E and F are calculated as follows:

$$\mathbf{G} = \begin{bmatrix} g_x \\ g_y \end{bmatrix}, \quad \mathbf{P} = \begin{bmatrix} p_x \\ p_y \end{bmatrix} \quad (12)$$

$$\phi = \text{atan2}(p_y - g_y, p_x - g_x) \quad (13)$$

$$\mathbf{E} = \mathbf{P} + \begin{bmatrix} l_e \cos(\phi + \frac{\pi}{2}) \\ l_e \sin(\phi + \frac{\pi}{2}) \end{bmatrix}, \quad \mathbf{F} = \mathbf{P} + \begin{bmatrix} l_e \cos(\phi - \frac{\pi}{2}) \\ l_e \sin(\phi - \frac{\pi}{2}) \end{bmatrix} \quad (14)$$

Using the results of the positions of E and F above, each angle of chains 1 and 2 can be derived by applying the law of cosine. Figure 3 shows triangles that consist of ACE chain and BDF chain. From this figure, joint angles  $\theta_{a1}$  and  $\theta_{a2}$  are derived as follows:

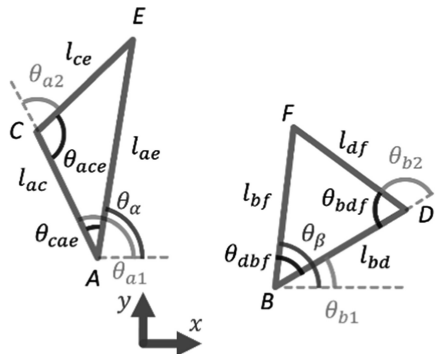


Fig. 3. Triangles for inverse kinematics of the planar motion generator model



$$\theta_{gpf} = \cos^{-1} \left( \frac{l_{gp}^2 + l_e^2 - l_{gf}^2}{2l_{gp}l_e} \right), \text{ where } l_{ae} = \|\mathbf{E} - \mathbf{A}\| \quad (15)$$

$$\theta_{a2} = \pi - \theta_{ace} \quad (16)$$

$$\theta_{cae} = \cos^{-1} \left( \frac{l_{ac}^2 + l_{ae}^2 - l_{ce}^2}{2l_{ac}l_{ae}} \right) \quad (17)$$

$$\theta_x = \text{atan2}(e_y - a_y, e_x - a_x) \quad (18)$$

$$\theta_{a1} = \theta_x + \theta_{cae} \quad (19)$$

where  $l_{ac}$ ,  $l_{ae}$ ,  $l_{ce}$ ,  $\theta_{cae}$ , and  $\theta_a$  are the link length of AC, the link length of AE, the link length of CE, the angle of CAE, the orientation angles of AE from  $x$ -axis. Since the chain BDF can be considered in the same way considering the triangle as shown in the figure, the  $\theta_{b1}$  and  $\theta_{b2}$  are also derived.

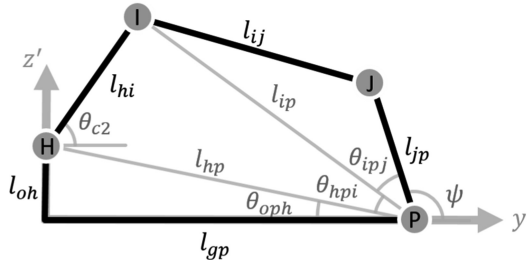


Fig. 4. Diagram of the orientation generator

### 3.3 Forward and Inverse Kinematics of Orientation Generator

The orientation generator is considered as the 4-bar linkage located in the  $y'z'$ -plane of  $P' - x'y'z'$  coordinate system. Figure 4 shows the diagram of the orientation generator. Since joint G is already considered in the kinematics analysis of the planar motion generator, the effect of joint G is not considered here. As the link length of  $l_{gp}$  (same as  $r$  of planar motion generator) is also calculated from the planar motion generator, it is considered as the known value. Based on this background, each of the joint angles, and orientation of the orientation generator are derived as follows:

$$l_{hp} = \|\mathbf{P} - \mathbf{H}\| \quad (20)$$

$$l_{ip} = \|\mathbf{P} - \mathbf{I}\| \quad (21)$$

where  $l_{oh}$ ,  $l_{hp}$  and  $l_{ip}$  are the length of OH, HP and IP, respectively. Based on the preprocessing mentioned above,  $\theta_{hpi}$  and  $\theta_{ipj}$  are calculated by applying the law of cosine.

$$\theta_{hpi} = \cos^{-1} \left( \frac{l_{hp}^2 + l_{ip}^2 - l_{hi}^2}{2l_{hp}l_{ip}} \right) \quad (22)$$

$$\theta_{ipj} = \cos^{-1} \left( \frac{l_{ip}^2 + l_{kp}^2 - l_{ij}^2}{2l_{ip}l_{kp}} \right) \quad (23)$$

Finally, the orientation output angle  $\Psi$  is calculated using Eqs. (22) and (23) as

$$\Psi = \begin{cases} \pi - \theta_{hpi} - \theta_{ipj} & 0 \leq \theta_{c2} \leq \pi \\ \pi + \theta_{hpi} - \theta_{ipj} & -\pi \leq \theta_{c2} \leq 0 \end{cases} \quad (24)$$

Regarding the inverse kinematics of the orientation generator, the process is similar to the forward one mentioned above: changing the known condition to  $\Psi$  instead of  $\theta_{c2}$ .

**Table 2.** Kinematic parameter values used in the analysis

Link lengths [mm]		Angles [Degree]	Joint positions [mm]
$l_e$	26	$\theta_{a1}, \theta_{b1}$ 0–180 Interval: 0.25	A(x, y, z) (–29, 0, 0)
$l_{ac}, l_{bd}, l_{ce}, l_{df}$	40	$\theta_{a2}$ 0–360 Interval: 0.25	B(x, y, z) (29, 0, 0)
$l_{hi}, l_{ij}, l_{kp}$	50	$\theta_{c2}$ –15–90 Interval: 0.25	H(x, y, z) (0, 0, 8.55)



**Fig. 5.** The workspace of the planar motion generator

## 4 Kinematic Performance Analysis

In order to analyze the performance of the proposed mechanism, numerical examples are provided to show the workspace of the planar motion generator and the rotational ability of the orientation generator. Kinematic parameters used in the analysis are shown in Table 2. The origin point is set at G as shown in Fig. 2.

### 4.1 Workspace of Planar Motion Generator

Since the planar motion generator provides its movement in  $xy$ -plane, its workspace also locates in that plane. Using the equations shown in the previous chapter, workspace was derived. In this analysis, allowable range of the active joint angles of A and B and the joint angle of C were considered and they were set from 0 to 180°. Within the range, active joint angles are given by the interval of 0.25°, and for each combination of the active joint angles, the position of P was obtained together with the angle of joint C so that the difference of the angle between EF and GP and 90° would be minimum. Each position of P obtained in this procedure is plotted to represent the workspace of the planar motion generator in Fig. 5. Though the expected workspace forms the circular shape that consists of  $r$  and  $\Phi$  as the radius and angle around the center point, it can be seen from the figure that some part is constrained. It is caused by the constraint effect of chains 1 and 2. Furthermore, since the angle between link GP and link EF is always 90°, the orientation of EF is subordinate to the circular motion around the origin G.

### 4.2 Rotational Capability and Sensitivity of Orientation Generator

In order to evaluate the rotational characteristics of the orientation generator, the rotational capability and sensitivity are analyzed. The maximum and minimum value of the base link length  $l_{gp}$  of the orientation generator shown in Fig. 4 is determined by the planar motion generator as  $r(=l_{gp})$ . In orientation generator model, if the length value of  $l_{gp}$  is given as a constant value, the rotational ability and sensitivity can be derived. In this chapter,  $l_{gp}$  was considered between the minimum (40 mm) and the maximum (80 mm), which were estimated from the analysis result of  $r$  of the planar motion generator. Additionally, the angle of the active joint I,  $\theta_{c2}$ , was given by  $-15^\circ \sim 90^\circ$  with the interval of 0.25°.

The rotational capability is evaluated by the range of the output angle  $\Psi$ . As for the sensitivity, it is defined by the rates of the change between  $\theta_{c2}$  and  $\Psi$  and calculated as  $s$  in the following equation.

$$s = \frac{\Delta \psi}{\Delta \theta_{c2}} \quad (25)$$

The bigger  $s$  is, the higher the sensitivity is. Figures 6 and 7 show the results of the rotational capability and the sensitivity. In Fig. 7, results are shown for eleven sample points with the same distance between the minimum and maximum values. It is known from these figures that for the value of  $r$  less than 60 mm, rotational capability is high while the sensitivity is high. As for the larger value of  $r$ , sensitivity is stable and low though the rotational capability is low.

From the results of the sensitivity, it is observed that there are cases where the maximum values are unnaturally huge compared with minimum and median values. For example, such high values are found for  $r = 40, 44, 52, 56$  mm. This phenomenon is occurred by similar posture when the links  $l_{kp}$  and  $l_{ij}$  overlap each other as shown in Fig. 8. Thus, if the maximum value is too high compared with the median value, the range of output is wider than another case. Since this phenomenon also is probable related to singularity, the suitable input and output angles of the orientation generator should be determined using the results.

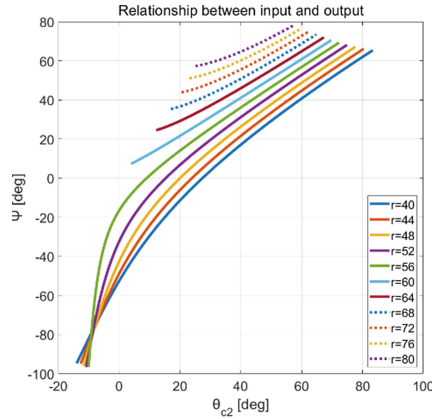


**Fig. 6.** The relationship between input and output angles

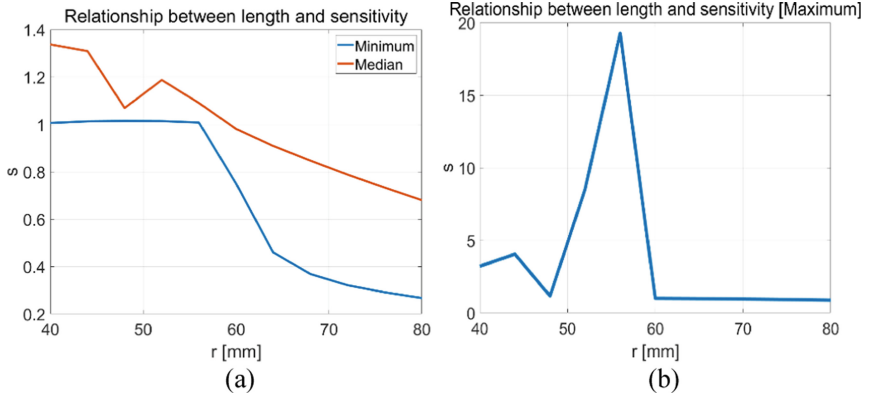


**Fig. 7.** The sensitivity result of the orientation generator (a): Minimum value and Median value, (b): Maximum value

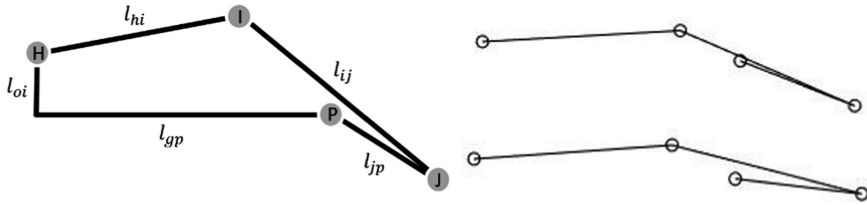


**Fig. 8.** The situation explanation diagram of the orientation generator when the huge sensitivity value occurs and their simulation configurations.

## 5 Discussion and Conclusion

In this paper, a novel over-constrained parallel mechanism composed of two identical chains and one different chain, which has two rotational mobility and one translational mobility, was proposed. The degrees of freedom of this mechanism was derived by the constraint conditions imposed on the output link by each connecting chain. The global motion feature of this mechanism was revealed as a circular motion around the origin on the base and rotational motion around an axis of the output link. The equations for kinematic analysis were derived by dividing the mechanism into two parts: planar motion generator and the orientation generator. Finally, the workspace and rotational capability were demonstrated as a numerical example to show the performance of the mechanism. From the analysis result of workspace, it shows that the mechanism provides a combined motion similar to circular-like motion by rotational and translation motion. From the analysis result of the rotational capability of the orientation generator, it was shown that the ranges of rotational DOF depend on the position of the output point of the planar motion generator (that is the output point of the mechanism). Furthermore, the relationship between the orientation capability and the sensitivity was discussed. In our future work, we will design and manufacture the prototype of the propose mechanism and evaluate its performance taking into consideration the real application.

## References

1. Stewart, D.: A platform with six degrees of freedom. *Proc. Inst. Mech. Eng.* **180**(1), 371–386 (1965)
2. Clavel, R.: DELTA, a fast robot with parallel geometry. In: *Proceedings of 18th International Symposium on Industrial Robot*, pp. 91–100 (1988)
3. Gosselin, C.M., Hamel, J.F.: The agile eye: a high-performance three-degree-of-freedom camera-orienting device. In: *1994 IEEE International Conference on Robotics and Automation*, pp. 781–786. IEEE (1994)
4. Srivatsan, R.A., Sandipan, B., Ashitava, G.: Analysis of the degrees-of-freedom of spatial parallel manipulators in regular and singular configurations. *Mech. Mach. Theory* **69**, 127–141 (2013)
5. Liu, X.J., Tang, X., Wang, J.: HANA: a novel spatial parallel manipulator with one rotational and two translational degrees of freedom. *Robotica* **23**(2), 257–270 (2005)
6. Wang, J., Liu, X.J.: Analysis of a novel cylindrical 3-DoF parallel robot. *Robot. Auton. Syst.* **42**(1), 31–46 (2003)



# Development of an Innovative 2-DOF Continuous–Rotatable Mechanism

Chun Liu<sup>(✉)</sup>, Ting-Hao Wang, and Pei-Chun Lin<sup>(✉)</sup>

National Taiwan University, Taipei City 10617, Taiwan (R.O.C.)  
{d05522022, wtyng, peichunlin}@ntu.edu.tw

**Abstract.** We report on the development of an innovative two degrees of freedoms (DOF) mechanism that is capable of performing continuous rotation in both DOFs. The design process began with the analysis and comparison of general 2-DOF mechanisms with various morphologies. The final selection was based on joint angles that yielded the largest region of continuous rotation. The design concept was realized as an empirical mechanism design. The transmission systems of the two DOFs were carefully designed so that the two DOFs can rotate continuously without colliding with one another. More specifically, double C-shaped racks were designed and utilized as key components to fulfill this goal. The dynamics of the 2-DOF mechanism was then analyzed to better understand the relation between the torque input and the rotation motion output. A prototype was built and its performance was empirically evaluated. The experimental results confirm the functionality of the continuous rotation of the two DOFs in the mechanism.

**Keywords:** 2-DOF · Mechanism design · Continuous rotation · Joint

## 1 Introduction

Animals usually have delicate, compact, and efficient joint systems, such as the waist or hip joint, which generate dexterous multi-degrees of freedom (DOF) motion. In contrast, artificial robotic motion systems have thus far mainly relied on one-DOF motors. Therefore, generating multi-DOF motions that mimic wrist or hip joints rely on mechanism designs that couple multiple individual motor motions in a compact form. The wrist joint, for example, is composed of two revolute chains (RR configuration) or a universal joint (U configuration) whose axes of rotation intersect perpendicularly [1]. The empirical two DOFs system driven by motors can be considered as joined by a linkage, and the connection method further determines the range of the joint workspace. Therefore, the connection method should be skillfully designed and optimized to meet the requirements of specific tasks.

2-DOF joints are popular and prevalent in humanoid robots owing to their biomimetic morphology with respect to the human body—for example, the wrists of WABIAN-2 [2] and ARMAR-3 [3], and the ankles of NAO [4], DLR-Biped [5] and LOLA [6]. Different humanoid robots use different linkage connection designs. The WABIAN-2 and ARMAR-3 mimic the motion behaviors of the human wrist favorably. Their design shifts the axis of rotation for intersecting the other axes, and they have

four support linkages around the motor close to the hand. The ankle of NAO has the same construction. The ankles of DLR-Biped and LOLA have one linkage connecting the motor that drives the foot from the motor near the knee, and they have double support linkages on the feet. In addition, the wrist of ARMAR-4 [7] has three DOFs, and after excluding the first revolute joint, which represents the pronation/supination generated from the forearm [8], the other two can form a 2-DOF structure. The motor that rotates the hand is supported by the C shell from both sides, and only one linkage is connected to the hand. This configuration successfully decreases the structural limitation regarding pitch motion. The three-DOF hip mechanism on HRP-3 [9] and ARMAR-4 [10] can similarly be decomposed. Discarding the joint that preforms lateral/medial rotation [11], the joint of HRP-3 has three support linkages—two for fixing the motor and one for acting as the femur. Moreover, the hip of ARMAR-4 has only two short support linkages to enlarge the rotation range. Because, so far, most of the 2-DOF mechanisms are for humanoid joints, the motion range of these DOFs is usually limited and does not have the possibility of continuous rotation, thus confining the motion range and motion speed.

Here, we report on an innovative 2-DOF mechanism that is capable of performing continuous 2-DOF rotation using a serial RR chain and a novel driving and connecting mechanism to avoid collision. This mechanism can still of course be utilized as a wrist or other joint, but it has extended performance regarding workspace and motion speed owing to continuous rotation. Moreover, this mechanism can be extended to other applications, such as pan-and-tilt cameras with extended surveillance viewing ranges. The contributions of this research include (i) the classification of the rotation behaviors of existing 2-DOF joints; (ii) the development of innovative mechanisms that provide a unique and new rotation behavior; and (iii) the analysis of mechanism dynamics.

The remainder of this work is organized as follows. Section 2 describes the rotation behavior of existing 2-DOF models and their motion and structural limitations. Section 3 describes the mechanism design of the innovative 2-DOF mechanism, which is followed by an analysis of the mechanism dynamics in Sect. 4. Section 5 shows the practical implementation results, and Sect. 6 concludes the work.

## 2 Rotation Behavior of Existing 2 DOF Structure

A multi-DOF joint inherently assumes that the rotational axes are not parallel to one another for independent motion. In addition, the rotational axes of the joint are usually set to be mutually orthogonal and to intersect one another (i.e. the morphology is similar to the universal joint). This is because complete driving independence of axes yields an easier computation regarding forward and inverse kinematics and dynamics. Thus, this work focuses on this configuration.

Empirically, to drive the described two DOFs requires a specific mechanism design because the motor and transmission system have non-zero physical sizes. Therefore, from the geometric point of view, the workspace or the rotation behavior of the multi-DOF joint depends on the size of the motors as well as the sizes of the transmission system and associated supporting structure. To simplify the analysis, the overall system can be modeled as two cylindrical blocks ( $M_1$  and  $M_2$ ) and two linkages ( $L_1$  and  $L_2$ ).

The cylindrical blocks represent the spaces taken by the motors. The first linkage  $L_1$  represents the transmission system and supporting structure, which transmits the rotational motion of the first motor to the place where the second motor resides so that the two DOFs are mutually orthogonal and intersect one another. The second linkage  $L_2$  represents the end effector. It should be noted that  $L_1$  here is used to transmit the rotation motion but not driven by the motor-1 directly.

Because the motor size (i.e. M1 and M2) is usually fixed and the mechanism design mainly addresses how the motor power transmits to drive the 2-DOF end effector, the following analysis focuses on the variation of the transmission and structure design (i.e.  $L_1$ ) as well as how the motion can be output to the end effector (i.e.  $L_2$ ). The mechanism can be classified into four types, which are based on use of single (S) or double (D) connection linkages: DD, DS, SD, and SS. The first letter D/S associated with linkage  $L_1$  represents the use of either one or two sides of spaces between the first DOF (M1) and the second DOF (M2) in the transmission system and structure. The second letter D/S associated with linkage  $L_2$  represents the use of either one or two sides of spaces between the M2 and the end effector by the structure.

The motor size and connection linkage lengths were set, as shown in Table 1, so that comparison among the four types of mechanism (DD, DS, SD, and SS) could proceed. Because blocks M1 and M2 occupy physical space, the linkage  $L_1$  has a minimum length so that the blocks are physically separated in various locations without collision or interference. Similarly, the linkage  $L_2$  has a minimum length so that the output can be transferred to the end effector “outside” the joint for practical uses, such as mounting a camera. The linkage thickness is set to zero but is still present.

**Table 1.** Geometrical parameters of the modeled 2-DOF joint

Parameter	Unit
Motor radius	8
Motor thickness	6
Linkage length, $L_1$	4 + 5
Linkage length, $L_2$	10
Width of linkage	0

**Table 2.** The D-H parameter of the modeled 2-DOF joint

$i$	$\alpha_{i-1}$	$a_{i-1}$	$d_i$	$\theta_i$
1	0	0	0	$\theta_1$
2	90	0	0	$\theta_2$

The geometrical relation of the described 2-DOF mechanism can be represented using Denavit–Hartenberg (D–H) notation [12]. Since the four types of mechanism have the same morphology but vary regarding the use of single or double connection methods, the D–H parameters of the four types are identical, as shown in Table 2. Figure 1(a) shows the associated coordinate systems, where the origin is set at the center of M2. The motion ranges of motor-1 and motor-2 are denoted as  $\theta_1$  and  $\theta_2$ , respectively. The first DOF generated by motor-1 rotates around the axis  $Z_1$ , and the second DOF generated by motor-2 rotates about axis  $Z_2$ . The motion ranges of motor-1 and motor-2 are denoted as  $\theta_1$  and  $\theta_2$ , respectively. Thus, the origin end point of linkages  $L_2$ , where  $\theta_1$  and  $\theta_2$  are  $0^\circ$ , is at (10, 0, 0) for global coordinate. When  $\theta_i$  is



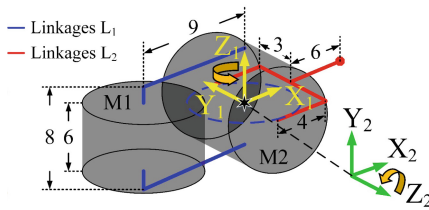
positive number means it rotates anticlockwise around its own  $Z_i$ -axis (orange arrows). Conversely, When  $\theta_i$  is negative number means it rotates clockwise about its own  $Z_i$ -axis. With these definitions and settings, the analysis of the 2-DOF joint using the four types can proceed, emphasizing their ability to rotate continuously.

- (i) DD: There are four linkages around M2, and the model is shown in Fig. 1(b). The achievable ranges of  $\theta_1$  and  $\theta_2$  are only  $\pm 153.6^\circ$  and  $\pm 90^\circ$ , respectively, owing to the volumes taken by blocks as well as the double-supported configurations; continuous rotation is therefore not possible with DD.
- (ii) DS: The transmission uses spaces on both sides of M1, and the end effector only uses space on one side. The ranges of  $\theta_1$  and  $\theta_2$  are same as those of DD, but  $\theta_2$  can rotate continuously when  $\theta_1$  is between  $+26.4^\circ$  and  $+153.6^\circ$ . Figure 1(c) shows the continuous rotation ability of  $\theta_2$  by drawing the reachable positions of the end effector (i.e. the green region). The brown curve shows one special condition when  $\theta_2$  is  $0^\circ$ .
- (iii) SD: The transmission only uses space on one side of M1, and the end effector uses space on both sides, opposite to the DS. The range of  $\theta_1$  remains  $\pm 153.6^\circ$ , and the range of  $\theta_2$  is  $-149^\circ$  to  $90^\circ$ . Additionally,  $\theta_1$  can rotate continuously when  $\theta_2$  is within the range  $-149^\circ$  to  $-31^\circ$ . Nevertheless,  $\theta_2$  does not have the ability to rotate repetitively due to the double support linkages. Therefore, there is no green region, as shown in Fig. 1(d), but the cyan region indicates the ability of  $\theta_1$  to continuously rotate, and the brown curve is plotted while  $\theta_1$  is  $0^\circ$ .
- (iv) SS: Both the transmission and the end effector use space on only one side of M1. The structure of the 2-DOF joint in this configuration has fewer geometric constraints than the other three cases. Although the range of  $\theta_1$  is still  $\pm 156^\circ$ , and the range of  $\theta_2$  is between  $-149^\circ$  and  $90^\circ$ ,  $\theta_1$  can rotate continuously when  $\theta_2$  is between  $-149^\circ$  and  $-31^\circ$ ;  $\theta_2$  can also rotate continuously when  $\theta_1$  is between  $26.4^\circ$  and  $153.6^\circ$ . Therefore the green area and the cyan area overlap, as shown in Fig. 1(e).

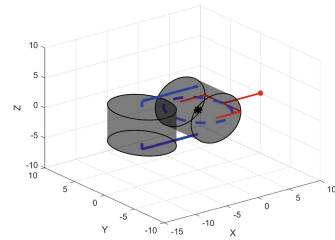
The proposed mechanism design in this work can be classified as type SS, although the arrangement of the transmission and supporting structure (i.e.  $L_1$ ) differs from the existing SS structure, as the linkage is shifted into the center region between the M1 and M2 blocks. Hereafter, this configuration is referred to as SSD. In this case,  $L_1$  does not interfere with the rotation of  $\theta_2$ . Therefore, although the rotation range of  $\theta_1$  is still restricted to  $\pm 153.6^\circ$ , the range of  $\theta_2$  can be extended on both sides to  $\pm 149^\circ$ . Moreover, the continuous rotation range for  $\theta_1$  is available when  $\theta_2$  is between  $-149^\circ$  and  $-31^\circ$ , and between  $31^\circ$  and  $149^\circ$ . Conversely, the continuous rotation range for  $\theta_2$  is available when  $\theta_1$  is between  $-153.6^\circ$  and  $-26.4^\circ$ , and between  $26.4^\circ$  and  $153.6^\circ$ . As long as  $\theta_1$  and  $\theta_2$  are within the described range, which is twice that of SS, both DOFs of the SSD can perform continuous rotations simultaneously, as shown in Table 3. The covered region is plotted in Fig. 1(f).

In summary, block M1 affects  $\theta_1$  equally for all four types. The linkages  $L_1$  determines the range and continuous rotation ability of  $\theta_1$ , and the linkage  $L_2$  determines the other DOF,  $\theta_2$ . Type SS is the only configuration where both  $\theta_1$  and  $\theta_2$  have the opportunity to perform continuous rotation simultaneously, as shown in Table 3.

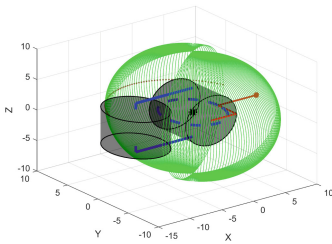
In addition, the proposed type SSD doubles the range for continuous rotation and extends the rotation range of  $\theta_2$ .



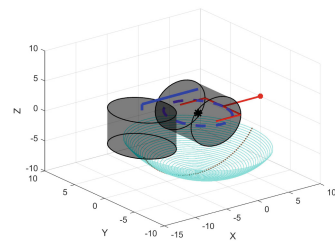
(a) Coordinate representation



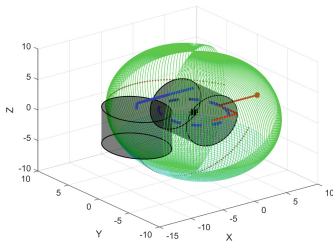
(b) Continuous rotation behavior of DD



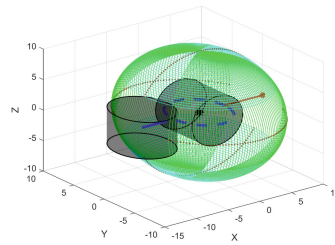
(c) Continuous rotation behavior of DS



(d) Continuous rotation behavior of SD



(e) Continuous rotation behavior of SS



(f) Continuous rotation behavior of SSD

**Fig. 1.** Coordinate representation (a), continuous rotation behavior of four stand types (b) DD (c) DS (d) SD (e) SS and the proposed type (f) SSD

**Table 3.** Rotation range of the DOFs in five different types

	DD	DS	SD	SS	SS design
$\theta_1$	$\pm 153.6^\circ$	$\pm 153.6^\circ$	$\pm 153.6^\circ$	$\pm 153.6^\circ$	$\pm 153.6^\circ$
$\theta_2$	$\pm 90^\circ$	$\pm 90^\circ$	$-149^\circ$ $+90^\circ$	$-149^\circ$ $+90^\circ$	$-149^\circ$ $+149^\circ$
$\theta_1$ range for $\theta_2$ RC	None	$+26.4^\circ$ $+153.6^\circ$	None	$+26.4^\circ$ $+153.6^\circ$	$-153.6^\circ \sim -26.4^\circ$ $+26.4^\circ \sim +153.6^\circ$
$\theta_2$ range for $\theta_1$ RC	None	None	$-149^\circ$ $-31^\circ$	$-149^\circ$ $-31^\circ$	$-149^\circ \sim -31^\circ$ $+31^\circ \sim +149^\circ$

Note.  $\theta_1$  range for  $\theta_2$  RC:  $\theta_2$  rotate continuously (RC) when  $\theta_1$  within the range.  
 $\theta_2$  range for  $\theta_1$  RC:  $\theta_1$  rotate continuously (RC) when  $\theta_2$  within the range.

### 3 Design and Implementation of the 2-DOF Mechanism

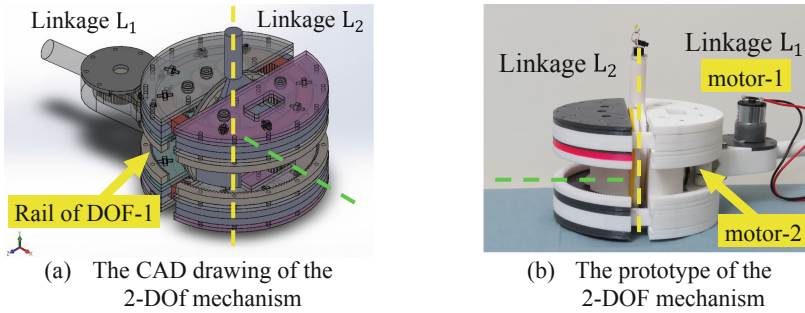


**Fig. 2.** The CAD drawing and the prototype of the 2-DOF mechanism

The mechanism design aims to realize the proposed SSD type, and Fig. 2(a) and (b) show the CAD design and the empirical implementation of the 2-DOF joint, respectively. The final cylinder has a diameter of 180 mm, a thickness of 108 mm, and weighs approximately 2.3 kg. The first DOF, which rotates around yellow axis, is designed to have continuous output rotation, so, conceptually, the output should have a cylindrical shape when the DOF is driven from the motor-1 outside. Motor-1 here is correlated with block M1 in Sect. 2, and by fixing Linkage L<sub>1</sub>, the cylinder can rotate along the Rail of DOF-1. In the meantime, to allow the second linkage L<sub>2</sub> located at the center of the cylinder to rotate continuously about green axis without colliding with the cylinder, the cylinder should be divided into two halves; these two halves should be designed to have a specific structure so that the relative configuration can be maintained. To satisfy these two constraints, two rotatable C-shaped structures are utilized to bridge the two halves. When the linkage L<sub>2</sub> rotates and passes the rack, the rack synchronously rotates to the orientation where the gap is presented. In the meantime, the other rack still connects the two cylindrical halves to fix the cylinder structure. This innovative double-C design allows the 2-DOF mechanism to have a wide range of continuous rotations.

Figure 3 demonstrates how the double-C works in detail. The gaps of the two C-shaped racks placed on opposite sides are shown in Fig. 3(a). When the linkage L<sub>2</sub> drives the end effector close to the upper C rack, it rotates to the orientation where the gap is presented, as shown in Fig. 3(b). Likewise, when it approaches the lower C rack, as shown in Fig. 3(c), the gap is also presented. In the second half of the rotation (i.e. the linkage is rotated up from the bottom, as shown in Fig. 3(d), a similar process is repeated, as shown in Fig. 3(e) and (f).

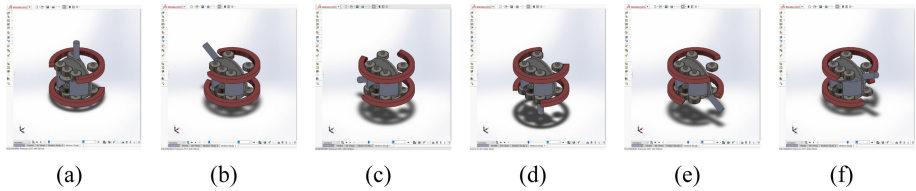


**Fig. 3.** Illustrative motion sequence of the 2-DOF mechanism while the second DOF performs continuous rotation

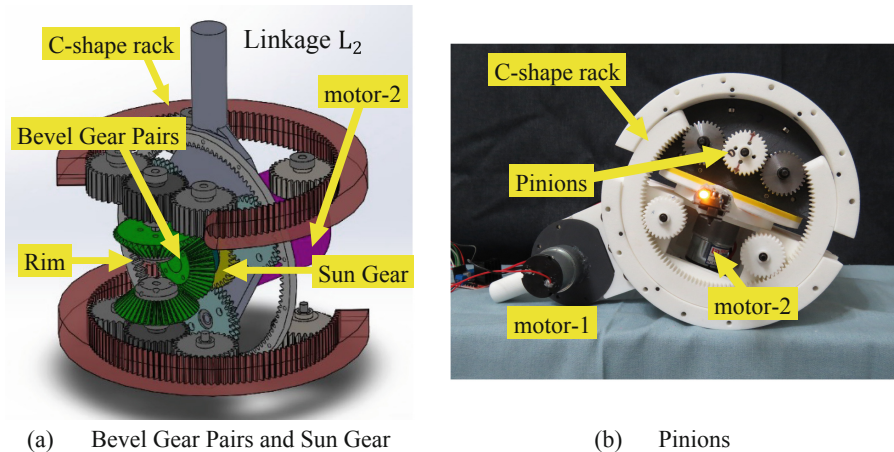


**Fig. 4.** Transmission system of the 2-DOF mechanism

The double-C mechanism described above requires a specific transmission system design. The C racks should be rotated synchronously as motor-2 is driven (i.e.  $\theta_2$ ). In the empirical design, the output of motor-2, which is aligned with block M2 in Sect. 2, drives the linkage  $L_2$ , where the linkage is also the arm of the planetary gear system. The rim is structurally fixed to one of the half-cylinders (i.e. does not rotate), and the output is the sun gear. The sun gear transmits the motion to the rack through bevel gear pairs Fig. 4(a) and the pinions Fig. 4(b). As for the first DOF, motor-1 is placed outside the cylinder. Eventually, all the gears driven by linkage  $L_2$  inside utilizes the double-C mechanism, and further realize the behavior of SSD.

## 4 Dynamic Simulation

Constructing a physical model of the mechanism is necessary to better understand the system dynamics and is helpful during the design and analysis process. In this section, the equation of motion was derived based on the known geometry and mass distribution. Given the initial postures and the rotating trajectories, the required torques to drive the system can be predicted as the reference on selecting the appropriate

actuators. Meanwhile, the kinematic can also be acquired with the given driving torque. Through the simulations and visualizations, several control strategies and the corresponding reactions of the system can be supervised before implementing the real mechanism.

To construct the governing equation, we first define the coordinate system. The 2-DOF RR joint can be simplified to two links, denoted as Link 1 and Link 2, and the ground link is denoted as Link 0. The coordinates corresponding to each link, shown in Fig. 5, are set to be concentric, while the z-axis is aligned with the rotating shaft according to the D–H notation. Here, we simply set the center of mass (CoM) to be located along the x-axis, so the representation can be written as  ${}^iP_{C_i} = L_{C_i}\hat{x}_i$ , where the  $L_{C_i}$  is the distance between the CoM and the origin. The rotation of the link is denoted as  $\theta_i$ , and the mass and inertia tensor of the mechanism are denoted as  $m_i$  and  $I_i$ , where  $i = 1, 2$ .

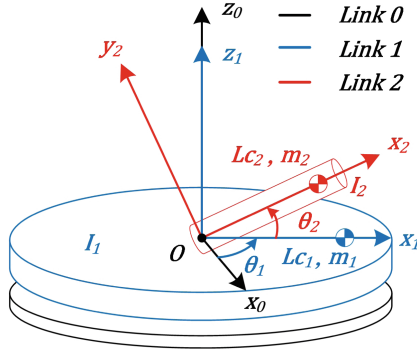


Fig. 5. The model for dynamics analysis

By using either the Newton–Euler approach or the Lagrangian formulation [12], the equation of motion can be obtained with the following formation, which includes mass, centrifugal and Coriolis, gravity, and friction terms:

$$\tau = M(\Theta)\ddot{\Theta} + V(\Theta, \dot{\Theta}) + G(\Theta) + F(\Theta, \dot{\Theta}) \quad (1)$$

$$M(\Theta) = \begin{bmatrix} m_1 L_{C_1}^2 + m_2 L_{C_2}^2 \cos \theta_2 + I_{1,zz} & 0 \\ -I_{2,xy} \sin \theta_2 - I_{2,yz} \cos \theta_2 & m_2 L_{C_2}^2 + I_{2,zz} \end{bmatrix} \quad (2)$$

$$V(\Theta, \dot{\Theta}) = \begin{bmatrix} (-2m_2 L_{C_2}^2 \sin \theta_2 \cos \theta_2) \dot{\theta}_1 \dot{\theta}_2 \\ ((m_2 L_{C_2}^2 - I_{2,xx} + I_{2,yy}) \sin \theta_2 \cos \theta_2 + I_{2,xy} (\cos^2 \theta_2 - \sin^2 \theta_2)) \dot{\theta}_1^2 \end{bmatrix} \quad (3)$$

$$G(\Theta) = \begin{bmatrix} 0 \\ m_2 L_{C_2} \cos \theta_2 g \end{bmatrix} \quad (4)$$

$$F(\Theta, \dot{\Theta}) = \begin{bmatrix} B_1 \dot{\theta}_1 + C_1 \text{sgn}(\dot{\theta}_1) \\ B_2 \dot{\theta}_2 + C_2 \text{sgn}(\dot{\theta}_2) \end{bmatrix} \quad (5)$$

Here,  $B_i$  is the viscous friction coefficient,  $C_i$  is the Coulomb friction coefficient.  $B_i$  and  $C_i$  are properly set to be specific small values for the initial trials, and further system identification is needed to refine the parameters for better prediction results.

The above equation gives the expressions for the torque of each actuator as a function of joint position, velocity, and acceleration, which means we can predict the required torque with the given motor trajectory. This also corresponds to the case when we apply position control to manipulate the mechanism. Note that when considering the extra load exerted on Link 2, which would be a common situation in practical use, we can simply adjust the corresponding values of  $L_{C_2}$  and  $m_2$  to modify the model.

Figure 6 gives a simple example of the simulation under constant  $\omega$  trajectory input. Figure 6(a) shows the two given trajectories, with the angular velocity values shown in Fig. 6(c). The endpoint trajectory of link 2 on each timestamp is drawn on Fig. 6(b) to check whether the collision between two links would happen, and the calculated torques are shown in Fig. 6(d). In this case, the set of trajectory would lead to collision when  $\theta_1$  and  $\theta_2$  both approach 0 or  $\pi$ , and it can be prevented through proper adjustments to the initial posture of both links. As far as the torque is concerned, since no angular acceleration is involved,  $\tau_1$  is a constant value due to the friction effect, and the  $\tau_2$  appears to oscillate with the motion of Link 2 and is mainly related to the gravity effect.

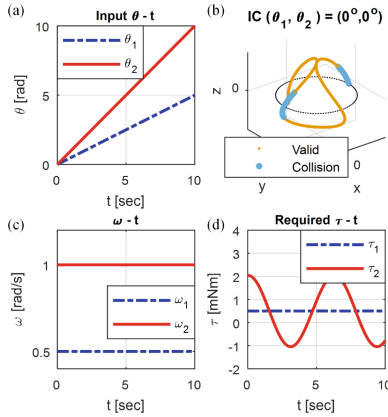


**Fig. 6.** Response of the mechanism running at constant  $\omega$  using position control

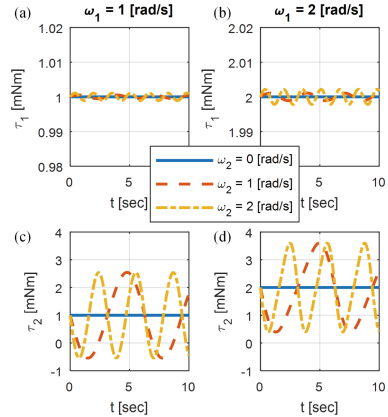


**Fig. 7.** Response of the mechanism running at different  $\omega_1$  and  $\omega_2$  conditions, with  $B_i$  are set 1 mNm · s/rad.

To find whether two links interact with one another, different step trajectories are selected as inputs, and the changes in torque response are observed. Noted that these

trajectories are selected to be non-collision that are feasible during real applications. In Fig. 7(a) and (c), both actuators are set to be driven at same  $\omega_1$ , and the values of  $\omega_2$  are adjusted. The results show that  $\tau_1$  remains nearly unchanged under different  $\theta_2$  input trajectories, and  $\tau_2$  appears to oscillate with the posture of Link 2. This corresponds to the observation from the governing equation that the gravity term is comparably larger than the others terms. Note that  $\tau_2$  is also combined with the centrifugal term, so increasing  $\omega_1$  will increase  $\tau_2$ . This can also be proven with the simulation under different  $\omega_1$  settings, as shown in Fig. 7(b) and (d).

More trajectories were tested, including sine and polynomial input, during the trials. Since the mass and the centrifugal and Coriolis terms are small compared to the gravity term, the torque that arose from the motion effect would not have evident influence under the low  $\omega$  area. Thus, when selecting actuators for the mechanism,  $\tau_2$  should be large enough to trigger the motion of Link 2, while  $\tau_1$  can be reduced to minimize the weight of the whole structure.

Moreover, to simulate the motion of the mechanism under force input, it is necessary to solve the dynamic equation for acceleration. We apply numerical integration techniques to integrate the acceleration and compute the future positions and velocities under the joint frame with the following equation:

$$\ddot{\Theta} = M^{-1}(\Theta) [\tau - V(\Theta, \dot{\Theta}) - G(\Theta) - F(\Theta, \dot{\Theta})] \quad (6)$$

By solving the equation, we can predict the motion of the links under certain torque inputs, which means we can estimate the behaviors of the system under force control. Here, different step commands are selected as inputs to see the motion response of the model. The results show that the influences of  $\theta_1$  under different  $\tau_2$  inputs are nearly neglectable, while different input  $\tau_1$  could possibly affect the trajectories of both Link 1 and Link 2. However, using force control could not guarantee the posture of the both links, which may lead to collisions on the real mechanism. Therefore, position control is utilized to ensure non-interference between the links during practical applications.

To conclude this section, the simulation visualizes the dynamic response of the mechanism under position and force control. It provides advice on selecting the appropriate actuators. In addition, the simulation results show that the motion of Link 1 could possibly affect the behavior of Link 2, so compensating terms based on the equation of motion could be added into the command to increase the performance of the system when applying different control strategies.

## 5 Experimental Validation of the 2-DOF Mechanism

The prototype, as shown in Fig. 2(b), was built based on the morphology design described in Sect. 2 and the mechanism design reported in Sect. 3. The proposed 2-DOF mechanism was experimentally evaluated. To aid visualization, an LED was mounted on the end effector. The motion of the mechanism was recorded for a period of time (i.e. 15 s) while the LED was on Linkage  $L_2$  (Fig. 2b). The trajectory of the end effector can be observed in the captured image. The results are shown in Figs. 8 and 9. The mechanism is placed vertically, with motor-1 located at the bottom to act as the



base that connects the mechanism to the ground. The camera faced the top of the mechanism. In this first stage, the motors were driven using voltage control.

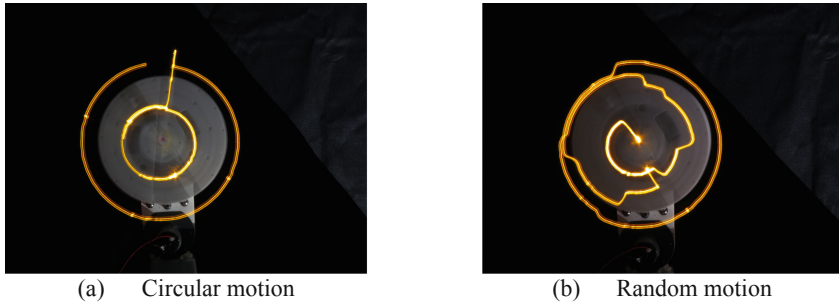


**Fig. 8.** The end effector trajectory where the first DOF performs continuous rotation.

The experiments included two parts, each demonstrating the continuous rotation of an individual DOF. In the first test, as shown in Fig. 8(a), the end effector started at the position shown by the red marker, while the second DOF ( $\theta_2$ ) was initially fixed at the edge of cylinder. After the first DOF ( $\theta_1$ ) rotated closed to a full circle, the second DOF raised the end effector to another orientation and then stopped. Then the first DOF continuously rotated for several circles. Figure 8(b) shows a scenario where the first DOF was driven continuously while the second DOF was moved randomly.

Figure 9 demonstrates the continuous rotation of the second DOF. In the experiment shown in Fig. 9(a), the end effector started from the center position, and then the second DOF was driven to rotate continuously while the first DOF was intermittently moved from a constant step to another step. In the experiment shown in Fig. 9(b), the first DOF was driven randomly.

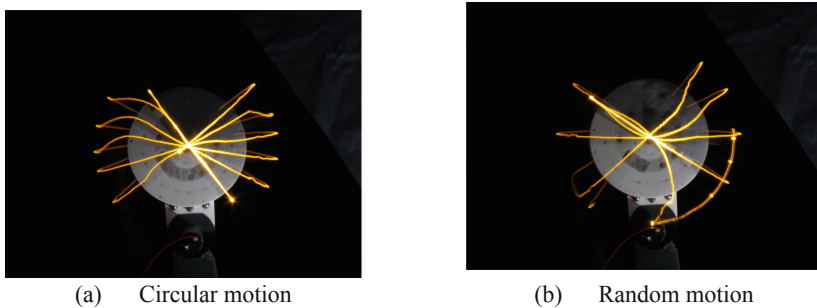


**Fig. 9.** The end effector trajectory where the second DOF performs continuous rotation

In short, the experimental results confirm the feasibility of continuous rotation in both DOFs of the proposed 2-DOF mechanism. In other words, the use of two



C-shaped racks to connect two half-cylinders and avoid collision between the end effector linkage and the cylinder while maintaining the cylinder structure proves to be feasible and functional.

## 6 Conclusion and Future Works

We report on the development of an innovative 2-DOF mechanism that is capable of performing continuous rotation in both DOFs. The design process began with an analysis and comparison of general 2-DOF mechanisms, which were categorized as DD, DS, SD, and SS according to the arrangement of the transmission between motor-1 and the output axis as well as the output linkage to the end effector. The analysis revealed that only the SS type is capable of generating continuous rotation in both DOFs. Aiming to enlarge the range of continuous rotation in both DOFs, this work proposed a new type (SSD), which doubles the range of type SS. The design was realized as a detailed mechanism that is suitable for manufacturing, where the use of double C-shaped racks plays an important role owing to their functionality regarding both linkage avoidance and structure support. The dynamics of the 2-DOF mechanism were analyzed. The results reveal that the gravity effect plays a key role in the dynamics of the mechanism and that the two DOFs have a couple effect, whereby the first DOF affects the dynamics of the second DOF. A prototype was built and its performance was empirically evaluated in two sets of tests, where each test focuses on generating continuous rotation in one DOF while the other is fixed, moved in small steps, or moved randomly. The experimental results confirm the functionality of the continuous rotation of the two DOFs in the mechanism.

We are currently working on embedding electronic systems within the mechanism as well as using a feedback control strategy to quantitatively analyze the performance of the systems. We will then develop a suitable motion generation strategy to create a useful joint mechanism. In the meantime, we are also exploring the possibility of shrinking the size of the mechanism so that it can be utilized in applications with size constraints.

**Acknowledgment.** This work is supported by the Ministry of Science and Technology (MOST), Taiwan, under contracts MOST 108-2634-F-002-002.

## References

1. Bajaj, N.M., Spiers, A.J., Dollar, A.M.: State of the art in artificial wrists: a review of prosthetic and robotic wrist design. *IEEE Trans. Rob.* **35**(1), 261–277 (2019)
2. Yu, O., et al.: Development of a new humanoid robot WABIAN-2. In: *Proceedings 2006 IEEE International Conference on Robotics and Automation, 2006. ICRA 2006*, pp. 76–81. IEEE, Orlando (2006)
3. Albers, A., et al.: Upper body of a new humanoid robot - the design of ARMAR III. In: *2006 6th IEEE-RAS International Conference on Humanoid Robots*, pp. 308–313. IEEE, Genova (2006)

4. Gouaillier, D., et al.: Mechatronic design of NAO humanoid. In: 2009 IEEE International Conference on Robotics and Automation, pp. 769–774. IEEE, Kobe (2009)
5. Ott, C., et al.: Development of a biped robot with torque controlled joints. In: 2010 10th IEEE-RAS International Conference on Humanoid Robots, pp. 167–173. IEEE, Nashville (2010)
6. Lohmeier, S., Buschmann, T., Ulbrich, H.: Humanoid robot LOLA. In: 2009 IEEE International Conference on Robotics and Automation, pp. 775–780. IEEE, Kobe (2009)
7. Albers, A., Sander, C., Simsek, A.: Development of the actuation of a new wrist for the next generation of the humanoid Robot ARMAR. In: 2010 10th IEEE-RAS International Conference on Humanoid Robots, pp. 677–682. IEEE, Nashville (2010)
8. Nazri Bajuri, M., Abdul Kadir, M.R.: Computational Biomechanics of the Wrist Joint. Springer, Heidelberg (2013)
9. Kaneko, K., et al.: Humanoid robot HRP-3. In: 2008 IEEE/RSJ International Conference on Intelligent Robots and Systems, pp. 2471–2478. IEEE, Nice (2008)
10. Asfour, T., et al.: ARMAR-4: A 63 DOF torque controlled humanoid robot. In: 2013 13th IEEE-RAS International Conference on Humanoid Robots (Humanoids), pp. 390–396. IEEE, Atlanta, GA (2013)
11. Abdul Kadir, M.R.: Computational Biomechanics of the Hip Joint. Springer, Berlin, Heidelberg (2014)
12. Craig, J.J.: Introduction to Robotics: Mechanics and Control, 3rd edn. Pearson/Prentice Hall, Upper Saddle River (2005)

# **Modelling and Simulation**



# Dynamic Model of a Crank Press in the Process of Braking

Assylbek Jomartov<sup>(✉)</sup> , Amandyk Tuleshov ,  
and Moldir Kuatova 

Institute Mechanics and Mechanical Engineering,  
Almaty 050010, Kazakhstan  
legsert@mail.ru

**Abstract.** The paper studies the dynamic of a brake of crank press. At present, the dynamic research of brake of the crank presses, with account of interaction with other links, is a priority. The crank press contains movable parts and links, the mass of which is from one hundred kilograms to several tons. These parts and links are cyclically stopped when braking with a crank press almost instantaneously, and they are subject to high dynamic loads. To simulate and analyze the movement of crank press with brake, a software package: SimulationX is used. SimulationX is a software package for modeling and analyzing the dynamics and kinematics of cars, industrial equipment, electric, pneumatic and hydraulic drives, hybrid engines, etc. As a result of dynamic calculation, important dynamic parameters of the crank press brake and working ram are determined. It is shown that dynamic loads sharply increase almost in all links of the crank press when the brake is switched on.

**Keywords:** Dynamics · Crank press · Brake · SimulationX

## 1 Introduction

Crank press is a machine with a slider-crank mechanism, designed for stamping various parts [1–3]. During the work of crank press, significant dynamic loads occur in links and mechanisms, especially when it is turned on. These dynamic loads are associated with operational feature of the crank press, which includes shock cyclic loads with sudden, almost immediate stops. In this connection, the study of the dynamics of brake of the crank press, is of great interest. Figure 1 shows scheme of the press [3].

Operating principle of the crank press (see Fig. 1): the crankshaft 10 rotates about an axis and activates through the connecting rod 2 a ram 1 with punch. The press drive consists of an electric motor 7, a V-belt drive and a flywheel 5. The press clutch 11 is located on the end of the crankshaft 10. Brake 4 serves to stop the press. Brake 3 serves to stop the crank mechanism of the press. The drive of the press is carried out from an electric motor with a flywheel. Since the parameters of motion of the actuating link – ram, depend only on the kinematic links of the main working mechanism, crank presses are referred to uncontrolled machines with limited movement of the ram, equal to the double radius of the crank or double eccentricity of the eccentric.

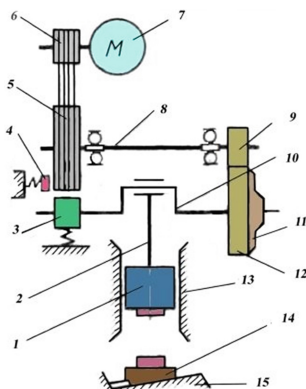


**Fig. 1.** Scheme of crank press: 1-ram, 2-connecting rod, 3-brake of crank mechanism, 4-flywheel brake, 5-flywheel, 6-sheave, 7-electric motor, 8-drive shaft, 9-drive gear, 10-crank shaft, 11-clutch, 12-driven gear, 13-crosshead guide, 14-wedge-type platten, 15-press board.

Asynchronous electric drive accelerates with power flywheel and all the guide links with the corresponding moment of inertia to the steady angular velocity during the technological cycle and dispatches kinetic energy of the rotational motion of the flywheel to it. In this case, the crank shaft and all driven links of the crank-slider mechanism are fixed, the slide is in the upper (initial) position. When the clutch 11 is turned on, the crank shaft (cranked axel 10) is rotated; driving and driven members move together, the ram with fixed upper die make a working stroke. After completion of the working stroke, the ram makes a return stroke. If the press works by single stokes, then when the ram reaches its initial position, the clutch 11 is turned off and at the same time the brake 3 is turned on. The ram stops in the upper (initial) position and the work cycle is completed.

## 2 Brake of Crank Press

The crank press brake absorbs the energy of the clutch driven parts after it is turned off and holds the actuator with the drive part in the position corresponding to the upper position of the ram. Band and disc brakes are used in crank presses. Disc brakes are more reliable than band brakes. Disc brakes provide greater friction moments and less inertia.

The working principle of disc brakes is similar to the operation of friction clutches with the difference that in the brake part of the discs are fixed (not rotating), and the other part rotates with the shaft. Most often, the brake is installed on the crank shaft (Fig. 2) [1].

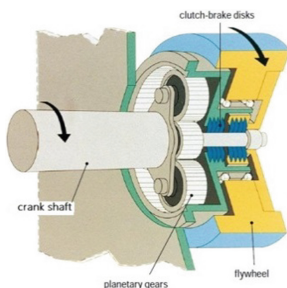


**Fig. 2.** Dick brake on the crank shaft.

Often the brakes are rigidly interlocked with the clutch, i.e. drive disks interlock with either clutch driven disks or brake (fixed) disks (Fig. 3) [1].

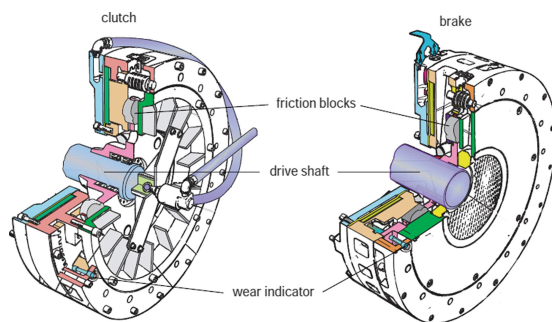


**Fig. 3.** Dick brake with the clutch.

The slotted hub of the brake is mounted on the left end of the eccentric shaft on the wedge keys [3]. Two steel discs with friction linings and a slotted connection with a hub are constantly clamped between the casing, intermediate and pressure discs with the help of tension springs with pushers (Fig. 4). The force of tightening the springs is determined based on the required pressure on the friction contact (2.4 ... 2.5 MPa). During braking, compressed air with a pressure of 0.45 ... 0.5 MPa is fed into the cavity under the piston.

Calculation of the disk brake is reduced to the determination of the braking torque and the choice of power elements ensuring the receipt of such torque.

The work of braking is equal to the kinetic energy of the driven parts of the press drive (taking into account the details of the ram), are determined by equality [3]:

$$\frac{I_{b.m}\omega_m^2}{2} = \frac{\pi}{180} M_m \cdot \alpha_m^0 \cdot u_m \quad (1)$$

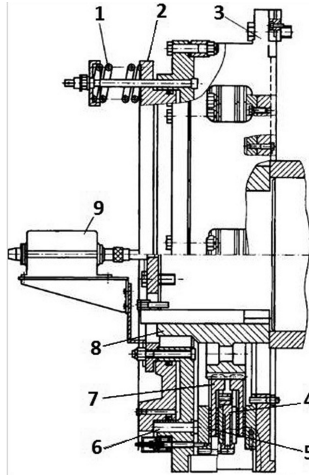


**Fig. 4.** Scheme of a two-disc brake: 1 - pressure springs; 2 - pressing piston; 3 - a housing with a cylinder; 4 - intermediate disk; 5 - pressure disc; 6 - push finger; 7 - driven discs with friction linings; 8 - hub with slots; 9 - control device.

where  $I_{b,m}$  - the moment of inertia of the driven parts of the drive is reduced to the brake shaft;  $\omega_m$  - angular velocity of the brake shaft;  $M_m$  - braking torque [Nm];  $\alpha_m^0$  - braking angle,  $\alpha_m^0 = 8^\circ - 12^\circ$  - for sheet metal stamping presses;  $u_m$  - the gear ratio from the brake shaft to the main shaft.

From Eq. (1) determine the braking torque

$$M_m = \frac{28,65 I_{b,m} \omega_m^2}{\alpha_m^0 \cdot u_m} \quad (2)$$

And the sizes of the single-disc brake with linings are determined [3]:

$$M_m = 2f \cdot q_m R_{cp} \cdot n \cdot F_{bc}$$

where  $f = 0.35$  is the friction coefficient;  $q_m = 0.6 - 1.2$  MPa is the pressure on the friction surface;  $R_{cr}$  is the average radius of the lining;  $n$  is number of lining;  $F_{bc}$  is the square of the working surface of the lining.

For disc brakes, dimensions are determined on the basis of recommendations, the required pressure on the discs is determined, springs are calculated, and the diameter of the piston is determined.

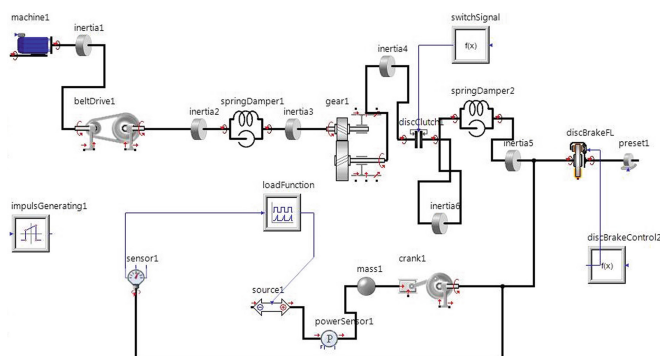
### 3 Dynamic Model of Crank Press with Brake

When modeling the dynamics of a crank press with the brake and simulation of the operation of the brake, various software systems are used [4–8].

To simulate and analyze the movement of a crank press with the brake, this work uses a software package: SimulationX [9].

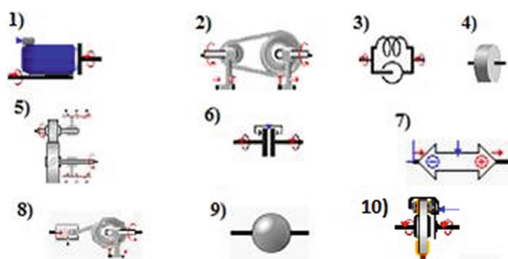
SimulationX – is software for modeling and analyzing the dynamics and kinematics of automobiles, industrial equipment, electric, pneumatic and hydraulic actuators, hybrid engines, etc. It is used for the design, modeling, simulation, analysis and virtual testing of complex mechatronic systems. It simulates the behavior and interaction of various physical objects of mechanics (1D and 3D), driving equipment, electrical, hydraulic, pneumatic and thermodynamic systems, as well as magnetism and analog and digital control systems. It performs the following tasks: system modeling in the time and frequency domains; simulation of transient processes in linear and nonlinear systems or stationary simulation to calculate a model in a periodic state (nonlinear or linear). Model libraries are divided by simulated physical applications. Tools and interfaces complement SimulationX for integrated analysis of systems and structure.

Figure 5 shows dynamic model of a crank press with brake on the SimulationX software package [9–12].



**Fig. 5.** Dynamic model of a crank press with brake on the SimulationX software package.

The elements of the SimulationX library that were used to compile the model are shown in Fig. 6.



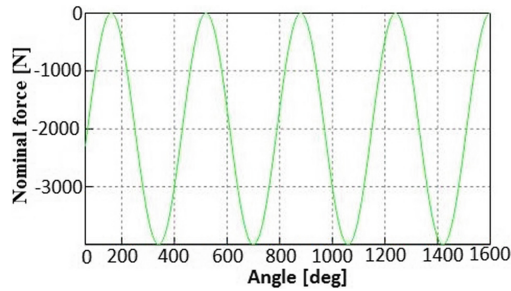
**Fig. 6.** The elements of the SimulationX library.



List of symbols (see Fig. 6) and description of the elements of the SimulationX library:

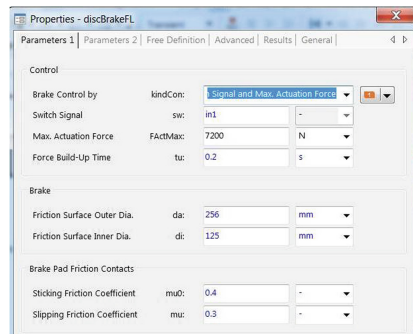
1. Asynchronous motor. This element simulates the simple asynchronous motor. The model is based on the stationary characteristics of the motor. This element models the asynchronous motor with sufficient accuracy when simulating the drive of a machine. It simulates engine starting, transient and steady-state processes, depending on the load and the speed of rotation of the shaft.
2. Belt drive. This element models the operation of belt transmission, with the account of elastic-dissipative characteristics. The model takes into account the reactions and movements in the bearings of the pulleys of the belt drive that allows you to simulate the interaction of the transmission with the base.
3. Spring - Damper – backlash. The model represents elastic and /or damped behavior between the rotational links, with the possibility of taking into account backlash. Springs always acts in parallel with the dampers.
4. Inertia. This element models the moment of inertia of a rotary link. It is also possible to simulate a variable moment of inertia.
5. Gear. The Transmission element is an ideal converter of rotational movements and forces operating between two components in a rotating mechanical system. It works as an ideal converter without taking into account dissipation and, fulfills the specified gear ratio or the conditions of power balance in input and output. The Transmission element allows you to model fixed and variable ratios for angles or velocities in input and output.
6. Disc clutch. The Model Disc Clutch is a component that turns on or interrupts the flow of torque (and therefore power transmission) between the drive components. The model can be used to simulate multi-plate clutch of machines or gearboxes. In addition, it is possible to simulate the friction of the brakes (for example, an automatic transmission). Elasticity, damping and clutch friction parameters can be considered. In transmission of the models, the clutch can be activated by a signal from the switch.
7. External force. This type of element allows you to simulate the forces between two components, or only on one component of the mechanical model. It provides universal, functional power transfer in the mechanical model.
8. Crank mechanism. The element models a slider-crank mechanism, taking into account the backlash in the hinges, the elastic-dissipative properties of the connecting rod.
9. Mass. This element models the mass of a linear link. Variable mass modeling is also possible.
10. Disc brake. The Model Disc brake is a component that turns on or interrupts the flow of torque (and therefore power transmission) between the drive components. The model can be used to simulate multi-plate brake of machines or gearboxes. In addition, it is possible to simulate the friction of the brakes (for example, an automatic transmission). Elasticity, damping and brake friction parameters can be considered. In transmission of the models, the brake can be activated by a signal from the switch.

Initial parameters of the model: crank press motor power  $W = 0.5$  kw, rated engine speed  $n = 450$  rpm. The numerical values of the dimensions, moments of inertia of the links of the crank press and the stiffness of the shafts are taken from [3]. The nominal force developed by the ram of the slider-crank working mechanism in the area before the extreme low point of the ram's stroke is modeled by a sine-wave signal generator (load Function) and linear force (load) [3] (Fig. 7). This load force depends on the angle of the crank. The maximum force is reached at the lower point of the ram's stroke and is equal to 4000 N.



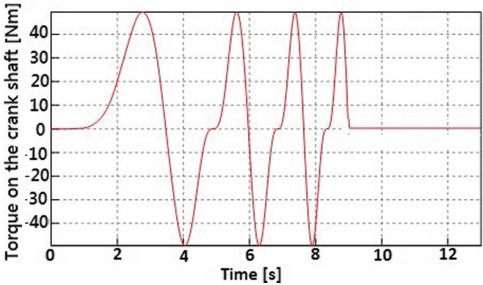
**Fig. 7.** The nominal force, developed by the ram of the slider-crank working mechanism.

Parameters of the brake of the crank press are shown in Fig. 8.



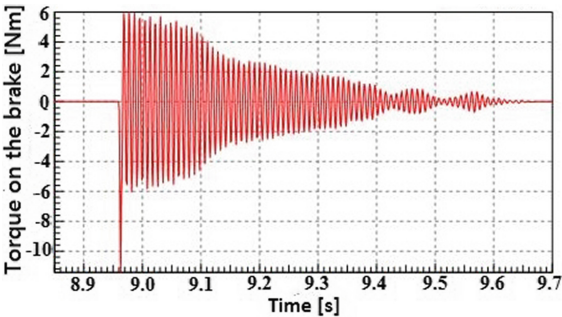
**Fig. 8.** Parameters of the brake of the crank press.

Simulation results: Brake of the crank press is activated and stops the moving flywheel. Figure 9 shows the torque on the crank shaft.



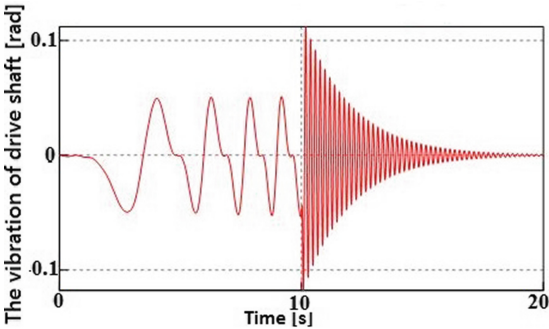
**Fig. 9.** The torque on the crank shaft.

Figure 10 shows the torque on the brake.



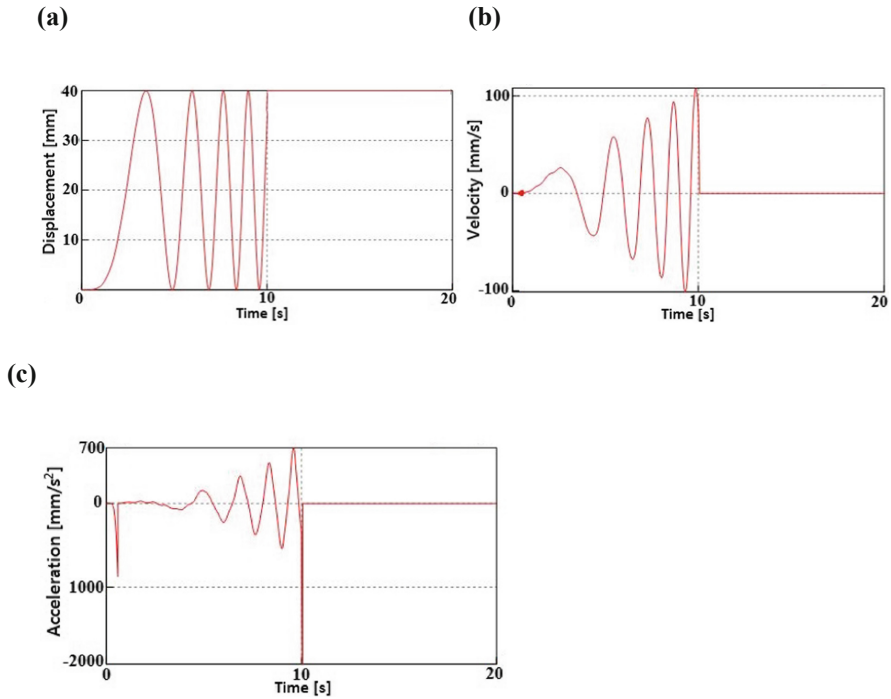
**Fig. 10.** The torque on the brake.

Figure 11 shows the vibration of drive shaft.



**Fig. 11.** The vibration of drive shaft.

Figures 12 a, b, c shows displacement, velocity, acceleration of the press ram.



**Fig. 12.** Estimated data of the press ram (a) - displacement, (b) - velocity; (c) – acceleration.

In Fig. 12 (c), the reason downward spike on the acceleration plot occurs due to sudden braking crank press on 10-th second.

## 4 Conclusion

The SimulationX software package allows one to simulate the dynamics of the brake of the crank press, taking into account its design parameters as part of the crank press, and the interaction with its entire links.

As the result of the dynamic calculation following is determined: the torque on the crank shaft, the torque on the brake, the vibration of drive shaft. Displacement, velocity, acceleration of the ram of the crank press are determined at the moment of brake turn-on.

Dynamic loads in the links of the crank press sharply increase at the moment of brake turn-on. When researching the dynamics of a crank press, it is necessary to take into account the design features of the brake, especially brake pad wear and adjustment, which requires further research of this unit.

Visibility of the models and graphical results are especially useful for students and engineers in the research of brake of the crank presses.





**Acknowledgments.** This material is based upon work supported by the Ministry of Education and Science of the Republic of Kazakhstan under grant no. AP05134959.

## References

1. Altan, T. (ed.): Metal Forming Handbook. Springer, Heidelberg (1998)
2. Altan, T., Oh, S., Gegel, H.: Metal Forming Fundamentals and Applications. American Society for Metals, Ohio (1983)
3. Bocharov, Ju.A.: Kuznechno-shtampovochnoe oborudovanie. M.: Izdatel'skij centr Akademija (2008). (in Russian)
4. Hlavac, J., Cechura, M., Kubec, V.: Technologia. The development of virtual simulation in design of mechanical presses. Bratislava (2011)
5. Halicioglu, R., Dulger, L., Bozdana, A.: Modelling and simulation based on matlab/simulink: a press mechanism. J. Phys: Conf. Ser. **490**, 1–4 (2014)
6. Li, L., Lu, Z., Li, L., Sun, T., Jing, X., Shangguan, W.: Modeling and analysis of friction clutch at a driveline for suppressing car starting judder. J. Sound Vib. **424**, 335–351 (2018)
7. Häfele, J., Küçükay, F.: Multi-body dynamics analysis of power train judder oscillations considering aggregate dynamics. Int. J. Veh. Noise Vib. **10**, 64–76 (2014)
8. Jang, J.D., Kim, G.W., Bae, D.S.: Rigid multi-body model for simulation of the dynamic hysteresis and the contact force of automotive clutch damper springs. I. Mech. E. Part D: J. Automobile Eng. **228**, 190–198 (2013)
9. SimulationX, <http://www.simulationx.com/>. Accessed 24 Jan 2019
10. Jomartov, A.A., Joldasbekov, S.U., Drakunov, Y.: Dynamic synthesis of machine with slider-crank mechanism. Mech. Sci. **6**(1), 35–40 (2015)
11. Jomartov, A.: Multibody dynamic model of Russian Sulzer loom STB. J. Vib. Eng. Technol. **5**(6), 523–533 (2017)
12. Jomartov, A., Tuleshov, A.: Vector method for kinetostatic analysis of planar linkages. J. Braz. Soc. Mech. Sci. Eng. **40**, 55–69 (2018)



# Workspace Modelling of a Parallel Robot with Relative Manipulation Mechanisms Based on Optimization Methods

Dmitry Malyshev<sup>1</sup> , Larisa Rybak<sup>1</sup> , Laxmidhar Behera<sup>2</sup> ,  
and Santhakumar Mohan<sup>3</sup> 

<sup>1</sup> Belgorod State Technological University Named After V.G. Shukhov,  
Belgorod, Russian Federation  
rlbgtu@gmail.com

<sup>2</sup> Indian Institute of Technology Kanpur, Kanpur 208016, India

<sup>3</sup> Indian Institute of Technology Palakkad, Palakkad, India

**Abstract.** The article describes the application of optimization algorithms for solving the problem of determining the workspace of a relative mechanism device, which includes a planar 3-RPS mechanism and a tripod module. Approximation sets of individual modules are used to approximate its workspace in the moving coordinate system. The considered method of approximating a solution set of nonlinear inequalities based on the concept of the non-uniform coverings, describes constraints on the robot geometric parameters. The exterior and interior approximations of the 3-RPS mechanism are obtained. Similarly, an approximation of the restrictions for the tripod module in the moving platform coordinate system is obtained. The constraints with a given accuracy are transferred to the coordinate system of the output using a three-dimensional binary array approximating the workspace. The workspace of the relative mechanism device was obtained on the basis of these results, taking into account the relative manipulation of modules and restrictions on the workpiece geometric parameters. Moving coordinate system is located in the center of the planar 3-RPS mechanism platform.

**Keywords:** Approximation set · Relative mechanism device · Workspace · Non-uniform coverings · Optimization

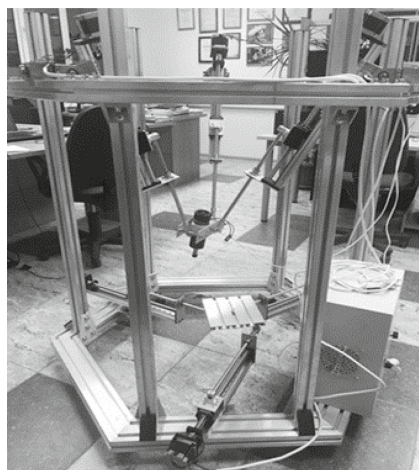
## 1 Introduction

Robots of a parallel structure are increasingly used in industry, including mechanical engineering for performing various technological operations [1–3]. Such robots have a number of positive properties, which include high performance, increased structural rigidity, increased accuracy of the operations performed. An important characteristic of robots of a parallel structure is workspace, within which the working tool must be located at technological operations. Determining the workspace of parallel robots is much more difficult than for serial robots. They are characterized by ambiguity in solving the kinematics problem, that is, the different positions of the driving rods can correspond to one position of the output link. In [4], the non-uniform coverings method

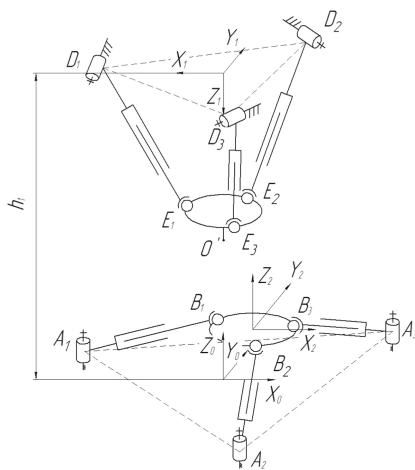
for approximating a solution set of nonlinear inequalities was considered, and in [5–7] the application of this method to determine the workspace of some types of planar robots.

## 2 Formulation of the Problem

Consider the application of the method for a parallel structure relative mechanism device (RMD) (Fig. 1a). The upper module is made on the basis of a tripod, the center of which mobile platform can perform translational motion along the  $Z$  axis and rotational around the  $X$  and  $Y$  axes, as well as additional output displacements when it rotates relative to the horizontal axes imposed by the kinematic chains of the module-tripod. The lower module is made on the basis of a planar 3-RPS mechanism, performs translational motion along the  $X$  axes and  $Y$  and rotational around the  $Z$  axis. Thus, RMD has 6 degrees of freedom. It can be used to perform part processing operations if the working tool (end-effector) is mounted on the movable platform of the tripod module, and the workpiece is on the movable platform of the 3-RPS mechanism. Consider the task of determining the workspace of the relative mechanism device, taking into account the restrictions on the geometric parameters of the workpiece, located on a moving platform. The scheme of the relative mechanism device is shown in Fig. 1b. The axes  $Z_0$  and  $Z_1$  lie on one straight line, perpendicular to the fixed base of the tripod module  $D_1D_2D_3$  and the platform of the planar 3-RPS mechanism and passing through the center of the circumscribed circle of triangle  $A_1A_2A_3$ . In the initial position, that is, if the center of the circumscribed circle of triangle  $A_1A_2A_3$  coincides with the center of the moving platform of the planar 3-RPS mechanism, the moving coordinate system  $X_2Y_2Z_2$  coincides with  $X_0Y_0Z_0$ . Define the workspaces of the individual modules.



(a) experimental sample.



(b) the scheme.

**Fig. 1.** Relative mechanism device.

### 3 Determination the Workspace of the Tripod Mechanism

The tripod module (Fig. 2) includes three rods of variable length, which are connected by rotational hinges with the base and spherical hinges to the working platform. The base and working platform are equilateral triangles. When the rod lengths change, the working platform moves along the  $Z_1$  axis by a distance  $z_1$  and turns around the  $X_1$  axis by the angle  $\psi$  and around  $Y_1$  the angle  $\theta$ . The additional degrees of freedom are a displacement along the  $X_1$  axis by a distance  $x_1$  and along  $Y_1$  by a distance  $y_1$  and a rotation relative to  $Z_1$  by an angle  $\alpha$ , which are determined by the formulas [8]:  $\alpha = \text{Tan}^{-1}(\frac{\sin \psi \sin \theta}{\cos \psi + \cos \theta})$ ;  $x_1 = \frac{r}{2}(\cos \theta \cos \alpha + \sin \psi \sin \theta \sin \alpha - \cos \psi \cos \alpha)$ ;  $y_1 = -r \cos \psi \sin \alpha$ .

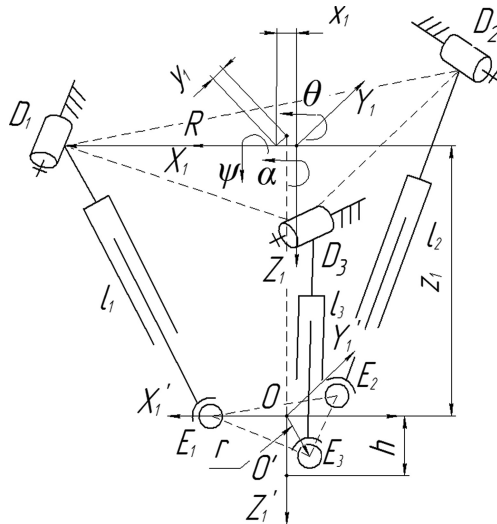


**Fig. 2.** Scheme of the module on the basis of tripod.

The input coordinates of the mechanism are the lengths of the drive links  $l_1, l_2, l_3$ , and the output are the coordinates of the point  $O'$  of the working tool:  $x_{o'}, y_{o'}, z_{o'}$ . Point  $O'$  is located at a distance  $h$  from the center of the moving platform. The inverse problem of kinematics has many solutions. So, it is necessary to preliminarily determine the set of admissible values of linear and angular coordinates of the center  $O$  of the moving platform, and then determine the set of coordinates  $O'$  of the working element for these values. Coordinates  $O'$  in the moving coordinate system  $X'_1 Y'_1 Z'_1$ :

$$\mathbf{O}'_1 = [0 \quad 0 \quad h \quad 1]^T \quad (1)$$

Calculate the coordinates of point  $O'$  in a fixed coordinate system  $X_1 Y_1 Z_1$



$$\mathbf{O}'_1 = \mathbf{O}'_1 \mathbf{M}_{1' \_1} \quad (2)$$

where  $\mathbf{M}_{1' \_1}$  - is the transition matrix from the moving coordinate system  $X'_1 Y'_1 Z'_1$  to the fixed system  $X_1 Y_1 Z_1$ , which includes displacement matrices along the axes  $X_1 Y_1 Z_1$  and turns around  $X_1 Y_1$  and  $Z_1$  axes:

$$\mathbf{M}_{1' \_1} = \begin{bmatrix} \cos \theta \cos \alpha + \sin \psi \sin \theta \sin \alpha & -\cos \theta \sin \alpha + \sin \psi \sin \theta \cos \alpha & \sin \theta \cos \psi & x_1 \\ \cos \psi \sin \alpha & \cos \psi \cos \alpha & -\sin \psi & y_1 \\ -\sin \theta \cos \alpha + \sin \psi \cos \theta \sin \alpha & \sin \theta \sin \alpha + \sin \psi \cos \theta \cos \alpha & \cos \theta \cos \psi & z_1 \\ 0 & 0 & 0 & 1 \end{bmatrix} \quad (3)$$

After the conversion, we get

$$\mathbf{O}'_1 = \begin{bmatrix} x_1 + \sin \theta \cos \psi h \\ y_1 - \sin \psi h \\ z_1 + \cos \theta \cos \psi h \\ 1 \end{bmatrix} \quad (4)$$

Next, we introduce restrictions on the geometric parameters of the mechanism

$$l_{\min} \leq l_i \leq l_{\max}, \quad (5)$$

where  $l_{\min}, l_{\max}$  are determined by the design parameters of the mechanism,  $l_i$  is the length of the  $i$ -th bar, which is defined as

$$l_i = \sqrt{(x_{Ei} - x_{Di})^2 + (y_{Ei} - y_{Di})^2 + (z_{Ei} - z_{Di})^2} \quad (6)$$

where  $x_{Ei}, y_{Ei}, z_{Ei}$  are the coordinates of the centers of the hinges point  $E_i$ ,  $x_{Di}, y_{Di}, z_{Di}$  are the coordinates of the centers of the hinges point  $D_i$  in the fixed coordinate system.

Define the coordinates of the hinges  $E_i$  in the moving coordinate system  $X'_1 Y'_1 Z'_1$ :

$$\begin{aligned} \mathbf{E}'_1 &= [r \quad 0 \quad 0 \quad 1]^T, \quad \mathbf{E}'_2 = [-0,5r \quad 0,5\sqrt{3}r \quad 0 \quad 1]^T, \\ \mathbf{E}'_3 &= [-0,5r \quad 0,5\sqrt{3}r \quad 0 \quad 1]^T. \end{aligned}$$

Denote in (3):  $M_{11} = \cos \theta \cos \alpha + \sin \psi \sin \theta \sin \alpha$ ,  $M_{12} = -\cos \theta \sin \alpha + \sin \psi \sin \theta \cos \alpha$ ,  $M_{13} = \sin \theta \cos \psi$ ,  $M_{21} = \cos \psi \sin \alpha$ ,  $M_{22} = \cos \psi \cos \alpha$ ,  $M_{23} = -\sin \psi$ ,  $M_{31} = -\sin \theta \cos \alpha + \sin \psi \cos \theta \sin \alpha$ ,  $M_{32} = \sin \theta \sin \alpha + \sin \psi \cos \theta \cos \alpha$ ,  $M_{33} = \cos \theta \cos \psi$ .

Express the coordinates of the hinges  $E_i$  in a fixed coordinate system  $X_1 Y_1 Z_1$

$$\mathbf{E}_1 = \mathbf{M}_{1' \_1} \mathbf{E}'_1 = \begin{bmatrix} x_1 + M_{11}r \\ y_1 + M_{21}r \\ z_1 + M_{31}r \\ 1 \end{bmatrix} = \begin{bmatrix} x_1 + M_{11}r \\ 0 \\ z_1 + M_{31}r \\ 1 \end{bmatrix} \quad (7)$$

$$\mathbf{E}_2 = \mathbf{M}_{1' \_1} \mathbf{E}'_2 = \begin{bmatrix} x_1 - 0, 5r(M_{11} - \sqrt{3}M_{12}) \\ y_1 - 0, 5r(M_{21} - \sqrt{3}M_{22}) \\ z_1 - 0, 5r(M_{31} - \sqrt{3}M_{32}) \\ 1 \end{bmatrix} \quad (8)$$

$$\mathbf{E}_3 = \mathbf{M}_{1' \_1} \mathbf{E}'_3 = \begin{bmatrix} x_1 - 0, 5r(M_{11} + \sqrt{3}M_{12}) \\ y_1 - 0, 5r(M_{21} + \sqrt{3}M_{22}) \\ z_1 - 0, 5r(M_{31} + \sqrt{3}M_{32}) \\ 1 \end{bmatrix} \quad (9)$$

where  $y_1 = -M_{21}r = -r \cos \psi \sin \alpha$ .

Determine the coordinates of the hinges  $D_i$  in a fixed coordinate system  $X_1Y_1Z_1$

$$\mathbf{D}_1 = [R \quad 0 \quad 0 \quad 1]^T \quad (10)$$

$$\mathbf{D}_2 = [-0, 5R \quad 0, 5\sqrt{3}R \quad 0 \quad 1]^T \quad (11)$$

$$\mathbf{D}_3 = [-0, 5R \quad -0, 5\sqrt{3}R \quad 0 \quad 1]^T \quad (12)$$

Substituting (7–9) and (10–12) into (6), we get

$$l_1 = \sqrt{(x_1 + M_{11}r - R)^2 + (z_1 + M_{31}r)^2}, \quad (13)$$

$$\begin{aligned} l_2 = & \left( (x_1 - 0, 5r(M_{11} - \sqrt{3}M_{12}) + 0, 5R)^2 \right. \\ & + \left( y_1 - 0, 5r(M_{21} - \sqrt{3}M_{22}) - \frac{\sqrt{3}}{2}R \right)^2 \\ & \left. + (z_1 - 0, 5r(M_{31} - \sqrt{3}M_{32}))^2 \right)^{1/2} \end{aligned} \quad (14)$$

$$\begin{aligned} l_3 = & \left( (x_1 - 0, 5r(M_{11} + \sqrt{3}M_{12}) + 0, 5R)^2 \right. \\ & + \left( y_1 - 0, 5r(M_{21} + \sqrt{3}M_{22}) - \frac{\sqrt{3}}{2}R \right)^2 \\ & \left. + (z_1 - 0, 5r(M_{31} + \sqrt{3}M_{32}))^2 \right)^{1/2} \end{aligned} \quad (15)$$

Taking into account (13–15), restrictions (5) we write in the form

$$\begin{cases} l_1 - l_{max} \leq 0 \\ l_{min} - l_1 \leq 0 \\ l_2 - l_{max} \leq 0 \\ l_{min} - l_2 \leq 0 \\ l_3 - l_{max} \leq 0 \\ l_{min} - l_3 \leq 0 \end{cases} \quad (16)$$

The system of inequalities (16) contains 3 variables:  $z_1, \theta, \psi$ . To determine the workspace in the coordinates  $x'_1, y'_1, z'_1$  you need to get the dependence of the form  $l_i = f(x'_1, y'_1, z'_1)$ , however, it is difficult to do it by an analytical method. In this regard, we will consider some methods for constructing the workspace in coordinates  $x'_1, y'_1, z'_1$ :

Method 1. If we express  $x_1, y_1, z_1$  through  $x'_1, y'_1, z'_1$  using formula (4), the system (16) will have 5 variables:  $x'_1, y'_1, z'_1, \theta, \psi$ . This problem can be solved using the non-uniform coverings method; however, a higher dimension creates a computational problem.

Method 2. Getting the limitation of the workspace in the coordinate space  $z_1, \theta, \psi$  as an ordered set of boxes of interior approximation and transfer for each of them the constraints in the coordinate space  $x'_1, y'_1, z'_1$  using the approximation of irregularly shaped areas to boxes [9]. However, in this case, the accuracy and clarity of the borders of the workspace decreases and also increases the computation time due to the need to iterate over all the boxes from the list of interior approximations.

Method 3. Transferring the workspace constraints in the coordinate space  $z_1, \theta, \psi$  to the coordinate space  $x'_1, y'_1, z'_1$  using an approximate three-dimensional binary array. This allows us to obtain an approximation set with given accuracy and to apply for determining the workspace of the RMD to the required element of the array without iterating over the elements.

Let us consider in more detail the third method. The coordinate space  $x'_1, y'_1, z'_1$  is characterized by some binary array  $A$ . Consider the construction of this array for some two-dimensional arbitrary area (Fig. 3). The size of the array is determined by the approximation accuracy  $\delta$  and the interval of coordinates  $[x_{min}; x_{max}]$  and  $[y_{min}; y_{max}]$ . The array has  $(\text{round}(\frac{x_{max}}{\delta}) - \text{round}(\frac{x_{min}}{\delta}) + 1)$  elements along the  $x$  axis and  $(\text{round}(\frac{y_{max}}{\delta}) - \text{round}(\frac{y_{min}}{\delta}) + 1)$  elements along the  $y$  axis. Initially all the elements of the array have the value 0. For the coordinates of each point  $P$  of the area, a row and a column of array  $A$  are calculated and 1 is assigned to this array element:

$$A[(\text{round}(\frac{y_P}{\delta}) - \text{round}(\frac{y_{min}}{\delta}) + 1), (\text{round}(\frac{x_P}{\delta}) - \text{round}(\frac{x_{min}}{\delta}) + 1)] = 1 \quad (17)$$

As a result, elements of a binary array that have the value of 1 describe the area.

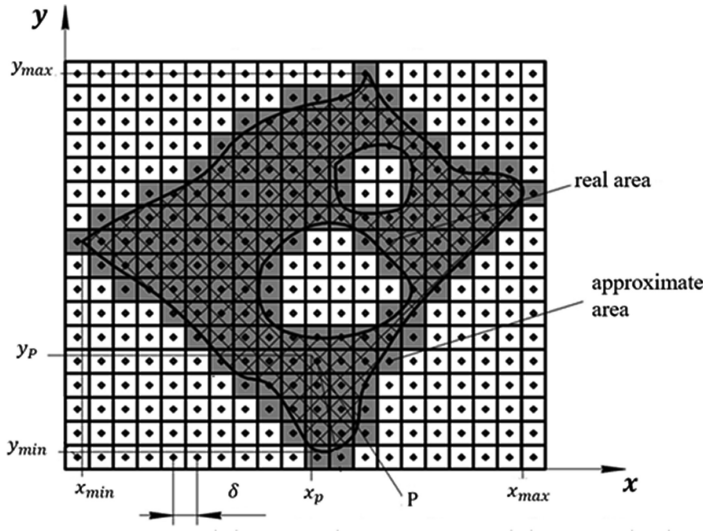
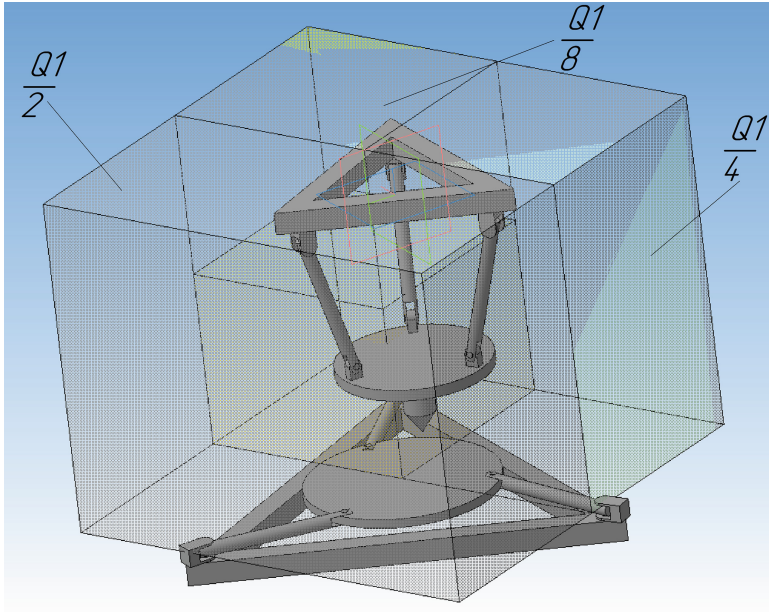


Fig. 3. Construction of an approximation array.

Taking into account formulas (4), (13–17), an algorithm for approximating the workspace of the tripod module has been synthesized. To approximate the systems of inequalities (16), we used the algorithm that works with a system of inequalities written in a general form:

$$\begin{cases} g_1(x) \leq 0, \\ \dots \\ g_m(x) \leq 0 \\ a_i \leq x_i \leq b_i, i = 1, \dots, n. \end{cases} \quad (18)$$

The initial box  $Q$  that encloses the whole solution set  $X$  is defined by interval constraints  $a_i \leq x_i \leq b_i, i = 1, \dots, n$ . Consider an arbitrary box  $B$ . Let  $m(B) = \max_{i=1, \dots, m} \min_{x \in B} g_i(x)$  and  $M(B) = \max_{i=1, \dots, m} \max_{x \in B} g_i(x)$ . If  $m(B) > 0$  then  $B$  contains no feasible points for a system (16). If  $M(B) \leq 0$  then every point of a box  $B$  is a feasible solution. Therefore, it can be added to the coverage as an inner box. If a box cannot be discarded it is partitioned into two smaller boxes unless its diameter is below the prescribed accuracy  $\delta$  (Fig. 4).



**Fig. 4.** Dividing the original box  $Q_1$ :  $\frac{Q_1}{2}$  - into 2 parts,  $\frac{Q_1}{4}$  - into 4 parts,  $\frac{Q_1}{8}$  - into 8 parts.

The algorithm works with two lists of three-dimensional boxes  $\mathbb{P}_1$  and  $\mathbb{P}_{1,I}$ , while the list  $\mathbb{P}_1$  is a set of boxes containing many point  $O$  positions, the list  $\mathbb{P}_{1,I}$  is a set of boxes containing a set of point  $O$  positions satisfying conditions (16), and a three-dimensional binary array  $A$  of the coordinates  $O'$  set, satisfying conditions (16). The algorithm flowchart is presented in Fig. 5.

To implement the synthesized algorithm, a program was developed in C++ language with the ability to visualize simulation results in the Gnuplot program. The program was developed within the framework of the project no. AP05133190, Science Committee, the Ministry of Education and Science, Republic of Kazakhstan. The simulation was performed for  $l_{1,2,3} \in [80 \text{ mm}, 120 \text{ mm}]$ ,  $R = 100 \text{ mm}$ ,  $r = 50 \text{ mm}$ . The simulation results are presented in Fig. 6. It can be seen from the figure that the workspace of the tripod module for the given parameters is limited to dimensions  $60 \times 60 \times 70 \text{ mm}$ .

From Fig. 6 it can be seen that for slice by the XOY plane in the transverse direction with the value  $z_{o'} = 110 \text{ mm}$ , the empty working space is not observed, that is, all positions of the workspace are achievable with any geometrical parameters of the mechanism. On sections with  $z_{o'} < 110 \text{ mm}$ , empty areas of the working space are observed that are unattainable with any geometric parameters of the mechanism in the range  $l_{1,2,3} \in [80 \text{ mm}, 120 \text{ mm}]$ ,  $\theta \in [-90^\circ, 90^\circ]$  and  $\psi \in [-90^\circ, 90^\circ]$ , which is additionally illustrated in Fig. 6d (purple area with a slice  $z_{o'} = 105 \text{ mm}$ , brown with  $z_{o'} = 130 \text{ mm}$ , black with  $z_{o'} = 145 \text{ mm}$ ). This is due to the specifics of parallel robots, namely the intersection of the drive links and the presence of so-called singularity zones.

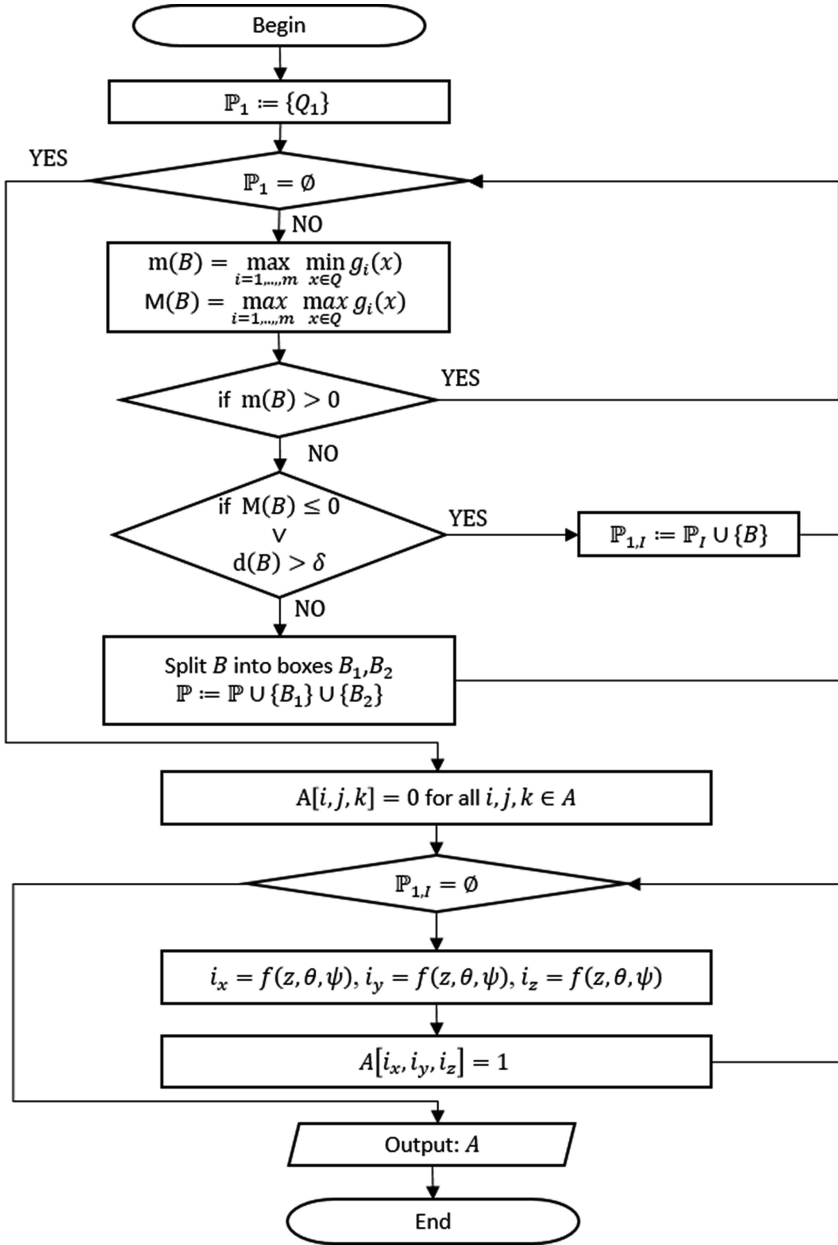


**Fig. 5.** An approximation algorithm for tripod workspace.

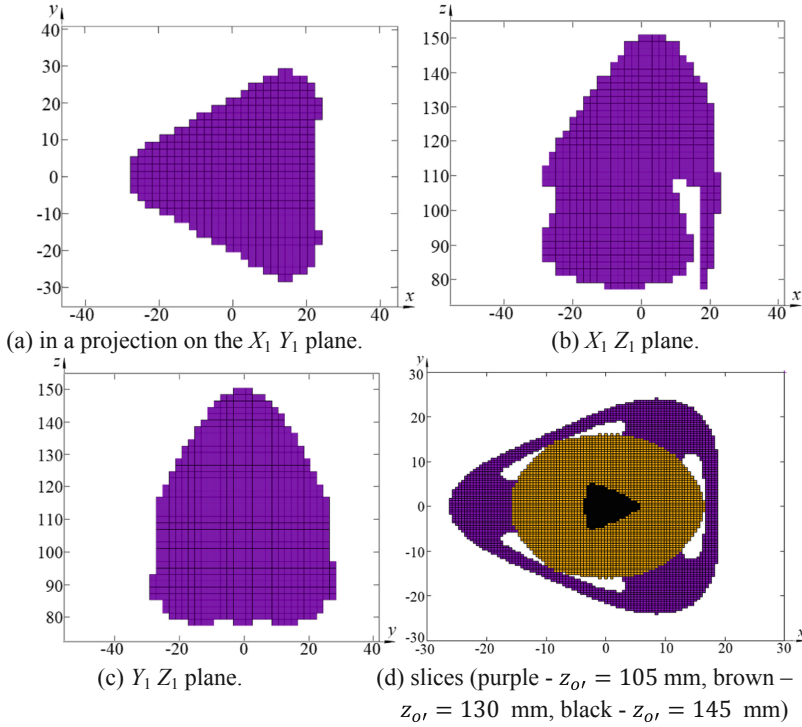


**Fig. 6.** Simulation results.

#### 4 Algorithm for Determining the RMD Workspace

To determine the RMD workspace, we used the 3-RPS mechanism workspace described in [10]. It is necessary to find a set of  $O'$  positions in the moving coordinate system  $X_2 Y_2 Z_2$  located in the center of the planar 3-RPS mechanism to determine the RMD workspace, taking into account the restrictions on the geometrical parameters of the workpiece. When determining the set of  $O'$  positions using combinations of box points describing the workspaces of the tripod module and 3-RPS mechanism, it becomes necessary to calculate the coordinates  $O'$  a significant number of times. For example, in the case of box division by a uniform grid of  $100 \times 100$  and the number of boxes in each of the lists is  $n = 1000$ , the number of calculations and results that need to be saved for each of the coordinates is 1018 times. So, it is necessary to apply the reverse method, i.e. check  $O'$  with coordinates  $x_2, y_2, z_2$  for the entry into the workspace of the tripod module. Define the coordinates  $O'$  in the fixed system  $X_1 Y_1 Z_1$  using transformation matrices that take into account the transition from the system  $X_2 Y_2 Z_2$  to  $X_1 Y_1 Z_1$ , extracted from the boxes describing the workspace of the 3-RPS mechanism. The visualization results for point verification are shown in Fig. 7. If area 4 exists, then point  $O'$  enters the workspace of the RMD.

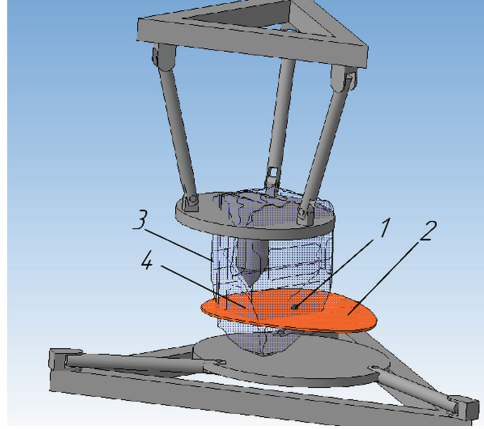


**Fig. 7.** Visualization of point verification: 1 – point  $O'$  in the moving coordinate system  $X_2 Y_2 Z_2$ , 2 – all possible positions of point  $O'$  in the fixed system  $X_0 Y_0 Z_0$ , 3 – tripod workspace in the fixed system  $X_1 Y_1 Z_1$ , 4 – intersection of areas 2 and 3.

We write the relation connecting the coordinates  $O'$  in the systems  $X_2 Y_2 Z_2$  and  $X_1 Y_1 Z_1$ , (Fig. 1b)  $O'_1 = M_{0-1} \cdot M_{2-0} \cdot O'_2$ , where  $O'_1 = [x_1 \ y_1 \ z_1 \ 1]^T$  – is the coordinate vector  $O'$  of the working body in the fixed coordinate system  $X_1 Y_1 Z_1$ ,  $O'_2 = [x_2 \ y_2 \ z_2 \ 1]^T$  is the coordinate vector  $O'$  in the moving coordinate system  $X_2 Y_2 Z_2$ , which must be checked for entry into the tripod module workspace (Fig. 6).

$$M_{2-0} = \begin{bmatrix} \cos \phi & -\sin \phi & 0 & x_0 \\ \sin \phi & \cos \phi & 0 & y_0 \\ 0 & 0 & 1 & 0 \\ 0 & 0 & 0 & 1 \end{bmatrix} - \text{matrix that takes into account the transition}$$

from the  $X_2 Y_2 Z_2$  coordinate system to  $X_0 Y_0 Z_0$ , where  $\phi$  is the angle of rotation of the  $X_0 Y_0 Z_0$  coordinate system relative to the  $Z_0$  axis,  $x_0, y_0$  are translational motion along the  $X_0$  and  $Y_0$  axes, respectively.

$$M_{0-1} = \begin{bmatrix} -1 & 0 & 0 & 0 \\ 0 & 1 & 0 & 0 \\ 0 & 0 & -1 & h_1 \\ 0 & 0 & 0 & 1 \end{bmatrix} - \text{matrix that takes into account the transition from}$$

the  $X_0 Y_0 Z_0$  coordinate system to  $X_1 Y_1 Z_1$ , where  $h_1$  is the distance from the center of the 3-RPS mechanism platform to the fixed platform center of the tripod module. Then

$$O'_1 = \begin{bmatrix} y_2 \sin \phi - x_2 \cos \phi - x_0 \\ x_2 \sin \phi + y_2 \cos \phi + y_0 \\ h_1 - z_2 \\ 1 \end{bmatrix} = \begin{bmatrix} x_1 \\ y_1 \\ z_1 \\ 1 \end{bmatrix} \quad (19)$$



The algorithm for determining the workspace in the moving coordinate system of the lower module of the RMD, which has the following features:

1. It works with three lists of three-dimensional parallelepipeds: the list of internal approximation of the planar 3-RPS mechanism  $\mathbb{P}_{2,I}$  obtained earlier, two changeable lists of  $\mathbb{P}$  and  $\mathbb{P}_I$ , as well as tripod three-dimensional binary array  $A$ .
2. In the process of executing the algorithm for points in the  $X_2Y_2Z_2$  coordinate system belonging to the parallelepipeds from the list  $\mathbb{P}$ , the coordinates in the  $X_1Y_1Z_1$  system are calculated using formula (19) using variable values from the  $\mathbb{P}_{2,I}$  list. If  $A \left[ \left( \text{round}\left(\frac{X_1}{\delta}\right) - \text{round}\left(\frac{X_{1\min}}{\delta}\right) + 1 \right), \left( \text{round}\left(\frac{Y_1}{\delta}\right) - \text{round}\left(\frac{Y_{1\min}}{\delta}\right) + 1 \right), \left( \text{round}\left(\frac{Z_1}{\delta}\right) - \text{round}\left(\frac{Z_{1\min}}{\delta}\right) + 1 \right) \right] = 1$ , then the condition is satisfied.
3. Parallelepipeds for which the condition is satisfied for all points is added to the list of interior approximation  $\mathbb{P}_I$ .

The simulation results at different heights of the cut  $z_{O'}$  are shown in Fig. 8. The computation time for the approximation accuracy  $\delta = 4$  mm and the grid dimension for calculating  $64 \times 64 \times 64$  functions on a personal computer were 1 h 18 min.

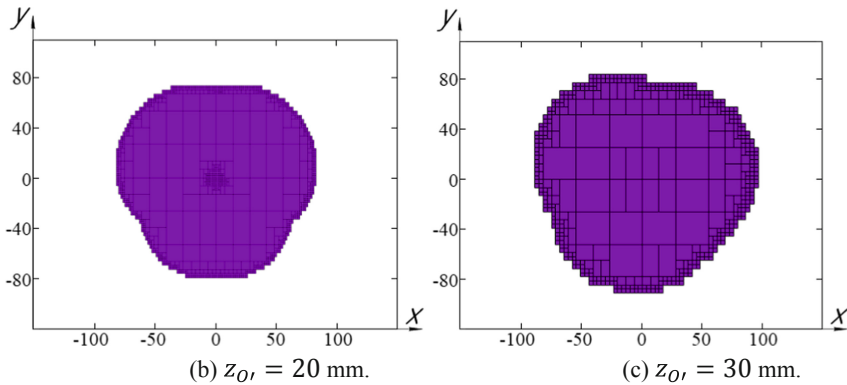


**Fig. 8.** Simulation results.

## 5 Conclusion

The developed algorithms have shown their effectiveness. Developed algorithm was used for the workspace approximation. Algorithm included the transfer of constraints from the coordinate space of the tripod's moving platform to the fixed coordinate space of the working tool using an approximation set in the form of a three-dimensional binary array. This made it possible to reduce the computation time by 2 times while improving the accuracy of approximation by 1.5 times and the workspace shape clarity in comparison with the results of [9]. The obtained results can be used for choosing the geometrical parameters of the mechanisms, providing the limits of the workspace set by the technological process.

**Acknowledgements.** This work was supported by the Russian Science Foundation, the agreement number 16-19-00148 and Science Committee, the Ministry of Education and Science, Republic of Kazakhstan, project no. AP05133190.

## References

1. Aleshin, A.K., Glazunov, V.A., Rashoyan, G.V., Shai, O.: Analysis of kinematic screws that determine the topology of singular zones of parallel-structure robots. *J. Mach. Manuf. Reliab.* **45**(4), 291–296 (2016)
2. Kong, H., Gosselin, C.M.: *Type Synthesis of Parallel Mechanisms*. Springer, Heidelberg (2007)
3. Merlet, J.-P.: *Parallel Robots*, 2nd edn. Springer, Heidelberg (2007)
4. Evtushenko, Y.: Numerical methods for finding global extreme (case of a non-uniform mesh). *U.S.S.R. Comput. Maths. Math. Phys.* **11**, 1390–1403 (1971)
5. Evtushenko, Y., Posypkin, M., Turkin, A., Rybak, L.: The non-uniform covering approach to manipulator workspace assessment. In: *Proceedings of the 2017 IEEE Russia Section Young Researchers in Electrical and Electronic Engineering Conference, El-ConRus 2017*, pp. 386–389 (2017)
6. Evtushenko, Y., Posypkin, M., Rybak, L., Turkin, A.: Approximating a solution set of non-linear inequalities. *J. Global Optim.* **7**, 129–145 (2018)
7. Rybak, L.A., Posypkin, M.A., Turkin, A.V.: Method for approximating the workspace of the parallel robot. *Int. J. Pharm. Technol.* **8**(4), 25045–25055 (2016)
8. Rao, P.S., Rao, N.M.: Position analysis of spatial 3-RPS parallel manipulator. *Int. J. Mech. Eng. Robot. Res.* **2**(2), 80–90 (2013)
9. Posypkin, M., Rybak, L., Malyshev, D., Gaponenko, E.: Approximation of the parallel robot working area using the method of nonuniform covering. In: Liu, G.R., Trovalusci, P. (eds.) *Proceedings at the 9th ICCM2018, 6th–10th August 2018, Rome, Italy*, pp. 949–960. ScienTech Publisher (2018)
10. Rybak, L.A., Gaponenko, E.V., Malyshev, D.I., Virabyan, L.G.: The algorithm for planning the trajectory of the 3-RPR robot, taking into account the singularity zones based on the method of non-uniform covering. In: *IOP Conference on Series: Materials Science and Engineering* 489, 012060 (2019)



# Disk Cam Mechanisms with a Translating Follower Having Double Oblique Flat Faces

Kuan-Lun Hsu<sup>(✉)</sup> and Yen-Nien Chen

National Taiwan University, Taipei 10617, Taiwan (R.O.C.)  
kuanlunhsu@ntu.edu.tw

**Abstract.** The research purposes a disk cam mechanism with a translating double oblique flat-faced follower and demonstrates how to design such a cam mechanism. The modified follower consists of a circular arc portion tangentially connected to two oblique flat-faced portions. Such geometrical arrangements effectively reduce moment arm about the center of gravity and decrease the overturning moment caused by contact forces between the cam and the follower. This design also increases the overturning moment generated by frictions at the cam–follower interface. However, the increment is much smaller than the reduced amount of the overturning moment. Numerical examples are provided to illustrate the simulated results. The obtained results are further compared with those of the disk cam mechanism with a flat-faced follower. The results indicate that the overturning moment of the novel follower will have a 45.86% reduction during the rising period and a 73.2% reduction during the falling period. While the maximum overturning moment caused by frictions for the novel follower is larger by 8.3% during the high dwell period, the increment is much smaller than the reduction of overturning moment caused by contact forces. The application of this follower can greatly be useful in avoiding follower jamming.

**Keywords:** Double oblique flat faces · Disk cam · Overturning moment

## 1 Introduction

Compared with the translating roller follower, the translating flat-faced follower has a constant, zero pressure angle. Thus, the side thrust due to the excessive pressure angles do not occur on a translating flat-faced follower. However, while the rising and falling motion of follower, the contact point moves away from the centerline of follower stem, the eccentric application of force may cause an overturning moment [1–4], which tends to jam the follower in its guides. To obtain a better performance, minimizing the moment arm of the force is proposed to solve the problem effectively. The application of this novel follower has advantage of lowering the lapsing of application of the force from the follower stem.

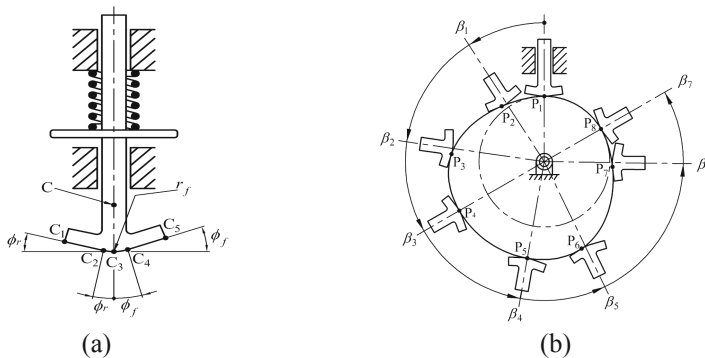
## 2 Disk Cam Mechanisms with a Translating Follower Having Double Oblique Flat Faces

Figure 1(a) shows a novel translating follower having double oblique flat-faced configuration. The follower comprises two oblique flat-faced portions  $C_1C_2$  and  $C_4C_5$ , whose oblique angles are  $\phi_r$  and  $\phi_f$  respectively; a circular arc  $C_2C_3C_4$  with its radius  $r_f$ , which is tangent to two oblique flat-faced portions  $C_1C_2$  and  $C_4C_5$ . The center of circular arc  $C$  is assumed to be located on the centerline of the follower stem.

Figure 1(b) shows a disk cam mechanism with such a translating follower having double oblique flat-faces. The stem centerline of the follower is assumed to pass through the fixed pivot of the cam. The cam is to rotate clockwise, and its profile can be divided into eight segments. The segments  $P_1P_2$ ,  $P_2P_3$  and  $P_3P_4$  are used to produce the rise motion of the follower. The segments  $P_4P_5$  and  $P_8P_1$  are circular arcs, which are used to produce follower dwells. The segments  $P_5P_6$ ,  $P_6P_7$  and  $P_7P_8$  are used to produce the fall motion of the follower. The details of contact condition between the cam and the follower are delivered below.

At first, the cam contacts with follower at  $C_3$  when the follower is at lowest position and on the verge of rising. While the cam rotates from  $0^\circ$  to  $\beta_1$ , the contact point between the cam and the follower lies on circular arc  $C_2C_3$  and moves from  $C_3$  to  $C_2$ , and the point  $C_2$  is the end of contact phase on circular arc  $C_2C_3$ . While the cam rotates from  $\beta_1$  to  $\beta_2$ , the cam contacts the oblique flat-faced portion  $C_1C_2$  of the follower. The contact point occurs on the surface of circular arc again for the cam rotation from  $\beta_2$  to  $\beta_3$  during the high dwell period of the follower motion, the cam contacts the follower at point  $C_3$  consecutively. The contact condition during falling period of the follower motion is similar to the previous one described during rising period, the cam contacts the follower on circular arc  $C_3C_4$  in the angle interval from  $\beta_4$  to  $\beta_5$ , the transition from circular arc contact to oblique flat-faced contact occurs from  $\beta_5$  to  $\beta_6$ , then the cam contacts the follower on circular arc  $C_3C_4$  again from  $\beta_6$  to  $\beta_7$ . Finally, the cam contacts the follower at point  $C_3$  consecutively during the low dwell period of the follower motion.

Based on the statements above, the contact conditions can be classified into three situations, including the circular arc contact, the oblique flat-faced contact with the oblique angles  $\phi_r$  and the oblique flat-faced contact with the oblique angles  $\phi_f$ . When



**Fig. 1.** A disk cam mechanism with such a translating follower having double oblique flat faces

designing such a cam mechanism, the cam profile should be calculated respectively with corresponding contact conditions. Summarily, the contact conditions with respect to cam rotation angle can be expressed as follows:

1. For  $0 < \theta < \beta_1$ ,  $\beta_2 < \theta < \beta_3$ ,  $\beta_3 < \theta < \beta_4$ ,  $\beta_4 < \theta < \beta_5$ ,  $\beta_6 < \theta < \beta_7$  and  $\beta_7 < \theta < 360^\circ$ , the cam contacts follower on circular arc  $C_2C_3C_4$  with radius  $r_f$ .
2. For  $\beta_1 < \theta < \beta_2$ , the cam contacts the follower on the oblique flat-faced contact portion  $C_1C_2$  with a oblique angles  $\phi_r$ .
3. For  $\beta_5 < \theta < \beta_6$ , the cam contacts the follower on the oblique flat-faced contact portion  $C_4C_5$  with a oblique angles  $\phi_f$ .

### 3 The Cam Profile

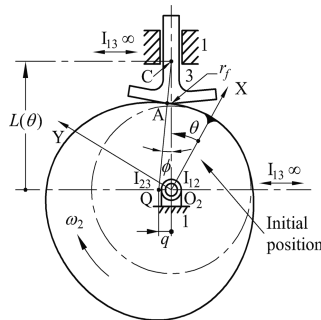
#### 3.1 The Cam Profile for the Circular Arc Contact

Figure 2 shows a cam mechanism with such a follower at a certain phase during the period of the circular arc contact condition. The pressure angle is the angle between the common normal at the contact point and the direction of motion of the follower; it is the angle between lines  $CQ$  and  $CO_2$ . From triangle  $CQO_2$ , the pressure angle  $\phi$  can be expressed as

$$\phi = \tan^{-1} \left[ \frac{q}{L(\theta)} \right] = \tan^{-1} \left[ \frac{V(\theta)}{L(\theta)} \right] \quad (1)$$

As a result, the parametric equations for the cam profile coordinates are

$$\mathbf{O_2A} = \begin{Bmatrix} X(\theta) \\ Y(\theta) \end{Bmatrix} = \begin{Bmatrix} (r_b + r_f + S(\theta)) \cos \theta - r_f \cos (\theta + \phi) \\ (r_b + r_f + S(\theta)) \sin \theta - r_f \sin (\theta + \phi) \end{Bmatrix} \quad (2)$$



**Fig. 2.** Disk cam with a translating follower having double oblique flat faces for the circular arc contact.

### 3.2 The Cam Profile for the Oblique Flat-Faced Contact with an Oblique Angles $\phi_r$

Figure 3 shows the cam mechanism at a certain phase during the period of the oblique flat-faced contact condition with a oblique angles  $\phi_r$ . In this case, the cam contacts the follower on the oblique flat-faced contact portion  $C_1C_2$ . The cam profile can be similarly determined. As the result, the parametric equations for the cam profile coordinates are

$$O_2A = \begin{Bmatrix} X(\theta) \\ Y(\theta) \end{Bmatrix} = \begin{Bmatrix} -q \sin \theta + [(L(\theta) - r_f \sec \phi_r) \cos \phi_r + q \sin \phi_r] \sin \theta \\ q \cos \theta - [(L(\theta) - r_f \sec \phi_r) \cos \phi_r + q \sin \phi_r] \cos \theta \end{Bmatrix} \quad (3)$$

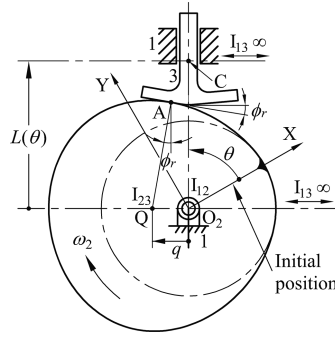


**Fig. 3.** Disk cam with a translating follower having double oblique flat faces for the oblique flat-faced contact with a oblique angles  $\phi_r$ .

### 3.3 The Cam Profile for the Oblique Flat-Faced Contact with an Oblique Angles $\phi_f$

As shown in Fig. 4, at this stage, the cam mechanism contacts the follower on oblique flat-faced portion  $C_4C_5$  with a oblique angles  $\phi_f$  which has a negative value. As a result, the parametric equations for the cam profile coordinates are

$$O_2A = \begin{Bmatrix} X(\theta) \\ Y(\theta) \end{Bmatrix} = \begin{Bmatrix} -q \sin \theta + [(L(\theta) - r_f \sec \phi_f) \cos \phi_f + q \sin \phi_f] \sin \theta \\ q \cos \theta - [(L(\theta) - r_f \sec \phi_f) \cos \phi_f + q \sin \phi_f] \cos \theta \end{Bmatrix} \quad (4)$$

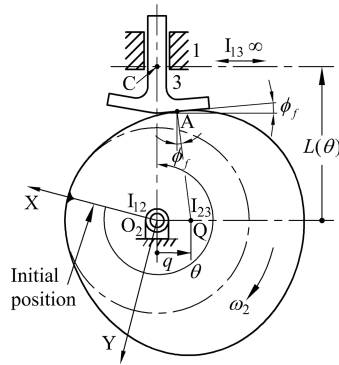


**Fig. 4.** Disk cam with a translating follower having double oblique flat faces for the oblique flat-faced contact with an oblique angles  $\phi_f$ .

## 4 Examples

In this section, the parametric equation will be applied to design such a novel cam mechanism profile coordinates with given design parameters.

**Example 1:** Disk cam mechanism with a translating follower having double oblique flat faces comprises two oblique flat-faced portions, whose oblique angle  $\phi_r$  during rising motion is  $5^\circ$  and oblique angle  $\phi_f$  during falling motion is  $7.5^\circ$  respectively, a circular arc has a radius of 5 mm, and the follower is to rise 20 mm with cycloidal motion while the cam rotates clockwise from  $0^\circ$  to  $120^\circ$ , dwell for the next  $50^\circ$ , return with cycloidal motion for  $130^\circ$  cam rotation and dwell for the remaining  $60^\circ$ . The radius of the base circle is 40 mm, and the angular speed of the cam is 1200 rpm. Since the contact condition includes the circular arc contact, the oblique flat-faced contact with a oblique angles  $\phi_r$  and the oblique flat-faced contact with a oblique angles  $\phi_f$ , when the cam contacts the follower with circular arc contact portions, pressure angle can be calculated by Eq. (1); When the oblique flat-faced contact occurs, pressure angle remains invariant and is equal to oblique angle. Therefore, pressure angle  $\phi$  with respect to cam rotation angle can be drawn in Fig. 5, and the intervals corresponding to each contact conditions can be specifically defined from the diagram. Each value of intervals are listed in Table 1. Recalling the expressions (2), (3) and (4) obtained above, the cam profiles can be calculated by employing corresponding equations, and resulting diagram has been done in Fig. 6.

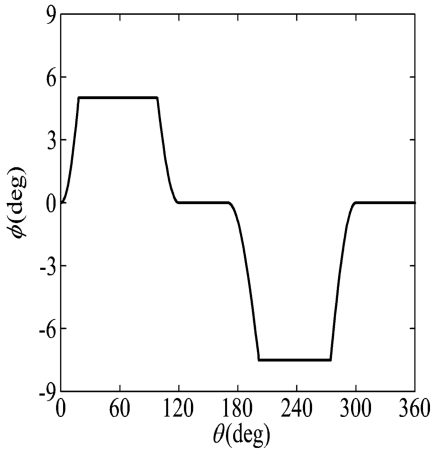


**Fig. 5.** Pressure angle diagram.

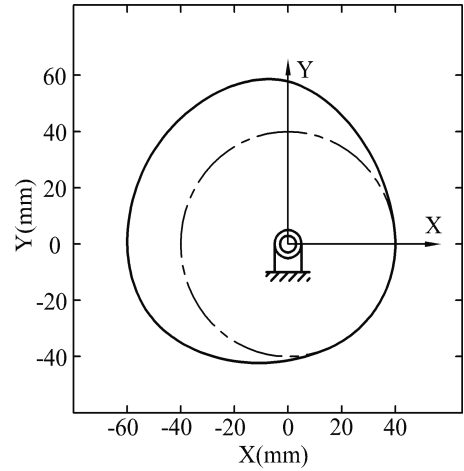


**Fig. 6.** Profile of disk cam with a translating follower having double oblique flat faces.

**Table 1.** Intervals of different contact conditions.

$\theta$	Circular arc contact	Oblique flat-faced contact ( $\phi_r$ )	Oblique flat-faced contact ( $\phi_f$ )
$0^\circ \sim \beta_1$	$0^\circ \sim 18.1^\circ$	N/A	N/A
$\beta_1 \sim \beta_2$	N/A	$18.1^\circ \sim 98.1^\circ$	N/A
$\beta_2 \sim \beta_3$	$98.1^\circ \sim 120^\circ$	N/A	N/A
$\beta_3 \sim \beta_4$	$120^\circ \sim 170^\circ$	N/A	N/A
$\beta_4 \sim \beta_5$	$170^\circ \sim 201.4^\circ$	N/A	N/A
$\beta_5 \sim \beta_6$	N/A	N/A	$201.4^\circ \sim 274.2^\circ$
$\beta_6 \sim \beta_7$	$274.2^\circ \sim 300^\circ$	N/A	N/A
$\beta_7 \sim 360^\circ$	$300^\circ \sim 360^\circ$	N/A	N/A

## 5 Force Analysis

Before the task of determining the overturning moment, it is necessary to calculate the net forces exerted on the follower [5]. Figure 7 shows a cam mechanism and the forces acting on a translating flat-faced follower. In these figures,  $d$  is the guide width or diameter of the follower,  $d_1$  is middle thickness of the follower,  $F_1$  is a force normal to the follower stem,  $F_2$  is another force normal to the follower stem,  $F_N$  is force normal to the cam profile,  $F_t$  is total external load on the follower,  $l_1$  is overhang length of the follower,  $l_2$  is the follower guide length,  $\mu$  is friction coefficient between the follower stem and its guide, and  $\mu_N$  is friction coefficient between the cam and the follower. The total compressed amount of the return spring,  $s$ , consists of its initial compressed amount  $S_p$  and the displacement of the follower and can be expressed as



$$s = S(\theta) + S_p \quad (5)$$

Here, only the static effective weight,  $Mg$ , its inertia, and the spring force are considered to contribute to the total external load  $F_t$  on the follower and can be expressed as

$$F_t = M[g + \ddot{S}(\theta)] + ks \quad (6)$$

where  $k$  is the spring constant of return spring.

An example is given as below. **Example 2:** A flat-faced follower is to rise 20 mm with cycloidal motion while the cam rotates clockwise from  $0^\circ$  to  $120^\circ$ , dwell for the next  $50^\circ$ , return with cycloidal motion for  $130^\circ$  cam rotation and dwell for the remaining  $60^\circ$ . The radius of the base circle is 40 mm, and the angular speed of the cam is 1200 rpm, the link lengths of the mechanism are:  $d_1 = 5$ ,  $d = 15$ ,  $S_p = 5$ ,  $l_1 = 30$ , and the initial value of  $l_2 = 80$ ; all dimensions are in mm. In addition, the following data has been assumed in the numerical computation:  $\mu = 0.1$ ,  $\mu_N = 0.1$ ,  $M = 0.3$  kg, and  $k = 12000$  N/m. The contact forces normal to the follower,  $F_N$ ,  $F_1$  and  $F_2$  with respect to  $\theta$  are shown in Fig. 8.

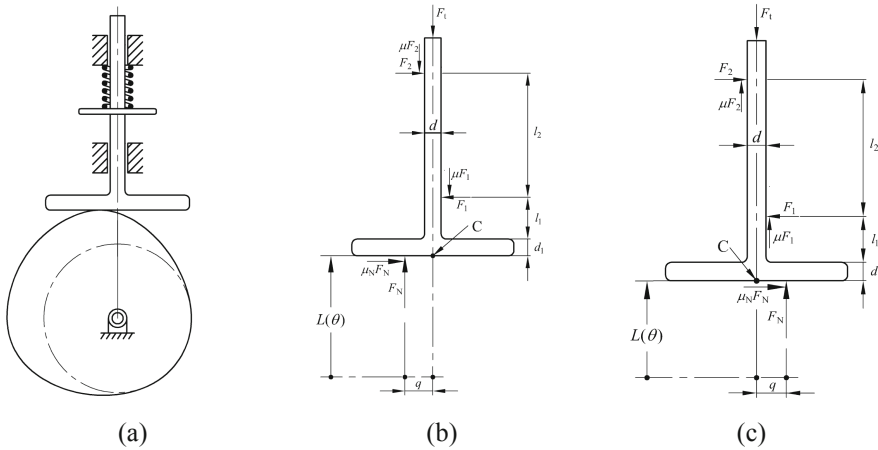


**Fig. 7.** A cam mechanism with a translating flat-faced follower and its free-body diagram.

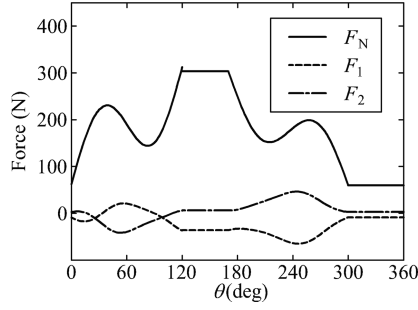


**Fig. 8.** External forces acting on a translating flat-faced follower.

For the novel follower shown in Fig. 9. Since the contact conditions involve the circular arc contact and the oblique flat-faced contact. The equilibrium equations of novel follower should be obtained with corresponding conditions. All notations are identical to those mentioned above. When the cam contacts the follower with the circular arc portion during rising movement, the free-body diagram of the follower is shown in Fig. 9(b), three linear equations of force equilibrium and moment equilibrium about point C for the follower can be written as

$$F_N \sin \varphi + \mu_N F_N \cos \varphi - F_1 + F_2 = 0 \quad (7)$$

$$F_N \cos \varphi - \mu_N F_N \sin \varphi - \mu F_1 - \mu F_2 - F_t = 0 \quad (8)$$

$$\mu_N F_N r_f + F_1 (l_1 + d_1 - r_f) - \mu F_1 \frac{d}{2} - F_2 (l_1 + l_2 + d_1 - r_f) + \mu F_2 \frac{d}{2} = 0 \quad (9)$$

When the oblique flat-faced contact with a oblique angles  $\phi_r$  occurs during rising movement, all external forces acting on the follower are shown in Fig. 9(c). Three linear equations of force equilibrium and moment equilibrium about point G for the follower can be written as

$$F_N \sin \varphi + \mu_N F_N \cos \varphi - F_1 + F_2 = 0 \quad (10)$$

$$F_N \cos \varphi_r - \mu_N F_N \sin \varphi_r - \mu F_1 - \mu F_2 - F_t = 0 \quad (11)$$

$$\begin{aligned} & [(L(\theta) - r_f \sec \varphi_r) \sin \varphi_r - q \cos \varphi_r] F_N + F_1 [l_1 + d_1 + r_f (\sec \varphi_r - 1)] \\ & - \mu F_1 \frac{d}{2} - F_2 [l_1 + l_2 + d_1 + r_f (\sec \varphi_r - 1)] + \mu F_2 \frac{d}{2} = 0 \end{aligned} \quad (12)$$

In reference to Fig. 9(d) and (e), the three external forces,  $F_1$ ,  $F_2$ ,  $F_N$ , are similar with the rising movement during the falling movement. While they only got a little different in the direction of  $F_N$ .

An example is given as below. **Example 3:** A double oblique flat-faced follower comprises two oblique flat-faced portions, whose oblique angle  $\phi_r$  is  $5^\circ$  and oblique angle  $\phi_f$  is  $7.5^\circ$  respectively; the radius of circular arc is 5 mm, and rest requirements are identical to those mentioned in Example 1. The contact forces normal to the follower,  $F_N$ ,  $F_1$  and  $F_2$  with respect to  $\theta$  are shown in Fig. 10.

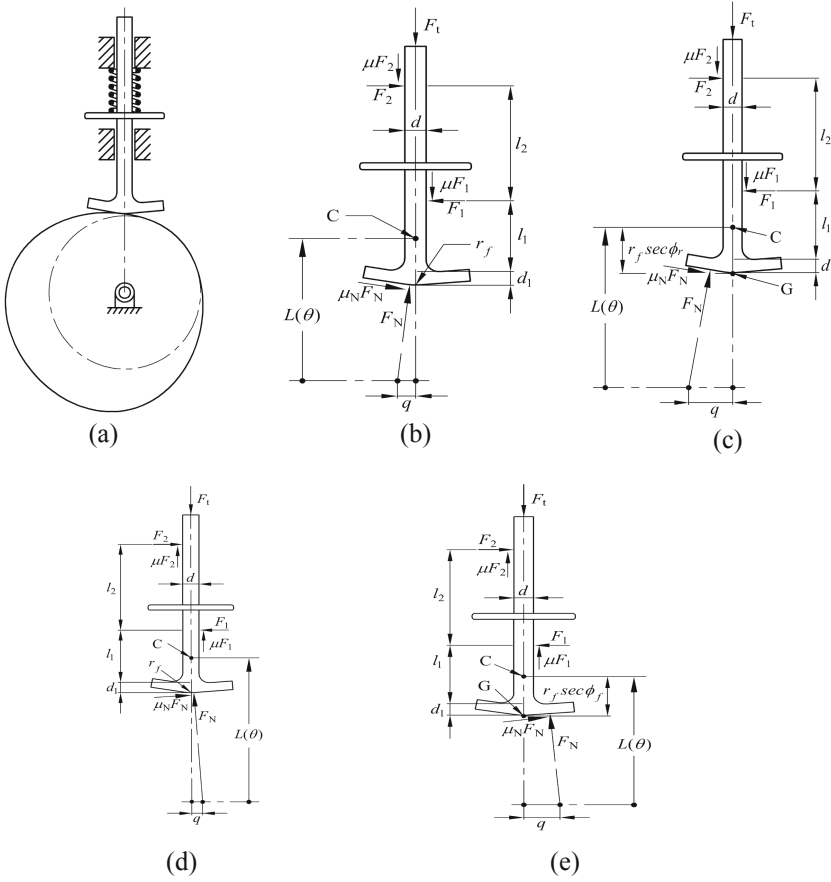


**Fig. 9.** A cam mechanism with a novel follower and its free-body diagram.

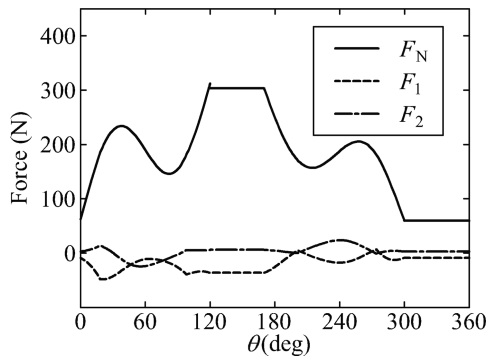


**Fig. 10.** External forces acting on a novel follower.

## 6 Overturning Moment Analysis

The overturning moment is the moment of energy which is produced by forces without passing through the center of gravity. The phenomenon may make follower lodged in its guide and damage follower rigidity. Since total external load  $F_t$  on the follower acts through the center of gravity, there is no effective moment about the center of gravity, net effects of the moments acting on the follower can be evaluated properly in this section. Suppose that the follower is made of homogeneous material and has uniform thickness, the center of gravity is equivalent to the centroid. Thus, the centroid of follower can be located in given coordinate system, and the distance from the center of gravity to the follower bottom  $f$  can be exactly described. This geometric size may help to measure effective moment arm perpendicular to the direction of the force.

Let us now considers the moments acting on the translating flat-faced follower shown in Fig. 11, the magnitude of the forces  $\mu F_1$  and  $\mu F_2$  are relatively small so that they can be ignored rationally. The major components of overturning moment about the center of gravity  $C_{c.g}$  are caused by the forces  $F_N$  and  $\mu_N F_N$ , and the magnitude of resulting moments  $M_{F_N}$  and  $M_{\mu_N F_N}$  can be, respectively, written as

$$M_{F_N} = -qF_N \quad (13)$$

$$M_{\mu_N F_N} = f\mu_N F_N \quad (14)$$

The configuration of the novel follower consists of double oblique flat-faced portions contacting with the cam profile, the geometrical arrangements effectively reduces the moment arm about the center of gravity to decrease the overturning moment, the influence of overturning moment can be conferred in similar procedures as discussed above. With reference to Fig. 12(a), when the cam contacts the follower with the circular arc portion, the magnitude of moments  $M_{F_N}$  and  $M_{\mu_N F_N}$ , can be, respectively, written as

$$M_{F_N} = (f - r_f)\sin \varphi F_N \quad (15)$$

$$M_{\mu_N F_N} = [f + r_f(\sec \varphi - 1)]\cos \varphi \mu_N F_N \quad (16)$$

Similarly, as shown in Fig. 12(b) and (c), when the cam contacts the follower with the oblique flat-faced portions, the magnitude of moments  $M_{F_N}$  and  $M_{\mu_N F_N}$  can be, respectively, expressed as

During rising movement,

$$M_{F_N} = \{[f + L(\theta) - r_f]\sin \varphi_r - q(\theta) \cos \varphi_r\}F_N \quad (17)$$

$$M_{\mu_N F_N} = [f + r_f(\sec \varphi_r - 1)]\cos \varphi \mu_N F_N \quad (18)$$

During falling movement,

$$M_{F_N} = \{[f + L(\theta) - r_f] \sin \varphi_f - q(\theta) \cos \varphi_f\} F_N \quad (19)$$

$$M_{\mu_N F_N} = [f + r_f (\sec \varphi_f - 1)] \cos \varphi_f \mu_N F_N. \quad (20)$$

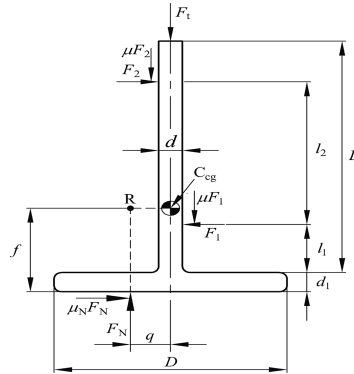


**Fig. 11.** Overturning moments acting on a translating flat-faced follower.

## 7 The Reduction on the Overturning Moment

The following two examples illustrate how the novel follower affects the overturning moments. For comparison, the third example has a common flat-faced follower whereas the fourth example has a novel follower.

**Example 4:** Atranslating follower having flat face is driven by a disk cam to meet the follower motion requirements as specified in example 2. The total length of the follower L is 110 mm, the total width of the follower D is 30 mm. Then, the distance from the center of gravity to follower bottom f would be 44.23 mm, and all other design data are identical with those specified in example 1.

**Example 5:** A translating follower having double oblique flat faces is driven by a disk cam to meet the same requirements. All other design data are assumed to be identical with those specified in example 4, then the distance from the center of gravity to follower bottom  $f$  would be 48.001 mm.

Jamming effect is caused by overturning moment generated from forces  $F_N$  and  $\mu_N F_N$ . Consequently, we shall plot the moments  $M_{F_N}$  and  $M_{\mu_N F_N}$  with respect to  $\theta$  of the flat-faced type and the double oblique flat-faced type respectively in Figs. 13 and 14. The overturning moments of the flat-faced follower are shown by the dashed lines, and that of the novel follower are shown by the solid lines.

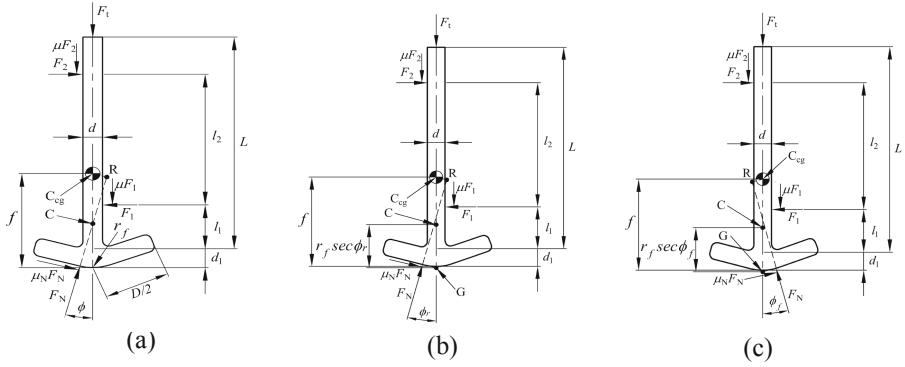


**Fig. 12.** Overturning moments on a novel follower.

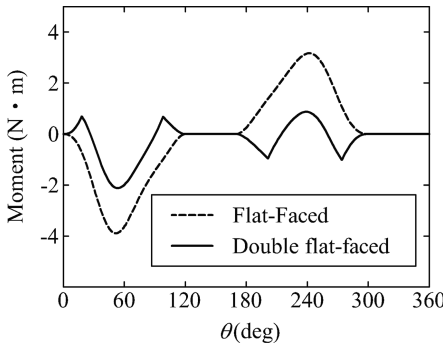


**Fig. 13.** Overturning moments  $M_{FN}$  of two different cam mechanisms.

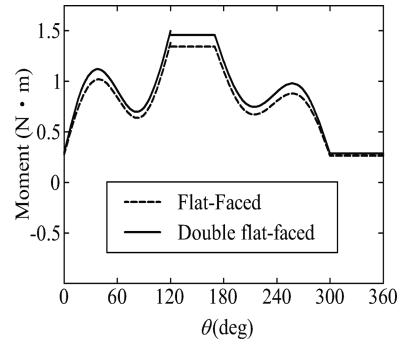


**Fig. 14.** Overturning moments  $M_{\mu FN}$  of two different cam mechanisms.

## 8 Discussion

As expected, the application of the novel follower greatly reduces the overturning moment on both the rising and the falling motions of the follower. For example, during the rising period, the extreme values of flat-faced type and novel type have a ratio of  $-2.108(\text{N}\cdot\text{m})/3.893(\text{N}\cdot\text{m}) = 0.5413$ , which means a 45.86% reduction. During the falling period, their extreme values have a ratio of  $0.8478(\text{N}\cdot\text{m})/3.1698(\text{N}\cdot\text{m}) = 0.2679$ , a 73.2% reduction. The simulation values of overturning moment for the yields agree well. The overturning moment of the novel follower caused by force  $\mu_N F_N$  is higher than that of the flat-faced follower. However, the results appear to influence the jamming effect slightly.

## 9 Conclusions

The research purposes a disk cam mechanism with a translating double oblique flat-faced follower to decrease efficient moment arm about the center of gravity of follower, and the reduction of overturning moment has been investigated, the simulation results are consistent with those stated in earlier section. The novel geometrical configuration of the follower may be useful in avoiding jamming effect.

**Acknowledgments.** The first author would like to express his gratitude to Prof. Dr. Long-Long Wu. His illuminating instruction makes this paper possible. In addition, the first author is grateful for the substantial support of National Taiwan University. Most importantly, the Young Scholar Fellowship Program of Ministry of Science and Technology of Taiwan (108-2636-E-002-012) encourages the first author to fearlessly devote to his research. All supports made this research work possible.

## References

1. Rothbart, H.A.: Cams: Design, Dynamics, and Accuracy, pp. 64–65. John Wiley & Sons, New York (1956)
2. Norton, R.L.: Cam Design and Manufacturing Handbook, Industrial, New York, pp. 161–162 (2002)
3. Soni, H.: Mechanism Synthesis and Analysis, pp. 227–229. Krieger Pub Co. (1974)
4. Chen, F.Y.: Mechanics and Design of Cam Mechanisms, pp. 194–195. Pergamon Press, New York (1982)
5. Jensen, P.W.: Cam Design and Manufacture, 2nd edn, pp. 146–150. Marcel Dekker, New York (1987)
6. Wu, L.I.: Calculating conjugate cam profiles by vector equations. Proc. Inst. Mech. Eng.—Part C, J. Mech. Eng. Sci. **217**(10), 1117–1123 (2003)



# Computationally Efficient Cable Force Calculation Outside the Wrench-Feasible Workspace

Roland Boumann<sup>(✉)</sup> and Tobias Bruckmann

Universität Duisburg-Essen, Forsthausweg 2, 47057 Duisburg, Germany  
{roland.boumann,tobias.bruckmann}@uni-due.de

**Abstract.** A cable-driven parallel robot (CDPR) can get outside of its wrench-feasible workspace in special situations, e.g. haptics applications or when a cable break occurs. In this case, the standard approaches for the computation of set forces for the cable robot are likely to fail. This calls out for methods to obtain appropriate cable forces for a desired wrench. In this paper, a novel method to calculate cable forces for a cable-driven parallel robot outside its wrench-feasible workspace is presented. Force distributions are obtained that generate wrenches close to the desired ones, while taking continuity in account. The method is based on geometrical analysis in the space of cable forces, and aims at simple implementation and numerical efficiency. Optimization algorithms are not required, indicating real-time usability. The method is tested in simulation, using a simplified dynamic robot model and a cable break scenario.

**Keywords:** Cable-driven parallel robot · Cable force calculation · Cable failure · Workspace · Puncture method · Force distribution

## 1 Introduction

Currently, multiple research groups focus on the development of cable-driven parallel robots (CDPR) [1, 2]. A CDPR uses the kinematic structure of a Stewart-Gough platform, but replaces the linear actuators by cables that are coiled on computerized winches.

In contrast to most conventional parallel kinematics, this allows for enormous workspaces as winches can coil virtually infinite cable lengths: At least, some dozen meters of cable length are easy to realize.

On the other hand, cables only introduce unilateral constraints as they can only pull, but never push. As a consequence, purely kinematic models are not sufficient to determine the workspace. Instead, typical workspace criteria for CDPR involve the cable tensions. Against an application background, a convenient definition is the so-called wrench-feasible workspace ( $\mathcal{WFW}$ ) which includes all end-effector poses where for a given range of end-effector wrenches  $\mathbf{w}$ , a suitable set of cable forces  $\mathbf{f}$  can be found.



Typically, all regularly planned maneuvers will consider the  $\mathcal{WFW}$  and accordingly, the cable force computation methods known from literature [3–6] will work. Generally, these algorithms try to find a set of cable forces that both fulfill the force equilibrium of the end-effector (see Sect. 2) and do not exceed a predefined minimum or maximum cable force, respectively. To ensure continuity of the cable forces, which is required when the set cable forces are computed e.g. for control purposes, the problem can be formulated as a constrained optimization problem and solved by Quadratic Programming [6].

In special situations, however, the applied or required values for  $\mathbf{w}$  might lead to a situation where no  $\mathbf{f}$  can be found. Examples are e.g. haptics simulations where interaction with a human might lead to undesired contact forces, or – intuitively more critical – situations where a cable break occurs.

Cable breaks are extremely rare under standard operational conditions. Norms such as the European DIN EN 12385 ensure a reliable operation of cable-driven systems and countless implementations of cables e.g. in elevators or cable cars prove the reliability of cables that are installed, used and maintained according to those norms. However, accidents like the crash of the SkyCam – a CDPR designed e.g. to move a TV camera above a sports stadium – which collapsed on December 30, 2011, during a football game, demonstrate how dramatic a failure in the cable system might be [7]. In case of a cable break, the remaining CDPR is still able to react and to apply forces onto the end-effector, but the end-effector might be abruptly out of the  $\mathcal{WFW}$  of the remaining CDPR. Therefore, common cable force computation methods will fail [8].

Therefore, it is reasonable to develop methods that allow the CDPR to react and to guide the end-effector back to its  $\mathcal{WFW}$  where it can be stopped and rescued in a controlled manner.

In [9], a force computation method is presented which is able to identify a suitable  $\mathbf{f}$  even outside the  $\mathcal{WFW}$  by adding a so-called slack variable to the constraints. However, the resulting optimization problem might lead to computation time issues, especially in the context of a realtime control system.

In this paper, a different approach is presented which is mainly inspired by geometrical analysis in the space of the cable forces. The remaining paper is structured as follows: In Sect. 2, a basic modeling of CDPR is introduced. Section 3 introduces the new algorithm capable for force calculations outside the  $\mathcal{WFW}$ . In Sect. 4, the new approach is tested and evaluated. Section 5 summarizes the conclusions and the future work.

## 2 Modeling and Cable-Robot Basics

The robot, as described in [10], possesses  $m$  cables and  $n$  degrees-of-freedom.  $r = m - n$  is the redundancy of the platform. The inertial coordinate-system is  $\uparrow \mathcal{B}$ , while the fixed coordinate-system on the platform is  $\uparrow \mathcal{P}$ . The position vector  ${}^B \mathbf{r}_P$  and the orientation  $\Phi$  of the end effector are merged into the posture of the platform in coordinates of the inertial frame  ${}^B \mathbf{x}_P = [{}^B \mathbf{r}_P^T \Phi^T]^T$ . The rotation matrix  ${}^B \mathbf{R}_P$  describes the orientation with respect to the inertial

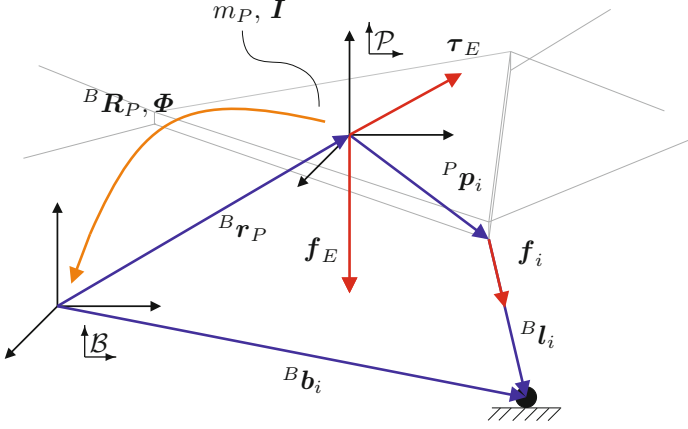


Fig. 1. Cable-robot model parameters

coordinate-system in the means of roll-pitch-yaw angles. The modeling of pulleys is neglected in the following under assumption of a point-shaped guidance of the cable. The cable vectors  ${}^B l_i$  as shown in Fig. 1 can be obtained by the inverse kinematic:

$${}^B l_i = {}^B b_i - \underbrace{({}^B r_P + {}^B R_P {}^P p_i)}_{{}^B p_{B_i}}, \quad 1 \leq i \leq m \quad (1)$$

All cable forces  $f_i$  in direction of the cable  $\nu_i$  are merged into the cable force vector  $\mathbf{f} \in \mathbb{R}^{m \times 1}$ . The force  $\mathbf{f}_i$  exerted on the platform by the  $i^{\text{th}}$  cable force is

$$\mathbf{f}_i = f_i \cdot \frac{\mathbf{l}_i}{\|\mathbf{l}_i\|_2} = f_i \cdot \nu_i, \quad 1 \leq i \leq m. \quad (2)$$

All forces and torques acting on the end effector impressed by the cables are  $-\mathbf{w}$ , wherein  $\mathbf{A}^T$  is the structure matrix of the robot.

$$-\mathbf{w} = \begin{bmatrix} \mathbf{f}_p \\ \tau_p \end{bmatrix} = \begin{bmatrix} \nu_1 & \dots & \nu_m \\ \mathbf{p}_1 \times \nu_1 & \dots & \mathbf{p}_m \times \nu_m \end{bmatrix} \begin{bmatrix} f_1 \\ \vdots \\ f_m \end{bmatrix} = \mathbf{A}^T \mathbf{f}. \quad (3)$$

Setting up a simplified model for force equilibrium (Assumptions see Sect. 4) and Newton-Euler equations, under the assumption that the center of gravity is equal to the origin of the end effectors coordinate system, it holds that

$$\underbrace{\begin{bmatrix} m_p \mathbf{E} & \mathbf{0} \\ \mathbf{0} & I \mathbf{K} \end{bmatrix}}_{\mathbf{M}_p(x_p)} \underbrace{\begin{bmatrix} {}^B \ddot{\mathbf{r}}_P \\ \ddot{\boldsymbol{\Phi}} \end{bmatrix}}_{\ddot{\mathbf{x}}_p} + \underbrace{\begin{bmatrix} \mathbf{0} \\ I(\dot{\mathbf{K}}\dot{\boldsymbol{\Phi}}) + (\mathbf{K}\dot{\boldsymbol{\Phi}}) \times (I(\mathbf{K}\dot{\boldsymbol{\Phi}})) \end{bmatrix}}_{\mathbf{w}_C(x_p, \dot{x}_p)} - \underbrace{\begin{bmatrix} \mathbf{f}_E \\ \tau_E \end{bmatrix}}_{\mathbf{w}_E} = \mathbf{A}^T \mathbf{f}. \quad (4)$$

-w

In force equilibrium the cable forces generate exactly the desired wrench  $-\mathbf{w}$ . The first and second time derivative of the end effector pose  $\mathbf{x}_p$  are  $\dot{\mathbf{x}}_p$  and  $\ddot{\mathbf{x}}_p$ , respectively. The mass matrix of the platform  $\mathbf{M}_p$  consist of the platform mass  $m_p$  and the inertia tensor  $\mathbf{I}$ . The inertia tensor depends on the orientation of the platform and needs to be expressed in the inertial system  $\mathcal{B}$ . From the kinematic Kardan equations, the matrix  $\mathbf{K}$  and its time derivative can be obtained [11].  $\mathbf{E}$  is an  $3 \times 3$  identity matrix. Vector  $\mathbf{w}_E$  contains the external forces and torques acting on the platform, while  $\mathbf{w}_C$  is the vector of Coriolis and centrifugal forces and torques.

## 2.1 Wire Force Distribution

The cable forces are limited by a minimum force  $f_{\min}$  and a maximum force  $f_{\max}$  to avoid cable sagging on one hand and to limit the maximum motor torque on the other hand. Solving Eq. 4 with respect to the cable force limits is a known problem in the field of cable-robotics. A suitable way to determine force distributions is the geometrical interpretation of the problem [3]. The force limits form a  $m$ -dimensional hypercube  $\mathcal{C} \subset \mathbb{R}^m$ , provided that the hyperplanes of the cube are defined by  $f_i = f_{\min} \vee f_i = f_{\max}, 1 \leq i \leq m$ . With  $n$  equations and  $m$  unknown variables, Eq. 4 is in general an under-determined linear system of equations. Therefore the dimension of the solution space is equal to the redundancy  $r$  of the robot. Solving Eq. 4 for  $\mathbf{f}$  it holds that:

$$\mathbf{f} = \underbrace{-\mathbf{A}^{+T}\mathbf{w}}_{\mathbf{f}_0} + \mathbf{H}\boldsymbol{\lambda}. \quad (5)$$

The force  $\mathbf{f}_0$  is a projection of the desired wrench onto the solution space.  $\boldsymbol{\lambda} \in \mathbb{R}^r$  is a vector of multipliers.  $\mathbf{A}^{+T}$  denotes the Moore-Penrose-Pseudo-Inverse of the structure matrix. The null space or kernel  $\mathbf{H} \in \mathbb{R}^{m \times r}$  of the structure matrix  $\mathbf{A}^T$  is defined as

$$\mathbf{H} = [\mathbf{h}_1, \dots, \mathbf{h}_r] \quad (6)$$

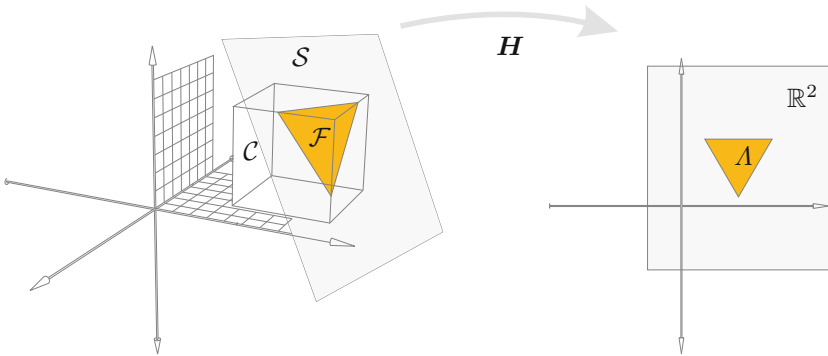


**Fig. 2.** Visualization of Cube, Solution Space, Manifold and Map for  $m = 3$  and  $r = 2$

with the vectors  $\mathbf{h}_i$  solving the equation:

$$\mathbf{A}^T \mathbf{h}_k = 0, \quad 1 \leq k \leq r. \quad (7)$$

The  $r$ -dimensional solution space  $\mathcal{S} \subset \mathbb{R}^m$  contains all solutions of Eq. 4 and is defined by the columns of the kernel  $\mathbf{H}$ . There are feasible wire force distributions which lie inside the force limits, if an intersection of the hypercube and the solution space exists. In this case and as shown in Fig. 2, the manifold

$$\mathcal{F} = \mathcal{C} \cap \mathcal{S} \neq \emptyset \quad (8)$$

contains all possible solutions.  $\mathcal{F}$  forms a convex polyhedron and the pose is called wrench-feasible, if  $\mathcal{F}$  is nonempty for the given wrench [3]. All multipliers  $\boldsymbol{\lambda}$  leading to wrench-feasible solutions form a polyhedron  $\Lambda$ , using the kernel  $\mathbf{H}$  as a transformation between  $\mathbb{R}^r$  and  $\mathbb{R}^m$  as shown in Fig. 3. To solve the problem in Eq. 5 with respect to the given force limits, one has to consider

$$\begin{aligned} \mathbf{f}_{\min} &\leq \mathbf{f}_0 + \mathbf{H}\boldsymbol{\lambda} \leq \mathbf{f}_{\max} \\ \Leftrightarrow \mathbf{f}_{\min} - \mathbf{f}_0 &\leq \mathbf{H}\boldsymbol{\lambda} \leq \mathbf{f}_{\max} - \mathbf{f}_0. \end{aligned} \quad (9)$$

To interpret this equation, the kernel  $\mathbf{H}$  forms a basis for the solution space  $\mathcal{S}$ . If a feasible wire-force-distribution is existing,  $\boldsymbol{\lambda} \in \Lambda$  can be used for scaling the force-distribution and thus the inner tension of the system within the limits. Several methods for computing force-distributions exist, which differ in real-time capability, force level, workspace coverage, continuity, maximum possible redundancy and computation time [6]. Approaches include e.g. calculating the forces as an optimization-problem [4] or applying the barycentric method [5].

### 3 Calculation Algorithm

There are several methods existing to compute feasible cable-force distributions. Still and as given in the introduction, scenarios with a wrench that is not feasible are possible. This is eager to occur when the end effector is moved outside of the static workspace, e.g. using a haptic device or suffering from a cable break. A solution of Eq. 4 cannot be found in that case and the given methods fail to operate. In the following, approaches to generate a reasonable force distributions are given.

#### 3.1 Optimizing

A method to deal with the described circumstance is proposed in [9]. In terms of finding an appropriate wire force distribution, the constraints of minimum and maximum cable forces cannot be changed. To relax Eq. 4, a so called slack variable  $\mathbf{s}$  is added to the equation. A way to solve the resulting problem via quadratic programming is also proposed in [9]. The optimization problem is described as

$$\begin{aligned}
& \text{minimize} && \mathbf{s}^T \mathbf{D}_1 \mathbf{s} + (\mathbf{f} - \tilde{\mathbf{f}})^T \mathbf{D}_2 (\mathbf{f} - \tilde{\mathbf{f}}) \\
& \text{with} && \mathbf{A}^T \mathbf{f} + \mathbf{w} + \mathbf{s} = 0 \\
& && \mathbf{f}_{\min} \leq \mathbf{f} \leq \mathbf{f}_{\max}.
\end{aligned} \tag{10}$$

The diagonal weighting matrices  $\mathbf{D}_1$  and  $\mathbf{D}_2$  can be used to adjust the solution. The solution will more likely follow the target forces  $\tilde{\mathbf{f}}$  by choosing  $\mathbf{D}_1 < \mathbf{D}_2$ . Otherwise the solution forces will more likely generate the desired wrench. The solution can be adjusted e.g. for minimum power or maximum stiffness by making a proper choice of the target forces. Though a solution of the problem can be carried out computationally efficient as shown in [9], the iterative characteristic might be a problem within industrial real time applications. Thus a simple method with a defined and preferably low number of calculation steps can be advisable.

### 3.2 Nearest-Corner-Method

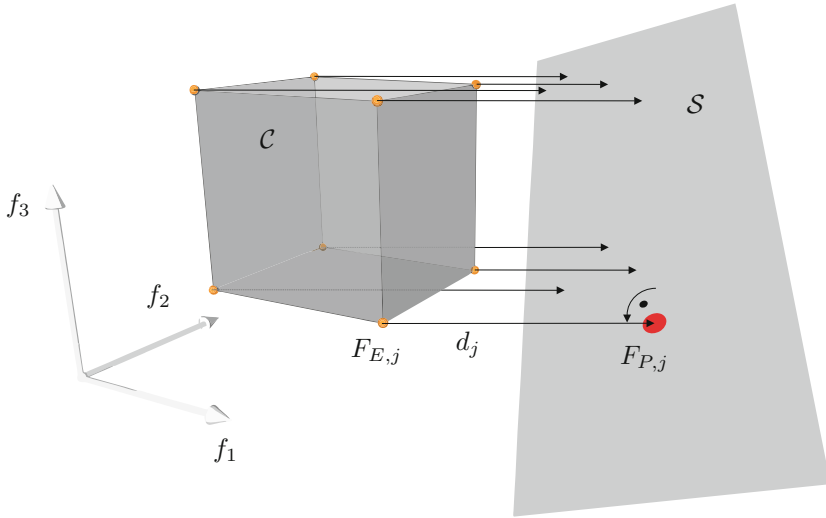


**Fig. 3.** Projection of corners on solution space for an empty set of  $\mathcal{F}$ , example for  $m = 3, r = 2$

An optimizing algorithm as explained beforehand is generally applicable. However, its usability in a realtime control system might be a problem as such optimization schemes usually employ iterative solvers. Within this paper, a different and simplified approach is proposed. It is inspired by geometrical analysis, using the orthogonal coordinate system as introduced in Sect. 2.1 to represent the space of the cable forces  $\mathbf{f}$ . The following introduction refers to  $r = 1$  and

$r = 2$ ; the applicability for higher redundancies  $r$  is currently being investigated. Note, the corners of  $\mathcal{C}$  are denoted as  $\mathbf{F}_{E,j}, j = 1, \dots, 2^m$ .

Assume a CDPR within its  $\mathcal{WFW}$ . In this case, a set of cable force solutions  $\mathcal{F}$  exists and a continuous solution along a trajectory can be found by the methods listed in Sect. 2.1. However, if the CDPR is outside its  $\mathcal{WFW}$ , these methods will fail. Still, the hypercube  $\mathcal{C}$  and the solution space  $\mathcal{S}$  exist, but as there is no intersection,  $\mathcal{F}$  is empty.

Nonetheless, using Euclidean norm, there is at least one corner of  $\mathcal{C}$  which has the closest distance to the hyper straight line (for  $r = 1$ ) or hyperplane (for  $r = 2$ ) representing  $\mathcal{S}$ , where the orthogonal projections of  $\mathbf{F}_{E,j}$  onto  $\mathcal{S}$  are denoted  $\mathbf{F}_{P,j}$ .

This  $\mathbf{f}$  is not a solution to Eq. 5, but in terms of the motion inducing parts of  $\mathbf{f}$ , i.e.  $\mathbf{f}_0$ , it is an approximation and compliant with the force boundaries! Therefore, it can be used e.g. for control purposes.

Note, that this closest corner might switch instantaneously depending on the motion of the system. To ensure continuity, instead of only using the closest corner, all corners are considered and weighted by the distance to  $\mathcal{S}$  using Euclidean norm where the distances between the corners  $\mathbf{F}_{E,j}$  and the projected forces onto  $\mathcal{S}$ ,  $\mathbf{F}_{P,j}$ , are given by

$$d_j = \|\mathbf{F}_{P,j} - \mathbf{F}_{E,j}\|, \quad 1 \leq j \leq 2^m. \quad (11)$$

The summarized distance  $L = \sum_{j=1}^{2^m} d_j$  is needed to obtain proper weighting  $g_j$  for each corner of  $\mathcal{C}$ .

$$g_j = \left(\frac{L}{d_j}\right)^p \quad (12)$$

Introducing higher exponential weights  $p$ , the corner that is closest to  $\mathcal{S}$  will dominate all others the closer it gets. If the  $\mathcal{S}$  and  $\mathcal{C}$  are about to intersect, i.e. in case a corner is just about to be a valid force distribution according to Eq. 5, this ensures continuous transition between force distributions within and outside the  $\mathcal{WFW}$ . The sum of all weights is  $G = \sum_{j=1}^{2^m} g_j$ . The resulting force distribution is

$$\mathbf{f} = \sum_{j=1}^{2^m} (\mathbf{F}_{E,j} \frac{g_j}{G}), \quad 1 \leq j \leq 2^m. \quad (13)$$

Generally, it is always tried beforehand to find a feasible cable force distribution according to Sect. 2.1. If those algorithms fail to determine a feasible solution, the proposed method is used, and a cable force distribution with minimal distance to the solution space  $\mathcal{S}$  will be found.

## 4 Simulation and Results

An example of a cable-robot rescue scenario after a cable break is taken into account for testing the proposed method. The robot model and the scenario are detailed in [8].

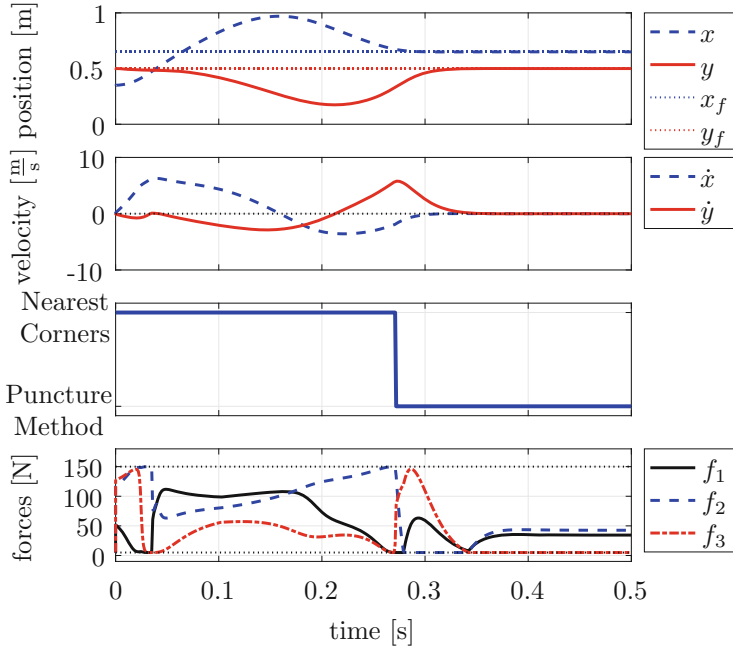


**Fig. 4.** Position, velocity, switch between both methods and forces in simulation with  $p = 8$

A two-dimensional planar and dynamic model with three cables is set up. The robot platform is described as a point mass with  $m_p = 1$  kg and is subject to gravity in negative direction of the  $y$ -axis. Thus the redundancy is  $r = 3 - 2 = 1$ . The pulley positions  $\mathbf{B}$  are shown in Fig. 6. Numbering of the cables is clockwise, beginning with cable 1 at the bottom left. The minimum force is  $f_{\min} = 5$  N and the maximum force is  $f_{\max} = 150$  N. The simulation is carried out with a fixed time step of  $\Delta t = 1$  ms and a numerical integration using the Euler-Cromer method. Each time step, the actual platform acceleration is computed using the current wire and gravitational forces. The cables are assumed to be massless and cannot sag. The modeling of friction, motors, gears and disturbances is neglected.

At the start of the simulation, the platform is placed with zero velocity at  $\mathbf{r}_p = [0.35 \ 0.5]^T$  m, which is outside of the static workspace of the robot model [8]. A situation like this could occur through a cable break. A goal position inside the workspace is defined at  $\mathbf{r}_f = [0.65 \ 0.5]^T$  m. To generate a desired wrench, an attractive potential field, as introduced in [12], is placed with its origin at the goal position, which could be e.g. a rescue position after a cable break. The resulting attractive force as the gradient of the fields potential  $\mathbf{U}$  can be described as:

$$\mathbf{F}_{\text{att}}(\mathbf{r}_p) = \nabla U_{\text{att}}(\mathbf{r}_p) = \begin{cases} -\zeta(\mathbf{r}_p - \mathbf{r}_f) & : \rho_f(\mathbf{r}_p) \leq \rho_0 \\ -\frac{\rho_0 \zeta(\mathbf{r}_p - \mathbf{r}_f)}{\rho_f(\mathbf{r}_p)} & : \rho_f(\mathbf{r}_p) > \rho_0. \end{cases} \quad (14)$$

At distance  $\rho_0 = 0.2$  m the field is shifted between a quadratic and a conic potential.  $\rho_f(\mathbf{r}_p)$  is the Euclidean distance between goal and actual position. The scaling parameter  $\zeta = 400$  can be used to adjust the field strength. Also a virtual damping, proportional to the robots velocity with factor  $D_P = 110$  Ns/m, is applied. The resulting wrench including the external forces is

$$\mathbf{w} = [\mathbf{F}_E] - [\mathbf{F}_{\text{att}}(\mathbf{r}_p) + \mathbf{F}_{D_P}(\dot{\mathbf{r}}_p)]. \quad (15)$$

In general, this desired wrench might be infeasible within the given cable force limits. Note that repulsive fields can be used to avoid collision. However the approach shown here will not guarantee collision free trajectories, as even infinite repulsive forces do not lead to forces beyond the force limits.

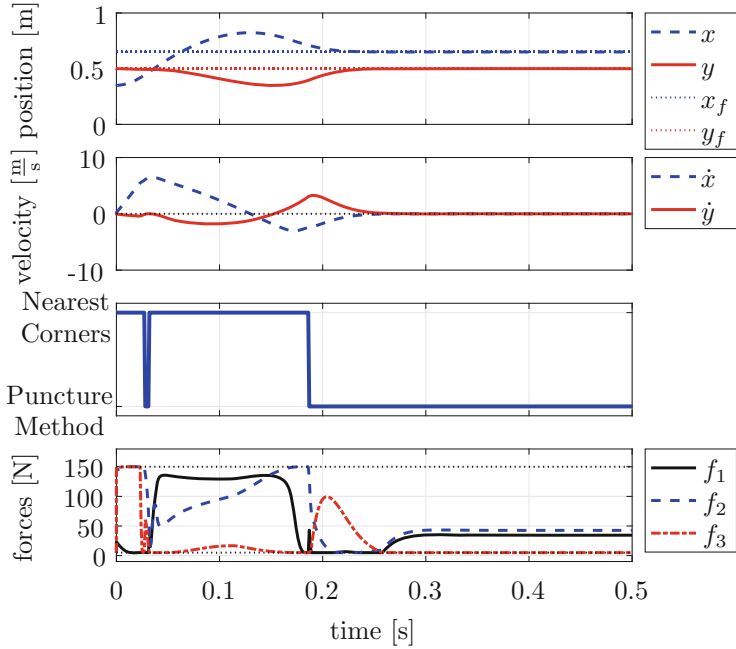


**Fig. 5.** Position, velocity, switch between both methods and forces in simulation with  $p = 20$

As a first method to check for a feasible solution of Eq. 4, the puncture method [13] is used, just as described in Sect. 2. If a feasible solution is found, these cable forces are set in the next simulation step. If the method fails to find



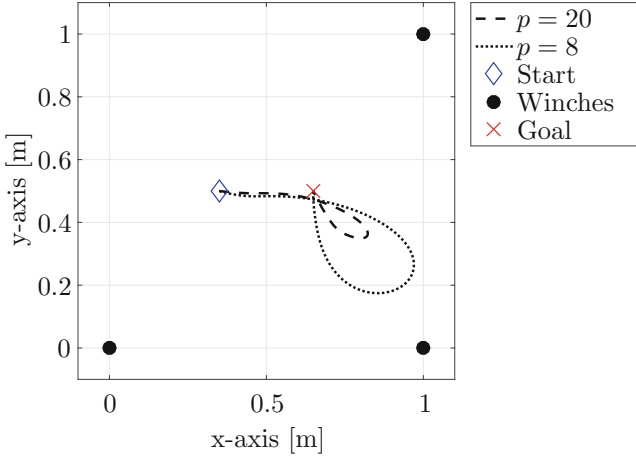


**Fig. 6.** Movement of end effector with different exponential weights  $p$ , numbering of winches clockwise, starting at bottom left

a solution, the nearest corner method from Sect. 3.2 is applied to find forces which result in a wrench close to the desired one. Figure 4 shows the results of a simulation with exponential weights  $p = 8$ . It can be observed that the robot is successfully guided into the goal position after 0.3 s. At 0.28 s, a feasible solution can be found with the puncture method and the algorithm switches. In this example, the forces are continuous at the moment the solution space intersects the hypercube.

Continuity in general cases can be assumed due to continuous motion of the hyperplane for continuous platform motions and a fixed hypercube, but formally needs to be proven in future work.

In Fig. 5, exponential weights of  $p = 20$  are used. The resulting forces show that the nearest corner gets more dominance in the solution, because of the weighting in Eq. 13. Thus the forces tend to get closer to the cable force limits. Therefore, the platform follows the desired wrench more accurately and reaches the goal position in shorter time at about 0.25 s with less deviation from the goal point throughout the trajectory.

This is also shown in Fig. 6, which compares the platform movements with both exponential weights  $p$ . It can be observed, that with a higher exponential weights, the platform overshoots way less and finds the way into the goal more directly.

## 5 Conclusion and Outlook

A new and simplified method for calculation of force distributions of CDPR outside of the  $\mathcal{WFW}$  was introduced. Tests for redundancies  $r = 1$  and  $r = 2$  have been made, and an example with  $r = 1$  was discussed. Based on geometrical

calculations in the cable force space, the algorithm promises to have superior realtime suitability because of its non-iterative behavior. Noteworthy, the computation time of this method is highly dependent on the method for checking feasible cable forces. The puncture method used in this paper does not employ full workspace coverage [13]. Therefore a combination with a different method is advisable. Suitable realtime methods are e.g. the barycentric method or the improved closed form [6]. Also using an active set method with proven maximum computation time would be possible [14].

Future work also includes tests with higher redundancies and a higher number of cables as well as investigation of numerical efficiency in comparison to existing approaches. Moreover, the method can be tested for applicability in more complex simulations. Finally, it needs to be tested on a realtime system.

**Acknowledgment.** This research received funding from the EFRE.NRW (2014–2020) Joint Research Funding Program of the European Union (EFRE) and the Ministry of Economy, Energy, Industry, and Handicrafts of the German Federal State of North Rhine-Westphalia (NRW) under grant agreement EFRE-0800365 (ML-1-1-019B, LEAN)]. Funded by the Federal Ministry for Economic Affairs and Energy based on a resolution of the German Bundestag. This funding is within the project “Entwicklung von Seilrobotern für die Erstellung von Kalksandstein-Mauerwerk auf der Baustelle” (IGF Vorhaben Nr.: 20061 BG), supported by the German Federation of Industrial Research Associations (AiF).

## References

1. Bruckmann, T., Mattern, H., Spengler, A., Reichert, C., Malkwitz, A., König, M.: Automated construction of Masonry buildings using cable-driven parallel robots. In: 33rd International Symposium on Automation and Robotics in Construction and Mining (ISARC), pp. 332–340, Auburn (2016)
2. Izard, J.B., Dubor, A., Herve, P.E., Cabay, E., Culla, D., Rodriguez, M., Barrado, M.: Large-scale 3D printing with cable-driven parallel robots. *Constr. Rob.* **1**, 69–76 (2017)
3. Verhoeven, R.: Analysis of the workspace of tendon-based stewart platforms. Ph.D. thesis, Germany: University of Duisburg-Essen, Duisburg (2004)
4. Bruckmann, T., Pott, A., Hiller, M.: Calculating force distributions for redundantly actuated tendon-based Stewart platforms. In: Lennarčič, J., Roth, B. (eds.) *Advances in Robot Kinematics*. Springer, Dordrecht (2006)
5. Mikelsons, L., Bruckmann, T., Hiller, M., Schramm, D.: A real-time capable force calculation algorithm for redundant tendon-based parallel manipulators. In: *IEEE International Conference on Robotics and Automation*, pp. 3869–3874. Pasadena, CA (2008)
6. Pott, A.: *Cable-driven Parallel Robots: Theory and Application*. Springer Tracts in Advanced Robotics (2018). - ISBN 978-3-319-76137-4
7. Koo, B.: Skycam Almost Takes Out Iowa Huddle In Insight Bowl 31 December 2011. <https://awfulannouncing.com/2011-articles/skycam-almost-takes-out-iowa-huddle-in-insight-bowl.html>. Accessed 5 Apr 2019

8. Boumann, R.; Bruckmann, T.: Simulation of cable breaks and development of emergency strategies for cable-driven parallel robots. In: *Cable-Driven Parallel Robots - Proceedings of the Fourth International Conference on Cable-Driven Parallel Robots* (2019). Accepted
9. Côté, A.F., Cardou, P., Gosselin, C.: A tension distribution algorithm for cable-driven parallel robots operating beyond their wrench-feasible workspace. In: *16th International Conference on Control, Automation and Systems (ICCAS)*, pp. 68-73. Gyeongju (2016)
10. Bruckmann, T., Lalo, W., Sturm, C.: Application examples of wire robots. In: Gattringer, H., Gerstmayr, J. (eds.) *Multibody System Dynamics, Robotics and Control*. Springer, Vienna (2013)
11. Hiller, M.: *Mechanische Systeme: Eine Einführung in die Analytische Mechanik und Systemdynamik*. Springer, Heidelberg (1983)
12. Spong, M.W., Hutchinson, S., Vidyasagar, M.: *Robot Modeling and Control*. Wiley, Hoboken (2005). ISBN 9780471649908
13. Müller, K., Reichert, C., Bruckmann, T.: Analysis of a real-time capable cable force computation method. In: Pott, A., Bruckmann, T. (eds.) *Cable-Driven Parallel Robots. Mechanisms and Machine Science*, vol. 32. Springer, Cham (2014)
14. Gouttefarde, M., Lamaury, J., Reichert, C., Bruckmann, T.: A versatile tension distribution algorithm for  $n$ -DOF parallel robots driven by  $n + 2$  cables. *IEEE Trans. Robot.* **31**(6), 1444–1457 (2015)



# A 3-Dimensional Dynamic Model of the Aerotrain and the Horizontal Tail Effect on the Longitudinal Stability

Quang Huan Luong<sup>1(✉)</sup>, Jeremy Jong<sup>2</sup>, Yusuke Sugahara<sup>1</sup>,  
DaisukSe Matsuura<sup>1</sup>, and Yukio Takeda<sup>1</sup>

<sup>1</sup> Tokyo Institute of Technology, Tokyo 152-8552, Japan

luong.h.aa@mech.titech.ac.jp

<sup>2</sup> Kokushikan University, Tokyo 154-8515, Japan

**Abstract.** The Aerotrain is a new generation train that floats at a low altitude along a U-shaped (concrete) guideway by the aerodynamic forces generated at the two levitation wings. Using the wing-in-ground effect, the Aerotrain can have an advantage in reducing the operating cost through its low-cost guideway while maintaining high-speed under high-payload compared with the conventional magnetically levitated train system which uses the magnetic levitation effect. By floating along a U-shaped guideway, at steady state, the movement in X direction is less important than the movement in Y and Z direction and the rotation about three axes, therefore it could be neglected. From this simplification, in this paper, the nonlinear 3-dimensional dynamic model of the Aerotrain based on the rigid body model has been developed in order to clarify the relationship between the body design and its stability. The dynamic model was applied to corroborate the effect of the horizontal tail on the longitudinal stability. Simulation results show that the presence of the horizontal tail greatly contributes to the longitudinal stability of the Aerotrain while its behavior of the Aerotrain without it results in divergence. In addition, the appropriate position of the horizontal tail was discussed after looking at the simulation results with different variations.

**Keywords:** Wing-In-Ground effect · Aerotrain · Aerial robotics

## 1 Introduction

In recent years, the expansion of the range, transportation mass, types of activities undertaken by human beings has created global environmental problems. Therefore, a transportation system with high-efficiency and low power consumption is one of the important solutions for these problems and will benefit society. For this purpose, in the future, the next-generation transportation system must include two significant features, namely, high speed and high efficiency [1, 2]. One of the potential candidates is the maglev train which could reach maximum velocity of up to 603 km/h [3]. However, in spite of the advantages of the technology, the costs of establishment and maintenance for the operation of the train are half of the operating costs according to a High-speed rail feasibility study reported by Rocky Mountain Rail Authority [4]. To reduce the



**Fig. 1.** Aerotrain concept [6].

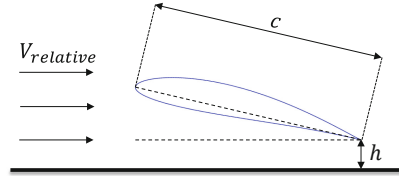


**Fig. 2.** Wing in ground effect.

operating cost and to satisfy the two important features mentioned above, the research on the Aerotrain was started in 1987 by Kohama et al. [5] at Tohoku University, Japan.

The Aerotrain, as shown in Fig. 1, has wings and levitates on a concrete U-shaped guideway by the Wing-In-Ground (WIG) effect. The advantage of a low-cost guideway in terms of construction and maintenance is expected to reduce the total operation cost. The aerodynamic lift force generated from two levitational wings at the cruise speed will lift the train a short distance from the ground, so that there is no friction between the vehicle's body and the guideway. Compared with normal maglev high-speed trains, the massive energy required to maintain the electrical magnetic force is not needed, which means that the Aerotrain could reduce a lot of power consumption. The difference between an airplane and the Aerotrain is the WIG effect. The WIG effect happens when an airfoil or wing-like object is close to the ground as shown in Fig. 2 when the altitude  $h$  is less than 25% of the wing chord  $c$  [7], a high-pressure air cushion will be created for the stagnation of the air which generates a greater lift force and a greater lift-drag ratio ( $L/D$ ) than the airfoil at higher altitude. This same principle is adopted for keeping the position of the train at the center of the guideway and keeping the direction parallel to the guideway. By changing the angle of the control surface on the guide wing (the vertical wings at the tip of the levitation wings), the side force and the yawing moment are also changed to make the Aerotrain stay on the proper track. The WIG effect could also provide a recovering moment to ensure the stability of the Aerotrain when an external disturbance in the rolling axis of motion happens. Compared with other WIG effect vehicles operating on water surface [8, 9], the Aerotrain has less external disturbances and it is safer because the operation of the train is based on the use of a solid guideway [10]. Unlike the normal airplane, the nonlinearity of the aerodynamic force and moment due to WIG effect need to be carefully considered.

There have been several studies on the control of the Aerotrain [11–13], but there is insufficient knowledge on the design of the vehicle body which has a desirable dynamic characteristic. Therefore, the long-term objective of this research is to determine the relationship between the Aerotrain's design parameters and its stability. A recent study [10] found that the influence of the relative positions of the levitation wings is significant in contrast to that of angles of attack. Generally, the longitudinal stability plays an important role in the stability of the vehicle and it could be studied separately with directional and lateral stability. According to this assumption, the previous study [14] found that the horizontal tail has a great contribution on the longitudinal stability of the Aerotrain. In order to confirm that the horizontal tail still retains its effect in combination

with lateral and directional stability, the purpose of this paper is to develop a 3-dimensional nonlinear dynamic model of the Aerotrain and attach the horizontal tail model into it. Through the simulation results, the effect of the horizontal tail has been clearly confirmed. The position of the horizontal tail has been considered as well.

## 2 Dynamic Model of the Aerotrain

Considering it as a flight vehicle, the dynamic equations of the Aerotrain are written in a body-fixed coordinate system  $O - XYZ$  in which the origin is the center of gravity of the vehicle. The X-axis is in the plane of symmetry of the body and points forward. The Z-axis is in the same plane as X-axis, perpendicular to X-axis and points down. The Y-axis is perpendicular to the symmetry plane and points out the right wing. However, only using the body-fixed coordinate system is not enough to express the gravitational force acting on the vehicle. Thus, the orientation of the body-fixed coordinate system with respect to the gravity vector needs to be determined as shown in Fig. 3. This orientation can be specified using the Euler angle (pitch angle  $\theta$ , roll angle  $\phi$  and yaw angle  $\psi$ ) of the body-fixed coordinate system with respect to an inertial system  $O_E - X_E Y_E Z_E$ , where the inertial system is oriented such that the  $Z_E$ -axis points down (parallel to the gravity vector), the  $X_E$  axis points North and the  $Y_E$ -axis completes the right-handed system, and therefore points East.

The Aerotrain is considered as a rigid body in steady state with a total of 6 degrees of freedom which include 3 translations and 3 rotation motions. The 3 translations are caused by the aerodynamic lift, drag, and gravity force. These force and aerodynamic moments are the reason of the 3 rotational motions which are pitching, rolling and yawing moment. The aerodynamic efficiency of the Aerotrain is higher than that of conventional airplanes due to the WIG effect that will be later explained in this chapter. In the Aerotrain model, the aerodynamic lifts generated from two levitational wings and 4 guide wings are under the WIG effect during cruise speed. Given that the operation occurs inside a U-shaped guideway, the movement in Z-axis and Y-axis and the rotation about 3 axes are more important than the movement in X-axis. Thus, in this paper, the 1 degree of freedom of the X-axis translation has been ignored for the Aerotrain model. Therefore, Z-axis and Y-axis forces as well as 3 moments (about 3 axes) have been modelled in the MapleSim [15] environment using its custom components.

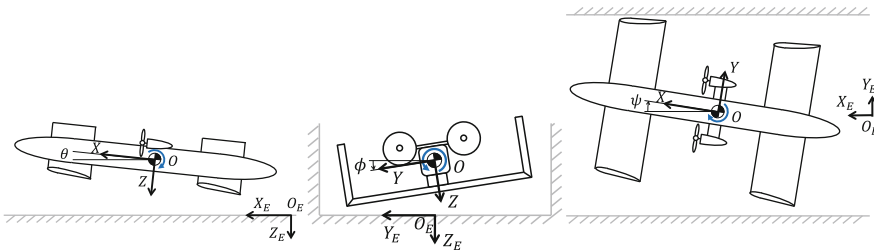


Fig. 3. Coordinate systems and Euler angles

## 2.1 Wing-In-Ground Effect Model

According to Honda [16], in the area affected by the ground effect, the lift coefficient changes nonlinearly, but this can be represented by the sum of the nonlinear term caused by the influence of the ground effect and the linear term unrelated to the influence of the ground effect.

$$L = \frac{1}{2} \rho V_{x0}^2 S C_L \quad (1)$$

$$C_L = C_{Lg,e} + C_{Lnormal} \quad (2)$$

where  $L$  is the aerodynamic lift,  $C_L$  is the lift coefficient,  $\rho$  is the air density,  $V_{x0}$  is the velocity at steady state and  $S$  is the wing area. The lift coefficient under the WIG effect  $C_{Lg,e}$  and in normal condition  $C_{Lnormal}$  could be expressed as followings:

$$C_{Lg,e} = a_1 \exp\left(-a_2 \frac{h}{c}\right) \quad (3)$$

$$C_{Lnormal} = a_3 \alpha + a_4 \quad (4)$$

where  $a_1, a_2, a_3, a_4$  are obtained constants from the curve fitting of the experimental results [16];  $\alpha$  is the angle of attack.

## 2.2 Aerodynamic Force Along the Z-Axis

The aerodynamic force along the Z-axis includes the lift force from the front and the rear levitation wing of the Aerotrains. Figure 4 shows the differential slice  $dy_i$  with its height  $h_f$  at the spanwise  $y_i$  of the front levitation wing with span  $b$  at the roll angle  $\phi$  that will be later used to calculate the differential lift.  $h_0$  is the height of the Center of Gravity (CoG) of Aerotrains at the steady state, and  $h$  is the displacement of the CoG from the steady state in the Z-axis.

Under the influence of the WIG effect, the lift coefficient of the front wing  $C_{Lfi}$  and the rear wing  $C_{Lri}$  at the spanwise  $y_i$  could be written as:

$$C_{Lfi}(y_i) = C_{Lfg,e} + C_{Lfnormal} = a_1 \exp\left(-a_2 \frac{h_f}{c_f}\right) + a_3 \alpha_f + a_4 \quad (5)$$

$$C_{Lri}(y_i) = C_{Lrg,e} + C_{Lrnormal} = b_1 \exp\left(-b_2 \frac{h_r}{c_r}\right) + b_3 \alpha_r + b_4 \quad (6)$$

The parameters  $a_1, \dots, a_4, b_1, \dots, b_4$  are defined by the curve fitting from the experiment [16];  $c_f, c_r$  are the chord length of the front and rear levitation wing relatively. Assume that the pitch angle  $\theta$  and roll angle  $\phi$  are small enough, the height of

the front wing  $h_f$  and the rear wing  $h_r$  are the linearized function of the actual height  $h$  of the CoG, the pitch angle  $\theta$ , the roll angle  $\phi$  and the location  $y_i$ :

$$h_f(h, \theta, \phi, y_i) = h_0 + h + l_f \theta - y_i \phi \quad (7)$$

$$h_r(h, \theta, \phi, y_i) = h_0 + h - l_r \theta - y_i \phi \quad (8)$$

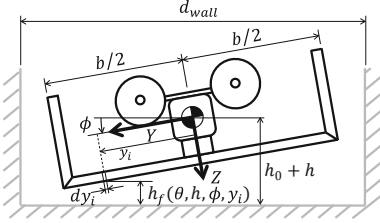


**Fig. 4.** The front view of Aerotrain [17].

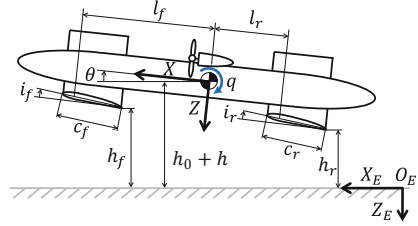


**Fig. 5.** The side view of Aerotrain [17].

The Angle of Attack (AOA) of the front wing  $\alpha_f$  and the rear wing  $\alpha_r$  are the function of the AOA  $\alpha$  and the pitching angular velocity  $q$ :

$$\alpha_f(\alpha, q) = \alpha + i_f - (l_f/V_{x0})q; \alpha_r(\alpha, q) = \alpha + i_r + (l_r/V_{x0})q \quad (9)$$

where  $i_f, i_r$  are the mounting angle;  $l_f, l_r$  are the distance from the CoG to the aerodynamic center which is located at the quarter-chord from the leading edge of the front and the rear levitation wing as shown in Fig. 5. By integrating along the wing span, the total aerodynamic force  $Z_a$  along the Z-axis can be obtained from the sum of the aerodynamic lift  $L_f, L_r$  of the front and rear levitation wing.

$$Z_a = L_f + L_r \quad (10)$$

$$L_f = \frac{1}{2} \rho V_{x0}^2 c_f \int_{-b_f/2}^{b_f/2} C_{Lfi}(y_i) dy_i; L_r = \frac{1}{2} \rho V_{x0}^2 c_r \int_{-b_r/2}^{b_r/2} C_{Lri}(y_i) dy_i \quad (11)$$

### 2.3 Aerodynamic Force Along the Y-Axis

Given that the Aerotrain runs in a U-shaped guideway, the aerodynamic force generated from the guide wings are also under the WIG effect. The aerodynamic force  $Y_a$  along Y-axis is the combination of the aerodynamic force from 4 guide wings  $Y_{fl}, Y_{fr}, Y_{rl}, Y_{rr}$ .

$$Y_a = Y_{fl} + Y_{fr} + Y_{rl} + Y_{rr} \quad (12)$$



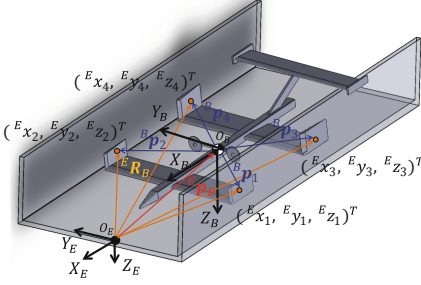


**Fig. 6.** Position vector of the point on the guide wing with respect to the origin of the inertial system [17].

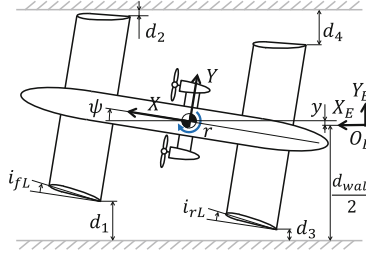


**Fig. 7.** The top view of Aerotrains [17].

Using the same idea as the aerodynamic force in the Z-axis, where the distance  $d_i$  plays the role of the height  $h_i$  and  $z_i$  plays the role of the spanwise  $y_i$ , the coefficient of differential force of the guide wing at the spanwise  $z_i$  could be written as follows [17]:

$$C_{yfl}(z_i) = a_1 \exp\left(-a_2 \frac{d_1(d, \theta, \phi, \psi, z_i)}{c_{sf}}\right) + a_3 \beta_{fl}(\beta, r) + a_4 \quad (13)$$

$$C_{yfr}(z_i) = -a_1 \exp\left(-a_2 \frac{d_2(d, \theta, \phi, \psi, z_i)}{c_{sf}}\right) - a_3 \beta_{fr}(\beta, r) - a_4 \quad (14)$$

$$C_{yrl}(z_i) = b_1 \exp\left(-b_2 \frac{d_3(d, \theta, \phi, \psi, z_i)}{c_{sr}}\right) + b_3 \beta_{rl}(\beta, r) + b_4 \quad (15)$$

$$C_{yrr}(z_i) = -b_1 \exp\left(-b_2 \frac{d_4(d, \theta, \phi, \psi, z_i)}{c_{sr}}\right) - b_3 \beta_{rr}(\beta, r) - b_4 \quad (16)$$

where  $\psi$  is the yawing angle;  $\beta$  is the sideslip angle;  $\beta_{fl}, \beta_{fr}, \beta_{rl}, \beta_{rr}$  are the angle of attack of the guide wings.

$$\beta_{fl}(\beta, r) = \beta + i_{fl} - (l_f/V_{x0})r; \beta_{fr}(\beta, r) = -\beta + i_{fr} + (l_f/V_{x0})r \quad (17)$$

$$\beta_{rl}(\beta, r) = \beta + i_{rl} + (l_r/V_{x0})r; \beta_{rr}(\beta, r) = -\beta + i_{rr} - (l_r/V_{x0})r \quad (18)$$

where  $i_{fl}, i_{fr}, i_{rl}, i_{rr}$  are the mounting angle of the front-left, front-right, rear-left, rear-right guide wing relatively;  $r$  is the yawing angular velocity. The distance  $d_1, \dots, d_4$  from the trailing edge of the guide wing to the wall as shown in Figs. 6, 7 could be calculated with respect to the inertial system  $O_E - X_E Y_E Z_E$ .

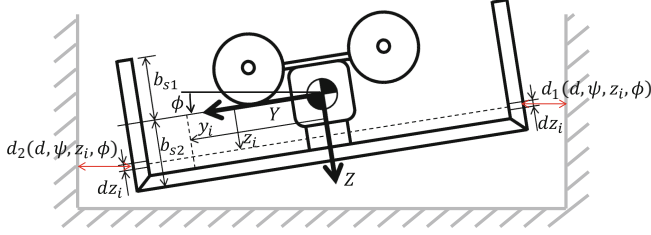


**Fig. 8.** The dimension of the guide wing [17].

The position vector of a point on the guide wing in the inertial system  ${}^E\mathbf{p}_i$  could be obtained from the position vector in the body-fixed system  ${}^B\mathbf{p}_i$  by the translation matrix  $\mathbf{T}(d, \phi, \theta, \psi)$  as follows:

$$\begin{bmatrix} {}^E\mathbf{p}_i \\ 1 \end{bmatrix} = \mathbf{T}(d, \phi, \theta, \psi) \begin{bmatrix} {}^B\mathbf{p}_i \\ 1 \end{bmatrix} \quad (19)$$

$$\mathbf{T}(d, \phi, \theta, \psi) = \begin{bmatrix} {}^E\mathbf{R}_B(\phi, \theta, \psi) & {}^E\mathbf{p}_B(d) \\ 0 & 1 \end{bmatrix}_s \quad (20)$$

where  ${}^E\mathbf{R}_B$  is the rotation matrix and  ${}^E\mathbf{p}_B(d)$  is the position vector of the origin of the body-fixed system with respect to the inertial system.

In the body-fixed system, for example, the position vector of a point on the front-left guide wing at the spanwise  $z_i$  could be written as follows:

$${}^B\mathbf{p}_1(z_i) = \left[ l_f, -\frac{b}{2}, z_i \right]^T \quad (21)$$

While in the inertial system, that position vector could be written as:

$$\begin{bmatrix} {}^E\mathbf{p}_1(d, \theta, \phi, \psi, z_i) \\ 1 \end{bmatrix} = \left[ {}^E x_1(d, \theta, \phi, \psi, z_i), {}^E y_1(d, \theta, \phi, \psi, z_i), {}^E z_1(d, \theta, \phi, \psi, z_i), 1 \right]^T \quad (22)$$

Using the Eqs. (19), (20), (21), (22), the distance  $d_1, \dots, d_4$  could be calculated.

$$d_1(d, \theta, \phi, \psi, z_i) = \frac{d_{wall}}{2} + {}^E y_1(d, \theta, \phi, \psi, z_i) \quad (23)$$

$$d_2(d, \theta, \phi, \psi, z_i) = \frac{d_{wall}}{2} - {}^E y_2(d, \theta, \phi, \psi, z_i) \quad (24)$$

$$d_3(d, \theta, \phi, \psi, z_i) = \frac{d_{wall}}{2} + {}^E y_3(d, \theta, \phi, \psi, z_i) \quad (25)$$

$$d_4(d, \theta, \phi, \psi, z_i) = \frac{d_{wall}}{2} - E_{y4}(d, \theta, \phi, \psi, z_i) \quad (26)$$

Therefore, by integrating along the wing span as shown in Fig. 8, the aerodynamic force along the Y-axis of 4 guide wings could be expressed as follows:

$$Y_{fl} = \frac{1}{2} \rho V_{x0}^2 c_{sf} \int_{-b_{s1f}}^{b_{s2f}} C_{yfli}(z_i) dz_i \quad (27)$$

$$Y_{fr} = \frac{1}{2} \rho V_{x0}^2 c_{sf} \int_{-b_{s1f}}^{b_{s2f}} C_{yfri}(z_i) dz_i \quad (28)$$

$$Y_{rl} = \frac{1}{2} \rho V_{x0}^2 c_{sr} \int_{-b_{s1r}}^{b_{s2r}} C_{yrli}(z_i) dz_i \quad (29)$$

$$Y_{rr} = \frac{1}{2} \rho V_{x0}^2 c_{sr} \int_{-b_{s1r}}^{b_{s2r}} C_{yrr i}(z_i) dz_i \quad (30)$$

where  $c_{sf}$ ,  $c_{sr}$  are the chord length of the front and rear guide wings.

## 2.4 Aerodynamic Moment About the X, Y, Z Axes

The aerodynamic moment about the Y-axis is the sum of the moment of two levitation wings, the moment of the fuselage and the moment cause by the lift of these wings. Based on the experimental result, the aerodynamic moment coefficient  $C_M$  about the Y-axis is also under the WIG effect and can be expressed as follows [11]:

$$M_a = \frac{1}{2} \rho S_f V_{x0}^2 C_{Mf} + \frac{1}{2} \rho S_r V_{x0}^2 C_{Mr} + M_{fus} + l_f L_f - l_r L_r \quad (31)$$

$$C_{Mf} = a_5 \exp\left(-a_6 \frac{h_f}{c_f}\right) + a_7 \exp\left(-a_8 \frac{h_f}{c_f}\right) + a_9 \alpha_f + a_{10} \quad (32)$$

$$C_{Mr} = b_5 \exp\left(-b_6 \frac{h_r}{c_r}\right) + b_7 \exp\left(-b_8 \frac{h_r}{c_r}\right) + b_9 \alpha_r + b_{10} \quad (33)$$

$$M_{fus} = \rho V_{x0}^2 V_{fus} \alpha \quad (34)$$

where  $C_{Mf}$ ,  $C_{Mr}$  are the aerodynamic moment coefficient of the front and rear levitation wing;  $V_{fus}$  is the volume of the equivalent fuselage [18] of the Aerotrains;  $a_5, \dots, a_{10}$ ,  $b_5, \dots, b_{10}$  are the constants from curve fitting. The moment about the X-axis is obtained from the aerodynamic lift from the main levitation wings  $L_{lw}$ , the front guide wings  $L_{gwf}$  and the rear guide wing  $L_{gwr}$  [17].

$$L_a = L_{lw} + L_{gwf} + L_{gwr} \quad (35)$$

$$L_{lw} = -\frac{1}{2}\rho V_{x0}^2 \left( c_f \int_{-\frac{b_f}{2}}^{\frac{b_f}{2}} C_{Lfi}(y_i) y_i dy_i + c_r \int_{-\frac{b_r}{2}}^{\frac{b_r}{2}} C_{Lri}(y_i) y_i dy_i \right) \quad (36)$$

$$L_{gwf} = \frac{1}{2}\rho V_{x0}^2 c_{sf} \int_{-b_{s1f}}^{b_{s2f}} (-C_{yfli}(z_i) + C_{yfri}(z_i)) z_i dz_i \quad (37)$$

$$L_{gwr} = \frac{1}{2}\rho V_{x0}^2 c_{sr} \int_{-b_{s1r}}^{b_{s2r}} (-C_{yrli}(z_i) + C_{yrri}(z_i)) z_i dz_i \quad (38)$$

The aerodynamic moment about the Z-axis  $N_a$  is the total moment of the guide wings, the moment of the side force from the guide wings and the moment of the fuselage, and it is also under the WIG effect as the pitching moment M:

$$N_a = N_{fl} + N_{fr} + N_{rl} + N_{rr} + l_f (Y_{fl} + Y_{fr}) - l_r (Y_{rl} + Y_{rr}) + N_{fus} \quad (39)$$

where  $N_{fl}, N_{fr}, N_{rl}, N_{rr}$  are the moments of the guide wings under WIG effect and could be computed in the same way as the moment of the levitation wings;  $N_{fus}$  is the moment of the fuselage and have the same value as the  $M_{fus}$ .

## 2.5 Horizontal Tail Model

The lift coefficient and moment coefficient of the horizontal tail is a function of the angle of attack and the angular velocity [14]. Depending on the angle of attack  $\alpha$ , the lift coefficient  $C_{L(tail)}$  is directly related to the mounting angle  $i_t$  and the downwash angle  $\varepsilon$  caused by the air flowing through the main wing.

$$C_{L(tail)} = a_t(\alpha - \varepsilon - i_t) \quad (40)$$

In the case of the Aerotrain, the horizontal tail is located at the rear side of the train and at a high location so that the downwash flow does not affect the tail. Thus, the downwash angle is zero,  $\varepsilon = 0$ . Another assumption is that the horizontal tail has symmetry airfoil and does not generate any aerodynamic force when the angle of attack is zero, which means that the chord line is parallel to the x-axis in the body-fixed system or the mounting angle  $i_t = 0$ . As for the thin, symmetric airfoil [19], the lift coefficient could be written as follows:

$$C_{L(tail)}(\alpha) = 2\pi\alpha \quad (41)$$

The horizontal tail is located at a distance  $l_t$  from the center of gravity of the Aerotrain to the aerodynamic center of the tail as shown in Fig. 9. Thus, the effect of pitching rate  $q$  in terms of the changing of angle of attack  $\alpha$  is described as:

$$\Delta\alpha_t = \frac{ql_t}{V_{x0}} \quad (42)$$

Thus, the lift coefficient of the horizontal tail caused by the pitching rate is:

$$C_{L(tail)}(q) = 2\pi \cdot \frac{ql_t}{V_{x0}} \quad (43)$$

Therefore, the total lift force coefficient is the sum of these two coefficients:

$$C_{L(tail)}(\alpha, q) = C_{L(tail)}(\alpha) + C_{L(tail)}(q) \quad (44)$$

The total pitching moment from the horizontal tail is also a function of the angle of attack  $\alpha$  and the pitching rate  $q$  and it could be written as:

$$C_{M(tail)}(\alpha, q) = -l_t C_{L(tail)}(\alpha) - l_t C_{L(tail)}(q) \quad (45)$$

### 3 Simulations

To evaluate the effectiveness of the horizontal tail in terms of longitudinal stability, the dynamic model of the Aerotrains was developed in the MapleSim [15] environment using a rigid body model as shown in Fig. 10. The advantage of MapleSim over the others is its friendly user interface and its sufficiency when creating custom components that are not available in the default library.

Based on the mathematical equations, the aerodynamic components, such as lift and moment of the levitation wings and the guide wings have been created. Then, the total net force in the Z-axis which includes the lift from the levitation wings, the horizontal tail and the total net force in the Y-axis from the guide wings was applied to the Aerotrains body through the “Apply World Force” component. Similar to the force, the total net moment about X, Y, Z axes was also applied to the body of the train through the “Apply World Moment” component.

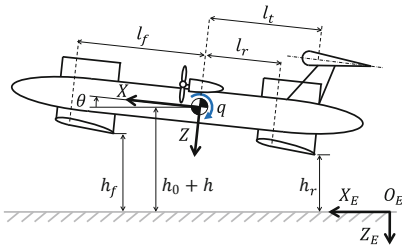


Fig. 9. Horizontal tail wing [14].

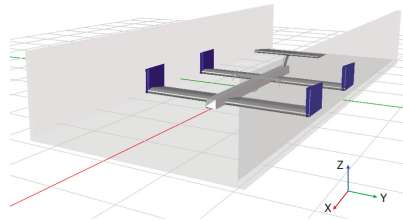
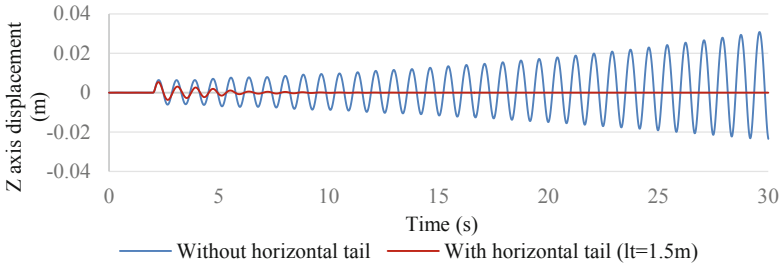
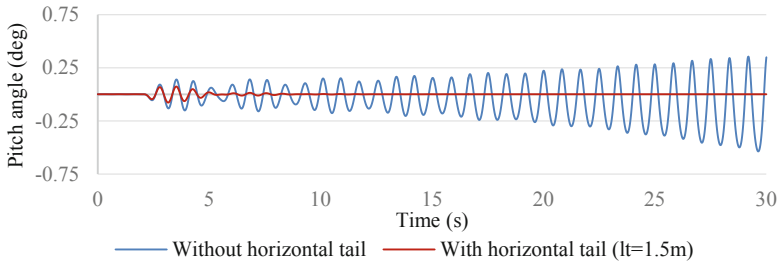


Fig. 10. Aerotrains in MapleSim.



**Fig. 11.** Displacement in Z axis.



**Fig. 12.** Pitch angle.

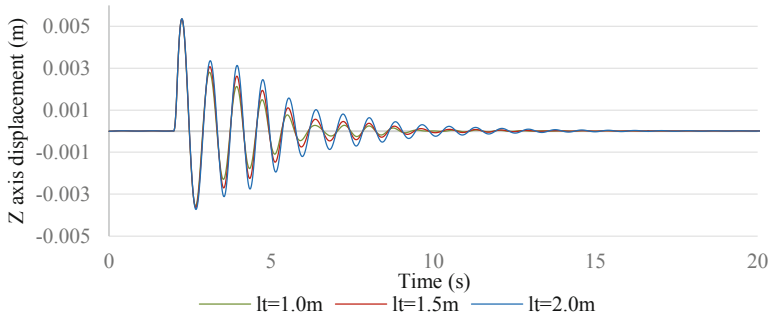


**Fig. 13.** Z axis displacement at various location of the horizontal tail.

The simulation was done in 30 s. At the steady state, a disturbance of 20.85 N (5% of the total lift at equilibrium state) was applied to the body in Z axis after 2 s in order to observe the responsibility of the model. The parameters used in the simulation are the same as the experimental prototype ARTE02 [12] as shown in following Table 1.

At the same condition, with the horizontal tail, the displacement in the Z axis and pitch angle have been convergent as shown in Figs. 11 and 12 thanks to the spring element  $\alpha$  and the damper element  $q$ . The simulation results have clearly proved that the effectiveness of the horizontal tail still remained in the 3-dimensional model.

With the 3-dimensional model, the body design parameters of the Aerotrain in general and the design of the horizontal tail in particular could be evaluated. For example, in this paper, various positions of the horizontal tail have been simulated with the assumption that the wingspan of the horizontal tail is 1 [m<sup>2</sup>]. The distance ranges from 1.0 [m] to 2.0 [m] at a 0.5 [m] step. As can be seen in Fig. 13, the horizontal tail reaches its best performance at the location of 1.0 [m] from the CoG of the Aerotrain. However, since the rear levitation wing is located at 1.13 [m] from the CoG, it would be better to attach the horizontal tail at 1.5 [m] to prevent the influence of the levitation wing. It is also revealed that the relative position of the CoG also plays a role in longitudinal stability which is consistent with the principle of the flight mechanics.

**Table 1.** Aerotrain parameters.

Parameters	Value		
Mass [kg]	42.5		
Wing area [m <sup>2</sup> ]	2.31		
Chord length [m]	0.7		
Wing span [m]	3.3		
Levitation height [m]	0.07		
$l_f$ [m]	1.4		
$l_r$ [m]	1.13		
$i_f$ [deg]	1.48		
$i_r$ [deg]	2.63		
$V_{x0}$ [m/s]	20		
Tail area [m <sup>2</sup> ]	1.0		
$l_t$ [m]	1.0	1.5	2.0
Disturbance at 2 s [N]	20.85		
Total lift at equilibrium state [N]	416.92		

## 4 Conclusions and Future Work

In this paper, the dynamic model of the Aerotrain in 3-dimensions has been developed with the nonlinear aerodynamic forces and moments under the WIG effect. Compared with the previous studies [14, 17], the side force from the 4 guide wings, the aerodynamic lift and moment from the levitational wings and the horizontal tail have been integrated into the rigid body model to make the dynamic model more specific so that it will be useful for other studies.

The horizontal tail still retains its effectiveness in terms of longitudinal stability as it was in 2-dimensional model of the Aerotrain. The position of the horizontal tail has a great effect on the longitudinal stability comparable with the position of its CoG.

Based on this dynamic model, the force in the X-axis will be considered to complete the 6-degrees of freedom of the 3-dimensional model. Then, next studies will be focused on the lateral stability and the directional stability to evaluate its response on a curved and banked guideway. A small-scale experiment prototype and controller will be designed to evaluate the reliability of the dynamic model in the longitudinal stability.

## References

1. Sugahara, Y., Kikuchi, S., Kosuge, K., Kohama, Y.: Levitation control of AEROTRAIN: the design and system of experimental manned Wing-In-Ground vehicle ART003R. *J. Robot. Mechatron.* **25**(6), 1097–1104 (2013)
2. International High-speed Rail Association Homepage. <https://www.ihra-hsr.org>. Accessed 28 Mar 2019
3. Omio Homepage. <https://www.omio.co.uk/trains/high-speed>. Accessed 13 Mar 2019
4. Rocky Mountain Rail Authority Homepage, <http://rockymountainrail.org>. Accessed 13 Mar 2019
5. Kohama, Y.: An application of ACV to railway transportation. In: 25th Aircraft Symposium, pp. 128–131 (1987). (in Japanese)
6. Kohama, Y.: Mechanical civilization induced earth pollution problem, and aero-train. In: Transactions of the Japan Society of Mechanical Engineers, Series B, vol. 71(707), pp. 1733–1737 (2005). (in Japanese)
7. Rozhdestvensky, K.V.: Aerodynamics of a Lifting System in Extreme Ground Effect. Springer-Verlag, Heidelberg (2000)
8. Rozhdestvensky, K.V.: Wing-In-Ground effect vehicles. *Prog. Aerosp. Sci.* **42**(3), 211–283 (2006)
9. Divitiis, N.D.: Performance and stability of winged vehicle in ground effect. *J. Aircr.* **42**, 148–157 (2005)
10. Boqi, R., Chenguang, L., Yuting, Z.: Influence of wing angle of attack and relative position on the aerodynamics of aerotrain. *Adv. Mech. Eng.* **9**(8), 1–12 (2017)
11. Sugahara, Y., Ikeuchi, Y., Suzuki, R., Hirata, Y., Kosuge, K., Noguchi, Y., Kikuchi, S., Kohama, Y.: Levitation control of experimental Wing-In-Ground effect vehicle along Z axis and about roll and pitch axes. In: 2011 IEEE International Conference on Robotics and Automation, pp. 8–13. IEEE, Shanghai, China (2011)
12. Sugahara, Y., Ikeuchi, Y., Suzuki, R., Hirata, Y., Kosuge, K., Noguchi, Y., Kikuchi, S., Kohama, Y.: Levitation control of experimental Wing-In-Ground effect vehicle along Y and Z axes and about three axis. In: 2012 IEEE/RSJ International Conference on Intelligent Robots and Systems, pp. 488–494. IEEE, Vilamoura, Portugal (2012)
13. Kikuchi, S., Ota, F., Kato, T., Ishikawa, T., Kohama, Y.: Development of a stability control method for the aero-train. *J. Fluid Sci. Technol.* **2**(1), 226–237 (2007)
14. Jong, J., Matsumoto, T., Honda, Y., Sugahara, Y., Kikuchi, S., Kohama, Y.: Study on the Body Frame Design and Stability of Aero-Train- 2nd Report: Effects of Horizontal Tail on Longitudinal Dynamic Model, pp. 0549–0553. SICE (2016). (in Japanese)
15. Maplesoft Homepage, <https://www.maplesoft.com/products/maplesim/>. Accessed 13 Mar 2019
16. Honda, K.: Longitudinal Stability of WIG with Tandem Configuration, Master thesis, Tohoku University (2002). (in Japanese)



17. Jong, J., Honda, Y., Sugahara, Y., Kikuchi, S., Kohama, Y.: Study on the body frame design and stability of aero-train-3rd report: development of 3-dimensional dynamic model. In: JSME Conference on Robotics and Mechatronics, no. 17-2, pp. 1P1-G06(1–4) (2017). (in Japanese)
18. Caughey, D.A.: Introduction to aircraft stability and control course notes for M&AE 5070, pp 19–20. Cornell University, New York 14853-7501 (2011)
19. Anderson, J.D.: Fundamental of Aerodynamics, 5th edn. McGraw-Hill, New York (2011)



# Towards Grey Box Modeling in Modelica

Frederic Bruder and Lars Mikelsons<sup>(✉)</sup>

Chair of Mechatronics, Augsburg University, 86159 Augsburg, Germany  
{frederic.bruder,lars.mikelsons}@informatik.uni-augsburg.de

**Abstract.** A dynamic system model of a motorcycle is described that has been implemented in the modeling language Modelica. Particular mathematical relations therein are learned by feedforward artificial neural networks which are trained using simulation data generated from the original model. These trained models are then used to replace the original relations in new models. This emulates a situation in which the original relations (e.g. those of a real system) are unknown but measurements indicate an interdependence between variables. The simulation results of those derived models are then evaluated and an approach to detect unreliable extrapolation of the artificial neural networks is proposed.

**Keywords:** Modelica · Grey box modeling ·  
Feedforward neural networks · Reliability

## 1 Introduction

### 1.1 Motivation

In the following, “model” refers to an ordinary differential equation:

$$\dot{\mathbf{x}}(t) = \mathbf{f}(\mathbf{x}(t), t, \mathbf{u}(t)), \quad (1)$$

$$\mathbf{x}(t = 0) = \mathbf{x}_0, \quad (2)$$

$$\mathbf{y} = \mathbf{h}(\mathbf{x}(t), t, \mathbf{u}(t)) \quad (3)$$

Here  $\mathbf{x}(t) \in \mathbb{R}^n$  stands for the state vector with initial state  $\mathbf{x}_0 \in \mathbb{R}^n$ . The input vector is written as  $\mathbf{u} \in \mathbb{R}^m$  and  $\mathbf{y} \in \mathbb{R}^r$  denotes the output vector.  $\mathbf{f}$  and  $\mathbf{g}$  are, in general, nonlinear vector functions. This kind of description is also known as “state space model”. The goal of mathematical modeling of physical systems is to create a model of a real or planned system that behaves like the original or replicates specific patterns of behavior. The pursuit of both model accuracy and simplicity results in conflict. Ultimately, a model should meet its accuracy requirements whilst remaining as simple as possible. To validate a model, measurements taken from the original system can be used. As an example, the trajectories from simulations of the model can be compared with the actual measurement data to compare their behavior. A more sophisticated approach may involve the extraction of high-level features from said trajectories. For example,

a good model of a pendulum should exhibit frequency and amplitude of oscillation similar to those of the original pendulum. Typically, after the modeling process, there are differences between the measurements of the model and the original system that, by magnitude or trend over time, cannot originate from measurement noise alone. In this case, parameter errors or model errors must be assumed. The former can be eliminated by choosing accurate physical parameters. Model errors, however, cannot be completely avoided and the question rises how their impact can be reduced.

## 1.2 State of the Art

Following [9], the following modeling approaches are considered:

- **“white box”**: The model is based on physical equations only. Every parameter is physically interpretable and the model is accurate in large regions of its state space.
- **“black box”**: The model aims to replicate the I/O-behavior of the original system with non-physically based relations. They are adapted using data of the original model, making it more flexible and possibly locally more accurate than a white box model. However, its generalization over state space is questionable.
- **“grey box”**: The model contains both physical and data-based relations. This way, unknown relations can be modeled flexibly while known effects are expressed in physical terms.

Figure 1 shows ways to adapt the different kinds of models to the original system and its measurements. In “white box” models, one could distort the physically correct parameters possibly resulting in locally but not globally more accurate results. In the case of “grey box” models, one would restrict adaptations to the data-based relations. The same applies to “black box” models, in which then every relation could be altered to adapt the model.

An example of “black box” modeling can be found in [11], where a time-invariant version of  $\mathbf{f}(\mathbf{x}(t))$  from Eq. 1 is considered to be part of a multistep-scheme. The variable weights of  $\mathbf{f}(\mathbf{x}(t))$ , the output of a feedforward artificial neural network (ANN), are then adjusted to satisfy the underlying equation of the multistep-scheme as well as possible. Measurements of the original system to be modeled have to be sampled at specific times and are included in that equation.

A “grey box” approach is described in [10]. A system is described in the same way as in Eqs. 1–3. However, it is known that a certain variable is not constant but instead a function of other model variables. The learning procedure is then split into two steps: In the first step, the function is assumed to be independent of the rest of the model and takes the form of a piecewise constant function. As the goal of an optimization task that aims to fit the measurement data of the original system, the values of the function during each time period are determined. With this knowledge about what the function “should have

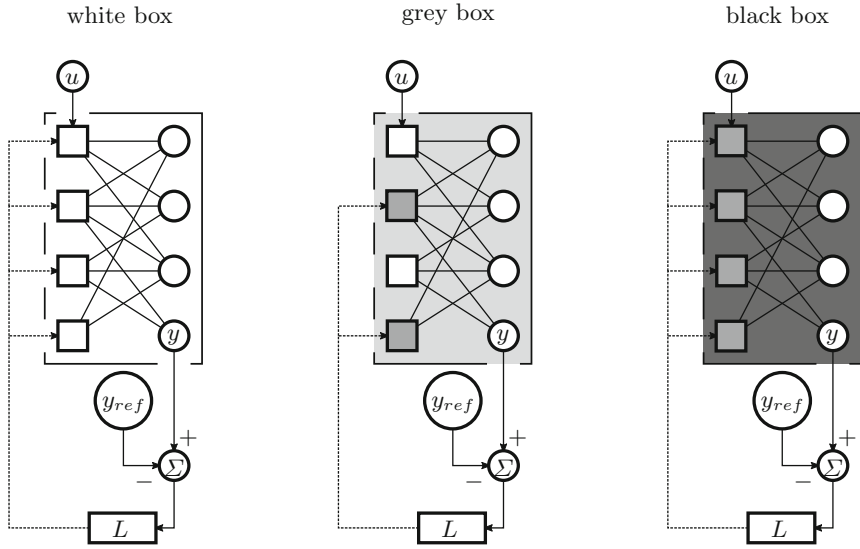


**Fig. 1.** Comparing adaption options for the different model classes. White squares: physically based equations. Grey squares: equations including “black box” expressions. Unlabeled circles: model variables. “ $u$ ”: input signal. “ $y$ ”: output signal. “ $y_{ref}$ ”: reference measurement data of the original system. “ $L$ ”: learning rule.

returned” at every instant, in the second step the determined time series of values is examined for correlations with other model quantities. The user (or a more complex algorithm) can then try to find a functional relation depending on those correlating model quantities to model the time series as well as possible. The result of this process is a model in which an expression has been adapted to available data next to existing “white box” knowledge.

The approach in this proposal has the same general goal as the one in [10]. Specific relations within a model shall be learned on the basis of reference data while keeping physically established relations unchanged. The idea of localized adaption of single expressions is especially applicable to object-oriented modeling (like in Modelica) and aims to keep learning results understandable to the user by separation from existing “white box” relations. Furthermore, it is of interest in which regions of state space one can expect reliable results from the learned relations.

### 1.3 Goals

Parts of the general idea outlined above shall be applied to the model of the planar dynamics of a motorcycle written in Modelica. The latter replaces a “real system” and contains specific relations that are supposed to be learned by multilayer perceptrons (MLP) based on virtual measurement data (simulation

data). These trained MLP are then used in new system models to model the original relations.

The following assumptions are made throughout this paper:

- It is known exactly which relations have to be adjusted.
- The set of model variables influencing each relation are known.
- The relations have no internal state and can be described in terms of mathematical functions.

## 2 Main Part

### 2.1 Reference System

The reference system is based on the example model `SingleTrackWithEngine` from [15] presented in [14]. The longitudinal velocity of the rear wheel joint is controlled using a saturating PI-controller driving a torque source that acts on the rotational acceleration of the rear wheel. Moreover, the steering angle is imposed using a positional source. More parts have been added/modified and will be described in what follows.

**Wheel Joints.** The wheels of the base model were replaced by a modified version of `SlipBasedWheelJoint`, which is part of `PlanarMechanics 1.4.0`. A force connector has been included that exposes the longitudinal wheel friction force, `f_long`, to the following component **dynamic loads**.

**Dynamic Loads.** The normal forces acting from the ground on the wheel joints depend not only on the vehicle mass and its center but also on the longitudinal forces between ground and wheels (see [12]).

$$0 = \hat{F}_{hz} l_h - (F_{hx} + F_{vx}) h - \hat{F}_{vz} l_v \quad (4)$$

$$0 = \hat{F}_{hz} + \hat{F}_{vz} - mg \quad (5)$$

Note that throughout simulation  $F_{hz}$  and  $F_{vz}$  are limited by the upper bound  $m \cdot g$  and the lower bound 0 to prevent negative values that cannot occur on a street. Where the bounds are not exceeded,  $\hat{F}_{hz}$  and  $\hat{F}_{vz}$  are used.

**Drag.** A drag force  $\mathbf{F}_d$  acts on the point where the fixed rods “chassis” and “trail” are connected in the single track model. The following equations are based on [1].

$$|\mathbf{F}_d| = \frac{\rho}{2} A_{ref} c_d |\mathbf{v}_d|^2 \quad (6)$$

$$\mathbf{F}_d = [F_{dx} \ F_{dy}]^T = \begin{cases} -|\mathbf{F}_d| \frac{\mathbf{v}_d}{|\mathbf{v}_d|} & \text{if } |\mathbf{v}_d| > 0 \\ \mathbf{0} & \text{else} \end{cases} \quad (7)$$

## 2.2 Models with ANN

In the following models the same relations are modeled using ANN. For the **front wheel joint**, the following relations replace those existing:

$$F_{vx} = NN_{WheelJoint\_f\_long}(v_{v,long}, v_{v,lat}, \omega_v) \quad (8)$$

$$F_{v,lat} = NN_{WheelJoint\_f\_lat}(v_{v,long}, v_{v,lat}, \omega_v) \quad (9)$$

In analogy, the same applies to the **rear wheel joint**.

In the case of the **dynamic loads**, the following relations are included:

$$F_{vz} = NN_{dynamicLoad\_front}(F_{hx}, F_{vx}) \quad (10)$$

$$F_{hz} = NN_{dynamicLoad\_rear}(F_{hx}, F_{vx}) \quad (11)$$

And for **drag**:

$$F_{dx} = NN_{drag\_x}(v_x, v_y) \quad (12)$$

$$F_{dy} = NN_{drag\_y}(v_x, v_y) \quad (13)$$

## 2.3 ANN Structure

For this contribution, MLP (as described in [5]) were chosen as function regressors. In future research, other architectures such as RBF networks have to be evaluated as well. Every single perceptron first linearly maps its inputs  $\mathbf{e}$ , of which the last is constantly 1 to account for affine transformation, using its own trainable weight vector  $\mathbf{w}$ . The result  $u$  is then nonlinearly mapped using activation function  $f_A$  to yield its output  $y$ :

$$u = \mathbf{w}^t \cdot \mathbf{e}, \quad y = f_A(u) = \underbrace{\frac{1}{1 - \exp(-u)}}_{\text{sigmoid function}} \quad (14)$$

Multiple of these perceptrons are arranged to form an MLP, see Fig. 2. The result (i.e.  $u$ ) of the last (output) node is not activated. In this application, all networks have **three** hidden layers holding **ten** perceptrons each.

**Training.** The goal of training these MLPs is to minimize the mean squared error (MSE) between ANN output and target output for all known sample points. The latter originate from simulation data of the reference system. Said samples are first randomly split into train and test set of which the latter is not used for training but to measure generalization capabilities of the ANN. During training, a common strategy called **mini-batching** is used. The MSE (and its gradient) is evaluated for “small” batches holding a stochastically selected set of sample points. This information is used by an instance of an Adam-optimizer [8] to update the trainable parameters of the ANN so that the MSE becomes minimal. An epoch is completed when all samples have been used once in a mini-batch after a number of updates depending on sample size and mini-batch size. The whole described process is repeated for a fixed number of epochs.

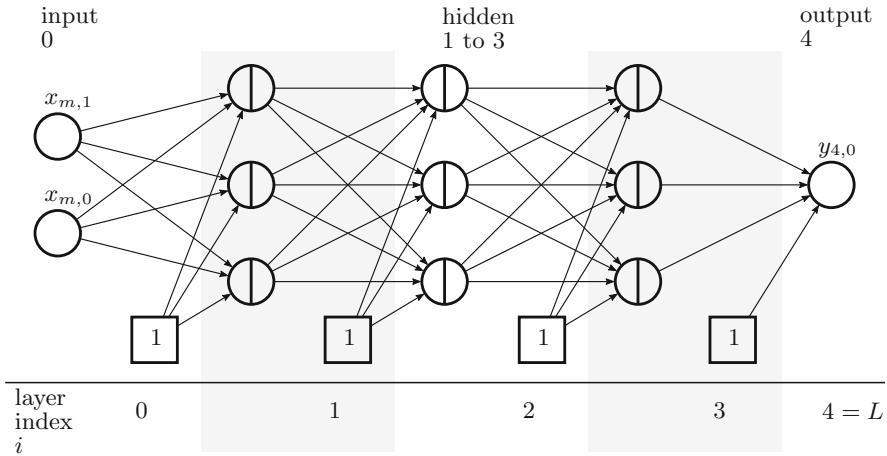


**Fig. 2.** An MLP displayed as a graph. Each node with a vertical line represents a perceptron, each edge stands for a connection. The square nodes have a constant activation of 1. This example network consists of an input layer (two input nodes), three hidden layers (each three perceptrons) and an output layer (one output node).

**Pros and Cons of MLPs.** MLPs can be used to approximate nonlinear functions. They are comparably easy to implement and their architecture is, to some extent, independent of the function to approximate. However, their hyper parameters require iterative tuning. Moreover, due to their feedforward structure, they do not have an internal state and thus can only approximate functions, not dynamic systems. Apart from that, it is not easy to tell how “well” they have learned a function after training. One can only judge their predictions based on the set of learning samples.

## 2.4 Application

In order to distribute learning samples “evenly” within different ANN input spaces, driver models have been developed. Each consists of (a) a steering component and (b) a target velocity setting. As for group (a), **EigtCurves** steers the model along the shape of an 8. **DoubleLaneChange** on the other hand steers the model to a parallel lane and returns the model to the old lane after a short time. As for group (b), **ConstVel** sets a constant target velocity. **ConstAcc** linearly varies the target velocity and **TrapzVel** periodically alters target velocity between two values. During transitions, the target speed is again varied linearly.

The simulation data generated in OpenModelica [4] using the reference model and a driver model is used to train the ANN implemented using Tensorflow [2] within the framework shown in Fig. 3 making use of the Python modules **DyMat** (or alternatively **OMPpython**), **numpy** and **tensorflow**.

In order to make functionality from the Tensorflow C++ API available in Modelica using the **ExternalObject** class, a wrapping library for use in C has

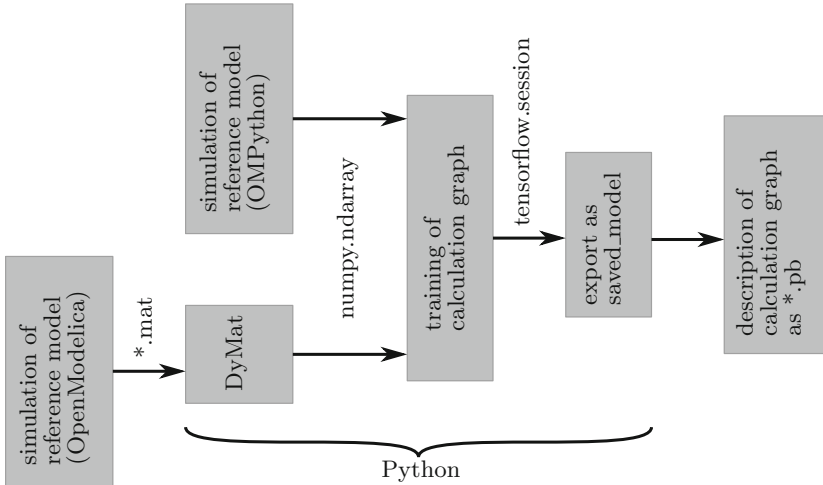


**Fig. 3.** Training

been developed which can be used from Modelica. Using said library it is possible to load a graph from a `*.pb` file and calculate the respective ANN output given a set of inputs.

## 3 Results

### 3.1 Training Process

During the training process, the six individual ANN have shown similar patterns in reducing the MSE as in example Fig. 4. This ANN has been trained on the data generated with the driving component `[EightCurves, TrapzVel]`. At first the MSE of both training and test set is heavily reduced over a few weight updates/learning steps. Both trends shortly become less steep before increasing in speed again. After about 11000 steps, it can be seen that approximation of both sets becomes worse on average. This is a possible outcome due to the stochastic nature of the learning algorithm. What looks like a promising weight update for one mini-batch can lead to worse approximation overall.

### 3.2 Simulation of a Different Maneuver

Two (with ANN “**dynamic loads**” and “**drag**”) of the three new models with ANN show very small differences in behavior compared to the reference system during a maneuver that has not been used to train any of the ANN: `[DoubleLaneChange, ConstVel]`. In Fig. 5, some of the simulated measurement data of the system with ANN for the “**wheel joints**” is shown. The second and third row show how the reference forces are completely different from the ANN



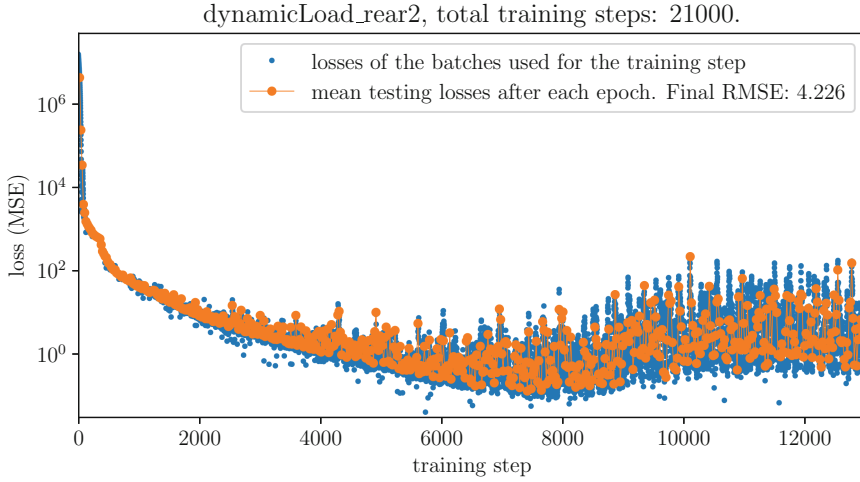


**Fig. 4.** The learning process for  $F_{hz}$ . Blue points: MSE of a single mini-batch used for the next weight vector update. Orange points: MSE of the entire test set after each **epoch**. The final root-mean-square error (RMSE) for the testing set is used as an indicator for regression accuracy (see legend above).

outputs that were supposed to model the exact same functions. For example, the lateral component, from the beginning, is, in contrast to the original, not zero and leads to movement of the vehicle model that can be seen in the first row. This behavior moves the model state into regions with even fewer samples of the learning set, which likely results in larger deviations from the desired outputs. The vehicle model basically reaches a point at which it stops and keeps rotating instead of performing a double lane change.

### 3.3 Requested Points in Feature Space

To get an idea of why the ANN approximating relations for the **wheel joints** do not lead to the desired results, its feature space is compared to that of the ANN for **dynamic loads** with regard to learning set and those data points requested during simulation. In the case of **drag** (not shown due to space limitations), every requested point is surrounded by points of the learning set. In Fig. 6, it can be seen that many of the requested points are still near the learning set (left image). This is not true for the right image in which the red trajectory quickly leaves the proximity of the learning set. Additionally, note that the feature space is covered a lot more sparsely due to its higher dimensionality.

### 3.4 An Approach to Detect Unreliable Extrapolation

Algorithm 1 tries to detect unreliable extrapolation at input point  $\mathbf{P}_{in}$  to an ANN based on its  $n$  nearest neighbors  $N$  in the learning set  $L$ . The target value vector  $\mathbf{r}$  of  $N$  given feature matrix  $\mathbf{A}$  is approximated using a polynomial of

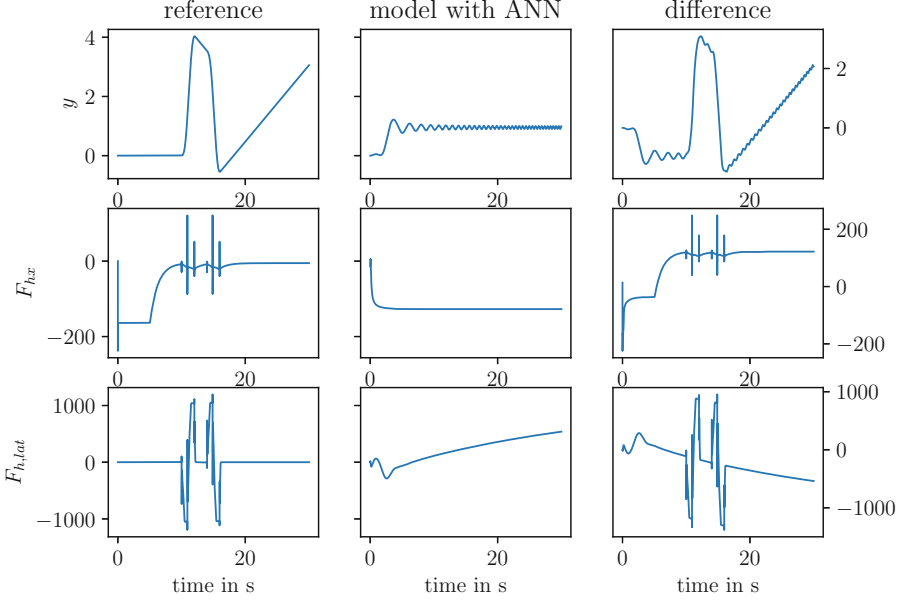
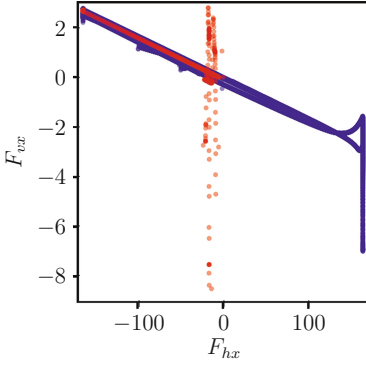
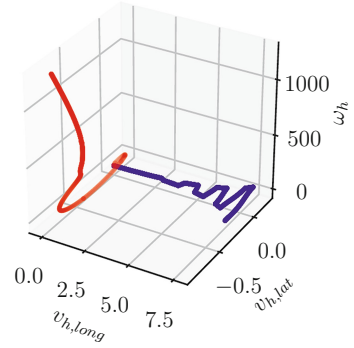


**Fig. 5.** Virtual measurement data of both the reference model and the model with **wheel joints** including ANN. The data was generated using OpenModelica and has been plotted using Matplotlib [7].



(a) dynamic loads



(b) wheel joints

**Fig. 6.** Inputs to ANN. Blue: learning set. Red: inputs during simulation of the double lane change.

order  $o$  (here assumed to be 1) linear in its coefficient vector  $\mathbf{x}$ . Feature Matrix  $\mathbf{A}$ , for  $o = 1$ , holds a 1 and a vector of features per each row for all points in  $N$ .  $\sigma$  measures how well the polynomial approximates  $N$ . If  $\sigma$  is low enough, the difference  $d$  between the polynomial and the ANN output at point  $\mathbf{P}_{in}$  is used to rate the extrapolation of the ANN.

**Algorithm 1.** detect unreliable extrapolation

---

```

1: Choose order  $o \in \mathbb{N}$ . (here 1)
2: Choose ratio  $q \in \mathbb{R}$  holding  $q \in [0, 1]$  (here 0.05).
3: Find the greatest number  $n \in \mathbb{N}$  holding  $n \leq q \cdot |L|$ .
4: for all  $P_{in}$  do
5:   Find the  $n$  nearest neighbors of  $P_{in}$  in  $L$  measured by euclidean 2-norm. These
   form  $N$ .
6:   Solve linear system  $\mathbf{A} \cdot \mathbf{x} = \mathbf{r}$ , to find optimal vector or coefficients  $\mathbf{x}^*$ .
7:   Calculate  $\sigma = \sqrt{|\mathbf{A} \cdot \mathbf{x} - \mathbf{r}|^2 \cdot n^{-1}}$ .
8:   if  $\sigma \geq \sigma_{max}$  then
9:     Do not flag the output as unreliable.
10:  else
11:    Calculate difference  $d$  between polynomial ANN output. In this case:  $d =$ 
     $[1, P_{in,1}, \dots, P_{in,p}] \cdot \mathbf{x}^* - NN(P_{in})$ .
12:    if  $d \geq d_{max}$  then
13:      Do flag the output as unreliable.
14:    else
15:      Do not flag the output as unreliable.
16:    end if
17:  end if
18: end for

```

---

In what follows, thresholds  $\sigma_{max}$  and  $d_{max}$  are not set and  $\sigma$  and  $d$  are regarded separately. In the example of **dynamic loads** on the left of Fig. 7,  $\sigma$  becomes very small because the underlying reference function is piecewise linear. In the case of  $F_{vz}$ ,  $d$  peaks to values of 19.6 N. For comparison, if the reference model does not accelerate, this value becomes 98.1 N, so this is a noticeable deviation with respect to “usual” values. In the context of **wheel joints**,  $\sigma$  of  $F_{hx}$  quickly becomes stationary at 1.26 which indicates an (expected) nonlinearity of the underlying function. Here, however, in the end,  $d$  becomes a lot larger (1.6e6 N). Even at points where  $\sigma$  is still below 0.1,  $d$  is already larger than 100. This behavior makes the ANN extrapolation unreliable with regard to the respective nearest neighbors.

This application demonstrates that  $\sigma$  and  $d$  can help detect unexpected or unreliable ANN extrapolation when  $\sigma$  is, by magnitude, a lot smaller than  $d$ . Nevertheless, the magnitude of  $d$  alone does not account for the actual effect on the system and it remains to be answered in future research how to estimate the impact that  $d$  has on the system.

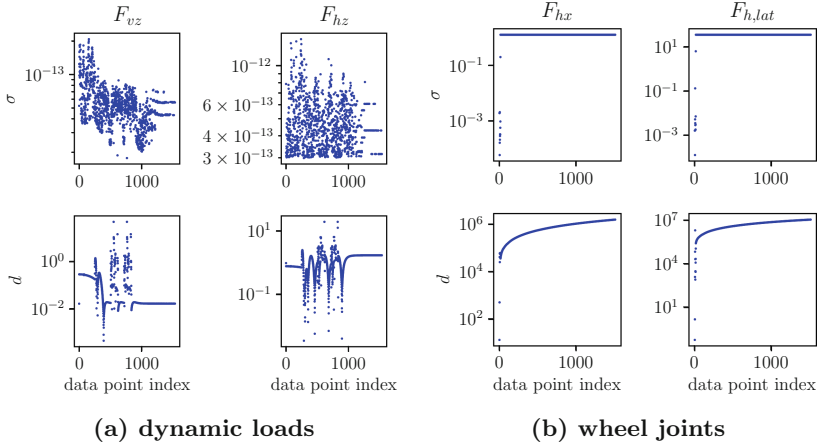


Fig. 7. Values of  $\sigma$  and  $d$  throughout the double lane change.

## 4 Conclusion

In a reference model of a dynamic system written in Modelica, different relations have been modeled using multilayer perceptrons. By means of popular Python modules, they were trained externally on the basis of simulation data of the reference model. This data was generated with the help of driver models which aim to cover regions of the ANN input space as well as possible. The trained ANNs, then in the form of `*.pb` files, were used to replace the respective relations in the reference model. This has been achieved by means of a wrapping library that makes functionality of the Tensorflow C++-API available to C and Modelica. Two (**drag, dynamic loads**) of the three components modeled this way produced desirable results during a maneuver on the basis of which none of the ANN had been trained. The last component (**wheel joints**) could not be modeled adequately according to simulation results. The input spaces have been compared and it became apparent that the ANN of **wheel joints** had requested points far outside the regions more densely occupied by the learning set.

Apart from that, an approach to detect unreliable extrapolation by ANNs has been proposed. It compares the output of an ANN to a polynomial approximation of the neighborhood of a requested input point. The question how to set thresholds  $\sigma_{max}$  and  $d_{max}$ , however, remains subject to further research. An option to find relevant values for  $d_{max}$  could involve sensitivity analysis of a measured variable to deviations in  $d$ . This strategy aims to address similar problems as the field of “anomaly detection”, for which [3] names several approaches such as kernel-based density estimation.

In order to apply the modeling approach described in this contribution to a real system, certain problems have to be solved. In order to find out which relations in an existing model should be altered to enhance model accuracy, different approaches exist. One option is to estimate the parameters of a statistical differential equation (SDE) as described in [9]. Once said relations are found, it is important to find a relevant set of predictors/input variables to the relations. In [6], reasons to reduce the number of said predictors are given. One class of approaches to find a good set of variables are so-called “wrapper”-methods which train models with different sets and rate those by e.g. accuracy metrics like the MSE. The ANNs in this contribution were not regularized. Others (e.g. [13]) have shown that the introduction of such techniques can help improve model generalization.

## References

1. Modern drag equation (2014). <https://wright.nasa.gov/airplane/drageq.html>
2. Abadi, M., Agarwal, A., Barham, P., Brevdo, E., Chen, Z., Citro, C., Corrado, G.S., Davis, A., Dean, J., Devin, M., Ghemawat, S., Goodfellow, I., Harp, A., Irving, G., Isard, M., Jia, Y., Jozefowicz, R., Kaiser, L., Kudlur, M., Levenberg, J., Mané, D., Monga, R., Moore, S., Murray, D., Olah, C., Schuster, M., Shlens, J., Steiner, B., Sutskever, I., Talwar, K., Tucker, P., Vanhoucke, V., Vasudevan, V., Viégas, F., Vinyals, O., Warden, P., Wattenberg, M., Wicke, M., Yu, Y., Zheng, X.: TensorFlow: Large-scale machine learning on heterogeneous systems (2015). software available from tensorflow.org, <https://www.tensorflow.org/>
3. Chandola, V., Banerjee, A., Kumar, V.: Anomaly detection: a survey. *ACM Comput. Surv. (CSUR)* **41**(3), 15 (2009)
4. Fritzson, P., Aronsson, P., Lundvall, H., Nyström, K., Pop, A., Saldamli, L., Broman, D.: The openmodelica modeling, simulation, and development environment. In: 46th Conference on Simulation and Modelling of the Scandinavian Simulation Society (SIMS2005), Trondheim, Norway, October 13–14, 2005 (2005)
5. Goodfellow, I., Bengio, Y., Courville, A.: Deep Learning. MIT Press (2016). <http://www.deeplearningbook.org>
6. Guyon, I., Elisseeff, A.: An introduction to variable and feature selection. *J. Mach. Learn. Res.* **3**(Mar), 1157–1182 (2003)
7. Hunter, J.D.: Matplotlib: a 2D graphics environment. *Comput. Sci. Eng.* **9**(3), 90–95 (2007). <https://doi.org/10.1109/MCSE.2007.55>
8. Kingma, D.P., Ba, J.: Adam: a method for stochastic optimization. arXiv preprint [arXiv:1412.6980](https://arxiv.org/abs/1412.6980) (2014)
9. Madsen, H.: Statistical modelling of physical systems. [http://iesi.org/assets/pdfs/101\\_madsen\\_4.pdf](http://iesi.org/assets/pdfs/101_madsen_4.pdf)
10. Prada Moraga, C.D., Hose, D., Gutierrez, G., Pitarch, J.L.: Developing grey-box dynamic process models (2018)
11. Raissi, M., Perdikaris, P., Karniadakis, G.E.: Multistep neural networks for data-driven discovery of nonlinear dynamical systems. arXiv preprint [arXiv:1801.01236](https://arxiv.org/abs/1801.01236) (2018)
12. Schramm, D., Hiller, M., Bardini, R.: Modellbildung und Simulation der Dynamik von Kraftfahrzeugen, vol. 124. Springer, Heidelberg (2010)

13. Srivastava, N., Hinton, G., Krizhevsky, A., Sutskever, I., Salakhutdinov, R.: Dropout: a simple way to prevent neural networks from overfitting. *J. Mach. Learn. Res.* **15**(1), 1929–1958 (2014)
14. Zimmer, D.: A planar mechanical library for teaching modelica, pp. 681–690, 09 2012. 10.3384/ecp12076681
15. Zimmer, D., van der Linden, F., Zheng, Q.: Planarmechanics - a free modelica library for planar mechanical multi-body systems (2019). <https://github.com/dzimmer/PlanarMechanics>

# **Sensors and Actuators**



# Development of an Interactive System for a Companion Robot Based on Telepresence Technology

Siyu Chen<sup>1</sup>, Ligang Yao<sup>1(✉)</sup>, Yehliang Hsu<sup>2</sup>, and Teddy Chen<sup>2</sup>

<sup>1</sup> Fuzhou University, Fuzhou 350108, People's Republic of China  
ylgyao@fzu.edu.cn

<sup>2</sup> Yuan Ze University, Chung-Li, Taiwan 32003, R.O.C.

**Abstract.** As the population ages, there is an increasing need for socio-emotional support for older adults. To meet the socio-emotional support requirement, a companion robot, named as Wobot, is developed. The Wobot composed of a tablet and docking station, with voice dialogue, Internet of Things control function. This paper is focusing on a new interactive system for the companion robot developed by using the telepresence technology. The elderly call a video phone by voice control, and the remote user can manipulate robot action when making video call. It can create more diverse interpersonal communication experience for the elderly and build a stronger relationship with the children.

**Keywords:** Companion robot · Interactive system · Telepresence technology

## 1 Introduction

The world population is ageing rapidly with the percentage of older adults increasing to 24% by 2030 from 10% in 2000 [1]. Therefore cost of providing aged care has been growing [2]. However, with the change of living patterns, the children have no time to take into account the mood of their elders and solve their loneliness. Robotic technology has been identified as being able to help older adults to live independently [3]. Japan has already launched several companion robots designed for the elderly, such as Paro, developed by Japan Institute of Industrial Technology, to meet the emotional and spiritual level of interactive robots [4]; Kribo, developed by KIBO Robot Project, can communicate with human beings through dialogue. However, most of these companion robots belong to self-disciplined robots. They can only give fixed feedback to external stimuli and lose their freshness as time goes on [5]. Norman [2005] proposed that robots should be partners or media for human interaction with others, rather than replacing people's original contact and interaction [6].

Compared with the companionship provided by companion robots, the real interactive conversation between people is more vivid and changeable, or because of the work requirement, there will be the need to talk to each other face to face, get the auditory and visual information of each other's location, so there will be a "Telepresence



Robot” [7]. Telepresence technology is common in the use of interpersonal communication and interaction in video conferencing. Later, robots using telepresence technology have been created. The main goal of this type of robot is to eliminate the restriction of space separation between people. What is more, it acts as the agent of the remote user to roam around the proximal user and interact with the proximal user. For example, the telepresence robot Beam created by Sutable Technologies (<http://suitabletech.com>) for mobile video conferencing; the telepresence robot RP-VITA (Care Presence Virtual and Independent Telemedicine Assistant) developed by iRobot in collaboration with InTouch Health for telemedicine [8]; and Telenoid R1, a telepresence robot developed by Osaka University and International Institute of Electrical and Communication Technology [9]. However, the cost of the above-mentioned robots is relatively high and the price is expensive, and the subsequent functional scalability is complex.

In recent years, due to the vigorous development of smart mobile devices such as the iPhone and Android, smart mobile devices have also affected the design of robotic products [10]. Intelligent mobile devices as the control center, the product itself only provides vehicles; software can be downloaded from the online application store; manufacturers in the development of novel features can quickly let users experience and get feedback; and hardware carrying the functions can be cheaper and more acceptable to users. All complex logic operations and sensing can be accomplished by smart mobile devices.

The companion robot designed in this study has multiple companion functions, such as voice dialogue, cooperating with elderly rehabilitation game and so on. This paper focuses on an interactive system by using the telepresence technology, cloud service and application implemented on the tablet computer, remote users can make a video call with proximal users and control the Wobot action. Through experience, the children working outside and the elderly at home can share their life and care in real time, so that they can shorten the distance between their souls.

## 2 Presentation of Wobot

Wobot consists of a tablet and docking station as shown in Fig. 1, using the Body-cerebellar-brain architecture. The robot base mechanism and servo motor are the “Body” in the system, for the realization of the action and the support of the robot; “Cerebellar” refers to the control chip, including the servo motor control chip and the Bluetooth chip, which is the bridge between “Body” and “Brain”; “Brain” is the tablet, which has its own Internet and video communication functions, sending commands to the robot base mechanism. This hardware-matched software model makes development more flexible and easy.

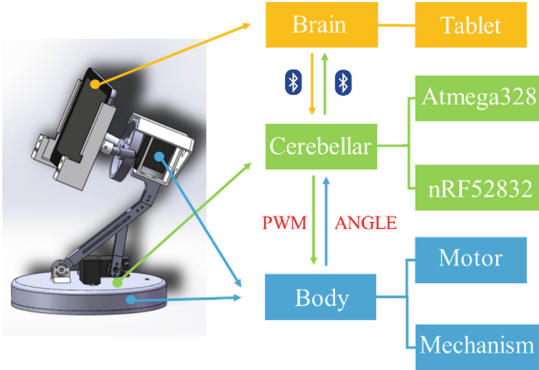


Fig. 1. Wobot model and architecture

The overall operating architecture of Wobot is shown in Fig. 2. It consists of six technical modules, namely the Proximal communication module, the Voice function module, the Emoticon animation module, the Bluetooth connection module, the Action module and the Remote communication module. Wobot has a Voice function module, which can realize voice dialogue, information query and IoT home appliance control in natural language.

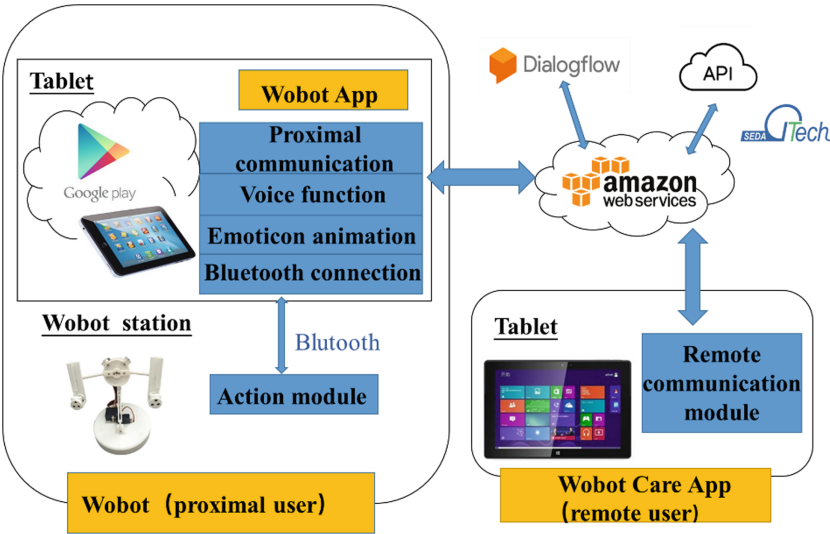


Fig. 2. Wobot system architecture diagram

The overall process of Wobot’s system architecture is as follows: the proximal user opens the Wobot App, communicates with Wobot through the “Voice function module”, and the “Emotion animation module” plays the situation animation during the

communication process, and transmits the Bluetooth by the “Bluetooth connection module”. Command the “Action module” in the base of the Wobot robot to make the corresponding action. The “Proximal communication module” in the Wobot App can make a video call to a remote user who has a Wobot Care App with a “Remote communication module”. The design of the Telepresence interactive system will be described in detail in the next section.

### 3 Interactive System

According to the interaction relationship between Wobot users and remote users, Wobot users divide into “proximal” and “remote” users, which are “proximal users” in the same space as Wobot and “remote users” of operating robots in another space. Proximal users can communicate with remote users via cameras, microphones on tablets and video communications App (Fig. 3). The remote user can send action commands to the background resident program Wobot App on the proximal user Tablet through Wobot Care App. After Wobot App confirms the action commands, which is transmitted to the docking station by Bluetooth, and then the docking station will track the proximal user or monitor the surrounding environment.

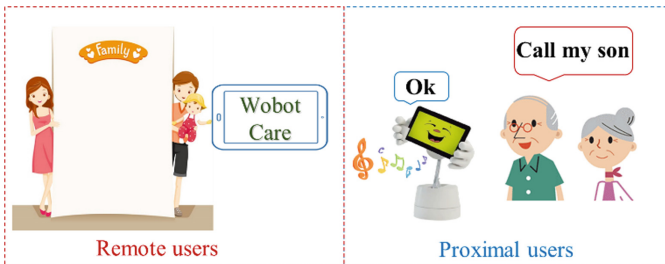


**Fig. 3.** Interactive situation

Information transfer process is described according to the information flow diagram in Fig. 4:

First, the proximal user opens Wobot App, wakes Wobot up successfully, and sends video instructions to Wobot App. Second, Wobot App has speech recognition function, which transfers the user’s voice in JSON format to Dialogflow by HTTP. Third, Dialogflow processes voice and transmits related content to AWS IoT via HTTP in JSON format. Next, AWS IoT service sends relevant content to Wobot Care App of remote users through MQTT transmission mode. Then, Wobot Care App sends back instructions to AWS IoT. Finally, AWS IoT is sent back to Wobot App, both of which establish video calls through FCM.

During the call, remote users can use MQTT to transmit action instructions to AWS IoT through Wobot Care App. AWS IoT transmits action instructions to Wobot App, which is the resident program of proximal users.

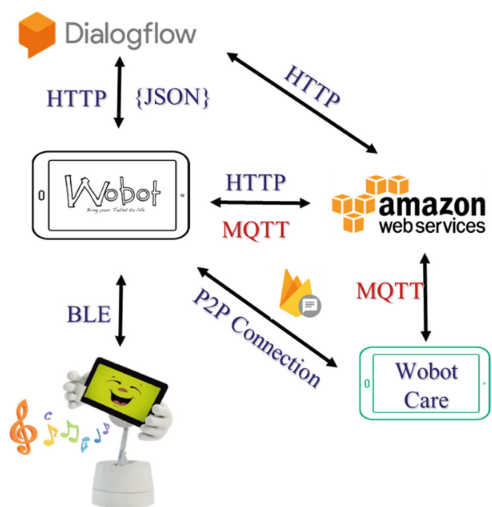


Fig. 4. Information flow diagram

3.1 Wobot and Wobot Care App Design and Development

Wobot system includes two important applications, Wobot Care App for remote control and Wobot App for proximal receiving instructions and executing them.

The software module diagram of Wobot App is shown in Fig. 5, including login, home and sign out screens. The background service includes account login or logout, wake-up words for wake-up of the robot; cloud server Amazon; voice processing platform Dialogflow for voice recognition; call establishment scheme WebRTC; BleConnect for Bluetooth connection and action command transmission.

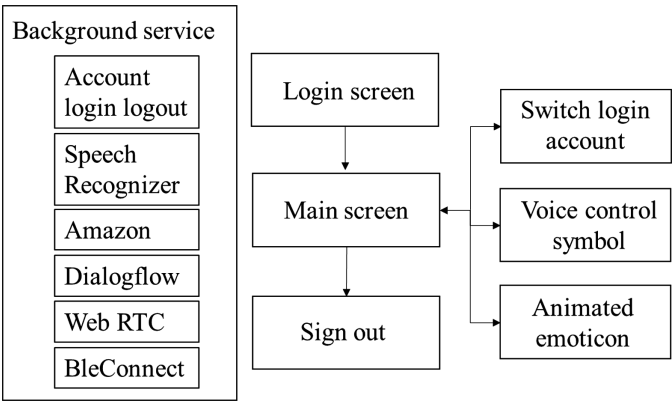


Fig. 5. Software module diagram of Wobot App

To achieve the above process, Wobot App builds three functions: Bluetooth connection, video communication and remote control.

Bluetooth connection uses bleConnect function in Android function library module com.inuker.bluetooth.library:1.4.0 to connect with Wobot Bluetooth and transmit instructions;

Video calls use the Call function in libjingle\_peerconnection function library module to establish communication links, and use the CallNotify function in com.-google.firebase:firebase-messaging:15.0.2 function library module to realize FCM calls pushing;

Remote control uses mqttManager. connect function in com.amazonaws:aws-android-sdk-iot: 2.6.6 function library module to establish an online connection with AWS IoT, and uses mqttManager. subscribe ToTopic function to receive control instructions from Wobot Care App.

In order to realize remote control function, AWS IoT in AWS service is used as MQTT Broker.

The software module diagram of Wobot Care App (Fig. 6) is similar to that of the Wobot App, except that there is action commands displayed in the main interface.

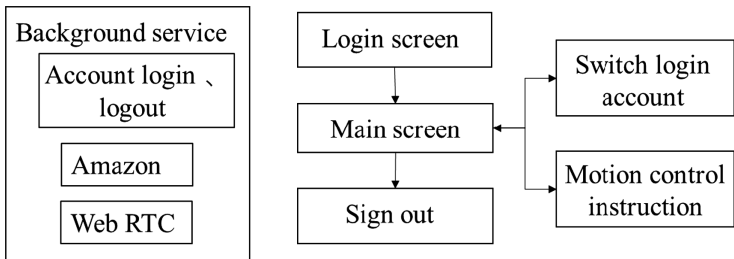


**Fig. 6.** Software module diagram of Wobot Care App

### 3.2 Action Control Program for Servo Motors

The motion of the Wobot is controlled by the servo motor. We write the servo motor control program designing for remote user in the control chip. The remote user can adjust the angle of the base of the robot and adjust the four directions of up, down, left, and right. Because of the adjustment, the angle control procedure as follows: after the program is burned into the motor control board, if the received command is the same as the motion command code, the content is encoded according to the motion command, and the angle is fine-tuned until the action is completed. If the receive command is not an identifiable command, it will return the error to the Wobot App and wait for the receive character again (Fig. 7).

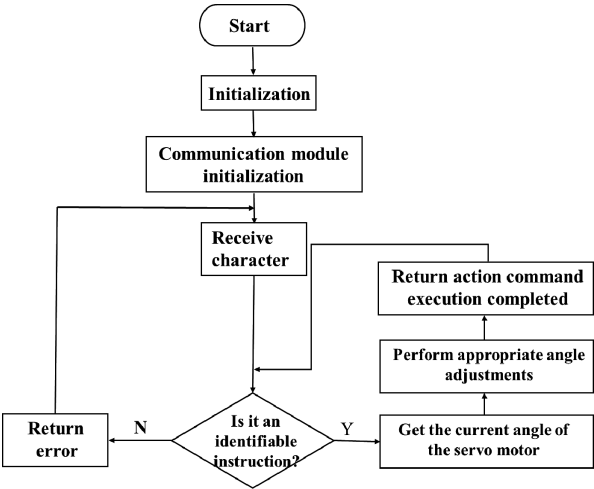


Fig. 7. Servo motors control program flow-process diagram

4 Preliminary Experiments

When the proximal user places a video call command, the proximal Wobot App and the remote Wobot Care App are connected. The remote user can control the button according to the video interface action of the Wobot Care App (Fig. 8), adjust the Wobot base motion, and provide more interactive and interesting communication methods.

At the result, the success rate of the videophone dialing is 86% according to the data provided by the Dialogflow, and the motion control command has a little delay, but the whole call process is smooth, and the pre-operation command can be completed, which meets the design requirements.

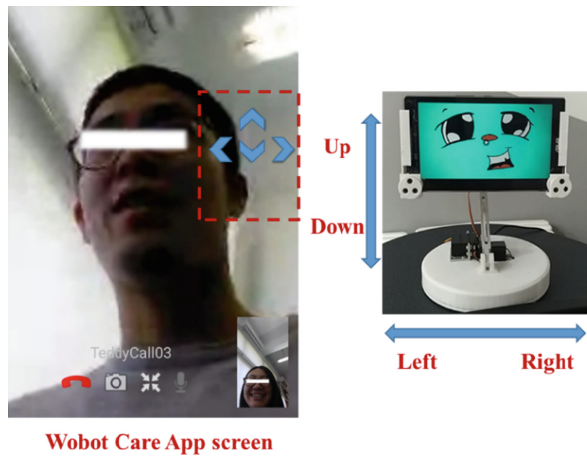


Fig. 8. Remote control screen and Wobot physical model

## 5 Conclusions




This study has developed an interactive system for a companion robot using the telepresence technology. Remote users can make a video call with proximal users and control the Wobot action. Users can use the Wobot Care App's user interface to transmit action commands, receive and execute commands in the background's Wobot App, and enrich the original video communication. Experiments show that it meets the design requirements. Combining cloud services to reduce robot development costs, Wobot App update features or maintenance are fully auto-updated through the app store. The next step is to enrich the interactive system, such as transmission emoticons or gif to proximal users.

## References

1. Shishehgar, M., et al.: A systematic review of research into how robotic technology can help older people. *Smart Health* **7–8**, 1–18 (2018)
2. Tomaka, J., et al.: The relation of social isolation, loneliness, and social support to disease outcomes among the elderly. *J. Aging Health* **18**, 359–384 (2006)
3. Abdi, J., et al.: Scoping review on the use of socially assistive robot technology in elderly care. *BMJ Open* **8**, e018815 (2018)
4. Moyle, W., et al.: Effect of a robotic seal on the motor activity and sleep patterns of older people with dementia, as measured by wearable technology: a cluster-randomised controlled trial. *Maturitas* **110**, 10–17 (2018)
5. Dentsu Inc. Robot Astronaut Kirobo Awarded Two GUINNESS WORLD RECORDS™ Titles. *Business Wire (English)* (2015)
6. Norman, D.A.: Robots in the home: What might they do? *Interactions* **12**, 65 (2005)
7. Song, A.: Research on human-robot interaction telerobot with force telepresence. *Sci. Technol. Rev.* **33**, 100–109 (2015)
8. Doctor on Wheels: *Technol. Rev.* **115**, 16 (2012)
9. Ishii, C.T.: Telenoid: tele-presence android for communication. In: *ACM SIGGRAPH Emerging Technologies*, vol. 15 (2011)
10. Papcun, P., et al.: Control and teleoperation of robot khepera via android mobile device through bluetooth and WiFi. *IFAC PapersOnLine* **49**, 188–193 (2016)



# Motion Experiment of Reducer-Integrated Motor Using Inscribed Planetary Gear Mechanism

Tatsuro Terakawa , Masaharu Komori  , Ryo Kataoka,  
Yuya Morita, and Shouta Tamura

Kyoto University, Kyoto daigaku-katsura, Nishikyo-ku, Kyoto 6158540, Japan  
komorim@me.kyoto-u.ac.jp

**Abstract.** The motors for industrial robots and transporting robots are required to have high-precision positioning, large torque output, and small size. However, conventional motor systems have disadvantages in size or load-supporting capacity. To solve the problems, we proposed a novel reducer-integrated motor. The proposed reducer-integrated motor has a reducer using the differential gear mechanism which realizes the simultaneous engagement of two kinds of external and internal gear pairs: one with a small difference in teeth number and the other with no difference in teeth number. Inside the reducer, linear actuators are installed, which contributes to downsizing of the motor. Additionally, two gear pairs with no difference in teeth number are fixed on the base and the gear pair with a small difference in teeth number is set between them. These two kinds of gear pairs engage simultaneously and support the load torque. It is thought that the structure of the proposed motor can realize high load-supporting capacity and high stiffness. In this paper, the structure and movement of the proposed motor are explained. Then, the experiments are conducted to clarify the optimal input pattern for the accurate rotation by using the prototype of the proposed motor. Through the measurement, the optimal input pattern is suggested.

**Keywords:** Motor · Reducer · Differential gear mechanism

## 1 Introduction

The motors that have high-precision positioning and large torque output are required in the fields of industrial robots and transporting robots, though conventional electromagnetic motors have high-speed and low-torque output. To overcome these gaps, motors combined are used with reducers. However, the conventional reducers utilize multistage trains of spur gear pairs or planetary gear mechanisms to gain high reduction ratios and therefore become large and heavy. They cause the entire motor system to be large and heavy.

To solve this problem, reducer-integrated motors using the differential gear mechanism of an inscribed planetary gear, or a KHV planetary gear [1–4] have been proposed. For example, cycloid motors [5] and wobble motors [6] consists of an external gear, an internal gear, and linear actuators. The internal gear, which is pushed by the linear actuators from the outside to the center, revolves around the external gear.



Meanwhile, the external gear rotates by the difference in teeth number from the internal gear. Thus, the reducer-integrated motors can output a reduced rotation directly from the input of the linear actuators. It derives an advantage in the downsizing of motors. However, this type of motors has disadvantages in limited load-supporting capacity and stiffness, because the linear actuators need to support the load torque applied to the output part in the circumferential direction. Then, some of the authors previously proposed a reducer-integrated motor using the strain wave gearing system [7]. That proposed motor is expected to achieve high load-supporting capacity and high stiffness because the load torque is supported by two internal gears fixed on the base thanks to the simultaneous engagement of three gear pairs. However, this motor has difficulties in design and production due to an elastic and flexible external gear.

To address this issue, we proposed a novel reducer-integrated motor using only rigid gears and realizing simultaneous tooth engagement [8]. We designed the differential gear mechanism in which the gear pair with a small difference in teeth number and the gear pairs with no difference in teeth number engaged simultaneously. This gear mechanism realizes a high reduction ratio, which helps the motor to achieve downsizing similarly to the existing reducer-integrated motors. At the same time, two internal gears fixed on the base support the load torque applied to the motor, and then the motor can gain high load-supporting capacity and high stiffness. In this paper, we discuss and evaluate the movement of the proposed motor. The structure and movement of the motor are explained first. Then, the experiments are conducted using the prototype and the optimal input pattern is suggested.

## 2 Proposed Reducer-Integrated Motor

Figure 1 shows the schematic structure of the proposed reducer-integrated motor. One ringed rigid external gear engages simultaneously with two kinds of internal gears, one A gear and two B gears. The internal A gear has one more tooth than the external gear, and the two internal B gears have the same teeth number as the external gear. The two internal B gears are placed coaxially on both sides of the internal A gear. Inside the external gear, linear actuators are arranged radially at equal intervals and fixed on the base. Each linear actuator (e.g., linear solenoids) can actively elongate and shrink in the radial direction. The external gear can rotate and move in the radial direction freely. The internal A gear is supported to rotate around the central axis. The two internal B gears are fixed on the base and do not rotate.

Next, we explain the movement of the proposed motor considering the situation where the neighboring two linear actuators are operated at the same time and switched clockwise, as shown in Fig. 2. When the linear actuators are operated and push the external gear, the external gear moves in the radial direction and engages with the internal A and B gears. The teeth number of the external gear is the same as those of the internal B gears fixed on the base, so that the external gear does not rotate but revolves around the internal circumferences of the internal gears. When the external gear revolves, the internal A gear rotates according to the difference in teeth number from the external gear, that is, every clockwise revolution of the external gear causes rotation of internal A gear by the teeth number difference. This means that the proposed motor

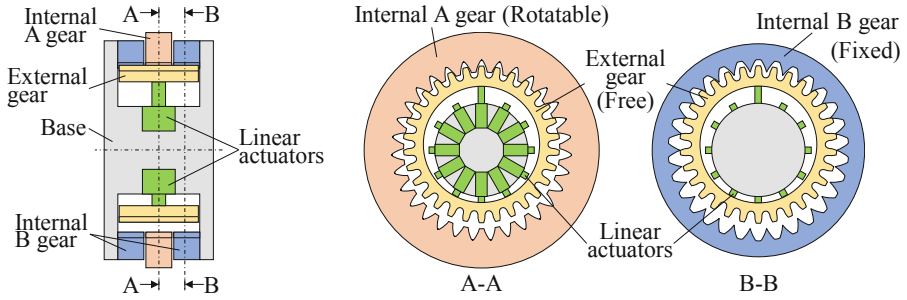


**Fig. 1.** Structure of the proposed reducer-integrated motor [8]

can directly output a reduced rotation. When we set the switching linear actuators as the input and the rotation of the internal A gear as the output, the reduction ratio  $R$  is represented by

$$R = \frac{z_2}{z_2 - z_1} = z_2 \quad (1)$$

where  $z_1$  and  $z_2$  are the teeth numbers of the external and the internal A gear, respectively.

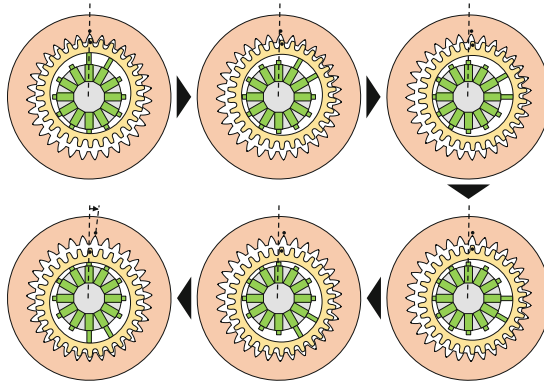


**Fig. 2.** Rotation of the internal A gear by the revolution of the external gear

The proposed motor has the following characteristics: First, the linear actuators are installed inside the reducer, which contributes to downsizing of the entire motor system. Next, the load torque applied to the internal A gear is supported by the internal B gears fixed on the base through the external gear, so that the linear actuators do not receive the circumferential force directly. Therefore, the proposed motor can support high load torque and gain high stiffness. Additionally, because the internal B gears are put on both sides of the internal A gear, the torque on the external gear from the

internal gears become symmetrical in the axial direction. These symmetrical torques are expected to suppress the tilt and torsion of the external gear and increase the stiffness of the motor. Finally, the proposed motor consists of rigid external and internal gears and does not need special gears, such as elastic gears. Then, it is thought to be relatively easy to produce the reducer of the motor.

### 3 Motion Experiment

In the proposed reducer-integrated motor, various input patterns are available. In order to investigate the optimal input pattern for the motor to rotate accurately, we conduct the experiments.

We introduce the prototype used in the experiments. The overview and properties of the developed prototype are shown in Fig. 3 and Table 1, and the specifications of the produced gears are shown in Table 2. In Fig. 3(b), the internal A gear is exposed by removing one of the two internal B gear and the external gear to show the internal structure. The basic structure of the prototype is the same as that in Fig. 1, and 12 linear solenoids are installed as the linear actuators. Though we used large linear solenoids to gain certain force output in order to confirm the movement, the linear solenoids are put outside the gears because of their size. Hence, the output of the linear solenoids is transmitted to the external gear through the connecting parts and the pushing parts as shown in Fig. 3(c). A programmable logic controller (PLC) operates the movement of the prototype. The PLC switches the linear solenoids on and off at the designated timing. It can also measure the rotation angle of the output part with the laser displacement sensor. In the measurement of the rotation angle, the distance is measured between the laser displacement sensor fixed on the base and the reflecting plate fixed on the internal A gear and moving in the circumferential direction with the output part rotation. The displacement of the reflecting plate from the initial position in the progressing direction of the laser is converted into the rotation angle.

By using this prototype, the experiments were conducted. In this paper, we targeted four fundamental input patterns, i.e., the stepping movements. Figure 4 shows the four input patterns. In Pattern 1, only one linear solenoid is used at the same time. In Pattern 2, the number of working linear solenoids alternates between one and two. The pushing force when two pairs are operated is half of the power when one pair is operated. Pattern 3 is the same movement as shown in Fig. 2, where two linear solenoids always push the external gear. In Pattern 4, two linear solenoids are used at the odd-numbered steps and three linear solenoids are used at the even-numbered steps. When three pairs are operated, the power of the linear solenoids on the sides is half of that of the linear solenoid in the middle. According to the result of the observation, the motor prototype rotated properly as expected.

Figure 5 shows the measured and theoretical rotation angle in each input patterns with 500-ms intervals of steps. In Pattern 1, the measured rotation angle draws the steps as expected, but there occur almost constant errors. Note that the results are offset so that the theoretical and measured values match at the initial time. It suggests that the error is caused mainly in the first step for some factors, such as friction between the teeth surfaces and lack of pushing power. In Pattern 2, the errors are relatively small at

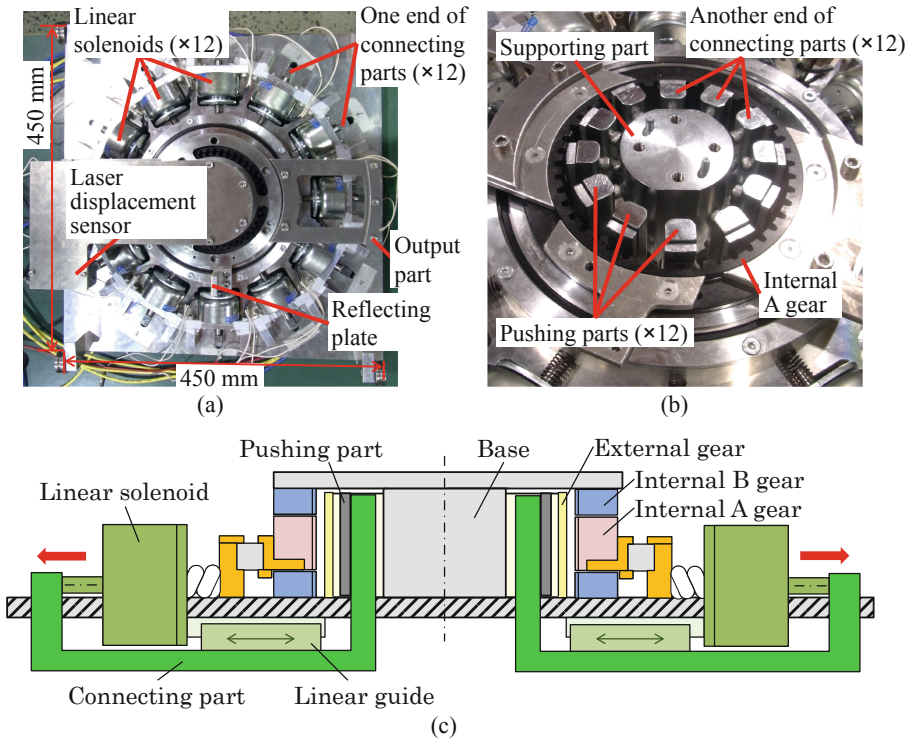


**Fig. 3.** (a) Overview of the motor prototype. (b) Internal structure. (c) Sectional view.

**Table 1.** Properties of the proposed reducer-integrated motor prototype

Entirety of prototype	Width	450 mm
	Depth	450 mm
	Height	150 mm
Linear solenoid	Model	Shindengen Mechatronics Co., Ltd., 6EF AWG. No. 20
Laser displacement sensor	Model	KEYENCE Corporation, LK-G150
	Resolution	1 $\mu\text{m}$
	Sampling period	1 ms

the even-numbered steps except for the second step, while rotation hardly occurs and large errors arise at the odd-numbered steps. This means that the motor rotates properly only when two linear solenoids are operated at the same time. Actually, in Pattern 3, where two linear solenoids are always operated, the measured rotational angle matches the theoretical angle well. On the other hand, relatively large errors occurred again in

**Table 2.** Specifications of the gears used in the proposed reducer-integrated motor prototype

	External gear	Internal A gear	Internal B gear
Module		3	
Reference pressure angle (°)		20	
Teeth number	43	44	43
Profile shift coefficient	−1.21	−0.91	0.7687
Addendum coefficient	0.60	0.35	2.0
Root circle diameter (mm)	115.14	132	132
Facewidth (mm)	52	26	$12.5 \times 2$
Inner diameter (mm)	110.4	–	–
Outer diameter (mm)	–	170	170

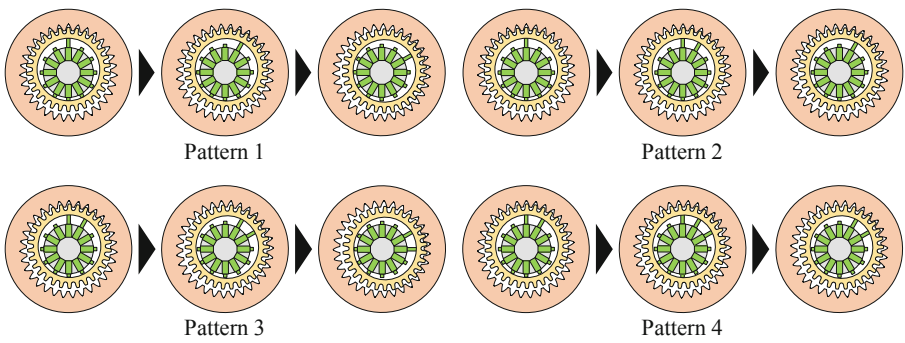


**Fig. 4.** Four input patterns for the experiments

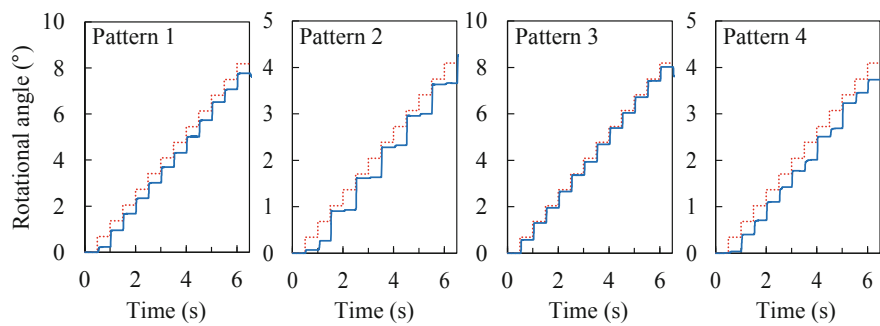


**Fig. 5.** Measured rotation angle for the experiments. The blue solid line indicates the measured rotation angle and the red dashed line indicates the theoretical rotation angle.

Pattern 4. Here, the measured rotation seems to delay by nearly one step compared to the theoretical value. This might be because the output force disturbance of the linear actuators caused a problem between the first and second steps when the power distribution of the linear actuators is changed.

By taking a closer look at the measured results, we compare the average step angle errors. The step angle error is the difference between the theoretical and measured values in the rotation angle of the internal A gear at each step. The theoretical step angle is given by  $360/nR$  where  $n$  is the number of steps to switch the linear solenoids in one round. The reduction ratio  $R$  coming from Eq. (1) is 44 in the prototype. Namely, the theoretical step angle is  $0.682^\circ$  in Pattern 1 and 3 where  $n = 12$ , and  $0.341^\circ$  in Pattern 2 and 4 where  $n = 24$ . When we take the average value of the step angle errors in 130 steps to the theoretical step angles in each pattern, the results are shown in Fig. 6. Obviously, the error in Pattern 2 is larger than the others as discussed above. Compared to Pattern 1 and 3, Pattern 4 causes a larger error. Thus, the change of the number of the operating linear solenoids may bring a negative effect in the accuracy of rotation. The error in Pattern 3 is smaller than those in Pattern 1. In fact, no linear solenoids can work on switching the linear solenoids between the steps in Pattern 1, so that the rotation may be uncertain. It causes a problem especially when load torque is applied to the motor. From the above, we conclude the optimal input pattern would be Pattern 3.

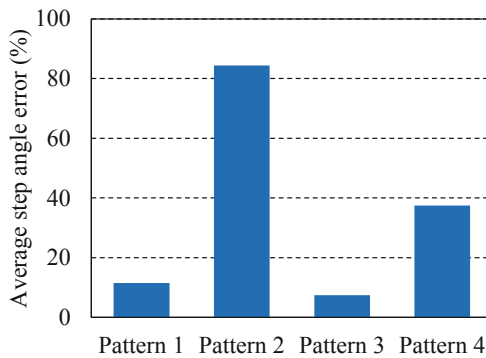


**Fig. 6.** Average step angle errors in the experimental results

## 4 Conclusions

In order to solve the problems of the conventional motor systems, we proposed a novel reducer-integrated motor using the inscribed planetary gear mechanism. In this paper, we conducted the experiments to find the optimal input pattern for the accurate rotation by using the prototype of the proposed motor. As a result of the observation and measurement, the input pattern where neighboring two linear actuators were always operated was suggested to be the optimal pattern.

**Acknowledgment.** The authors would like to thank AMTEC INC. for their support in this research.

## References

1. Kinki Gear Association ed.: Design and manufacturing of gears (I), TAIGA Publishing, Tokyo (1971). (in Japanese)
2. Yu, D.: KHV planetary gear. *Gear Technol.* **1987**(6), 21–48 (1987)
3. Yu, D.: KHV planetary gear - Part II. *Gear Technol.* **1988**(1), 28–48 (1988)
4. Morozumi, M.: The Theory and Design Calculation Method of Planetary Gears and Differential Gears. The Nikkan Kogyo Shimbun, Tokyo (1989). (in Japanese)
5. Hayashi, I., Iwatsuki, N., Kawai, M., Shibata, J., Kitagawa, T.: Development of a piezoelectric cycloid motor. *Mechatronics* **2**(5), 433–444 (1992)
6. Suzumori, K., Hori, K.: Development of pneumatic wobble motors. *JSME Int J., Ser. C* **42**(2), 392–397 (1999)
7. Terakawa, T., Komori, M., Morita, Y.: Reducer-integrated motor using the principle of strain wave gearing system. *J. Jpn. Soc. Des. Eng.* **52**(11), 683–694 (2017). (in Japanese)
8. Terakawa, T., Komori, M., Tamura, S., Kataoka, R., Morita, Y.: Reducer-integrated motor using simultaneous engagement of gear pairs with small and no differences in teeth number. *J. Adv. Mech. Des. Syst. Manuf.* **12**(1), JAMDSM0014 (2018)



# Conductive Fabric Strain Sensor Design and Electromechanical Characterization

Jun Liang Lau<sup>1</sup>(✉), Hwee Choo Liaw<sup>2</sup>, and Gim Song Soh<sup>1</sup>(✉)

<sup>1</sup> Singapore University of Technology and Design,  
Singapore 487372, Singapore  
junliang\_lau@mymail.sutd.edu.sg,  
sohgimsong@sutd.edu.sg

<sup>2</sup> DigiPen Institute of Technology Singapore, Singapore 139660, Singapore

**Abstract.** The design of strain sensor made from conductive fabrics (CF) requires precise characterization prior to their intended use. However, the electrical signals produced by the direct resistance measurements of CF are irregular and have high deviation which affects its performance as a wearable strain sensor. In this paper, we explore an alternative design, where the electromechanical property of a CF is characterized under the application of a small constant current. The result showed an improvement in the maximum standard deviation of its electrical signals from 0.2 to 0.06 for a commercially available CF. Apart from enhancing the reliability of the commercial CF, we also found that a variety of strain axes, besides its principal course axis, can be used in the design of the fabric sensor.

**Keywords:** Conductive fabrics · Wearable strain sensor · Sensor characterization

## 1 Introduction

The capabilities of collecting daily information during our human motion activities hold particular interest in clinical and sports application [1]. Over recent years, the used of flexible strain sensor made from conductive fabrics (CF), have received many research interests in applications for human motion monitoring [2–4] and medical technology [5, 6].

CF exhibits piezo-resistive effect and has a highly elastic property. The piezo-resistive effect led to electrical property changes during deformation and its high elastic property makes them highly suitable for use as wearable sensors. However, its development as a wearable sensor requires tactful characterization process for its electromechanical property [7]. Such property is dependable on the yarn direction, thread material [8], coating material and geometry. For a good review, refer to [9, 10]. Most CF knitted yarn structure is constructed through wales direction (WD) and courses direction (CD) which is based on two knit types, namely the weft and warp knit [11] as shown in Fig. 1. To achieve conductive behavior, three approaches are used based on their thread embodiment types: (i) twisting of metal wires around the yarn; (ii) coating the yarn with a thin metal layer; and (iii) embedding metal fiber directly into the thread. For details, see [12, 13].



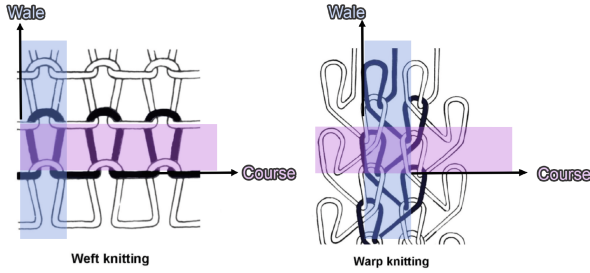


**Fig. 1.** The weft knitted structure (left) and warp knitted structure (right) with their respective wale and course direction.

The most common method of CF sensor design that exists in literature involved a direct measurement of its electrical resistance along the fabric principal course or wale axis [7–10]. This is as shown by the circuitry on the left of Fig. 2. Such design though convenient but results in irregularities and high deviation [9, 10] in the resulting sensor electromechanical property. This poses a problem as it affects the reliability and accuracy of the resulting wearable strain sensor for use in clinical application.

In this paper, we explore an alternative sensor design, where the electromechanical property of a commercially available CF (Electrolycra) along a variety of its wale and course direction is studied under the application of a constant current for its performance. This is motivated by the work of Jinnan et al. [14], where their wearable graphene-coated fiber sensors were shown to maintain stable and accurate performance under both low and high strains through the introduction of constant current to their device. Our goal is to understand the key geometric parameters affecting its electromechanical property, in particular if it is dependent on the fabric length, width or a combination of both.

## 2 Sensor Architecture and Design

The concept of our CF strain sensor architecture, as shown in Fig. 2, was to supply a small constant current through the sensor terminals while measuring the resulting output voltage as the resistance of the fabric strip changes under elongation.

### 2.1 Sensor Design

The design of our strain sensor is as shown in Fig. 3. It consists of two end holders with a strip of CF attached to it. To secure and ensure that any attached CF strip are measured from the same contact point, we have designed a holder made from a 2 mm thickness of transparent acrylic, assembled with copper tape and wire. Refer to Fig. 3a for its exploded view, Fig. 3b for the acrylic holder copper tape and wire, and Fig. 3c for the completed assembled strain sensor.

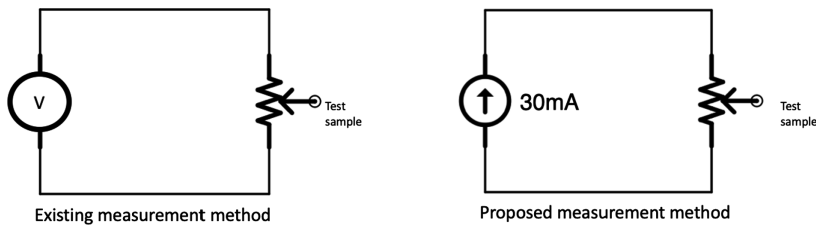


**Fig. 2.** Existing measurement method found in literature (left) and our proposed measurement method (right).

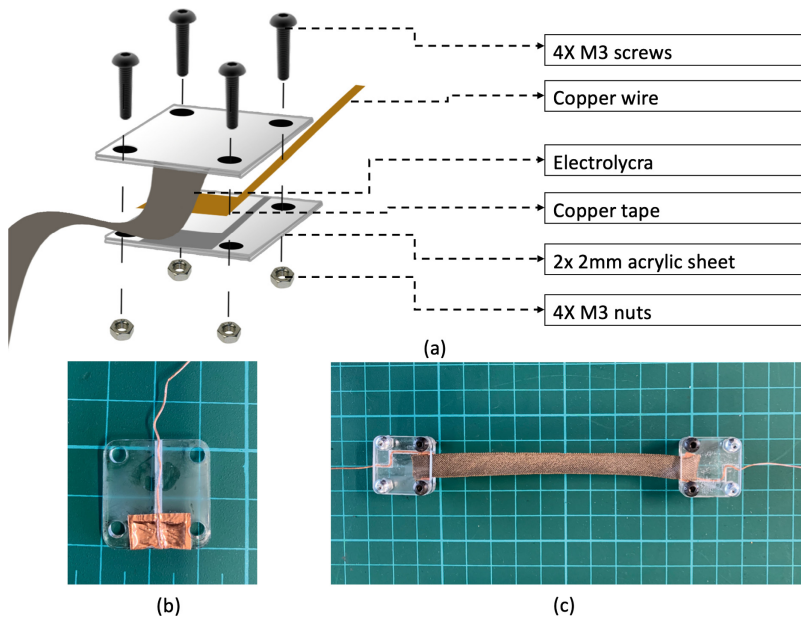


**Fig. 3.** (a) Exploded view of the strain sensor, (b) 2 mm transparent acrylic with copper tape and wire, (c) Assembled strain sensor for a  $10 \times 1$  cm example.

## 2.2 Material Selection

To choose a suitable CF material for our sensor, we have evaluated a variety of commercially available CF such as (1) EeonTex™ NW170-PI-20, (2) EeonTex™ LTT SLPA, (3) Electrolycra (Mindsets Ltd, UK) and (4) fabric 4900 stretch conductive fabric (Holland Shielding Systems B.V) and found that Electrolycra have a repeatable resistance-strain behaviour as compared to the rest. This form our choice of material for our sensor where we seek to perform further detail characterization.

### 3 Sensor Characterization

To investigate the electro-mechanical relationship of our sensor under the effect of using a constant current source. An experimental testbed was devised to measure our sensor strain-voltage relationship as shown in Fig. 4. It consists of an Agilent DC Power Analyser (Model: N6705B) to provide a constant current source of 30 mA across the strain sensor and a linear stage to provide the necessary strain input to our sensor. The voltage values from the strain sensor and the encoder data from the stepper motor were simultaneously recorded at 200 Hz (5 ms) using a real-time embedded evaluation board (National Instrument: MyRio).

All samples were cut using GCC Laser Cutting System and tested under the same speed of 10RPM up to a strain of 60%.

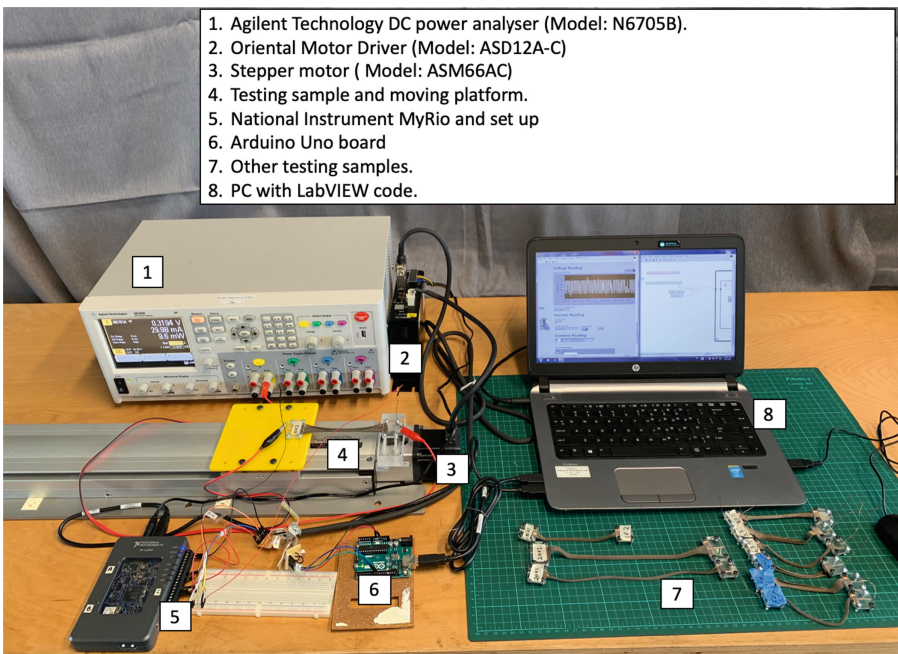


**Fig. 4.** The experiment setup for sensor characterization.

#### 3.1 Strain Axis Electromechanical Property

First, we study the electro-mechanical properties of the CF along a variety of different axes. Our goal is to understand if there is an optimal fabric axis that yields the best electromechanical performance. To the best of the author's knowledge, the electromechanical effect of the courses and wales combination direction under constant current effect was not studied in any current literature and this work seeks to address this. The study involves a constant  $10 \times 1$  cm sample strip at increment angles of  $22.5^\circ$  as shown in Fig. 5.

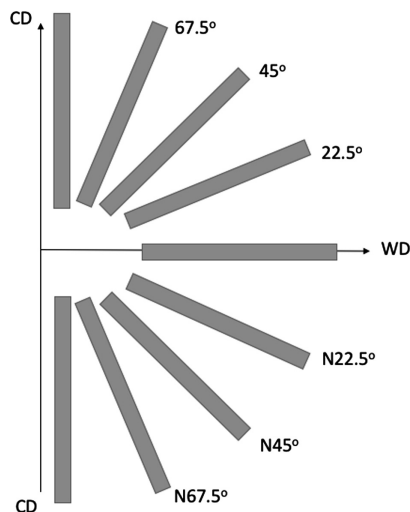


**Fig. 5.** Orientation of the various  $10 \times 1$  cm sensor samples.

For each of these samples, they were repeated for ten trials. For each trial, they were strain to 60% and back. The measured voltage and encoder data were expressed as normalised relative voltage ( $\frac{V_i - V_0}{V_0}$ ) and length ( $\frac{L_i - L_0}{L_0}$ ), where  $V_0$  and  $L_0$  denote the initial voltage and length of the fabric prior to strain and  $V_i$  is the voltage of the fabric at a particular instance of time. The return path of the strain sensor was not taken into consideration as we are not interested in its hysteresis effects at this stage. The mean of the results for these ten trials is plotted in Fig. 6.

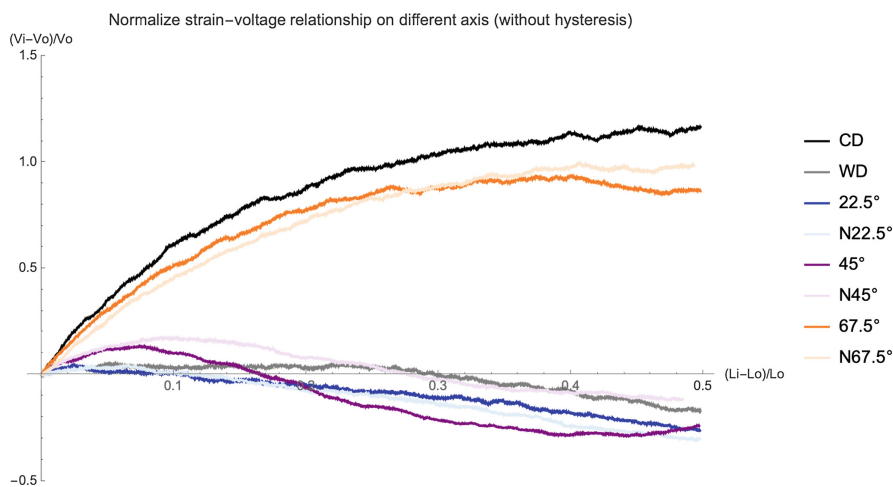


**Fig. 6.** Mean Normalize Strain-Voltage graph of the CF along the various fabric axis.

### 3.2 Geometric Parameters Affecting Electromechanical Property

Next, we investigate further the electromechanical behaviour of the CF along its best performing CD axis. In particular, the axis where the largest relative normalized voltage is observed. To understand this, four samples of different length and width with geometric dimensions as indicated in Table 1 are characterized.

**Table 1.** CF sample with different dimension.

Sample	Length (cm)	Width (cm)
Sample 1	10	1
Sample 2	10	2
Sample 3	20	1
Sample 4	20	2

Similarly, for each of these samples, they were repeated for ten trials where they were strain to 60%. The individual 10 cycles results were plotted in Fig. 7(a–d).

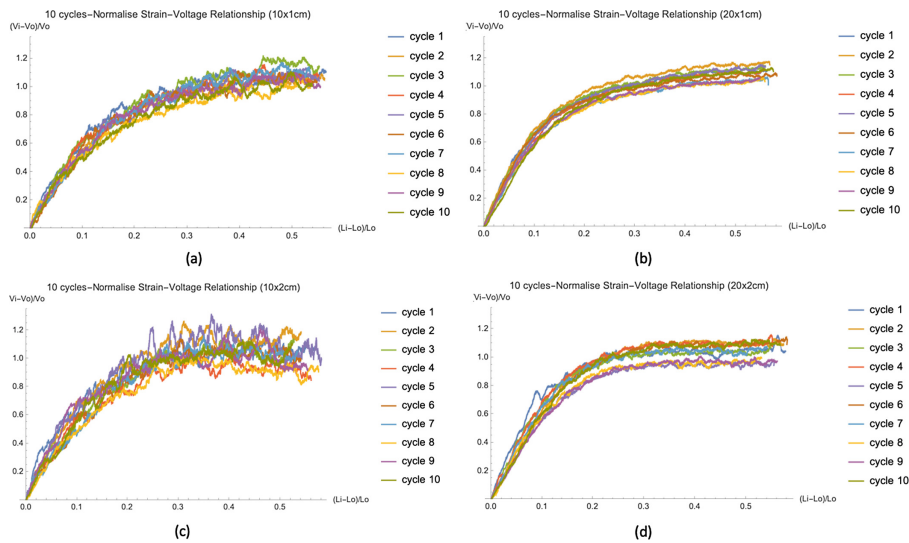


**Fig. 7.** Normalize strain-voltage relationship for each individual sample: (a)  $10 \times 1$  cm sample, (b)  $10 \times 2$  cm sample, (c)  $20 \times 1$  cm sample, (d)  $20 \times 2$  cm sample.

### 3.3 Sensor Electrical Hysteresis

Next, we investigate further the sensor electrical hysteresis behaviour of the CF along its best performing CD axis. Four samples of different length and width with geometric dimensions as indicated in Table 1 are characterized. For each of these samples, they were repeated for ten trials where they were strain to 60%. The mean individual dimension results were plotted in Fig. 8.

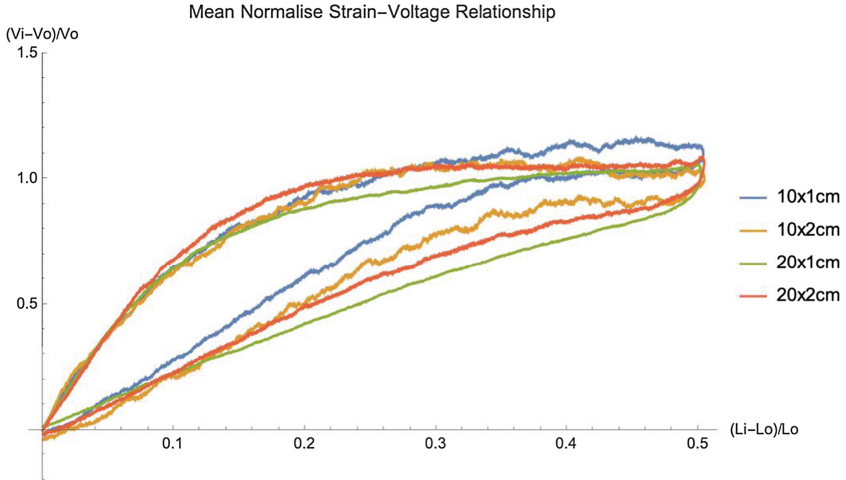


**Fig. 8.** Mean Normalise strain-voltage relationship for  $10 \times 1$  cm,  $10 \times 2$  cm,  $20 \times 1$  cm and  $20 \times 2$  cm sample with hysteresis.

## 4 Discussion

From the characterization results, it was shown that the fabric CD axis yields the best electromechanical performance. This is due to having the highest normalization voltage values, which provides a better sensor working range and sensitivity between 0% to 50%. Also, along this axis, we have observed that its length does not have any influence on its normalized electromechanical performance, but its width does affect its stability due to the higher noise variation (Fig. 7). We also noticed that any angle between  $67.5^\circ$  and  $N67.5^\circ$  axes apart from the CD axis are possible candidates for use as a strain sensor, due to their similar sensitivity and electromechanical behaviour (Fig. 6). This also indicates the amount of manufacturing precision required for cutting along the appropriate fabric axis is not very curial. However, we find that any axes outside of the above range are not suitable due to their nonlinear behaviour in particular within its 10–30% strain range and much lower normalized voltage behaviour as shown by the plots of WD,  $22.5^\circ$ , N $22.5^\circ$ ,  $45^\circ$  and N $45^\circ$  axes. On hysteresis, we found that it consistently peaks at 0.30% strain and reaches a plateau at 0.50% strain, for all samples tested, as shown in Fig. 8.

Next, to compare the resulting variation performance of our sensor design with that as reported by Grassi et al. [9], we calculated the overall mean data and standard deviation across our four characterized CD axis samples. The results were plotted in Fig. 9. Our result shows an improvement when compared to their normalized resistance data, with a maximum standard deviation of 0.06 at 20% strain for our sensor as compared to 0.2 at 30% strain as reported by the authors. This verifies the benefit of our sensor design. We have also observed similar electromechanical trend and they reach a plateau after reaching 50% strain.

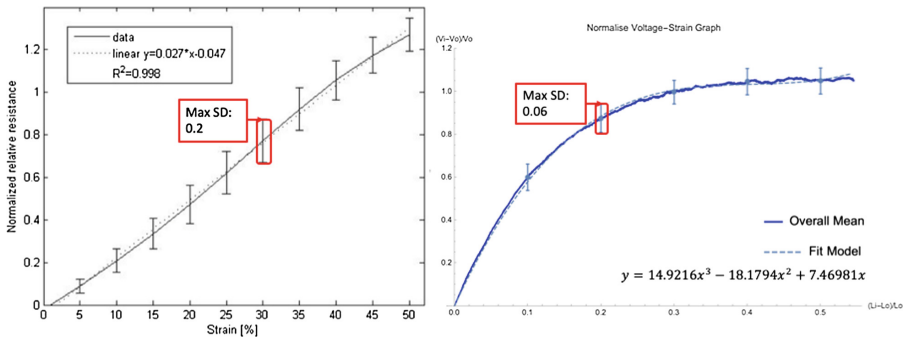


**Fig. 9.** Comparison of sensor electromechanical performance between [9] (left) and our design (right). Note that the value of current was cancelled during the normalization progress.

## 5 Conclusion

This paper explores an alternative sensor design for conductive fabric (CF) sensors. This was achieved by applying a small constant current and measuring the resulting voltage as compared to pure resistance measurement as found in the literature. Using this approach, we have seen an improvement in the strain-voltage relationship with a lower noise standard deviation for the commercially available Electrolycra CF. Future works seek to develop and test this strain sensor on applicable human joint sensing and circuitry miniaturization for mounting onto the human joint.

## References

1. Veltink, P.H., De Rossi, D.: Wearable technology for biomechanics: e-textile or micromechanical sensors? (conversions in BME). *IEEE Eng. Med. Biol. Mag.* **29**(3), 3743 (2010)
2. Ryu, S., Lee, P., Chou, J.B., Xu, R., Zhao, R., Hart, A.J., Kim, S.-G.: Extremely elastic wearable carbon nanotube fiber strain sensor for monitoring of human motion. *ACS Nano* **9**(6), 59295936 (2015)
3. Shyr, T.-W., Shie, J.-W., Jhuang, Y.-E.: The effect of tensile hysteresis and contact resistance on the performance of strain-resistant elastic-conductive webbing. *Sensors* **11**(2), 16931705 (2011)
4. Shyr, T.-W., Shie, J.-W., Jhuang, Y.-E.: A textile based wearable sensing device designed for monitoring the flexion angle of elbow and knee movement. *Sensors* **14**, 4050–4059 (2014)
5. Lofhede, J., Seoane, F., Thordstein, M.: Textile electrodes for eeg recording a pilot study. *Sensors* **12**(12), 1690716919 (2012)
6. Coosemans, J., Hermans, B., Puers, R.: Integrating wireless ecg monitoring in textiles. *Sens. Actuators A Phys.* **130**, 4853 (2006)
7. Guo, L., Berglin, L., Mattila, H.: Textile strain sensors characterization-sensitivity, linearity, stability and hysteresis. *Nord. Text. J.* (2), 5163 (2010)

8. Gioberto, G., Dunne, L.E.: Overlock stitched stretch sensor. *J. Text. Appeal Technol. Manag.* **8**(3) (2013). Winter
9. Grassi, A., Cecchi, F., Maselli, M., Röling, M., Laschi, C., Cianchetti, M.: Warp-knitted textile as a strain sensor: characterization procedure and application in a comfortable wearable goniometer. *IEEE Sens. J.* **17**(18), 59275936 (2017)
10. Maselli, M., Mussi, E., Cecchi, F., Manti, M., Tropea, P., Laschi, C.: A wearable sensing device for monitoring single planes neck movements: assessment of its performance. *IEEE Sens. J.* (2018)
11. Castano, L.M., Flatau, A.B.: Smart fabric sensors and e-textile technologies: a review. *Smart Mater. Struct.* **23**, 053001 (2014)
12. Stoppa, M., Chiolerio, A.: Wearable electronics and smart textiles: a critical review. *Sensors* **14**(7), 11957–11992 (2014)
13. Locher, I.: Technologies for system-on-textile integration. Ph.D. thesis, ETH Zurich (2006)
14. Zhang, J., Cao, Y., Qiao, M., Ai, L., Sun, K., Mi, Q., Zang, S., Zuo, Y., Yuan, X., Wang, Q.: Human motion monitoring in sports using wearable graphene-coated fiber sensors. *Sens. Actuators Phys.* **274**, 132140 (2018)





# Based on a Calibration Machine and Process to Develop a Six-Axis Force/Torque Sensor

Yu-Jen Wang<sup>1</sup>, Ching-Wei Hsu<sup>1</sup>, Pei-Hua Huang<sup>1</sup>, Li-Chi Wu<sup>1</sup>(✉),  
Chung-Yang Sue<sup>2</sup>, and Chih-Che Lin<sup>2</sup>

<sup>1</sup> National Sun Yat-Sen University, Kaohsiung 80424, Taiwan, R.O.C.  
sh970726@gmail.com

<sup>2</sup> Smart Microsystems Technology Center,  
Industrial Technology Research Institute, Zhudong, Taiwan

**Abstract.** This study developed a six-axis force/torque sensor and calibration system. To improve the stability of the calibration system, voice coil motors (VCMs) were used as the system's output force device. A simply and directly designed structure lent reliability to the six-axis calibration force/torque sensor. Furthermore, the system combined two precise one-axis load cells to receive the output reactionary force from the VCMs, and then used a proportional-integral-derivative controller to reduce the steady-state time. Finally, a mechanism was designed to adjust the orientation of the calibration force. The six-axis force/torque sensor is based on the principle of mechanical deformation of the structure. Resistance strain gauges were used as measuring devices because of their wide measurement range and high level of accuracy. According to the results of a strain analysis using ANSYS, we designed a crab-type force sensor as the main structure of our sensor. Through measuring the strain gauges on the elastic body surfaces, we obtained the corresponding voltages of each applied calibration force. In this study, we conducted least squares estimation (LSE) and maximum likelihood estimation (MLE) to determine the transfer function between the calibration force/torque and the voltages of the sensor. Overall, we integrated the entire system with LabVIEW and simplified its usage to minimize operation errors. Furthermore, the six-axis calibration process was conducted to verify the proposed method.

**Keywords:** Multi-axis force/torque sensor calibration system ·  
Multi-axis force/torque sensor · Transfer function ·  
Maximum likelihood estimation · Least mean square

## 1 Introduction

In this study, a six-axis force/torque sensor and calibration system were developed. To improve the stability of the calibration system, we used voice coil motors (VCMs) as the output force device of the system. A simply and directly designed structure lent reliability to the six-axis calibration force/torque sensor. Furthermore, the system combined two precise one-axis load cells to receive the output reactionary force from the VCMs, and then used the proportional-integral-derivative controller (PID controller) to reduce the steady-state time. Finally, a mechanism was designed to adjust the orientation of the

calibration force. The six-axis force/torque sensor is based on the principle of mechanical deformation of the structure. We used resistance strain gauges as measuring devices because of their wide measurement range and high level of accuracy. We designed a crab-type force sensor as the main structure of our sensor according to the results of strain analysis with ANSYS. By measuring the strain gauges on the elastic body surfaces, we obtained the corresponding voltages of each applied calibration force. Subsequently, we conducted least squares estimation (LSE) and maximum likelihood estimation (MLE) to determine the transfer function between the calibration force/torque and the voltages of the sensor. We integrated the entire system with LabVIEW and simplified the usage of this equipment to minimize the operation error. Finally, the six-axis calibration process was conducted to verify the proposed method.

## 2 Geometric Structure of the Six-Axis Force/Torque Sensor

The six-axis force/torque sensor proposed in this study was constructed on four spider leg-shaped stands, which were characterized by four horizontal beams connected to the center of a stress block and four vertical beams connected to the fixed base. Figure 1 illustrates the structure of the sensor and its stress position indicators, and Figs. 2 and 3 display the specifications of the structure. When stress was briefly applied to the central block, the horizontal and vertical beams surrounding the block became deformed, and surface strain was generated and detected by the strain gauges. Finally, a conversion matrix was established using the calibration platform.

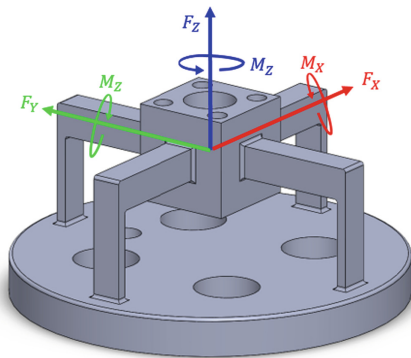
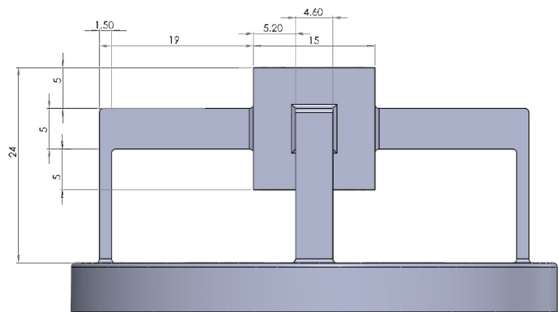


Fig. 1. Structure of the sensor and its stress position indicators

### 2.1 Locations of Strain Gauges

There was a stress concentration in the area less than 0.5 mm from the stress block (Fig. 4). In order to make the strain gauge read signal linear and stable, the location of strain gauges was selected to be 0.5 mm from the stress block.



**Fig. 2.** Side view of the sensor

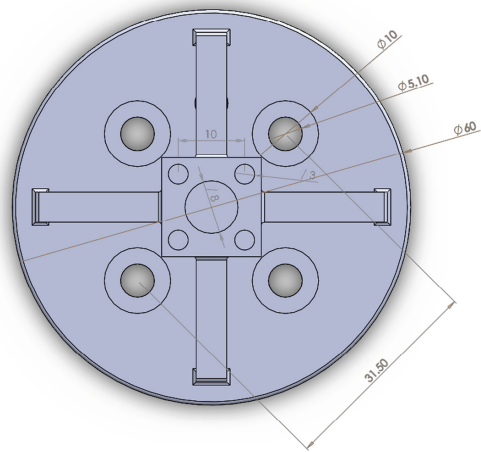


**Fig. 3.** Upper view of the sensor (Unit: mm)

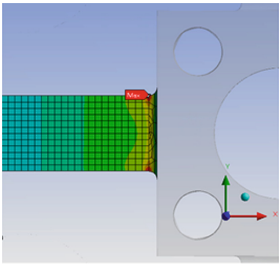


**Fig. 4.** Distribution of strain on structural surface

**2.2 Wheatstone Bridge Connection Methods**

After the correlation between resistance and strain was determined, the 16 strain gauges on the sensor were arranged in full and half Wheatstone bridges (Fig. 5). Specifically, the gauges were arranged as four full bridges and two half bridges to magnify or diminish strain signals.

This method could make specific axis decouple, such as force of x and y axis would not make the value of Tz change; Torque of x and y axis would not make the value of Fz change; Force of z axis would not make the value of Tx and Ty change; Torque of z axis would not make the value of Fx and Fy change.

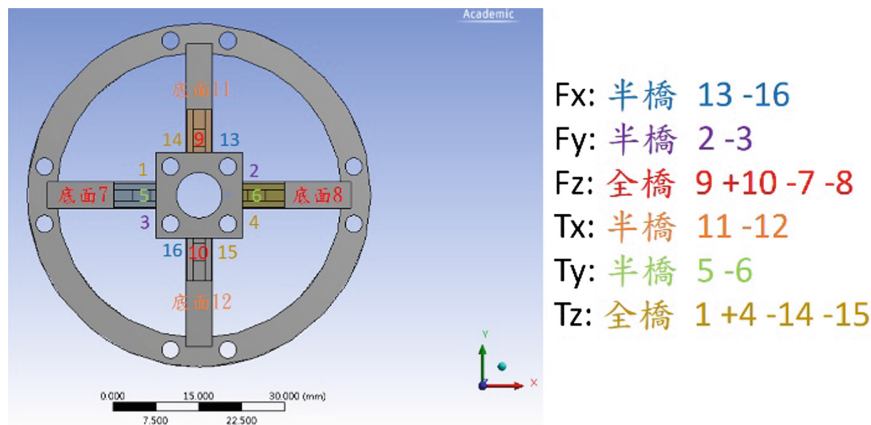


Fig. 5. Allocation of the strain gauges in six axes

2.3 Strain Analysis on the Z-Axis Force

When the force sensor experienced a z-axis force, the primary Wheatstone bridge receiving the axial strain was the full bridge of Gauge 7 + Gauge 8 – Gauge 9 – Gauge 10. Because the geometric structure of the sensor was fully symmetrical, the analysis results on all the spider legs would theoretically be identical. Therefore, only one of the spider legs was required for analysis. The forces applied in the analysis were set as 1, 5, 10, 100, and 300 N. Figure 6 illustrates the structural deformation of the sensor according to the analysis.

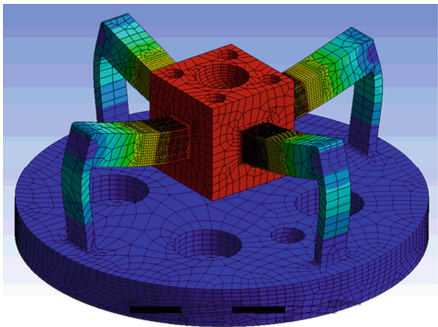


Fig. 6. Allocation of the strain gauges in six axes

## 2.4 Six-Axis Force/Torque Sensor Prototype

After the aforementioned analysis and simulation, the machining process was conducted. Figure 7 presents a diagram of the six-axis force and torque sensor of this study. The bottom of the structure is characterized by Wheatstone resistance, and the surface of the circuit is protected from moisture by a moisture-proof frame.

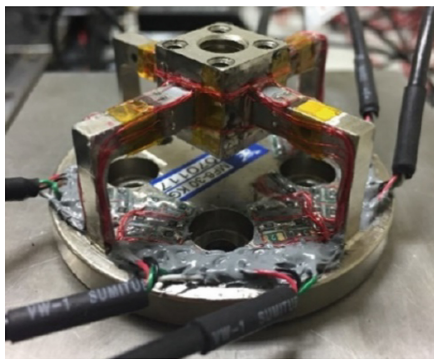


Fig. 7. Six-axis force/torque sensor prototype

## 2.5 Signal Processing

The analog signals from the Wheatstone bridge contained noise. To avoid signal distortion, we used signal amplifier and second order filter to amplify signal and reduce output noise.

## 3 Design of the Calibration Platform

A calibration platform was designed to facilitate stable and credible calibration, gather strain signals generated by the sensor structure, and establish a conversion matrix. Figure 8 illustrates the structural design of the platform. VCMs, load cells, precision motion platforms, linear slides, dial indicators, optical aluminum plates, and other processing components were used to magnify the precision and measurement range of the calibration platform. The thrust or tension force detected by the output devices at the two ends of the platform was transmitted directly to the designated fixture at the center through the levers. The force was then transferred to the force/torque sensor through the fixture. Thus, the force was applied directly to the sensor. The force detected by the output devices was coordinated with the installation of the sensor to exert a six-axis force on the sensor, and thus calibration was on all six axes. Load cells were installed between the VCMs and levers to detect the axial forces, thereby enhancing the calibration accuracy of the platform. The cells experienced reaction forces from the VCMs and compensated the error values through feedback to the controller for adjusting the calibration errors. The relative spatial positions of the levers

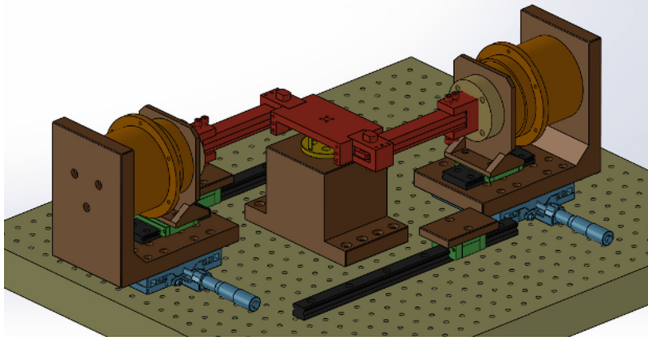


**Fig. 8.** Structure of the calibration platform

were then calibrated through the linear slides and dial indicators and fine-tuned using the precision motion platforms and screws on the levers.

#### 4 Calibration System and Transformation Matrix

The force sensor calibration platform applies a correction force to the sensor, collects strain gauge values on the sensor, collects strain values, and mathematically determines a corresponding conversion matrix between the two.

In addition, another key point is to establish the conversion relationship between the force of the sensor and the strain gauge output voltage on the sensor. The sensor designed in this study is linear under the force state to ensure the correction force can be applied and sensing can be performed. The mathematical model of static correction between strains is defined as:

$$Y_{N \times 6} = X_{N \times 6} \times \beta_{6 \times 6}.$$

However, the structural processing and strain gauge bonding might cause the signal of sensor to be not linear. Consider the nonlinear relationship between correction force and strain gauge values. The mathematical model is defined as:

$$Y_{N \times 6} = X^3 \beta + X^2 \beta + X \beta.$$

The structure of the force sensor would cause coupling signal. With the  $6 \times 6$  conversion matrix given above, could decouple signal to identify all axis forces accurately. And through the numerical distribution of the matrix, the coupling relationship between every axis could be understood.

## 5 Using the Nonlinear Least Squares Method to Establish a Transformation Matrix

In this study, the power Y matrix of the system was established. Twenty sets of forces were applied to each axial direction, the correction force was increased from 10 to 200 N, and the correction torque was increased from 0.75 to 15 N·m. This matrix consists of 20 sets with every axial forces and 10 sets with every combined forces. Thus, a  $140 \times 6$  matrix was obtained. Each row in the corresponding voltage X matrix represented the voltage value generated by the six axial sensing bridges. A transformation matrix can be obtained using the nonlinear least squares method. Thus, the X matrix was  $140 \times 18$ .

At the end of the experiment, another 120 sets of experimental data were substituted into the transformation matrix to calculate the corrected force values and compare the errors.

## 6 Conclusion

In this study, VCMs were used as the linear stability power source. Through the spatial geometric relationship, a special fixture and rod were combined with the sensor to achieve the six-axis force/torque correction capability of the sensor. The accurate load cell received the reaction force of the VCM and provided feedback to the controller, which provided compensatory action to ensure accuracy of the output device. Finally, the six-axis force/torque sensor calibration platform was created. This platform has a power correction range of 350 N and a torque correction range of N·m with an error of less than 0.2%. Using this precise calibration platform, a transformation relationship matrix for multi-axis force/torque sensors can be realized. The multi-axis force sensor equipped in this system can sense forces up to 300 N and a torque sensing range up to 22.5 N·m. The sensing error after conversion through the conversion matrix is less than 1%.

**Acknowledgements.** The authors appreciate the support from Ministry of Science and Technology, R.O.C under the grant No. NSC 107-2221-E-110-071 and 107-2622-E-110-CC3. Also appreciate the support from NSYSU-KMU JOINT RESEARCH PROJECT under the grant No. NSYSUNKUST 108-I008, National Applied Research Laboratories under the grant NARL-IMS-107-005 and from Industrial Technology Research Institute.

## References

1. Ren, C., Gong, Y., Jia, F., Wang, X.: Theoretical analysis of a six-axis force/torque sensor with overload protection for polishing robot. In: IEEE M2VIP International Conference, Nanjing, China (2016)
2. Luca, A.D., Schaffer, A.A., Haddadin, S., Hirzinger, G.: Collision detection and safe reaction with the DLR-III lightweight manipulator arm. In: Intelligent Robots and Systems International Conference, Beijing, China, 9–15 October 2006

3. Kuribayashi, K., Oe, N., Shimizu, S., Taniguchi, T.: Micro force sensor using strain gauge for articulated robot hand. In: IEEE IECON International Conference, Maui, HI, USA (1993)
4. Liang, Q., Zhang, D., Song, Q., Ge, Y.: A potential 4-D fingertip force sensor for an underwater robot manipulator. *IEEE J. Ocean. Eng.* **35**, 574–583 (2010)
5. Ito, A., Tsujiuchi, N., Koizumi, T., Oshima, H., Nojiri, Y., Tsuchiya, Y., Hiram, N., Kurogi, S.: Acquisition of slip phenomenon between developed distributed-type force sensor and the contacted object. In: IEEE IECON Annual Conference on IEEE Industrial Electronics, Paris, France, November 2006
6. Kim, Y.C., Ihn, Y.S., Choi, H.R., Lee, S.M., Koo, J.C.: Implementation of force sensor with multi strain gauges for enhancing accuracy and precision. In: IEEE MESA International Conference on Mechatronic and Embedded Systems and Applications, QingDao, China, July 2010
7. Xu, G., Song, A., Li, H.: Control system design for an upper-limb rehabilitation robot. *J. Adv. Robot.* **25**, 229–251 (2011)
8. Jacq, C., Luthi, B., Maeder, T., Lamercy, O., Gassert, R., Ryser, P.: Thick-film multi-DOF force/torque sensor for wrist rehabilitation. *J. Sens. Actuators A* **162**, 361–366 (2010)
9. Sekiguchi, K., Ueda, M., Uno, H., Takemura, H., Mizoguchi, H.: Development and calibration of 6-axis force sensor for simultaneous measuring of plantar deformation. In: IEEE International Conference on Systems, Man and Cybernetics, Singapore (2008)
10. Cui, Z., Han, Z., Pan, H., Shao, Y., Zhu, D.: Design of a 3-axial force/torque sensor for arthroscopy force sensing. In: 2011 IEEE International Conference on Mechatronics and Automation, Beijing, China, 7–10 August 2011
11. Myung, I.J.: Tutorial on maximum likelihood estimation. *J. Math. Psychol.* **47**, 90–100 (2003)
12. Wang, Y., Zuo, G., Chen, X., Liu, L.: Strain analysis of six-axis force/torque sensors based on analytical method. *IEEE Sens. J.* **17**, 4394–4404 (2017)
13. Okumura, D., Sakaino, S., Tsuji, T.: Development of a multistage six-axis force sensor with a high dynamic range. In: IEEE Industrial Electronics, Edinburgh, UK (2017)
14. Berkelman, P.J., Whitcomb, L.L., Taylor, R.H., Jensen, P.: A miniature microsurgical instrument tip force sensor for enhanced force feedback during robot-assisted manipulation. *IEEE Trans. Robot. Autom.* **19**, 917–921 (2003)
15. Chen, D., Song, A., Li, A.: Design and calibration of a six-axis force/torque sensor with large measurement range used for the space manipulator. *J. Procedia Eng.* **99**, 1164–1170 (2015)
16. 劉硯濤, 郭冰, 尹偉, 吳兵, “六維力傳感器靜態標定及解耦研究,”. *Structure and Environment Engineering* (2013)
17. Xin, Z.: Design of a new type six-axis force sensor. In: Intelligent Computation Technology and Automation International Conference, Changsha, Hunan, China (2009)
18. Sun, Y., Liu, Y., Zou, T., Jin, M., Liu, H.: Design and optimization of a novel six-axis force torque sensor for space robot. *Measurement* **65**, 135–148 (2015)
19. Li, K., Pan, B., Fu, Y., Wang, S.: Experimental study of static and dynamic characteristics of a miniature 6-axis force and torque sensor. In: International Conference on Information and Automation, Lijiang, China, August 2015
20. Beck, J.V., Arnold, K.J.: Parameter estimation in engineering and science, 13 July 1977



# **Novel Robotic Systems**



# Parallel Mechanism Designs for Humanoid Robots

Marco Ceccarelli<sup>1,2(✉)</sup> and Matteo Russo<sup>1,3</sup>

<sup>1</sup> LARM2: Laboratory of Robot Mechatronics, University of Roma Tor Vergata,  
Viale del Politecnico 1, 00133 Rome, Italy  
marco.ceccarelli@uniroma2.it,  
matteo.russo@nottingham.ac.uk

<sup>2</sup> Beijing Advanced Innovation Center for Intelligent Robots and Systems,  
Beijing Institute of Technology, Beijing 100081, China

<sup>3</sup> The Rolls-Royce UTC in Manufacturing and On-Wing Technology,  
University of Nottingham, Nottingham NG8 1BB, UK

**Abstract.** The design of humanoid robots is inspired to human anatomy and operation with open challenges in mechanical performance that can be achieved by using parallel architectures. In this paper, parallel architectures are recognized in human anatomy and operations and they are used as inspiration for designing parallel mechanisms within humanoid robots. Requirements and performance of parallel mechanisms in humanoid designs are discussed. The example of LARMbot humanoid is reported to show the feasibility and efficiency of the proposed designs.

**Keywords:** Humanoids · Mechanism design · Parallel mechanisms · LARMbot

## 1 Introduction

Humanoid robot design has been a major challenge in Robotics for decades, and in the last ten years, successful humanoid designs were developed both by academy and industry as platforms for research and applications for service, navigation, human-robot interaction and learning. Examples can be indicated in NAO by SoftBank Robotics [1], that is used in many Robotics competitions such as RoboCup; iCub [2], for research on learning; WALK-MAN, a rescue robot for unstructured environments [3]; Pepper, for investigation on human-robot interaction [4]; WABIAN-2 [5]; Ami, developed for applications in Domotics [6]; REEM-B by PAL-Robotics, as a service robot in human assistance [7]; ARMAR, a collaborative robot for Domotics [8, 9]. All these robots are characterized by serial kinematic architectures with large workspace and mobility due to the 5R, 6R, 7R and 8R kinematic chains that are used for arms and legs with the aim of mimicking human motion and dexterity. However, the payload of these structures is rather small (for example, NAO can lift only 0.15 kg per arm) and they are often characterized by poor dynamics and stiffness. For these reasons, there are still challenging design issues and parallel architectures can be used to improve the mechanical design and performance in accuracy, payload and dynamics of humanoid designs.

## 2 Parallel Mechanisms in Human Anatomy

Humanoids are designed with structures and operations replicating human ones. Human nature has a complex design in structure composition, with several kinds of material and architectures that humanoid design can replicate only very partially. The most referenced part of human anatomy for humanoid robot structures is the skeleton system, which inspires solutions mainly with rigid links in serial kinematic chain architectures. However, considering that the functionality of human movable parts is mainly due to a combined/integrated structure of bones and muscles, the reference structure for humanoid robot design can be considered a parallel architecture that combines bones as rigid movable links and muscles as linear actuators. Figure 1 is an example of such an inspiration from human anatomy, with parallel architectures of bone and muscle for designing a movable arm with a parallel mechanism that is based on the antagonist actuation of a pair of muscles for a planar motion.

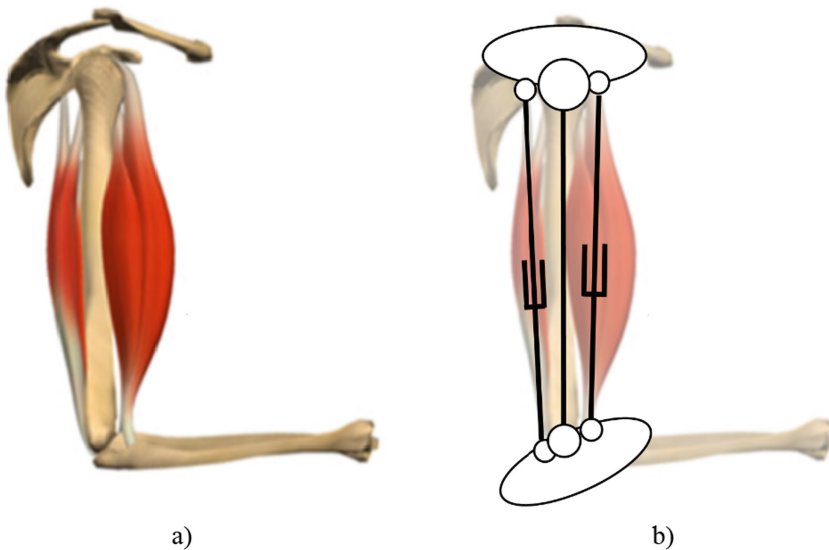


**Fig. 1.** Examples of parallel architectures with antagonist functioning: (a) in human anatomy; (b) replicating mechanism.

The antagonist functioning of muscles is characterized by the fact that the muscles mainly act with pulling actions when they are contracted, and therefore full mobility requires alternated actions of two muscles in pulling and releasing. For complex motions, such as 3D movements, a bone is actuated by more complex groups of muscles that still control the operation through antagonist functionality. Thus, although the basic principle can be still referred to the example in Fig. 1, human anatomy can be of difficult replication in efficient compact designs for humanoid robots. However, the inspiration from human anatomy for designs with parallel mechanisms can be summarized in

solutions that are characterized by two platforms in relative motion, which are connected and actuated by a number of pairs of linear actuators working either independently (as rigid variable links) or in antagonism (as cable-driven links).

### 3 Requirements and Design Performance for Humanoid Robots

Humanoid designs are aimed at replicating/mimicking human operations mainly in locomotion, manipulation, and sensing for human-like tasks and interactions. Figure 2 summarizes the main aspects that should be considered for design and operation by looking at human nature, making a humanoid solution efficient, durable, and functional.

In particular, for locomotion requirements, attention is required in a properly designed leg workspace, in order to replicate the area of mobility of a human leg, which is usually characterized by suitable values of step length and step height. In addition, the locomotion can be performed in several modes just like humans, such as walking, running and jumping, with characteristic performance in terms of speed and motion smoothness. Among practical requirements, payload capability is required not only to sustain the weight of the full humanoid but also considering the task loads and actions that the leg system will have to support. As per a successful functionality, the locomotion system must be provided of control software and hardware as well as motion strategies for a stable balancing during bipedal operations.

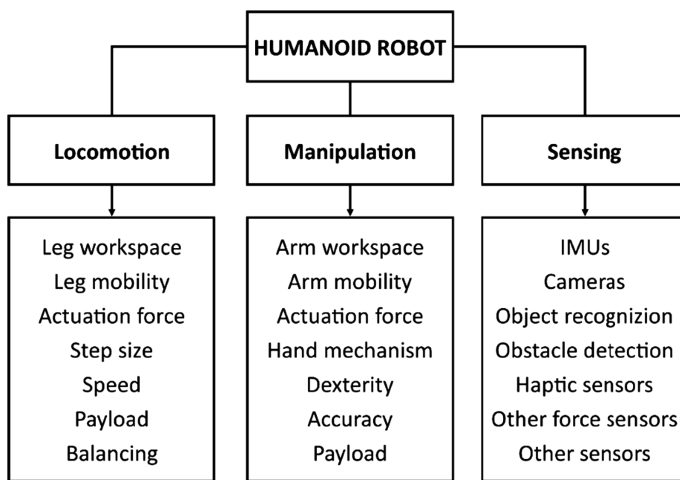


**Fig. 2.** Main requirements for humanoid robots.

Similarly, the manipulation system is characterized by requirements in terms of arm workspace and mobility, that include each point that the arm can reach and all the configurations in which that point can be reached (with different orientations for

different manipulation tasks). The payload of the arm structure should be enough to support a variety of human-like manipulation tasks, with a good accuracy and repeatability. Manipulation capability should be characterized also in terms of dexterity as expressed by multiple reachable arm configurations with suitable motion and dynamics characteristics.

Humanoid robot sensing can be considered as based mainly on sensor equipment with characteristics and composition outlined in Fig. 2 as for main human-like operation. Inertial measurement units (IMUs) are needed to have a feedback on the motion that the humanoid performs, in order to react to external forces or not-balanced configurations with a proper balancing motion. Cameras are needed for autonomous navigation through obstacle detection, and for area inspection through object recognition. Other common sensor in humanoid robots are haptic sensors, for measuring the interaction of the humanoid robot with the environment. Important sensing is related also to force detection both in manipulation and locomotion with or without control feedbacks. Significant are sensors in grasping task up to a tactile capability.

Referring to an average human characterization, Table 1 lists an example of numerical evaluation of design requirements for humanoid design as referring to the requirements in Fig. 2 as linked to solutions with parallel mechanisms.

**Table 1.** Requirements for humanoid design (Fig. 2) [10–12].

Characteristics	Human reference value	Expected value in humanoids
Step length (natural)	<94% leg height	75–100% leg height
Step length (fast)	>116% leg height	100–125% leg height
Speed	<105 steps per minute	80–120 steps per minute
Arm mobility	6 D.o.F.	>6 D.o.F.
Torso flexion/extension	30–45°	10–30°
Torso lateral bending	<40°	<30°
Power consumption	<6.00 W/kg	<10.0 W/kg

The expected performance in Table 1 are estimated considering design solution with parallel architectures enhancing the whole humanoid design.

## 4 An Example: LARMbot

The advantage in using parallel mechanisms in humanoid designs are discussed by referring authors' direct experience with LARMbot. LARMbot is a humanoid robot that has been developed as based on parallel architectures at LARM laboratory of University of Cassino and Southern Latium. LARMbot, in Fig. 5, is conceived as a service robot for autonomous walking and manipulation tasks. As documented in [13], the first full prototype of LARMbot was assembled in 2015, while a second version with a different leg architecture is now being developed [14, 15]. It is based on two parallel subsystems, one for legs and one for torso.

LARMbot is 850 mm tall, with a lightweight structure of less than 3.70 kg. Its payload capability is 0.85 kg for manipulation, and 3 kg for the torso/leg structure, which is considerably stronger than in traditional humanoids thanks to parallel architectures. The payload to weight ratio is 0.23 for manipulation and 0.81 for weight lifting, which is considerably higher than in other existing humanoid robots. For example, Nao, which is based on serial kinematic architectures, has a payload to weight ratio of only 0.03 [1]. Furthermore, LARMbot is energy-efficient, with a peak 20 W power consumption in LARMbot II prototype, as tested in [15] (Fig. 3).

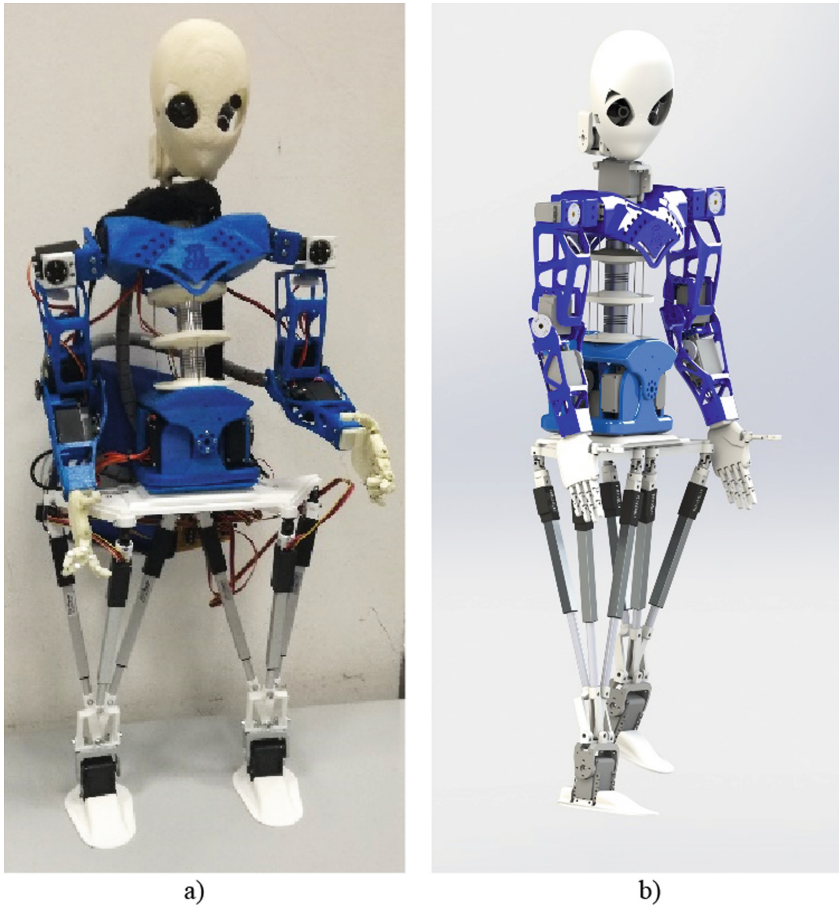


**Fig. 3.** LARMbot humanoid as based on parallel mechanisms: (a) A prototype; (b) A CAD model.

The torso is characterized by the CAUTO design that is introduced in [16] and shown in Fig. 4a, which is a cable-driven, underactuated hybrid serial-parallel manipulator based on the kinematic scheme in Fig. 5b. Its trunk architecture is based

on a 4SPS-(3S) parallel mechanism with 4 degrees of freedom, which are actuated by the four motors that regulate the length of each cable. The mechanism is inspired by the human torso (Fig. 5a), with a serial-kinematic compliant spine in the center, represented by the 3S chain in Fig. 5b, and the cables acting as antagonist muscles for motion control. As outlined in [17], the motion of the torso can be used to enhance and support walking balance too.

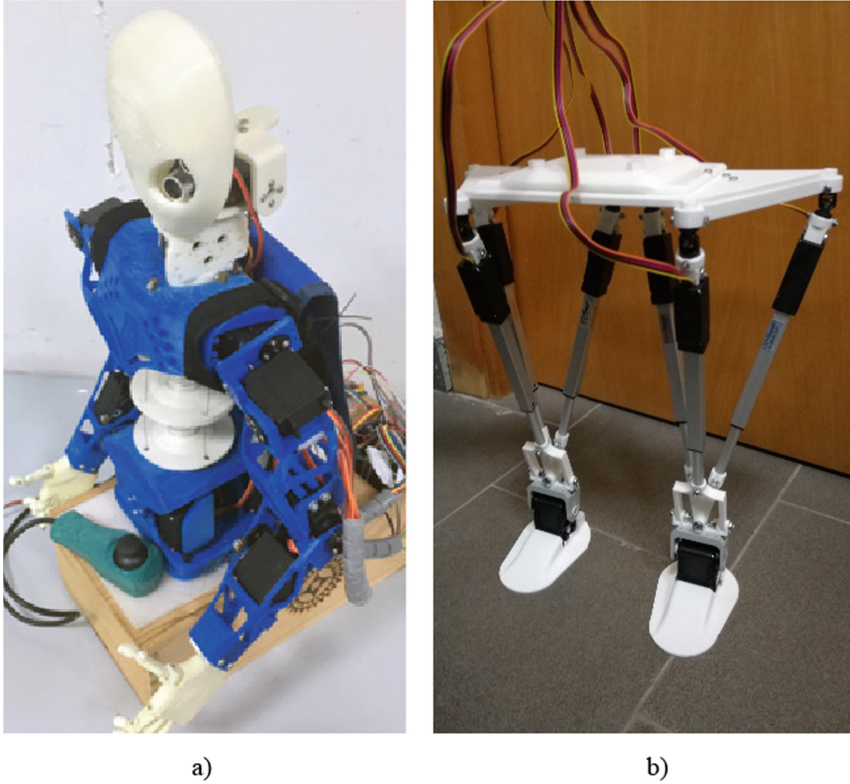


**Fig. 4.** Parallel structures in LARMbot: (a) The torso; (b) The legs.

The leg mechanism is shown in Fig. 4b and it is analyzed in detail in [18]. The design is inspired by human upper leg structure in Fig. 6a, with the three actuators representing the main muscle groups of the upper leg, namely hamstrings, quadriceps and adductors, as mainly for their operation on the leg actuation. Each leg is characterized by the 3UPR lower-mobility parallel mechanism that is shown in Fig. 6b and connects the hip to the ankle. It is actuated by three linear actuators in the links, which converge to a single point of the knee/ankle mechanism. This special joint design has a large workspace when compared to similar parallel manipulators and it is characterized by no singular configurations, as detailed in [19, 20]. The performance of LARMbot can be summarized as in Table 2, with reference to the requirements of Table 1.



Thanks to its properly designed parallel architectures, it is possible to obtain a good performance not only in payload and energy consumption, but also workspace, mobility and speed that are comparable to human ones.

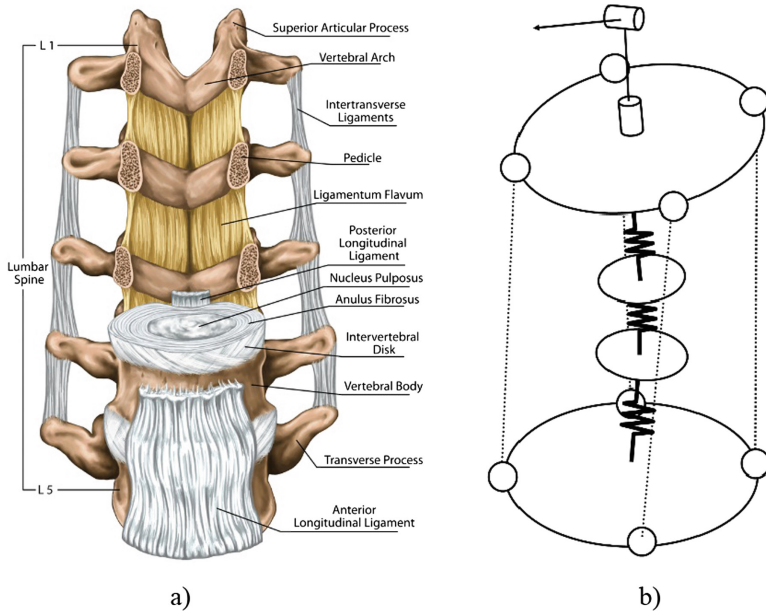


**Fig. 5.** Spinal structure: (a) Human spine with ligaments; (b) LARMbot spine mechanism.

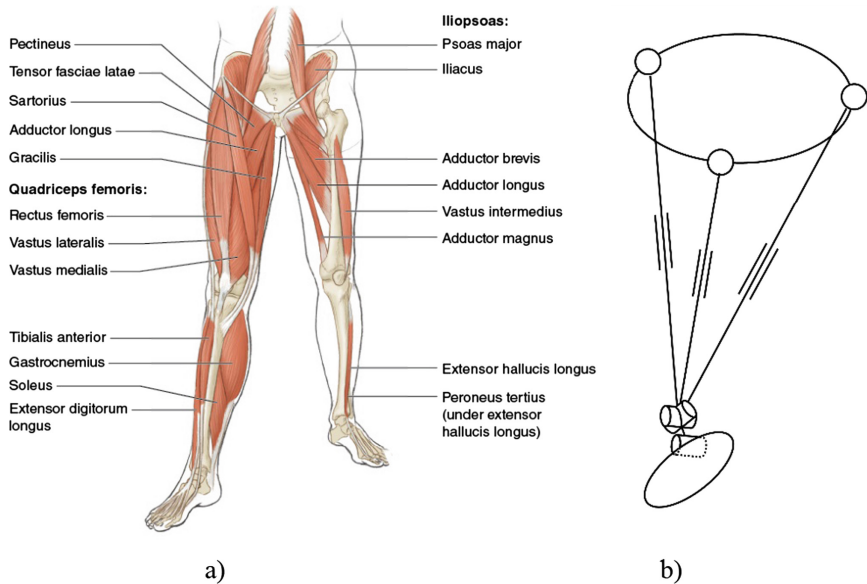


**Fig. 6.** Leg structure: (a) Human leg with muscles; (b) LARMbot leg mechanism.



**Table 2.** LARMbot performance characteristics [13–15].

Characteristics	LARMbot
Height	0.85 m
Weight	3.70 kg
Step length (natural)	100% leg height
Step length (fast)	100% leg height
Speed	100 steps per minute
Arm mobility	6 D.o.F.
Torso flexion/extension	45°
Torso lateral bending	45°
Power consumption	7.00 W/kg

In particular, Figs. 7 and 8 refer to a test of squatting motion with a payload of 1.0 kg on the hand to show the feasibility and convenience of the parallel mechanisms in LARMbot, as mainly referring to the leg design with a coordination with the trunk. The squatting motion consisted in a vertical displacement of 40 mm at a speed of 10 mm/s.

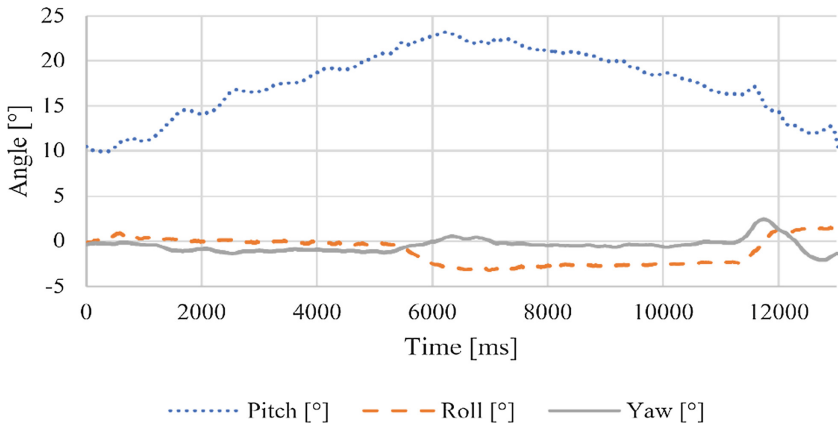


**Fig. 7.** Acquired angular displacement for a squat weight-lifting test with a 1 kg payload.

Figure 7 shows the limited angular motion of the trunk from the measures that were acquired by an IMU on the top of the shoulder. The operation of the leg parallel mechanism is obtained with an almost linear displacement that has been properly balanced by the trunk motion with only a pitch adjustment. The smooth operation, that can be also noted from the plots in Fig. 7, is proved by the sensed acceleration by the same IMU with the very limited values and time history in Fig. 8.

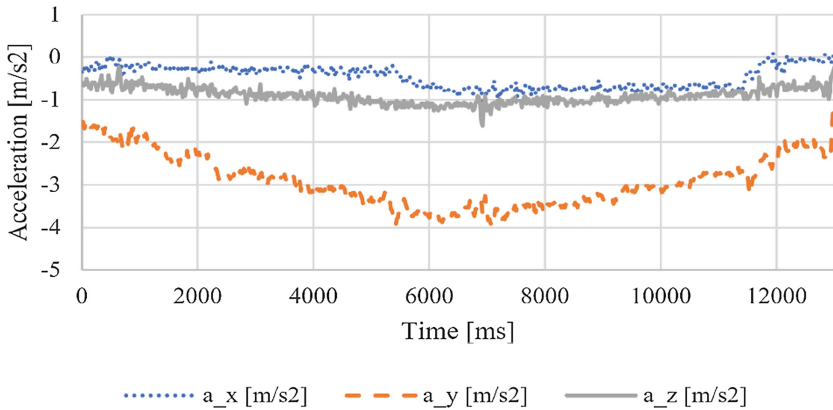


**Fig. 8.** Acquired angular acceleration for a squat weight-lifting test with a 1 kg payload.

The motion of the leg mechanism with the trunk motion give very small accelerations, that characterize a smooth squatting along the Z-axis and a bending balancing action along the X-axis with a maximum acceleration of  $4 \text{ m/s}^2$ .

Summarizing, the parallel mechanisms in the LARMbot design give significant high performance in payload capability and motion quality.

## 5 Conclusions

This paper introduces parallel mechanisms for humanoid robots to improve structure and operation as inspired by human nature. The complex of bones actuated by antagonist muscles is recognized as a parallel mechanism whose conceptual design is used as inspiration for new designs in humanoid robots. The LARMbot design is presented as an emblematic successful example of using parallel mechanism both to replicate human anatomy and to get efficient compact humanoid design with properly enhanced performance.

## References

1. Kulk, J., Welsh, J.: A low power walk for the NAO robot. In: Kim, J., Mahony, R. (eds.) *Proceedings of the 2008 Australasian Conference on Robotics & Automation (ACRA-2008)*, pp. 1–7, December 2008
2. Metta, G., Natale, L., Nori, F., Sandini, G., Vernon, D., Fadiga, L., Bernardino, A.: The iCub humanoid robot: an open-systems platform for research in cognitive development. *Neural Netw.* **23**(8–9), 1125–1134 (2010)
3. Tzagarakis, N.G., Caldwell, D.G., Negrello, F., Choi, W., Baccelliere, L., Loc, V.G., Noorden, J., Muratore, L., Margan, A., Cardellino, A., Natale, L.: WALK-MAN: a high-performance humanoid platform for realistic environments. *J. Field Robot.* **34**(7), 1225–1259 (2017)

4. Lafaye, J., Gouaillier, D., Wieber, P.B.: Linear model predictive control of the locomotion of Pepper, a humanoid robot with omnidirectional wheels. In: 2014 14th IEEE-RAS International Conference on Humanoid Robots (Humanoids), pp. 336–341. IEEE, November 2014
5. Ogura, Y., Aikawa, H., Shimomura, K., Morishima, A., Lim, H.O., Takanishi, A.: Development of a new humanoid robot WABIAN-2. In: Proceedings of the 2006 IEEE International Conference on Robotics and Automation, ICRA 2006, pp. 76–81. IEEE, May 2006
6. Jung, H.W., Seo, Y.H., Ryoo, M.S., Yang, H.S.: Affective communication system with multimodality for a humanoid robot, AMI. In: 2004 4th IEEE/RAS International Conference on Humanoid Robots, vol. 2, pp. 690–706. IEEE, November 2004
7. Tellez, R., Ferro, F., Garcia, S., Gomez, E., Jorge, E., Mora, D., Faconti, D.: Reem-B: an autonomous lightweight human-size humanoid robot. In: Humanoids 2008, 8th IEEE-RAS International Conference on Humanoid Robots, 2008, pp. 462–468. IEEE, December 2008
8. Asfour, T., Regenstien, K., Azad, P., Schroder, J., Bierbaum, A., Vahrenkamp, N., Dillmann, R.: ARMAR-III: an integrated humanoid platform for sensory-motor control. In: 2006 6th IEEE-RAS International Conference on Humanoid Robots, pp. 169–175. IEEE, December 2006
9. Asfour, T., Schill, J., Peters, H., Klas, C., Bücker, J., Sander, C., Bartenbach, V.: ARMAR-4: a 63 DOF torque controlled humanoid robot. In: 13th IEEE-RAS International Conference on Humanoid Robots (Humanoids), 2013, pp. 390–396. IEEE, October 2013
10. Farris, D.J., Sawicki, G.S.: The mechanics and energetics of human walking and running: a joint level perspective. *J. R. Soc. Interface* **9**, 110–118 (2011). rsif20110182
11. Knudson, D.: Fundamentals of Biomechanics. Springer, Dordrecht (2007)
12. Winter, D.A.: Kinematic and kinetic patterns of human gait: variability and compensating effects. *Hum. Mov. Sci.* **3**, 51–76 (1984)
13. Cafolla, D., Wang, M.F., Carbone, G., Ceccarelli, M.: LARMBot: a new humanoid robot with parallel mechanisms. In: Robot Design, Dynamics and Control: Proceedings of ROMANSY 2016, 21st CISM-IFTOMM Symposium on Robot Design, Dynamics, and Control, pp. 275–284 Springer (2016)
14. Ceccarelli, M., Cafolla, D., Russo, M., Carbone, G.: Larmbot humanoid design towards a prototype. *MOJ Appl. Bionics Biomech.* **1**(2), 00008 (2017)
15. Russo, M., Cafolla, D., Ceccarelli, M.: Design and experiments of a novel humanoid robot with parallel architectures. *MDPI Robot.* **7**(4), 79 (2018)
16. Cafolla, D., Ceccarelli, M.: Design and simulation of a cable-driven vertebra-based humanoid torso. *Int. J. Hum. Robot.* **13**(4), 1650015–1–1650015–27 (2016). <https://doi.org/10.1142/s0219843616500158>
17. Cafolla, D., Ceccarelli, M.: An experimental validation of a novel humanoid torso. *Robot. Auton. Syst.* (2017). <http://dx.doi.org/10.1016/j.robot.2017.02.005>
18. Russo, M., Ceccarelli, M., Takeda, Y.: Force transmission and constraint analysis of a 3-SPR parallel manipulator. *Proc. Inst. Mech. Eng. Part C J. Mech. Eng. Sci.* (2017). <https://doi.org/10.1177/0954406217750190>
19. Russo, M., Ceccarelli, M.: Kinematic design of a tripod parallel mechanism for robotic legs. In: Mechanisms, Transmissions and Applications, Mechanism and Machine Science, vol. 52, pp. 121–130. Springer, Cham (2018)
20. Russo, M., Herrero, S., Altuzarra, O., Ceccarelli, M.: Kinematic Analysis and multi-objective optimization of a 3-UPR parallel mechanism for a robotic leg. In: Mechanism and Machine Theory, February 2018, vol. 120, pp. 192–202 (2018)



# Development and Optimization of an Intelligent Parking Slot Allotter and Billing System Based on Machine Learning and OCR

D. Bhanu Priya<sup>1</sup> and Guan-Chen Chen<sup>2</sup>(✉)

<sup>1</sup> SRM Institute of Science and Technology, Chennai 603203, India  
bhanupriyad4@gmail.com

<sup>2</sup> Tamkang University, Tamsui District, New Taipei City 251, Taiwan (R.O.C.)  
niborchen@gmail.com

**Abstract.** As a key part of automated vehicle technology intelligent parking slot allotter has become a popular research topic. Intelligent parking slot allotter can grant permission to access the parking area with less human inference. This system can capture image of the vehicle, identify the type of vehicle and allot best fit and optimal parking slot based on its size. It extracts the vehicle's license plate number, entry time, exit time and calculate total time of the vehicle present with in the parking space. Here, sensors are utilized to identify the presence of the vehicle during entry and exit. Two cameras are utilized to extract features. One camera is used to identify the region of interest, vehicle license plate and identify the characters from the license plate. Tesseract engine and optical character recognition (OCR) functions are used to detect characters from the image. Another camera is utilized to extract features like dimensions of the vehicle using machine learning operations such as convolutional neural network (CNN). Based on the size of the vehicle, best fit parking slot is allotted which gives optimal usage of parking area. These days the quantity of vehicles is expanding exceptionally, so that, searching for an empty parking slot turns out to be increasingly troublesome. By installing the intelligent parking slot allotter, in places like, shopping malls, train stations, and airports the need for searching of parking slot significantly reduces. A past study has demonstrated that traffic because of vehicle's parking slot searching in downtowns of significant urban communities can represent half of the absolute traffic. With such a hefty traffic jam and time delay in parking slot identifying, intelligent parking slot allotter will be in great demand.

**Keywords:** License plate recognition · Vehicle type classification · Optimal parking slot

## 1 Introduction

As a key part of computerized vehicle recognition technology, intelligent parking slot allotter system has turned into a well-known research point. These days the quantity of vehicles is expanding exceptionally, so that searching for an empty parking slot turns

out to be increasingly troublesome. For example, shopping malls, train stations, and airports. In such vast territories, a few zones of the parking might be effectively utilized at the same time and some might have numerous empty slots. Past study has demonstrated, traffic jam because of vehicle's parking slot searching in downtowns of significant urban communities can represent half of the absolute traffic. With such a hefty traffic and time delay in parking slot detection, intelligent parking slot allotter system turned into a need.

Normally, as per the vehicle measure, vehicle types can be partitioned into three classifications: SUV, sedan, mini (see Fig. 1). Identifying and differentiating the vehicle has turned into a critical part of machine learning in view of its potential applications. Diverse conditions, for example, obstructions, difference in lighting, exceptional camera settings, shadows, parallax errors and different orientations, all these factors made car type classification more complex.



**Fig. 1.** Types of cars

Vigorous car type differentiation technique depends on multi-class principal feature analysis with self-grouping. Car's front part is separated by inspecting car frontal area span and also the region of the license number plate (see Fig. 2). Wang [1], in 2014 proposed vehicle type classification from surveillance videos on urban roads, in which vehicle type is identified from traffic surveillance videos by extracting features like color, shape and texture from histogram of gradient (HOG). Image is converted to small blocks, individual histogram is applied and concatenated to obtain HOG descriptor. Peng [2], in 2012 proposed vehicle type classification using pca with self-clustering in which vehicle type can be classified in to two categories like small and large cars based on self-clustering. Vehicle features such as length and width are extracted.

Visual related car group classification divides cars into two classes: strategies utilizing vehicle's side region view and strategies utilizing vehicle's frontal area (or rear) view (see Fig. 2). For the side region view ones, edge-based and model-based

methodologies are generally utilized. Methodologies dependent on edge can incorporate parameterized edge model to depict the topological framework of car, and afterwards fed system into a multi-layer perceptron networks-based classifier. Classification rate is satisfactory with high resolution images, but this method is bounded for performing on low quality images.



**Fig. 2.** Car frontal region and rear region

There are numerous methodologies for recognition utilized in contemporary vehicle number plate identification frameworks. The vast majority comprises of three fundamental stages: car license plate identification, character separation and optical character recognition (OCR). All of these stages must possess superior performance rates so as to build reliable and accurate structure. Pechiammal [3] in 2017 proposed an efficient approach for automatic license plate recognition system where, vehicle plate is extracted by gabor filtering. RGB image is converted to gray-scale image, gabor filter is applied to remove noise. Character segmentation and OCR were used to extract vehicle license plate. Wang [4], in 2017 proposed license plate segmentation & recognition of Chinese vehicle based on BPNN where, vehicle plate character recognition is done by neural network. If wrong recognition of a character then it is added to the library of machine learning for better training. It is called back propagation neural network (BPNN). In this work, the car license plate detection algorithm which is associated with the separation part. Character segmentation can give us important information about the profile of car license plate characters. This is accomplished by making connected component analysis (CCA) and optical character recognition (OCR) on the pictures. The profile is used to locate and extract each character in the plate.

As the novelty of this paper, is to put together all these concepts and allot best fit and optimal parking area of the vehicle based on its size captured from the image. In this paper the overall system work process is divided into four major segments. Section 2 gives an overview of vehicle license plate localization and character recognition.

Section 3 describes about vehicle type identification and clear-cut idea of how it works. Under Sect. 4, a novel method for allotting best fit and optimal parking slot is presented. Section 5 exhibits our analytical result. At last, this paper is completed in Sect. 6 with conclusions and future extension, followed by references.

## 2 Car's License Number Plate Detection and Text Identification

In this section localizing license number plate is the initial thing utilized to extricate areas where license number plates are present. Vertical edge characteristics are moreover considered as suitable for number plate identification. These strategies estimate vertical edges of car's license plate and look for most dense regions in the picture. Color edge identifier is utilized, as the car's license number plate can also include distinct colors. That are the reason pixels with such different colors can be anticipated in two different ways and the locales with high density are taken as number plate characters. After license plate characters are discovered they ought to be examined by some identification strategy. Heuristic examining and priority selection methodology is utilized for the license plate character recognition. This methodology incorporates a few unique heuristics: the altitude of the band, quantity of peak in vertical projection, an estimation of region under the chart close to peaks, the angle proportion or aspect ratio of the license number plate. After these heuristics are assessed, they are joined together figuring their weighted entirety.

In this system raspberry pi is utilized as main processing unit. Optical character recognition (OCR), OpenCV and tesseract function is used to detect characters in license plate (see Fig. 3). The trained model is then copied to raspberry pi for deployment. Two range finding sensors are used to know the presence of the car. When a car is present at the entry section webcam turns towards the entry side and captures the image of license plate. Convert the image to text format, and display the license plate of the vehicle on the LCD module. If it matches driver need not to press any push button. If it doesn't match, the driver needs to press the push button to restart the license plate recognition process. So that, the camera captures the image of the vehicle's license plate and stores the car's license plate (see Fig. 4) and corresponding entry time of the vehicle. It gives access to the vehicle to enter the parking area by lifting the boom-barrier.



**Fig. 3.** Vehicle license plate number identified from an image using tesseract functions and optical character recognition.



With reference (see Fig. 4), when a car is present at the exit section, webcam turns towards the exit side and captures the image of license plate. Convert image to text format, compares the license plate with existing license plate of the vehicles. If it matches with the existing data it gives total time and billing amount of the vehicle.

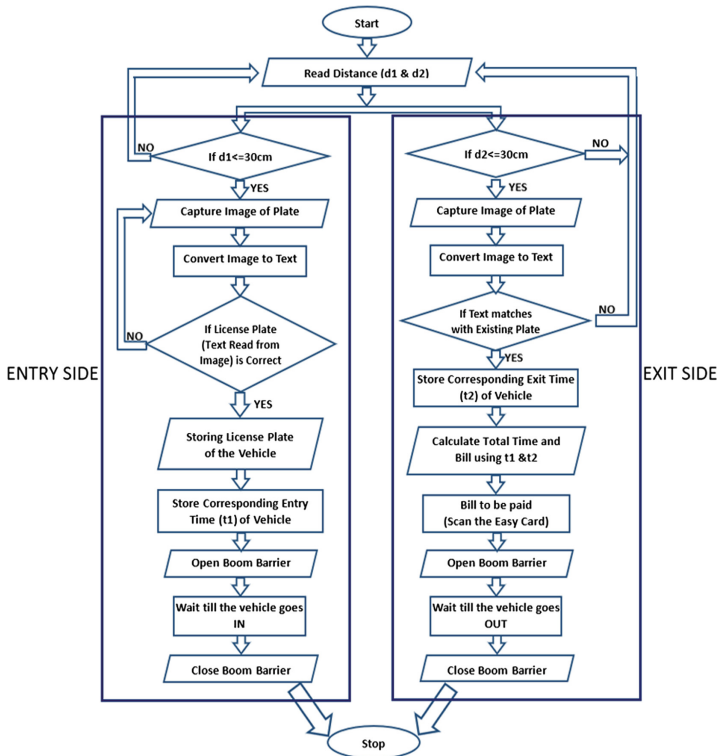


**Fig. 4.** Work flow of accessing vehicle to the parking area and displaying total time of car present with in the parking area.

## 2.1 Image Acquisition

This stage coordinates getting a picture by an acquisition method. In our proposed framework, a high-quality automated camera and adequate light source is used.

## 2.2 Number Plate Extraction

This stage expels the area of interest, i.e., the license plate, from the captured picture. The proposed methodology incorporates covering of a region with high or low probability of license plate and a short time later analyzing the whole hidden region of license plate.



### 2.3 Number Plate Character Segmentation

License plate segmentation, once a while insinuated as character isolation takes the region of interest and tries to identify it into explicit characters. The proposed system is done in the OCR portion.

### 2.4 Optical Character Recognition

There are various methodologies used to see limited characters. In the proposed structure optical character recognition are used.

## 3 Vehicle Type Detection

Normally, as per the vehicle measure, vehicle types can be partitioned into three classifications: SUV, sedan, mini. In this system, if the vehicle occupies more than 60% of the frame, it is classified as SUV, 25% to 60% is considers to be sedan and less than that as a mini car as referred in Table 1. Vehicle pictures caught under both good lightening conditions and bad lightening conditions independently are considered. Vehicle frontal area part is separated by inspecting car frontal area span and the region of the license number plate. In this system raspberry pi is utilized as main processing unit. Machine learning algorithms like convolutional neural network (CNN) is used. YOLO v2 model is utilized YOLO is a real-time object detection system. It processes images at 40–90 frames per second (FPS) and has a mean average precision (mAP) of 78.6%. A single neural network is applied to the full image, which makes it faster than other neural networks. This network divides the image into regions, predicts bounding boxes and gives probability of each region. These bounding boxes are weighted by the predicted probabilities. YOLO v2 mAP is increased by 4% when compared with mAP of YOLO v1. Teaching the system requires high processing power, which was done in MSI gp73 laptop, having 16 GB ram, 6 GB graphics card. For training purpose, python language, tensor flow, pycharm, anaconda is utilized. The trained model is then copied to raspberry pi for deployment. Additionally, open database including adequate pictures are utilized to develop own database that is, including pictures of vehicle front view. Actual procedure of vehicle type characterization includes frontal area segmentation, vehicle recognition, characteristics extraction and differentiation, which make it also slow for accomplishing real time operations. Vision based vehicle type characterization is of two types: techniques utilizing vehicle's side region view and techniques utilizing vehicle's frontal area (or back) view.

For vehicle feature extraction, a settled region of interests in a specific video arrangement is done. Setting ROI has a few points of interest, for example, constraining the vehicle pictures to an appropriate size range. Additionally, by setting appropriate areas, the required zone will be diminished and the principle features of vehicles can be ensured. At that point, a pre-trained convolutional neural network which can yield precise vehicle features has been executed to identify vehicles in the chosen area. The vehicle pictures will be acquired from a video. The recognition procedure is connected to the front piece of the video, a vehicle informational collection for the specific video scene would be produced so as to finish the vehicle identification steps.

Table 1. Vehicle classification

Type	Frame ratio
SUV	>60%
Sedan	25%> && <60%
Mini	<25%

Initially, the system is trained with adequate dataset of cars and not cars (see Figs. 5 and 6). The dataset consists of 1000 high resolution images of each set of vehicles. Then training the system with an approximate epoch value of 100 for better, accurate and rigid system. Principal feature analysis (PFA) is utilized to detect the vehicle. Whenever the system is trained with some set of images it performs some mathematical operations on the image, it also identifies the common thing in all the images of the dataset, plot the graph of the images with the key features and set a range of values to every key feature of the image. It also generates a model with set of scores of the input image at each pixel value which includes the key features.

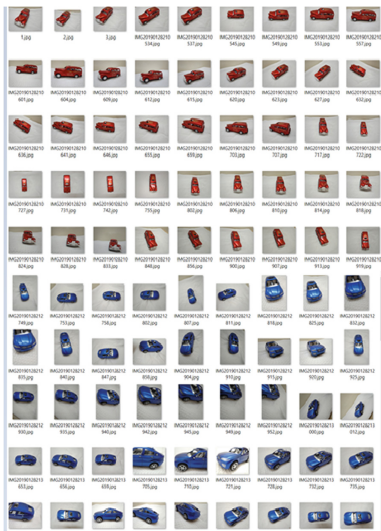


Fig. 5. Adequate dataset

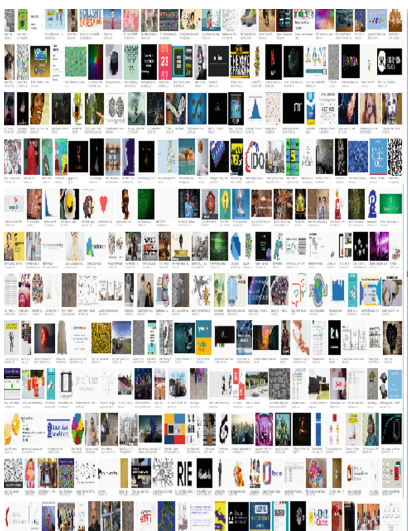
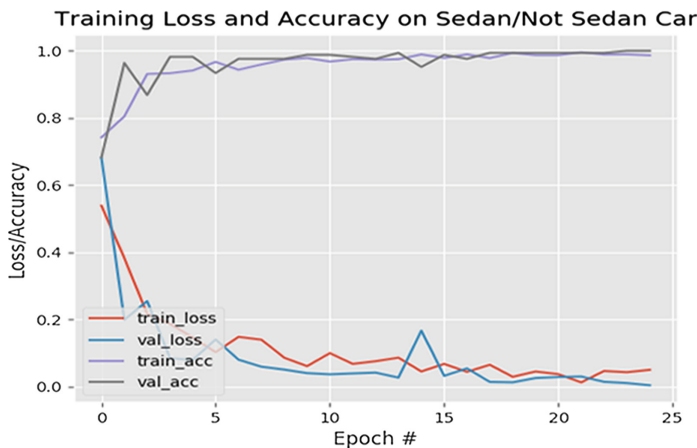


Fig. 6. Random dataset

In neural network an image is received and transform it through series of hidden layers. Each hidden layer is made up of set of neurons. Each neuron is fully connected with other neurons in previous layer. When an input is given it holds raw pixel value. Then it is sent through convolutional layer where it performs dot product between their weights followed by pooling operation where downsizing the spatial dimensions of the image. It gives the final class score of the image.

With reference (see Fig. 7) gives an idea of the training output. The system is trained using ‘cars’ and ‘not cars’ dataset. The not cars dataset consists of random images. After the training operation, the collection of images having a car will have an accuracy value greater than 0.9 (see Fig. 7). Random images will have less accuracy as the images don’t possess a common feature to be recognised.



**Fig. 7.** Model is plotted against adequate and random dataset

While performing deep learning of the image, it has two data sets- training data and validating data. Training data is utilized to train the system. Validation data is utilized for testing the system. For every epoch validation loss gets lower and accuracy gets higher. Epoch is teaching the system with one full pass of training set. It has few iterations.

While testing is done it extracts key features or objects from the image, by performing some mathematical operations it gets some set of value or score of every pixel of the image, that is the final class score. If the final score of the image matches with trained data it gives true or else false. The probability of matching depends on the dataset provided or accuracy of the system. With reference (see Fig. 8), the blue car is at the entry side and through the vehicle identification camera, the car is being detected with a probability of 99.95% (see Fig. 9).

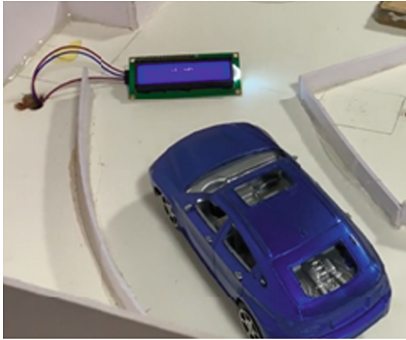


**Fig. 8.** Identifying type of car

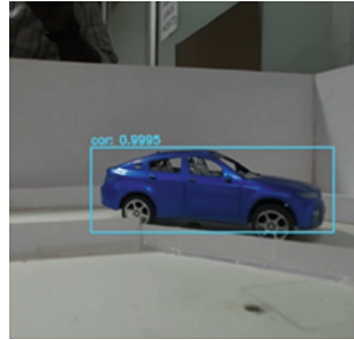


**Fig. 9.** Getting Pixel length of car

## 4 Allot Best Fit Parking Area

The parking slot detection and allotment has also become troublesome these days and a lot of research is taking place in this area, Kanteti [5] in 2017 proposed a hybrid algorithm for parking area allotment for car, by attaching CMOS sensors for number plate identification, speed sensors, ultrasonic sensors for vehicle detection and working on OCR software by utilizing a micro controller and processor. Liu [6] in 2017 developed an image-based system for the detection of vacant spaces in a parking area. Following an initial edge detection stage, they combined edge density, closed contour density, and foreground/background pixel ratio, at every car parking spot, to identify whether a car is present or not. Combining these features a vacant space is detected at low computational cost. Sawangchote [7] in 2017 designed and implemented a calculation model for number of car and parking pattern in the specified parking area. In the calculation, the dimension and the specific condition of parking area is required. The model calculated the maximum number of car and also calculated the parking pattern for the parking area. This model is used to support non-technical user during the parking area design and can be as engine to develop mobile application for general user in the future. Zhang [8] in 2018 proposed a novel DCNN (Deep Convolutional Neural Networks) based parking-slot detection approach, namely DeepPS, which takes the surround-view image as the input. There are two key steps in DeepPS, identifying all the marking-points on the input image and classifying local image patterns formed by pairs of marking points. Second, to facilitate the study of vision-based parking-slot detection, a largescale labeled dataset is established. For each image, the marking-points and parking-slots are carefully labeled. The efficiency of DeepPS have been corroborated on their collected dataset.

Generally, there are two methodologies utilized for recognition of empty slots: sensor based and picture-based system. Comparing sensor-based parking lot arrangement systems, picture-based methodologies are more reliable and cost friendly. Sensor based parking recognizes the existence or absence of the vehicle. Aside from recognizing the vehicle, the sensor can give additional data like displaying the vacancy slots for parking. The chance of occurrence of error is more by the usage of sensors. As it

requires a greater number of sensors to be placed i.e., at every parking slot it requires a sensor. Disruptive communication between the sensors may lead to errors. That is, the signal from transmitter may not be received by the receiver, then the sensor may be prone to errors. It may show vacant slot as occupied and vice versa. Moreover, the power consumed by the sensors is high due to repeated utilization. Sensors requires continuous monitoring at entrance section and exit sections.

In the image-based parking lot arrangements the camera can be utilized to detect the unoccupied space through image recognition. The picture is captured and it is permitted to image segmentation and edge recognition by boundaries. The moving vehicle is to be parked at explicit zone, at first the parking region must be recognized at the zone then the parking slot must be detected. Check whether there is any empty slot, and it is accessible or not. In the parking region the image processing technique have been implemented that will experience the image segmentation and edge detection.

With reference (see Fig. 10), in parking slot allotment, if a vehicle is present, it captures the image of the car. It performs mathematical operations and separates VIP cars from normal cars based on the QR code present on the vehicle. It also detects the length of car and classify the cars in to 3 types SUV, sedan, mini based on its size. Intelligent parking system allots best fit and optimal parking area to the vehicle.

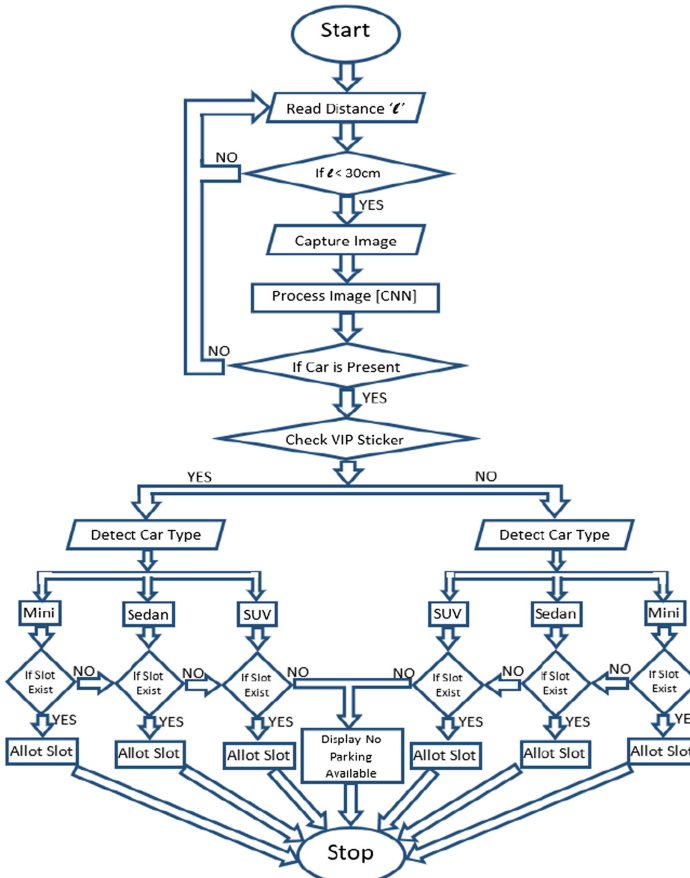


**Fig. 10.** Work flow of allotting best fit and optimal parking slot to the vehicle

## 5 Experimental Results

An experiment conducted with an epoch value can reach an accuracy range of 40–50%. By changing an epoch value to 100 under good lighting conditions an accuracy of 80–85% can be achieved. Previously, the detection rate using webcam was as low as 50–60%, using deep learning-based region of interest selection algorithms, the detection rate was increased to 80% as mentioned in Table 2. YOLO v2 model is used for training and testing as it has a mean average precision (mAP) of 80%. Other deep learning models took more processing time thus increasing time taken for registering one car. For text recognition in vehicles license plate this system is capable of identifying all character fonts of different sizes.

**Table 2.** Confusion matrix for number plate identification

N = 100	Characters on number plate	Not the characters on number plate
Characters on number plate	38	11
Not the characters on number plate	9	42

## 6 Conclusion

In this paper, the presented methodology is effectively able to allot best fit and optimal parking area to the vehicle based on its size. As the trained data consists of cars only, the algorithm would be incapable of detecting other vehicles. It extracts features like length and size.

In character recognition of license plate, it is able to identify characters only in few fonts, with an accuracy of 80%. For future work the extracted feature can likewise be utilized to prepare neural system for higher precision. In acknowledgment, a variety in character geometry prompts misclassification. So as to reduce these miscalculations, classifier should be trained with various textual styles which was detected from individual training dataset.

**Acknowledgement.** The authors are grateful to the Tamkang University, Taiwan (ROC) under the “2017–2018 TEEP@Asia Plus Program” for the financial support of this work.

## References

1. Wang, Y.C., Han, C.C., Hsieh, C.T., Fan, K.C.: Vehicle type classification from surveillance videos on urban roads. In: Proceedings – 2014 7th International Conference on Ubi-Media Computing and Workshops, pp. 266–270 (2014)
2. Peng, Y., Jin, J.S., Luo, S., Xu, M., Cui, Y.: Vehicle type classification using PCA with self-clustering. In: Proceedings – 2012 IEEE International Conference on Multimedia and Expo Workshops (ICMEW), pp. 384–389 (2012)

3. Pechiammal, B., Renjith, J.A.: An efficient approach for automatic license plate recognition system. In: Proceedings – 2017 Third International Conference on Science and Technology Engineering & Management (ICONSTEM), pp. 121–129, January 2018
4. Wang, N., Zhu, X., Zhang, J.: License plate segmentation and recognition of Chinese vehicle based on BPNN. In: Proceedings – 12th International Conference on Computational Intelligence and Security (CIS), pp. 403–406 (2016)
5. Kanteti, D., Srikar, D.V.S., Ramesh, T.K.: Intelligent smart parking algorithm. *IEEE Transp. Intell. Transp. Syst.* **11**(4), 942–953 (2017)
6. Liu, J., Mohandes, M., Deriche, M.: A multi-classifier image based vacant parking detection system. In: Proceedings – IEEE International Conference on Electron Circuits and Systems, pp. 933–936 (2013)
7. Sawangchote, P., Yooyativong, T.: Automated parking area optimization for garage construction using geometric algorithm. In: Proceedings – 2nd International Conference on Digital Arts and Media Technology, pp. 286–290 (2017)
8. Zhang, L., Huang, J., Li, X., Xiong, L.: Vision based parking slot detection: a DCNN based approach and a large-scale benchmark dataset. *IEEE Trans. Image Process.* **27**(11), 5350–5364 (2018)



# Design and Requirements for a Mobile Robot for Team Cooperation

Luca Di Nunzio<sup>1</sup>, Giancarlo Cardarilli<sup>1</sup>, Marco Ceccarelli<sup>2(✉)</sup>,  
and Rocco Fazzolari<sup>1</sup>

<sup>1</sup> Department of Electronics Engineering,  
University of Roma Tor Vergata, Rome, Italy  
{di.nunzio, fazzolari}@ing.uniroma2.it

<sup>2</sup> Department of Industrial Engineering,  
University of Roma Tor Vergata, Rome, Italy  
marco.ceccarelli@uniroma2.it

**Abstract.** The paper presents requirements and issues for a mobile robot design that is finalized to work in a swarm with cooperation among several other units with the same structure and features. A design for a small mobile robot TOR-VEbot is proposed by considering the requirements for locomotion in cooperation as combined with integrated sensing and motion planning. Preliminary results are also discussed to highlight problems and targets of the swarm project under development at the University of Rome Tor Vergata.

**Keywords:** Service robotics · Surveying robots · Swarm robots · Design

## 1 Introduction

Swarm Robotics consists of the use of several autonomous robots cooperating each other to accomplish common tasks. Application fields for robot swarms include search and rescue, precision agriculture, military surveillance as in general for surveying activities. In a robot swarm, each robot must be able to take decisions autonomously considering its state and the external environment [1].

The design of mobile robots can be developed by using different structures and operation features as depending on the environments and tasks, as for example reported in [2]. There are a variety of solutions of mobile robots with wheels, crawlers, or legs that have been developed for operation as single units or team units, even considering the case to use and/or to adjust the design and/or operation for team/swarm applications. Examples of wheeled mobile robots that can be used also in cooperative teams/swarms can be considered as for example in [3–5]. Similarly, legged mobile robots of references can be considered for example Cassino Hexapode [3] and many other as in [4]. The swarm design requires e-communication and interaction capabilities, as indicated for example in [5]. This means that also the mechanical design of a mobile robot will be affected by the swarm application and indeed it is convenient to consider the mobile robot unit as a platform for the e-comm equipment and interaction interfaces.



In this paper, the design of a robot mobile unit is outlined with those peculiarities as swarm unit that give requirements and solutions for TORVEbot robot with features for low-cost, easy operation, e-learning path planning, and e-comm interfaces.

## 2 Design Problems and Targets

A crucial aspect of robots cooperating in a swarm is the capability to adapt themselves to dynamic environments. Such capability is usually provided to such robots also by Machine Learning (ML) algorithms. ML refers to the ability of computers to learning from data [6]. Thanks to ML robots are able to learn “what to do” when analyzing data coming from sensors and consequently, they are able to “take decisions” and to be autonomous.

In this paper, the TORVEbot wheeled robot is presented as designed to cooperate in a swarm and to operate in risky situations. The main features of the proposed mobile robot are:

- **Flexibility:** The robot it is able to operate in different environments and to accomplish different tasks
- **Experience sharing:** Robot unit can communicate with other robot units in the swarm and with the internet. The capability to communicate with other robot units allows the possibility to share experience and speed-up the accomplishing of the task [7]

The flexibility is an ability that can be obtained providing a robot of reconfigurable electronic devices and of a common interface for all the sensors the robot needs. The choice of a common interface for all the sensors, allows the possibility to equip the robot of the appropriate sensors without the necessity to redesign the electronic board during updates or for different tasks. For example, when a robot has to detect a fire, it can be equipped with smoke sensors, temperature sensors, etc. Vice-versa when the robot must reveal the presence of chemical elements it can be equipped with specific sensors. In this way, the sensors substitution does not require any mechanical and/or electrical design.

In Fig. 1 a conceptual design of a swarm robot unit is summarized indicating the main requirements in task, motion, and interaction that will give an integrated design solution with capabilities in team swarm cooperation, localization, and e-comm (communication). The specific components of a mobile robot unit for a swarm can be listed in

- Sensors for locomotion needs,
- Location identification, and coordination of team interaction;
- Interface equipment for team communication and cooperation in actions performing the assigned tasks
- Control systems both in hardware and software to regulate and execute the motion and actions as asked for the task and needed for team cooperation.
- Power unit to ensure the necessary duration of the operation of all the components in the robot, besides the locomotion energy
- Electronics boards for the e-learning capability and e-comm among the swarm units and the central supervisor

A specific feature for TORVEbot design is related to the swarm cooperation that is also based on quick learning and communication among the swarm units. Therefore, specific attention is addressed to e-learning with proper hardware and algorithms, like suggested for example in [8–12].

Figure 1 is aimed to point out that requirements and design solutions for a swarm robot unit are affected to each other and although each component can be designed or provided from standard solutions their integration give specific problems and need specific solutions.

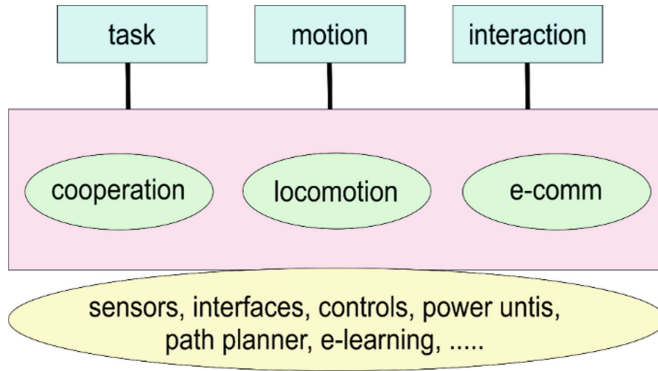


**Fig. 1.** A scheme for design integration considering problems and requirements for a swarm mobile unit

In Fig. 2 such an effect of the component interaction is stressed by considering the design structure with a platform body where most of those components for the swarm operation can be installed. This requires a specific shape and design of the platform body and its connections or extensions for the locomotion system, the e-comm equipment, team interface devices, and link to the supervisor. The locomotion system can be conceived with two actuated wheels and one front wheel to ensure a stable posture on three contact points during motion. The swarm e-comm system is aimed to permit communication among the swarm units so that the actions of the swarm can be operated in suitable collaboration of the units using also the interface devices that the robot units are equipped with for the assigned task. A device of communication with the supervisor is considered useful both to command and monitor each unit directly and even the whole swarm as seen from the unit.

The design target is to conceive a mobile robot unit that with a robust mechanical design is able to perform efficiently the motion planning as assigned by the task and elaborated by the swarm cooperation even with e-learning capabilities. The design structure is also characterized by a body that serves as platform for those components and operation making the designed wheeled mobile robot a unit of a swarm team.

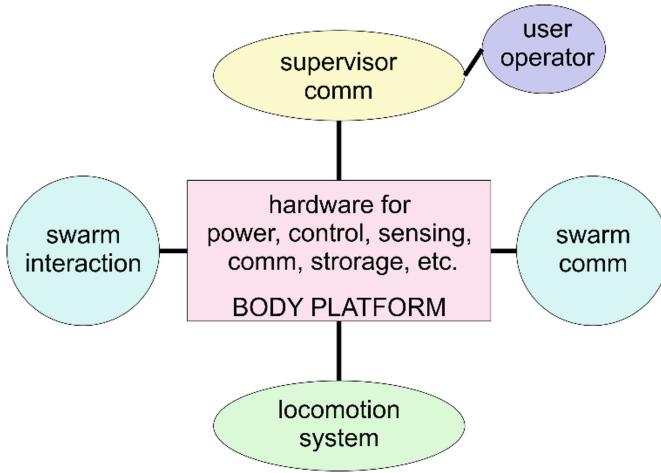


**Fig. 2.** A scheme for a conceptual design of a swarm mobile unit

### 3 Design Solution

In this paper, we present a prototype of the TORVEbot mobile robot with features and purposes that are discussed in the previous section. The structure of the robot unit has been built using a 3D printer with PLA material and is equipped with the following devices:

- HC SR04 ultrasonic sensor with a range of 2 cm to 4 m and 1 cm resolution
- FS 90R servo motor
- An arty board with an Artix FPGA as from [12]
- DHT11 digital temperature and humidity sensor
- GY-BMP280-3.3 pressure sensor
- NRF24L01+ wireless transceiver

In Fig. 3(a) the frontal and the lateral views of the CAD model design are reported whereas in Fig. 3(b) the corresponding built prototype is shown in its first version. All the control and the Artificial Intelligence (AI) algorithms of the robot are implemented on a Digilent Arty Board where the MicroBlaze soft processor has been implemented. Arty is a low-cost development board equipped with the Xilinx Artix-7 FPGA, [12].

MicroBlaze is a 32-bit Reduced Instruction Set Computer (RISC) soft processor, that can be used in several application fields such as industrial, medical, automotive, consumer, and communication infrastructure markets among others. MicroBlaze is a highly configurable and easy to use processor and can be used across FPGAs and All Programmable (AP) SoC families. This Microprocessor supports more configuration options. Some of the key configuration options are Instruction/Data Cache, Floating Point unit, Memory Management Unit, etc. With highly flexible and configurable core, the user can implement virtually any processor use case, from a very-small-footprint state machine or microcontroller to a high-performance, compute-intensive microprocessor-based system running Linux. It is very suitable for the implementation, inside of the

FPGA, of mixed digital systems composed by a Processor and a reconfigurable architecture. Microblaze supports the integration of custom peripherals that can be designed in HDLs (Hardware description languages) like VHDL or Verilog and connected with the Microprocessor using the AXI interface. AXI [13] is part of ARM AMBA, a family of micro controller buses first introduced in 1996. The first version of AXI was first included in AMBA 3.0, released in 2003. AMBA 4.0, released in 2010, includes the second version of AXI, AXI4.

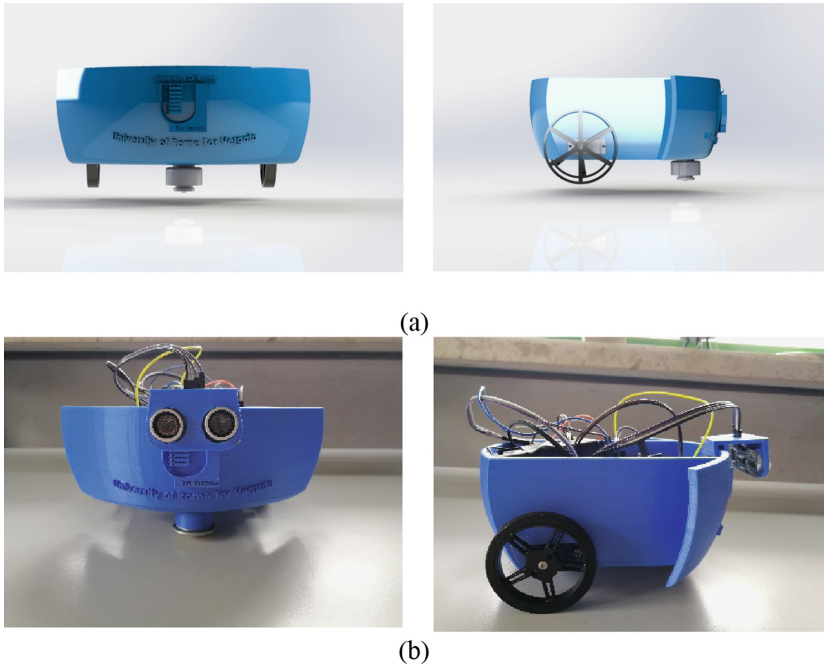


**Fig. 3.** The TORVEbot swarm robot unit: (a) views of the CAD design; (b) a built prototype

There are three types of AXI4 interfaces, [13]:

- AXI4—for high-performance memory-mapped requirements.
- AXI4-Lite—for simple, low-throughput memory-mapped communication (for example, to and from control and status registers).
- AXI4-Stream—for high-speed streaming data.

In Fig. 4 a block diagram is shown for the design of the complete control unit that is composed of the Microprocessor and the custom peripherals. The system includes by the microprocessor and several custom peripherals that are:

- A Machine Learning Accelerator.
- Two PWM controllers for the wheels.

- Some Application Specific Sensors Interface ASSC. In our case, we have three interfaces for the HC SR04, the DHT11 and the GY-BMP280-3.3.
- An e-comm interface for the wireless transceiver (Wireless Interface).

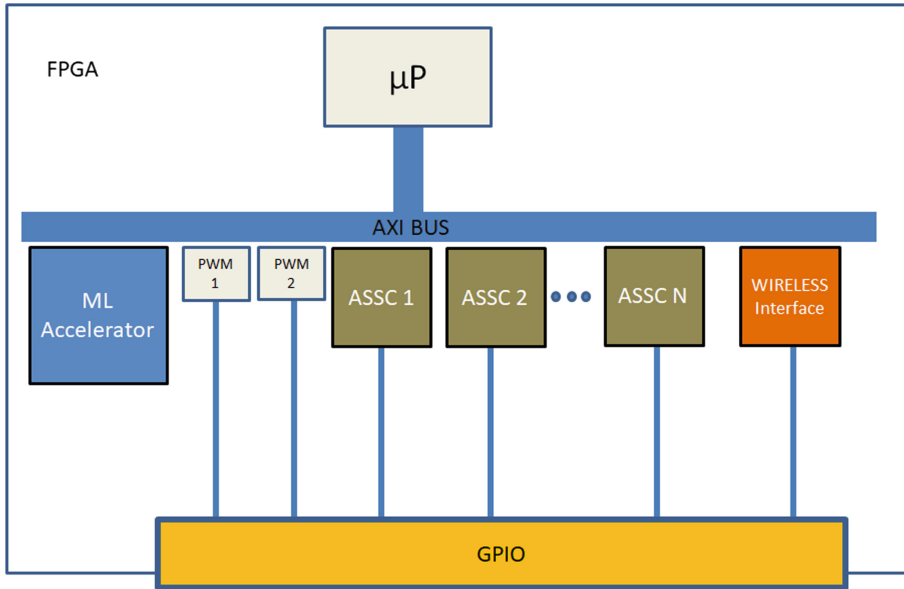


**Fig. 4.** A design scheme of the control system for the swarm robot unit in Fig. 3

The Wi-Fi interface with a wireless transceiver allows the robot to communicate with other robots in order to share its experience and with a gateway that is used to collect data from all the robot swarm. The interface with a wireless transceiver allows a robot to communicate with a gateway that to collects data from all the robot units of the swarm and to manage the sharing of the experience. The proposed TORVEbot robot prototype is provided of the NRF24L01+ Transceiver that is characterized by:

- 2.4 GHz carrier
- Throughput 1 Mb/s
- Range 30 m in open spaces
- GFSK Modulation
- 3.3 V supply range
- 900 nA deep sleep mode
- 11.3 mA Radio TX at 0 dBm
- 13.3 mA Radio RX at 2 Mbps on-air data-rate

The hardware and the software of the control unit as in the design in Fig. 4 can affect the mechanical design of the TORVEbot robot unit both for the needed room for the hardware and its good functioning (cooling air and no electro-magnetic interference with servomotors) and for the operation performance in posture and speed. Figure 5

shows a solution for the construction of a prototype as mainly focused on a proper installation of the built electronic board with the design of Fig. 4 as in Fig. 5(a) within the mechanical design as in Fig. 5(b). Components of the control design in Fig. 4 are included in the control board in Fig. 5(a) as indicated in the main chip; while the mechanical design of the robot body has been properly shaped to store the control board vertically with proper room also for efficient cable connections to other components. In the control board in Fig. 5(a) typical components for a control unit are also included, such as I-O channels for servomotor handling, switches for debug, and RAM chip for data elaboration.

Main characteristics of the solution in Fig. 5 can be recognized in a compact design of the electronic board (that can be further miniaturized) and in installing it in the central body of the mobile robot design in a vertical posture for an easy check/extraction and to give the possibility of more electronic boards for sensors and other equipment.

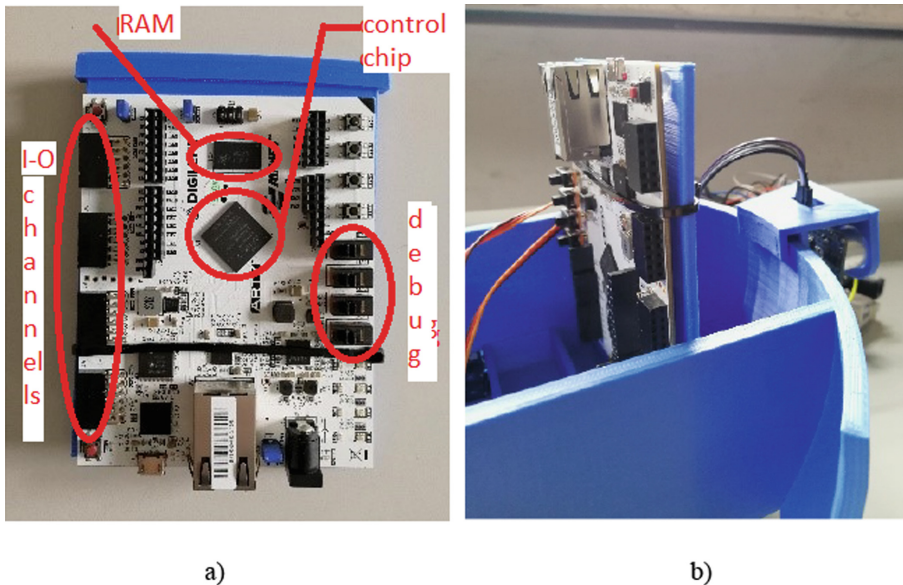


**Fig. 5.** Mechanical design of the body platform of the TORVEbot prototype in Fig. 3 with the control board: (a) the control board with designed control chip in Fig. 4; (b) the assembly within the robot body

## 4 Sensing Design and Software

The use of reconfigurable electronic devices allows the possibility to reconfigure the robot for different tasks with fast easy operation with no necessary changes of the hardware and software as well as the corresponding mechanical design. The proposed TORVEbot robot is provided with a Field Programmable Gate Array (FPGA). In addition to the reconfiguration capability, the FPGA offers the possibility to efficiently execute algorithms that are characterized by a considerable level of parallelism and the

possibility to execute several algorithms in parallel. These features are very useful in the case of ML algorithms for three reasons, namely:

- 1 FPGAs are able to execute matrix computation in a very efficient way. ML algorithms as for example CNN, SVM, SOM [8], etc. are characterized by parallel operations as vector matrix multiplications.
- 2 The robot can efficiently use Ensemble Machine Learning [9] to improve the performances.
- 3 More than one task can be accomplished in parallel, for example, the robot could detect the presence of smoke and fire and at the same time, it could reconstruct the unknown environment in which it is operating.

The experience sharing is the capability of the robot to share its experience with the other robots of the swarm. Swarm robotic operation can be modeled as a multi-agent learning problem, as for example in [7]. In a reinforcement ML algorithm, like the case for example of the Q-learning, the learning phase of the entire swarm can be accelerated if all the agents (the robots composing swarm) are able to fetch pieces of information and upgrading the Q-matrix ( $Q_{sw}$ ) simultaneously. In other words, a single robot is able to learn by the experience of the other robots by fast communication and sharing data for the task and status of itself and the whole swarm. The above feature is due to a data elaboration coming from the sensors in combination with a cognitive system using the sensed information. In the TORVEbot design great attention has been addressed to the hardware and software for the experience sharing in the swarm as a novel aspect influencing the design and sensor equipment of each mobile robot unit. The sensors that can be considered for the swarm coordinate operation, have been identified in:

- Proximity sensors that can detect near obstacles and swarm units
- Vision and laser scanners that can be used to identify the environment and to guide the path planning of each unit in coordination with the near ones
- Sensors for localization of the unit with respect to a reference frame and with respect to other swarm units
- Sensor equipment for the assigned task either for the specific unit or for the whole swarm

The above sensors are installed onboard of each swarm unit by using the room in the platform body of each unit whereas the corresponding software is loaded in the control unit mainframe and is run and coordinated by the software of the control unit that acts also with the communications and e-learning algorithms.

In fact, the size of the mechanical design of TORVEbot robot has been determined by considering the installation of the above sensors (and some more in the future <) and equipment near/in conjunction with the electronic board of the control unit that can include also the electronics for the sensors equipment as per its design. Thus, as shown in Fig. 5(b) the body shape of TORVEbot is sized with a hemisphere shape of 80 cm diameter to host everything on board with a protection shell and by using wheels of 4 cm diameter.

## 5 Conclusions

This paper presents a TORVEbot wheeled mobile robot for swarm that is designed as a unit with characteristics for team cooperation and e-communication. The TORVEbot unit design is presented by referring to requirements for operation in swarm operation with the aim to identify a platform solution with main features on low-cost, easy-operation, e-learning capability, and team e-interaction. Design issues and peculiarities are discussed with preliminary experiences with a first unit prototype.

**Acknowledgements.** The authors acknowledge thankfully Mr. Mohamed Elarayshi for the help in the construction of the prototype of TORVEbot within a teaching project of the curriculum Mechatronics.

## References

1. Seo, S., Yang, H., Sim, K.: Behavior learning and evolution of swarm robot system for cooperative behavior. In: IEEE/ASME International Conference on Advanced Intelligent Mechatronics, AIM, pp. 673–678 (2009)
2. Ceccarelli, M., Kececi, E.F. (eds.): Designs and Prototypes of Mobile Robots, ASME Press Robotics Engineering Book Series. ASME (2015)
3. Carbone, G., Ceccarelli, M.: A low-cost easy-operation hexapod walking machine. *Int. J. Adv. Robot. Syst.* **5**(2), 161–166 (2008)
4. Carbone, G., Ceccarelli, M.: Legged Robotic System, Cutting Edge Robotics ARS Scientific Book, Wien, pp. 553–576 (2005)
5. Kececi, E.F., Ceccarelli, M. (eds.): Mobile Robots for Dynamic Environments, ASME Press Robotics Engineering Book Series. ASME (2015)
6. Abu-Mostafa Y.S., Magdon-Ismael M., Lin H.-T.: Learning from Data. AML Book (2012)
7. Matta, M., Cardarilli, G.C., Di Nunzio, L., Fazzolari, R., Giardini, D., Re, M., Silvestri, F., Spanò, S.: Q-RTS: a real-time swarm intelligence based on multi-agent Q-learning. *Electron. Lett.* **55**, 589–591 (2019)
8. Cardarilli, G.C., Di Nunzio, L., Fazzolari, R., Re, M., Spano, S.: AW-SOM, an algorithm for high-speed learning in hardware self-organizing maps. *IEEE Trans. Circuits Syst. II.* (in print)
9. Cardarilli, G.C., Di Nunzio, L., Fazzolari, R., Giardini, D., Matta, M., Re, M., Silvestri, F., Spanò, S.: Ensemble machine learning implementation on FPGA using partial reconfiguration. In: 2019 Lecture Notes in Electrical Engineering (2019)
10. Tuyls, K., Weiss, G.: Multiagent learning: basics, challenges, and prospects. *AI Mag.* **33**(3), 41–52 (2012)
11. Watkins, C.J., Dayan, P.: Q-learning. *Mach. Learn.* **8**(3–4), 279–292 (1992)
12. DIGILENT: ARTY board manual (2019)
13. XILINX: IP documentation: AXI Reference guide (2019)





# Learning Emotion Recognition and Response Generation for a Service Robot

Jhih-Yuan Huang, Wei-Po Lee<sup>(✉)</sup>, and Bu-Wei Dong

National Sun Yat-sen University, Kaohsiung City 80424, Taiwan  
wplee@mail.nsysu.edu.tw

**Abstract.** Building dialoguing services for robots to provide natural human-robot interactions and to enhance user experiences is now advocated. With this type of services, a robot can work as a consultant and provide domain-specific knowledge to end users. In this study, we adopt a service-oriented framework to develop emotion-aware dialogues for a service robot. Our work includes several unique features: it trains classifiers to recognize users' emotions in conversation, learns a deep neural model to generate answers in response to users' questions, and uses the emotional information to determine the answer sentences produced by the dialoguing model. A series of experiments are conducted for performance evaluation. The results are compared with other machine learning methods, and they show the promise and potential of the presented approach.

**Keywords:** Service robot · Emotion recognition · Dialogue modeling · Machine learning

## 1 Introduction

Researchers and engineers are building service robots that can interact with people and achieve the given tasks. To deploy practical service robots, two major concerns need to be considered seriously, including the system architecture for launching the services and the creation of service functions. Presently, the services are mostly laboring services, in which robots take actions in the physical environment to assist people. However, robots are now expected to play more important roles in providing knowledge services, and communicating with users through a natural way of spoken language. It thus becomes increasingly critical to equip social competences to robots, with which the robot can respond appropriately to users. Following our previous studies that adopt a service-oriented architecture to develop action-oriented robot services, in this work we present a trainable framework for modeling emotion-aware human-robot dialogues to provide knowledge services.

Considering choosing supportive software architecture, several studies have proposed to adopt the cloud-based service-oriented architecture. Among others, the most representative work is RoboEarth [1], driven by an open-source cloud robotics platform [2]. With this platform, the robots can distribute highly loaded computation to the cloud and access the RoboEarth knowledge repository to download required resources. There are also other platforms developed for cloud robotic systems, in which the robotic hardware and software resources are connected and available through the web.

Our previous work implemented a cloud-based system supporting a variety of user-created services [3]. To ensure its expandability and shareability, we have constructed a service configuration mechanism and deployed the system on the ROS (Robot Operating System) computing nodes in practice.

To achieve natural language-based human-robot interaction, the most common way is to build a dialogue system as a vocal interactive interface. Essentially, the dialogue system includes a knowledge base with domain questions and the corresponding answers, and the dialogue service is to design an accurate mapping mechanism that retrieves correct answers in response to the users' questions. The system is performed in a question-answering manner, and most traditional approaches are based on hand-crafted rules or templates (e.g. [4]). Recently, the deep learning-based methods have been successfully employed to infer neural models for question and answer sentences. These neural systems mainly used sequence to sequence (seq2seq) model as a backbone, to perform mappings from entire sequences of words or characters to other sequences, for example [5, 6].

In addition to the dialoguing content, emotion plays an important role in determining the relevance of the answer to a specific question. By integrating emotion information into the application, a service system can enable its application services to automatically adapt to changes in the operational environment, leading to the enhancement of user experiences. There are works that propose considering emotion information along with the content of the dialogues. For example, Zhou *et al.* presented a model that assumed the emotion category of human utterance was known and taken as additional input to train a model of responses [7]. Sun *et al.* adopted a LSTM neural network for conversation modeling [8], in which an emotional category label was added to the encoder, regarded emotional information as an additional source to the conversational model.

In this work, we develop an emotion-aware human-robot dialogue service to enable the robot to work as a consultant to deliver domain-specific knowledge service. Specifically, the major focus is on constructing a deep learning model for mapping question and answer sentences, tracking the human emotion during the process of human-robot dialoguing, and using this additional information to determine the relevance of the sentences obtained by the model. To verify the presented approach, a series of experiments are conducted and several methods are implemented for comparison. The results show that the presented approach performs the best among different methods.

## 2 Learning Emotion-Aware Human-Robot Dialogues

### 2.1 The Service Robot Framework

In this work, we adopt a service-oriented robotic framework that can provide various services and resources, and develop our emotion-aware dialoguing service on it. This computing platform includes two parts: the on-board processors mounted on the robot side (to deal basis functions requiring fast responses, such as those related to perception and actuation), and the computing nodes located in the cloud side to perform high

loaded computing services (such as service planning and deep learning). To realize the proposed design in practice, we configure the framework with ROS to deliver different types of services. Figure 1 illustrates the system architecture of our robotic system and its ROS configuration. The module of service planning has been described in our previous work. Here, we focus on the dialoguing module (i.e., the lower part), in which the major functional blocks are indicated.

To provide different services on the cloud, we define different types of computing nodes in the framework. Through the ROS frame protocol, management of data interchange between nodes, the framework can easily combine different services to launch new functions. In this work, we focus on a newly developed emotion-aware dialoguing service, in which the robot can identify users (by face recognition) and their emotions (by utterance analysis), and then generate suitable responses (by a question-answering model) accordingly. At present, the functions of user identification and emotion recognition are constructed independently from the dialoguing model (due to the lack of a dataset with complete information of human face, utterance emotion and dialoguing content). The current strategy is that the identified user is assigned to a certain type of user group and the corresponding model is retrieved to perform dialoguing. Then the candidate sentences produced by the model are re-ranked (based on the recognized emotion) by a set of hand-crafted rules and the sentence with the highest rank is selected as the robot's response.

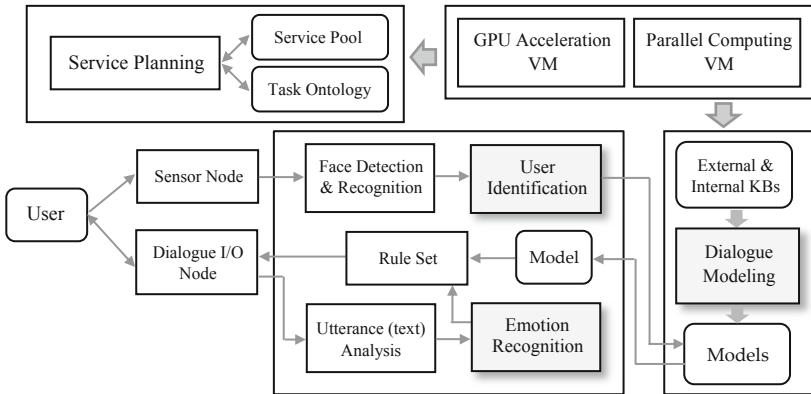


Fig. 1. Our emotion-aware service robot framework.

2.2 Emotion Recognition

Before constructing emotion classifiers, we perform several text processing procedures. The first is to use semantic rules for sentence segmentation. For example, if there is a disjunctive such as “but” or “although” in the sentence, the emotion of the entire sentence is usually biased toward the former or the latter clause. To solve such a problem, we adopt a set of five semantic rules (from [9]) to perform more precise sentence segmentation. Then, we employ the natural language processing toolkit

NLTK to build a dictionary, of which the most frequently stop words are removed, and then a procedure of stemming is performed to strip off word endings, and reduce them to a common core or stem.

Once the word processing is completed, the GloVe method (Global Vectors for Word Representation, [10]) is employed to map words into vectors. GloVe is a log-bilinear model with a weighted least-squares objective. This objective is to learn word vectors such that their dot product equals the logarithm of the words' probability of co-occurrence, based on the observation that word-word co-occurrence probabilities have the potential for encoding some form of meaning. The training process is performed on aggregated global word-word co-occurrence statistics from a corpus. Through this mapping method, the words are represented by real numbers and words with similar meanings can thus have similar representations. GloVe's model training efficiency is high, the calculation scale is proportional to the corpus size, and when the corpus is small or the vector dimension is small, it still achieves good results.

After the text processing procedures, to recognize various classes of emotions in conversation, we adopt a deep learning network that can achieve excellent performance in natural language processing through automated feature learning. Figure 2 illustrates the deep learning model used in this study. As shown, the input of this model are the dialoguing sentences that have been processed by the steps described and converted to the vectors by the word embedding method as described above. As the sentences have different length, to keep a consistent data format without affecting the meaning of the original sentences, the vectors are expanded with zero values to a maximum length pre-defined. In this network, three convolutional layers with lengths of 3, 4, and 5, are arranged to extract the local features of the sentence. Then, the features are combined and served as the input of the LSTM learning layer.

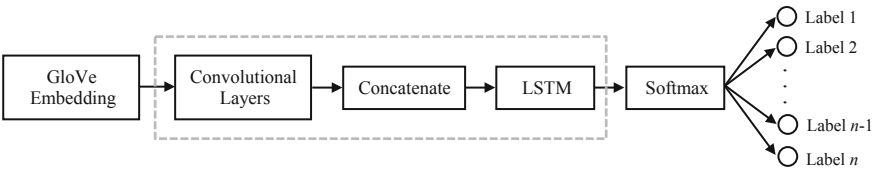


**Fig. 2.** The deep learning model for emotion recognition.

In this study, we adopt LSTM with ReLU (Rectified Linear Unit) to train a better model. The ReLU employs rectifier (an activation function defined as the positive part of its argument) and is able to obtain better training of deeper networks, compared to other widely used activation functions, such as the logistic sigmoid and the hyperbolic tangent. The piecewise linear property of ReLU has been proved to be effective in overcoming the vanishing gradient problem by several studies, and its property of scale-invariance allows for faster and effective training of deep neural architectures on large and complex datasets. Also, ReLU has the property of sparse activation, making the neural network sparse to alleviate the problem of overfitting.

In the above learning process, the gradient descent optimization algorithm Adam is used as an optimizer [11]. Unlike the classical stochastic gradient descent algorithms that maintain a single and fixed learning rate during the learning process, Adam maintains a learning rate for each weight and dynamically adjusts the learning rate. The parameter change at each learning-iteration has a certain range. It means that the parameter is not dramatically updated along with a large change of gradient; therefore the parameter values are relatively stable. Empirical results demonstrate that Adam works well in practice and can efficiently solve practical deep learning problems, compared to other stochastic optimization methods.

Finally, we use the activation function “Softmax” at the output layer to map the outputs of neurons into the interval of  $[0, 1]$ . From the aspect of probability theory, the output of the Softmax function can be used to represent a probability distribution over possible classes. In our application, the node with the highest probability (i.e., the one with the largest value) is selected as our prediction emotion class. In this work, the LabelEncoder of sklearn and the categorical\_crossentropy loss functions of Keras are employed to normalize the class label and it is converted into a one-hot code of the binary matrix to perform the numerical calculation.

Though the machine learning procedure is an efficient method in data modeling, to ensure the success of this approach, the problem of class imbalance must be overcome. For an imbalanced dataset, the machine learning method often focuses on reducing the classification error, and this may cause the model biases toward the common categories with large numbers of data samples. Therefore, we use the cost-sensitive technique to work with the machine learning method to learn a classifier that takes the costs into account internally. This is done by re-weighting the instances in a way that reflects the error costs. It is to define a weight matrix to specify the importance of different data classes and to adjust the weights to overcome the data imbalance problem.

### 2.3 Learning Emotion-Aware Dialogues

For the robot’s dialoguing model, a LSTM network with a CNN network is developed to train the answer selection mechanism to generate the most appropriate sentences (as outputs) in response to the users’ input sentences. Figure 3 illustrates the model, in which the LSTM contains memory blocks in the recurrent hidden layer that can store the temporal state of the network. With this characteristic, this model can better capture information over longer time steps to meet our goal here.

To train the above deep learning model, the sentences are organized as the question-answering pairs. The question sentence  $Q$  is the input question encoded into an internal vector form  $Q_V$  by the word embedding procedure. To enhance the performance, we establish the word2vec weights for the entire corpus, and use them as the pretrained model of the embedding layer. The output then flows to the LSTM and CNN layers.

In this procedure, a training dataset needs to be organized. In the knowledge base (i.e., the dataset), for each question  $Q$  there is a corresponding positive answer  $A_+$  with a highest probability to be the correct answer among all answers in the dataset (i.e., the confirmed correct answer). As shown in Fig. 3, after the embedding layer, an output vector  $E$  is obtained and then calculated through the LSTM function to derive a hidden vector  $L$  as the following:

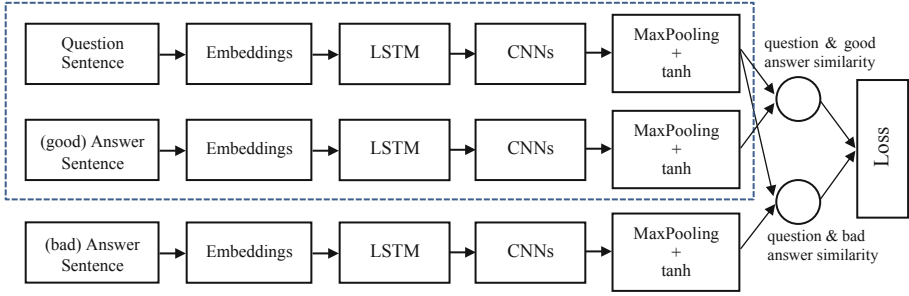


Fig. 3. The deep learning model for human-robot dialoguing.

$$E = \text{EMBED}(x_1, \dots, x_n; W_e) \quad (1)$$

$$L = \text{LSTM}(E; W_L) \quad (2)$$

In the above equations,  $E$  can be represented as  $\{e_1, e_2, \dots, e_n\}$ ,  $E \in R^{n \times d}$  in which  $n$  is the maximal sentence length and  $d$  is the dimension of embedding. Besides,  $W_e$  is the weight matrix  $W \in R^{v \times d}$  ( $v$  is the number of words in the dictionary),  $e$  is the vector embedded for word  $x$ , and  $W_L$  is the LSTM weight matrix.

Though the LSTM layer described above can extract the features of word sequences in sentences, in our network we further connect the tensor  $L$  (output of LSTM, Eq. (2)) to a convolutional layer to extract more complicated features for performance enhancement. As shown in the figure, the “MaxPooling” (a sample-based discretization process to down-sample an input representation) function is performed, and the “tanh” function is used to transfer and output the decoding result.

During the model training procedure, the question  $Q$ , the correct answer  $A+$ , and the wrong answer  $A-$  (sampled from the answer space) are encoded into vector representations  $V_Q$ ,  $V_{A+}$  and  $V_{A-}$ , respectively, and the similarities between the question and the two answers are calculated separately. Here, the similarity of two vectors is defined as:

$$\text{Similarity}(V_Q, V_A) = 1 / (1 + \|V_Q - V_A\|) \times 1 / [1 + \exp(-\gamma(\text{dot}(V_Q, V_A) + c))] \quad (3)$$

In the above equation, the parameters  $\gamma$  is 1.0 and  $c$  is 1.  $V_A$  is a positive or negative answer (i.e.,  $V_{A+}$  or  $V_{A-}$ ). Then, the distance between the two similarities is compared (meaning the difference between an answer and the ground truth) to a pre-defined margin  $m$ . If the distance is less than the margin  $m$ , the network parameters are updates; otherwise another negative example is sampled until the distance is less than  $m$  (a maximum number of steps often used to reduce the running time). The above operations are to ensure that the similarity distance (to be minimized) can reach a certain level. The function is defined as:

$$Loss = \max\{0, m - \text{Similarity}(V_Q, V_A) + \text{Similarity}(V_Q, V_{A-})\} \quad (4)$$

As described previously, in the test phase, this dialogue service calculates the similarity between a question sentence (asked by the user) and each answer sentence (in the knowledge base). A set of answers with highest similarity scores are selected, and they are re-ranked by the pre-defined rules (as illustrated in Fig. 1). The first-rank sentence is then adopted as the robot's response.

## 2.4 Knowledge Expansion

As can be seen, the main knowledge component in the above dialoguing service is a database (i.e., an indexed knowledge base) with domain questions and the corresponding answers. Here, we consider the conversation as the instance-based dialogue modeling, in which instances are pairs of question-answer sentences obtained from a semantically indexed knowledge base. This knowledge base includes the prior knowledge used to train the robot and it thus limits the ability of the dialoguing model in utterance generation. Therefore, it is important to exploit more background or domain knowledge in external knowledge resources to enrich conversation comprehension for robots. To provide additional knowledge, we attach an external knowledge base to the system to deal with the cases when the trained model is not able to provide responses. As our current focus is to investigate how this strategy can work with the model (rather than to find the optimal way to exploit the external knowledge), therefore, we choose the easiest method: directly attaching DBpedia to our system. This knowledge base includes rich content extracted from Wikipedia, and it can further enrich knowledge used for searching answers in the human-machine dialogues.

In our current implementations, we adopted the code available from the "quepy" website to perform knowledge retrieval. Our system first takes the user's question and then uses the `dbpedia.get_query` to transfer the question to the internal form specified by the knowledge base. If the answer is available from the external knowledge base, it is then used as the answer to response to the user's question, through the analysis of target and metadata obtained from the knowledge base.

## 3 Experiments and Results

To evaluate the presented emotion-aware dialoguing service for human-robot interaction, several sets of experimental trials were conducted. As mentioned, due to the lack of a dataset with complete information of human face, utterance emotion and dialoguing content, in the experiments we used three datasets to evaluate these modules separately. They are described in the following subsections.

### 3.1 User Identification

In this work, a cloud-based system was built for a service robot, and we configured a ROS framework on top of Linux OS to connect the sensing camera nodes. Often, a system built with ROS consists of a number of processes on a set of hosts, which are

connected at runtime in a peer-to-peer topology. Here, the ROS master was a PC running roscore and serving as the resource center for all the other ROS nodes connected to the network. The cloud parallel computing virtual machine has 8 CPU and 8 GB memory, and the GPU acceleration virtual machine has 8 CPU, 32 GB memory and NVIDIA Tesla K80 GPU.

For user identification, experiments were conducted to evaluate the performance of face recognition. The goal was to train and recognize human faces in a static manner, and we adopted OpenCV to train the classifiers. An online face dataset ([12]) was used. It included 90 image sets of different persons, in which each set included face images taken from different viewpoints, from  $90^\circ$  to  $-90^\circ$  (stepping by  $5^\circ$ ). The results show that the trained classifiers performed the best in the recognition of front face images. The faces in the images can be detected correctly with a reasonable rate of accuracy when the variation of the rotating angle was less than  $30^\circ$ , and the faces can be recognized with a good accuracy if the view angle was within the range of  $10^\circ$  to  $-10^\circ$ .

### 3.2 Training Classifiers for Emotion Recognition

To assess the performance of emotion recognition module, we adopted the dataset used in [13], which was derived from the Movie Dialog Corpus. The sentences in this dataset were categorized into six classes of emotions: fear, disgust, joy, sadness, anticipation and none (neutral). The deep learning approach described in Sect. 2.2 was employed to train a model for multi-class emotion recognition. In addition, two popular learning methods, Random Forest (RF) and Support Vector machine (SVM), were used for performance comparison.

For RF and SVM, we used the  $N$ -gram method to extract more text features from the original data for building classifiers to enhance their performance, in addition to the word features extracted from the text processing procedure.  $N$ -gram can express the sequence relationship between words, and the models of unigram, bigram and trigram ( $n$  is 1, 2, and 3, respectively) are often used. After a preliminary test, in this work we used the above three models to extract more text features, and the combined feature vectors were used as the input of the above two machine learning (RF and SVM) to enhance their performance.

Figure 4(a) illustrates the accuracy, precision, recall, and F-score of the three methods. As can be seen, RF performed the best in all metrics. The main reason could be that RF is a type of ensemble machine learning algorithm, and the way it handled (samples) data for the grouped multiple classifiers made it performing better than others for the imbalance dataset here.

After comparing the aforementioned three methods, we investigated the effects of two data processing techniques (i.e., data balance and semantic rules), when they were applied to the dataset. For data balance, we adopted the sklearn package to produce a set of specific class weights for different types of emotions. The five semantic rules mentioned in Sect. 2.2 were used to perform more precise sentence segmentation. The results of accuracy, precision, recall, and F-score are illustrated in Fig. 4(b). Overall, LSTM obtained the best results on all performance metrics. In addition to the data balance effect, the reason for performance improvement could be that the semantic rules can remove the irrelevant words and filter out their effects on the sentence



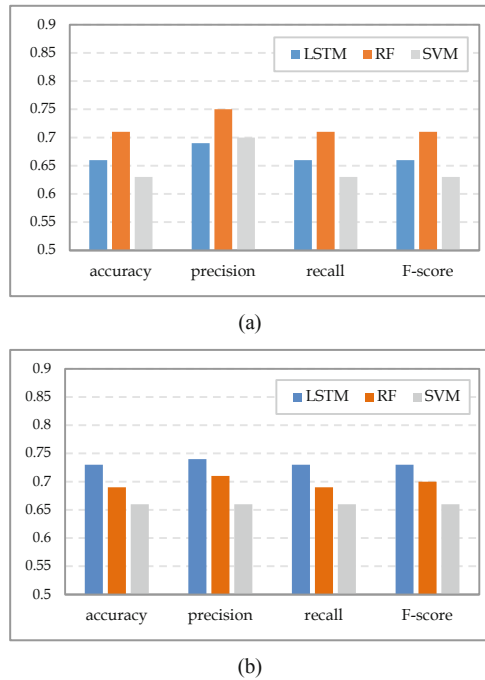


**Fig. 4.** Results of three methods without (a) and with (b) enhanced techniques.

emotions. Thus, the learning methods were able to focus on the emotions delivered by the most related parts of the sentences to be predicted.

Based on the results of single turn emotion classification, we adopted the combined approach of LSTM method and two enhanced techniques to evaluate the influence of considering text context for predicting emotions of consecutive dialoguing sentences grouped from the dataset. The strategy was to use the weighted sum of the sentences involved in the same group; that was, to predict the emotion for each sentence and then to sum the emotions up with different weights. The weights of the consecutive sentences were decreased from 1 (current step) stepping by 0.2, in which the time effect was considered. The results from two sets of experimental trials were compared: one set with the consideration of the context factor, and the other set without. Table 1 presents the results. As shown, the strategy of taking context into account in the above way yielded better results in the cases of 4-step and 5-step, but not in the case of 3-step. After examining the details of the prediction error for the case of 3-step, we noticed that for the wrongly predicted sentences, the emotion outputs (by LSTM) for the first-rank and second-rank classes are in fact very close (with a discrepancy less than 0.03). The reason could be that the context information contained in the three consecutive sentences in this dataset was not strong enough to distinguish the emotions, and this situation made the prediction sensible in the multi-class prediction task.

**Table 1.** Results of emotion prediction for continuous sentences

Weighting	3-step	4-step	5-step
Without	0.76	0.68	0.73
With	0.71	0.72	0.80

### 3.3 Evaluation of Training a Dialogue Model

The third set of experiments was to examine the system performance of model training in retrieving (selecting) answers. In this series of experiments, a large dataset was adopted [14]. It was collected from the Insurance Library website that included 12,889 questions and 21,325 answers, after a data preprocessing procedure was performed. This procedure was to remove unsuitable data that could not form the proper input question-answer pairs, to clean the irrelevant terms (such as html tags), and to transfer the text context into internal identifiers (to form the vectors). In the experiments, the above dataset was divided into two parts, in which a part of 2,000 questions and 3,308 answers were used for testing. The complete experiments of dialoguing are described in our work [15], and here we focus on reporting the results most related to the model training for human-robot interaction.

As described in Sect. 2.3, in the model training phase, for each question sentence, a positive and a negative answers were needed to constitute a training instance. However, in a real world application, the correct answer  $A+$  for a question  $Q$  can be determined easily (by the confirmation of the person asking the question), while the wrong answers are often not explicitly specified. Therefore, in the experiments here, all other answers in the dataset were considered candidates of wrong answers to  $Q$ . To find the most suitable wrong answer  $A-$  for each question in the dataset, we used the above model training procedure to perform preprocessing of wrong answer selection. Due to the large amount of answers, in this work we randomly chose ten (instead of all) answers for each question to perform training to reduce computational time.

In the learning process, the random shuffling strategy was used to combine correct and wrong answers for each question to work as the training data. The model and method presented in Sect. 2.3 were used for training. Figure 5(a) illustrates the results of the two popular performance metrics, accuracy and MRR. Here, the accuracy was in fact the top-1 precision mentioned in other relevant studies. It means that the model's predictive result (i.e., the top score answer) must be exactly the expected one as recorded in the dataset. As shown, the LSTM model can achieve the best performance with a correct prediction rate of 0.6, and the MRR is 0.7. In addition to the LSTM model, a traditional embedding model was also implemented for performance comparison. The results are shown in Fig. 5(b). As presented, the accuracy of the embedding model is 0.12, and the MRR is 0.21. These results indicate that the LSTM model is more efficient; it obtained a better result within less iterations.

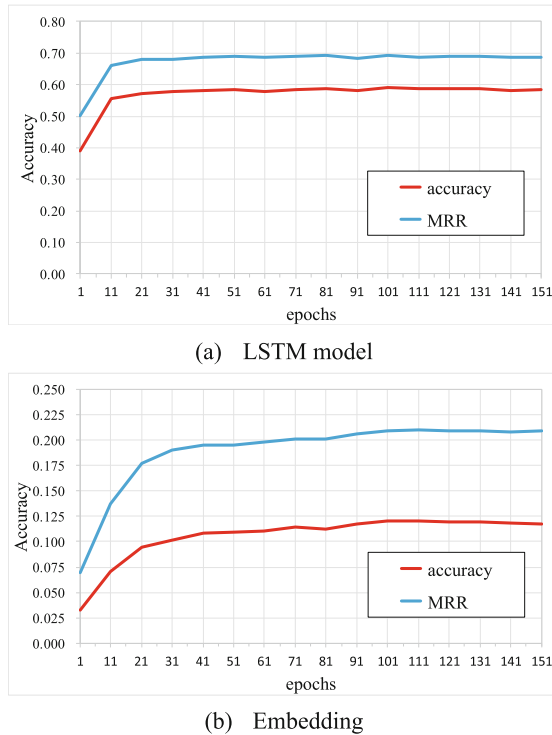


Fig. 5. Performance comparison of the two methods during training.

## 4 Conclusion

This work presented an emotion-aware dialoguing framework for a service robot to achieve natural human-robot communication. In this type of service, the robot works as a consultant and delivers domain-specific knowledge to users. To deploy this service, we adopted a cloud-based service-oriented architecture and developed the emotion recognition and dialogue modeling modules on it. We employed a deep learning method to train different neural models to track users' emotions and to generate answers in response to the users' questions. To evaluate our approach, we conducted a series of experiments, and the results show that the emotion-aware models performed the best among different methods.

The experiments for learning model for emotion-aware dialogues were conducted under various restrictions and required that a combined solution be used to collect the data for verifying the approach developed in this study. To overcome this challenge, we are attempting to develop a knowledge transfer method to automatically enrich datasets by identifying questions and retrieving answers from texts, and the acquired knowledge can be shared by different service domains.

## References

1. Waibel, M., Beetz, M., Civera, J., D'Andrea, R., et al.: RoboEarth-a world wide web for robots. *IEEE Robot. Autom. Mag.* **18**(2), 69–82 (2011)
2. Mohanarajah, G., Hunziker, D., D'Andrea, R., Waibel, M.: Rapyuta: a cloud robotics platform. *IEEE Trans. Autom. Sci. Eng.* **12**(2), 481–493 (2015)
3. Yang, T.-H., Lee, W.-P.: A service-oriented framework for developing home robots. *Int. J. Adv. Robot. Syst.* **10**(12), 1–11 (2013)
4. Perera, V., Soetens, R., Kollar, T., et al.: Learning task knowledge from dialog and web access. *Robotics* **4**, 223–252 (2015)
5. Gao, J., Galley, M., Li, L.: Neural approaches to conversational AI. In: *Proceedings of the 41st ACM SIGIR International Conference on Research and Development in Information Retrieval*, pp. 1371–1374 (2018)
6. Shang, L., Lu, Z., Li, H.: Neural responding machine for short-text conversation. In: *Proceedings of the 53rd Annual Meeting of the Association for Computational Linguistics*, vol. 1, pp. 1577–1586 (2015)
7. Zhou, H., Huang, M., Zhang, T., Zhu, X., et al.: Emotional chatting machine: emotional conversation generation with internal and external memory. In: *Proceedings of AAAI*, pp. 730–738 (2018)
8. Sun, X., Peng, X., Ding, S.: Emotional human-machine conversation generation based on long short-term memory. *Cogn. Comput.* **10**(3), 389–397 (2018)
9. Appel, O., Chiclana, F., Carter, J., Fujita, H.: A hybrid approach to the sentiment analysis problem at the sentence level. *Knowl.-Based Syst.* **108**, 110–124 (2016)
10. Pennington, J., Socher, R., Manning, C. D.: GloVe: global vectors for word representation. In: *Proceedings of International Conference on Empirical Methods in Natural Language Processing*, pp. 1532–1543 (2014)
11. Kingma, D.P., Ba, J.: Adam: a method for stochastic optimization. In: *Proceedings of International Conference for Learning Representations* (2015)
12. Face recognition dataset: [https://robotics.csie.ncku.edu.tw/Databases/FaceDetect\\_Pose\\_Estimate.htm#Our\\_Database](https://robotics.csie.ncku.edu.tw/Databases/FaceDetect_Pose_Estimate.htm#Our_Database). Accessed 15 Apr 2018
13. Phan, D.A., Shindo, H., Matsumoto, Y.: Multiple emotions detection in conversation transcripts. In: *Proceedings of the 30th Pacific Asia Conference on Language, Information and Computation*, pp. 85–94 (2016)
14. Feng, M., Xiang, B., Glass, M. R., Wang, L., et al.: Applying deep learning to answer selection: a study and an open task. *arXiv:1508.01585v2* [cs.CL] (2015)
15. Huang, J.-Y., Lin, T.-A., Lee, W.-P.: Using deep learning and an external knowledge base to develop human-robot dialogues. In: *Proceedings of IEEE International Conference on Systems, Man, and Cybernetics*, pp. 3709–3714 (2018)



# Design and Testing of 2-Degree-of-Freedom (DOF) Printable Pneumatic Soft Finger

Ebrahim Shahabi<sup>1</sup>, Yu-Ta Yao<sup>1</sup>, Cheng-Hsiu Chuang<sup>1</sup>,  
Po Ting Lin<sup>1,2,3</sup>✉, and Chin-Hsing Kuo<sup>4</sup>

<sup>1</sup> Department of Mechanical Engineering, National Taiwan University of Science and Technology, 43 Keelung Road, Section 4, Taipei 10609, Taiwan  
potinglin@mail.ntust.edu.tw

<sup>2</sup> Center for Cyber-Physical System Innovation, National Taiwan University of Science and Technology, 43 Keelung Road, Section 4, Taipei 10609, Taiwan

<sup>3</sup> High-Speed 3D Printing Research Center, National Taiwan University of Science and Technology, 43 Keelung Road, Section 4, Taipei 10609, Taiwan

<sup>4</sup> School of Mechanical, Materials, Mechatronic and Biomedical Engineering, Faculty of Engineering and Information Science, University of Wollongong, Wollongong, NSW 2522, Australia

**Abstract.** Recently, soft robotics have been rapidly developed. Different from the traditional robots, soft robots have the advantages of higher flexibility, safer operations, lightweight, low manufacturing cost, simple fabrication, etc. Soft robots have been applied to various applications, such as medical devices, grippers, rehabilitation devices, etc. This paper proposes a printable pneumatic soft finger with two degrees of freedom (DOF). The developed finger is capable of not only bending but also twisting. A vision-based experimental setup was used to observe and measure the complex actuations with respect to two characteristic variables in the soft finger design. Kriging was used to build the response surfaces of total movement and twisting angle of the soft finger. The built Kriging models could help designers or engineers understand how each variable affects the complex actuations of the proposed printable pneumatic soft finger.

**Keywords:** Soft pneumatic actuator · 3D printing · Computer vision · Kriging

## 1 Introduction

Recently, one of the hottest topics in the field of robotics is soft robotics. Soft robotics is a subclass of the robotics field using flexible and soft materials to make different parts of the robot such as joints, actuators, fingers, etc. In the last decade, soft robotics used in many kinds of applications such as artificial organs [1, 2], medical devices [3–6], grippers [7, 8], soft wearable devices [9], etc. There are different kinds of research in the field of soft robotics such as materials and methods [10–13], robot modeling [14, 15], etc. Many new methods, including additive manufacturing techniques [16, 17], soft lithography [18–20] and making composite materials by unified methods [21–23], were proposed to fabricate some complicated models of soft robots.

Also, there are many kinds of methods for actuations of soft robotics, such as traditional variable-length tension cable driving [24, 25], hydraulic, pneumatic and vacuum actuations [18, 26], electroactive polymer [27], dielectric elastomer actuator [28], etc. Using different kinds of materials, design and manufacturing methods can make different movement ability for soft robots. Marchese et al. [29] demonstrated a soft robotic fish powered by an onboard energy source for a case study. Jung et al. [27] designed a new type of dielectric elastomer actuator (DEA) to mimic annelid motions. Most of the researches in this field focus on one-dimensional motions like bending or twisting, but some research did both of them in one soft finger such as the soft robotic glove, that was designed by Polygerinos et al. [3], for combined assistance and at-home rehabilitation with two degrees of freedom (DOF). Shih et al. [30] made a soft hand with three fingers and added a sensor to control the twisting and bending for different kinds of objects. In this paper, we designed and fabricated a new model of pneumatic soft finger made by Fused Deposition Modeling (FDM) technology. Two characteristic design variables were chosen, i.e. the rib angle and rib distance, and how they affect the soft finger actuations were studied. Computer vision methods were used to measure the total movement and twisting angle of the soft finger. Kriging was used to build the response surfaces of total movement and twisting angle of the soft finger.

## 2 Design and Testing of the Printable Pneumatic Soft Fingers

This paper focused on designing a pneumatic soft finger that could be manufactured by 3D printing. Figure 1 shows the printable pneumatic soft finger design. Two air channels were made and separated with a middle wall inside the soft finger. As the left air inlet is pressured, the air channel on the left-hand side will be inflated causing actuation at the left-hand side. On the other hand, pressurized air applied to the right air inlet inflated the right air channel and caused right actuation. Bending occurs as both air channels are inflated with the same pressure. Twisting happens as the inflation pressure on each side is different from each other. Our preliminary tests also showed both the rib angle  $\theta$  and the rib width  $d$ , shown in Fig. 1(a), are sensitive to the actuations of bending and twisting of the soft finger. Therefore, the soft finger with the design of experiments (DOE) of  $\theta \in [35, 40, 45, 50]$  (degrees) and  $d \in [3, 4, 5]$  (mm) are investigated. To manufacture the soft finger designs, the 3D printer (FlashForge Creator Pro) was used with the settings listed in Table 1. The material of the soft finger thermoplastic polyurethane (TPU, Flex mark 8 made by TREED, Italy).

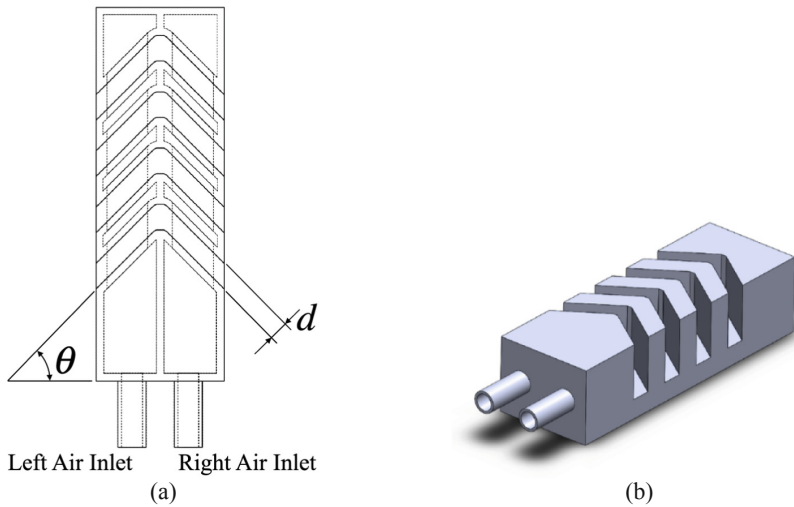


**Fig. 1.** Design variables of the printable pneumatic soft finger: (a) top view; (b) angular view.

**Table 1.** Parameters for 3D printing of thermoplastic polyurethane (flex, Mark 8).

Parameter	Value	Unit
Layer height	0.12	mm
First layer height	0.18	mm
Perimeter shells	3	
Top solid layers	4	
Bottom solid layers	4	
Infill fill density	100	%
Infill fill pattern	Hexagon	
Combined infill	Every 2 layers	
Print speed	20	mm/s
Travel speed	30	mm/s
Extrude temperature	240	°C
Platform temperature	45	°C
Cooling fan controls	Automatch	

Figure 2 shows the experimental setup of the actuations of the 2-DOF pneumatic soft fingers. A Raspberry Pi board was used to control the relay modules, which were connected to the solenoid valves. Pressurized air was applied to the pneumatic filter and then sent to the solenoid valves. The signal from the Raspberry Pi board opened the solenoid valves to apply pressurized air to the left and right air channels in the soft finger. Two cameras were used to capture the deformation of the soft finger from the front and the right, respectively.

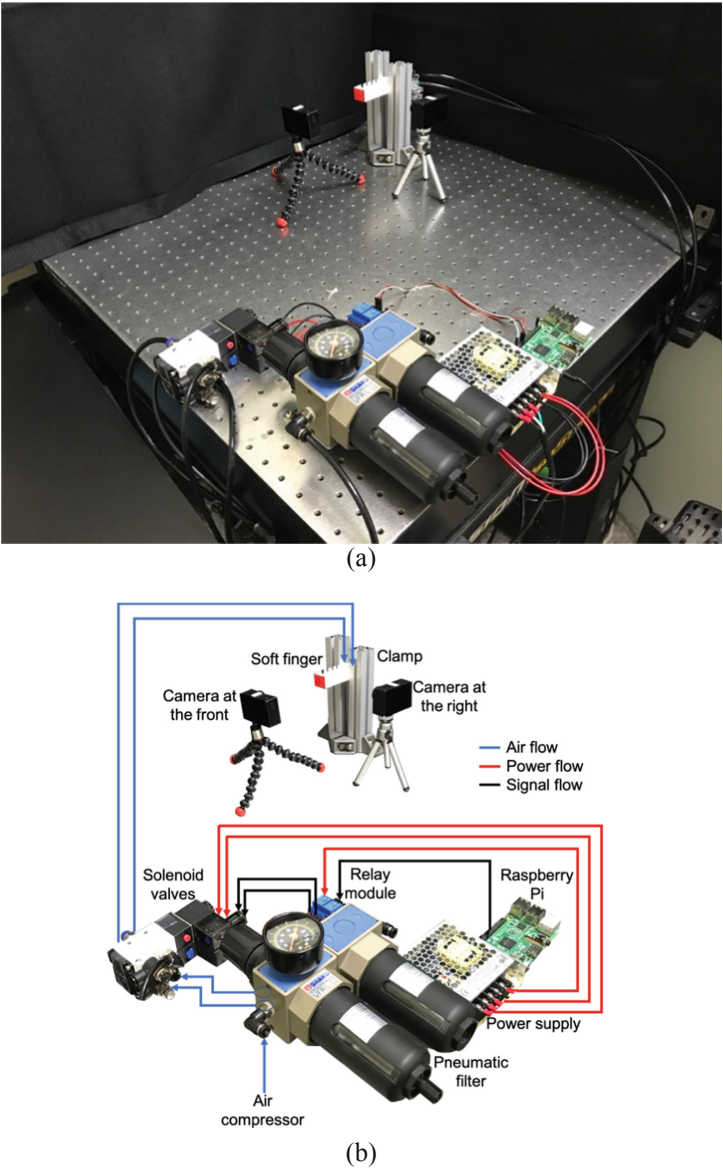


**Fig. 2.** Experimental setup for the pneumatic actuation of the 2-DOF soft finger: (a) A picture of the setup; (b) Details about the connections of air, power and signal.



### 3 Vision-Based Measurements of Soft Finger Deformations

Figure 3 illustrates the feature points located at the tip of the 2-DOF soft finger, which are automatically identified by computer vision and utilized for coordinate measurements. The left-upper and right-upper corner points of the soft finger are identified and denoted as  $\mathbf{P}_1$  and  $\mathbf{P}_2$ , respectively.  $\mathbf{P}_1$  is considered as the origin of the world coordinate so  $\mathbf{P}_1 = [0, 0, 0]^T$ . The x- and y-coordinates of  $\mathbf{P}_2$  can be determined from the picture taken from the front, as shown in Fig. 3(a). The z-coordinate of  $\mathbf{P}_2$  can be obtained from the picture taken from the right, as shown in Fig. 3(b). The middle point of  $\mathbf{P}_1\mathbf{P}_2$ , denoted as  $\mathbf{M}$ , is then computed by:

$$\mathbf{M} = \frac{1}{2}(\mathbf{P}_1 + \mathbf{P}_2) \quad (1)$$

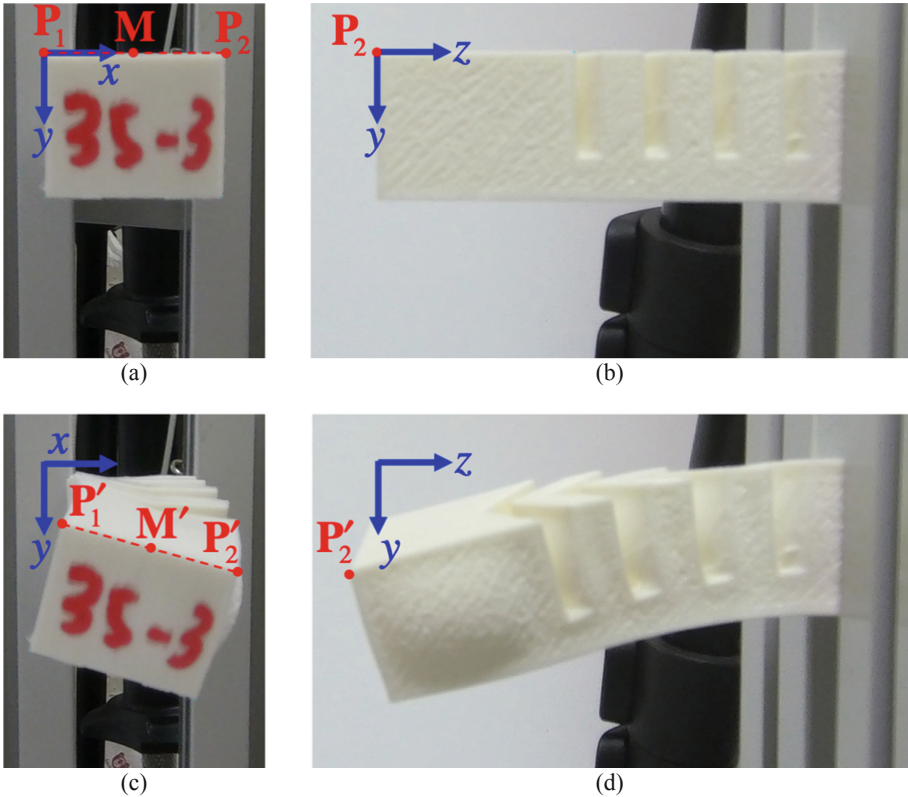


**Fig. 3.** Captured images of the soft finger actuations: (a) Original configuration (front view); (b) Original configuration (right view); (c) Left actuation (front view); (d) Left actuation (right view).

Figure 3(c) and (d) illustrates the front and right views of the 2-DOF soft finger under right actuation, respectively. The same corner points are captured by computer vision methods and are denoted as  $\mathbf{P}'_1$  and  $\mathbf{P}'_2$ , respectively. The x- and y-coordinates of these two corner points can be obtained from the front view, as shown in Fig. 3(c). However, only the z-coordinate of  $\mathbf{P}'_2$  can be determined from the right view shown in Fig. 3(d).  $\mathbf{P}'_1$  may be behind the soft finger geometry at some actuation configurations when being observed from the right. Therefore, the Eq. (2) is solved to determine the z-coordinate of  $\mathbf{P}'_1$ :

$$\|\mathbf{P}'_1 - \mathbf{P}'_2\| = \|\mathbf{P}_1 - \mathbf{P}_2\| = 25 \text{ mm} \quad (2)$$

Or,

$$P'_{1z} = P'_{2z} \pm \sqrt{25^2 - (P'_{1x} - P'_{2x})^2 - (P'_{1y} - P'_{2y})^2} \quad (3)$$

The middle point between  $\mathbf{P}'_1$  and  $\mathbf{P}'_2$  is then determined by:

$$\mathbf{M}' = \frac{1}{2}(\mathbf{P}'_1 + \mathbf{P}'_2) \quad (4)$$

To investigate the nonlinear and complex deformation of the 2-DOF pneumatic soft finger, the total movement from  $\mathbf{M}$  to  $\mathbf{M}'$ , as shown in Eq. (5), is used to represent how much the tip of the soft finger reaches.

$$\text{Total Movement} = \|\mathbf{M}' - \mathbf{M}\| \quad (5)$$

On the other hand, the angle between the vectors  $\overline{\mathbf{P}_1\mathbf{P}_2}$  and  $\overline{\mathbf{P}'_1\mathbf{P}'_2}$ , as given in Eq. (6), is used to represent how much the soft finger twists.

$$\text{Twisting Angle} = \cos^{-1} \frac{\overline{\mathbf{P}_1\mathbf{P}_2} \cdot \overline{\mathbf{P}'_1\mathbf{P}'_2}}{\|\overline{\mathbf{P}_1\mathbf{P}_2}\| \|\overline{\mathbf{P}'_1\mathbf{P}'_2}\|} \quad (6)$$

As mentioned earlier, we chose 12 different combinations of design variables, i.e.  $\theta$  and  $d$ . Each design was made by 3D printing with the presented settings in Sect. 2. The total movement and twisting angle of the soft finger in each design were measured using the presented experimental setup. The results are listed in Table 2. “Right actuation” means pressure was only applied to the right air channel shown in Fig. 1(a) as “right actuation” is for pressure applied to the left air channel only. “Both actuated” stands for the same pressure was applied to both of the air channels. It can be seen that the total movements of the right and left actuations were very similar due to symmetric geometry. For the same reason, the twisting angles of the right and left actuations were also very similar. When pressure was applied to both air channels, larger movements were achieved but the twisting angles were close to zero due to pressure balancing.

**Table 2.** Results of tip movements and twisting angles with various design variables.

$\theta$	$d$	Total movement (mm)			Twisting angle (°)		
		Right actuation	Left actuation	Both actuated	Right actuation	Left actuation	Both actuated
35	3	13.22	12.73	23.29	15.91	15.46	0.34
35	4	12.94	11.49	25.45	18.89	18.34	0.67
35	5	13.46	12.78	27.04	20.78	21.34	0.28
40	3	14.76	14.38	25.70	21.15	19.97	0.51
40	4	10.33	9.77	19.47	20.85	20.14	0.54
40	5	18.03	14.10	32.77	34.34	29.63	3.06
45	3	15.84	16.27	28.40	27.63	25.41	0.17
45	4	14.11	12.11	23.53	28.36	27.07	1.36
45	5	12.90	11.69	24.91	24.63	24.59	1.15
50	3	14.44	14.60	25.71	31.57	27.88	0.99
50	4	14.17	13.85	22.76	33.64	33.52	1.81
50	5	12.58	11.76	16.84	35.15	34.08	2.26

#### 4 Study of Soft Finger Actuation Using Kriging Response Surface

In this paper, the nonlinear Kriging model [31] was used to build the response surfaces of the total movements and twisting angles with respect to the chosen design variables, as shown in Fig. 4. First, the Gaussian model in Eq. (7) was used to find the best fit of the semivariogram  $\gamma$ :

$$\gamma(h) = A \left[ 1 - \exp\left(\frac{-h^2}{B^2}\right) \right] \quad (7)$$

where  $h$  is the Euclidean distance between sampling points;  $A$  is an asymptotic parameter;  $B$  is a shape parameter.  $\gamma(h)$  is the squared difference of the responses of two sampling points that has a distance of  $h$ . Based on the determined semivariogram parameters, the covariance between two sampling points was then given as follows:

$$C_{ij} \equiv \text{COV}(\mathbf{s}_i, \mathbf{s}_j) = \exp\left(\frac{-\|\mathbf{s}_i - \mathbf{s}_j\|^2}{B^2}\right) \quad (8)$$

where  $\mathbf{s}_i = [\theta_i, d_i]^T$  and  $\mathbf{s}_j = [\theta_j, d_j]^T$  are the  $i^{\text{th}}$  and  $j^{\text{th}}$  sampling points, respectively. Finally, the Kriging model of each response  $f$  was given by:

$$f(\mathbf{x}) = \mathbf{F}^T \mathbf{C}^{-1} \mathbf{C}_x(\mathbf{x}) \quad (9)$$

where  $\mathbf{F}$  is a vector of responses listed in Table 2;  $\mathbf{C} \equiv C_{ij}\mathbf{e}_i\mathbf{e}_j$  written in Einstein notation;  $\mathbf{C}_x \equiv C_{x,i}\mathbf{e}_i$  is a vector of covariance between the  $i^{th}$  sampling point and the design variable  $\mathbf{x} = [\theta, d]^T$  where:

$$C_{x,i} \equiv \text{COV}(s_i, \mathbf{x}) = \exp\left(\frac{-\|\mathbf{s}_i - \mathbf{x}\|^2}{B^2}\right) \quad (10)$$

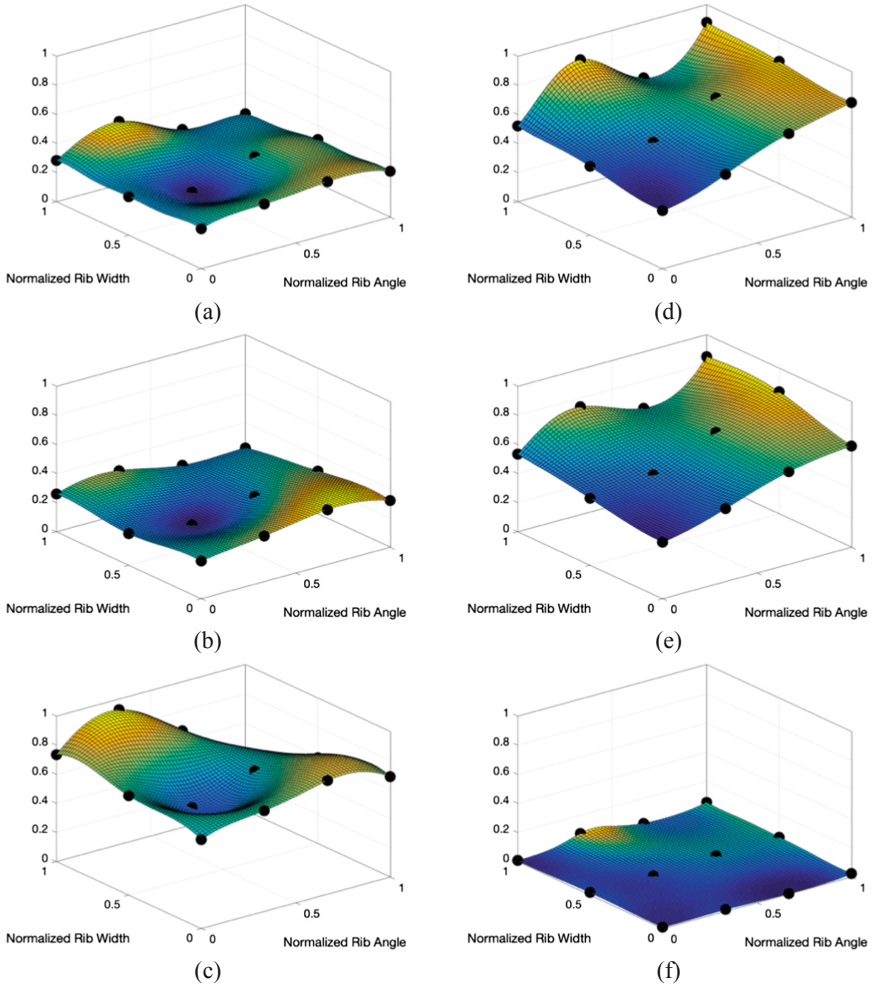


**Fig. 4.** Kriging response surfaces with respect to the design variables: (a) Normalized total movement of right actuation; (b) Normalized total movement of left actuation; (c) Normalized total movement of both left and right actuations; (d) Normalized twisting angle of right actuation; (e) Normalized twisting angle of left actuation; (f) Normalized twisting angle of both left and right actuations.

In Fig. 4, the Kriging models are the normalized responses with respect to the normalized design variables. The normalizations of the rib angle, the rib width, the total movement, and the twisting angle were determined by  $(\theta - 35)/15$ ,  $(d - 3)/2$ ,  $(\text{movement} - 5)/30$ , and  $\text{angle}/40$ , respectively. Observed from these results, the movements and twisting angles nonlinearly behave with respect to the design variables. As one side of the air channel was actuated, the main deformation modes were twisting, as shown in Fig. 4(d) and (e). As shown in Fig. 4(c), the main deformation modes were bending. The studies of the finger actuations with respect to different design variables and control parameters could be used for the kinematics analyses of the soft finger designs.

## 5 Conclusions

In this paper, we presented a new model of printable pneumatic soft finger that has two DOF of bending and twisting. The finger was made of thermoplastic urethane (TPU) and manufactured by 3D printer. 12 different models with different rib angles and rib distances were manufactured. An experimental setup was used to provide 3 different kinds of actuation: left, right and both-side actuations. Two cameras were used to observe the actuations and measure the tip movement and twist angle in each soft finger design. The responses of the tip movement and twist angle were then built with respect to the design variables using Kriging models. The built Kriging models could help designers or engineers understand how each variable affects the complex actuations of the proposed printable pneumatic soft finger. We plan to analyze the kinematics of various soft finger designs based on the results of the actuations with respect to different design variables and control parameters.

**Acknowledgement.** This paper was supported by Ministry of Science and Technology (MOST), Taiwan (grant numbers MOST 106-2221-E-033-025, MOST 107-2218-E-011-021, MOST 107-2221-E-011-088); and Center for Cyber-Physical System Innovation and High-Speed 3D Printing Research Center, which are Featured Areas Research Centers in Higher Education Sprout Project of Ministry of Education (MOE), Taiwan (since 2018).

## References

1. Mutlu, R., Alici, G., in het Panhuis, M., Spinks, G.M.: 3D printed flexure hinges for soft monolithic prosthetic fingers. *Soft Robot.* **3**(3), 120–133 (2016)
2. Delph, M.A., Fischer, S.A., Gauthier, P.W., Luna, C.H.M., Clancy, E.A., Fischer, G.S.: A soft robotic exomusculature glove with integrated sEMG sensing for hand rehabilitation. In: 2013 IEEE 13th International Conference on Rehabilitation Robotics (ICORR), pp. 1–7 (2013)
3. Polygerinos, P., Wang, Z., Galloway, K.C., Wood, R.J., Walsh, C.J.: Soft robotic glove for combined assistance and at-home rehabilitation. *Robot. Auton. Syst.* **73**, 135–143 (2015)
4. Park, Y.-L., Chen, B.-R., Pérez-Arancibia, N.O., Young, D., Stirling, L., Wood, R.J., Goldfield, E.C., Nagpal, R.: Design and control of a bio-inspired soft wearable robotic device for ankle–foot rehabilitation. *Bioinspiration Biomim.* **9**(1), 016007 (2014)

5. Agarwal, G., Besuchet, N., Audergon, B., Paik, J.: Stretchable materials for robust soft actuators towards assistive wearable devices. *Sci. Rep.* **6**, 34224 (2016)
6. Cianchetti, M., Ranzani, T., Gerboni, G., Nanayakkara, T., Althoefer, K., Dasgupta, P., Mencias, A.: Soft robotics technologies to address shortcomings in today's minimally invasive surgery: the STIFF-FLOP approach. *Soft Robot.* **1**(2), 122–131 (2014)
7. Shintake, J., Rosset, S., Schubert, B., Floreano, D., Shea, H.: Versatile soft grippers with intrinsic electroadhesion based on multifunctional polymer actuators. *Adv. Mater.* **28**(2), 231–238 (2016)
8. Shian, S., Bertoldi, K., Clarke, D.R.: Dielectric elastomer based “grippers” for soft robotics. *Adv. Mater.* **27**(43), 6814–6819 (2015)
9. Walsh, C.: Human-in-the-loop development of soft wearable robots. *Nat. Rev. Mater.* **3**(6), 78 (2018)
10. Ilievski, F., Mazzeo, A.D., Shepherd, R.F., Chen, X., Whitesides, G.M.: Soft robotics for chemists. *Angew. Chem.* **123**(8), 1930–1935 (2011)
11. Shepherd, R.F., Stokes, A.A., Freake, J., Barber, J., Snyder, P.W., Mazzeo, A.D., Cademartiri, L., Morin, S.A., Whitesides, G.M.: Using explosions to power a soft robot. *Angew. Chem.* **125**(10), 2964–2968 (2013)
12. Polygerinos, P., Wang, Z., Overvelde, J.T., Galloway, K.C., Wood, R.J., Bertoldi, K., Walsh, C.J.: Modeling of soft fiber-reinforced bending actuators. *IEEE Trans. Robot.* **31**(3), 778–789 (2015)
13. Connolly, F., Walsh, C.J., Bertoldi, K.: Automatic design of fiber-reinforced soft actuators for trajectory matching. *Proc. Natl. Acad. Sci.* **114**(1), 51–56 (2017)
14. Brown, E., Rodenberg, N., Amend, J., Mozeika, A., Steltz, E., Zakin, M.R., Lipson, H., Jaeger, H.M.: Universal robotic gripper based on the jamming of granular material. *Proc. Natl. Acad. Sci.* **107**(44), 18809–18814 (2010)
15. Long Jr., J.H., Combes, S., Nawroth, J., Hale, M., Lauder, G., Swartz, S., Quinn, R., Chiel, H.: How does soft robotics drive research in animal locomotion? *Soft Robot.* **1**(3), 161–168 (2014)
16. Bartlett, N.W., Tolley, M.T., Overvelde, J.T., Weaver, J.C., Mosadegh, B., Bertoldi, K., Whitesides, G.M., Wood, R.J.: A 3D-printed, functionally graded soft robot powered by combustion. *Science* **349**(6244), 161–165 (2015)
17. Wehner, M., Truby, R.L., Fitzgerald, D.J., Mosadegh, B., Whitesides, G.M., Lewis, J.A., Wood, R.J.: An integrated design and fabrication strategy for entirely soft, autonomous robots. *Nature* **536**(7617), 451 (2016)
18. Shepherd, R.F., Ilievski, F., Choi, W., Morin, S.A., Stokes, A.A., Mazzeo, A.D., Chen, X., Wang, M., Whitesides, G.M.: Multigait soft robot. *Proc. Natl. Acad. Sci.* **108**(51), 20400–20403 (2011)
19. Morin, S.A., Shepherd, R.F., Kwok, S.W., Stokes, A.A., Nemiroski, A., Whitesides, G.M.: Camouflage and display for soft machines. *Science* **337**(6096), 828–832 (2012)
20. Shepherd, R.F., Stokes, A.A., Nunes, R.M., Whitesides, G.M.: Soft machines that are resistant to puncture and that self seal. *Adv. Mater.* **25**(46), 6709–6713 (2013)
21. Cho, K.-J., Koh, J.-S., Kim, S., Chu, W.-S., Hong, Y., Ahn, S.-H.: Review of manufacturing processes for soft biomimetic robots. *Int. J. Precis. Eng. Manuf.* **10**(3), 171–181 (2009)
22. Stokes, A.A., Shepherd, R.F., Morin, S.A., Ilievski, F., Whitesides, G.M.: A hybrid combining hard and soft robots. *Soft Robot.* **1**(1), 70–74 (2014)
23. Connolly, F., Polygerinos, P., Walsh, C.J., Bertoldi, K.: Mechanical programming of soft actuators by varying fiber angle. *Soft Robot.* **2**(1), 26–32 (2015)
24. Odhner, L.U., Jentoft, L.P., Claffee, M.R., Corson, N., Tenzer, Y., Ma, R.R., Buehler, M., Kohout, R., Howe, R.D., Dollar, A.M.: A compliant, underactuated hand for robust manipulation. *Int. J. Robot. Res.* **33**(5), 736–752 (2014)

25. Stuart, H.S., Wang, S., Gardineer, B., Christensen, D.L., Aukes, D.M., Cutkosky, M.: A compliant underactuated hand with suction flow for underwater mobile manipulation. In: 2014 IEEE International Conference on Robotics and Automation (ICRA), pp. 6691–6697 (2014)
26. Mosadegh, B., Polygerinos, P., Keplinger, C., Wennstedt, S., Shepherd, R.F., Gupta, U., Shim, J., Bertoldi, K., Walsh, C.J., Whitesides, G.M.: Soft robotics: pneumatic networks for soft robotics that actuate rapidly (*Adv. Funct. Mater.* 15/2014). *Adv. Funct. Mater.* **24**(15), 2109 (2014)
27. Jung, K., Koo, J.C., Lee, Y.K., Choi, H.R.: Artificial annelid robot driven by soft actuators. *Adv. Funct. Mater.* **2**(2), S42 (2007)
28. Girard, A., Bigue, J.-P.L., O'Brien, B.M., Gisby, T.A., Anderson, I.A., Plante, J.-S.: Soft two-degree-of-freedom dielectric elastomer position sensor exhibiting linear behavior. *IEEE/ASME Trans. Mechatron.* **20**(1), 105–114 (2015)
29. Marchese, A.D., Onal, C.D., Rus, D.: Autonomous soft robotic fish capable of escape maneuvers using fluidic elastomer actuators. *Soft Robot.* **1**(1), 75–87 (2014)
30. Shih, B., Drotman, D., Christianson, C., Huo, Z., White, R., Christensen, H.I., Tolley, M.T.: Custom soft robotic gripper sensor skins for haptic object visualization. In: 2017 IEEE/RSJ International Conference on Intelligent Robots and Systems (IROS), pp. 494–501 (2017)
31. Stein, M.L.: *Interpolation of Spatial Data: Some Theory for Kriging*. Springer, New York (2012)

# **Industrial and Service Related Robotics and Mechatronics**





# Intelligent Automation Module-Based Gear Edge Grinding System

C. K. Huang<sup>(✉)</sup>, Y. B. Guu, C. Y. Yang, Yi-Ying Lin,  
and C. H. Chen

Industrial Technology Research Institute, Hsinchu 31040, Taiwan (R.O.C.)  
itriA50317@itri.org.tw

**Abstract.** As industry progresses toward intelligent production and development, on-site workers that perform repetitive tasks will be replaced by intelligent machines. Currently, automation applications still have the following problems: (1) on-site personnel are required to line up the workpieces before a robot arm can pick it up; (2) the trajectory generated by offline programming software must be adjusted by on-site personnel in accordance with the processing results; and (3) because of workpiece positioning errors and tool wear, achieving acceptable processing results is difficult. This study developed intelligent application modules that solve the aforementioned automation application problems. These modules predict processing quality, generate trajectory, enable robot arms to load and unload randomly positioned workpieces, and automatically calibrate the system. An automatic gear edge grinding system was developed by integrating each module; the system increases the processing efficiency and solves the current problem of manual grinding being required after gear processing.

**Keywords:** Intelligent automation module · Grinding · Calibration

## 1 Introduction

As technology has progressed and evolved, industrial automation has become the objective of numerous corporations, with the advantages of reducing workforce sizes and improving product quality and safety. The usage of robot arms has increased progressively; according to estimation by the International Federation of Robotics, 3.218 million industrial robots will be used worldwide in 2020 [1]. Because they boost production and have capability for long working hours, high precision and repeatability, and low error rates, robot arms are crucial in industrial automation.

According to a report from the Gaogong Industry Research Institute, more than 35% of all industrial robots sold in 2017 were bought for use in load and unload, and this sector has been the most common application for industrial robots for numerous years [2]. Although the trajectory of robots used for palletizing can be directly designed through manual teaching, robot arms can also be programmed for automation applications other than the loading and unloading of products, for example, in advanced applications such as grinding, soldering, and spraying. In 2017, the market for grinding robots was approximately CN¥24.2 billion in China; in 2020, it is expected to exceed CN¥85 billion [2].

Compared with typical automation applications, advanced automation applications require more complex processing paths. Because developing advanced automation applications through manual teaching is difficult, the assistance of offline programming software is essential [3]. Despite numerous offline programming software programs existing in the current market, the following problems still occur when using robots for automated applications: (1) For a robot arm to pick up or process a workpiece, the workpiece must either be correctly lined up in the collection tray or the workpiece must have a positioning device; (2) The path produced by the offline programming software must be adjustable according to the actual processing quality; (3) Finally, due to workpiece positioning errors and tool wear, planned paths may require manual adjustment before they are used. To solve these three problems, this study developed intelligent application modules for integrating kinetic property analysis [4, 5], processing quality analysis [6], and automatic calibration technology [7]. The modules can predict the processing quality, generate paths [8], load and unload randomly placed workpieces [9], and automatically compensate for errors. By integrating the modules, a gear edge automatic grinding system was developed that automates the posthobbing grinding and trimming processes, therefore reducing workforce requirements and increasing work efficiency and quality. During automation application planning using the system, the user is required only to input the workpiece model and select the work method; the system then automatically generates a motion path and displays the predicted processing quality results, with the user able to adjust the trajectory according to the predictions. After planning, the user can construct workstations according to the analysis results. After a workpiece has been randomly placed, the automatic calibration module guides the robot arm to pick up the workpiece, align its tool with the processing trajectory, and calibrate the process according to the tool's wear. After processing, the module automatically lines up the next workpiece.

## 2 Intelligent Application Modules

This chapter explains the intelligent application modules developed in this study:

- (1) Optimal trajectory generation module: During advanced automation applications, CAD/CAM analysis is required to generate robot programs. However, the paths generated by the robot arm path generation software currently in use must be manually adjusted according to the processing quality. This study developed a system for quickly analyzing robot kinematics (e.g., singularities, joint limits, collisions, and grinding processing quality) and producing motion paths, thus assisting the user in rapid workstation distribution analysis and robot arm path generation.
- (2) Automatic calibration module: During actual processing, the robot arm is easily influenced by positioning error and tool wear, which can destabilize the software-generated path. This study developed automatic calibration technology for automatically identifying a workpiece's position, automatically aligning the tool with the processing trajectory, and adjusting and compensating for the errors produced during tool mounting. Additionally, this study established random picking

technology, which enables the random placing of workpieces; the module employs visual recognition and positioning to automatically pick up a workpiece and conduct error adjustment, ensuring trajectory accuracy and high processing quality.

After inputting a workpiece model into the path generator module for processing, the system automatically generates a motion path and displays the processing predictions. Users can then make adjustments according to these predictions to generate the optimal path. In accordance with the analysis results, the user can construct workstations and use the automatic calibration module to compensate for workpiece positioning and tool errors, thus enabling the robot arm to pick up randomly placed objects, line up the tool with the processing trajectory, make adjustments for tool wear, and line up the workpiece for the next work procedure. The module-based system is illustrated in Fig. 1.

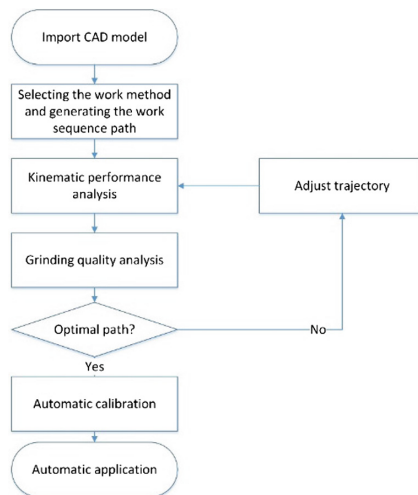


**Fig. 1.** Intelligent modules and system

## 2.1 Optimal Paths Are Generated Using Processing Quality Predictions

The optimal path generation module developed in this study as follow: (1) Robot arm kinematic analysis: This includes forward and inverse kinematic analysis of the robot arm, joint limitation analysis, singularity analysis, stiffness analysis, and path generation for continuous motion. After selecting the processing type and position distribution, a processing trajectory is automatically generated; (2) Collision detection: After a continuous motion processing trajectory for the robot arm is generated, analysis is required to determine whether a collision may occur between the robot arm, workpiece, tools, and surrounding hardware equipment or whether the objects are too close to each other. The module automatically adjusts the path to ensure functional processing; (3) Prediction of grinding processing quality: After generating a processing trajectory that has acceptable dexterity but does not have singularities or collisions, the

processing quality is analyzed. By predicting grinding quality using the processing tool and the amount of workpiece interference, the user can predict whether the planned grinding is insufficient and adjust the path according to the analysis results.

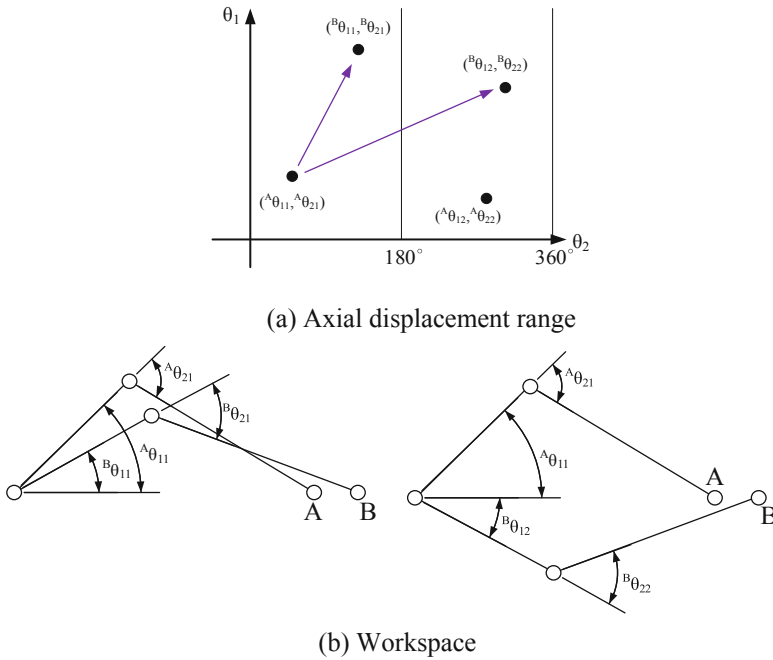


**Fig. 2.** Two inverse kinematic solution sets for two-DOF robots

Six-axis articulated robot arms satisfy two conditions namely that the three upper axes intersect and the second and third axes are parallel. According to inverse kinematics analysis, three quadratic polynomials can be used to calculate the inverse kinematic solution sets of the arm's eight postures. Additionally, by selecting different inverse kinematic solution sets, a path can be planned that avoids singularities, axial displacement constraints, and obstacles. However, if the incorrect inverse kinematic solution set is selected during path planning, the robot will exhibit a rapid speed change or make an unpredicted motion.

Figure 2(a) illustrates the two sets of inverse kinematic solutions for a 2-DOF robot.  $^A\theta_{ij}$  and  $^B\theta_{ij}$  represent the  $j^{\text{th}}$  set of inverse kinematic solutions at points A and B, respectively. If the robot is commanded to move from A =  $(^A\theta_{11}, ^A\theta_{21})$  to B, the inverse kinematic solution sets of the two solution branches would be  $(^B\theta_{11}, ^B\theta_{22})$  and  $(^B\theta_{11}, ^B\theta_{22})$ . However, if the robot is commanded to move from  $(^A\theta_{11}, ^A\theta_{21})$  to  $(^B\theta_{11}, ^B\theta_{22})$ , the robot must move further and pass through at least one singularity of the two at  $\theta_2 = 0^\circ$  and  $180^\circ$ . By conducting path planning using inverse kinematic solution sets from the same branch, energy can typically be saved and singularities, joint limit constraints, and collisions avoided.

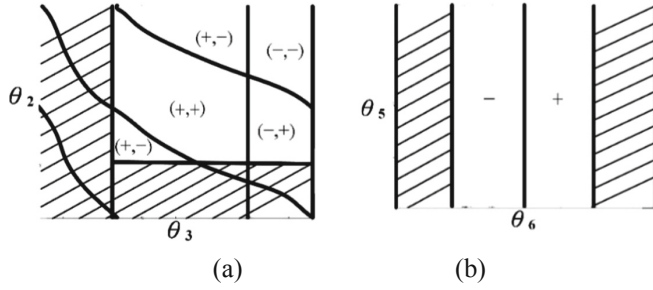


**Fig. 3.** Axial displacement range

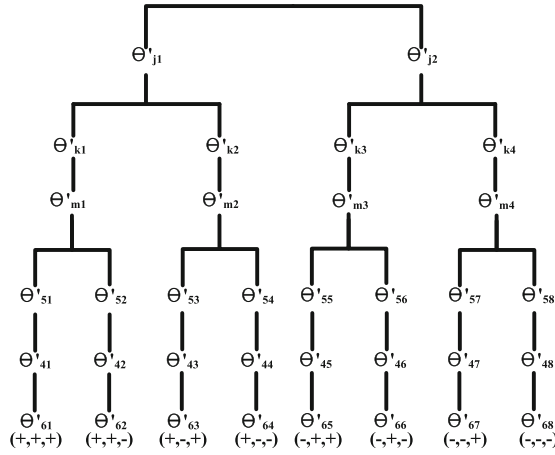


**Fig. 4.** Inverse kinematic solutions of a 6-DOF robot

The inverse kinematic solution with the largest singular-free joint space should be selected when conducting path planning to reduce the number of times the inverse kinematic solution must be changed. Figure 3(a) shows the joint spaces for the first three joints of a 6-DOF robot. The four regions indicate the intervals between the positive and negative solutions of the two discriminants before conducting inverse kinematic analysis. Figure 3(b) shows the three upper joint space, which is separated into two ranges by the singularity curve ( $\sin\theta_5 = 0$ ). Figure 4 displays the branches of the eight inverse kinematic solutions for a 6-DOF robot, with each “+” sign representing a positive solution in the quadratic polynomial of the discriminant ( $\pm\sqrt{b_i^2 - 4a_i c_i}$ ). To calculate the approximate value of the joint space for the (+, +, +) branch, the interval area of (+, +) from Fig. 3(a) should be added to the interval area of (+) in Fig. 3(b). During path planning, the inverse kinematic branch with the largest joint space is employed to reduce the number of times the inverse kinematic solution must be changed. If path planning requires selection of a different set of branch solution, the inverse kinematic solution set with discriminant value closest to 0 is selected. When the discriminant value is close to 0, the inverse kinematic solutions of different sets are close.

For the joint limits, displacement  $\theta_i$  is within its joint limits if  $(\theta_{\max} - \theta_i)(\theta_{\min} - \theta_i) < 0$ , where  $\theta_{\max}$  and  $\theta_{\min}$  representing the maximum and minimum joint limit of  $i^{\text{th}}$  axis, respectively. The closeness to joint limits is evaluated by

$$\eta_i = \frac{(\theta_{\max} - \theta_i)(\theta_{\min} - \theta_i)}{(\theta_{\max} - \theta_{i\text{ave}})(\theta_{\min} - \theta_{i\text{ave}})} \quad (1)$$

where  $\theta_{i\text{ave}} = \frac{\theta_{\max} + \theta_{\min}}{2}$ . Measure  $\eta_i = 1$ ,  $\eta_i = 0$ , and  $\eta_i < 0$  indicate  $\theta_i$  is in the middle of  $\theta_{\max}$  and  $\theta_{\min}$ , reaches its joint limits and exceeds its joint limits, respectively.

The singularity, stiffness, and dexterity of the robot arm can be represented using Plücker coordinates. Because the three upper axes of the robot arm intersect, the  $6 \times 6$  Jacobian matrix can be simplified into four  $3 \times 3$  affiliated matrices (2) to quickly analyze the kinematic properties of the robot arm. For example, robot arm rigidity can be analyzed using the maximum and minimum singularity value of the  $C^T C$  compliance matrix in (3). In (3),  $k_i$  is the rigidity coefficient of the  $i^{\text{th}}$  axis. The proximity to the singularity can be determined using the determinant of the Jacobian matrix in (4). The dexterity of the robot arm is analyzed using the ratio between the maximum and minimum singularity values of the Jacobian matrix  $\mathbf{J}\mathbf{J}^T$ , ensuring the kinematic performance of the robot arm.

$$\begin{aligned} \begin{bmatrix} \omega_6 \\ \mathbf{v}_p \end{bmatrix} &= \mathbf{J}\dot{\theta} = \begin{bmatrix} \hat{\mathbf{e}}_1 & \hat{\mathbf{e}}_2 & \hat{\mathbf{e}}_3 & \hat{\mathbf{e}}_4 & \hat{\mathbf{e}}_5 & \hat{\mathbf{e}}_6 \\ \mathbf{r}_1 \times \hat{\mathbf{e}}_1 & \mathbf{r}_2 \times \hat{\mathbf{e}}_2 & \mathbf{r}_3 \times \hat{\mathbf{e}}_3 & \mathbf{r}_4 \times \hat{\mathbf{e}}_4 & \mathbf{r}_5 \times \hat{\mathbf{e}}_5 & \mathbf{r}_6 \times \hat{\mathbf{e}}_6 \end{bmatrix} \dot{\theta} \\ &= \begin{bmatrix} \mathbf{J}_1 & \mathbf{J}_3 \\ \mathbf{J}_2 & \mathbf{0} \end{bmatrix} \dot{\mathbf{q}} \end{aligned} \quad (2)$$

$$\mathbf{C} = (\mathbf{J}\mathbf{J}^{-1}\mathbf{J}^T)^{-1} \quad (3)$$

$$\begin{aligned} \text{Det}[\mathbf{J}] &= -\{a_3 \sin \theta_3 - \cos \theta_3 \sin \alpha_3 d_4\} [(-d_4 \sin \alpha_1 \sin \alpha_3 \sin \theta_3 \\ &\quad - a_3 \sin \alpha_1 \cos \theta_3 - a_2 \sin \alpha_1)(\cos \theta_2) \\ &\quad - (d_4 \sin \alpha_1 \sin \alpha_3 \cos \theta_3 - a_3 \sin \alpha_1 \sin \theta_3)(\sin \theta_2) \\ &\quad - a_1 \sin \alpha_1] \sin \theta_5 \sin \alpha_4 \sin \alpha_5 \end{aligned} \quad (4)$$

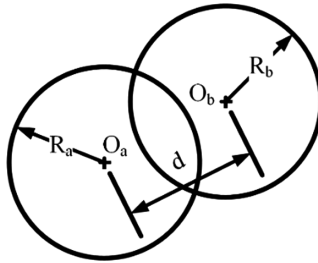


Fig. 5. Detecting potential collisions using the voxel-based method

For the collision detection, the voxel-based method is employed to conduct collision analysis. This method divides the models into finite elements and analyzes the relationship between each element to determine any interference. If interference between two elements is detected, a collision would occur. In this case, the workpiece and tool must be reconfigured to generate a new trajectory. The analysis accuracy of the voxel-based method is related to the size of the elements; employing smaller elements enables more accurate analysis results but requires more computation time. The linear distance between the centers of two spherical elements can be used to conduct element collision analysis. If this linear distance is smaller than the sum of the radii of the elements, interference will occur between the two elements (Fig. 5):

$$\|O_a - O_b\| \leq (R_a + R_b) \quad (5)$$

The voxel-based method and workpiece element interference conditions are used to analyze workpiece–tool contact during processing. The amount of contact is crucial for analyzing the grinding processing conditions. The amount of grinding that will occur on a given path is calculated and displayed on the operational interface. The user can then make adjustments in areas with insufficient or excessive grinding.

## 2.2 Automatic Calibration Technology

Currently, automation using a robot arm requires an operator to line up workpieces at the tray or a positioning device; only then can the robot arm perform follow-up motions. During automation applications, the path generated using programming software may be unusable or processing quality may be unstable because of workpiece scale tolerance, relative errors between items, and tool wear. The automatic calibration module developed in this study includes the following technology: automatic workpiece position recognition, automatic processing trajectory alignment, and tool center point (TCP) calibration. Additionally, this study developed technology incorporating machine vision and positioning, enabling the robot arm to automatically pick up workpieces with random positions and the system to conduct calibration for ensuring trajectory preciseness and processing quality.

The technology for automatic workpiece position recognition, pickup and automatic trajectory calibration: (1) establishes the position and orientation relationships between the coordinates of the image sensor mounted on the loading platform, the physical workpiece, and the workpiece's two-dimensional image on the sensor; (2) establishes a method for calibrating the internal and external variables of the image sensor; (3) enables the use of workpiece contour alignment technology. After a deploying physical workstation, the user can employ the workpiece calibration technology to analyze the positioning error of the workpiece. Subsequently, the user can adjust the workpiece position or trajectory for reducing this error. A description of related technology follows.

- (1) Automatically picking of randomly positioned workpieces [9]: An image sensor is set above the loading platform, and the coordinates of the robot arm relative to the image sensor is calibrated. Visual recognition is employed to determine the

workpiece's position. The workpiece coordinates are converted into the coordinates of the robot arm. Finally, the robot arm is controlled to pick up the workpiece.

- (2) Identifying the actual processing trajectory and performing calibration in accordance with the default processing trajectory [10]: When the robot arm picks up a randomly positioned workpiece from the loading platform, the processing trajectory should be aligned twice to ensure correct grinding of the gear edge. The proposed method uses the image sensor to capture the grinding trajectory under default conditions. Automatic calibration technology is then employed to align the workpiece with the grinding trajectory and adjusts the grinding trajectory errors determined from both alignment processes. After the error between the processing position and actual position has been analyzed, processing trajectory correction methods are used to adjust the processing position for ensuring processing quality. In gear grinding applications, a gear is picked up by the robot arm and moved to the image sensor position for image capture. Analyzing the position of the gear edge yields the offset between the actual and predicted grinding trajectories.

The TCP automatic calibration system is employed by two image sensors (Fig. 6). The A- and B-axes are defined as the center axes of the field of view for image sensors 1 and 2, respectively. The C-axis is defined as the direction perpendicular to both the A- and B-axes. Planes 1 and 2 are the planes perpendicular to the A- and B-axes, respectively. The TCP obtained by image sensors 1 and 2 are located on planes 1 and 2, respectively [7].

The TCP calibration process has four steps: (1) establishment of the calibration system, which consists of numerous image sensors and axes that intersect; (2) determination of the conversion relationship between the robot arm reference coordinate system and image sensor reference coordination system; the image-sensor-coordinate motion vectors are converted into robot-arm-coordinate motion vectors; (3) use of the visual server to control the robot and obtain the calibration reference point; this point must have the same position as the TCP but a different orientation; and (4) calculation of the actual TCP position.

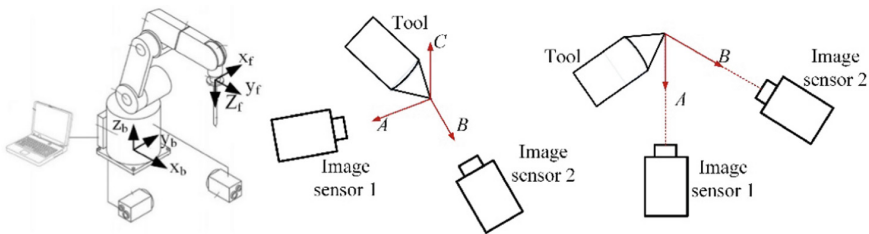


**Fig. 6.** TCP calibration system



### 3 Gear Edge Grinding Application System

The common features of manufacturing factories include sultriness, noisiness, and repetitive operations, which are factors that are unpleasant for workers and thus lead to the labor gap. The environment in processing factories often causes workers to feel bored and lose concentration, causing psychological fatigue that leads to adverse symptoms (e.g., physiological exhaustion). Not only does this endanger worker safety, it also results in inconsistent product quality. Numerous factories now employ automation to address this concern. Introducing industrial robots into the parts of the production process that are dangerous or require repeated performance of a particular task enables more efficient utilization of human resources.

This chapter explains the integration of the intelligent automation modules and the development of the gear edge automatic grinding system. Robot arms can be used for the following automation applications: loading and unloading of workpieces, deburring and chamfering. Factories can employ the intelligent application modules to achieve the following:

- (1) Intelligent pickup and placement of workpieces: After placing a workpiece in the loading area, the feedback coordinates obtained through machine vision recognition are transmitted to the robot, enabling it to pick up the workpiece. After processing has been completed, the actual condition of the unload area is determined and transmitted to the robot, enabling the robot to place the processed workpiece at a usable grid position.
- (2) Pickup function featuring decentering calibration: Before image capture, the fixed position of the worm wheel is obtained by the angle of rotation of each gear in the workpiece. After recording the start of the Trajectory and the center deviation distance of each gear, sine functions are employed to perform curve fitting and calculate the possible deviations, and the deviations are compensated to adjust the tool coordinates and perform verification. The process is repeated until the deviations are within a predetermined error range.
- (3) Automatic alignment of the processing trajectory: According to the set angle rotation of the workpiece, machine vision is employed to label the displacement of the teeth grinding starting point near the center of the image. The deviation between the current teeth grinding starting point and center of the image is calculated. The deviation is added to the tool position of the rotating workpiece, thus aligning the gear grinding starting point with the center of the image.
- (4) Gear edge grinding: The workpiece alignment value is substituted into the work coordinates configured in each grinding process setting. Grinding then proceeds.

The automatic gear edge grinding system developed in this study employs the ITRI 12A62 robot arm (Fig. 7).

The work process of the automatic tool edge grinding system developed in this study consists of the following four stages. (1) Initialization: The system can be used on gears of different sizes. Before grinding processing, automatic machine vision recognition or notification by the user of the appropriate gear code is required to determine the processing parameters, such as the processing trajectory generated by offline

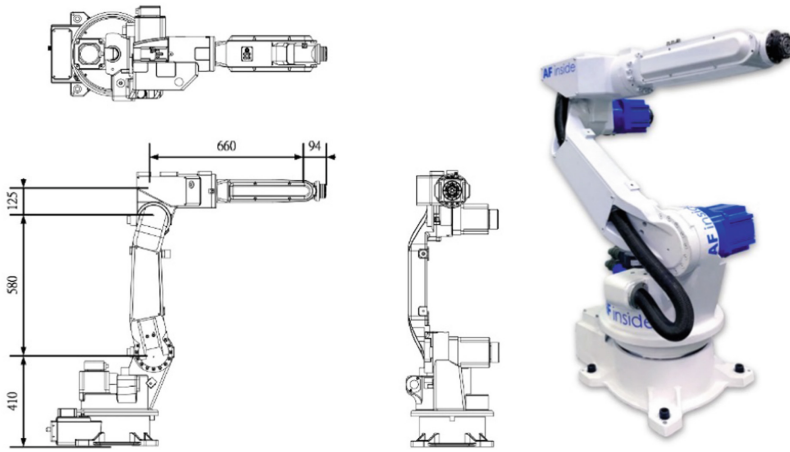


**Fig. 7.** 12A62 robot arm

software and gear geometry variables. (2) Automatic self-measurement and calibration: During the first operation of the system and after the system has operated for a certain amount of time, automatic self-measurement and calibration are required to ensure standard operation of the system; these processes include using a calibration block to evaluate the accuracy of the image sensor above the loading platform, calibrating the relationship between the mounted image sensor and robot arm, and conducting decentering measurements of the robot arm gears. The proposed detection method uses the image sensor to identify the size and position of the first gear's teeth. The gear is then rotated in place, and its position and size deviation is recorded to estimate the deviation condition (Fig. 8). (3) Gear grinding processing: After the evaluation has been completed, gear edge grinding can be performed. The grinding process involves the pickup of a randomly positioned workpiece, alignment of the processing trajectory, grinding, and alignment of the processed gear.

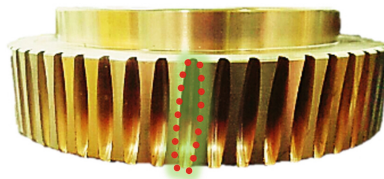


**Fig. 8.** Gear tooth size and position determination

The proposed system implements automated production into the gear grinding process, which was originally conducted only manually. By enabling loading and unloading of randomly positioned workpieces and performing automatic trajectory calibration, this system saves the cost of a loading plate and positioning device. The results obtained using the automatic grinding system are displayed in Fig. 9.

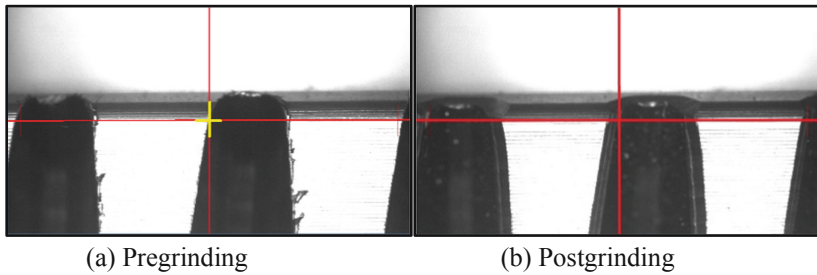


**Fig. 9.** Results of automated grinding of a gear edge

The system achieved grinding of similar quality to manual grinding while increasing the processing efficiency by 20%. Furthermore, processing quality can be maintained using this system even after operation for a long period.

## 4 Conclusion

This study developed intelligent application modules and integrated the modules into an automatic gear grinding system, which has the following three features: (1) capable of generating the optimal path by predicting processing quality; (2) automatic calibration technology for tools and workpieces; and (3) an automatic gear edge grinding application workstation. The module scales of the automatic gear edge grinding application workstation are as follows. (1) The automatic path generation technology produces a processing trajectory without singularities and collisions and with smaller joint angle changes than the user set value. (2) The success rate of the pickup and processing trajectory functions exceeded 99%, and actions could be completed in less than 40 s. (3) The automatic TCP calibration technology completed calibration within 1 min, with errors less than 0.1 mm. (4) The errors in the gear edge grinding width were within  $\pm 0.3$  mm, similar processing quality to manual processing and increasing the work efficiency by 20%. Aside from producing a human-machine interface for related functions, this study strengthened the automation application, improving the automation application modules and the technological competitiveness of Taiwan while reducing the time required for process planning.

At present, automated application module are used in Taiwan mainly in factories of Japanese firms, such as FANUC, Mujin, and Keyence, which account for 80% of the Taiwanese market share and thus control the price, delivery date, and profits of Taiwanese intelligent applications. Because the technology of advanced intelligent automation applications is a difficult field of research and development, Taiwan has yet to release an advanced intelligent application module. By implementing a domestically developed intelligent module, this study aims to increase the acceptance among Taiwanese firms of domestically produced controllers as well as increase the reliance on these controllers and the confidence in their properties. When purchasing automation application modules and robot arms, terminal users will hopefully be encouraged to

purchase Taiwan-developed controllers with a higher price–performance ratio rather than controllers from Japanese and European brands.

**Acknowledgement.** The researchers would like to express gratitude toward the Technology Development Program of the Ministry of Economic Affairs and the Industrial Technology Research Institution for providing funding and support.

## References

1. International Federation of Robotics: World Robotics Report 2018 (2018)
2. Gaogong Industry Research Institution, GGII: Industrial Robot Industry research 2018 (2018)
3. Neto, P., Pires, J.N., Moreira, A.P.: CAD-based off-line robot programming. In: IEEE Conference on Robotics, Automation and Mechatronics (2010). <https://doi.org/10.1109/ramech.2010.5513141>
4. Huang, C.-K., Ou, Y.W.-C., Tsai, K.-Y.: Inverse kinematic analysis and singularity research of industrial robots, institution and machine design. *Newsl. Chin. Soc. Mech. Mach. Theory* **24**(5), 16–28 (2013)
5. Huang, C.K., Tsai, K.Y.: Analytical inverse kinematic computation for a special class of 7-DOF redundant manipulators. In: The 14th IFToMM World Congress, 25–30 June 2015. <https://doi.org/10.6567/iftomm.14th.wc.os1.013>
6. Eberst, C.: Offline-Programmierung leicht gemacht, Pulverbeschichtung bei Jungheinrich in Moosburg. *JOT Journal für Oberflächentechnik* **44**(4), 66–69 (2016)
7. Huang, C.K., Guu, Y.B., Chen, Y.-L., Chu, C.Y., Chen, C.H.: An automatic calibration method of TCP of robot arms. In: 4th International Conference on Production Automation and Mechanical Engineering, Paper Id ICPAME-2018-1714, 3–4 August 2018
8. Eberst, C., Ferri, M., Stoeffler, B., Tornese, R., Umgeher, G.: System and method for the automatic generation of robot programs, U.S. Patent 9701019 (2011)
9. Huang, S.-J., Yan, C.-Z., Huang, C.K., Ting, C.-C., Chen, C.-H.: Application of deep learning for object image recognition and robot automatic grasping. In: The 15th International Conference on Automation Technology, Taichung Taiwan, Paper Id 1053, 6–8 December 2018
10. Ryberg, A., Ericsson, M., Christiansson, A.K., Eriksson, K., Nilsson, J., Larsson, M.: Stereo vision for path correction in off-line programmed robot welding. In: IEEE International Conference on Industrial Technology (2010). <https://doi.org/10.1109/icit.2010.5472442>



# Development of an Automated and Adaptive System for Robotic Hybrid-Wire Arc Additive Manufacturing (H-WAAM)

Audelia Gumarus Dharmawan, Yi Xiong, Shaohui Foong,  
and Gim Song Soh<sup>(✉)</sup>

Singapore University of Technology and Design, Singapore, Singapore  
sohgimsong@sutd.edu.sg

**Abstract.** In wire arc additive manufacturing, weld beads are deposited layer-by-layer leading to the final part geometry. The printed geometry of the weld bead depends on various factors and is therefore hard to predict and control accurately. These errors will lead to large deviation between the actual and the expected print layer thickness, deteriorates the print's geometry and hinders subsequent print layer. This paper describes an adaptive system for Hybrid-Wire Arc Additive Manufacturing that is capable of automatically sensing, correcting and updating the printed layer behavior to address the above issues. The details of the developed system and the employed universal framework is described, and experiments were conducted to demonstrate its capabilities and effectiveness.

**Keywords:** Additive manufacturing · Automation · Hybrid manufacturing

## 1 Introduction

Metal Additive Manufacturing (AM) has gained increasing attention recently to fabricate complex components for various industries [1]. Compared with the traditional subtractive manufacturing, AM offers a shorter production time and requires less human intervention as the process can be completely automated from a CAD model. It is also more cost-effective due to the low buy-to-fly ratio through the production of near net-shape components [2]. Based on the feedstock type, metal AM can be categorized into powder-feed and wire-feed technology. Although powder-feed process can produce parts with higher accuracy, wire-feed approach is more practical for fabricating large components due to its higher deposition rate. The energy source for the deposition in wire-feed AM can be provided by an electron beam, a laser, or an electric arc [3]. The arc-based technology, often referred to as Wire Arc Additive Manufacturing (WAAM) [4], is less costly and has a higher deposition rate than the other two processes.

In WAAM, the parts are built by depositing overlapping weld beads in the horizontal (multi-bead) as well as vertical (multi-layer) directions on top of a substrate. The suitable distance between the beads in both horizontal (stepover increment) and vertical (layer increment) directions can be calculated from the geometry of the single weld bead obtained experimentally [5,6]. Despite using the recommended stepover distance, it is still challenging to obtain a flat surface of the deposited layer, deteriorating the subsequent layer deposition. As the layers are built up vertically, the heat transfer conditions also change [7]. For the first few layers, the heat can quickly dissipate onto the larger substrate acting as a heat sink. For the subsequent layers, the heat conduction to the substrate is slower as it needs to pass through the previously deposited layers, leading to more accumulation of heat near the print. The different temperature conditions are known to affect the output behaviour of the weld bead. The deposited layer at the different height level may have different layer thickness due to this varying cooling rate [8]. This leads to an accumulated error of the predicted cumulative printed height as represented by the experimental results in [9], thus affecting the accuracy of the set distance of the layer increment. A short distance between the welding nozzle and the layer surface increases the chance of collision as well as spatters sticking onto the nozzle, while a long distance has been known to influence the shielding gas effect and result in more porosities [10].

In order to solve the aforementioned issues, complex vision and control can be employed to regulate the welding parameters and the deposition to ensure the regularity and the accuracy of the printed layer thickness [10]. However, such a feedback control requires developing a complicated online measurement system, and a simpler solution would be to face-mill the layer to compensate for the thickness variation and obtain the surface evenness [11]. This approach has been implemented by some in the literature and usually termed as Hybrid Layered Manufacturing (HLM) [5,12]. Nevertheless, those existing systems usually do not include an integrated sensing system to automatically quantify the surface roughness and the required milling thickness as well as update the resulting layer height for the subsequent layer deposition, and these laborious steps most likely had been performed manually. An effort on developing an automated system was recently reported [13]. However, the process was specifically developed for and is thus only applicable for manufacturing thin-walled structures. Incorporating and automating these routines for printing general shapes would be a step towards a more intelligent WAAM process requiring very minimal human intervention.

This paper presents the development of an integrated system for adaptive Hybrid-Wire Arc Additive Manufacturing (H-WAAM) which can automatically sense, correct and update the print behavior. The system consists of a robot manipulator equipped with a welding system to perform the additive operation, and a gantry system with a laser displacement sensor and a milling head assembly installed to perform the registrative and subtractive function respectively. A universal framework is proposed and employed to automate the procedures of depositing, sensing and milling from only the CAD model of the part, which thus requires very little human intervention and accommodates for any print shape.

## 2 System Overview and Workflow

Shown in Fig. 1a, an integrated system for automated and adaptive H-WAAM is developed in Singapore University of Technology and Design (SUTD). It consists of a robot manipulator (ABB IRB 1660ID), a welding machine (Fronius TPS 400i) with a welding torch (Fronius WF 25i Robacta Drive), a gantry robot made up of three linear rails (PMI KM4510) and three servos (SmartMotor SM34165DT), a 2D laser scanner (Micro-Epsilon scanCONTROL 2910-100), and a milling head assembly (Proxxon FF500). All of the control commands to the system are formulated and dispatched by a central master computer which is connected to the rest of the hardware components through either an ethernet or an RS232 communication interface.

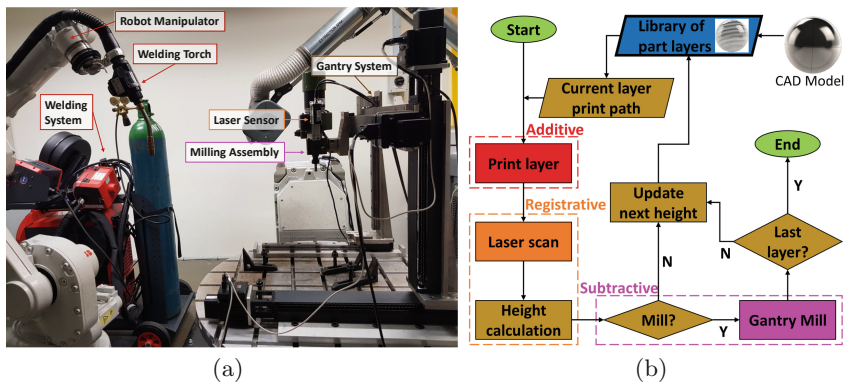


**Fig. 1.** (a) Hardware equipments and (b) Workflow of the developed adaptive Hybrid-Wire Arc Additive Manufacturing (H-WAAM) system.

Figure 1b shows the proposed workflow of the automated adaptive H-WAAM. The only input required is the 3D CAD model of the part. The CAD model is first sliced into layers with a resolution depending on the accuracy required, and the print path for each layer is generated and stored in a library of the part layers. The automated workflow starts with the robot manipulator printing the first layer. When the print job is done, the gantry robot moves the 2D laser sensor to scan and reconstruct the 3D surface of the printed layer, and the maximum and minimum heights of the layer are obtained. Based on the surface roughness, it is then decided whether face milling is required to improve the flatness of the surface. With or without milling, the final height of the current layer is then fed into the system and the corresponding print path for that particular layer height is extracted from the library of the part layers. The robot manipulator then carries out the subsequent layer's print job on top of the previous layer, and the workflow repeats until the last layer has been reached.

### 3 Automation and Generalization Strategies

To automate the adaptive H-WAAM system consisting of the various hardware and operations, a universal framework is employed. The individual functional module, namely the additive, registrative and subtractive unit, can understand what one another is doing with very little preparation and intervention from human. The following subsections discuss the universal strategies used in the developed H-WAAM system with only the CAD model of the part as the input, which is general enough to be used for printing any part's shape. The main automated adaptive function, which is developed in-house, is also described.

#### 3.1 Unified Path Generation

The jobs for the additive, registrative and subtractive functions are to be generated solely from the CAD model, so that very little pre-processing and prior preparation by human is required. To achieve this, three different paths are generated automatically from the sliced CAD model: the additive path, the registrative path and the subtractive path. The additive path is basically the typical print pattern employed in AM, and it can take any deposition patterns depending on the needs. The most common hatching patterns are spiral (contour-based) and raster (zig-zag) patterns. The layer is hatched into the print path with a stepover distance specific to the material being deposited.

For the registrative function, it is good for the laser sensor to know the shape of the layer that was just printed by the additive module so that it does not have to scan the whole workspace and thus saves on the operational time. To attain this, unidirectional raster lines are generated from the sliced CAD model with the required resolution of the 3D scan output as the stepover distance. These raster lines represent the positions of the 2D laser line across the layer's shape and form the registrative path automatically generated from the CAD model of the part. More details on how the path is used for the sensing and adaptive function will be discussed in Sect. 3.3 later.

Similar to the additive function, the subtractive task can also be performed on the layer surface either in a spiral or raster manner. Hence, to construct the subtractive path automatically, spiral or raster pattern can likewise be generated from the sliced CAD model, but now with the diameter (full or around 80%) of the face or end mill tool as the stepover distance. This path then becomes the route that has to be taken by the subtractive module to mill and flatten the layer surface according to its shape.

To achieve the proposed unified path generation for the three H-WAAM functions, a hatching software tool is developed in-house which takes in the sliced CAD model of the part to be printed. Figure 2 shows the examples of the three different paths for the additive, registrative and subtractive functions generated by the software for manufacturing a test coupon part.



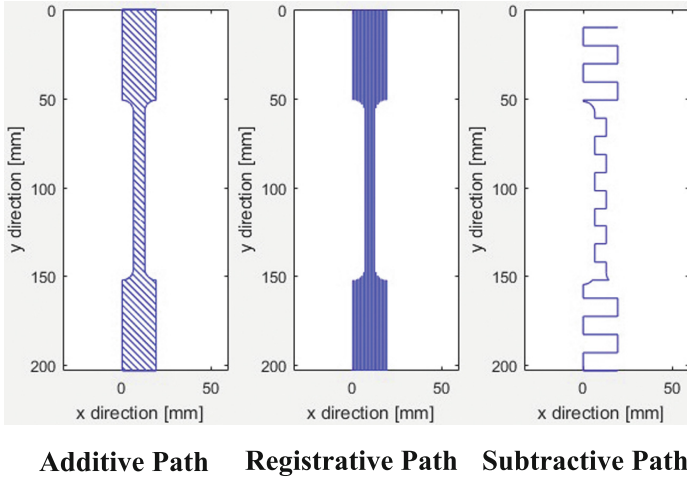


**Fig. 2.** Unified path generation from the sliced CAD model for the adaptive H-WAAM system. The additive path represents the deposition path of the part layer hatched with a stepover distance specific to the material characteristics. The registrative path represents the positions for the 2D line laser sensor hatched from the part layer with the required scan resolution as the stepover distance. The subtractive path represents the route to be taken by the miller hatched from the part layer with a stepover distance related to the diameter of the face or end mill tool.

### 3.2 Coordinate Systems

After the unified paths for the three adaptive H-WAAM functions have been automatically generated from the CAD model, the various hardware components need to know the position of the printed part relative to each of them so that they move to the correct location to deposit, scan or mill the part. Figure 3 shows the coordinate systems of the developed adaptive H-WAAM system, where the positions of the coordinate frames have been calibrated relative to one another. The coordinates of the generated unified paths will always be positioned relative to the table frame  $T$ , which is where the part is going to be printed on. Hence, the coordinates of the unified paths will be generally notated as  ${}^T P_{U_\kappa}$  with  $\kappa = \{a, r, s\}$  for additive, registrative and subtractive paths respectively, and  $P$  is in the format of  $[x, y, z]$  coordinates. To formulate the motions of the robot manipulator as well as the gantry robot to perform the deposit, scan and mill operations based on the generated unified paths, the coordinates of the paths need to be expressed relative to the additive, registrative and subtractive tool frames respectively.

From the coordinate systems, the motion of the robot manipulator to perform the additive function can be obtained from

$${}^A P_{U_a} = {}^T P_{U_a} + {}^M P_T - {}^M P_A \quad (1)$$

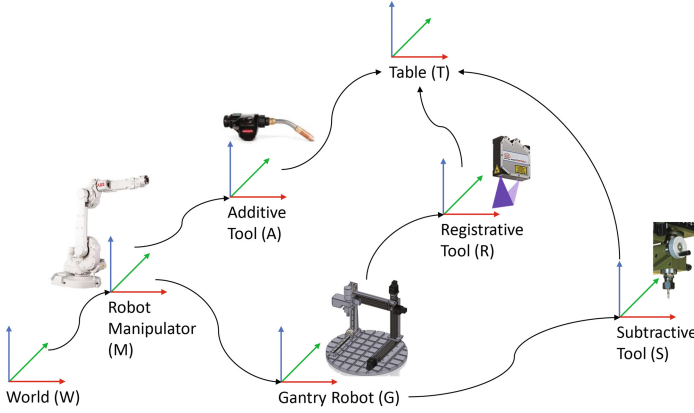


**Fig. 3.** Coordinate systems of the developed adaptive H-WAAM system.

where  ${}^M P_T$  and  ${}^M P_A$  are the calibrated positions of the table frame and the additive tool frame respectively relative to the robot manipulator frame. The motion of the gantry robot to carry out the registrative task is formulated as

$${}^R P_{U_r} = {}^T P_{U_r\_new} + {}^M P_T - {}^M P_G - {}^G P_R \quad (2)$$

where  ${}^M P_G$  is the calibrated position of the gantry robot frame relative to the manipulator frame,  ${}^G P_R$  is the calibrated position of the registrative tool frame relative to the gantry robot frame, and  ${}^T P_{U_r\_new}$  is the new registrative path after being processed further, which is discussed in Sect. 3.3. The movement of the gantry robot to execute the subtractive operation can be obtained as

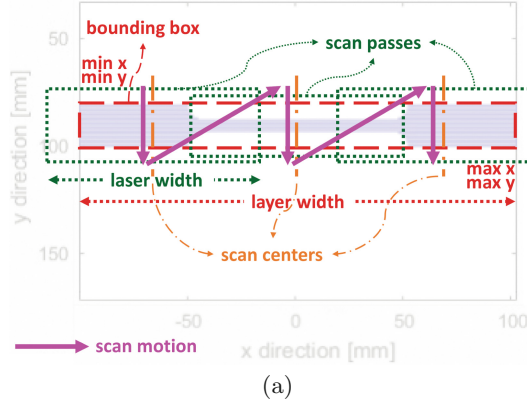
$${}^S P_{U_s} = {}^T P_{U_s} + {}^M P_T - {}^M P_G - {}^G P_S \quad (3)$$

where  ${}^G P_S$  is the calibrated position of the subtractive tool frame relative to the gantry robot frame. With these coordinate systems and unified paths, the whole process of the adaptive H-WAAM system can be fully automated from only the CAD model of the part to be built.

### 3.3 Sensing and Adaptive Function

This section describes the planning and processing of the laser sensing operation further derived from the generated registrative path ( ${}^T P_{U_r}$ ) to automatically perform the main adaptive function of the H-WAAM system. As mentioned in Sect. 3.1, the generated registrative path only represents the desired positions of the 2D laser line on the layer's surface. To achieve this, the motion of the laser sensor needs to be further formulated.

From the automatically-generated registrative path, the bounding box which encloses the contour shape of the printed layer is first extracted, as depicted by the dashed red box in Fig. 4a with the test coupon path as an example.



```

ScanPlan( $^T P_{Ur}$ )
1:  $min\_x, max\_x, min\_y, max\_y \leftarrow bounding\_box(^T P_{Ur})$ 
2:  $layer\_width \leftarrow max\_x - min\_x$ 
3:  $scan\_pass \leftarrow ceiling(layer\_width / laser\_width)$ 
4: for  $i \leftarrow 1$  to  $scan\_pass$  do
5:    $scan\_center[i] \leftarrow min\_x + \frac{(2i-1) \cdot layer\_width}{2 \cdot scan\_pass}$ 
6:    $^T P_{Ur\_new}[2i-1] \leftarrow [scan\_center[i], min\_y, ^T P_{Ur\_z}]$ 
7:    $^T P_{Ur\_new}[2i] \leftarrow [scan\_center[i], max\_y, ^T P_{Ur\_z}]$ 
8: return  $^T P_{Ur\_new}$ 

```

(b)

**Fig. 4.** (a) Illustration of the path planning for the laser sensing operation derived from the registrative path and (b) Pseudocode of the automated planning algorithm.

From there, the width of the current printed layer can be obtained. The 2D laser scanner has a maximum width limit that it can measure at a single instance. Hence, if the layer width is longer than the laser width, multiple passes of the scanning will be formulated to cover the full part's width, as depicted by the several overlapping dotted green boxes in Fig. 4a. The path for the 3D scan motion (purple solid arrows) is then the center of each of the scan passes (dashed-dot brown lines in Fig. 4a). As the relative positions of the scan passes are known, the scan output can be easily stitched together to reconstruct the layer's surface. The pseudocode in Fig. 4b summarizes the algorithm used to automatically formulate the laser scanning motion from the initial generated unified registrative path. This  $^T P_{Ur\_new}$  is then fed into Eq. (2) to generate the gantry robot motion for the registrative operation. The laser sensor is programmed to collect the 2D scan data at a distance interval following the stepover increment in the initial generated unified registrative path  $^T P_{Ur}$ .

The original generated registrative path itself will be useful again later on for processing the laser scan data to perform the automated adaptive function. As the lines in  $^T P_{Ur}$  represent the 2D laser line strictly on the layer surface, the output of the 3D scanning, which may include data not belonging to the printed layer's surface due to the contour shape of the layer, can then be cropped

automatically and accordingly following the end coordinates of the lines in  ${}^T P_{Ur}$ . Hence, the scan data used for the adaptive function will only include those that belong to the surface of the layer, as will be described further in Sect. 4.

## 4 Results and Discussion

To test and demonstrate the capabilities of the developed system, a  $5 \times 5 \times 5 \text{ cm}^3$  block was printed adaptively and each of the printed layers was automatically scanned to compare the actual and the theoretical heights of the layers. Table 1 summarizes the parameters used in the experiments. A total of 18 layers were printed and Fig. 5a shows the final printed cube. Figure 5b shows the full output of the automated scan result of one of the printed layers, which is the 9<sup>th</sup> layer (halfway to the print), while Fig. 5c shows the scan result for the printed surface only after the full scan data has been cropped automatically using the end coordinates from the lines in the generated unified registrative path  ${}^T P_{Ur}$ . After automatically removing the unwanted scan data that do not belong to the printed layer, the depth data can be fairly processed and the maximum and minimum heights of the current layer can be obtained. These values are useful to decide accordingly whether milling is required to increase the flatness of the top layer surface for subsequent print. Figure 5d shows a sample of a layer that was automatically milled using the generated unified subtractive path  ${}^T P_{Us}$ .

As each of the printed layers was automatically scanned, the actual height of the layers can be compared with the theoretical values. Figure 5e shows the plot of the actual average height of each of the printed layers compared with the theoretical expected height, which is the layer number times the height of the first layer. As can be seen, the actual layer height increasingly deviates from the expected height as the layer progresses upwards, similar to [8] where the thickness of the individual layer decreased as more layers were added. If the print was not performed adaptively, it would have stopped printing at a certain layer when the gap between the actual and the expected (set) height is large enough to impede the arc establishment between the welding electrode tip and the layer's top surface.

We also compared our results with Panchagnula and Simhambhatla [9], where they proposed a model to predict the height of the  $n^{\text{th}}$  layer which compensated for the anticipated decrease in the layer thickness. The height calculated based on the model is plotted on Fig. 5e (dotted yellow line). As can be seen, though the model predicted the layer's height more accurately than the rudimentary expected height, the calculated height still increasingly deviates from the actual layer height as the print progresses, which is consistent with what the authors reported. Hence, with the developed automated adaptive H-WAAM system, the actual layer's height can be measured and updated on the fly to ensure the continuation and completion of the print.

**Table 1.** Parameters used in the experiments.

Parameters (Unit)	Value
Filler material	ER316LSi
Torch speed (mm/s)	7
Wire feed rate (m/min)	3
Voltage (V)	14.8
Current (A)	100
Bead height (mm)	2.24
Bead width (mm)	4.1
Stepover rate	0.67

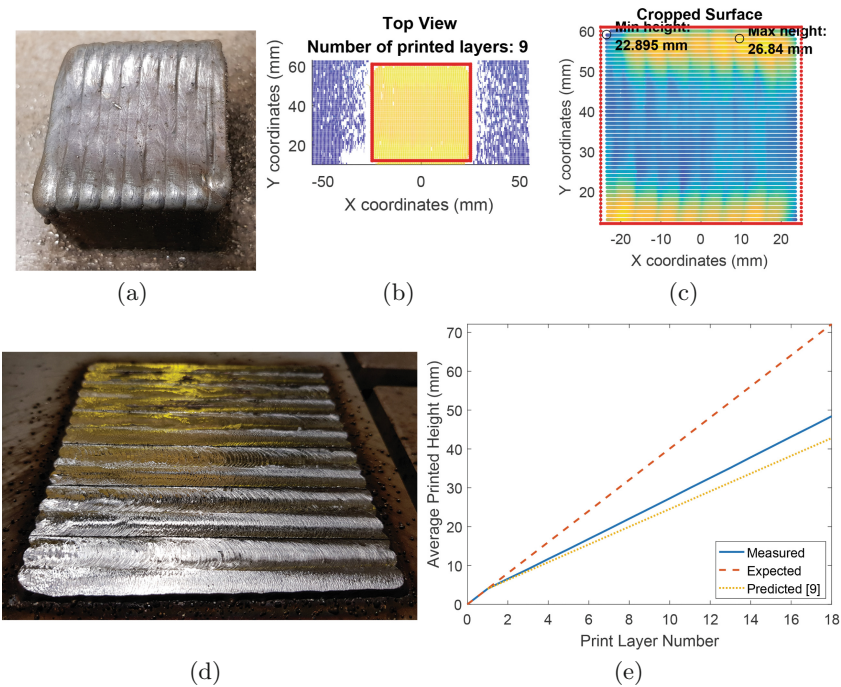


**Fig. 5.** (a) The final printed cube. (b) Sample of the output of the laser scan for one of the printed layers (9<sup>th</sup> layer). (c) Cropped scan of the printed layer's surface only. (d) Sample of a milled layer. (e) Comparison of the actual (measured) average, expected and calculated [9] printed height of each layer.

## 5 Conclusions

This paper developed and proposed a universal framework for an automated adaptive Hybrid-Wire Arc Additive Manufacturing (H-WAAM) system. The only input required to the system is the CAD model of the part to be built, and the system is able to automatically sense and adapt to the variation of the print behaviour to ensure the continuation and completion of the print job. Specifically, the system is able to measure the current print height after each layer's print, decide whether subtractive operation is required to improve the smoothness of the top surface and perform accordingly, and finally update the actual height for the subsequent layer's print to obtain a more accurate print result. The proposed process is general enough for printing any part's shape as it only requires the CAD model of the part as the input. Experiments were conducted to demonstrate the capabilities of the developed system and reported.

**Acknowledgements.** The authors gratefully acknowledge the support of SUTD Digital Manufacturing and Design Centre (<https://dmand.sutd.edu.sg>).

## References

1. Ding, D., Pan, Z., Cuiuri, D., Li, H.: Wire-feed additive manufacturing of metal components: technologies, developments and future interests. *Int. J. Adv. Manuf. Technol.* **81**(1–4), 465–481 (2015)
2. Busachi, A., Erkoyuncu, J., Colegrove, P., Martina, F., Ding, J.: Designing a WAAM based manufacturing system for defence applications. *Procedia Cirp* **37**, 48–53 (2015)
3. Karunakaran, K.P., Suryakumar, S., Pushpa, V., Akula, S.: Low cost integration of additive and subtractive processes for hybrid layered manufacturing. *Robot. Comput. Integr. Manuf.* **26**(5), 490–499 (2010)
4. Williams, S.W., Martina, F., Addison, A.C., Ding, J., Pardal, G., Colegrove, P.: Wire+ arc additive manufacturing. *Mater. Sci. Technol.* **32**(7), 641–647 (2016)
5. Suryakumar, S., Karunakaran, K.P., Bernard, A., Chandrasekhar, U., Raghavender, N., Sharma, D.: Weld bead modeling and process optimization in hybrid layered manufacturing. *Comput. Aided Des.* **43**(4), 331–344 (2011)
6. Li, Y., Han, Q., Zhang, G., Horváth, I.: A layers-overlapping strategy for robotic wire and arc additive manufacturing of multi-layer multi-bead components with homogeneous layers. *Int. J. Adv. Manuf. Technol.* **96**(9–12), 3331–3344 (2018)
7. Xiong, J., Zhang, G., Zhang, W.: Forming appearance analysis in multi-layer single-pass GMAW-based additive manufacturing. *Int. J. Adv. Manuf. Technol.* **80**(9–12), 1767–1776 (2015)
8. Song, Y.A., Park, S., Hwang, K., Choi, D., Jee, H.: 3D welding and milling for direct prototyping of metallic parts. In: *International Solid Freeform Fabrication Symposium* (1998)
9. Panchagnula, J.S., Simhambhatla, S.: Manufacture of complex thin-walled metallic objects using weld-deposition based additive manufacturing. *Robot. Comput. Integr. Manuf.* **49**, 194–203 (2018)
10. Xiong, J., Zhang, G.: Adaptive control of deposited height in GMAW-based layer additive manufacturing. *J. Mater. Process. Technol.* **214**(4), 962–968 (2014)

11. Song, Y.A., Park, S., Choi, D., Jee, H.: 3D welding and milling: Part I - a direct approach for freeform fabrication of metallic prototypes. *Int. J. Mach. Tools Manuf.* **45**(9), 1057–1062 (2005)
12. Akula, S., Karunakaran, K.P.: Hybrid adaptive layer manufacturing: an Intelligent art of direct metal rapid tooling process. *Robot. Comput. Integr. Manuf.* **22**(2), 113–123 (2006)
13. Ma, G., Zhao, G., Li, Z., Yang, M., Xiao, W.: Optimization strategies for robotic additive and subtractive manufacturing of large and high thin-walled aluminum structures. *Int. J. Adv. Manuf. Technol.*, 1–18 (2018)



# A Motion Control System to Use Robots at up to 100 Times the Earth's Gravity

Victor M. Cedeno-Campos<sup>1(✉)</sup>, Uriel Martinez-Hernandez<sup>2</sup>,  
and Adrian Rubio Solis<sup>1</sup>

<sup>1</sup> Civil and Structural Engineering Department  
and Automatic Control and Systems Engineering Departments,  
The University of Sheffield, Sheffield, UK  
{v.cedeno-campos, a.rubiosolis}@sheffield.ac.uk

<sup>2</sup> Department of Electronic and Electrical Engineering,  
The University of Bath, Bath, UK  
u.martinez@bath.ac.uk

**Abstract.** Challenges for using robots in operational centrifuges are robust structures with low mass, mechanical design for movement at high vibration and high gravity (gs), orientation of components to avoid deflection, and advanced controllers to reduce vibration. The importance of centrifuge modelling resides in the capacity of physical simulation of large scale models with a small scale model. This paper presents the novel design and development of a flexible actuation control system (FACS) to control multiple stepper motors that use robots within an operational centrifuge. The novel design is robust and symmetric in order to withstand forces equivalent to 30 times earth's gravitational acceleration (30g). Moreover, the FACS and its control software are flexible and generic in order to serve for different applications. The components of the system were selected and the components' layout (location and orientation) was designed to support 30gs and fit within a box of 42 cm × 34 cm × 22 cm. A graphical user interface was developed in LabVIEW to control four motors. Different types of motion control such as judge, jog, synchronized, unsynchronized, absolute and relative positioning were implemented. The FACS was validated with a cone penetration test (CPT) and the results are discussed. An actuator was used to perform the CPT whilst the centrifuge was rotating and achieving 30gs. The case study probed the flexible application of the FACS, its robustness to g field and its performance.

**Keywords:** Robotics within centrifuges · Mechatronics · Motion control systems

## 1 Introduction

The use of robots is vital for hazardous tasks in dangerous environments or with difficult access for persons [1–3]. A growing application for actuators and robots is in large scale civil geotechnical centrifuges (Fig. 1(a)) [4–7]. Centrifuges are used in small scale physical modeling that simulates real world physical conditions on scaled models (prepared samples of clay or sand containing sensors, actuators and Cartesian robots).



When the centrifuge rotates, it creates an artificial gravity field due to the centrifugal force. Similitude in the performance of the scaled model behavior and prototype is achieved because the gravity acting on the model increases the self-weight body forces such that stresses in the small scale model reflect those at full scale. This gravitational acceleration results in a very challenging environment for robots to operate due to vibration and deflection of electronic devices and cantilever structures [8, 9].

Challenges for robots in centrifuges are the need for compact size, precision, repeatability, lightweight but also robust structures and supports for electronics to avoid deflection. Robots are used to perform real time tasks during centrifuge operation, such as penetration of instrumented probes, excavation of samples and loading during testing. Hence, this paper presents a flexible actuation control system (FACS) for plug-and-play stepper motors. The flexibility resides in its ability to work for several experimental tests due to its plug-and-play capacity and its control software which just requires two parameters to configure each actuator (stroke and motor steps). FACS is the third of its kind to be reported in literature and it was developed for use on the 4 m diameter centrifuge in the University of Sheffield (Fig. 1) [10]. The novelty of FACS resides in the generic and scalable design of its control software and motors' plug-and-play capability. This flexibility facilitates the connection and disconnection of different experimental setups.

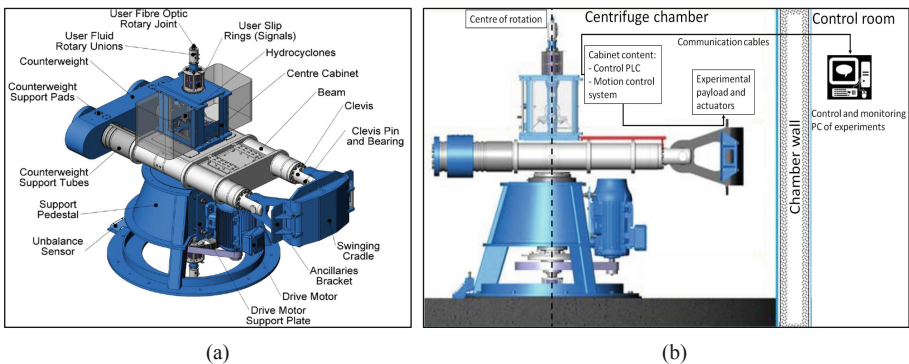


**Fig. 1.** Centrifuge (a) 3D view and parts. Reproduced from [10] (b) Side view and control room.

## 2 Centrifuge Modelling Background

The development of motion control systems for centrifuges endow the ability to perform experimental tests to models such as lateral loading, excavation, multi degree of freedom (DOF) loading and vertical-horizontal-moment (VHM) loading. Specific equipment for VHM, excavation and multi-DOF were reported in [11–14]. A linear actuator was used to apply lateral load to a monopile (emulation of wind and wave loads on wind turbine tower). The lateral load was produced by an actuator of 10 kN at a maximum loading rate of 8.3 mm/s. This actuator consisted of the following control hardware: a controller (National Instruments NI PCI-7390), servomotor driver (Mitsubishi, MR-J2S-40A), and AC servomotor (Mitsubishi, HCKFS43) [11].

Two servo motors were used to drive an actuator designed specifically for excavation. The aim was to simulate the excavation of underground infrastructure such as service tunnels and subways. Thus, the actuator's design was very robust and sturdy to cope with dynamics of cyclic loading [12]. In a VHM, three independent actuators load samples in vertical, horizontal and moment modes. The vertical actuator is limited to work at 3 mm/s, the horizontal between 0 and 3 mm/s, and the rotation at 1°/s [13].

A multi-DOF was developed for multiplanar loading. The multi-DOF can operate on either displacement or load control on two horizontal axes, but only on load control on the vertical axis. Also, it allows rotation about horizontal axes. The multi-DOF was validated through a cyclic test of large-amplitude lateral movements under low vertical load [14]. The VHM and multi-DOF systems were controlled by one of the only two motion control system reported in literature. This motion control system is called Package Actuator Control System (PACS). The system was capable of controlling up to four servo motor with PID controllers in cyclic (waveform) or desired sequence modes. The system offered load or/and displacement control for the four motors [15].

The other reported motion control system is called Scalable Actuator Control System architecture (SACS). The system uses National Instruments equipment (NI controller cRIO-9024) [16]. SACS's first approach was reported for a single motor, but was scalable in hardware. The SACS software was edited to make use of a second motor working in displacement control in forward and reverse directions [17]. The use of motorized equipment is widespread for in-flight operations, but the equipment is not properly reported. In most of them, motors and their control were specific for each developed hardware and experimental setup. Instead, FACS is a generic system that can operate with diverse experimental setups. The use of NI hardware and LabVIEW for motion control is increasing, however, there are only few systems designed to work within an operational centrifuge. Thus, the following section describes the hardware and software development of the scalable and plug-and-play FACS to operate within centrifuges.

### 3 Motion Control System Design and Development

Most of the components of the novel flexible actuator control system (FACS) architecture are from National Instruments (NI). The components are described in the order of connection. PC in Centrifuge control room, real time PXI controller (NI 8135), a PXI card (NI 7354), a breakout board (NI UMI-7774) and four stepper motor drives (ACE-102). The complete architecture is shown in Fig. 2.

#### 3.1 FACS Architecture and Electronics

The breakout board and drives are supplied with two power supply units (PSU) RPS-400 of 10.5 A nominal, 16.7 A peak at 24 V DC. In specific one PSU supplies the breakout board and two drives, whilst the second PSU supplies the other two drives.

The PXI card is directed plugged into the PXI controller, whilst the PCI card is connected to the breakout board through NI cables (SHC68-C68-S, 68-pin VHDCI). The breakout board consists of several DB type connectors. These connectors are

mainly DB15 connected to motor drives and DB25 to feedback sensors (i.e. forward and backward limit switches, home switch and encoders). The DB connectors facilitate plugging and unplugging the cables. In order to protect encoder's signal integrity, bespoke cables to the DB connectors were double insulated (aluminum foil and braid shield).

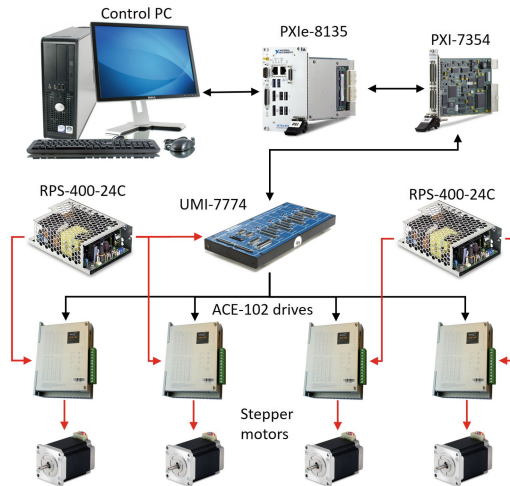


**Fig. 2.** Motion control system architecture. (Bi)Directional communication is in black arrows, transmitted energy is in read arrows.

The power supply input for the two PSUs is 120 V AC and is supplied through a 3-pin Amphenol connector (62 GB-16F12-03SN and 62 GB-10F12-03PN). The 120 V AC Amphenol is connected to the PSUs through DIN rail terminals blocks for ground and 120 V AC. There is a 32 A fuse in the rail terminals for the 120 V AC connections. Each PSU has its own on/off button. Each stepper motor drive output has its own 4-pin Amphenol connector (62 GB-16F08-04PN and 62 GB-12E08-04SN). This allows plugging and unplugging cables with each experimental setup.

An additional device to increase the flexibility of the FACS is a changeover switch, which allows supplying power to a single stepper motor driver with an external power supply. The objective of the switch is to use large voltages (i.e. 80 V) and current of up to 20 A for a single driver. This external power supply is provided with a 2-pin Amphenol connector (62 GB-16E12-02SN and 62 GB-10F12-02PN). See Fig. 3 for the complete electrical wiring diagram.

The layout (location and orientation) of the FACS considers the increased forces imposed by the artificial gravity field and wiring routes to connect the components (Fig. 4). The cables are restrained with cable ties and secured to the aluminum box through cable tie mounts. The orientation of the breakout board, PSUs and stepper motor drives are parallel to the artificial centrifugal gravity field, so that circuit boards are not subjected to bending forces. Excessive bending force leads to breakage of the boards.

### 3.2 FACS Software

The control interface was developed in NI LabVIEW 2016 and NI Motion Assistant 2016. In specific the visual instrument (VI) library 73xx of Vision and Motion library was used. The motion assistant software facilitated creating motion subprograms and LabVIEW was used to create control loops, switch cases and if conditions. In LabVIEW, the software which the user interacts is called front panel whilst the software which the developer interacts is called block diagram. The block diagram consists of three loops working in parallel. The loops interaction is controlled by one loop that transfer configuration data such as moving velocity and acceleration, whilst it enables the desired movement and disable the other movements. The data is transferred by local variables that are updated in milliseconds.

The implemented types of moves are absolute, relative, unsynchronized jog, synchronized jog and nudge. See Fig. 5 for code of jog and absolute movement of a single axis respectively. The nudge movement refers to a very small movement (1 mm), the jog movement refers to a continuous movement at constant velocity, the absolute/relative movement refers to a move in absolute/relative coordinates, the synchronized jog refers to moving all the motors at the same time at the same constant velocity whilst the unsynchronized job is the same but each motor moves at its own constant velocity.

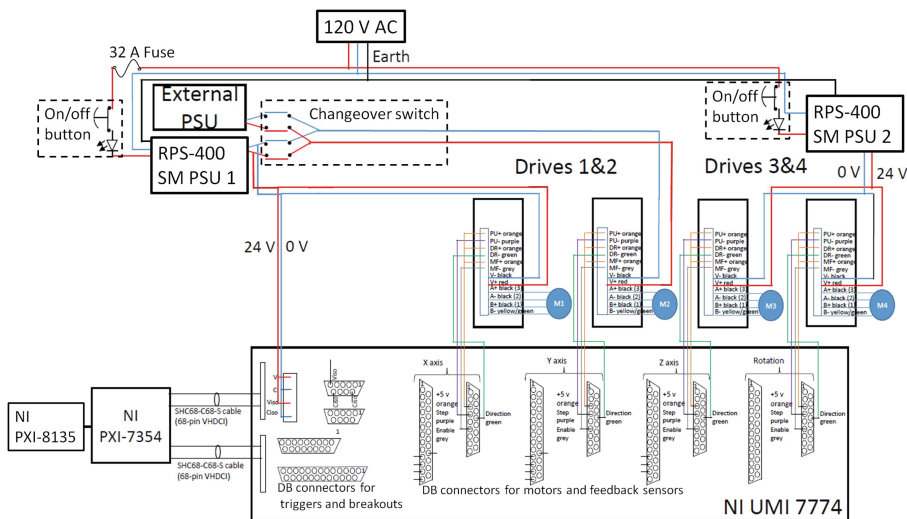
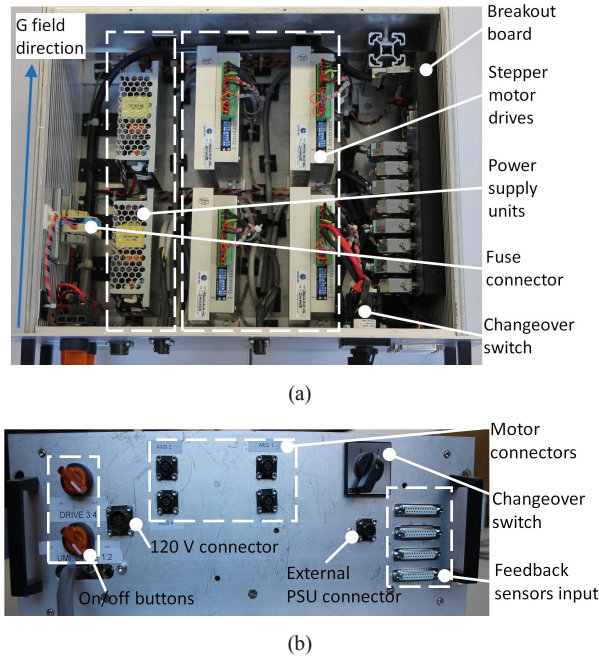
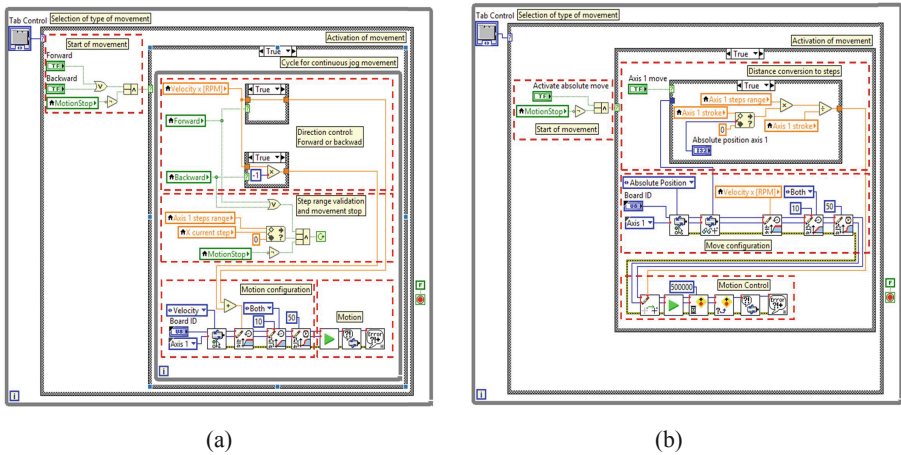


Fig. 3. Electrical wiring diagram of motion control system.



**Fig. 4.** Motion control system. (a) Top view (b) Front view.

The rest of the movements are combinations and variations of the jog and absolute movements. The user can control desired velocity and distance (in case of absolute and relative movements). The first loop gets the current position of each axis in steps and converts it to distance position. The second loop monitors the selection of the movement and the third loop executes the selected movement at desired velocity. See algorithm for pseudocode.



**Fig. 5.** Movement codes in LabVIEW: (a) Jog (b) Absolute.

**Algorithm: Flexible motion control system**

---

```

do:
capture current step
convert step to current position
while:(Stop is false)
do:
    do not stop
while:(StopMotion is false)
do:
check movement selection
Case 1: (Absolute movement active)
    at each selected moving axes:
        capture current position in steps
        convert desired position to steps
        0 < calculated steps < maximum available steps
        add calculated steps to current position in steps
        configure movement (velocity, acceleration)
        move calculated steps
end Absolute movement
Case 2: (Jog movement active)
    while:(forward or backward buttons is pressed
        or 0 <current step < maximum available steps)
    do:
        if: (forward is true)
            velocity > 0
        if: (backward is true)
            velocity < 0
        if: (none is true)
            velocity = 0
        if: (both are true)
            velocity = 0
        configure movement (velocity, acceleration)
        move at desired velocity
    end Jog movement
.....
Case N:
while:(Stop is false)

```

---

The user interface (front panel) consists of a fixed part that shows the current position of each axis (monitoring) and the axis configuration (input values) (Fig. 6). Only two parameters are required to configure each axis (stroke and steps per stroke). Due to this easy configuration, the user interface allows for any stepper motor driven actuator to be plug and used. See Fig. 7 for front panel of jog and absolute movements.

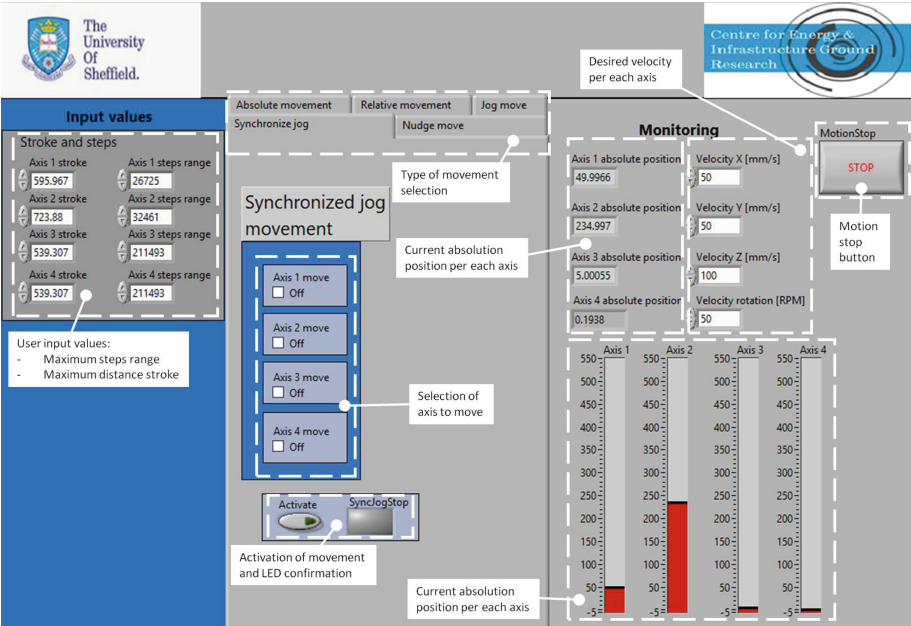


**Fig. 6.** User interface of motion control system. The user can change through types of movements by clicking the tab. The input values and monitoring sections are fixed.

In case of screw driven actuators, a rotation of a stepper motor multiplied by a reduction factor (gears or pulleys) is equivalent to the lead of the screw. The total number of steps is the total number of steps of the stepper motor multiplied by any reduction ratio from gears or pulleys. In case of belt driven actuators, the driven distance depends on the revolutions of the stepper motor and the ratio of the pulleys’ diameters.

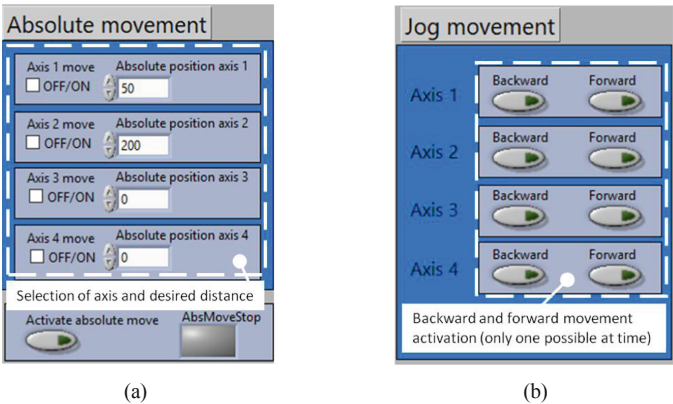


**Fig. 7.** User interface for the FACS (a) Absolute move (b) Jog move.



#### 4 Validation Case Study: Cone Penetration Test

The FACS was validated with a cone penetration test (CPT) which is a common test in geotechnics engineering. The CPT consists of driving down a conical ended penetration probe with a vertical actuator. The CPT is driven down into a model made of sand to measure penetration resistance (Fig. 8(a)). The objective is to measure sample (sand) mechanical properties [18].

The CPT consists of an aluminum cylinder that has a cone tip at the bottom (Fig. 8(b)). The function of the cone tip is to penetrate a sample. Instrumentation consists of strain gauges inside the cylinder behind the cone tip to measure penetration resistance and a 5 kN load cell connecting CPT to actuator. The test was made whilst the centrifuge was working and generating an artificial gravity of 30g. Hence, the FACS hardware withstand 30g as specified by design. Moreover, a PID controller was implemented with a laser sensor as distance feedback. The PID controller is synthesized for each experiment with an autotune with a PID relay technique. The protocol of the CPT test is:

1. Prepare a model consisting of layers of sand at low and high relative density.
2. Place sand model on centrifuge and connect actuator and CPT probe over model.
3. Implement safety system checks and accelerate centrifuge to 120 RPM, equivalent to 30g at a radius of 1.85 m.
4. At test gravity (30g), conduct CPT test measuring force and displacement during penetration over 20 cm stroke. The rate of penetration is 0.08 mm/s. Measure forces from 5 kN load cell and cone tip strain gauge.
5. Retract CPT probe and decelerate centrifuge.

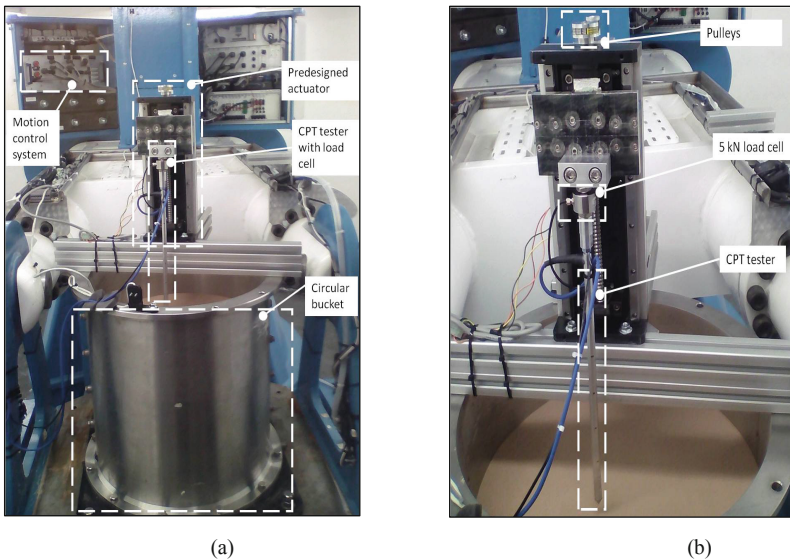


**Fig. 8.** Cone penetration test setup in centrifuge. (a) Complete setup (b) Detail of cone penetration probe.



5 Results and Discussion

The application case study demonstrated the FACS operation. The measured force from the load cell was adjusted with a calibration factor of 2 N/mV. This force captures clearly the loose and dense layers of sand as the probe advanced through the sand model with increased resistance observed at layer interfaces (Fig. 9).

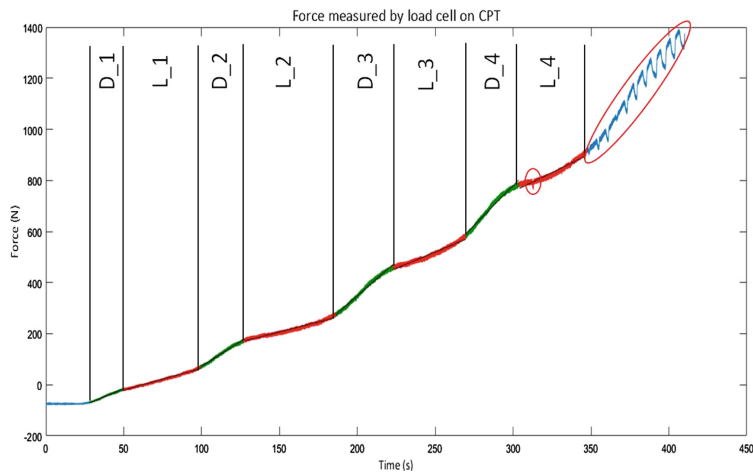


**Fig. 9.** Forces measured by a 5 kN load cell during CPT. Dense layers (D\_x) in green line and loose layers (L\_x) in red line. 1<sup>st</sup> order curve fitting in black thin line. Highlights in red show slippage of actuator.

It is observed that the loose layers offer lower resistant than dense layers, also that resistance increases at greater depths. This is attributed to the additional vertical stress generated by the overburden surcharge stress of overlying layers that provides additional confinement of the sand. A Matlab curve fitting measured the linearity of the actuator’s displacement control. The first three layers behave linear but afterwards nonlinear. The curve fitness coefficients of 1<sup>st</sup> order and 2<sup>nd</sup> order are shown in Table 1. 3<sup>rd</sup> order fitting did not improve significantly. There is an increase in fitness coefficients as the CPT buries deeper for both the loose and dense layers. The physical meaning is that as the CPT goes deeper in the sand the load cell force becomes more non linear.

The CPT shows the performance of the FACS and the actuator at high depth (denser layers). As the probe advanced after layer Loose\_4 the mechanical capacity of the actuator is reached and there is slippage. Overall, the case study demonstrated the easiness of operation of the FACS and its control software, and the flexibility of the plug-and-play capacity.

**Table 1.** Fitness coefficients from curve fitting

Layer	1 <sup>st</sup> order		2 <sup>nd</sup> order		Difference between 1 <sup>st</sup> and 2 <sup>nd</sup> order	
	Loose	Dense	Loose	Dense	Loose	Dense
1	382	847	376	709	6	138
2	790	1653	712	1129	78	524
3	1436	1854	1236	1131	200	723
4	2152	2602	1239	1355	913	1247

## 6 Summary and Future Work

A novel flexible actuation control system (FACS) was presented in this paper. The flexibility allows to plug-and-play any experimental tests and configure the control software of each actuator by setting the stroke and motor steps. The electrical design and system architecture were explained. Also, the control software and user interface were explained. A validation case study (cone penetration test, CPT) was presented and discussed. The force measured by the CPT's load cell captured the alternating layers of sand with dense and loose density. Future work will focus on the design of a more robust actuator and expanding the capabilities of the FACS to implement force control to cope with nonlinearities of the sand. Also, future work will focus on developing control for multi-axis actuators to perform VHM loading.

**Acknowledgments.** The authors would like to thank Prof. Black, of the Centre for Energy and Infrastructure Ground Research at the University of Sheffield, for all his support during this project and his helpful comments.

## References

1. Trevelyan, J.P., Kang, S.-C., Hamel, W.R.: Robotics in Hazardous Applications. In: Siciliano, B., Khatib, O. (eds.) *Handbook of Robotics*, pp. 1101–1126. Springer, Berlin (2016)
2. Hamel, W.R., Murray, P., Kress, R.L.: Internet-based robotics and remote systems in hazardous environments: review and projections. *J. Adv. Robot.* **16**(5), 399–413 (2012). <https://doi.org/10.1163/15685530260182909>
3. Baudoin, Y., Habib, M.K.: *Using Robot in Hazardous Environment*, pp. 486–489. Woodhead Publishing (2014)
4. Ng, C.W.W., et al: Development of a four-axis robotic manipulator for centrifuge modeling at HKUST. In: *Physical Modelling in Geotechnics 2002, ICPMG*, pp. 71–76 (2002)
5. Ubilla, J., Abdoun, T., Zimmie, T.: Application of in-flight robot in centrifuge modeling of laterally loaded stiff pile foundations. In: Ng, Zhang, Wang (eds.) *Physical Modeling in Geotechnics*, Taylor and Francis, Sixth ICPMG 2006, pp. 259–264 (2006)
6. Hao, J., et al.: Design of a robot and test procedure for the dynamic testing of anchorages in geotechnical centrifuge. *J. ASTM Geotech Test.* **32**(4), 325–334 (2009)

7. Kong, L.G., Zhang, L.M.: Rate-controlled lateral-load pile tests using a robotic manipulator in centrifuge. *Geotech. Test. J.* **30**(3), 1–10 (2009)
8. Wood, D.M.: *Geotechnical Modelling*, Taylor & Francis (2005). ISBN 9780419237303 - CAT# RU29142
9. Kim, D.S., Kim, N.-R., Choo, Y.W., Cho, G.-C.: A newly developed state-of-the-art geotechnical centrifuge in Korea. *KSCE J. Civ. Eng.* **17**(1), 77–84 (2013). <https://doi.org/10.1007/s12205-013-1350-5>. ISSN: 1976-3808
10. Black, J. A., Baker, N., Ainsworth, A.: Establishing a 50g-ton geotechnical centrifuge at the University of Sheffield. In: Gaudin, C., White, D., (eds.) *Proceedings of the 8th International Conference on Physical Modelling in Geotechnics, ICPMG2014*, pp. 181–186 (2014). ISBN 9781138001527
11. Choo, Y.W., Kim, D., Park, J., Kwak, K., Kim, J., Kim, D.: Lateral response of large-diameter monopiles for offshore wind turbines from centrifuge model tests. *Geotech. Test. J.* **37**(1), 106–120 (2014)
12. Lam, S.Y., Haigh, S.K., Elshafie, M.Z.E.B., Bolton, M.D.: A new apparatus for modelling excavations. *Int. J. Phys. Model. Geotech.* **12**(1), 24–38 (2012)
13. Zhang, Y., Cassidy, M.J., Bienen, B.: Development of a combined VHM loading apparatus for a geotechnical drum centrifuge. *Int. J. Phys. Model. Geotech.* **13**(1), 13–30 (2013)
14. O'Loughlin, C.D., Cocjin, M.L., Gourvenec, S.M., Stanier, S.A.: A simple approach to multi degree-of-freedom loading in a geotechnical centrifuge. *Geotech. Test. J.* (2018, in press)
15. De Catania, S., Breen, J., Gaudin, C., White, D.J.: Development of a multiple-axis actuator control system. In: *Physical Modelling in Geotechnics*, pp. 325–330 (2010)
16. Patra, S., Knappett, J. Brown, M. J.: Development of a scalable actuator control system for use in a geotechnical centrifuge. In: *Information technology in Geo-Engineering, Proceedings of the 2nd International Conference (ICITG)*, vol. 3, pp. 183–190. IOS Press (2014)
17. Al-Baghdad, A., Brown, M. J., Knappett, J. A.: Development of an inflight centrifuge screw pile installation and loading system. In: *3rd European Conference on Physical Modelling Geotechnics Eurofuge*, pp. 239–244 (2016)
18. Robertson, P.K.: Soil classification using the cone penetration test. *Can. Geotech. J.* **27**, 151–158 (1990)



# Fault Signature Analysis of Industrial Machines

Wei-Ting Hsu, Chen-Yang Lan<sup>(✉)</sup>, Meng-Kun Liu,  
and Shu-Tzu Chang

National Taiwan University of Technology and Science,  
Taipei City 10607, Taiwan (R.O.C.)  
{M10703432, jimmylan, mkliu}@mail.ntust.edu.tw,  
ss850624@gmail.com

**Abstract.** The condition monitoring and fault diagnosis is an important function of the intelligent mechanics. Understanding equipment's condition helps engineers avoiding inevitable catastrophe that could cause unplanned downtime and affect the system reliability and safety. In addition, alleviation of the machine's incipient faults helps the machine running efficiently and reduces energy consumption. This paper presents field case studies of industrial induction motors including pumps and fans from several facility factories, and uses electrical data not only to analyze machine's condition and but also to detect the faults. Current spectrum analysis is mainly employed to detect the anomaly. In addition, we propose a ratio of current divided by voltage (C/V) spectrum to represent the steady gain property of the system. This ratio is expected to mitigate the effect of Variable-frequency drive's noise and disturbance on current spectrum and to reduce the false alarm caused by Variable-frequency drive (VFD). The combination of current spectrum and spectrum ratio is beneficial in the conditional analysis of industrial motors.

**Keyword:** Fault detection · Current spectrum · Induction motor

## 1 Introduction

Induction motors are used extensively in industry due to its simplicity of structure, low price, high reliability and easy to maintain. With the increased operation of the induction motors, more attention is drawn to fault detection and diagnosis technique about induction motors and associated rotary machines. Generally, the causes of motor failure are composed as 42% relative to bearing failure, 37% to stator failure, 10% to the rotor failure, and 12% to other failure [1]. For instances of squirrel-cage induction motor, commonly detected faults include bearing fault, stator short turns, broken rotor bar, air gap eccentricity, and misalignment.

Machine failure due to above faults would usually bring unbalanced inductive voltage and current, higher fluctuation of torque, decline of torque output, and also increase of heat. Operation under faulty condition could usually result in extra energy waste, cease of motor, and even breakdown of production process or accident if attention is not paid on time. Therefore, motor fault detection and diagnosis is very important in

preventing failures. Correction of those faults in early stage could avoid unexpected shutdown failure and also reduce extra energy waste due to operation under anomaly. Efficiently operating of induction motor can save energy up to around 5%–20% [2].

Conventionally, there are many methods for motor fault diagnosis, such as vibration analysis, motor current signature analysis (MCSA), electromagnetic field change detection, temperature distribution measure, noise inspection, and model-based fault detection. MCSA is a method utilize the motor electrical data for motor condition monitoring and signature analysis, and the method is documented in ISO 20958 standards [3]. Due to the high magnetic resistance of air, slight change of air gap between motor stator and rotor causes the overall magnetic flux difference which affects the current of winding wire and produce fault signatures. Other than detecting bearing failure, misalignment of coupling and air gap eccentricity, the MCSA method can also be used to detect broken rotor bar fault, stator short turns and transmission fault, etc.

Because of the noise from supply voltage, current spectrum usually contains some frequency peaks associated with those noise. This would usually jeopardize the capability to detect early fault and even cause confusion leading to false judgement in current spectrum. We propose to use current divided by voltage as a measure not only to attenuate the effect of voltage noise, but also to enhance the fault signature frequency. In this paper we applied MCSA on field collected cases for analysis and compare it to the proposed current divided voltage FFT spectrum.

## 2 Analysis Method

### 2.1 Fast Fourier Transform Analysis (FFT)

In signal analysis, it is common to use Discrete Fourier Transform (DFT) to convert discrete time signal into frequency domain representation [4].

$$X_k = \sum_{n=0}^{N-1} x_n \cdot [\cos(2\pi kn/N) - i \sin(2\pi kn/N)] \quad (1)$$

$$|X_k| = \sqrt{\text{Re}(X_k)^2 + \text{Im}(X_k)^2} \quad (2)$$

where

- $x$  is original signal
- $|X_k|$  is amplitude for frequency component  $k$
- $N$  is the number of data
- $k$  is frequency component.

However, the computation loss is large in doing this conversion. To resolve this problem, Fast Fourier Transform (FFT) is employed to rapidly calculate such transformation by factorizing the DFT matrix into a product of sparse factors. Therefore, it can reduce the data complexity of DFT from the order  $N^2$  of to the order of  $N \log(N)$  [5]. FFT is thus a very suitable way to characterize the stationary signals, but not suitable for transient signal.

## 2.2 Current Divided by Voltage Analysis

When applying FFT to analyze field data, current spectrum is inevitably affected by supplying voltage noise, such as VFD's noises. Therefore, if the supply voltage condition is not good, there could be lots of noises appearing in the low frequency band. These noises might overlap with mechanic's feature frequency. Thus, it is hard to determine the motor's condition and to differentiate fault signature from noise. To attenuate this difficulty, FFT is applied to both current and voltage's signal and then voltage spectrum amplitude is divided by the current spectrum amplitude so that to obtain the gain of motor system

$$\frac{V(j\omega)}{I(j\omega)} = |G(j\omega)| \angle G(j\omega) \quad (3)$$

where

$|G(j\omega)|$ : gain of the system  
 $\angle G(j\omega)$ : phase of the system.

## 2.3 Fault Feature

In this paper, ISO 20958 standard is followed to find the fault characteristic frequencies. In ISO 20958, several different fault characteristic frequencies are documented, and these characteristic frequencies are similar in calculation, such as broken rotor bar, broken bearing, misalignment, air gap eccentricity, stator short turn, etc. The neighborhood band of characteristic frequency is also taken into account to find representative features to determine the condition of the fault.

There are several characteristic frequencies used in the following analysis.

### (1) Bearing Anomaly

This element is the most vulnerable to be damaged during the operation, and different cause of broken parts has unique characteristic frequency. These characteristic frequencies are generally obtained from the bearing size and its geometry. The bearing characteristic frequency is found to be function of the bearing specifications as bellow [3, 12, 14]:

Rolling ball defect frequency:

$$f_{rb} = f_e + \frac{D_p}{D_b} f_m [1 - (\frac{D_p}{D_b} \cos(\beta))^2] \quad (4)$$

Inner race defect frequency:

$$f_{ri} = f_e + \frac{N_B}{2} f_m [1 + \frac{D_p}{D_b} \cos(\beta)] \quad (5)$$

## Outer race defect frequency

$$f_{ro} = f_e + \frac{N_B}{2} f_m \left[ 1 - \frac{D_p}{D_b} \cos(\beta) \right] \quad (6)$$

In these formulations,  $f_m$  is the shaft rotation frequency,  $f_e$  is the supply frequency,  $n$  is the number of the rollers,  $D_b$  is the roller diameter,  $D_p$  is the pitch diameter of the bearing, and  $\beta$  is the contact angle of the bearing.

## (2) Shaft/Coupling Misalignment

$$f_{mis} = f_e + m f_r \quad (7)$$

where  $f_e$  is the supply frequency,  $f_r$  is the rotational speed frequency of the rotor,  $m$  is the harmonic number 1, 2, 3, ....., and  $f_{mis}$  is the current component frequency due to misalignment.

## (3) Rotor Cage Defect

A broken rotor would increase rotor side resistance irregularly. This change also leads to the current variation in the stator side due to the magnetic flux effect. Hence, its signature frequency can be denoted by as following [9, 15]

$$f_{rotor} = (1 + 2ks) f_e \quad (8)$$

where  $k$  is 1, 2, 3.. etc.,  $f_e$  is the fundamental supply frequency, and  $s$  is the rotor slip.

## (4) Transmission Problem

There are many causes for different transmission problems, such as contaminated flow, cyclic load, gear failure, clutch failure or mechanical looseness etc. [11–13]. It is usually difficult to know the detail specifications of the transmission components for users, and thus it is hard to determine the exact fault frequency band for transmission problems. However, this could still be assumed that the transmission problem may generally cause low frequency signals since industrial machine rotating speed usually operates below 30 Hz. In addition, transmission vibration signal is carried and modulated with the current signal. Therefore, the characteristic frequencies for transmission related problem are usually appeared as two symmetry peaks centered at the main power frequency due to FFT mirror property [7]. Thus, any symmetric peaks appear around the main frequency indicate potential transmission problems. Moreover, the height of the peaks represents the seriousness of the fault.

In this paper, the difference from the amplitude of main frequency minus the amplitude of faulty characteristic frequency is used as the current spectrum feature to quantify the level of motor's fault

$$\text{Fault Level} = |X(f_e)| - |X(f_{\text{failure}})| \quad (9)$$

where  $f_e$  is electric frequency,  $f_{\text{failure}}$  is failure frequency.

#### (5) Stator Problem

The most common way to analyze inter turn stator fault is park's vector approach. Using the alpha-beta transformation transforms the instantaneous line currents of stator into Park's vector [8]. An undamaged motor stator shows a perfect circle theoretically. On the other hand, damaged motor stator generates elliptic shape at the park's vector. The park's vector approach is calculated as following

$$\begin{aligned} i_d &= \sqrt{\frac{2}{3}}i_a - \frac{1}{\sqrt{6}}i_b - \frac{1}{\sqrt{6}}i_c \\ i_q &= \frac{1}{\sqrt{2}}i_b - \frac{1}{\sqrt{2}}i_c \end{aligned} \quad (10)$$

where  $i_a, i_b, i_c$  is electric three-phase current,  $i_d, i_q$  current is electric d-q axis current.

## 3 Data Analysis

### 3.1 Equipment Specification

In this paper, voltage and current measurement data from pumps, fans, and air compressors in the industrial fields were collected and analyzed. The data sampling rate is at 2500 samples per second, and thus has a frequency resolution of 0.3 Hz in FFT spectrum. There are eight motors with different fault conditions and one of samples is healthy. Electrical data is used to detect equipment conditions, and for classification. In addition, different methods are used to indicate fault level in different spectrum reading. In the current spectrum, principle frequency amplitude minus fault characteristic frequency's amplitude is used to measure its fault level. In C/V spectrum, fault characteristic frequency's amplitude minus principle frequency amplitude is used as the indicator. The general equipment information is as follows in Tables 1 and 2.

### 3.2 Healthy Motor

Both current spectrum and C/V spectrum of sample 1 appear smooth and show no obvious peaks in low frequency band except for the main frequency and harmonics (see Figs. 1 and 2). This indicates both the motor and its VFD are in good condition.



Table 1. Equipment sheet

	Sample 1	Sample 2	Sample 3	Sample 4
Equipment type	Pump	Fan	Pump	Fan
Rate power	150 KW	45 KW	30 KW	55 KW
Rate voltage	460 (V)	460 (V)	380 (V)	380 (V)
Rate current	214 (A)	71 (A)	55.7 (A)	103 (A)
Actual voltage	456.6 (V)	481.7 (V)	250.74 (V)	393.99 (V)
Actual current	58.5 (A)	30.7 (A)	34.75 (A)	66.13 (A)

Table 2. Equipment sheet continued

	Sample 5	Sample 6	Sample 7	Sample 8
Equipment type	Fan	Fan	Fan	Fan
Rate power	55 KW	90 KW	75 KW	55 KW
Rate voltage	440 (V)	480 (V)	440 (V)	380 (V)
Rate current	86 (A)	130.74 (A)	124 (A)	103 (A)
Actual voltage	424.11 (V)	407.91 (V)	423.71 (V)	293.82 (V)
Actual current	60.50 (A)	38.08 (A)	111.66 (A)	53.20 (A)

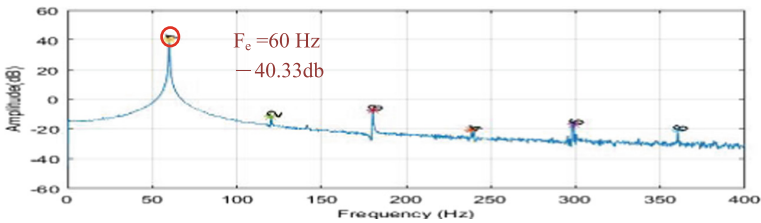


Fig. 1. Sample 1 current spectrum.

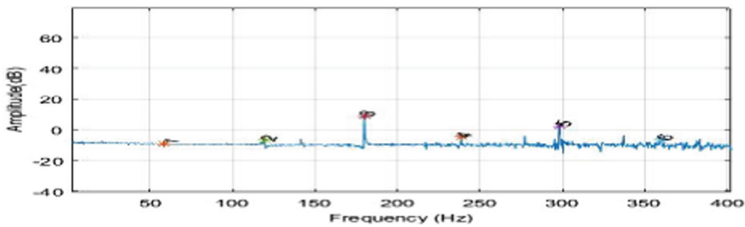


Fig. 2. Sample 1 current/voltage spectrum

### 3.3 Misalignment Failure

The current spectrum and the C/V spectrum have peaks which coincide with misalignment characteristic frequency for sample 2 (see Figs. 3 and 4). Comparing sample 2 with sample 3 (see Figs. 4 and 6), it is noticed that if the C/V is used rather than current spectrum, it indicates that sample 3's condition is more serious than sample 2. However, if the current spectrum is used (see Figs. 3 and 5), it would appear that sample 2's condition is more serious than sample 3. Nonetheless, both method can be used to detect the misalignment. From system perspective, C/V index represents the system's gain and has more physical meaning.

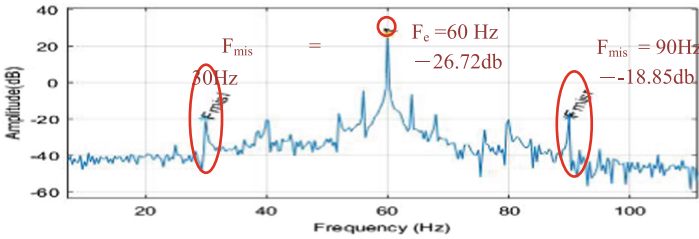


Fig. 3. Sample 2 current spectrum

### 3.4 Transmission Fault

When transmission fault occurs, it causes several low frequency peaks appearing in symmetry centered at the main frequency. Sample 4 shows a serious case (see Fig. 7) and Sample 5 also shows the transmission fault (see Fig. 9). In the case of sample 5, frequency peaks raise as multiple pairs, which indicates potential multiple different transmission fault problems but not as serious as Sample 4. They also show higher system gain on fault frequency band (see Figs. 8 and 10). Although frequency peak energy or gain are not high for Sample 5, its condition should be checked as operation continued.

### 3.5 Bearing Fault

It is noticed that several high energy peaks around the characteristic frequency of bearing rolling element failure for sample 6 (see Fig. 11). C/V spectrum shows higher system gain on that frequency band (see Fig. 12). Due to the geometry structure and non-steady operation, bearing fault usually causes spectral peaks around the fault frequency band. High energy peaks at inner bearing failure frequency are noticed (see Fig. 13). C/V spectrum also shows higher gain at that particular failure frequency (see Fig. 14).

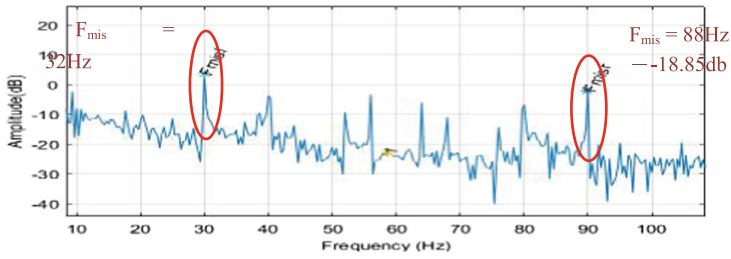


Fig. 4. Sample 2 current/voltage spectrum

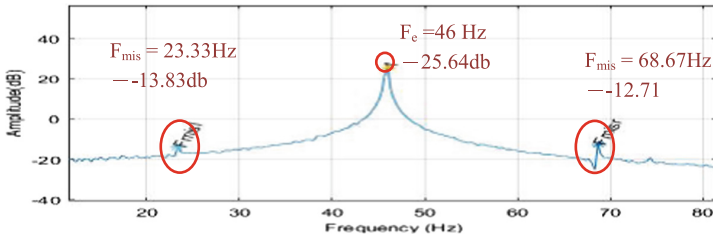


Fig. 5. Sample 3 current spectrum

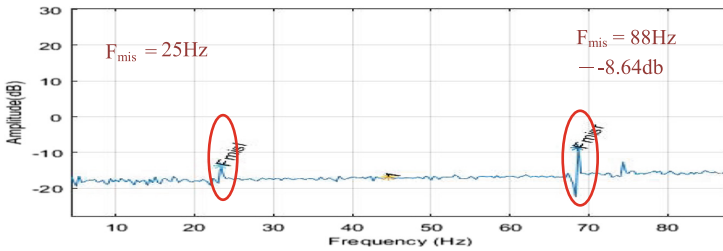


Fig. 6. Sample 3 current/voltage spectrum

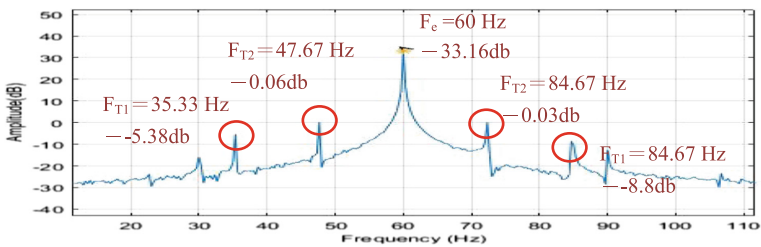


Fig. 7. Sample 4 current spectrum

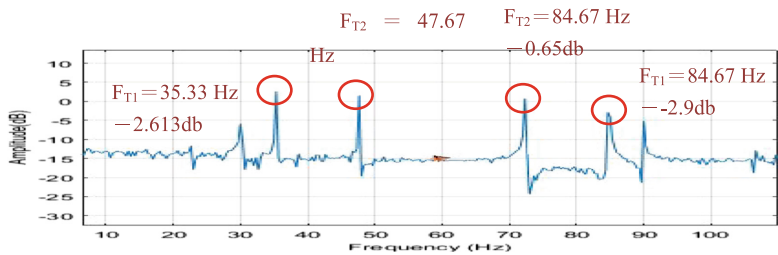


Fig. 8. Sample 4 current/voltage spectrum

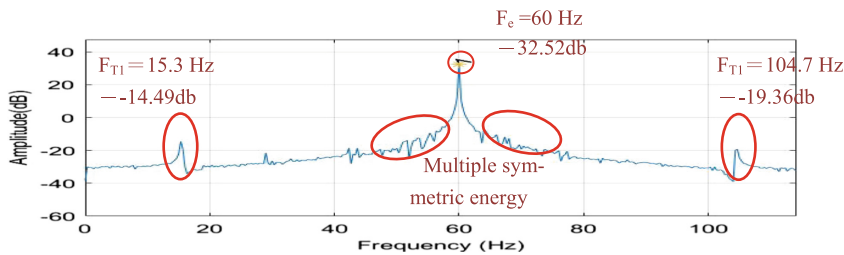


Fig. 9. Sample 5 current spectrum

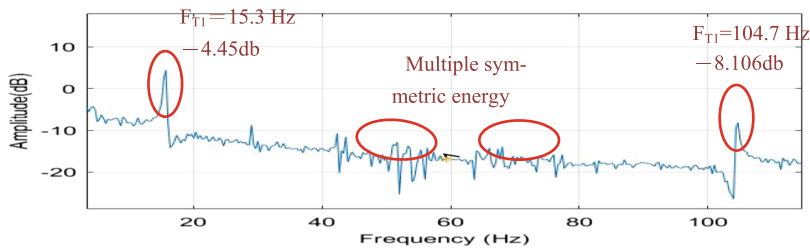


Fig. 10. Sample 5 current/voltage spectrum

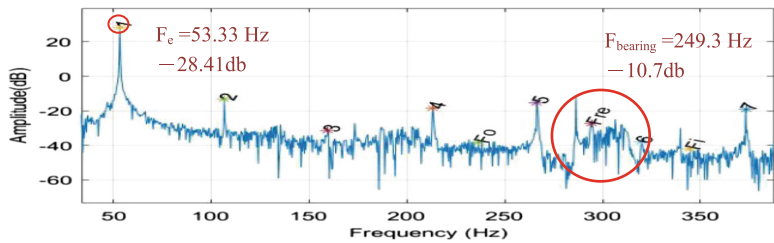
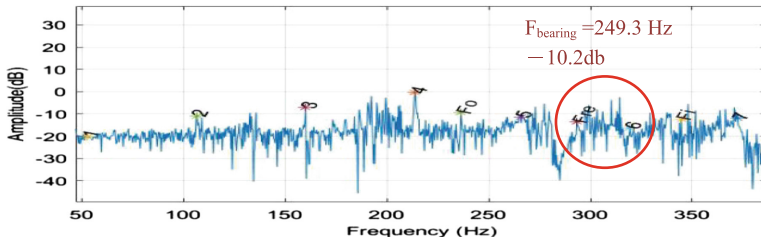
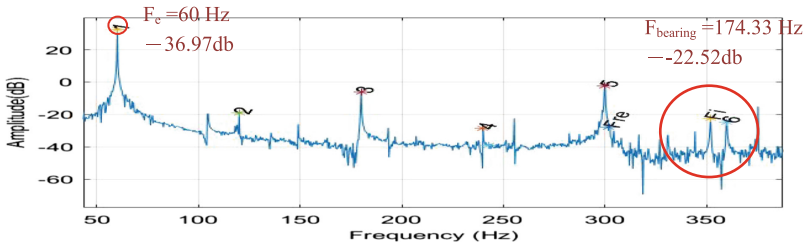


Fig. 11. Sample 5 current/voltage spectrum



**Fig. 12.** Sample 6 current/voltage spectrum



**Fig. 13.** Sample 5 current spectrum

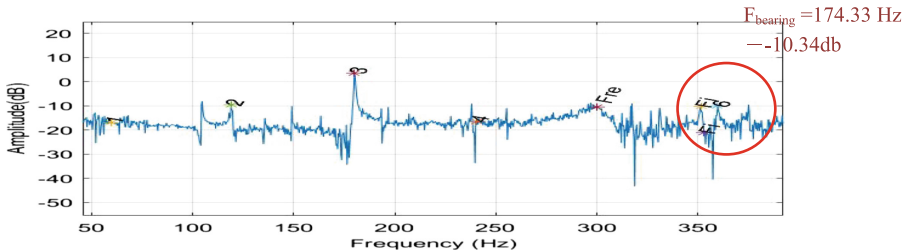


**Fig. 14.** Sample 5 current/voltage spectrum

### 3.6 Broken Rotor Fault

Sample 8 shows a blunt main frequency peak due to elevated energy in broken rotor fault frequencies (see Fig. 16), compared to the healthy sample 1 (see Fig. 15). This feature indicates the broken rotor problem in sample 8. It is also noticed that both current spectrum and C/V spectrum have energy peaks observed in the symmetry of main frequency and its harmonics in the case of broken rotor fault (see Figs. 17 and 18). The broken rotor problem is also noticed for sample 9 (see Figs. 19 and 20). Although it is not as serious as sample 8, similar pattern could still be observed.

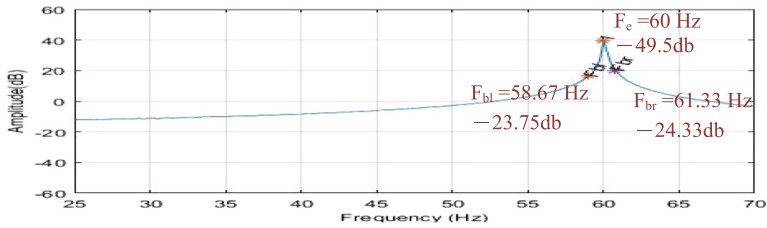


**Fig. 15.** Sample 1 (Health) current spectrum

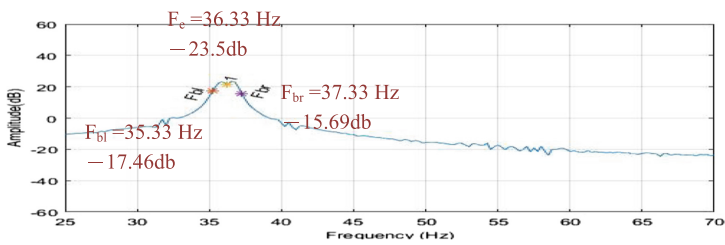


**Fig. 16.** Sample 8 (Failure) current spectrum

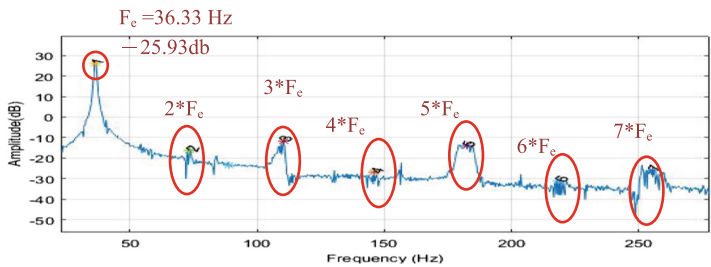


**Fig. 17.** Sample 8 current spectrum

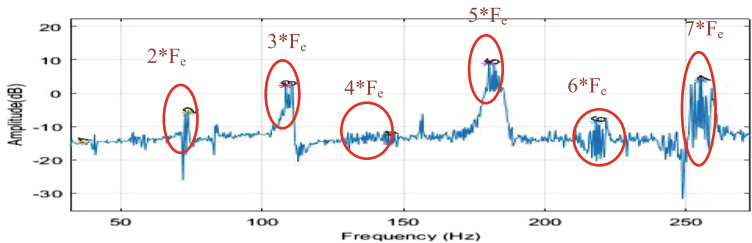


**Fig. 18.** Sample 8 current/voltage spectrum

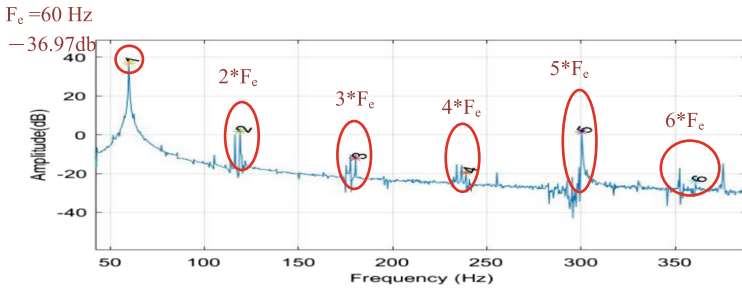


Fig. 19. Sample 7 current spectrum

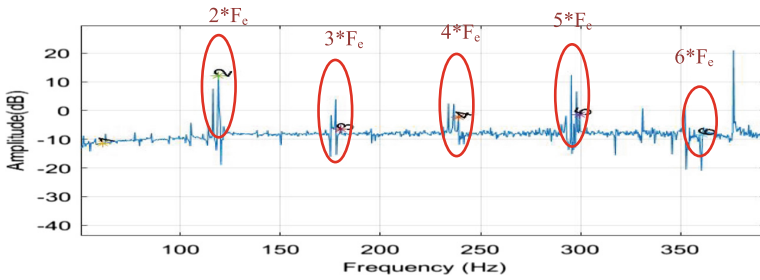


Fig. 20. Sample 7 current/voltage spectrum

### 3.7 Stator Short Turns Failure

From the current measurement, the stator's condition is interpreted using park's vector and analyzing the circularity of current parks vector. Higher circularity implies healthier stator. Sample 1 shows the healthy stator (see Fig. 21) and Sample 4 shows the stator problem (see Fig. 22).

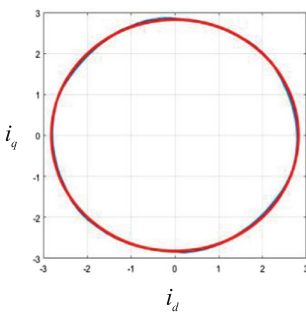


Fig. 21. Sample 1 (Health) parks vector

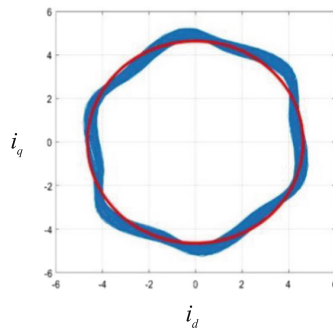


Fig. 22. Sample 4 (Faulty) parks vector

## 4 Conclusion

This paper presents the result of industrial field case studies, and shows different level of anomaly condition and different fault signature using FFT on motor current and the spectrum ratio. Conventionally, current spectrum is employed to detect if any failure features exist in spectrum. Due to the noise and condition of VFD, the current spectrum analysis might sometimes be polluted and misleading. To alleviate this problem, a C/V spectrum ratio is proposed, and represents the gain of input-output relations at different frequency. This spectrum ratio is expected to mitigate the effect of VFD's noises and enhances the magnitude at featured characteristic frequencies associated with machine faults. Therefore, the combination of current spectrum and C/V spectrum ratio can provide us more accurate result regarding to motors condition. Furthermore, those methods were applied to field data for the purpose of emphasizing challenges in the practical machine condition analysis.

## References

1. Motor Reliability Working Group: Report of large motor reliability survey of industrial and commercial installations, Part I. *IEEE Trans. Ind. Appl.* **1**(4), 865–872 (1985)
2. Sullivan, G.P., Pugh, R., Melendez, A.P., Hunt, W.D.: Operations & Maintenance Best Practices A Guide to Achieving Operational Efficiency, Release 3.0, Federal Energy Management Program, U.S. Department of Energy
3. ISO20958 Condition monitoring and diagnostic of machine systems – Electrical signature analysis of three-phase induction motors Van
4. Mitra, S.K., Kuo, Y.: *Digital Signal Processing: A Computer-Based Approach*, vol. 2, pp. 617–641. McGraw-Hill, New York (2006)
5. Loan, C.: *Computational Frameworks for the Fast Fourier Transform*, vol. 10. SIAM, Philadelphia (1992)
6. Miljković, D.: Brief review of motor current signature analysis. *HDKBR Info Mag.* **5**(1), 14–26 (2015)
7. Smith, S.W.: *The Scientist and Engineer's Guide to Digital Signal Processing*, vol. 35, chap. 10. California Technical Publishing, San Diego (1997)
8. Cardoso, A.J.M., Cruz, S.M.A., Fonseca, D.S.B.: Inter-turn stator winding fault diagnosis in three-phase induction motors, by Park's vector approach. *IEEE Trans. Energy Conv.* **14**(3), 595–598 (1999)
9. Gaeid, K.S., et al.: Fault diagnosis of induction motor using MCSA and FFT. *Electr. Electron. Eng.* **1**(2), 85–92 (2011)
10. Rai, V.K., Mohanty, A.R.: Condition monitoring techniques for rolling element bearings: an overview. In: *Proceedings of National Conference on Role of NDE in Modern Maintenance Management*, IACR, Rayagada, Orissa (India)
11. Nandi, S., Toliyat, H.A., Li, X.: Condition monitoring and fault diagnosis of electrical motors—a review. *IEEE Trans. Energy Convers.* **20**(4), 719–729 (2005)
12. Jung, J., et al.: Electrical monitoring of mechanical looseness for induction motors with sleeve bearings. *IEEE Trans. Energy Convers.* **31**(4), 1377–1386 (2016)



13. Thomson, W.T., Culbert, I.: Current signature Analysis for Condition Monitoring of Cage Induction Motors: Industrial Application and Case Histories. Wiley, Hoboken (2017)
14. Thomson, W.T., Fenger, M.: Current signature analysis to detect induction motor faults. *IEEE Ind. Appl. Mag.* **7**(4), 26–34 (2001)
15. Schoen, R.R., et al.: Motor bearing damage detection using stator current monitoring. *IEEE Trans. Ind. Appl.* **31**(6), 1274–1279 (1995)



# Robot-Assisted Double-Pulse Gas Metal Arc Welding for Wire and Arc Additive Manufacturing

Jukkapun Greebmalai<sup>1</sup>, Eakkachai Warinsiriruk<sup>1</sup>,  
and Yin-Tien Wang<sup>2</sup>(✉)

<sup>1</sup> Department of Industrial Engineering, Mahidol University, Bangkok, Thailand

<sup>2</sup> Mechanical and Electro-Mechanical Engineering,  
Tamkang University, New Taipei City 25137, Taiwan  
ytwang@mail.tku.edu.tw

**Abstract.** The study presents the process of double-pulse gas metal arc welding (DP-GMAW) for wire-and-arc additive manufacturing (WAAM). The robot-assisted DP-GMAW process built up an aluminum laminate wall using the filler wire ER5356 of diameter 1.2 mm with industrial argon gas shielding on aluminum 5083 substrate material. There are two stages in the study including the single-pass build-up and the multi-pass build-up. In first stage, the effect of DP-GMAW parameters on the build-up dimension was investigated, including current (ampere), voltage (volt), travel speed (centimeters per minute), frequency (Hz), duty cycle (percent) and delta current (ampere). The dimension of bead width and bead height were used to represent the effect of parameters as well as the processability of DP-GMAW. The results were sketched in a process window of current and travel speed for the DP-GMAW single-pass forming. In the second stage, the experiments focused on the effect of DP-GMAW conditions on a laminate wall dimension. The suitable DP-GMAW condition was determined for building-up the desired laminate wall.

**Keywords:** Double-pulse gas metal arc welding (DP-GMAW) · Aluminum build-up process · Additive manufacturing · Aluminum wire-and-arc additive manufacturing (WAAM)

## 1 Introduction

The additive manufacturing (AM) is used as the build-up process for creating or repairing the metal part of complicated geometry to reduce the cost of material and investment [1–3]. Especially to create part and prototypes. For reach the demands of the aerospace, automotive, and rapid tooling industry. The recent focus of AM research has been shifted to fabricate complex shaped metal components, including titanium and nickel alloys that cannot be economically produced using conventional methods. The competitive position of AM for metal components relative to alternative manufacturing processes is a function of the geometrical complexity and production volume [3–6].

AM is the official industry standard term (ASTM F2792) for all applications of the technology. It is defined as the process of joining materials to make objects from 3D

model data, usually layer upon layer, as opposed to subtractive manufacturing methodologies. To build-up material layer, the thermal process such as welding and laser melting, especially the wire-and-arc additive manufacturing (WAAM), are suitable because they meld the material and continuously form the layer upon layer. In this study, we focus on the gas metal arc welding (GMAW) process which has high flexibility because it could select the many characteristics of the current signal to matching with a working material. By applying the GMAW process on an aluminum bead forming, a preliminary experiment was studied on the comparison of the direct current (DC) and double pulse current (DP). Both the DC and DP current waveforms are shown in Fig. 1. The more detail of the DP current is shown in Fig. 4. The result showed that the welding using DC has the difficulty for control a uniform of the bead. On the other hand, for the weld using DP current formed a bead uniformly than direct current, as shown in Fig. 1. It was concluded that the DP-GMAW process has more uniform bead than that by DC on low heat condition. Therefore, the DP-GMAW process was used in this study in forming the laminate wall, especially building-up aluminum alloy based WAAM.

The study investigated effect of DP-GMAW parameters on bead dimension for build-up aluminum alloy and determined the build-up process window for single-layer. For the multi-layer process, the study focused on the effect of heat condition on laminate wall dimension and determined a suitable process condition for the multilayer wall.

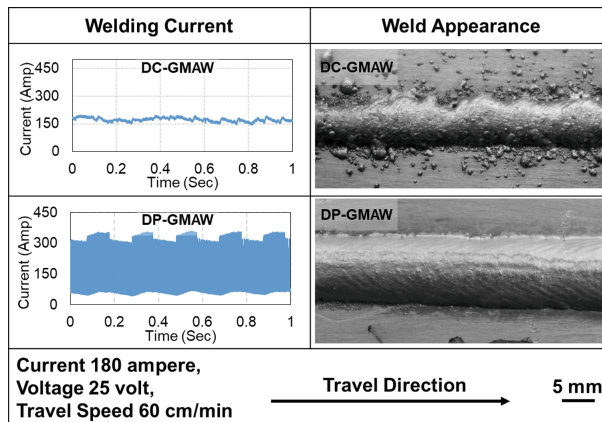


**Fig. 1.** The GMAW current comparison of weld bead appearance

## 2 Experimental Setup and Parameter

### 2.1 Experiment Material and Equipment

In this study, Aluminum alloy wire ER5356 with a diameter of 1.2 mm was used as the build-up material, the aluminum 5083 with a thickness of 15 mm used as substrate material, and industrial argon gas (99% purifier) used to shield during process build-up.

The laminate thin wall weld continually layer upon layer was chosen as the build-up geometry to perform the ability of the build-up process.

For the welding process, the experiment set-up shown in Fig. 2 consists of a DP-GMAW machine Astern 400 ADR made by Megmeet Electric Co. and weld power source WB-P500L made by OTC Daihen Co.. The DP-GMAW machine had a maximum current range at 400–720 A and voltage 50 V maximum adjusting. The power source WB-P500L had maximum current 400 A and voltage 34 V maximum adjusting. In this case of the machine parameters were compared by heat input concept to determine the same heat condition of welding parameters. Welding robotic OTC FD-V8 was employed to control a precision build-up path for the single-pass and multi-layer experiment. A process was planned to build from the base layer upon layer with increasing constant distance or constant layer height. The first starting layer used 15 mm as the contact tip to work distance (CTWD). Figure 3 represented the schematic of the process with process variables.

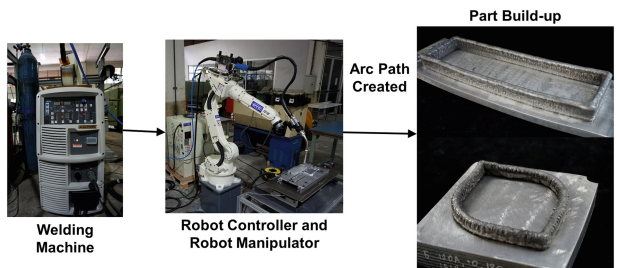


Fig. 2. Experimental setup.

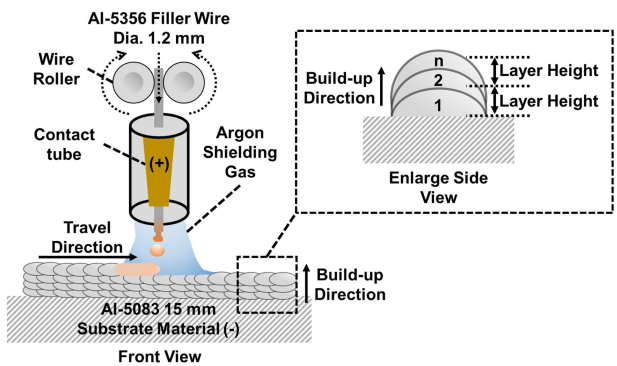


Fig. 3. Schematic of the WAAM process

## 2.2 Double-Pulse Parameters

In order to investigate the effect of DP parameters, the DP current signal during build-up was detected to get an actual level of a current pattern. Calibrated current sensing with a hall sensor (current transformer) was connected through the DAC device by the sampling rate of 5000 samples per second. The computer was used for converting and storing the weld signal data. The measured DP current signal collected from OTC WB-P500L welding machine, as shown in Fig. 4, is a suitable monitoring system this current pattern using the conditions of current 120 A, voltage 17.8 V, travel speed 100 cm per minute, frequency 5 Hz, duty cycle 50% and delta current 30 A. Moreover, from the measured current waveform shown in Fig. 4, the parameters including DP-frequency, DP-duty cycle and delta current were defined.

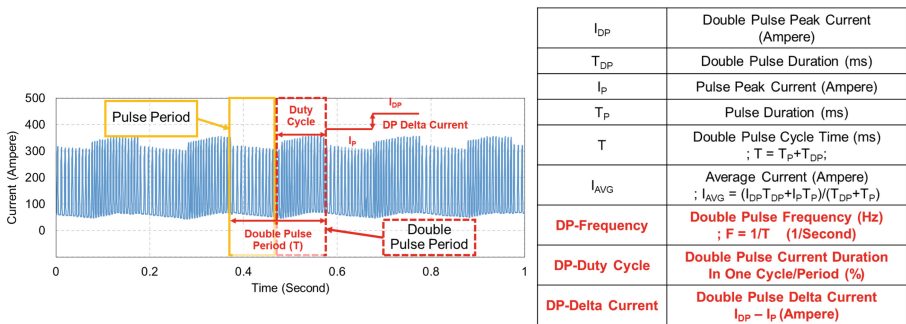


Fig. 4. Double pulse gas metal arc welding parameters

## 2.3 Experiment Parameters Study

In the experiment of the single-pass experiment, the effect of DP-GMAW variables consist of the current range 5 to 80 A, voltage 20 to 27 V, travel speed 20 to 160 cm per minute, frequency 0.5 to 10 Hz and duty cycle 30 to 70% and delta current 3 to 45 A. The Taguchi's method (Orthogonal Array Design) was chosen for the design of the experiment. Set of the first studied variables shown in Table 1.

In the multi-layer build-up experiment, the effect of DP-GMAW variables consist of 4 conditions of DP parameters with constant DP parameters consist of frequency 5 Hz, duty cycle 50%, delta current 30 A and layer height 1.5 mm. The set of the multi-layer studied parameters are shown in Table 2.

**Table 1.** Single-pass experiment parameters

Single-pass Study Parameters						
	Current Study	Voltage Study	Frequency Study	Duty Cycle Study	Delta Current Study	Travel Speed Study
Current (ampere)	120, 140, 160, 180, 200, 210	180	180	180	180	140
Voltage (volt)	25	15, 17, 19, 21, 23, 25, 27	21	21	21	19
Frequency (Hz)	5	5	1, 5, 10	5	5	5
Duty Cycle (%)	50	50	50	30, 50, 70	50	50
Current Intensity (%) or Cal. Delta Current (ampere)	14	14	14	14	3, 8, 14, 16, 32 or 4, 14, 23, 24, 45	14
Travel Speed (cm/min)	60	60	60	60	60	20, 60, 100, 140, 160
Fixed Welding Parameters						
CTWD (mm)	15					
Argon Shielding Gas Flow (LPM)	15					
Torch Angle (Degree)	90					

**Table 2.** Multi-layer experiment parameters

Multi-layer Study Parameters			
Condition 1		Condition 2	
Current (ampere)	120	Current (ampere)	120
Voltage (volt)	17.8	Voltage (volt)	17.8
Travel Speed (cm/min)	120	Travel Speed (cm/min)	100
Condition 3		Condition 4	
Current (ampere)	140	Current (ampere)	140
Voltage (volt)	18.6	Voltage (volt)	18.6
Travel Speed (cm/min)	100	Travel Speed (cm/min)	60
Welding Parameters			
Layer Height (mm)	1.5		
Frequency (Hz)	5		
Duty Cycle (%)	50		
Delta Current (ampere)	30		
Start CTWD (mm)	15		
Argon Shielding Gas Flow (LPM)	15		
Torch Angle (Degree)	90		

## 2.4 Build-Up Dimension

The dimension of the bead was used to represent the ability and effect of the process parameters. Figure 5 illustrates the measured dimension of the single-pass bead and multi-layer bead in the experiment. Moreover, bead width and height for multi-layer were measured in the minimum dimension defined as the effective dimension. In this study, the penetration depth was not measured due to the study focusing on bead effective formation and the penetration depth was not useful for AM process.

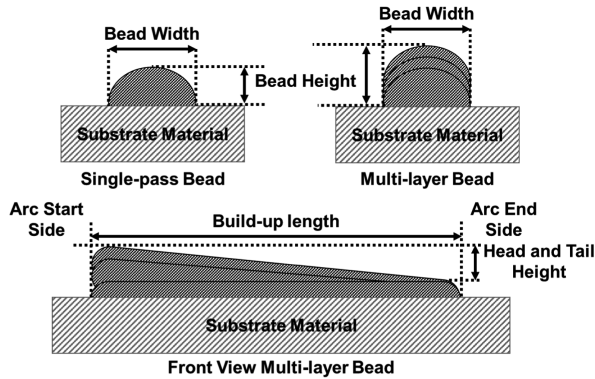


Fig. 5. Single-pass and multi-layer bead geometry

### 3 Experimented Results and Discussion

#### 3.1 Single-Pass

In discussing the effect of current on the experiment, the welding current was set in the range of 120–210 A, with other parameters kept constant as shown in Table 1. The spatter occurred at the weld toe when too low current and improper voltage were applied. The increment of welding current resulted in a welding width and height increment. Figure 6 showed the weld appearance on current change. When the current was set in range of 120–210 A, excellent bead formation could be obtained. If lower current was applied, the lack of fusion might occurred even the travel speed was at low or high value. Similarly, if higher current was applied, two types of uncontrollable bead might occurred: overflow bead (high current with low travel speed) and the humping bead (high current with high travel speed).

In discussing the effect of voltage on the experiment, the arc voltage was set in the range of 15–27 V, with other parameters fixed as shown in Table 1. If the voltage was set at a low 15 V, the weld edge resulted in unevenness. If the voltage was set in the range of 25–27 V, the spatter of the weld toe occurred. The increment of the arc voltage resulted in an increment on the bead width but the bead height was decreased. Figure 6 showed the resultant weld appearance when voltage changed.

In discussing the effect of travel speed on the experiment, the travel speed was set in the range of 20–160 cm per minute with other parameters fixed, as shown in Table 1. The welding speed at 20 cm per minute resulted in uneven welding bead overflow because of too slow welding speed. If the welding speed of more than 160 cm per minute, bead humping (non-uniform bead) occurred due to too fast speed. The travel speed increment resulted in the decrement of bead width and bead height. Figure 6 showed the weld appearance depending on the travel speed. The travel speed is one of the main factors for the process because the speed could control the heat to form a bead and control the productivity rate.

In discussing the effect of frequency from the experiment, the frequency was set in 1–10 Hz, with other parameters fixed, as shown in Table 1. The increment of frequency

resulted in an increment in the number of double pulses cycle in one second with a shorter duration. If the frequency was as low as 1 Hz, the wavy weld edge occurred due to long difference deposition between pulse and double pulse (interval). The increment of frequency does not significantly increase the bead width and bead height. Figure 7 showed the weld appearance depending on the frequency change. The penetration depth would not be affected significantly by increasing the frequency if the input heat was no changed.

In discussing the effect of the duty cycle from the experiment, the duty cycle was set in the range of 30–70% with other parameters fixed, as shown in Table 1. If the duty cycle was increased, the double pulse duration was also increased. The increment of the duty cycle would not affect the bead width and the bead height significantly. Figure 7 showed the weld appearance depending on the duty cycle change. The circle mark indicated the pore (diameters less than 1 mm) occurred on weld toe as a lack of fusion. The increment of duty cycle would affect the penetration depth.

In discussing the effect of delta current from the experiment, the value of the delta current was set in the range of 4–45 A with other parameters fixed, as shown in Table 1. Note that the study did not focus on high delta current because too high delta current caused the uniform weld bead. For increasing the delta current, the difference of current between the pulses current and the double pulse current increased. The low delta current 4 A resulted in exceeding the curved welding toe because of no enough heat for forming. Moreover, high delta currents could make the bead pattern look like fish scales. However, the increment of the delta current would not affect the bead width and bead heights. Figure 7 showed the weld appearance depending on the delta current change. The circle mark indicated the pore (diameters less than 1 mm) on weld toe as a lack of fusion. We concluded that if the delta current was increased, the penetration depth would be increased.

It is observed from the single-pass build-up experiment, the DP-GMAW parameters significantly affected on the weld bead dimension. The variables include welding current, arc voltage, and travel speed. Alternatively, the variables that does not affect the bead geometry significantly consist of the frequency, duty cycle, and delta current. Figure 8 presents an overall effect of DP-GMAW parameters on the bead dimension. Therefore, a mapping for setting parameters was created in the study. The process window was constructed further with current in the range of 60–210 A and travel speeds in the range of 20–180 cm per minute.

For arc voltage recommend adjusting from the welding machine to maintain the stability of the arc perform. The results from the experiment can create a process window for aluminum single-pass build-up as shown in Fig. 9. The plot is divided into four main areas including lack of fusion area, adequate area, humping bead area, and overflow bead area. For the multi-layer experiment, the parameters in the adequate area were chosen as: current in the range of 120 to 140 A with travel speed in the range of 60 to 120 cm per minute.



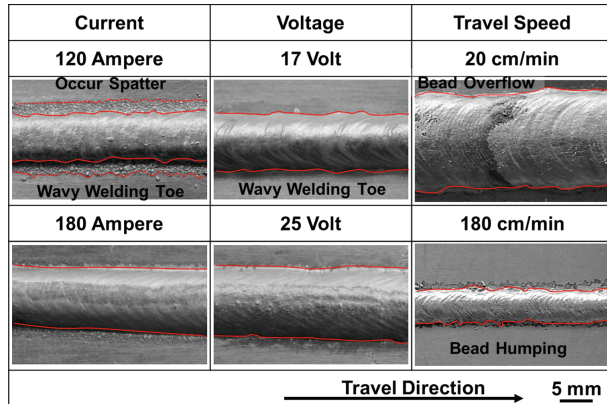


Fig. 6. Bead appearance on current, voltage, and travel speed change

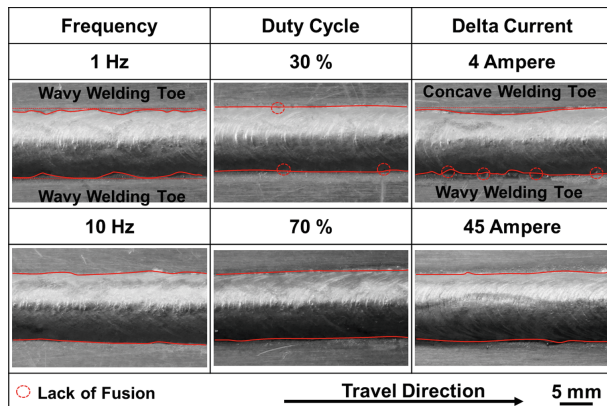


Fig. 7. Bead appearance on frequency, duty cycle, and delta current change

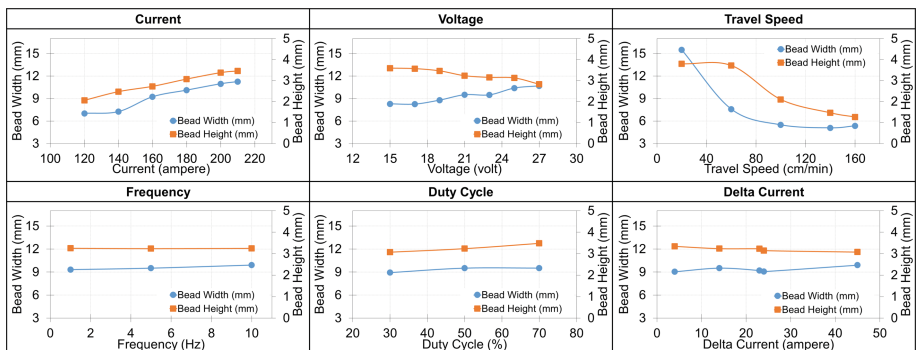
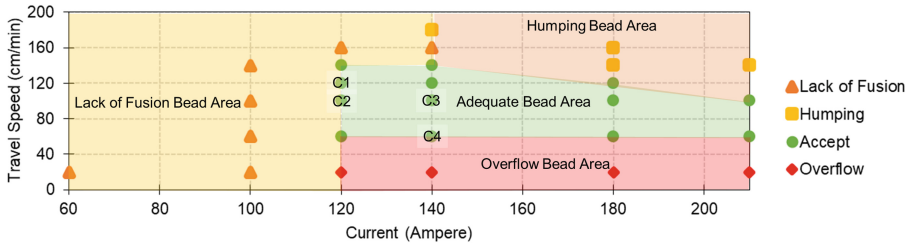


Fig. 8. Effect of DP-GMAW parameters on bead dimension



**Fig. 9.** DP-GMAW process parameters area for aluminum single-pass bead forming

### 3.2 Multi-layer Build-Up

The parameters condition consist of current at 140, 120 A and travel speed at 60, 100, 120 cm per minute with constant parameters as frequency 5 Hz, duty cycle 50%, the delta current of 140 A and layer height 1.5 mm. In the high heat condition 4 (0.2604 kJ/mm), the bead flow occurred and the laminate wall slope caused cumulative heat on the laminate appearance as shown in the bottom right side of Fig. 10. To avoid the bead flow, the heat could be reduced by increasing travel speed as condition 3 (0.1562 kJ/mm) or by decreasing current as condition 2 (0.1281 kJ/mm) or applying both conditions like condition 1 (0.1068 kJ/mm).

The effect of heat condition on laminate dimension are caused by the heat input. The increment of heat condition would decrease the effective laminate height. Besides, the height difference between the head and the tail have increased. The high heat condition had more cumulative temperature effect on the bead formation pattern or penetration change occurred laminate slope. The relation of heat condition and laminate dimension is represented in Fig. 11.

The recommendation for the layer height on laminate dimension should follow the laminate height properly. If the layer height was too low, the contact tip stuck occurred. If the layer height was too high, the lack of gas shielding might happen and cause the problem of bead oxidation and uncontrollable of bead formation.

In Fig. 11, the heat condition 1 (0.10 kJ/mm/layer) has the lowest difference height (2.22 mm) with highest effective height (7.63 mm) was determined in term of the adequate condition to build-up aluminum alloy. However, this study focused on the process performance. The study of metallurgy cross-section evaluation and mechanical properties testing will be discussed on another paper. Moreover, the proposed process shows the advantage by comparing the cold metal transfer (CMT) on a single bead dimension [7] under the average heat input between 0.180–0.306 kJ/mm, the DP had 18% larger dimension in bead width and 20% higher dimension in bead height.

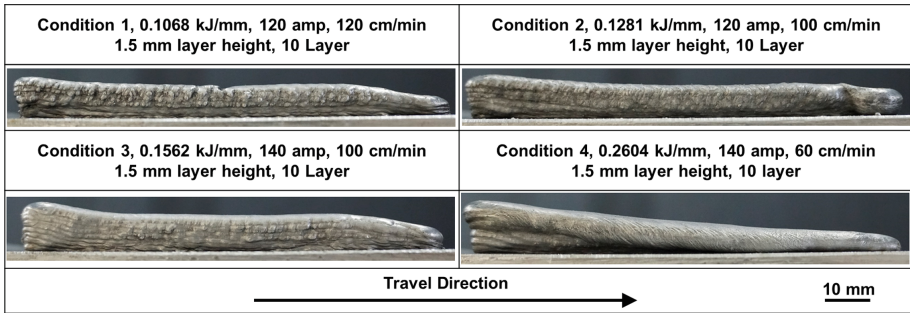


Fig. 10. Laminate wall appearance in each condition

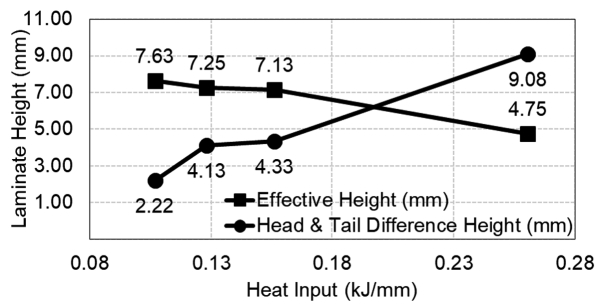


Fig. 11. Heat input condition effect on laminate head and tail difference height

## 4 Conclusion

The DP-GMAW parameters were investigated for the effect on build-up bead dimension for the single-pass build-up and the effect on multi-layer laminate dimension. It was concluded from the research that:

The main effect of process parameters on the bead dimension included current and travel speed. The main parameters should be adjusted in a range of 120–210 A and travel speed 60–140 cm per minute.

The double-pulse variables including frequency, duty cycle and delta current were not significant effects on bead dimension. However, the DP-variable should be adjusted on the adequate range to maintain the uniformly of bead dimension and appearance. The recommend range for frequency is 5–10 Hz, for duty cycle is 30–70%, and for delta current is 15–40 A.

The increment of heat condition resulted in the decrement of laminate height. The heat condition was the main effect on a laminate slope. To reduce the laminate slope, the lowest heat condition should be used for build-up. The adequate process condition determined in the study including the parameters: 120 A of current, voltage 17.8 V, travel speed 120 cm per minute, frequency at 5 Hz, duty cycle 50%, delta current 30 A and layer height 1.5 mm. Figure 12 is a resultant workpiece with uniform dimension which was built-up using the adequate process condition.

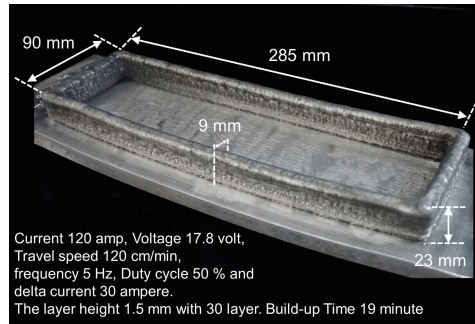


**Fig. 12.** Workpiece by the suitable DP-GMAW parameters

## References

1. Ding, D., Pan, Z., Cuiuri, D., Li, H.: Wire-feed additive manufacturing of metal components: technologies, developments and future interests. *Int. J. Adv. Manuf. Technol.* **81**(1–4), 465–481 (2015)
2. Xiong, J., Zhang, G., Zhang, W.: Forming appearance analysis in multi-layer single-pass GMAW-based additive manufacturing. *Int. J. Adv. Manuf. Technol.* **80**(9–12), 1767–1776 (2015)
3. Ding, D., Pan, Z., Cuiuri, D., Li, H.: A multi-bead overlapping model for robotic wire and arc additive manufacturing (WAAM). *Robot. Comput. Integr. Manuf.* **1**(31), 101–110 (2015)
4. Ding, D., Pan, Z., Cuiuri, D., Li, H., van Duin, S., Larkin, N.: Bead modelling and implementation of adaptive MAT path in wire and arc additive manufacturing. *Robot. Comput. Integr. Manuf.* **1**(39), 32–42 (2016)
5. Li, Y., Sun, Y., Han, Q., Zhang, G., Horvath, I.: Enhanced beads overlapping model for wire and arc additive manufacturing of multi-layer multi-bead metallic parts. *J. Mater. Process. Technol.* **1**(252), 838–848 (2018)
6. Ding, D., Shen, C., Pan, Z., Cuiuri, D., Li, H., Larkin, N., van Duin, S.: Towards an automated robotic arc-welding-based additive manufacturing system from CAD to finished part. *Comput. Aided Des.* **1**(73), 66–75 (2016)
7. Wagiman, A., Wahab, B., Saidin, M., Mohid, Z., Mamat, A.: Effect of GMAW-CMT heat input on weld bead profile geometry for freeform fabrication of aluminium parts. In: *Applied Mechanics and Materials*, vol. 465, pp. 1370–1374. Trans Tech Publications (2014)



# Development of a Close-Fitting Assistive Suit with Adjustable Structure for Arm and Back as Needed - e.z.UP<sup>®</sup>

Yun-Ting Liao<sup>1(✉)</sup>, Toshifumi Ishioka<sup>2</sup>, Kazuko Mishima<sup>2</sup>,  
Chiaki Kanda<sup>2</sup>, Kenji Kodama<sup>2</sup>, and Eiichiro Tanaka<sup>3</sup>

<sup>1</sup> Graduate School of Information, Production and Systems,  
Waseda University, Fukuoka 808-0135, Japan  
jesse80213@fuji.waseda.jp

<sup>2</sup> Asahicho Corporation, Hiroshima 726-0004, Japan

<sup>3</sup> Faculty of Science and Engineering, Waseda University,  
Fukuoka 808-0135, Japan

**Abstract.** The muscle injuries of manual handling workers, caused by the repeated motion and heavy load in the daily tasks, strongly influence their quality of life. To prevent muscle injuries in many occupations, a close-fitting assistive suit weighing 0.75 [kg] with the passive actuation mechanism and adjustable structures is proposed to assist not only the back muscle but the arm muscle of manual handling workers according to the user intention. An experiment with electromyography for measuring the muscle activities is conducted with six subjects to practically confirm the effectiveness of the suit. The experimental results revealed and proved that the proposed suit can successfully and appropriately assist not only the arm but also the back muscle with a lifting-up motion, simultaneously.

**Keywords:** Close-fitting assistive suit · Passive actuation mechanism · Electromyography · Arm assistance · Back assistance

## 1 Introduction

Muscle injuries, especially lower back pain (LBP), often troubled manual handling workers in many occupations, such as manufacturing, construction, and nursing care. Regarding the employees, LBP can influence their quality of life [1]. In contrast, employers can face an increase of financial loss indirectly due to the lost productivities of employees who suffer from LBP [2]. It can be prevented by training, practicing and the proper motions/postures.

Due to the merits of lightweight and compact in size, the assistive suits with the passive actuation mechanism was proposed to assist the user with the elastic component. Imamura et al. [3] proposed a passive power assist supporter, called “Smart Suit Lite,” which focused on low back assistance and torso stability. Most of the devices/suits focused on the assistance of low back muscle. In fact, the localized muscle can influence other muscle groups when localized muscle fatigue. Chen [4] revealed that an indirect effect of low LBP occurs when the worker’s arm muscle

experiences localized fatigue. Hence, this research focuses on the development of an assistive suit to assist not only the back but the arm muscles.

Within these contexts, in our previous research [5], we proposed a concept and prototype of an assistive suit consisting of rubber and nylon belts to assist user's arm and back muscles. The feasibility was verified by the interview in the university hospital and electromyography measurement with eight muscle groups. However, the unconcealable belt structure may cause the hazard in daily tasks. To overcome this difficulty, we proposed a worker-wear assistance suit with the adjustable elastic structure with concealable belt structure to mainly support the user's localized arm muscle [6]. During the development period, the design principles are given: (1) the adjustable structure can not only overcome the individual difference of the user, but the adjustment of assistive level for different load weight in daily task; (2) the concealable belt structure can prevent the hazards and dangers in the daily tasks; (3) according to prevention of localized muscle fatigue [4], the back and arm muscles should be considered to be assisted.

## 2 Close-Fitting Assistive Suit

This study proposed a close-fitting assistive suit. The concealable structure is considered to prevent the hazard in daily tasks (e.g., the unconcealable structure may catch the item on hand or external equipment and items). In addition to the concealable belt structure, the close-fitting design can also prevent the hazard comparing with a loose-fitting design. The adjustable structure is considered to overcome different body dimensions of individual users and different working conditions (e.g., the load weight and the motions). The users can wear their clothes outside of the suit, and the structure can be hidden under the personal clothes/wears. Furthermore, the suit has approximately 0.75 [kg] of the total weight. Compared with averaged Japanese body weight, 57.2 [kg] [7], the suit accounted for only 1.3% of the averaged weight. It can avoid the additional burden while wearing. According to the user's intention and practical motions, the belt layout is designed and proposed as described in the following subchapter. The proposed suit mainly consists of two parts, arm and lower-limb assistance and the back-assist parts, as shown in Fig. 1(a).

### 2.1 Arm and Lower Limb Assistance

The concept of belt layout for arm and lower limb assistance is illustrated in Fig. 1(b). By connecting the belt from the arm to back of the knee, the arm assistive belt can be pulled and extended while bending the knee and leaning trunk motions. It means that the layout is designed based on the user's motion, and automatically assists the user's arm muscle while he/she intends to lifting/lowing the target load. The arm assistance belt, called Belt 1, connects with three elastic components, two rubber belts and a deformable fabric called quadrilateral structure, as shown in Fig. 2(a). According to the user's motion, the assistive force can be generated while squatting down without utilizing the other muscle group (e.g. triceps brachii muscle) to extend the rubber belts. The proposed belt layout can be extended by the user's weight, instead of using

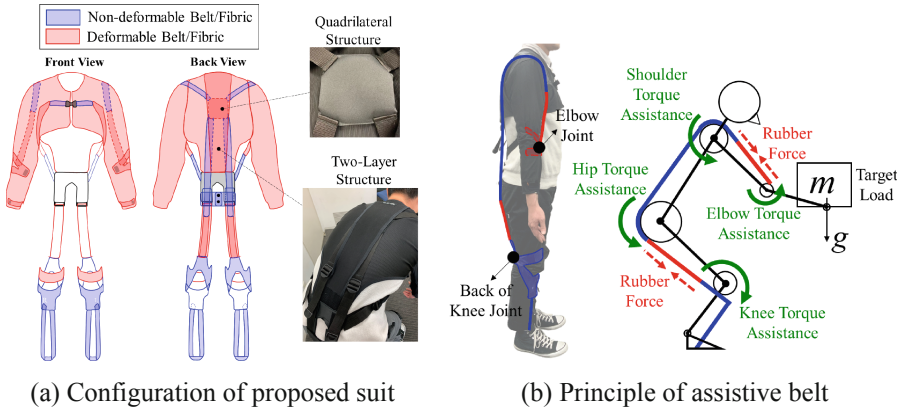


**Fig. 1.** Concept of the proposed suit-e.z.UP<sup>®</sup>

additional muscle. Therefore, assistance can be adequately provided as needed. According to the woven pattern of quadrilateral structure, its shape cannot be deformed along the horizontal and vertical direction. While the user turns his/her torso and twists his/her waist to pick up the target on the side of the user, the belt elongations of right and left arms are different. For instance, turning torso rightward, Belt 1 on the right arm is elongated. Meanwhile, the left-hand Belt 1 is diminished. Thanks to the proposed quadrilateral structure, the structure can deform along the diagonal direction to compensate Belt 1 on the left hand. It implies that the structure can automatically compensate for the shortened belt and keep the assistive force. It can prevent and compensate the arm assistance belt loosening when the user twisting their waist and upper trunk.

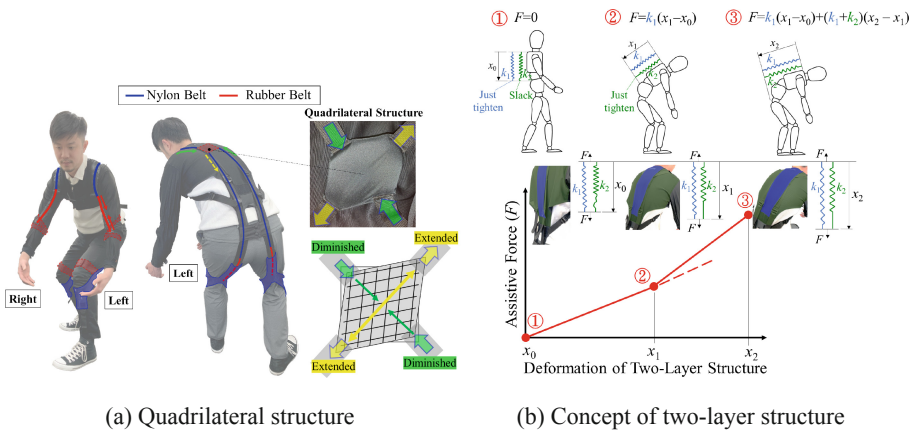


**Fig. 2.** Configuration of assistive belt/fabric



## 2.2 Back Assistance

The load on the back and the skin deformation can be increased while the torso bends forward, simultaneously. Hence, an elastic structure with the changeable spring coefficient should be considered. In our previous study [5], a concept of the rubber belt with the changeable spring coefficient was proposed. Thereafter, this study designs and proposes a stiffness changeable structure, called the two-layer structure, as shown in Fig. 2(b). The structure provides lighter assistance when the user stands straight, which only the outer layer ( $k_1$ ) is deformed, and the inner layer ( $k_2$ ) is slack. When the user tends to bend or leaning forward and lift the load, the inner layer is further extended along the back curve. On the other hand, the two-layer structure can gradually and automatically increase the assistive force as needed according to the user's motion.

## 3 Simulation Evaluation

To evaluate the feasibility of the elastic structure layout of the suit, a human model is primarily defined based on the averaged body dimensions of Japanese young and healthy adults and elderlies [7], as shown in Fig. 3. It can be utilized to mimic the practical user wearing the suit. The averaged lengths of the shank ( $l_1$ ), thigh ( $l_2$ ), trunk ( $l_3$ ), upper arm ( $l_4$ ) and forearm ( $l_5$ ) are 0.3687 [m], 0.3968 [m], 0.5215 [m], 0.2986 [m] and 0.2373 [m], respectively. The average weight in the human model ( $m$ ) is 57.2 [kg]. We assumed each joint has its corresponding radius referring to the averaged body dimension [7]. The radii of the knee ( $r_k$ ), hip ( $r_h$ ), shoulder ( $r_s$ ) and elbow ( $r_e$ ) joints are 0.0576 [m], 0.1047 [m], 0.0766 [m] and 0.0459 [m], respectively. The corresponding positions of the center of gravity (COG) of each limb are defined according to de Leva's technical note [8]. The locations of each limb COG are defined in Fig. 3,  $l_{1g}$ ,  $l_{2g}$ ,  $l_{3g}$ ,  $l_{4g}$  and  $l_{5g}$ , are  $0.5541 \cdot l_1$ ,  $0.5905 \cdot l_2$ ,  $0.5514 \cdot l_3$ ,  $0.5772 \cdot l_4$  and  $0.4574 \cdot l_5$ , respectively. Based on the investigation of Drill et al. [9], the mass of each limb,  $m_1$ ,  $m_2$ ,  $m_3$ ,  $m_4$ , and  $m_5$ , are  $0.0878 \cdot m$ ,  $0.2236 \cdot m$ ,  $0.5342 \cdot m$ ,  $0.0648 \cdot m$  and  $0.0362 \cdot m$ , respectively.

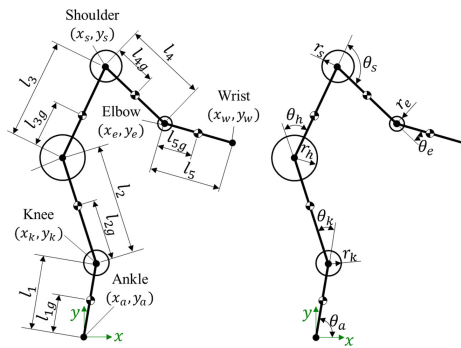
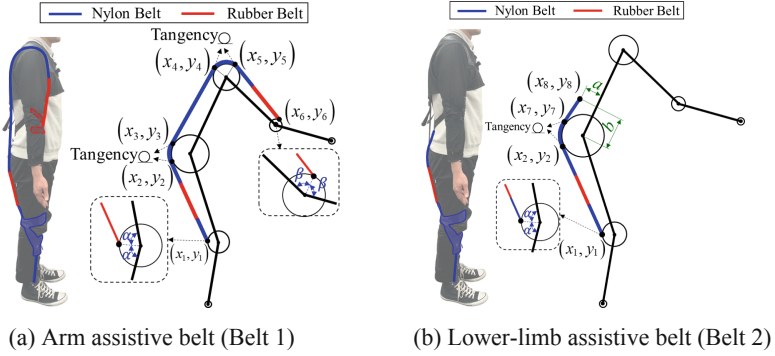


Fig. 3. Definitions of a human body model





**Fig. 4.** Boundary conditions of arm assistive belt in suit-user model

To define the posture and motion of the human model, the ankle joint  $(x_a, y_a)$  is defined as the original point (0,0) in the coordination system; the position of knee joint  $(x_k, y_k)$ , hip joint  $(x_h, y_h)$ , shoulder joint  $(x_s, y_s)$  and elbow joint  $(x_e, y_e)$  in the sagittal plane are presented as a vector  $\{\mathbf{x}_{human} \ \mathbf{y}_{human}\} \in \mathbb{R}^{10}$  and calculated by following equation:

$$\begin{Bmatrix} \mathbf{x}_{human} \\ \mathbf{y}_{human} \end{Bmatrix} = \begin{bmatrix} C_1 \\ S_1 \end{bmatrix} \{l_1 \ l_2 \ l_3 \ l_4 \ l_5\}^T \quad (1)$$

where  $C_1 \in \mathbb{R}^{5 \times 5}$  and  $S_1 \in \mathbb{R}^{5 \times 5}$  are the lower triangular matrices consisting of cosine and sine included each joint angle ( $\theta_a, \theta_k, \theta_h, \theta_s$  and  $\theta_e$ ), respectively.  $\{l_1 \ l_2 \ l_3 \ l_4 \ l_5\}^T \in \mathbb{R}^5$  is the length vector related to each limb length of the model. Based on the contact points of the suit and the user, the boundary conditions are defined, as shown in Fig. 4. The corresponding coordination of the contact points is presented as a vector  $\{x_1 \ x_2 \ x_3 \ x_4 \ x_5 \ x_6 \ x_7 \ x_8 \ y_1 \ y_2 \ y_3 \ y_4 \ y_5 \ y_6 \ y_7 \ y_8\}^T \in \mathbb{R}^{16}$ , which can be written as  $\{\mathbf{x}_{belt} \ \mathbf{y}_{belt}\}^T \in \mathbb{R}^{16}$  and calculated as follows:

$$\begin{Bmatrix} \mathbf{x}_{belt} \\ \mathbf{y}_{belt} \end{Bmatrix} = \begin{bmatrix} B & 0 \\ 0 & B \end{bmatrix} \begin{Bmatrix} \mathbf{x}_{human} \\ \mathbf{y}_{human} \end{Bmatrix} + \begin{bmatrix} C_2 \\ S_2 \end{bmatrix} \{r_k \ r_h \ r_s \ r_e \ l_c\}^T \quad (2)$$

where  $B \in \mathbb{R}^{8 \times 5}$  is a logical matrix consisting 0 and 1,  $C_2$  and  $S_2$  are triangular matrices consisting of cosine and sine with each joint angle ( $\theta_a, \theta_k, \theta_h, \theta_s$ , and  $\theta_e$ ), respectively.  $l_c$  can be written as  $l_c = (a^2 + b^2)^{0.5}$ .  $a$  and  $b$  are the torso thickness and the distance from the hip joint to the navel. To obtain the belts' length variation, a motion with the angle variations of each joint was recorded with a practical lifting motion. By substituting the variation of the angles of each joint into Eqs. (1) and (2), the deformations of the Belt 1 and Belt 2 shown in Fig. 5(a) and (b), respectively, show the maximum elongation appearing at the begin of Phase 1. In fact, the begin of a lifting task requires greater power to generate momentum, which may cause a greater muscle output force. In other words, the proposed suit can adequately satisfy the requirement at the begin of a lifting task according to the user's motion.

## 4 Experimental Evaluation

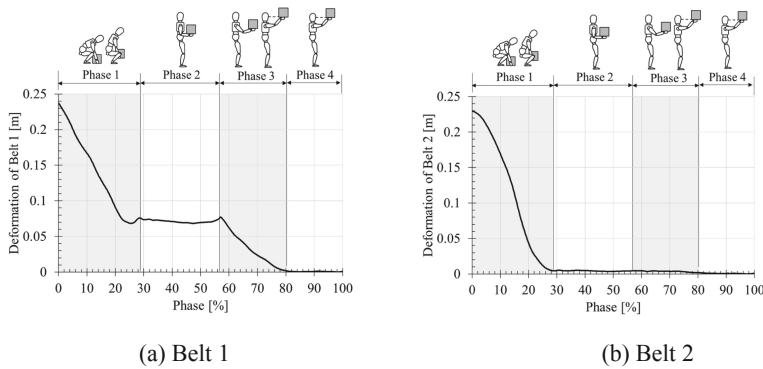


**Fig. 5.** Deformation of the assistive belts

An experiment is conducted with four young subjects (age: 23 to 25 years, mass:  $71.1 \pm 4.5$  [kg], height:  $1.774 \pm 0.079$  [m]) and two middle-aged subjects (age: 55 and 58 years, mass:  $72.5 \pm 3.5$  [kg], height:  $1.735 \pm 2.121$  [m]). None of them had any significant history of low back pain or present illness. All subjects consented for participation in the study. The experimental protocol with a similar motion in the simulation part is shown in Fig. 6(a). The period of each phase was defined as 5 [s]. The weight of the load for this experiment is 10 [kg]. Each subject is asked to perform the same motion three times. The rest time between each set of experiment is 10 min.

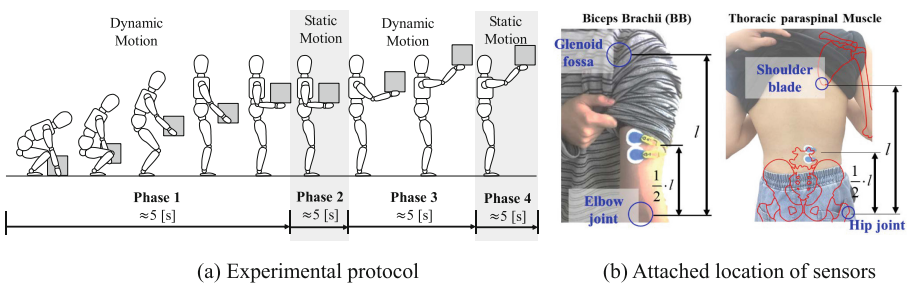


**Fig. 6.** Experimental conditions

To evaluate the effectiveness of the two-layer structure, the activity of the back muscle must be a part of the measurement. Thoracic paraspinal muscle (PM) is decided to be measured, which relates to the motion of the back stretching. According to the simulation results, the elbow joint has an obvious improvement. Therefore, the Biceps Brachii (BB) muscle is considered as a measured muscle group, which relates to the

motion of elbow flexion. Additionally, in our previous study [5], we measured eight muscle groups. In the previous results, the BB and PM muscles showed obvious improvement. Therefore, BB and PM muscles are decided to verify the usability of the proposed suit. The electromyography (EMG) sensors are respectively attached to BB and PM muscles. The attached locations of EMG sensors are unified as illustrated in Fig. 6(b).

The maximum voluntary contraction (MVC) of each muscle group is measured in advance to define the maximum muscle activities of BB and PM muscles of each subject and further compare the measurement results of each subject. To eliminate the individual difference, MVC is divided by integrated electromyography (iEMG) as described in the following equation:

$$\%MVC = iEMG/MVC \quad (3)$$

The effectiveness while using and without using the proposed suit is evaluated and calculated by the p-value of t-test analysis with the follows conditions: (1) one-tailed, which can demonstrate a “significant better” result; and (2) the “paired data,” because the subject numbers are the same while wearing and without wearing the suit. To judge the improvement of muscle activities with and without wearing those suits, the p-value lessening than 0.05 is used. The decreasing ratio ( $\eta$ ) was calculated to compare the efficiency by the following equation:

$$\eta = \frac{(\%MVC_{without} - \%MVC_{with})}{\%MVC_{without}} \times 100\% \quad (4)$$

where  $\%MVC_{without}$  and  $\%MVC_{with}$  represent the  $\%MVC$  values with and without wearing the suit, respectively.

The results of BB and PM muscle of the subjects with and without wearing the proposed suit are shown in Fig. 7. Comparing the dynamic motions (Phases 1 and 3) and static motion (Phases 2 and 4), the dynamic motions have higher muscle activities. It means that the dynamic motions may easily cause muscle injury of both BB and PM muscles at the same time. According to the results of BB muscle shown in Fig. 7(a), we can confirm the effectiveness of the proposed suit with above 38% of the improved ratio. According to the simulation result of Belt 1, the maximum assistive force can appear in Phase 1 due to the maximum deformation of the belts. However, the experimental results of BB muscle show the maximum improvement in Phase 3. It may be caused by the friction of belts and fabrics. In the results of PM muscle (Fig. 7(b)), the muscle activities can be successfully decreased above 30% in each phase. Through the experimental results, the effectiveness of the two-layer structure can be confirmed. It proves that the proposed two-layer structure can gradually and adequately generate the assistive force based on the user's motion. According to the influence of the localized arm muscle fatigue [2], the proposed suit may prevent localized muscle fatigue, and further prevent the lower back injuries.

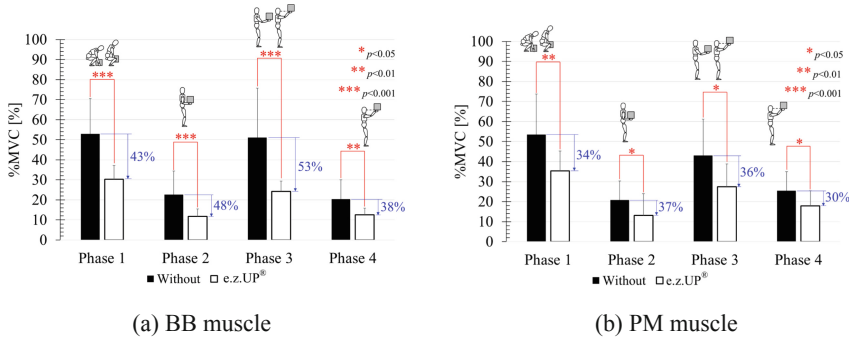


**Fig. 7.** Experimental Results

## 5 Conclusions

A close-fitting assistance suit with the adjustable structure is proposed in this study for the muscle assistance of manual handling workers in their daily tasks, especially for the arm and back assistance. This suit is mainly composed with elastic component (rubber belts and deformable fabrics) and non-deformable component (nylon belts and non-deformation fabrics). To verify the belt layout of the proposed suit, the simulation is primarily conducted based on the averaged human body model to observe the belts' deformation with a lifting motion while wearing the suit. The simulation results proved that the proposed suit can successfully and adequately assist the user without additional burden. To practically confirm the feasibility of the suit, an experiment is conducted with seven subjects (four young and two middle-aged subjects). The results prove that the proposed suit can successfully decrease the back muscle activities above 30% at least. Especially, the arm muscle can successfully assist the user around 46% decreasing on average.

## References

1. Suka, M., Yoshida, M.: Lower back pain deprives the Japanese adult population of their quality of life: a questionnaire survey at five healthcare facilities in Japan. *Environ. Health Prev. Med.* **13**(2), 109–115 (2008)
2. Montgomery, W., Sato, M., Nagasaka, Y., Vietri, J.: The economic and humanistic costs of chronic lower back pain in Japan. *ClinicoEcon. Outcomes Res.* **9**, 361–371 (2017)
3. Iamura, Y., Ayusawa, K., Yoshida, E.: Evaluation framework for passive assistive device based on humanoid experiments. *Int. J. Hum. Robot.* **15**(3), 176026-1–1750026-25 (2018)
4. Chen, Y.-L.: Changes in lifting dynamics after localized arm fatigue. *Int. J. Ind. Ergon.* **25**, 611–619 (2000)
5. Tanaka, E., Muramatsu, K., Watanuki, K., Saegusa, S., Iwasaki, Y., Yuge, L.: Development of a rubber belt suit for lift-up motion to assist both upper limb and back and evaluation of muscle activity. *J. Jpn. Soc. Des. Eng.* **52**(6), 405–418 (2017). (in Japanese)

6. Liao, Y.-T., Kodama, K., Ishioka, T., Lee, H.-H., Tanaka, E.: Development and evaluation of a worker-wear assistance suit with the adjustable and concealable elastic structure for the manual handling workers. In: Conf. Rec. 2018 IEEE/ASME International Conference on Advanced Intelligent Mechatronics (AIM), Auckland, New Zealand
7. Kouchi, Y., Yokoyama, K., Yamashita, J., Yokoi, T., Ogi, H., Yoshioka, M., Atsumi, H., Hotta, A.: Human body dimensions data for ergonomic design. Report of National Institute of Bioscience and Human-Technology, vol. 2, no. 1, pp. 119, 123, 126 (1996). ISSN 0919-5351
8. de Leva, P.: Adjustment to Zatsiorsky-Seluyanov's segment inertia parameters. *J. Biomech.* **29**(9), 1223–1230 (1996)
9. Drillis, R., Contini, R., Bluestein, M.: Body segment parameter: a survey of measurement techniques. *Artif. Limbs* **8**(1), 44–66 (1964)



# An Experimental Characterization of the BIT Astronaut Robot

Zheng Tao<sup>1</sup>, Ceccarelli Marco<sup>1,2(✉)</sup>, Li Hui<sup>1</sup>, and Mo Yang<sup>1</sup>

<sup>1</sup> Key Laboratory of Biomimetic Robots and Systems,  
Beijing Advanced Innovation Center for Intelligent Robots and Systems,  
Beijing Institute of Technology, Beijing 100081, China  
18634409496@163.com, moyang602@163.com,  
marco.ceccarelli@uniroma2.it, lihui2011@bit.edu.cn

<sup>2</sup> Lab Robot Mechatronics, University of Rome Tor Vergata, Rome, Italy

**Abstract.** In this paper a prototype of BIT (Beijing Institute of Technology) astronaut robot with three leg-arm limbs is presented with performance characteristics from a demo test. An experimental demo for basic operation modes is presented simulating the BIT astronaut robot moving outside an orbital station with a lab testbed set up for experimental activity of robot characterization. Results of the demo tests are used to characterize the feasibility of the robot design and its operation also with experiences at ground gravity.

**Keywords:** Space robotics · Astronaut robots · Design ·  
Experimental robotics · Performance analysis

## 1 Introduction

The space station is the carrier of human development and utilization of space resources. The use of space stations to complete the full development and utilization of space resources plays a vital role in the advancement of science and technology, (Ceccarelli 2012). Astronauts are in great danger every time they leave the cabin to complete the mission. Therefore, the safety of astronauts can be guaranteed by replacing the astronauts with robots to complete high-risk missions (King 2001).

The Canadian II Arm is a large space manipulator that can capture large mass objects and assists astronauts to get out of the capsule (Sallaberger 1998). But it is awkward and cannot replace the astronauts to complete missions outside the space capsule. The dual-arm robot Robonaut was developed by NASA to replace the astronauts to complete part of missions, which reduces the frequency of the astronauts out of the space capsule, (Bluthmann et al. 2003). However, in a microgravity environment, it is difficult for the Robonaut to complete the task, and the astronauts are needed to work together with Robonaut to complete tasks. The Canadian II Arm and Robonaut are designed with complex structures that can be complicate to be repaired once a fault occurs. Other interesting astronaut robots are the European ESA EuroBot and German Justin with similar problems although with improved characteristics as the above reported astronaut robot examples.

In this paper the BIT three-limb astronaut robot is presented by an experimental characterization of a prototype a demo test of basic operation modes in the lab ground gravity environment.

## 2 The BIT Astronaut Robot

The BIT astronaut design is shown in Fig. 1 with its peculiar structure with three limbs of equal design and a central body housing any other equipment, as reported in (Ceccarelli et al. 2012). Figure 1(a) gives the design features as focused on the limb design with a 2-d.o.f. shoulder, elbow, wrist, and an end-effector with claw that can work either as a leg in locomotion operations or as an arm in manipulation tasks. Figure 1(b) shows a lab prototype at BAICIRS (Beijing Advanced Innovation Center for Intelligent Robots and Systems) in BIT for testing in a testbed frame reproducing the outside environment of an orbital station with handles that are used also by astronauts for moving on its surface. The prototype has been built bulky also because of the testing in the lab at ground gravity ( $g = 9.8 \text{ m/s}^2$ ) for investigations on its feasibility and performance evaluation.

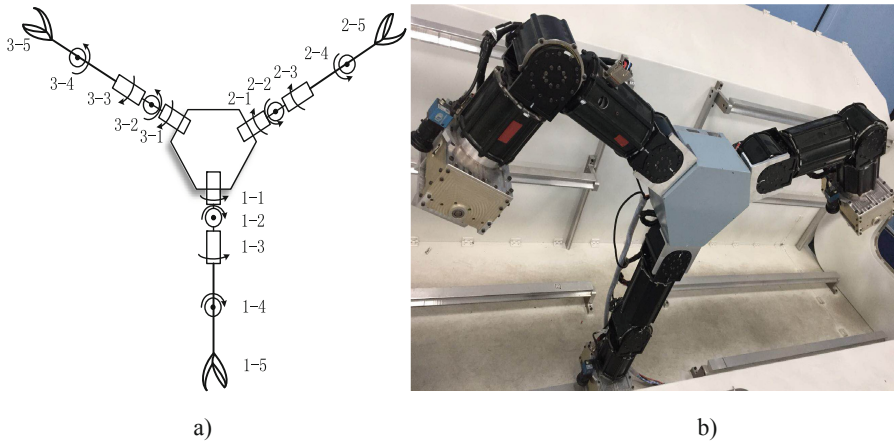


**Fig. 1.** The BIT astronaut robot: (a) a CAD design; (b) the built prototype

The three-limb robot structure is characterized by the fact that the limbs can be used indifferently thanks to their common design, that is inspired by the chameleon anatomy and operation, as reported in (Ceccarelli et al. 2012). In locomotion operations the three-limb robot can move using two different modes, namely walking with legs or revolving using the three limbs. In locomotion task the end-effector will act as a foot once it has grasped the handle with respect which the motion is planned to. In walking mode two limbs are operated as legs with a human-like movement leaving the third limb available for manipulation tasks, carrying load, and/or balancing purposes. In the revolving mode the three limbs are used as fixed legs around which the whole robot structure rotates in advancing by articulating the legs.

The central body is designed with a shape and size both to housing equipment for control units and sensors and to be the frame for the limbs around which they can be housed in home configuration.

The three-limb BIT astronaut robot is conceived with its peculiar design to perform locomotion and manipulation tasks outside a space orbital station for maintenance and repair works of the structures and functions for the efficiency of the orbital station with a multi-task ability.

The operation of the BIT astronaut robot is controlled by adjusting the angular displacement of the joints with a PID control law in a closed-loop design. A DC motor and an angular displacement sensor are installed at each joint of a robot limb. The PID controlled motion is activated by PWM signals that are generated by hardware controller unit using angular displacement measures by sensors as feedback signals.

### 3 An Experimental Characterization with a Demo Test

An experimental characterization has been experienced in a lab environment that has been designed with a structure replicating partially the areas of an orbital station within which the BIT astronaut robot will operate.

Figure 2 shows this lab lay out with orbital station structure with typical armrest as handles for EVA (Extra Vehicular Actions) astronaut tasks, the prototype of the BIT astronaut robot, and computer facilities for testing.

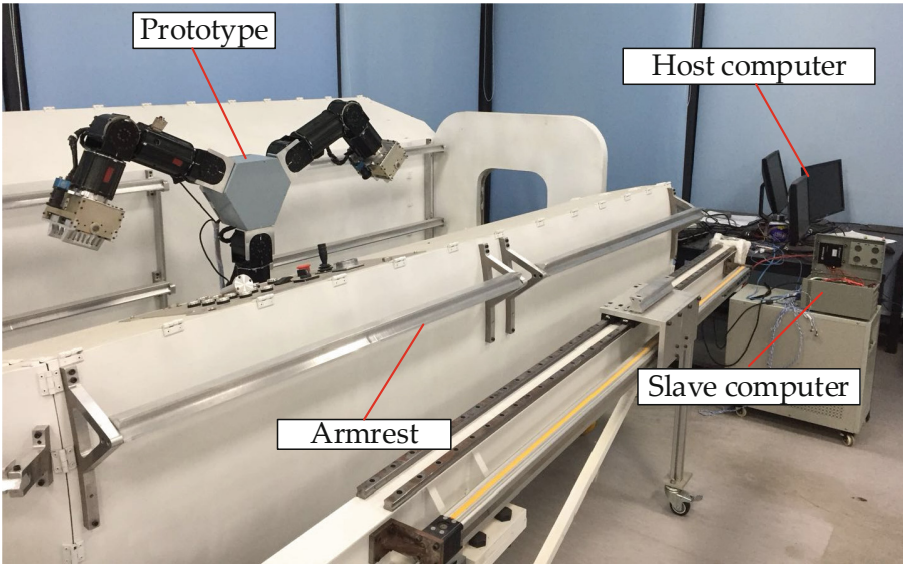


**Fig. 2.** Lab layout for testing with BIT astronaut robot in Fig. 1



A demo test has been designed for basic operation motion within the structure of the orbital station in BAICIRS lab in BIT with ground gravity with the aim to show the practical feasibility of the BIT astronaut robot and its typical motion performance.

The demo test is shown in the snapshot in Fig. 3 as referring to a walking mode operation as in (Ceccarelli et al. 2015) in Figs. 3(a) to (c) for changing handle towards a stationary positioning, and to a revolving motion as in (Ceccarelli et al. 2015) in Figs. 3 (d) to (f) for translating along a handle. In both motion tests at least one limb is free from the motion operation and available for manipulation tasks or other task, like for example a visual inspection using a video camera on the end-effort that is moved pointed properly by suitable arm motion. The demo motion is performed as assisted by the video cameras on each end-effector of the limbs either by pre-programmed path planning or by user tele-operation with the characteristics of low-speed operation that is typical of outdoor space movements and is required by low-energy consumption.

## 4 Test Results

The demo test has been monitored by tracking the motion in terms of joint angle displacements and energy consumption in terms of actuator currents, as measures that are acquired on-line also for motion control purposes.

Examples of those acquisitions and monitored data are reported in Figs. 4 and 5 as referring to the three limbs acting as leg-arms during the demo test portion with revolving mode operation in Figs. 3(d) to (f). In particular, arm 1 is fixed grasping the handle while the other two arms move with the second one approaching the handle yet.

In Fig. 4 the angular displacements of the joints are reported as acquired by the encoders on the actuated joints and in Fig. 5 the actuator currents are displayed as collected from the feeding circuits.

In Fig. 4(a) it is to note that only the first joint of the shoulder is active as contributing to the revolving motion by rotating the central body with a quasi-constant speed with an initial acceleration and a final deceleration. Correspondingly, in Fig. 5(a) the current of the first actuator is measured with variation in the accelerated and decelerated phases and then with a current level maintaining the posture with braking. In the same time the other joints do not move but the corresponding actuators may need torque to maintain the arm configuration, as shown by the acquired actuator currents in the joint plots in Fig. 5(a).

In the arm 2 that moves in the air as mainly for balance purposes, the active joints are the shoulder and elbow ones with a smooth motion that is characterized by variations of about 60 deg and 90 deg, respectively, while the other joints do not move significantly. Correspondingly, in Fig. 5(b) significant changes in actuator current levels are detected for those moving joints, while in the other joints the actuator currents are used to provide the proper torques for the static configuration also with brake activations.

In the arm 3 that moves toward the handle, the active joints are the shoulder, elbow, and wrist with a smooth motion yet that is characterized by displacements of about 100 deg, 40 deg, and 180 deg, respectively. Correspondingly, in Fig. 5(c) the actuator

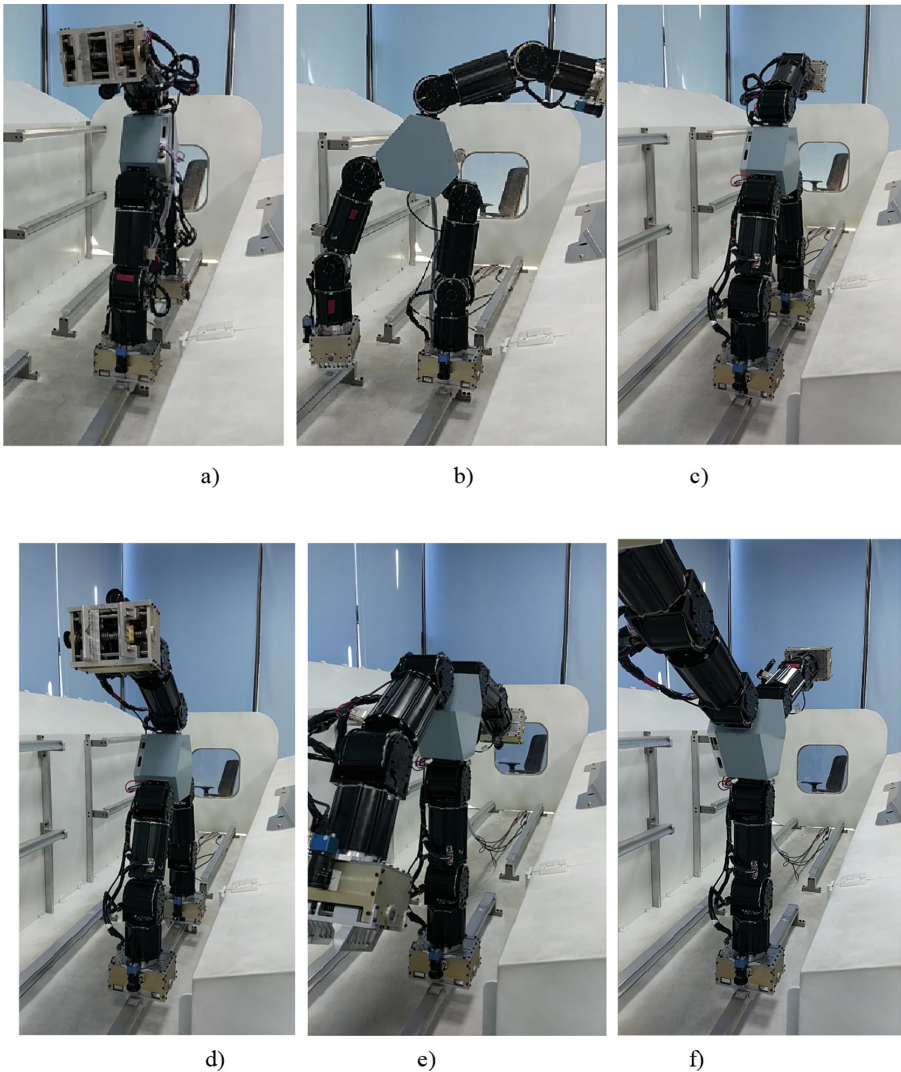


**Fig. 3.** A snapshot of a demo test with BIT astronaut robot, Fig. 2

currents are shown with significant values and variations, although also the other joints experienced the need of currents to ensure torque or braking activation.

Referring to the plots in Fig. 5, it is to note that most of the measured currents are below 1 A, whereas a maximum of about 3 A is experience only for the shoulder joint of arm 3.

The demo results, whose examples are reported in Figs. 4 and 5, show that the prototype of BIT three-limb astronaut robot moves successfully in operating its characteristic locomotion modes for walking and revolving, even with bulky design that has been developed for testing at ground gravity.

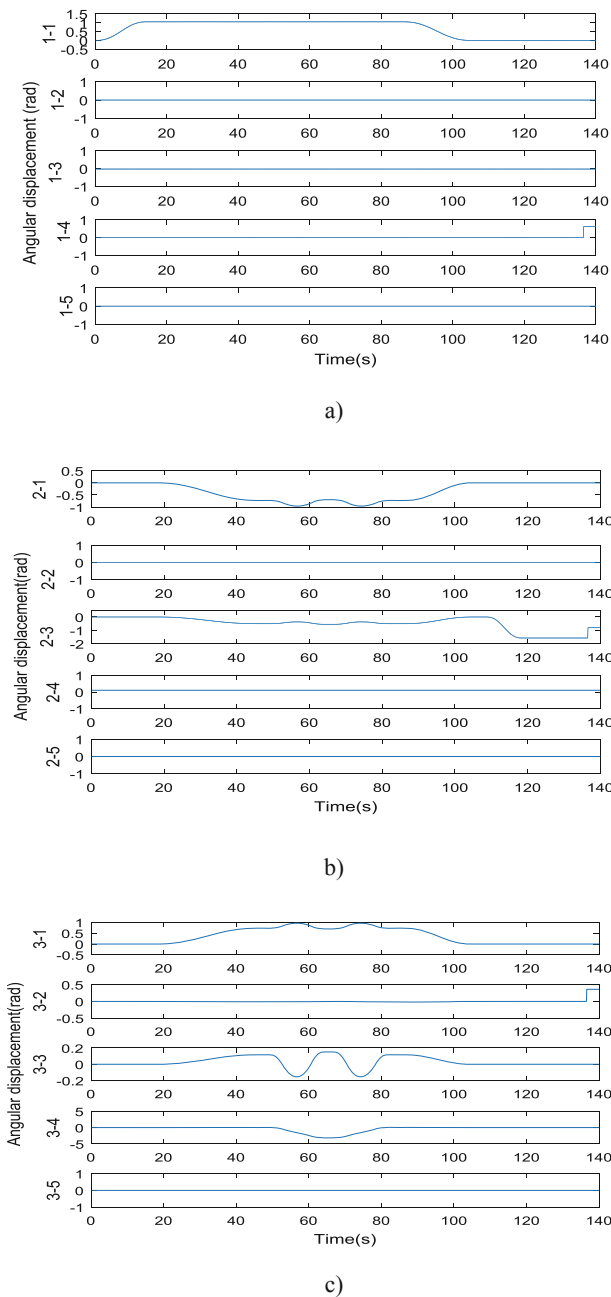


**Fig. 4.** Acquired joint angles during demo test of revolving motion in Figs. 3(d) to (f): (a) arm 1; (b) arm 2; (c) arm 3.

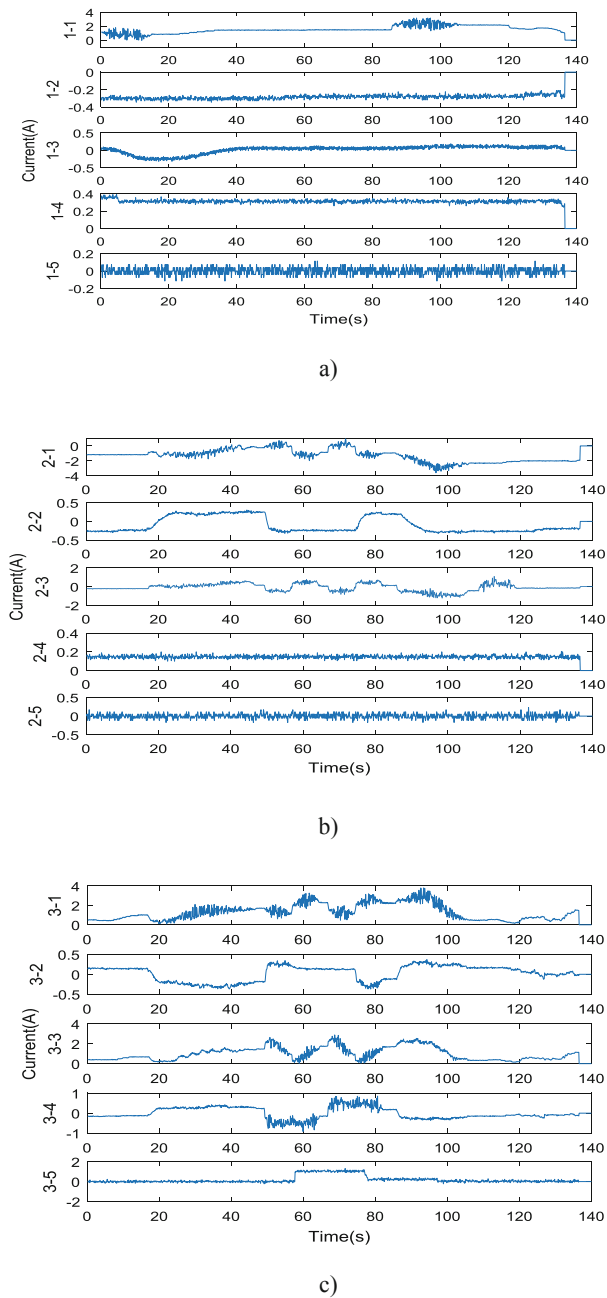


**Fig. 5.** Acquired motor current demo test of revolving motion in Figs. 3(d) to (f): (a) arm 1; (b) arm 2; (c) arm 3.

## 5 Conclusions

The BIT astronaut robot with three limbs is presented with its peculiar design and characteristic operation modes through a demo test in lab environment at ground acceleration field. The results characterize successfully the limb operation as leg or arm with the end-effector acting as foot or gripper, respectively. The reported demo test gives a numerical characterization in term of properly controlled motion and energy consumption. Future work is planned not only with this ground operated prototype for task improvements but also for a new mass-reduced design to be operated in micro-gravity filed in the space.

## References

- Bluethmann, W., Ambrose, R., Diftler, M., Askew, S., Huber, E., Goza, M., Rehnmark, F., Lovchik, C., Magruder, D.: Robonaut: a robot designed to work with humans in space. *Auton. Robot.* **14**, 179–197 (2003)
- Ceccarelli, M. (ed.): *Service Robots and Robotics: Design and Application*. IGI Global, Hershey (2012). Engineering Science Reference
- Ceccarelli, M., Li, H., Carbone, G., Huang, Q.: Conceptual kinematic design and performance evaluation of a chameleon-like service robot for space stations. *Int. J. Adv. Robot Syst.* **12** (2015). <https://doi.org/10.5772/60203>
- King, D.: Space servicing: past, present and future. In: *Proceeding of the 6th International Symposium on Artificial Intelligence and Robotics and Automation in Space* (2001)
- Sallaberger, C.: Canadian space robotic activities. *Acta Astronaut.* **41**, 239–246 (1998)

# **Advances in Medical Robotics**



# An Experimental Test Procedure for Validation of Stiffness Model: A Case Study for R-CUBE Parallel Mechanism

İbrahimcan Görgülü<sup>1(✉)</sup>, M. İ. Can Dede<sup>1</sup>, and Giuseppe Carbone<sup>2,3</sup>

<sup>1</sup> Izmir Institute of Technology, Izmir, Turkey  
{ibrahimcangorgulu,candede}@iyte.edu.tr

<sup>2</sup> DIMEG, University of Calabria, Rende, Italy

<sup>3</sup> Technical University of Cluj-Napoca, Cluj-Napoca, Romania  
giuseppe.carbone@unical.it

**Abstract.** Haptic device manipulators are used for generating haptic feedback. This feedback is composed of force which is regulated with respect to motion information. Accurate generation of the feedback requires exact position acquisition of the end-effector. Due to the compliant bodies of a manipulator, a stiffness model is needed to predict this position. Previously, Virtual Joint Method was adopted to obtain the stiffness model of an R-CUBE parallel haptic mechanism. In this paper, experimental test setup and experimental procedure are described for validating this stiffness model, its engineering feasibility and soundness of the proposed model.

**Keywords:** Virtual Joint Method · Parallel mechanism ·  
Experimental stiffness validation

## 1 Introduction

A haptic device reflects force/motion information to a user to generate haptic stimuli [1]. This information is generated by making use of the end-effector position. It is common to use forward kinematics and joint sensor data (e.g. encoders) to compute this position. However, joint sensors cannot detect the compliant displacements of compliant manipulators. Hence, the kinematic model is not sufficient to compute the actual position. Correspondingly, force/torque information to be displayed to the user is generated inaccurately. Since the accuracy of haptic stimulus is related to the accurate acquisition of position information, a stiffness model is required to estimate the actual end-effector position.

A stiffness model is an ideal mathematical model. However, the manufactured manipulators may have imperfectness in their geometry, sub-component, and material. These imperfectnesses causes divergence in compliant deflections between the model and the manipulator. In order to reduce this divergence, the stiffness model has to be verified and modified via experiments. A general procedure is described in [2] to obtain an exact stiffness model. Another procedure

is proposed in [3] to verify and modify the stiffness model of robotic systems experimentally. In [4], stiffness model of a parallel manipulator that has sagging cables was experimentally verified.

In an experiment of stiffness mapping, the manipulator is positioned at several poses or followed a pre-defined trajectory with a relatively low speed. Simultaneously, an external wrench is applied to the end-effector. Meanwhile, compliant displacements are measured. The measurement instrument type defines the type of experiment method. Some merits and standards on the measurement of geometric errors and instrument types are given in [5]. Comparison of position measurement sensors are given in [6]. These position sensors may be used to obtain compliant displacements for stiffness experiments. Also, they may or may not require contact with the test subject. In addition, some of these sensors directly measure the end-effector position while other ones measure indirectly. This indirect measurement requires a model that relates the measured data in sensor-space to the compliant displacement in task space.

In [7], and [8], a camera is used for contactless and direct measurement approach. In this method, a reference picture is attached to the end-effector. Then, the pose information of this picture is computed via image processing. Depending on the change in the pose of the reference image, the compliant displacement is computed. The accuracy of the results in this technique is dependent on the lighting conditions, and the resolution of the camera. However, the computation cost is relatively higher compared to the other methods.

In [9], coordinate measuring machines (CMM) are used to measure the position via its probe directly. Hence, CMM needs physical contact. This may expose additional external wrench on the end-effector. Nevertheless, if this contact force is relatively smaller than the designated minimum force output, then the wrench of the probe cannot neglected.

An indirect measurement approach is proposed in [10]. In this study, a cable-based parallel manipulator called Milli-CaTraSys is coupled with the mobile platform of CaPaMan parallel manipulator. Then, the change in mobile platform position/orientation is computed by measuring the displacements of cables. Although this system is highly accurate, it requires precise calibration to begin the tests.

In [11], and [12] laser distance sensors are used to measure the end-effector position. This laser sensor demands a reference surface to observe the displacement. One drawback of the laser sensor is that it can only measure the translational displacements along the axis of the laser beam. Therefore, several of them must be used to get the translational and rotational deflections. Despite this drawback, a laser sensor is easy to use, has high resolution, and gives accurate and precise data.

Virtual Joint Method (VJM) is one of the methods to obtain an analytical stiffness model. It has a relatively shorter computation time. Therefore, it can run in a real-time control loop [13]. In this regard, this study is devoted to the construction of a test setup for the experimental validation of the VJM model of an R-CUBE mechanism [14]. A laser sensor is used to measure the compliant



displacements directly from the mobile platform. First, a short description of the R-CUBE mechanism is given in Sect. 2. In Sect. 3, VJM model of the manipulator is briefly explained. In Sects. 4 and 5, experimental setup and procedure are described. In Sect. 6 results of experiments are illustrated and in Sect. 7 conclusion is addressed.

## 2 R-CUBE Mechanism

The R-CUBE manipulator is introduced by [14]. This manipulator comprises only revolute joints. It has 3 serial chains. Each chain actuates one of the translational degree of freedom (DOF) of the mobile platform. In Fig. 1 kinematic model of the manipulator is illustrated.

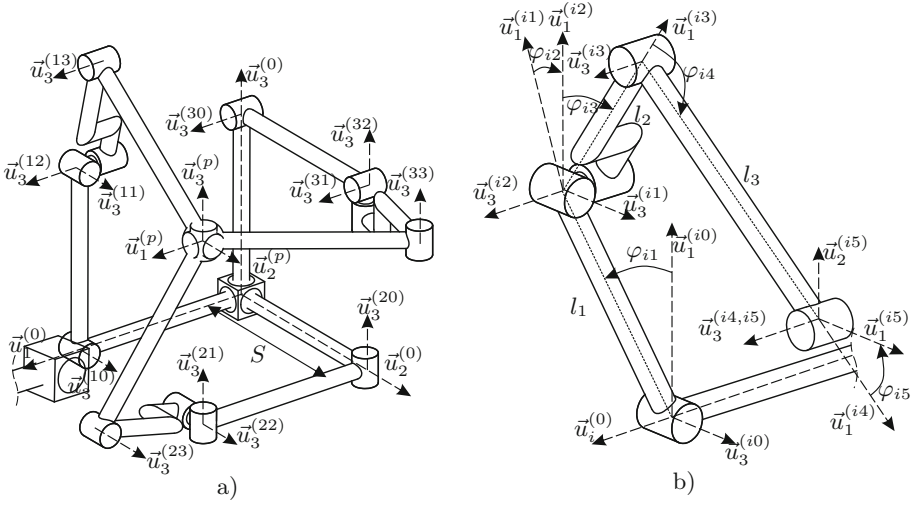


**Fig. 1.** Kinematic sketches and frames of the R-CUBE mechanism: (a) the manipulator, (b) variables of  $i^{th}$  serial chain where  $i$  is one of the serial chains.

In Fig. 1(a), initial frames of the serial chains are located on  $\vec{u}_k^{(0)}$  orthogonal unit vectors along  $k^{th}$  axis for  $k = 1, 2, 3$ .  $\vec{u}_k^{(ij)}$  denotes the unit vector belonging  $i^{th}$  serial chain and  $j^{th}$  frame as shown in Fig. 1(b). Due the kinematic constraints,  $\vec{u}_k^{(0)} \parallel \vec{u}_k^{(p)}$  where  $p$  is mobile platform frame. Also,  $\vec{u}_3^{(15)}, \vec{u}_3^{(25)}, \vec{u}_3^{(35)}$  are always aligned with  $\vec{u}_1^{(35)}, \vec{u}_1^{(15)}, \vec{u}_1^{(25)}$  vectors, respectively. The forward kinematics of the mechanism is simply given as:

$$r_i = S + l_1 \sin \varphi_{i1} \quad \text{for } i = 1, 2, 3 \quad \text{and} \quad \bar{r} = [r_1 \ r_2 \ r_3]^T \quad (1)$$

where  $S$  is a constant length between the  $0^{th}$  frame and  $\vec{u}_3^{(i0)}$  axis.  $\bar{r}$  denotes the column matrix form of position vector with respect to the origin.

### 3 Stiffness Model

VJM is a lumped model approach based on the Jacobian matrix mapping and the virtual work principle. The stiffness information of a link is lumped on virtual springs defined on the virtual joints at the tip of this link. A lumped model approach for parallel manipulators is described for the first time in [15]. In [16], VJM approach is systematized for parallel manipulators, and the effects of passive joints on stiffness are considered.

In this regard, the compliant kinematic model of R-CUBE mechanism is obtained through virtual joints. Given in Fig. 2, compliance model of a single serial kinematic chain of R-CUBE is presented. Each virtual joint has 6 DOF that are 3 translations and 3 rotations. Kinematics of a virtual joint is defined as:

$$\mathbf{H}_v(\bar{\theta}_{ij}) = \mathbf{T}_1(\theta_{ij}^1) \mathbf{T}_2(\theta_{ij}^2) \mathbf{T}_3(\theta_{ij}^3) \mathbf{R}_1(\theta_{ij}^4) \mathbf{R}_2(\theta_{ij}^5) \mathbf{R}_3(\theta_{ij}^6) \quad (2)$$

where  $\mathbf{H}_v$  denotes the homogeneous transformation matrix,  $\mathbf{T}_k$  and  $\mathbf{R}_k$  denote homogeneous transformation matrices for pure translation along and pure rotation about  $\vec{u}_k^{\text{th}}$  axis for  $k = 1, 2, 3$ .  $\bar{\theta}_{ij}$  is virtual joint variables that includes the translational and rotational DOF. Superscripts of  $\theta_{ij}$  denote element number.

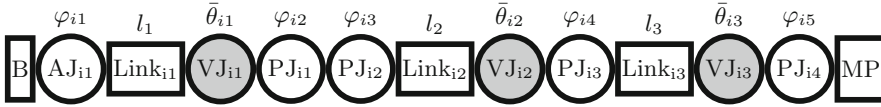


**Fig. 2.** Compliant kinematics of the manipulator where AJ is active joint, PJ is passive joint, VJ is virtual joint, MP is mobile Platform, and B is base.

Stiffness matrix of  $i^{\text{th}}$  serial chain,  $\mathbf{K}_{Ci}$ , is obtained via the compliant kinematics in Fig. 2. This matrix is given in Cartesian space coordinates as derived in [13]. Then, Cartesian stiffness matrix of the manipulator,  $\mathbf{K}_C$ , is computed as  $\mathbf{K}_C = \sum_{i=1}^3 \mathbf{K}_{Ci}$ . Components of  $\mathbf{K}_C$  is given in Eq. 3 for small amount of deflections. This matrix must be re-computed if external load  $|\bar{F}_{ext}| >> 0$ .

$$\mathbf{K}_C = \begin{bmatrix} K_{C_1}^{(11)} & 0 & 0 & 0 & K_{C_1}^{(15)} & K_{C_1}^{(16)} \\ 0 & K_{C_2}^{(22)} & 0 & K_{C_2}^{(24)} & 0 & K_{C_2}^{(26)} \\ 0 & 0 & K_{C_3}^{(33)} & K_{C_3}^{(34)} & K_{C_3}^{(35)} & 0 \\ 0 & K_{C_2}^{(24)} & K_{C_3}^{(34)} & K_{C_2}^{(44)} + K_{C_3}^{(44)} & K_{C_3}^{(45)} & K_{C_2}^{(46)} \\ K_{C_1}^{(15)} & 0 & K_{C_3}^{(35)} & K_{C_3}^{(45)} & K_{C_1}^{(55)} + K_{C_3}^{(55)} & K_{C_2}^{(56)} \\ K_{C_1}^{(16)} & K_{C_2}^{(26)} & 0 & K_{C_2}^{(46)} & K_{C_1}^{(56)} & K_{C_1}^{(66)} + K_{C_2}^{(66)} \end{bmatrix} \quad (3)$$

### 4 Experimental Setup

The test setup is composed of a 3D printed R-CUBE manipulator, a laser range sensor, a reference plane to reflect the laser light, and a pulley-guide system to

apply an external wrench to the manipulator. In Fig. 3(a), the constructed test setup is shown. In Fig. 3(b), a sketch of the CAD model of the test setup is given denoting some components of the setup.

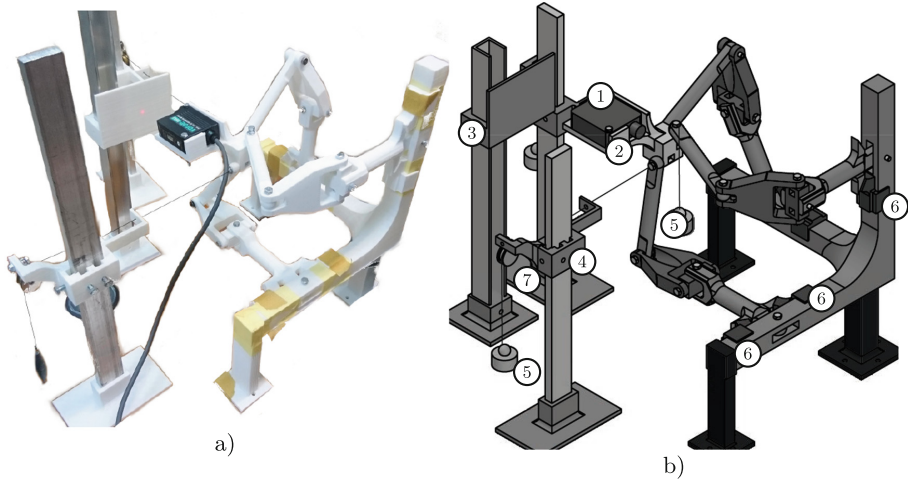


**Fig. 3.** Test setup in different. (a) Built setup, (b) CAD model where 1: Laser sensor, 2: Mobile platform, 3: Reference plane, 4: Guide, 5: Weights, 6: Stoppers, 7: Pulley.

The prototype is manufactured with Polylactic acid (PLA) material via a 3D printer. Each 3D printed part has 15% infill. PLA material results in relatively larger compliant displacements compared to composite and metals. However, this behavior of PLA makes it more convenient to be used in stiffness evaluation tests because it is easier to measure larger compliant displacements (from 0.1 to 1 mm) with higher accuracy. In this range of displacements, the sensor noise during the measurements becomes insignificant and thus, it can be neglected. PLA differs from metals by being thermoplastic material that has visco-elastic properties. This behavior requires the consideration of the rate of applying the external wrenches. If there is a quick loading-unloading scenario such as operation in high frequencies, viscous forces become more dominant than the elastic forces. Hence, a damping model is also required in addition to stiffness model. However, the study focuses on structural stiffness. Hence, the measurements are obtained when the manipulator is in its final position and stabilized, and thus, the viscous forces are abolished.

M5 screws are used at the joint structures to connect the links. Screw connection increases the static friction in the joints. In the stiffness model, it was assumed that there was no friction in the passive joints. Accordingly, this friction induces errors in the stiffness model. Nonetheless, these joints have less joint clearance compared to a joint structure with bearings. This property minimizes the level of uncertainty in the manipulator's pose. The friction force, on the

other hand, is smaller compared to applied external wrenches. Hence, neglecting the friction forces do not generate a significant error.

A Nippon brand LAS-5010V model laser range sensor is used for measuring the compliant displacements. Laser range sensor signals are acquired via a National Instruments data acquisition card. These distances are measured from the reference plane. This reference plane is located depending on the test poses of the manipulator.

The intention is to measure the translational compliant displacements along  $\vec{u}_k^{(p)}$  for  $k = 1, 2, 3$ . For this purpose, the mobile platform of R-CUBE mechanism is designed to align the laser sensor with motion axes. The orientation of the mobile platform is changed to measure compliant displacements along the respective motion axis. That way, compliant translational displacement parallel to  $\vec{u}_k^{(p)}$  for  $k = 1, 2, 3$  axes can be determined, separately. The orientation of the mobile platform changes due to the weight of the laser range sensor and external wrench. However, these orientation changes are assumed to be close to zero. Hence, orientation effects on the measurements are neglected since a relative measurement is done for compliant displacements.

External force vectors are aligned with  $\vec{u}_1^{(p)}$ ,  $\vec{u}_2^{(p)}$  and  $\vec{u}_3^{(p)}$  axes as shown in Fig. 4. This alignment ensures that there is no external torque input to the manipulator. These external forces are generated by calibrated weights hung by a cable-pulley system. One end of the cable is connected to a mass, and the other end is connected to last frames of 1<sup>st</sup> and 2<sup>nd</sup> serial chains. This cable passes through a pulley and the 2 holes of the guide system. Location and the height of the guide system are adjusted so that the cable passes through the centers of these holes, so it is aligned with the respective motion axis. Guides allow us to adjust the height so that this test system can be used for any test pose.

Since hung masses generate the external forces, force vectors along  $\vec{u}_1^{(p)}$  and  $\vec{u}_2^{(p)}$  are always applied in a positive direction. The external force vector along  $\vec{u}_3^{(p)}$  is always in the negative direction and aligned with the gravity vector. These directions of external force vectors do not change during the test procedure. Hence, the validation of stiffness model is conducted only for this force combination.

The manipulator should be tested throughout its workspace to capture its stiffness characteristics. These tests are often conducted by following a test trajectory in the workspace with low speeds. However, measurements in such a

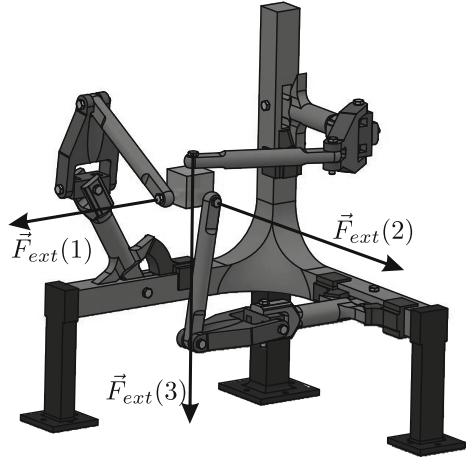


**Fig. 4.** External wrench components and their application points.

scenario include the stiffness property of the actuator. Since the objective of this study is to obtain structural stiffness, the mobile platform should be positioned and locked at several discrete poses in the workspace. Unfortunately, there are infinitely many discrete poses in the workspace. However, some of these poses have unique stiffness characteristics. By testing the manipulator at these poses, desired stiffness properties may be obtained. Therefore, some critical poses are identified to run the experiment. 27 poses are determined in total depending on the fully folded, fully expanded, and nominal poses of active links. 10 critical test poses (TPs) are selected for experiments. These TPs are given in Table 1. Later, the results at these TPs may be used to generate full stiffness model of the manipulator via interpolation. The manipulator is positioned to these poses manually by the help of mechanical limits on the first links and stopper parts. Stoppers are designed to lock the manipulator when the active joint is located at  $0^\circ$  or  $\pm 30^\circ$ .

**Table 1.** Active joint values (AJV) of selected TPs,  $\mathbf{TP} = \mathbf{TP}(\varphi_{11}, \varphi_{21}, \varphi_{31})$ ,  $-30 \Rightarrow -30^\circ$ ,  $+30 \Rightarrow +30^\circ$ ,  $0 \Rightarrow 0^\circ$

AJV	TP1	TP2	TP3	TP4	TP5	TP6	TP7	TP8	TP9	TP10
$\varphi_{11}$	-30	0	+30	0	0	0	0	+30	+30	0
$\varphi_{21}$	-30	0	+30	0	0	+30	-30	-30	-30	-30
$\varphi_{31}$	-30	0	+30	+30	-30	+30	-30	-30	+30	+30

## 5 Experimental Procedure

In this section, the experimental procedure is described. First, the experiment factors are determined to conduct a comprehensive experiment. These factors are laser range sensor orientation ( $a$ ), test pose ( $b$ ), attached mass ( $c$ ), and recorded sample ( $d$ ), where  $a, b, c, d$  are their labels. The laser sensor orientation is aligned with motion axes to measure compliant deflections in these directions. A test pose is selected from Table 1. In each test pose, the manipulator is locked via stoppers. Then, the masses are attached to end-effector by using the pulley-guide system for each motion axis. Different masses enable to observe the effect of different wrenches on compliant deflections. In each set value of  $a, b, c$ , a measurement is recorded for 3 times and each recording is labeled with  $d$  parameter. This repetitive recording is done to increase confidence on the measured data. Table 2 shows the possible values of these factors and their ranges. These values are presented with respect to their selection order.

The experimental test procedure starts by setting all factor labels to 1 ( $a = 1, b = 1, c = 1, d = 1$ ). Hence, the initial test configuration measures the deflections along  $\vec{u}_1^{(p)}$  axis at TP1 with 285 g forces in all directions. After the manipulator is stabilized (when the visco-elastic behavior diminishes), the distance between the laser sensor and reference plane is recorded with label  $d = 1$ . Next, masses are removed, and reattached 2 more times to record the data for

**Table 2.** Experiment factors.

Factors	Range of labels	Values of factors in order
Laser orientation, <b>a</b>	1–3	$\vec{u}_1^{(0)}, \vec{u}_2^{(0)}, \vec{u}_3^{(0)}$
Test pose, <b>b</b>	1–10	TP1–TP10
Attached mass, <b>c</b>	1–4	285 g, 185 g, 85 g, 0 g
Sample number, <b>d</b>	1–3	1, 2, 3

$d = 2$ , and  $d = 3$ . This attach-and-remove procedure prevents incorrect data measurement that might be caused by nonlinear effects at joints such as friction and joint clearance. Then, 185 g, 85 g, and 0 g masses are attached for  $c = 2, 3, 4$  and 3, and measurements are recorded for  $d = 1, 2, 3$ . This higher to lower

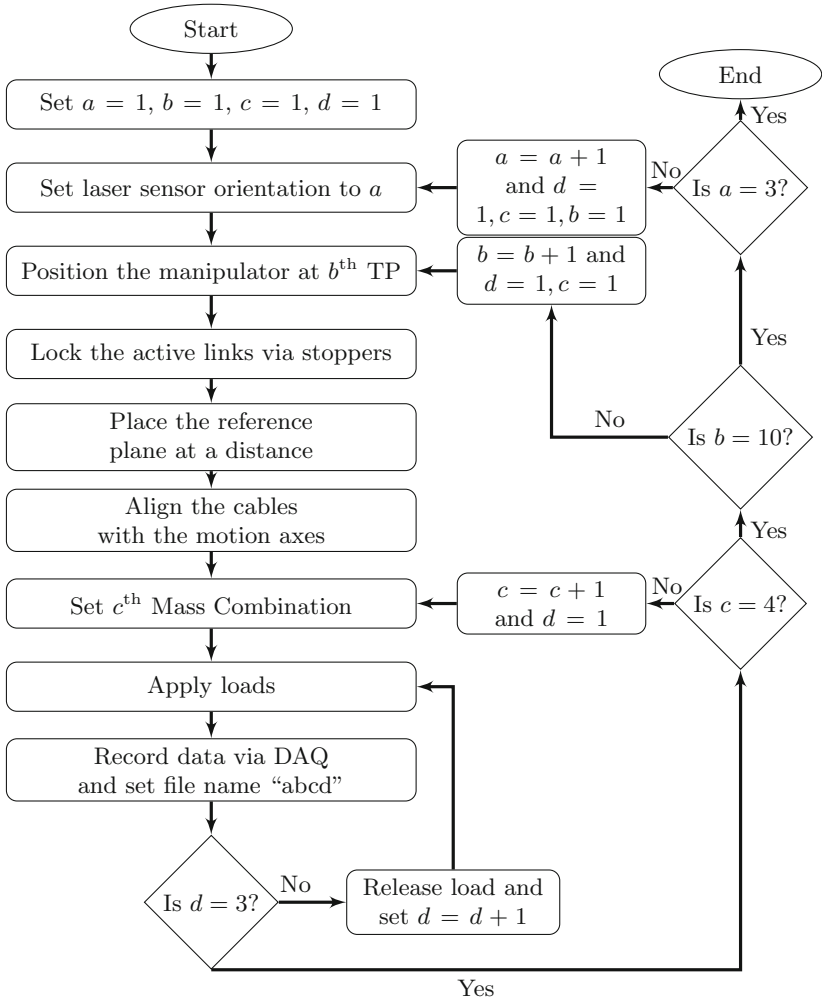


**Fig. 5.** Flow chart of experimental procedure.

loading sequence for  $c$  ensures that the mechanism is in its final compliant pose, and there is no displacement due to joint clearance. Notice that, when  $c = 4$ , there is no mass attached. This measurement determines the distance to the reference plane for the unloaded case. Hence, this value is used to subtract the offset value of the sensor data to compute compliant displacement. Then, same procedure is conducted for TP2 to TP10 for  $b = 2, 3, \dots, 10$  and in different motion axes for  $a = 2, 3$  for measurement at different poses in different directions. A flow chart of the procedure is described in Fig. 5.

## 6 Test Results and Comparison with the VJM Model

Obtained raw data (voltage readings) from laser range sensor are recorded in LabVIEW. Then, they are post-processed in MATLAB for conversion of the raw data into distance information. The compliant displacements are computed by subtracting the unloaded distance from loaded distances. The numerical results are given in Table 3 for deflections along  $\vec{u}_1$ ,  $\vec{u}_2$ , and  $\vec{u}_3$  motion axes, respectively.

**Table 3.** Absolute values of experimental deflection measurements along  $\vec{u}_1$ ,  $\vec{u}_2$ , and  $\vec{u}_3$  in mm.

	TP1	TP2	TP3	TP4	TP5	TP6	TP7	TP8	TP9	TP10
$\vec{u}_1$ 85 g	0,23	0,34	0,40	0,51	0,19	0,72	0,18	0,26	0,54	0,92
$\vec{u}_1$ 185 g	0,34	0,76	0,94	1,02	0,41	1,44	0,46	0,47	1,05	1,70
$\vec{u}_1$ 285 g	0,51	1,22	1,39	1,64	0,85	2,23	0,87	0,71	1,47	2,46
$\vec{u}_2$ 85 g	0,37	0,34	0,46	0,47	0,46	0,56	0,13	0,40	0,92	0,77
$\vec{u}_2$ 185 g	0,45	0,58	0,90	0,93	0,83	0,92	0,60	0,82	1,70	1,48
$\vec{u}_2$ 285 g	0,66	0,85	1,14	1,25	1,23	1,35	0,89	1,30	2,50	2,01
$\vec{u}_3$ 85 g	0,02	0,63	0,68	0,88	0,38	0,87	0,41	0,17	0,80	0,56
$\vec{u}_3$ 185 g	0,23	1,66	1,62	1,70	0,81	1,74	0,63	0,51	1,63	1,29
$\vec{u}_3$ 285 g	0,39	2,34	2,30	2,44	1,33	2,16	0,81	0,77	2,56	2,15

In stiffness modeling, it is assumed that the compliant deflections are linearly proportional to applied force/torque. Hence, force to deflection ratio (the stiffness) is constant for small deflections. If the measured deflections are normalized with respect to their corresponding wrenches, the resultant ratio of different deflections and forces should be equal in the same test pose. When the compliant deflection results with 85 g, 185 g, and 285 g of loads are plotted with respect to test poses, they should overlap on each other in normalized space. In an ideal case, the VJM model and the experiment measurements should also overlap in normalized space. However, a perfect overlap should not be expected due to manufacturing errors, joint clearances, etc. Yet, a correlation is still expected with minor errors. The normalization of VJM deflections and experimental ones

are achieved by dividing each deflection set to their maximum value. Also, overall deflections are computed and normalized for comparison. Figure 6 shows the VJM and experimental results in normalized space. It can be observed that measurements are a close correlation. However, VJM deflections are less correlated with the experiment results as expected.

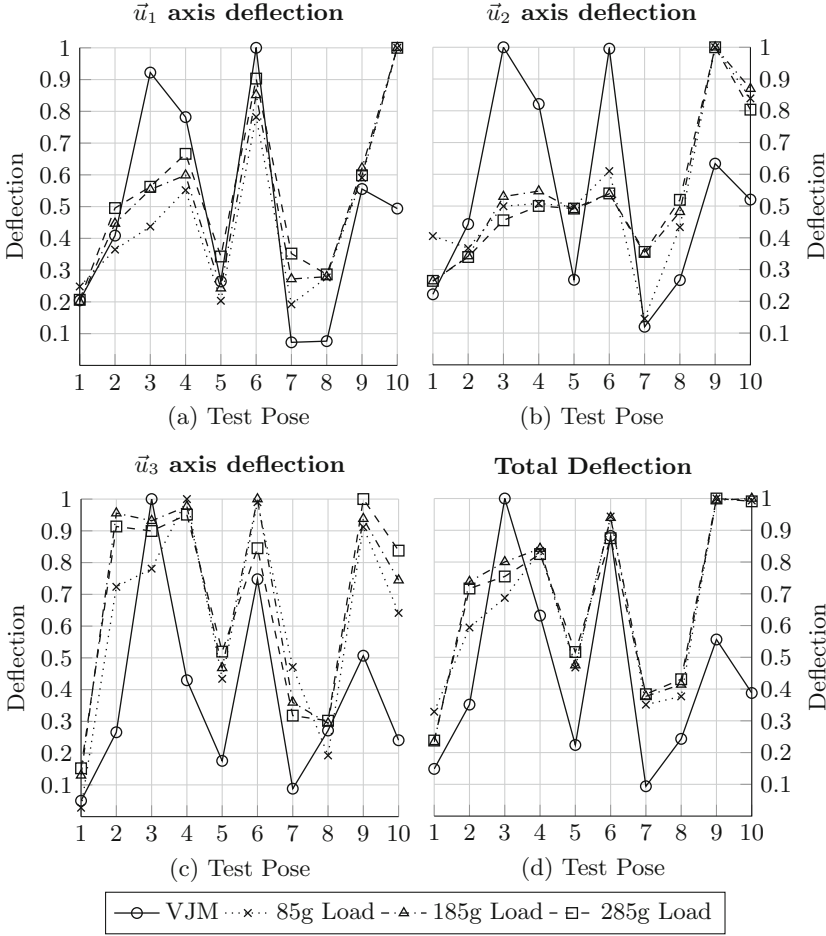


**Fig. 6.** Normalized VJM and experimental deflections.

The best fit between VJM and experiments are observed for  $\vec{u}_1$  deflections, as shown in Fig. 6(a). Except for TP4 and TP10, VJM exhibits identical deflection behavior with the experiments. The maximum error between VJM and experiment is observed at TP3 and TP10. However, TP1, TP2, TP4, TP5, TP6, and TP9 results are close to each other.



$\bar{u}_2$  deflections are shown in Fig. 6(b). It has been observed that the experimental and VJM deflection data have a similar trend. In both data set, deflections increase or decrease about in same TPs. TP1 and TP2 results of VJM and experiment have the minimum relative error compared to the other TPs. VJM-experiment deflections in other TPs highly differ from each other.

Figure 6(c) shows deflections along  $\bar{u}_3$ . Experimental results of TP2 highly differ in terms of general behavior that needs careful attention. Also, TP2, TP4, TP9, and TP10 have high relative errors between experiment and VJM results.

Finally, overall deflections are illustrated in Fig. 6. In VJM, TP3 has its highest deflection while experiments show that maximum deflection occurs at TP9. Besides, TP3 has a lower value for experiments than TP4 while TP3 in VJM is the most compliant pose. In overall deflections, the dominant axis is  $\bar{u}_3$ . TP6 for all poses, however, is the best fitting pose with the VJM results.

## 7 Conclusion

In this study, experimental test setup and procedure are described to measure the compliant deflections of a mechanism. The results of these test are used for VJM stiffness model verification that was previously procured.

VJM and experimental results are compared in normalized space to validate the analytical model. Except for a few test poses, VJM and experimental results have a similar stiffness behavior. One of the reasons for the discrepancy of the calculated and measured data is the weight of the laser range sensor, which is not taken into account in the simulation test with the VJM model. Another reason is the assumption that the orientation of the mobile platform does not change during the application of different loads. One last reason is the flexion of the base of the manipulator since it is not produced from high-strength material. Nevertheless, the experimental test setup and its procedure are proposed in this study. The future work includes the addition of an inclinometer to the mobile platform to measure the orientation change and fix the laser range sensor reading accordingly, including sensor weight to the VJM model, and carrying out the experimentation with the actual prototype of the mechanism produced from aluminum material and carbon composite tubes.

**Acknowledgement.** The paper presents results from the research activities of the project ID 37.215, MySMIS code 103415 “Innovative approaches regarding the rehabilitation and assistive robotics for healthy ageing” co-financed by the European Regional Development Fund through the Competitiveness Operational Programme 2014–2020, Priority Axis 1, Action 1.1.4, through the financing contract 20/01.09.2016, between the Technical University of Cluj-Napoca and ANCSI as Intermediary Organism in the name and for the Ministry of European Funds. The study is supported in part by The Scientific and Technological Research Council of Turkey via grant number 117M405. Also, the first author wishes to thank ACRI association for a grant which supported him for a period of study at LARM in Cassino, Italy within 2018.

## References

1. Kern, T.A.: Engineering Haptic Devices: A Beginner's Guide for Engineers. Springer, London (2009)
2. Pinto, C., Corral, J., Altuzarra, O., Hernández, A.: A methodology for static stiffness mapping in lower mobility parallel manipulators with decoupled motions. *Robotica* **28**(5), 719–735 (2010)
3. Carbone, G.: Stiffness analysis and experimental validation of robotic systems. *Front. Mech. Eng.* **6**(2), 182–196 (2011)
4. Yuan, H., Courteille, E., Deblaise, D.: Elastodynamic analysis of cable-driven parallel manipulators considering dynamic stiffness of sagging cables. In: 2014 IEEE International Conference on Robotics and Automation (ICRA), pp. 4055–4060. IEEE (2014)
5. Schwenke, H., Knapp, W., Haitjema, H., Weckenmann, A., Schmitt, R., Delbressine, F.: Geometric error measurement and compensation of machines—an update. *CIRP Ann.* **57**(2), 660–675 (2008)
6. Nyce, D.S.: Position Sensors. Wiley, Hoboken (2016)
7. Taner, B., Dede, M.I.C.: Image processing based stiffness mapping of a haptic device. In: New Advances in Mechanisms, Mechanical Transmissions and Robotics, pp. 447–454. Springer (2017)
8. Švaco, M., Šekoranja, B., Šuligoj, F., Jerbić, B.: Calibration of an industrial robot using a stereo vision system. *Procedia Eng.* **69**, 459–463 (2014)
9. Slavković, N.R., Milutinović, D.S., Kokotović, B.M., Glavonjić, M.M., Živanović, S.T., Ehmann, K.F.: Cartesian compliance identification and analysis of an articulated machining robot. *FME Trans.* **41**(2), 83–95 (2013)
10. Hernández-Martínez, E.E., Ceccarelli, M., Carbone, G., López-Cajún, C.S., Jáuregui-Correa, J.C.: Characterization of a cable-based parallel mechanism for measurement purposes#. *Mech. Based Des. Struct. Mach.* **38**(1), 25–49 (2010)
11. Zhang, X., Yang, W., Cheng, X., Chen, Y.: Stiffness identification for serial robot manipulator based on uncertainty approach. In: International Conference on Intelligent Robotics and Applications, pp. 378–388. Springer (2011)
12. Klimchik, A., Pashkevich, A., Wu, Y., Caro, S., Furet, B.: Design of calibration experiments for identification of manipulator elastostatic parameters. arXiv preprint [arXiv:1211.6101](https://arxiv.org/abs/1211.6101) (2012)
13. Görgülü, İ., Dede, M.: Computation time efficient stiffness analysis of the modified R-CUBE mechanism. In: The International Conference of IFToMM ITALY, pp. 231–239. Springer (2018)
14. Li, W., Gao, F., Zhang, J.: R-CUBE, a decoupled parallel manipulator only with revolute joints. *Mech. Mach. Theory* **40**(4), 467–473 (2005)
15. Gosselin, C.: Stiffness analysis of parallel mechanisms using a lumped model. *Int. J. Robotics Automat.* **17**, 17–27 (2002)
16. Pashkevich, A., Chablat, D., Wenger, P.: Stiffness analysis of overconstrained parallel manipulators. *Mech. Mach. Theory* **44**(5), 966–982 (2009)



# Multi-camera Vision-Guided Manipulation: Application to Acne and Wrinkles Treatment

Ho-Yu Chuang and Jen-Yuan (James) Chang<sup>(✉)</sup> 

Department of Power Mechanical Engineering,  
National Tsing Hua University, Hsinchu 30013, Taiwan (R.O.C.)  
harveychuang@gapp.nthu.edu.tw,  
jychang@pme.nthu.edu.tw

**Abstract.** Current treatment method for acne and wrinkles requires medical staff to operate with medical injection devices, which requires a lot of time and manpower. In this paper, a method to automate acne and wrinkles treatment using robotic manipulator with two RGB-D camera system is proposed. Through experiments with a UNIVERSAL ROBOT UR5 equipped with the medical injector, it is demonstrated that the proposed approach enables the camera on UR5 to detect and track acne and wrinkles on the flat head face mannequin. Using intrinsic and extrinsic matrix of the RGB-D camera, the coordinates of the targets can be automatically identified with precision. Such targets can be wrinkles or acne which can be detected by skeletonization or template matching methods in the camera system. The system will match the targets and plan the trajectory for the manipulator to follow. The method used in this research to estimate the normal vector of target is PCA (Principal Component Analysis). By trajectory planning, the angles of the manipulator joints can be determined through UR5 inverse kinematics solutions. With such method and optimizing the redundancy of freedom to reduce the motion time by Hill Climbing algorithm, the manipulator is able to move vertically along the skin and the injector can be controlled to aim to the target with precision. To ensure safety, the other camera is fixed on table to monitor working area of UR5 to avoid the manipulator end-effector hitting obstacles. This process enables the possibility of automated medical treatment.

**Keywords:** Vision-guided system · Multi-camera · Manipulator

## 1 Introduction

Automated medical robots are the future robotics development direction. Non-invasive treatment can be accomplished by a combination of mechanical vision system and a robotic manipulator. In the coming of an aging society such as Taiwan, the burden on the medical system can be reduced through automated processes. The purpose of this automated medical system is to detect abnormalities on the surface of the skin and guide the manipulator with the medical injector for treatment.

In this article, we aim at acne and wrinkles treatment. With two-camera system, a robotic manipulator is guided so as to move to the simulated acne and wrinkles located on face mannequin. The direction of the medical injector should be aligned and

perpendicular to the skin surface. Another fixed camera is equipped to observe obstacles near the manipulator, and to detect patient movement and object invasion. When the manipulator route is blocked, the system will immediately stop the manipulator movement. The face mannequin is used to simulate real conditions in the treatment before getting into medical trials.

Identification of acne and wrinkles has been previously studied in many articles. Typical strategy for identifying acne is to use gray scale pre-processing, and to use binary thresholds to remove underling noise, commonly marking the interested areas with rectangular boxes [1]. However, this method is susceptible to light. The way to remove light is divided into two types, one of which is to determine whether the oily skin in the acne causes light reflection, and use the surrounding pixels to restore the portion that is reflected by the light [2]. The other method reported in the literature is to convert to YIQ, I1I2I3 color space for identification [3], compare RGB, rgb, YIQ, and I1I2I3 color space, in YIQ, I1I2I3 and show robustness against non-uniform illumination. For wrinkle detection, patient's face features are first detected and analyzed in particular in the corner of the eye in a specific area [4–6]. [7] uses the Hessian line to track wrinkles. As opposed to the methods reported in literature, in this paper, template matching and skeletonization are adopted to detect the samples of acne and wrinkles.

There are two types of hand-eye systems, eye-on-hand and eye-to-hand, both of which have a long history of development. The posture of the object can be recognized. If the manipulator is equipped with gripper and the 3D camera, system can guide manipulator in an appropriate posture to grip the objects [8–10]. Avoiding the collision of the manipulator and gripper should be noticed. The depth camera can be used to predict the obstacle on the path of the manipulator and change the path to avoid collision [11]. If two kinds of cameras can be integrated, it is possible for vision guided and avoiding collision at the same time.

This paper explores the coordinate calibration of the camera and the manipulator. Through the cooperation of two 3D cameras, the manipulator is moved to a specific coordinate and posture while avoiding the medical injector touching the skin. The contribution of this paper is to validate the feasibility of automating the exampled non-invasive medical system in terms of positioning, identification, manipulator trajectory planning and control. The method that will be discussed in the following sections is examined with face mannequin. It was suggested in [12] that the manipulator's end-effector poses can be optimized by utilizing the redundant degrees of freedom. To minimize the task competition time, this method is employed and examined because the medical injector possesses redundant degree of freedom in yaw rotation.

## 2 Vision-Guided Manipulator

The system as depicted in Fig. 1 is composed of the following five major subsystems:

- (1) Eye-on-hand camera: Eye-on-hand camera takes photos from the top of face mannequin. In addition to color and depth information, position and posture of the camera on the manipulator hand will be recorded.

- (2) Image processing: This subsystem uses the intake images to identify acne and wrinkles based on data from 3D depth cameras. The depth information is used to assist calculation of coordinates and orientation in the base reference frame.
- (3) Trajectory planning: This subsystem helps to select the most suitable solution from the manipulator's inverse kinematics calculations.
- (4) Eye-to-hand camera: The eye-to-hand camera subsystem oversees surrounding obstacles that may be in the path of the manipulator. If any abnormality is detected, the arm is then interrupted immediately.
- (5) Motion control: This subsystem use PD control method to control the angle of the manipulator.

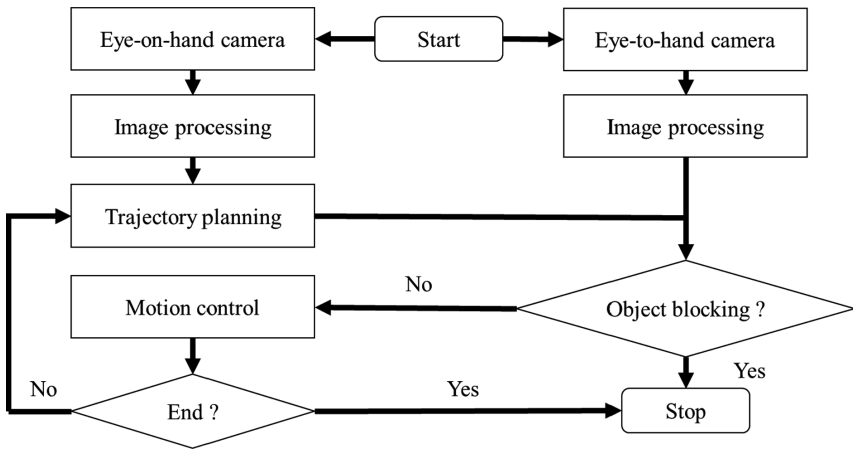


**Fig. 1.** Flow chart of the system

## 2.1 Acne and Wrinkles Identification

The method used for identify acne is the template matching. Several patterns of the acne sample are prepared to serve as the training set for acne searching. First, the manipulator moves to the top of the face mannequin and then the eye-on-hand camera is engaged to capture the image of the face mannequin. Secondly, by using the template matching method based on the prepared acne samples, the acne marks in the face mannequin image are searched. Based on the depth information, all of the acne coordinates to the base frame of the manipulator can be located.

The method for wrinkles identification differs from that used in acne searching. It first uses hue threshold to remove background and then search dark line on the face. By skeletonizing contour of the wrinkles, the position of the wrinkle can be converted into several vectors. The wrinkle's target normal vector to the skin surface can then be estimated by using PCA method.

## 2.2 Obstacles Detection and Identification

The eye-to-hand camera can capture and realize the manipulator's working space. From the images captured by the eye-to-hand camera, obstacles on the path of the manipulator's end effector can be detected and identified. The eye-to-hand camera is used to compensate the shortcomings of field of view from the eye-on-hand camera. The obstacles are predicted by conversion of the end effector frame to the eye-to-hand frame. In the camera frame, marking the depth of the manipulator movement path, and comparing the depth information map of the camera can lead to the determination whether an object is close to the path or not.

## 2.3 Manipulator Trajectory Planning and Control

In the literature [13], the process of solving UR5 inverse kinematics was described. According to this method, one can solve the UR5 inverse kinematics for selected pose  $H_6^0$  in eight different joint-space solutions  $(\theta_1^j, \theta_2^j, \theta_3^j, \theta_4^j, \theta_5^j, \theta_6^j)$ . By limiting the sign of  $\theta_5$  (wrist) and  $\theta_3$  (elbow), eight solutions are limited to two solutions.

In the present work, the injector is attached to the manipulator's end effector, leading to expansion to the 7th axis. The transformation matrix between 6th and 7th axes in such case contains only translation information. The pose of the manipulator must be limited to avoid collision of the injector. As such, the lower limit of the distance between the injector and the wrist to avoid interference with each other is set using the follow equation:

$$|P_{7'}^{3'}| = \sqrt{P_{7'x}^{3'2} + P_{7'y}^{3'2} + P_{7'z}^{3'2}} \geq \text{distance threshold} \quad (1)$$

If there is no interference problem with the injector in the two solutions, the average motor movement will be the criterion for selecting the solution. Taking the sum of the motor angles difference  $\sum_{i=1}^6 |\theta_i - \theta_{i,now}|$  as the comparison condition, the solution  $\theta_i$  of with smaller  $\sum_{i=1}^6 |\theta_i - \theta_{i,now}|$  can then be selected (Fig. 2).

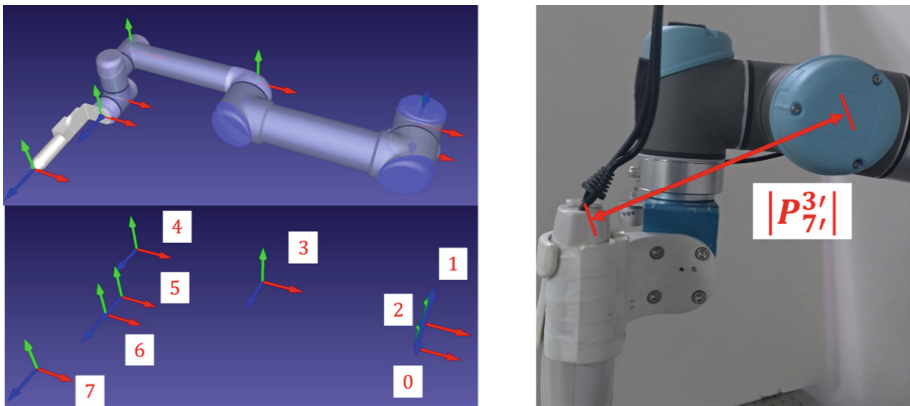


**Fig. 2.** UR5 frame definition and  $|P_{7'}^{3'}|$

## 2.4 Manipulator Pose Optimization

For the medical injector, its yaw rotation angle can be adjusted freely. As shown in Fig. 3, the pose of the manipulator is limited only by the position and  $\hat{Z}$ . Therefore, the primary goal is placed on adjusting the yaw rotation angle  $\gamma$  of the 7<sup>th</sup> axis of the robot so that the manipulator can reach the target point within the shortest amount of time.

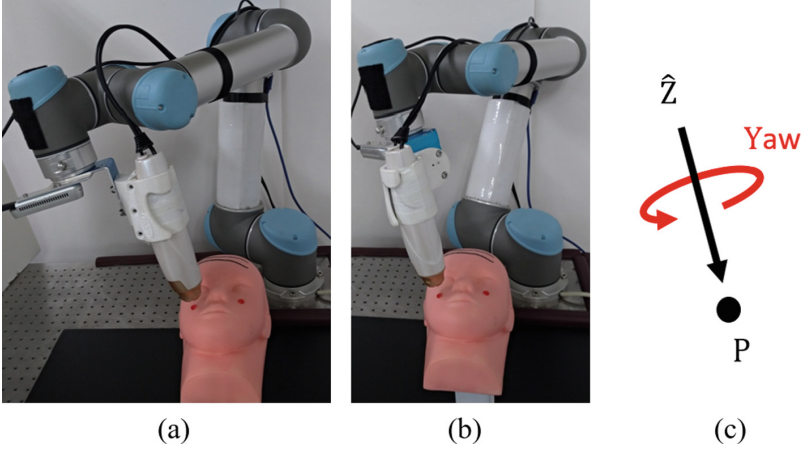


**Fig. 3.** (a) and (b) are still images of the manipulator in operation at two different yaw angles both representing the injector's axis of symmetry with the same position and  $\hat{Z}$  vector as illustrated in (c).

As opposed to the approach in [12] in which the maximum, joint angular velocity is considered, to reach this goal, the cost function is set equal to the required motion time of the manipulator in this research such that the corresponding maximum angular acceleration can be also considered. We use HC (Hill Climbing algorithm) to find the best  $\gamma$  to minimum the cost. The advantage of HC is that it requires less computation time and the local optimal solution can be found in a short time. The flow chart for the HC search algorithm is shown in Fig. 4. When the local optimal solution is found, the search will be stopped. By adjusting the HC structure, not only the motion time of the manipulator can be reduced, but also interference of the medical injector with the manipulator can be avoided.

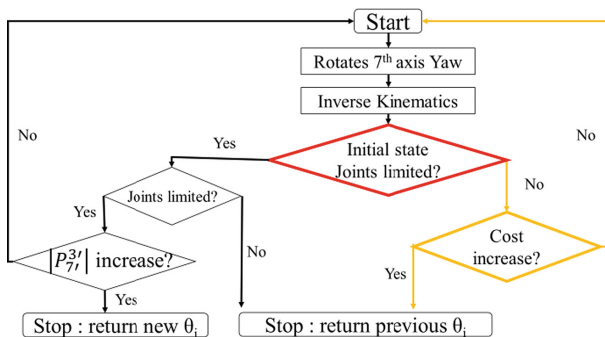


**Fig. 4.** Flow of HC search process.

### 3 Result and Discussion

Figure 5 shows the results of the identification of the acne and wrinkles on the face mannequin using the proposed method. The process of eye-to-hand obstacles detection is shown as Fig. 6.

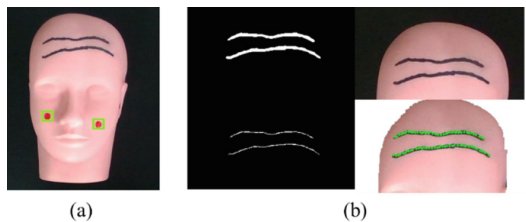


**Fig. 5.** (a) Acne detection result. (b) Wrinkles detection result.

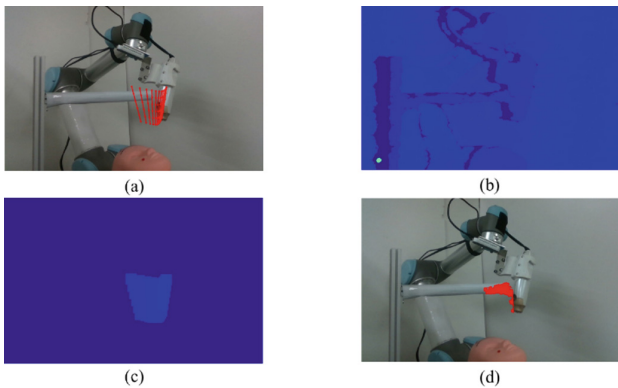


**Fig. 6.** The process of the obstacles detection: (a) trajectory projects onto image, (b) depth information from eye-to-hand camera, (c) depth prediction to camera, and (d) red color shows the area might cause a collision.



To validate the effectiveness of the proposed methods, an experiment as shown in Fig. 7 was conducted. In the experiment as illustrated in Fig. 7, the manipulator is moved from  $(0^\circ, -90^\circ, -90^\circ, 90^\circ, 90^\circ, 0^\circ)$  to the 26 points. The sum of the actual motion time with the HC algorithm and  $\text{Yaw} = 0^\circ$  is compared with the cost function with the results listed in Tables 1 and 2. Based on the cost function, approximately 6.26% of the motion time can be improved from the simulation. After conducting experiments, it was found that the experimental result, which is 6.54% reduction, is very close to what simulated by the proposed method. In the present work using the proposed method, the result including the consideration of maximum velocity and acceleration (6.26%) is more precise than only considered maximum velocity (11.77% reduced).

The process of treating acne and wrinkles is shown in Fig. 8. At present, only one eye-to-hand camera is set up in this system. The field of view of it may be obscured while observing the path of manipulator movement. However, such issue can be resolved with more eye-to-hand cameras as filming from all directions can certainly avoid the obscuration of a single camera, and the judgment of obstacles can be more precise.

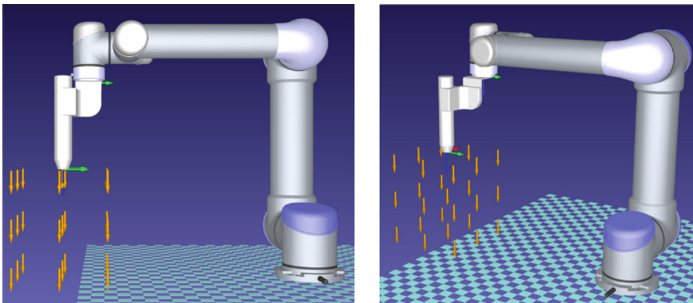


**Fig. 7.** Manipulator moves to 26 points. Compare the motion time of  $\text{Yaw} = 0$  and HC.

**Table 1.** Comparison of motion time.

Method	[12] Cost (only velocity)	Cost (acceleration and velocity)	Motion time (s)
$\gamma (\text{Yaw}) = 0$	9.26	21.58	29.38
HC	8.17	20.23	27.46

**Table 2.** Reduced proportion of cost and the motion time.

Method	[12] Cost (only velocity)	Cost (acceleration and velocity)	Motion time
Reduced proportion	11.77%	6.26%	6.54%

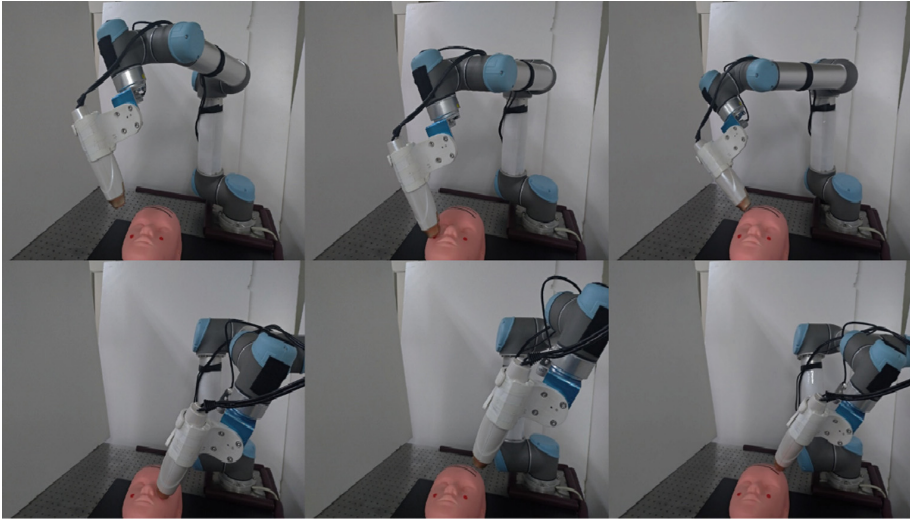


**Fig. 8.** The process of acne and wrinkles treatment.

## 4 Conclusion

This paper proposes and implement a combined eye-to-hand and eye-on-hand visual-guided system for medical treatment. The position of the acne and wrinkles are automatically recognized from the vision system. With such system, the manipulator would be guided automatically to move to target points through trajectory planning based on the required time for completion of the treatment set by medical users. Multiple cameras, the eye-on-hand and the eye-to-hand cameras are used in this study to analyze obstacles in the manipulator path of movement, and to avoid collisions during treatment. This paper validates the possibility of automated medical treatment for acne and wrinkles. With Hill Climbing algorithm searching for Z-axis rotation angle of the medical injector to optimize the manipulator pose, it is found the manipulator movement time can be further reduced by 6% at slow motion. Under the same motor speed limitation, it is confirmed that using the Hill Climbing algorithm the manipulator pose is able to complete the movement faster under than traditional motion planning algorithm.

The process proposed in this work not only can be used for the treatment of acne and wrinkles, but also for wound debridement. In the common medical practice in treating the debridement, medical staff would manually clean wounds of the patient's ulceration. Such treating operation needs to be in a slow and light manner, otherwise it will cause pain and discomfort to the patients. Since it is operated manually, the treatment time is long while the movements are repeated, which is very labor intensive. In particular, the medical staff who are currently engaged in medical care are seriously inadequate, and the problem of long-term care is imminent. Therefore, the work presented in this paper has engineering implications especially for medical treatments that are repeatable and labor-intensive.

**Acknowledgements.** The authors of greatly appreciate the support by Gold Nanotech Company for the work described herein.

## References

1. Chantharaphaichi, T., Uyyanonvara, B., Sinthanayothin, C., Nishihara, A.: Automatic acne detection for medical treatment. In: 2015 6th International Conference of Information and Communication Technology for Embedded Systems (IC-ICTES), pp. 1–6. IEEE (2015)
2. Khan, J., Malik, A.S., Kamel, N., Dass, S.C., Affandi, A.M.: Segmentation of acne lesion using fuzzy C-means technique with intelligent selection of the desired cluster. In: 37th Annual International Conference of the IEEE Engineering in Medicine and Biology Society (EMBC), pp. 3077–3080. IEEE (2015)
3. Khan, J., Malik, A.S., Kamel, N., Dass, S.C., Affandi, A.M.: Segmentation of acne lesion using fuzzy C-means technique with intelligent selection of the desired cluster. In: 2015 37th Annual International Conference of the IEEE Engineering in Medicine and Biology Society (EMBC), pp. 3077–3080. IEEE (2015)
4. Chang, C.-Y., Li, S.-C., Chung, P.-C., Kuo, J.-Y., Tu, Y.-C.: Automatic facial skin defect detection system. In: International Conference on Broadband, Wireless Computing, Communication and Applications, pp. 527–532. IEEE (2010)
5. Cula, G., Bargo, P., Nkengne, A., Kollias, N.: Assessing facial wrinkles: automatic detection and quantification. *Skin Res. Technol.* **19**(1), e243–e251 (2013)
6. Jiang, X., Liao, Q.-M.: Skin wrinkles analysis based on digital image processing. In: 2012 International Conference on Wavelet Active Media Technology and Information Processing (ICWAMTIP), pp. 50–53. IEEE (2012)
7. Ng, C.-C., Yap, M.H., Costen, N., Li, B.: Wrinkle detection using hessian line tracking. *IEEE Access* **3**, 1079–1088 (2015)
8. Viereck, U., ten Pas, A., Saenko, K., Platt, R.: Learning a visuomotor controller for real world robotic grasping using simulated depth images. arXiv preprint [arXiv:1706.04652](https://arxiv.org/abs/1706.04652) (2017)
9. Miyazaki, W., Miura, J.: Object placement estimation with occlusions and planning of robotic handling strategies. In: 2017 IEEE International Conference on Advanced Intelligent Mechatronics (AIM), pp. 602–607. IEEE (2017)
10. Reis, M.F., Leite, A.C., From, P.J., Hsu, L., Lizarralde, F.: Visual servoing for object manipulation with a multifingered robot hand. *IFAC-PapersOnLine* **48**(19), 1–6 (2015)
11. Ahmad, R., Plapper, P.: Safe and automated assembly process using vision assisted robot manipulator. *Proc CIRP* **41**, 771–776 (2016)
12. Gueta, L.B., Cheng, J., Chiba, R., Arai, T., Ueyama, T., Ota, J.: Multiple-goal task realization utilizing redundant degrees of freedom of task and tool attachment optimization. In: 2011 IEEE International Conference on Robotics and Automation, Shanghai, pp. 1714–1719 (2011)
13. Hawkins, K.P.: Analytic inverse kinematics for the universal robots UR-5/UR-10 arms. Georgia Institute of Technology (2013)



# A Novel Three Degrees of Freedom Haptic Device for Rendering Texture, Stiffness, Shape, and Shear

Vijay Kumar Pediredla<sup>(✉)</sup>, Karthik Chandrasekaran,  
Srikan Annamraju, and Asokan Thondiyath

Indian Institute of Technology Madras, Chennai, India  
pediredla.vijaykumar21@gmail.com

**Abstract.** Rendering haptic feedback, particularly tactile feedback of various objects or the environment, extends its usage in a wide variety of applications in order to provide a realistic experience for the user. Conventional methods for reproducing tactile sensations involve utilizing piezoelectric, electro-tactile, and other types of actuators, which do not lend themselves the flexibility to reproduce various surface textures in real time. In this paper, we present the design and development of a novel three Degrees of Freedom (DoF) tactile haptic device to acquire haptic feedback from a known virtual/remote environment. The haptic sensations are rendered to the user through a two-DoF spherical segment of the device consisting of an array of surfaces. The roll and pitch motion of the spherical segment provides tactile cues like texture and shear. Additional DoF provides the stiffness and shape variations based on the feedback it receives. A semi-compliant four-link mechanism, mounted on a gimbal setup, provides the necessary stiffness/shape variation effects. A prototype of the device has been fabricated and tested. The preliminary experimental results confirm the fidelity of haptic feedback to the user while interacting with the environment.

**Keywords:** Kinesthetic and tactile feedback · Haptic devices · Teleoperated systems

## 1 Introduction

Recent developments in teleoperated and virtual reality devices are bringing revolutionary changes in fields such as military, entertainment, medical, hazardous material handling, and space & underwater explorations. Even in the face of these advances, the experience of the sensation of real-time objects is limited. Haptics is the sense of touch, which is the combination of two forces, namely kinesthetic and tactile forces. Kinesthetic forces are associated with the shape, size, weight, and position of the object sensed by the muscles, tendons, and joints of the body, which are related dynamically with the force and displacement variations. Tactile forces are associated with the surface (texture, and smoothness), vibration and stiffness properties of the object sensed by the mechanoreceptors situated on the inner surface of the body. Most of the haptic devices designed for the applications mentioned above make use of only the kinesthetic

force-feedback to date. Nonetheless, the tactile force feedback through the haptic device is essential in identifying surface properties like texture and roughness, curvature, stiffness, shear, and shape rendering [1]. Reproducing these tactile representations of an object that is at a distance or in a virtual environment enables the user to acquire sensations about the tactile properties of the object, thus making the haptic feedback more transparent. This is particularly important in applications like surgical tele robotic systems, training medical apprentices, rehabilitation, mobile communication, and gaming. In the case of surgical applications, tactile sensations play a crucial role in giving information about the surface textures and stiffness of the tissues [2]. This information helps the surgeon to assess the healthiness of the tissue, detecting the tumor, and thus juncture the disease effectively [3]. The abnormalities of many organs of the body, such as lumps, and cancerous growth can be easily detected either by feeling the surface or by palpating. Also, in the case of teleoperation systems, the regular practice of kinesthetic force feedback is problematic because of the issues like time delay, actuator saturation, force sensing, and model uncertainties that unswervingly affects stability and transparency. Therefore, kinesthetic feedback can be substituted by the tactile feedback by eliminating the active devices, thus achieving the stability and safe maneuvering of the system [4].

The generation of tactile forces compared to kinesthetic forces in the haptic device or grasper is always challenging. This is because of the complications involved in the design, construction, and actuation of the tactile haptic devices. In addition, displaying tactile forces demands strong requirements on the resolution, frequency range, and dynamic range (amplitude) of the tactile display device. State-of-the-art research in creating tactile effects focused on reproducing vibration, temperature, stiffness, texture, slip contact, and its combinations of the environment [1]. Each tactile display uses a specific actuation technology to make the user perceive the tactile forces through stimulating mechanoreceptors on the surface of the skin. The commonly used tactile display technologies are electromagnetic, piezoelectric, electrostatic, and pressurized air/fluids passing through pneumatic tubes. An ideal design of a tactile display device should be able to generate widespread sensations to the user, which can replicate the remote or virtual environments. Therefore, the goal of the design is to provide the majority of features of the tactile stimulus in order to reinforce the realism about the environment.

The paper is organized as follows: Sect. 2 gives a brief overview of the recent works in the tactile display, along with some research gaps. Sections 3 and 4 describe the design methodology and analysis of the proposed device using various metrics.

## 2 Background and Related Work

Tactile texture displays are classified into two categories; one is a direct texture display, where few textures are attached to the surface of the haptic device and the surface is moved according to the movements taking place in the environment [5]. The other is an indirect texture display, where the skin is deformed by triggering through various actuators, and in some cases, symbolic inputs are given to the user according to the variation of the texture. Indirect texture interfaces cannot simultaneously represent the

majority of the aforementioned tactile effects. Therefore, these interfaces cannot be used for the applications in which sense of touch is critical. Some tactile feedback devices had been developed by researchers based on the actuation techniques like pneumatic [6, 7], magnetic [8], motor micro actuators [9], piezoelectric and voice coils [10]. Ohka et al. [11] proposed a haptic display system in which the heights of the pin matrix are varied to match the pressure distribution of the surfaces, which can provide large strokes to feel a variety of environments. However, the spatial density of the actuator limits the display resolution of the tactile cues. Each actuation technique mentioned here has its own specific tactile property in replicating the feel of the virtual or remote environment. Representing most of the tactile effects in one haptic device is not possible without either increasing bulkiness or mechanical complexity. Most of the research work is focussed on displaying the various combination of tactile effects amongst slip contact [12], skin stretch [10], vibrations [13, 14], shape and texture [5], which do not provide the important haptic modality, stiffness. Few proposed devices by researchers can render stiffness combined with size and shape [15], and stiffness combined with texture [16, 17] are unable to provide either texture or shape. These interfaces are limited in their resolution and workspace. Nevertheless, any of these combinations cannot give the feel of interacting with the natural environment because of the lack of rendering the proper combination of the haptic stimulus. Tactile display devices [2, 5], which belong to the category of direct texture display, enables the user to experience the combinations of tactile effects. Okamoto et al. [14] developed a vibrotactile display in which the change in roughness and texture is perceived through the vibrations by an actuator. However, when the variation of texture changes rapidly, intense vibrations from the actuator subjugates the feel of a real object. Whitmire et al. [5] developed one degree of freedom haptic revolver which renders touch sensation of different textures. These textures are realized by interchanging the main contact wheel with wheels equipped with different textures on its surface to render various environments. The limited surface area on the wheel remains as a drawback in rendering diverse textures. Lederman et al. [18] demonstrated that rendering of stiffness combined with the texture can provide good haptic fidelity for the user. This is because of the dominating nature of perceptual cues of material properties than geometric properties.

### 3 Design and Implementation of the Haptic Device

In this paper, a three Degrees of Freedom (DoF) tactile haptic device is proposed, wherein two rotations (roll and pitch) adjust the position of a spherical segment equipped with an array of textures for displaying different surface tactile effects. The third DoF is to represent the stiffness of the object in the direction of force applied. By using the same actuator used for reproducing the stiffness, vibrations and shape can also be stimulated to the user, in order to get the feel of diverse textures and geometric shapes. Out of the three DoF, two DoF (pitch and roll) give information about the texture, and shear in two dimensions. The third DoF gives the information related to the stiffness of the object. All three DoF combined together can provide shape information about the virtual/remote object.

### 3.1 Kinematic Model of the Haptic Device

The kinematic model of the haptic device is shown in Fig. 1. The  $J_i$ 's represent the joints in the kinematic model, wherein  $J_1$ ,  $J_2$ , and  $J_3$  are active joints with three rotary actuators in which  $J_1$  and  $J_2$  provide the pitch and roll DoF, and  $J_3$  provides the linear motion using a four-link mechanism.  $J_4$ ,  $J_5$ , and  $J_6$  are passive joints, in which  $J_4$  and  $J_5$  are rotary joints, and  $J_6$  is a prismatic joint. The length of the links between the joints  $J_3$  and  $J_4$ ,  $J_4$  and  $J_5$ ,  $J_3$  and  $J_6$  are given by  $l_1$ ,  $l_2$ , and  $l_3$  respectively, as shown in the kinematic model in Fig. 1.

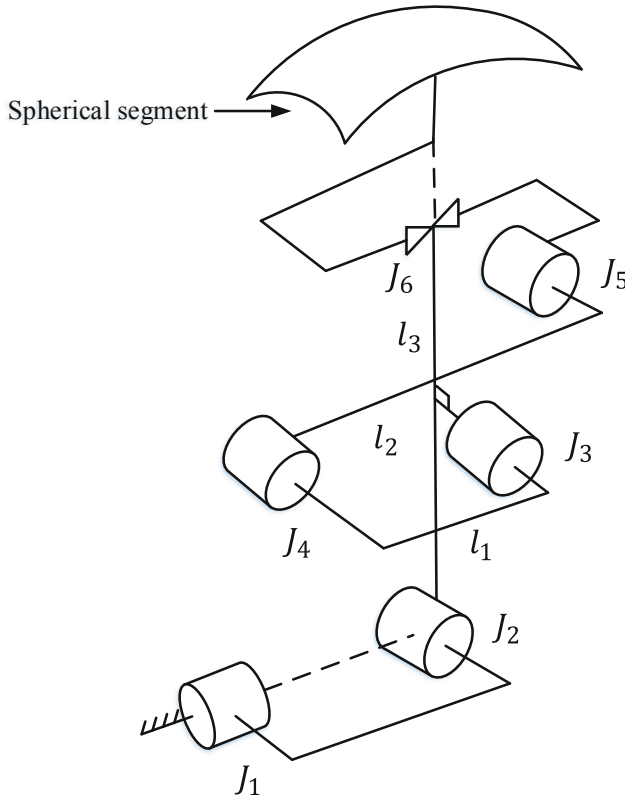


**Fig. 1.** Kinematic model of the 3-DoF haptic device

A Computer Aided Design (CAD) of the haptic device is shown in Fig. 2. The user's finger is placed on the spherical segment in order to experience the virtual/remote environment. An assortment of different textures pasted on top of the hemispherical surface allows the user to switch between textures on the fly, as and when the texture of the virtual or remote object varies. This experience of sensations brings about the perception of different objects textures and consequently immerses the user in the illusory world. In addition, this device greatly reduces the intervention of human in the loop (HITL) and thus making the haptic device reliable and simple to operate.

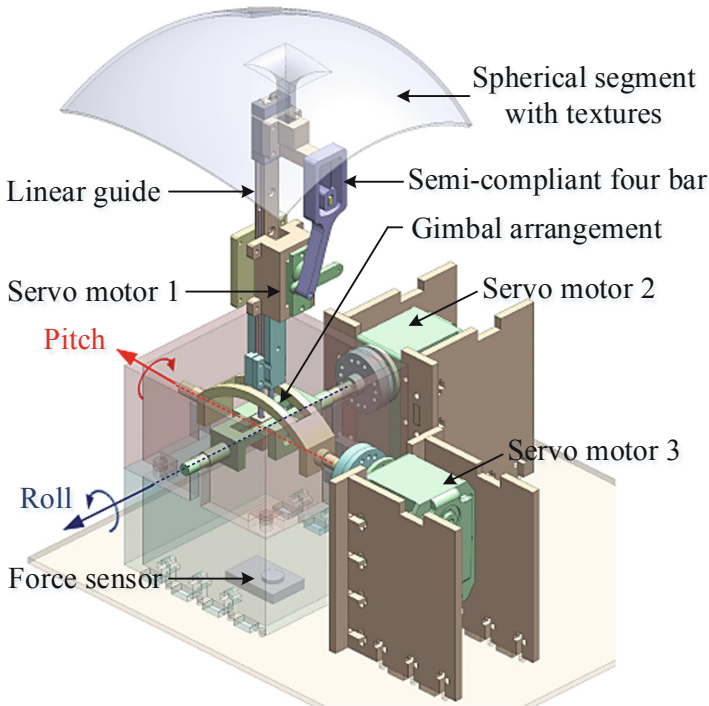


**Fig. 2.** A CAD model of the 3-DoF haptic device

### 3.2 System Design

The proposed haptic device is designed to generate tactile feedback in three degrees of freedom. The device has a spherical segment with several patches of textures attached to it. The user is meant to place his/her finger over the spherical segment and the spherical segment is moved relative to the finger. This produces different subsets of haptic sensations (stiffness and texture, texture and shape, etc.) to the user. The spherical segment can move in both pitch and roll DoF with the aid of a gimbal arrangement as shown in Fig. 2. Both the pitch and roll DoF are actuated by two motors (Dynamixel RX-64 model), namely servomotor 2 and servomotor 3, which are capable of position control. By design, the gimbal ensures decoupling between the pitch and roll DoF. The rotation of motors is joint limited to prevent the intersection of the spherical segment with other components in the assembly. To provide varying stiffness to the spherical segment the haptic device has a semi-compliant crank slider mechanism connected to servomotor 1. By varying the impedance of the servomotor 1, different stiffness can be obtained, when a user exerts a force on the spherical segment.

### 3.3 Semi-compliant Four-Link Mechanism

An oil-free linear guide (Igus DryLin miniature slide) guides the translatory motion of the spherical segment. The servomotor 1 driving the translatory motion of the spherical



segment is rigidly connected to the linear guide and has a semi-compliant four-link that converts the rotary motion of the servo to linear motion. The semi-compliant four-link is designed with a flexure in tension as shown in Fig. 3, which overcomes the limitations of flexures when they are loaded in compression [19]. Because of the way the flexure is positioned in the four-link assembly, any force that the motor/user exerts on the spherical segment appears as a tensile load on the flexure as shown in Fig. 3.

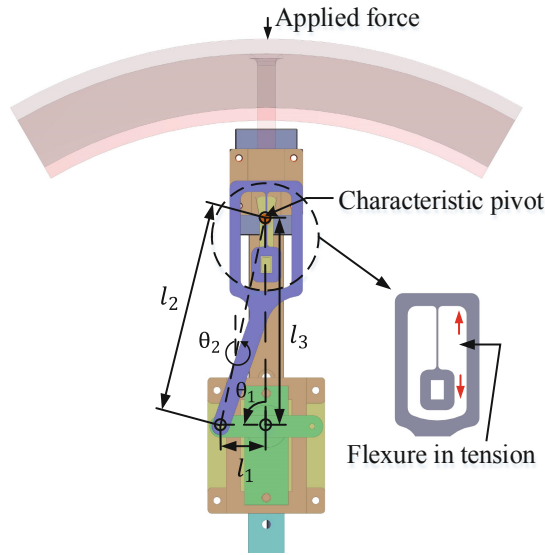


**Fig. 3.** Semi-compliant four-link mechanism

Utilizing the flexure on the four-link assembly also has the added advantage of a backlash-free mechanism with a minimal number of moving components. A large deflection Finite Element Analysis (FEA) was carried out on the flexure to assess its performance using standard commercial FEA software. A tensile load of 7 N was applied at the base of the flexure, which represents the maximum haptic force that the device can exert on the user's hand. A displacement input corresponding to the maximum deflection of the flexure was applied to the flexure as shown in Fig. 4. FEA results show that von Mises stress was well within the allowable limit of the material of the prototype. The flexure is contained within an envelope that transfers the haptic force from the servomotor 1 to the flexure.

A pseudo-rigid-body model [20] is used to model the semi-compliant four-link mechanism. The flexure of the four-link is replaced by a revolute joint (characteristic pivot) placed at half of its length and a torsional spring as shown in Fig. 3.

The relationship between the rotary motion  $\theta_1$  of the servo motor1 and the linear deflection of the guide  $x$  are given by Eqs. 1 and 2,

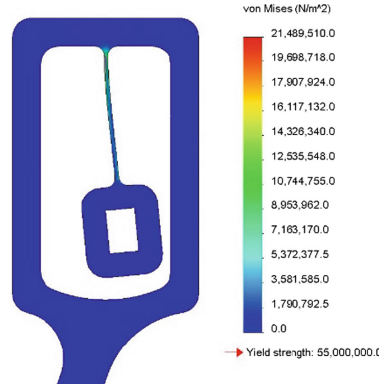


**Fig. 4.** Finite element analysis of the flexure in tension

$$\theta_2 = \sin^{-1} \left( \frac{-l_1 \sin(\theta_1)}{l_2} \right) \quad (1)$$

$$x = l_1 \cos(\theta_1) + l_2 \cos(\theta_2) - l_3 \quad (2)$$

where  $l_1 = 12.5$  mm,  $l_2 = 58$  mm,  $l_3 = 57$  mm.

### 3.4 Working of the Prototype

When a user applies a force, the stiffness and texture corresponding to the virtual/remote environment are experienced through the haptic device interface. A force sensor (Honeywell - FSAGPDXX1.5LC5B5 - force range up to 7 N), placed below the line of action of the applied force, measures the force applied by the user. The servomotor 1 modulates the position of the spherical segment corresponding to the stiffness of the environment being simulated based on Eqs. 1 and 2. The rate of change of the position can also be varied corresponding to the rate of change of the force. The user realizes the shape of the object either by directly experiencing the irregular surface texture or by controlling the position provided by the servomotor 1 in order to feel the variations in the shape equivalent to the virtual/remote environment. The method of representing the shape by position control of motor requires very high resolution and precise control over the position, and coordination between all the three servo motors. This can be further improved in the future designs for realistic haptic (in this case, it is shape) feedback. Shear haptic feedback is provided by controlling the speed of the servomotor 2 and servomotor 3. The overall experimental setup of the three DoF haptic device is shown in Fig. 5.

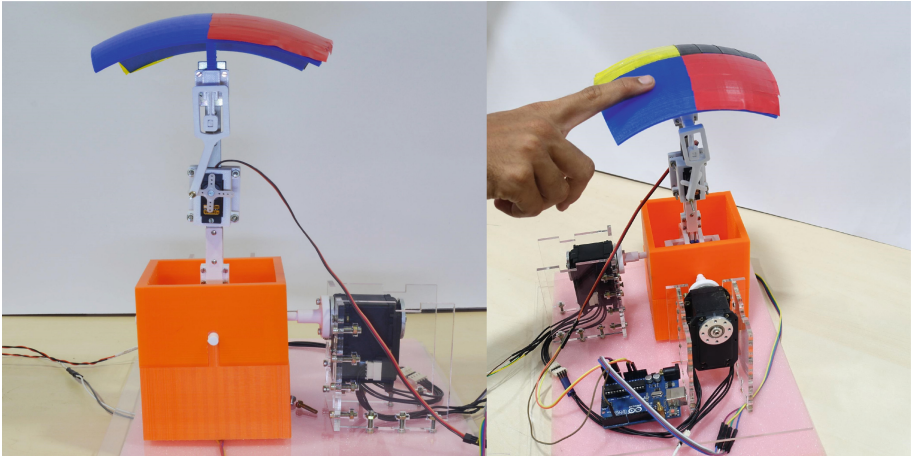


**Fig. 5.** Experimental setup of the 3-DoF haptic device

## 4 Performance Analysis

Preliminary experiments have been carried out on the haptic device to analyze the performance. The spherical segment is separated into four sections, and each section is attached with a different texture resembling the four virtual/remote objects or environments. It is assumed here that, the location of each environment with respect to another environment and the stiffness of the environment is known. The stiffness of the four different linear virtual/remote environments (stiffness varying linearly),  $k_1, k_2, k_3, k_4$  are 2, 1.5, 1, 0.75 N/mm respectively. However, the non-linear virtual/remote environments (stiffness varying non-linearly) can also be precisely implemented by using a linear motor in place of the existing four-link mechanism.

### 4.1 Force Analysis

To analyze the stiffness rendered by the haptic device, a force is applied on each textural surface affixed to the spherical segment. The input force is gradually varied from 0 to 7 N, remains constant at 7 N, and again varies from 7 to 0 N as shown in Fig. 6(a). As a result of applied force, and the predefined stiffness of the section on the spherical segment, there will be displacement. The displacement of the segment from its equilibrium position is measured. Figure 6(b) shows the force-displacement curves of four sections with different stiffness on the spherical segment. Haptic devices demand a high degree of accuracy in generating feedback to make the user's interaction with the environment natural and dynamic. This figure clearly depicts that the proposed haptic device represents the virtual/remote environments accurately.

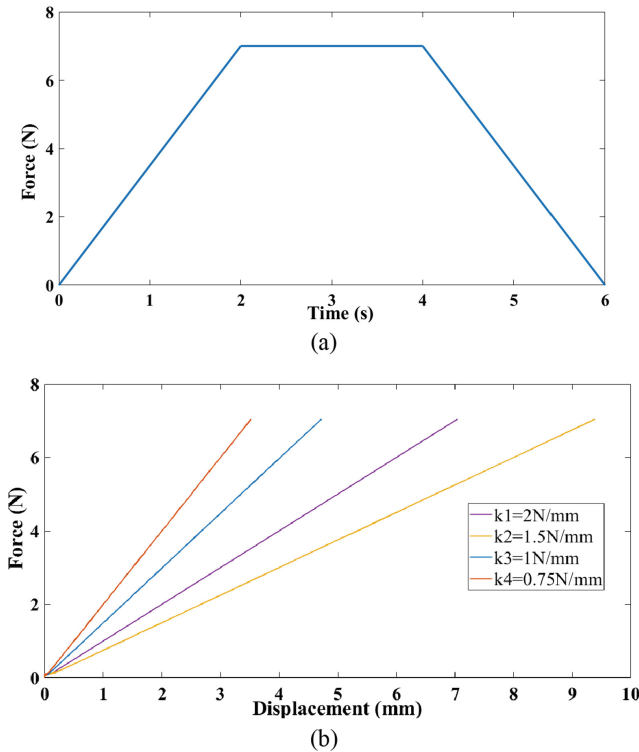


**Fig. 6.** (a) Input force profile (b) Force-displacement curves for different textures

## 5 Results and Discussions

The functioning of the prototype and its results portray the efficacy of using the proposed haptic device in rendering the virtual/remote environments. The system design permits the user to experience a range of haptic effects like texture, stiffness, shape, and shear. This haptic device can be used in many applications; particularly in teleoperated surgical systems, where the surgeon can feel the properties of the tissues especially stiffness. This diagnosis assists the surgeon in identifying many diseases. One of the limitations of the prototype is its bulkiness. However, miniaturizing the prototype consequently reduces the workspace, and because of the availability of limited workspace for each texture on the hemispherical segment, experiencing the texture of the surface is thus limited. The device can be modified by replacing mere textures with belt mechanism for each texture. This mechanism enables the user to experience the haptic effects of different surfaces of longer length and simultaneously making the device portable. This design widens the applications similar to the existing handheld haptic devices.

Several design concepts were considered for realizing a device that can provide rapid switching between different textures. Textures that needs to be simulated can be fixed to a long belt in two different ways as shown in Fig. 7. A long belt that has

several tracks of different textures can be wound on two cylinders – a supply reel and a take-up reel. Implementation as shown in Fig. 7(a) provides textures of very long length but only fewer textures are possible with this design. Implementation as shown in Fig. 7(b) shows that the belt is discretized in smaller zones enabling many more textures of smaller lengths. Rapid switching between different textures becomes time consuming especially switching between textures that are placed at the extreme ends of the belt since the belt has to physically wind from one side to the other to reach the other extreme. In addition, providing stiffness to the texture with this kind of implementation becomes challenging. Further work is in progress to analyze the possibility of this configuration in the proposed device.

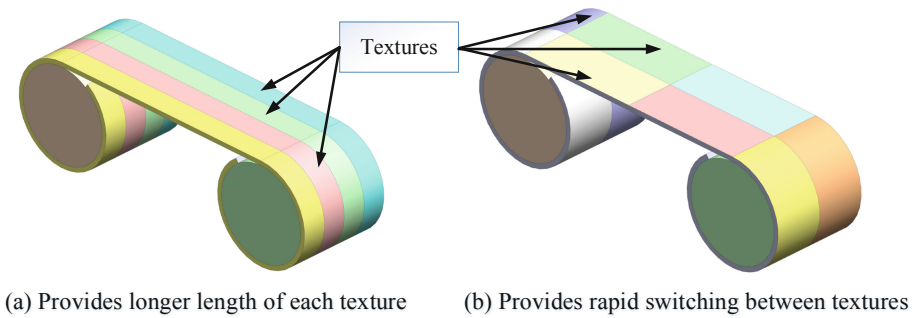


**Fig. 7.** CAD models of the design proposed

## 6 Conclusions and Future Work

The proposed design is unique in terms of rendering different tactile effects in two degrees of freedom using an array of textures that are affixed to a spherical segment that can pitch and roll, and translate in another degree of freedom to simulate the stiffness of a virtual/remote environment. Delivering this kind of feedback would enrich the user's ability to comprehend different properties of the virtual/remote objects, and thus enabling the user to sense and manipulate the objects accordingly. This work can be extended in miniaturizing the prototype and concurrently enhancing the workspace by belt mechanism to increase its uniformity and fidelity in rendering various environments. Impedance control algorithms can be implemented to the system to enhance the accuracy and feel of the virtual or remote objects.

## References

1. Bello, F., Kajimoto, H., Visell, Y. (eds.) Haptics: Perception, Devices, Control, and Applications: 10th International Conference, Proceedings, EuroHaptics 2016, London, UK, 4–7 July 2016, vol. 9774. Springer (2016)
2. Ravensbergen, S.K., Rosielle, P.C.J.N., Steinbuch, M.: Improving maneuverability and tactile feedback in medical catheters by optimizing the valve toward minimal friction. *J. Med. Devices* **3**(1), 011003 (2009)

3. Tendick, F., Sastry, S.S., Fearing, R.S., Cohn, M.: Applications of micro mechatronics in minimally invasive surgery. *IEEE/ASME Trans. Mechatron.* **3**(1), 34–42 (1998)
4. Prattichizzo, D., Pacchierotti, C., Cenci, S., Minamizawa, K., Rosati, G.: Using a fingertip tactile device to substitute kinesthetic feedback in haptic interaction. In: *International Conference on Human Haptic Sensing and Touch Enabled Computer Applications*, pp. 125–130. Springer, Heidelberg, July 2010
5. Whitmire, E., Benko, H., Holz, C., Ofek, E., Sinclair, M.: Haptic revolver: touch, shear, texture, and shape rendering on a reconfigurable virtual reality controller. In: *Proceedings of the 2018 CHI Conference on Human Factors in Computing Systems*, p. 86. ACM, April 2018
6. Moy, G., Wagner, C., Fearing, R.S.: A compliant tactile display for teletaction. In: *IEEE International Conference on Robotics and Automation. Proceedings, ICRA 2000*, vol. 4, pp. 3409–3415. IEEE (2000)
7. King, C.H., Culjat, M.O., Franco, M.L., Bisley, J.W., Dutson, E., Grundfest, W.S.: Optimization of a pneumatic balloon tactile display for robotic surgery based on human perception. *IEEE Trans. Biomed. Eng.* **55**(11), 2593–2600 (2008)
8. Stregue, J., Talbi, A., Pernod, P., Preobrazhensky, V.: New magnetic microactuator design based on PDMS elastomer and MEMS technologies for tactile display. *IEEE Trans. Haptics* **3**(2), 88–97 (2010)
9. Quek, Z.F., Provancher, W., Okamura, A.: Evaluation of skin deformation tactile feedback for teleoperated surgical tasks. *IEEE Trans. Haptics* (2018)
10. Fukumoto, M., Toshiaki, S.: ActiveClick: tactile feedback for touch panels. In: *CHI 2001, Extended Abstracts*, pp. 121–122. ACM (2001)
11. Ohka, M., Kato, K., Fujiwara, T., Matsukawa, S., Mitsuya, Y.: A tactile-haptic display system using micro-actuator array. In: *2005 IEEE International Symposium on Micro-NanoMechatronics and Human Science*, pp. 23–28. IEEE, November 2005
12. Murphy, T.E., Webster, R.J., Okamura, A.M.: Design and performance of a two-dimensional tactile slip display. In: *Proc. Eurohaptics*, 2004
13. Summers, I.R., Chanter, C.M.: A broadband tactile array on the fingertip. *J. Acoustical Soc. Am.* **112**(5), 2118–2126 (2002)
14. Asano, S., Okamoto, S., Yamada, Y.: Vibrotactile stimulation to increase and decrease texture roughness. *IEEE Trans. Hum. Mach. Syst.* **45**(3), 393–398 (2014)
15. Sun, Y., Yoshida, S., Narumi, T., Hirose, M.: Handheld haptic interface for rendering size, shape, and stiffness of virtual objects. In: *Proceedings of the 2018 ACM International Conference on Interactive Surfaces and Spaces*, pp. 411–414. ACM, November 2018
16. Benko, H., Holz, C., Sinclair, M., Ofek, E.: Normaltouch and texturetouch: high-fidelity 3d haptic shape rendering on handheld virtual reality controllers. In: *Proceedings of the 29th Annual Symposium on User Interface Software and Technology*, pp. 717–728. ACM, October 2016
17. Wiertelowski, M., Leonardis, D., Meyer, D.J., Peshkin, M.A., Colgate, J.E.: A high-fidelity surface-haptic device for texture rendering on bare finger. In: *International Conference on Human Haptic Sensing and Touch Enabled Computer Applications*, pp. 241–248. Springer, Heidelberg, June 2014
18. Lederman, S.L., Klatzky, R.L.: Relative availability of surface and object properties during early haptic processing. *J. Exp. Psychol. Hum. Percept. Perform.* **23**(6), 1680–1707 (1997)
19. Dearden, J., Grames, C., Jensen, B.D., Magleby, S.P., Howell, L.L.: Inverted L-Arm gripper compliant mechanism. *J. Med. Devices* **11**(3), 034502 (2017)
20. Howell, L.L.: *Compliant Mechanisms*. Wiley, New York (2001)



# Real-Time Resolution of the Forward Kinematic Model for a New Spherical Parallel Manipulator

Houssem Saafi<sup>1,2</sup>, Med Amine Laribi<sup>3</sup>✉, and Said Zeghloul<sup>3</sup>

<sup>1</sup> Mechanical Laboratory of Sousse (LMS), National Engineering School of Sousse, University of Sousse, 4000 Sousse, Tunisia  
houssem.saafi@gmail.com

<sup>2</sup> Preparatory Institute for Engineering Studies of Gafsa, University of Gafsa, 2000 Gafsa, Tunisia

<sup>3</sup> Department of GMSC, Pprime Institute, CNRS - University of Poitiers, ENSMA - UPR 3346, Poitiers, France  
{med.amine.laribi,said.zeghloul}@univ-poitiers.fr

**Abstract.** This paper discusses the comparison between three methods used to solve the Forward Kinematic Model (FKM) of a New Spherical Parallel Manipulator (New SPM). The three methods are: a classical method (Classical FKM) using three sensors installed in the base, an improved method (Improved FKM) using an extra sensor installed on the moving platform and a serial method (Serial FKM) using three sensors installed on one leg of the parallel manipulator. Both the accuracy and the calculation time are compared. The serial approach was chosen, thanks to its simplicity and the fast calculation time, despite the small error compared to the other methods.

**Keywords:** Spherical Parallel Manipulator · Forward Kinematic Model · Minimally Invasive Surgery

## 1 Introduction

Master devices are systems used to control the motion of virtual objects [1, 2] or real robots [3, 4]. Many master devices have a parallel architecture thanks to their high stiffness, their load capability and their low weight. Spherical parallel manipulators (SPMs) are a class of parallel mechanisms. They offer three degrees of freedom of pure rotation (3-RRR). Some haptic devices have a parallel spherical structure, such as the haptic device proposed by [5] and [6] dedicated to control the orientation of a camera, and the haptic device proposed for use in Minimally Invasive Surgery (MIS) by [7].

A first prototype of the master device (Fig. 1) was proposed in the work of [7] to control the motion of a surgical slave robot (Fig. 2). This prototype has a spherical parallel architecture. The geometric parameters of this device were optimized to reach a MIS prescribed workspace. In this previous work, the self-rotation was not considered during the optimization process. This led to the presence of the parallel singularity in the workspace of the SPM. The effects of the parallel singularity are the amplification of errors in the kinematic transformation from the joint Space to the Cartesian space

(Forward Kinematic Model (FKM)) and the amplification of the actuated joint torques. In [8, 9], we proposed the addition of a redundant sensor to eliminate the effect of parallel singularities on the FKM. By this way, we improved the accuracy of the FKM within the singular region and we reduced the complexity of the model. In addition, it makes it possible to run in Real-Time.



**Fig. 1.** First prototype of the master device.

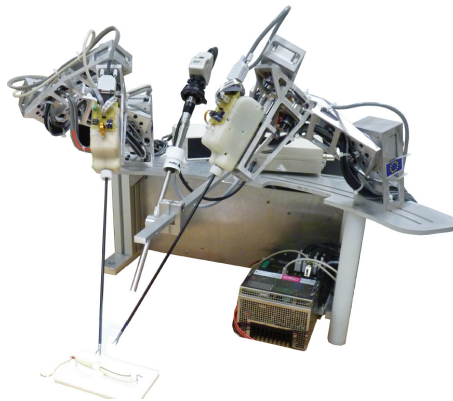


**Fig. 2.** Surgical robots.

Parallel singularities also amplify the required joint torques to values that violate the torque limits. To cope with this issue, in [10], we proposed the use of a redundant actuator as well as a specific control scheme. In [10, 11], we chose to replace one passive joint by an active one. In this case, a minor mechanical design change is needed. This approach eliminates the effects of parallel singularities for torque control and guarantees the continuity of the actuated joint torques. Those solutions give suitable results. However, the additional actuator increases the weight of the moving platform.



In this paper a new solution is proposed. The kinematic of one leg of the classical Spherical Parallel Manipulator is changed. The forward kinematic model of the new master device is solved using three approaches. A comparison like the one made in [12] for the classic SPM is carried on. The more suitable FKM is chosen and implemented to control the motion of the surgical slave robot.

The paper is organized as follows: in Sect. 2, the kinematic of the new SPM is studied. In Sect. 3, the three approaches to solve the Forward Kinematic Model are presented. An experimental comparison of the three models is carried out in Sect. 4. Finally, Sect. 5 provides a conclusion to the paper.

## 2 Kinematic of the New Spherical Parallel Manipulator

In order to eliminate the parallel singularity from the workspace of the spherical parallel manipulator, the kinematic of one leg is changed. One leg with RRR architecture is replaced by a leg with URU architecture. Two legs are kept the same in order to maintain the spherical behavior of the device. The New SPM has three degrees of freedom of pure rotation described by the Euler angles  $\psi$ ,  $\theta$  and  $\varphi$ . The kinematic of the new manipulator is presented in Fig. 3. [5] proposed a similar architecture to eliminate interference between legs for the haptic device.

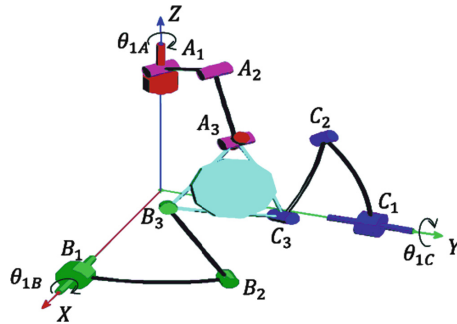


**Fig. 3.** New Spherical parallel manipulator.



**Fig. 4.** New prototype of the haptic device.

A real master device has been developed (Fig. 4). The prototype was equipped with sensors and actuators. This prototype is designed to control the motion of the surgical robot. For this, we need to solve the Forward Kinematic model of the new SPM in Real-Time. In the next Section, we discuss the resolution of the Forward Kinematic Model.

### 3 Forward Kinematic Model Resolution

In this section, we present three methods to solve the Forward Kinematic Model of the New SPM. The first method is a classic method where three sensors are installed on the base (Classical FKM), the second method is based on the use of an extra sensor placed on the moving platform (Improved FKM) and the third method is a serial method where three sensors are installed on one leg of the parallel manipulator.

#### 3.1 Classical Method to Solve the Forward Kinematic Model

The Forward Kinematic Model express the orientation of the moving platform described by the Euler angle  $(\psi, \theta, \phi)$ , using the active joint angles  $(\theta_{1A}, \theta_{1B}, \theta_{1C})$ . [13] proposed a method based on the input/output equations of spherical four-bar mechanisms to solve the forward kinematic model of the classical spherical parallel manipulator. This technique is considered for the new SPM. Only one spherical four-bar mechanism is considered for this structure (Fig. 5). It is composed of the distal links of the legs B and C, the moving platform and a fictive link between the joints with axis  $Z_{2B}$  and the axis  $Z_{2C}$ . The input/output equation of the spherical four-bar mechanism is:

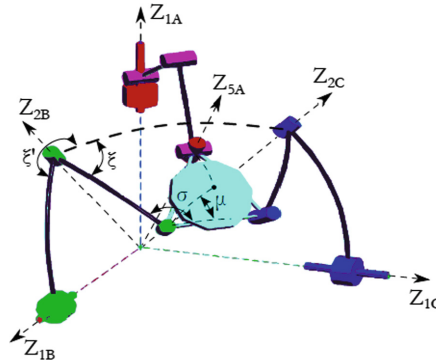


Fig. 5. Considered Four-Bar mechanism.

$$L_1(\xi)\cos \sigma + M_1(\xi)\sin \sigma + N_1(\xi) = 0 \quad (1)$$

To solve the FKM of the new SPM, another equation is required. This equation can be obtained by expressing  $Z_{5A}$  using the forward kinematic of the leg B then by solving the equation obtained by:

$$Z_{5A} \cdot Y_{1A} = 0 \quad (2)$$

After arrangement, we get the following expression:

$$L_2(\xi)\cos \sigma + M_2(\xi)\sin \sigma + N_2(\xi) = 0 \quad (3)$$

From Eqs. (1) and (3), we can express  $\cos \sigma$  and  $\sin \sigma$ . The square sum of  $\cos \sigma$  and  $\sin \sigma$  gives the following equation where only  $\xi$  is unknown:

$$\begin{aligned} & N_2^2 L_2^2 + 2L_1 M_1 L_2 M_2 - 2L_1 N_1 L_2 N_2 \\ & + N_2^2 M_1^2 - L_2^2 M_1^2 - 2M_1 N_2 M_2 N_2 - M_2^2 L_1^2 \\ & - N_1^2 L_2^2 - N_1^2 M_2^2 = 0 \end{aligned} \quad (4)$$

All the solutions of  $\sigma$  and  $\xi$  are obtained by solving the Eq. (4). The orientation of the moving platform can be obtained by solving the forward kinematic of the leg B.

### 3.2 Improved Method to Solve the Forward Kinematic Model

An extra sensor is installed in the joint with the axis  $Z_{3B}$ . This sensor gives the angle  $\sigma$ . In this case, only  $\xi$  is unknown. The unique solution of  $\xi$  is solved using the Eqs. (1) and (3). The orientation of the moving platform can be obtained by solving the forward kinematic of the leg B, as the previous method.

This method gives a direct and unique solution to the FKM. However, it requires the use of four sensors instead of three sensors. In the next paragraph, we propose a serial method to solve the Forward Kinematic Model of the new SPM.

### 3.3 Serial Method to Solve the Forward Kinematic Model

This method consists in determining the orientation of the moving platform using the forward model of one leg of the new SPM by using a serial approach. The leg B was equipped with three sensors Fig. 6.

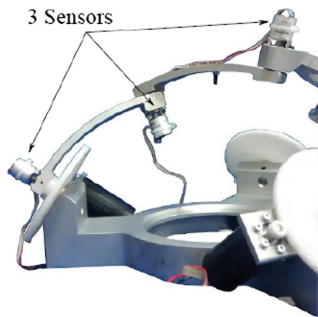


**Fig. 6.** Leg B with three sensors.

The orientation of the moving platform can be expressed using the forward model of the leg B.

In the next section, we compare experimentally the three methods of solving the FKM.

#### 4 Experimental Comparison Between the Three Techniques of Solving the FKM

The three method are implemented using C++ language on a PC with a processor running at 3.16 GHz. The Table 1 presents the calculation times of the models.

**Table 1.** Calculation time of the three Forward Kinematic Models

Model	Calculation time	Description
Classic FKM	<90 $\mu$ s	3 sensors in the base
Improved FKM	<60 $\mu$ s	4 sensors
Serial FKM	<15 $\mu$ s	3 sensors in the leg B

As expected, the serial method has the best calculation time which is 4 times less than the improved FKM (FKM with four sensors). A study is made in order to compare the orientation of the moving platform obtained by the three models. The sensors were calibrated by fixing the moving platform in a reference position. A mechanical part was designed to block the moving platform (Fig. 7).

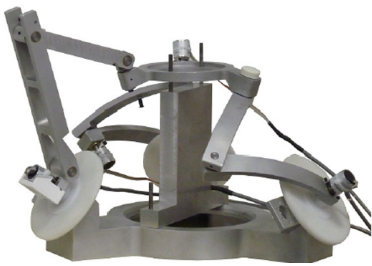


**Fig. 7.** Calibration process.

After the calibration process, the sensor was connected to a PC based controller via a National Instrument data acquisition card to measure the angular values of the joints. In order to compare the accuracy of the three models, we blocked mechanically the self-rotation by locking the joint with axis Z5A (Fig. 8). In this case, the three models must give a null value to the self-rotation. The self-rotations given by the three is the error of the FKMs since it must be zero.

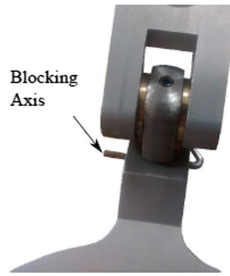


**Fig. 8.** Blocking  $Z_{5A}$  joint.

The orientation of the moving platform was varied. The results of the three models are shown in Fig. 9. We can see that the self-rotation for the three models is equal to zero. Figure 10 shows the error distributions for the three models. The three models have a normal distribution. As expected, the serial FKM gives the less accurate solution. However, we can see that the difference is not flagrant. The Table 2 shows the parameters of the distribution of each model. The mean value of the distribution corresponds to the calibration errors and the standard deviation corresponds to sensitivity of the model related to the sensor errors.

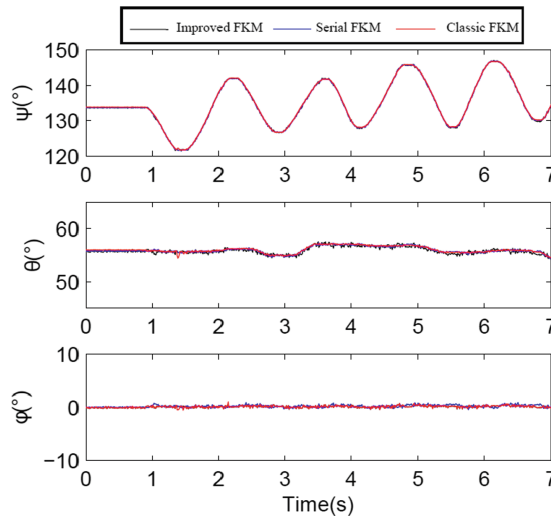


**Fig. 9.** Orientation of the moving platform using the three models.

The errors of the improved FKM and the classical FKM are very close because there is no parallel singularity in the workspace of new SPM.

The Table 2 shows the accuracy of the Serial FKM which is acceptable. The simplicity and the short calculation time of the serial FKM are the most advantages despite its small error of resolution compared to other models.

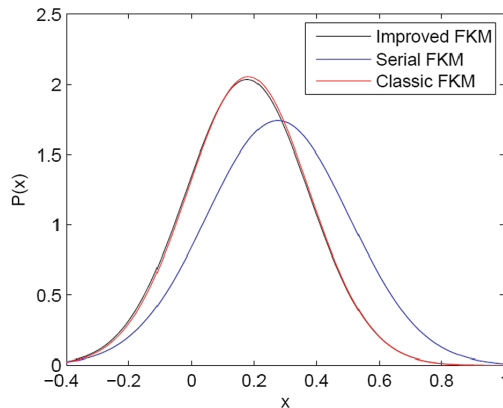


**Fig. 10.** Error Distributions for the tree models.

**Table 2.** Calculation time of the three Forward Kinematic Models

Model	Mean value $\mu$	Standard deviation $\sigma$
Classic FKM	0.182°	0.193°
Improved FKM	0.178°	0.196°
Serial FKM	0.276°	0.229°

## 5 Conclusion

In this paper, a new singularity-free spherical parallel manipulator used as a master device was developed and presented. In order to control the motion of a surgical slave robot in Real-Time, three methods to solve the Forward Kinematic Model are compared. These models are: a classical approach using three sensors installed on the base, an improved method using three sensors installed on the base and an extra sensor installed on the moving platform and a serial approach using sensors installed on one leg of the Parallel Manipulator. The comparison shows that the serial FKM leads to a fast calculation time however it has slightly more calculation error. This model was chosen and implemented to control the motion of the slave robot. Future work will focus on the implementation of the haptic control.

## References

1. Park, W., Kim, L., Cho, H., Park, S.: Design of haptic interface for brickout game. In: IEEE International Workshop on Haptic Audio-visual Environments and Games, HAVE 2009, pp. 64–68. IEEE (2009)
2. Gosselin, F., Jouan, T., Brisset, J., Andriot, C.: Design of a wearable haptic interface for precise finger interactions in large virtual environments. In: First Joint Eurohaptics Conference, 2005 and Symposium on Haptic Interfaces for Virtual Environment and Teleoperator Systems, World Haptics 2005, pp. 202–207. IEEE (2005)

3. van den Bedem, L., Hendrix, R., Rosielle, N., Steinbuch, M., Nijmeijer, H.: Design of a minimally invasive surgical teleoperated masterslave system with haptic feedback. In: International Conference on Mechatronics and Automation, ICMA 2009, pp. 60–65. IEEE (2009)
4. Tobergte, A., Helmer, P., Hagn, U., Rouiller, P., Thielmann, S., Grange, S., Albu-Schaffer, A., Conti, F., Hirzinger, G.: The sigma. 7 haptic interface for MiroSurge: a new bi-manual surgical console. In: 2011 IEEE/RSJ International Conference on Intelligent Robots and Systems (IROS), pp. 3023–3030. IEEE (2011)
5. Birglen, L., Gosselin, C., Pouliot, N., Monsarrat, B., Laliberté, T.: SHaDe, a new 3-DOF haptic device. *IEEE Trans. Robot. Autom.* **18**(2), 166–175 (2002)
6. Gosselin, C., St Pierre, E., Gagne, M.: On the development of the agile eye. *Robot. Autom. Mag.* **3**(4), 29–37 (1996)
7. Chaker, A., Mlika, A., Laribi, M.A., Romdhane, L., Zeghloul, S.: Synthesis of spherical parallel manipulator for dexterous medical task. *Front. Mech. Eng.* **7**(2), 150–162 (2012)
8. Saafi, H., Laribi, M.A., Zeghloul, S.: Improvement of the direct kinematic model of a haptic device for medical application in real time using an extra sensor. In: 2014 IEEE/RSJ International Conference on Intelligent Robots and Systems (IROS 2014), pp. 1697–1702. IEEE (2014)
9. Saafi, H., Laribi, M.A., Zeghloul, S.: Forward kinematic model improvement of a spherical parallel manipulator using an extra sensor. *Mech. Mach. Theory* **91**, 102–119 (2015)
10. Saafi, H., Laribi, M.A., Zeghloul, S.: Redundantly actuated 3-RRR spherical parallel manipulator used as a haptic device: improving dexterity and eliminating singularity. *Robotica* **33**(05), 1113–1130 (2015)
11. Saafi, H., Laribi, M.A., Zeghloul, S.: Optimal haptic control of a redundant 3-RRR spherical parallel manipulator. In: 2015 IEEE/RSJ International Conference on Intelligent Robots and Systems (IROS 2015). IEEE (2015)
12. Saafi, H., Vulliez, M., Zeghloul, S., Laribi, M.A.: A new serial approach of the forward kinematic model of spherical parallel manipulators for real-time applications. *Proc. Inst. Mech. Eng. Part C J. Mech. Eng. Sci.* **232**(4), 677–684 (2018)
13. Bai, S., Hansen, M.R., Angeles, J.: A robust forward displacement analysis of spherical parallel robots. *Mech. Mach. Theory* **44**(12), 2204–2216 (2009)



# Kinematic Design of a Double Pantographic Mechanism for the Intracranial Echography on Incubated Newborns

Terence Essomba<sup>(✉)</sup> and Jia-Yu Hsieh

National Central University, Zhongli City 32001, Taiwan (R.O.C.)  
tessomba@cc.ncu.edu.tw

**Abstract.** Some newborn babies require particular cares and are therefore placed in neonatal incubators. Intracranial ultrasound examinations are regularly performed in order to monitor the development of their brain. Due to the repetitiveness and unavailability associated with this clinical task, the design of a robotic system capable of performing this task is proposed. The manipulation of an ultrasound probe inside a neonatal incubator is studied using a motion capture system. The kinematic specifications associated with this clinical task are established. A mechanical architecture based on two combined pantographic linkages is proposed. One pantographic mechanism performs the linear positioning of the end effector around a center of rotation. The orientation of the ultrasound probe around another center of rotation is mainly provided by a second pantographic linkage. The forward and inverse kinematic models are calculated to study the linear and angular positioning of the mechanism. The trajectories measured during the motion capture experiments are then tested on the mechanism to validate its suitability with the intracranial echography on newborns inside incubators.

**Keywords:** Intracranial echography · Pantographic mechanism · Kinematics · Remote center of motion · Motion capture

## 1 Introduction

Before the age of 9 to 18 months, the skull is composed of several bones. A gap formed between the cranial bones sections is located in the frontal skull and is called the fontanelle. These bones are subject to an ossification that progressively closes the skull as illustrated in Fig. 1(a). The fontanelle is composed of soft tissues that allow the propagation of ultrasonic waves. In order to perform an examination of the newborn patient's intracranial anatomy, particularly the development of the brain, the use of ultrasound is possible [1, 2]. A specific ultrasound probe can be used like the model shown in Fig. 1(b). In Taiwan, intracranial ultrasound is performed on a large number of newborns as a routine examination. The cost is relatively low and it allows to detect many types of brain development issues such as brain disease, trauma or tumor [3]. Intracranial Ultrasound (ICU) is an easily available and time-saving clinical examination for such cases. Some newborn babies are subject to intensive care and placed into neonatal incubators. ICU examinations must be regularly performed on these patients. In the current procedure, the



doctor has to come to an observation room that accommodates around 15–20 babies. The ICU is performed by inserting the ultrasound in the incubator. The diagnostic is not performed in real time: a total of 6 ultrasonic section views are recorded or printed out to be analyzed later. The same procedure and the same gestures are repeated as many as there are pediatric patient in the room. This makes intra-incubated ICU a highly repetitive task that could be performed by a tele-operated robotic manipulator. This can suppress the need for a doctor to move through large premises and allow the monitoring of pediatric patients in other branches of a large hospital group.

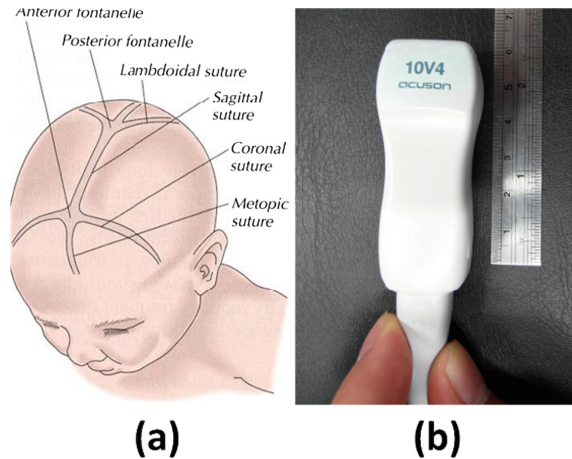


**Fig. 1.** Location of the fontanelle on a newborn patient (a). Specific ultrasound probe used for newborn intracranial examination (b).

The first robotic tele-echography system MIDSTEP, is an anthropomorphic robot holding an ultrasound probe. Later, a robotic manipulator has been proposed for tele-echography using a pantographic architecture [4] to generate a Remote Center of Motion (RCM). RUDS (Remote Ultrasound Diagnostic System) uses a double arc guiding architecture for its RCM and has a total of 7 Degrees of Freedom (DoF) [5]. The TER robot uses pneumatic artificial muscles for linear positioning [6]. A system based on a double pantographic architecture has been designed by the University of Manitoba [7]. Another parallel architecture has been developed based on two 5-bar vertical linkages [8]. A hybrid structure based on the same concept has been also proposed [9]. An unsymmetrical parallel robot of three legs has been designed to manipulate an ultrasound probe [10]. The robotic system WTA-2R has been developed based on a hybrid structure composed of a 6-DoF serial pantographic positioning device and a 6-DoF parallel manipulator [11]. Although the tele-echography has attracted both medical experts and robotic researchers, no case of robotized tele-echography performed on pediatric patients has been reported yet. The intracranial examination is performed regularly on newborn patients that are gathered in observation rooms. This requires the doctor to come to the room, which is time consuming since hospitals have large and complex premises. The insertion of an ultrasound probe into the neonatal incubation

brings the doctor in an uncomfortable pose that alters his/her dexterity during the examination. The objective of the present work is to propose a mechanism for a tele-echography robot capable of performing ICU examination on intra-incubated pediatric patients. The kinematic associated with the present medical application and the motion capture experiment protocol and results will be presented in the next Section. Section 3 will introduce the mechanical architecture concept and its kinematic analysis. Section 4 will present the kinematic simulations that validated the suitability of the mechanism with the clinical task. The last Section is dedicated to conclusion.

## 2 Specification Analysis

This medical application presents a major challenge in terms of kinematics. An ultrasound probe of small size must be held and manipulated safely and accurately toward a newborn patient. The mechanical architecture that provides this task must be defined to reply to specific kinematic requirement.

### 2.1 Motion Capture Experiments

A series of experimentation have been carried out with the assistance of our medical collaborator from CGMH, Linkou branch. The objective is to investigate the kinematic behavior of the ultrasound probe during the ICU examination. The motion capture system has been used to measure the motion of the ultrasound probe during this medical. A motion tracker has been attached to the ultrasound probe and the optronic system NDI Polaris Vicra has recorded the motion of the probe by tracking the position and orientation the motion tracker attached to it. A newborn model used for doctor training has been placed in a neonatal incubator Dager Isolette 8000 (the model used by CGMH). A doctor has used the ultrasound probe to simulate an ICU examination while the optronic system recorded the position of the motion tracker (Fig. 2).

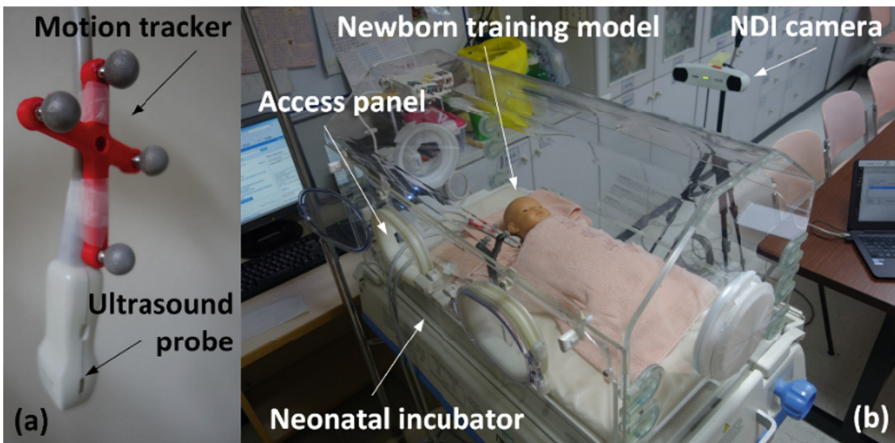


**Fig. 2.** Optronic motion tracker attached to an ultrasound probe (a). Intra-incubated newborn model used for preliminary experiments (b).

The NDI camera was placed on the side of the neonatal incubator. The doctor who participated to the experiment was sitting on the other of the incubator and performed a simulated ICU through the access panel. As for a standard routine ICU examination, these simulated ICU was performed by scanning the model head in two different directions: one horizontal rotation and one vertical rotation. In total, six simulated ICU have been recorded: three on horizontal rotation and three in vertical rotations. For all these motions, both the position and orientation of the ultrasound probe are considered for analysis. It is intended to measure:

- The 3-D volume of space that the doctor need to reach to cover to the newborn patient's fontanel zone;
- The range of angular motion required to scan the entire newborn patient's brain through the fontanel.

To fulfill these objective, motion capture system detects and locates the position of the reflective markers installed on the motion tracker. A reference frame associated with the motion tracker is then calculated. The system calculates in real time the transformation matrix that locates the motion in the reference frame of the camera. Based on that matrix, the position and orientation of the ultrasound probe can be calculated as long as at least three markers are detected. It is known that the probe is rotated around its tip that is considered as the center of rotation of the RCM. So the probe must be located by the position of this tip. Therefore, the system is configured to locate the center of the reference frame associated with the probe to its tip. The Euler angles are used to measure the orientation of the ultrasound probe. Its motion is describe as one rotation of angle  $\psi$  around the  $z$  axis, one rotation of angle  $\theta$  around the  $y$  axis and one rotation of angle  $\varphi$  around the  $x$  axis.

## 2.2 Kinematic Requirements of Intra-incubated Echography

During a series of simulated ICU examinations, the motion capture system has recorded the motion of the ultrasound probe inside the neonatal incubator. Before representing the identified kinematic data, the reference frame associated with the camera and the probe have been re-oriented in order to obtain a visualization that is more suitable with the reality. The  $x$  axis is now directed to the front of the camera and the  $z$  axis is oriented toward the vertical direction as shown in Fig. 3(a). The trajectories have been displayed in green for the vertical scanning and in red for the horizontal scanning. Based on the collected data, the ultrasound tip position has a range of motion of around 35 mm along all  $x$ ,  $y$  and  $z$  components. According to the medical expert involved in the experiment, this corresponds to the average size of a newborn's fontanel.

The orientation of the ultrasound has also been recorded during the simulated ICU. The evolution its Euler angles are displayed in Fig. 4. The motions associated with the horizontal and vertical scanning are represented by the curves in green and red respectively. According to the graphics, the following angular ranges of motion can be identified:  $\psi \in [-135; 53]$ ,  $\theta \in [11; 108]$  and  $\varphi \in [-33; 125]$ .

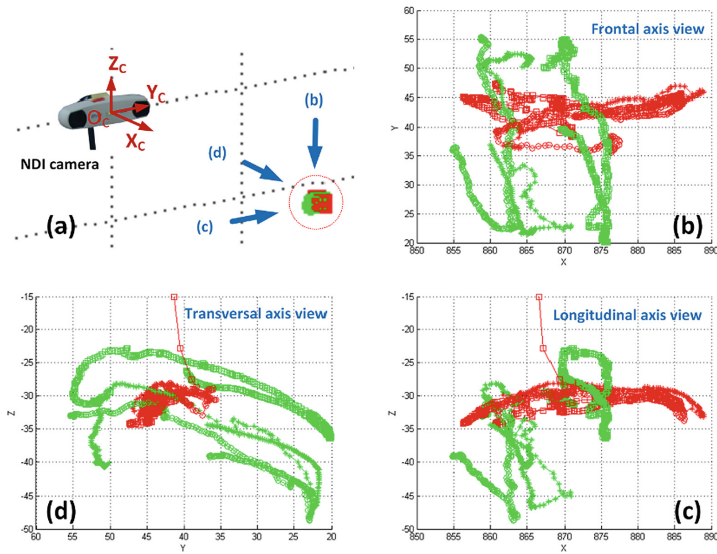


**Fig. 3.** Evolution of the ultrasound probe linear position during the simulation ICU examinations. (b) Frontal view, (c) longitudinal view, (d) transversal view (camera view).

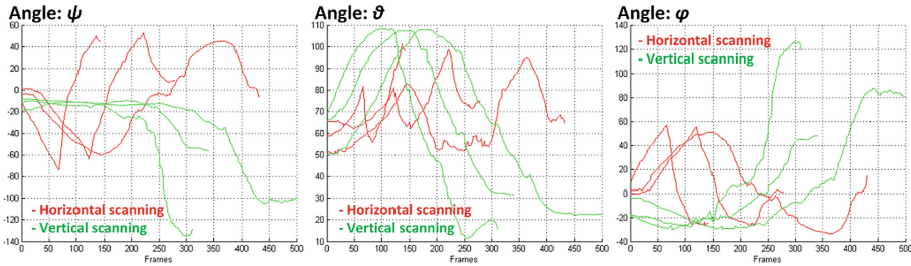


**Fig. 4.** Evolution of the ultrasound probe angular motion during the simulated ICU examination.

Based on the doctors' description and our preliminary observation, it can anticipated the kinematic of the task has the following characteristics:

- The ultrasound probe is oriented as an 3-DoF Remote Center of Motion;
- The center of rotation of the RCM is the contact point between the ultrasound probe and the patient's fontanelle;
- The center of rotation is displaced in a 3-D linear motion to target the fontanelle location;
- Two of the angular DoF require a large range to "scan" the all the brain through the fontanelle;
- The third angular DoF requires only two approximate positions: one for scanning along the 1<sup>st</sup> angular DoF and one for the 2<sup>nd</sup> DoF.

In terms of design, the part of the manipulator that passes through the incubator access panel must as thin as possible to allow the insertion of the probe inside. The manipulator must remain as less invasive as possible: mechatronic instruments (motors, sensors, etc.) shall be then located outside as much as possible.

### 3 Kinematic Analysis of the Double Pantographic Mechanism

The kinematic models of this novel mechanism are studied. The mechanism is made of two pantographic linkages providing a specific kinematic task each.

#### 3.1 Definition of the Mechanical Architecture

In order to respond to these characteristics stated above, a specific mechanical architecture is proposed. This concept is composed of two pantographic mechanisms as illustrated in Fig. 4. The first one is a proximal mechanism (in red) dedicated to the linear positioning of the distal RCM. The second one is a distal mechanism (in green) that provides the angular DoF of the distal RCM. The proximal pantographic mechanism is modified to allow an additional degree of mobility. Traditionally, the base linkage of pantographic manipulators remains immobile. The linkage that constitutes the base can rotate around its longitudinal axis in order to generate a second angular DoF. Such an architecture will then provide an RCM of two DoF. As for any standard pantographic mechanism, the configuration of the proximal mechanism is controlled by active joints rotating the linkage AB around its longitudinal axis and the linkages AE around a transversal axis passing through point A. By rotating AE around A, linkage FH will follow a similar rotation around the proximal RCM point H. If the linkage FH is extended by HK, the distal RCM point K will have circular trajectory around the point H. By this method, two angular DoF are provided by the angles  $\theta_1$  and  $\theta_2$  as shown in Fig. 4(a) and (b). In the present concept, an additional degree of mobility is provided by controlling the orientation of the base linkage AB as shown on Fig. 4(c). The linkage AB is rotated around the point A by an additional active joint controlling the angle  $\theta_3$ . The effect is the rotation of the segment AH around point A. As result, the proximal RCM point H is displaced with a circular trajectory around the point A. The distal RCM point K will then follow the same trajectory. At the end, the three active joints coordinates  $\theta_1$ ,  $\theta_2$  and  $\theta_3$  can control the linear positioning of the point K using curvilinear trajectories.

When adapted to the present clinical application, the first pantographic mechanism provides the linear motion of the manipulator end effector inside the incubator via an RCM that is approximatively located at the access panel (in blue on Fig. 5). Another important characteristic of the mechanism is the safety it can provide by choosing this architecture concept and by locating its base above the neonatal incubator. In the case of a power supply failure, the parallelogram linkage DEFG will be pulled down by gravity. In consequence, the distal pantographic linkage will automatically rotate around the RCM point H, which will lift the end effector point K away from the patient's head.

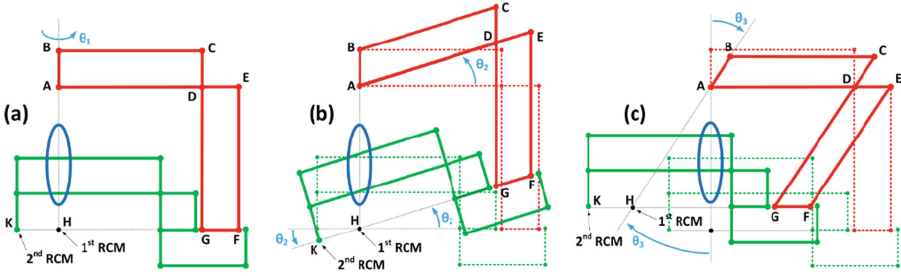


**Fig. 5.** Kinematic associated with the proximal pantographic linkage.

It is necessary to add 3 additional DoF to this mechanism in order to obtain the 6 DoF required for the present medical application. The 3 angular DoF are provided by the distal mechanism (in green on Fig. 6) the same way of any classic pantographic architecture. As the proximal mechanism controls the position of the linkage FG, it is used as the base for the distal mechanism. It first angular DoF rotates the mechanism around the longitudinal axis of the same linkage with the angle  $\theta_4$ . The second one rotates the end effector of an angle  $\theta_5$  around the transversal axis of the mechanism. The last one is the spinning rotation  $\theta_6$  of the end effector around its longitudinal axis.

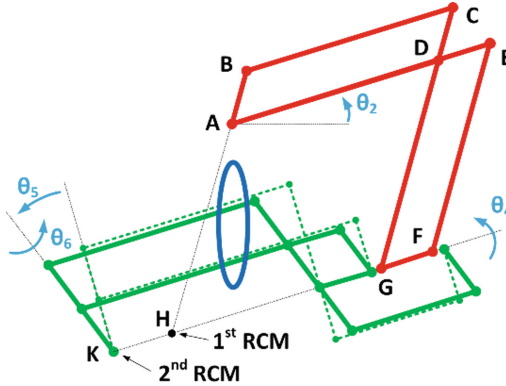


**Fig. 6.** Kinematic associated with the distal pantographic linkage.

### 3.2 Kinematic Model of the Mechanism

The distal pantographic mechanism has no effect on the linear positioning of the point K. So the linear part of the forward kinematic model is found by studying the proximal mechanism only. The linear forward kinematic model can be written as follow:

$$\begin{cases} x_K = (h \sin \theta_3 + k \cos \theta_2) \cos \theta_1 \\ y_K = (h \sin \theta_3 + k \cos \theta_2) \sin \theta_1 \\ z_K = -h \cos \theta_3 - k \sin \theta_2 \end{cases} \quad (1)$$

With  $h$  and  $k$ , the length of linkages AH and HK respectively. The angular part of the forward kinematic model is calculated using algebraic method. The different rotational motion of the end effector are identified in an intrinsic configuration as followed:

$$\mathbf{R}_{06} = \mathbf{R}_z(\theta_1) \times \mathbf{R}_x(\theta_2) \times \mathbf{R}_y(\theta_4) \times \mathbf{R}_x(\theta_5) \times \mathbf{R}_z(\theta_6). \quad (2)$$

Where  $\mathbf{R}_U(\gamma)$  is a  $3 \times 3$  rotation matrix of angle  $\gamma$  around the axis  $\mathbf{u}$  (with  $\mathbf{u}$ :  $\mathbf{x}$ ,  $\mathbf{y}$  or  $\mathbf{z}$ ) and  $\mathbf{R}_i$ , a reference frame (with  $i = 1$  to 6). The input coordinate  $\theta_4$  of the proximal mechanism does not affect the angular position of the end effector. In the present kinematic model, the angle  $\theta_4$  is set to directly transform  $\mathbf{R}_2$  into  $\mathbf{R}_4$  to avoid confusion. The full rotation is determined by multiplying all rotation matrices mentioned above. On the other hand, the Euler angles have been chosen to represent the angular position of the end effector. Using the Euler and the mechanism full rotation matrices, the angular kinematic model can be found by writing:

$$\mathbf{R}_{06} = \mathbf{R}_{\text{Euler}} = \begin{bmatrix} C\psi C\varphi - S\psi C\theta S\varphi & -C\psi S\varphi - S\psi C\theta C\varphi & S\psi S\theta \\ S\psi C\varphi - C\psi C\theta S\varphi & -S\psi S\varphi + C\psi C\theta C\varphi & -C\psi S\theta \\ S\theta S\varphi & S\theta C\varphi & C\theta \end{bmatrix}, \quad (3)$$

With  $C(\gamma) = \cos(\gamma)$  and  $S(\gamma) = \sin(\gamma)$ . The angular position of the mechanism end effector can be then calculated as followed:

$$\begin{cases} \theta = \cos^{-1}(C\theta_2 C\theta_4 C\theta_5 - S\theta_2 S\theta_5) \\ \psi = \text{ATAN2}\left(\frac{C\theta_5(S\theta_1 S\theta_2 C\theta_4 + S\theta_1 S\theta_4) + S\theta_1 C\theta_2 S\theta_5}{S\theta}, \frac{C\theta_5(C\theta_1 S\theta_2 C\theta_4 - S\theta_1 S\theta_4) + C\theta_1 C\theta_2 S\theta_5}{S\theta}\right) \\ \varphi = \text{ATAN2}\left(\frac{S\theta_6(C\theta_2 C\theta_4 S\theta_5 + S\theta_2 C\theta_5) - C\theta_2 S\theta_4 C\theta_5}{S\theta}, \frac{C\theta_6(C\theta_2 C\theta_4 S\theta_5 + S\theta_2 C\theta_5) + C\theta_2 S\theta_4 S\theta_6}{S\theta}\right) \end{cases} \quad (4)$$

For the linear positioning of the end effector, the inverse kinematic model is calculated by using a geometric method. The first mechanism is modelled as a parallelogram linkage. The segments [AH] and [HK] are considered in this regards. By using geometric formula associated with parallelogram, the inverse linear kinematic model can be written as followed:

$$\begin{cases} \theta_1 = \tan^{-1}(x_K/y_K) \\ \theta_2 = \text{ATAN2}\left(\frac{z-h \cos \theta_3}{k}, \frac{\sqrt{x_K^2 + y_K^2} - h \sin \theta_3}{k}\right) \\ \theta_3 = \text{ATAN2}\left(\frac{\sqrt{x_K^2 + y_K^2}}{\sqrt{c}}, \frac{z_K}{\sqrt{c}}\right) + \text{ATAN2}\left(\frac{\sqrt{2h^2 + 2k^2 - c}}{h}, \frac{\sqrt{c}}{2h}\right) \end{cases}, \quad (5)$$

With  $c = x_K^2 + y_K^2 + z_K^2$ . The angular part of the inverse kinematic model is establish using the algebraic method. The first and second input variables of the distal mechanism  $\theta_4$  and  $\theta_5$  are identified first. It is assumed that the rotations of the entire mechanism from  $\theta_1$  to  $\theta_5$  (excluding  $\theta_3$ ), named  $\mathbf{R}_{05}$ , and the rotations of the Euler angles  $\psi$  and  $\theta$ , named  $\mathbf{R}_{\psi\theta}$ , will both generate the same end effector longitudinal axis. This yields to the following equation:



$$\mathbf{R}_{05} \times \begin{bmatrix} 0 \\ 0 \\ 1 \end{bmatrix} = \mathbf{R}_{\psi\theta} \times \begin{bmatrix} 0 \\ 0 \\ 1 \end{bmatrix}. \quad (6)$$

By developing Eq. (6) and isolating the rotation matrices associated with the input variables  $\theta_4$  and  $\theta_5$ , it can be written as:

$$\mathbf{R}_y(\theta_4) \times \mathbf{R}_x(\theta_5) \times \begin{bmatrix} 0 \\ 0 \\ 1 \end{bmatrix} = (\mathbf{R}_z(\theta_1) \times \mathbf{R}_x(\theta_2))^{-1} \times \begin{bmatrix} C\psi & -S\psi C\theta & S\psi S\theta \\ S\psi & C\psi C\theta & -C\psi S\theta \\ 0 & S\theta & C\theta \end{bmatrix} \times \begin{bmatrix} 0 \\ 0 \\ 1 \end{bmatrix}. \quad (7)$$

The two first input variables of the distal mechanism  $\theta_4$  and  $\theta_5$  can be therefore calculated as followed:

$$\begin{cases} \theta_4 = \text{ATAN2}\left(\frac{-\sin\theta\sin(\theta_1-\psi)}{\cos\theta_5}, \frac{\cos\theta\cos\theta_2 + \cos(\theta_1-\psi)\sin\theta\sin\theta_2}{\cos\theta_5}\right) \\ \theta_5 = \sin^{-1}(\cos\theta_1\cos\theta_2\cos\psi\sin\theta - \cos\theta\sin\theta_2 + \cos\theta_2\sin\theta\sin\theta_1\sin\psi) \end{cases} \quad (8)$$

The last input variable of the distal mechanism is calculated by considering the spinning deviation around the end effector longitudinal axis between the two rotations sequences described above. The last input variables  $\theta_6$  is calculated as the sum of the spinning deviation  $\varphi_D$  and spinning output variable  $\varphi$ .

$$\theta_6 = \varphi_D + \varphi. \quad (9)$$

The spinning deviation is identified by calculating the angle between the  $\mathbf{x}$  axes of the reference frames given by the rotation matrix  $\mathbf{R}_{05}$  and  $\mathbf{R}_{\psi\theta}$ . It is written as below:

$$\cos\varphi_D = \left[ \mathbf{R}_{05} \times \begin{bmatrix} 1 \\ 0 \\ 0 \end{bmatrix} \right] \cdot \left[ \mathbf{R}_{\psi\theta} \times \begin{bmatrix} 1 \\ 0 \\ 0 \end{bmatrix} \right]. \quad (10)$$

Equation (9) is then developed as followed:

$$\varphi_D = \cos^{-1}(a \cos\psi + b \sin\psi), \quad (11)$$

With  $a = \cos\theta_1\cos\theta_4 - \sin\theta_4\sin\theta_2\sin\theta_4$  and  $b = \cos\theta_4\sin\theta_1 + \cos\theta_1\sin\theta_2\sin\theta_4$ .

## 4 Simulations

In order to verify the ability of the mechanism to perform ICU examination in incubators, kinematic simulations have been performed based on the trajectories presented in Sect. 2.2. The mechanism inverse kinematic model is implemented into a Matlab program. A function is written to calculate for each ultrasound probe coordinates  $(x, y, z, \psi, \theta, \varphi)$ , the corresponding mechanism input variables  $(\theta_1, \theta_2, \theta_3, \theta_4, \theta_5, \theta_6)$ . This function is called by the algorithm for each point of the trajectories.



For these simulations, the mechanism design variable have been set as:  $h = 400$  and  $k = 250$ . These dimensions have been adjusted to insure several requirements:

- The mechanism proximal RCM point is located at the incubator entrance in its origin configuration;
- The mechanism distal RCM point is located in the sagittal center of the incubator in its origin configuration;
- The mechanism workspace is large enough to cover all possible position of the patient's fontanel.

For each ultrasound probe trajectory, the position  $(x, y, z)$  and orientation  $(\psi, \theta, \varphi)$  are both given. The linear position of the ultrasound probe is managed only by the mechanism proximal pantograph, so the evolution of the three first input variables  $(\theta_1, \theta_2, \theta_3)$  can be calculated based on  $(x, y, z)$  coordinated. They are displayed on Fig. 7. This first set of simulations has revealed the linear positioning associated with the adjustment of the distal RCM point only require a very limited range of motion from the proximal pantograph. The range of the proximal input variables are identified as:  $\theta_1 \in [-3^\circ; 7^\circ]$ ,  $\theta_2 \in [-5^\circ; -2^\circ]$  and  $\theta_3 \in [-13^\circ; -4^\circ]$ .

The angular positioning of the ultrasound probe is mainly carried out by the distal pantograph after the tip of the ultrasound is positioned on the patient's fontanel by the proximal pantograph. But the linear position adjustment observed during these rotations will necessarily affect the evolution of the distal input variables  $(\theta_4, \theta_5, \theta_6)$ . Therefore, the calculation of these variables requires the prior calculation of the proximal variables  $(\theta_1, \theta_2, \theta_3)$ . The evolution of the distal input variables are calculated for all horizontal and vertical scanning trajectories and are displayed in Fig. 8. The distal input variable ranges of values required to perform ICU examination appear much larger than the proximal ones. They can be measured as:  $\theta_4 \in [-70^\circ; 60^\circ]$ ,  $\theta_5 \in [-25^\circ; 60^\circ]$  and  $\theta_6 \in [-140^\circ; 20^\circ]$ .

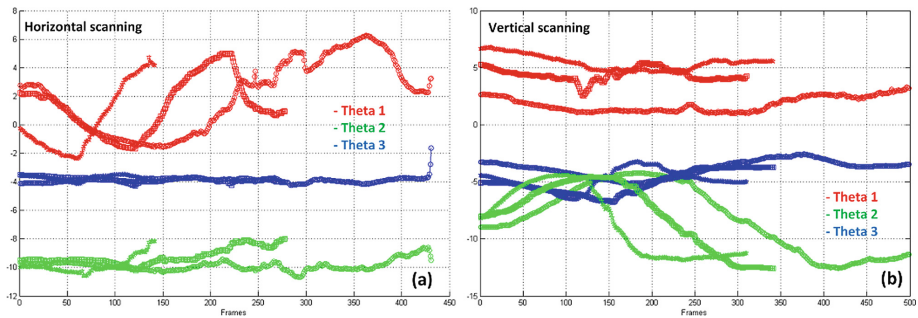


**Fig. 7.** Evolution of the proximal mechanism input variables  $(\theta_1, \theta_2, \theta_3)$  during horizontal (a) and vertical (b) scanning trajectories.

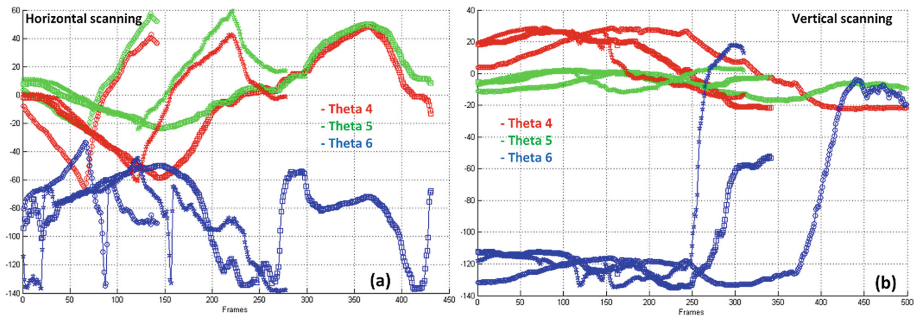


**Fig. 8.** Evolution of the distal mechanism input variables ( $\theta_4$ ,  $\theta_5$ ,  $\theta_6$ ) during horizontal (a) and vertical (b) scanning trajectories.

According to the kinematic simulations presented above, it can be predicted that the distal pantographic mechanism will be much more solicited in term of motion than the proximal pantograph. However, the proximal pantograph will need to support the weight of the rest of the mechanism, which will require more torque but less amplitude of motion at the proximal joints. The use of reducers in the proximal joints is therefore recommended for the design of a robotic manipulator based on this mechanism. At the same time, the charge supported by the distal joints remains limited. A CAD prototype of the mechanism based on these design requirement is shown on Fig. 9. It can be noted that due to the specific mechanical architecture, all motors remains outside of the incubator. The sixth joint is not included in this prototype as the design of its transmission system will be addressed in a more advanced version.

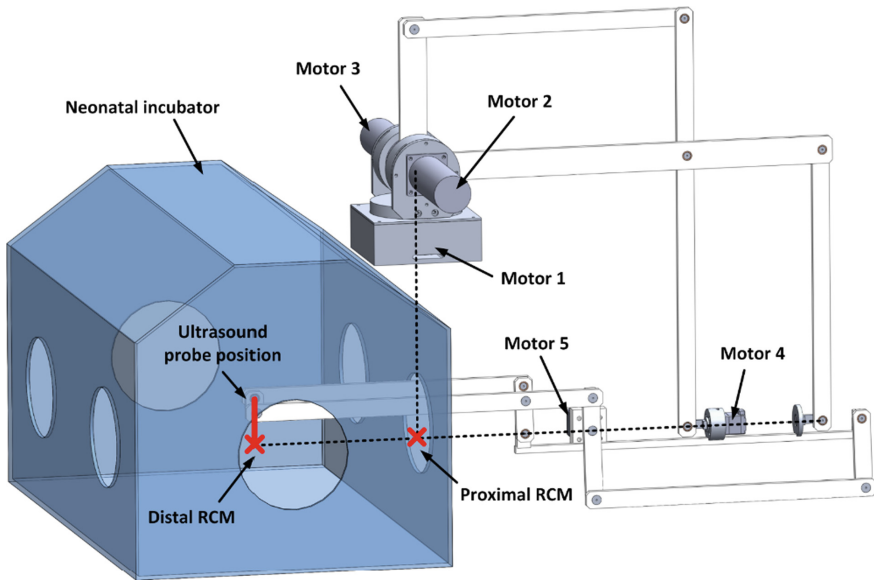


**Fig. 9.** CAD view of the double pantographic mechanism for ICU examination.

## 5 Conclusion

A tele-operated manipulator dedicated to the examination of intra-incubated newborn's fontanelle has never been proposed. Based on the results of motion capture experiments, a concept of mechanical architecture has been proposed as a response to this mechanical challenge. A novel mechanism is based on a combination of a proximal and distal pantographic linkages. The proximal pantographic provides the 3-DoF linear positioning allowed by an architectural improvement. The distal one manages the angular positioning of the end effector. It generates a RCM around a point which position is controlled by the proximal linkage. Geometric and algebraic methods are used to calculate the linear and angular kinematic model respectively. A series of simulation have been carried out to investigate the aptitude of the mechanism to perform intracranial echography in incubators.

## References

1. Slovis, T.L., Kuhns, L.R.: Real-time sonography of the brain through the anterior fontanelle. *Am. J. Roentgenol.* **136**, 277–286 (1981)
2. Pape, K.E., Cusick, G., Blackwell, R.J., Houang, M.T.W., Sherwood, A., Thorburn R.J., Reynolds, E.O.R: Ultrasound detection of brain damage in preterm infants. *Lancet* **313**(8129), 1261–1264 (1979)
3. Hsieh, W.-S., Jeng, S.-F., Hung, Y.-L., Chen, P.-C., Chou, H.-C., Tsao, P.-N.: Outcome and hospital cost for infants weighing less than 500 grams: a tertiary centre experience in Taiwan. *J. Paediatr. Child Health* **43**(9), 627–631 (2007)
4. Salcudean, S.E., Bell, G., Bachmann, S., Zhu, W.H., Abolmaesumi, P., Lawrence, P.D.: Robot-assisted diagnostic ultrasound-design and feasibility experiments. In: *Medical Image Computing and Computer-Assisted Intervention, MICCAI 1999*, pp. 1062–1071 (1999)
5. Mitsuishi, M., Warisawa, S., Tsuda, T., Higuchi, T., Koizumi, N., Hashizume, H., Fujiwara, K.: Remote ultrasound diagnostic system. In: *IEEE International Conference on Robotics & Automation, ICRA 2001*, pp. 1567–1574 (2001)
6. Vilchis, A., Troccaz, J., Cinquin, P., Masuda, K., Pellissier, F.: A new robot architecture for tele-echography. *IEEE Trans. Robot. Autom. Spec. Issue Med. Robot.* **19**(5), 922–926 (2003)
7. Najafi, F.: Design and prototype of a robotic system for remote palpation and ultrasound imaging. M.Sc. Dissertation, University of Manitoba. Available as Report 20104, University of Manitoba Library MSpace (2004)
8. Lessard, S., Bigras, P., Bonev, I.A.: A new medical parallel robotic and its static balancing optimization. *ASME J. Med. Device* **1**(4), 272–278 (2007)
9. Najafi, F., Sepehri, N.: A robotic wrist for remote ultrasound imaging. *Mech. Mach. Theory* **46**(8), 1153–1170 (2011)
10. Masuda, K., Miyazaki, W., Sugano, Y., Yoshinaga, T.: Effectiveness of tele-echography system with and without robotics according to patient circumstances. In: *Proceedings of the 3rd International Conference on E-Health and Bioengineering, EHB 2011*, Iasi, Romania, 24–26 November 2011
11. Nakadate, R., Matsunaga, Y., Solis, J., Takanishi, A., Minagawa, E., Sugawara, M., Niki, K.: Development of a robot assisted carotid blood flow measurement system. *Mech. Mach. Theory* **46**(8), 1066–1083 (2011)



# Kinematic Design of a Six-Degrees of Freedom 3-RRPS Parallel Mechanism for Bone Reduction Surgery

Sinh Nguyen Phu and Terence Essomba<sup>(✉)</sup>

Department of Mechanical Engineering,  
National Central University, Zhongli City 32001, Taiwan (R.O.C.)  
tessomba@cc.ncu.edu.tw

**Abstract.** In orthopedic surgery, bone reduction surgery consists in relocating the broken bones to their initial position while insuring a correct alignment. In the traditional method, orthopedic surgeons have to manually manipulate the fixator to re-position the fragments. With the advancements of robotics in the medical field in the last few years, robots have also been applied to the field of precision fracture reduction surgery. It assists orthopedic surgeons in re-positioning the broken bones back into their proper place. In this paper, a 3-RRPS parallel robot is proposed to perform bone reduction surgery. The kinematic analysis and velocity model are presented in this paper. A series of simulation on Adams and Matlab have been carried out to validate the kinematic and velocity model of the mechanism. A simulated bone reduction procedure using the 3-RRPS parallel robot is also performed in Adams software. The simulated result shows the suitability of the present mechanism with bone reduction surgery.

**Keywords:** Parallel robot · Tripod mechanism · Bone reduction · Kinematic · Simulation

## 1 Introduction

Robotic-assisted surgery is a new and emerging technology that helps the surgeons to carry out a variety of complex operations with more comfort and precision than the traditional surgeon. In orthopedic surgery, fracture reduction plays an important role in the treatment of broken bones and bone deformities. With advances in robotic technology, robots have also been useful in the field of precision fracture reduction surgery. It assists orthopedic surgeons in re-positioning the broken bones back into their proper place and help them heal. Using robot for fracture reduction can also help to reduce the radiation exposure to the physicians and to the patient during surgery.

In the past few decades, many different techniques and well-designed devices have been developed for performing bone reduction such as the traction table, unilateral external fixators, circular external fixator or hybrid architecture. The most common fixators used are unilateral fixators and circular external fixator. Unilateral external fixator as seen in Fig. 1(a) is usually designed as a series of linkages connected with lockable universal joints to allow surgeons to manipulate the fixator in fracture

reduction. Two well-known commercial unilateral fixation devices are Orthofix fixator and Dynafix fixator. Unilateral fixators are advantageous for applying some simple fracture deformities. However, it is not easy to predict the configuration of unilateral fixators in bi-planar for correcting the complex fracture. Therefore, in the correction of complex multi-planar deformities, the circular frames usually are used. The circular external fixator shown in Fig. 1(b) is commonly composed of two important components, rings, and connecting rods. The ring could be a full ring, partial ring or an arch. This fixator type has the cylindrical shape so it is evaluated more versatile than unilateral fixator for simultaneously controlling in three-dimension.

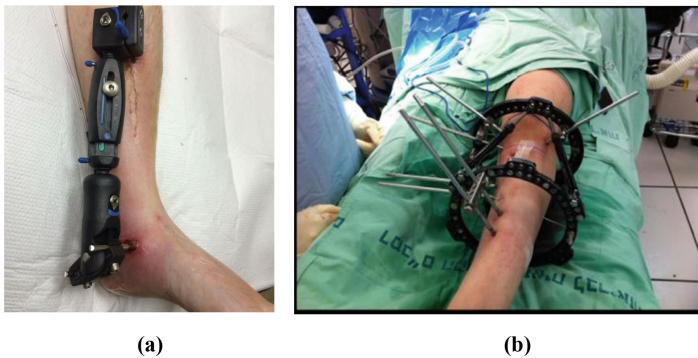


**Fig. 1.** External fixators: (a) Unilateral external fixators [1], (b) Circular external fixator [2].

In conventional operation, surgeons must perform high force for adjusting mechanism as well as the influence of excessive x-ray exposure to both patient and surgeons in the theatre during the procedure. Therefore, robot-assisted fracture reduction has attracted much attention from many scholars. Numerous papers on the use of robots in fracture reduction have been reported. Bubak et al. [3] developed the serial robot based on unilateral Dynafix fixator with a computer graphic model. Actuators were added to the fixator joints. In 1993, Viceconti et al. [4] proposed an automatic mechanism for the reduction of fractures. This device is similar to Ilizarov external fixator but the connecting rods between rings are equipped three stepper motors for controlling relative motion between the rings. Füchtmeier et al. [5] presented the modification of an industrial serial manipulator model RX130 from Stäubli Co. Ltd, with six Degrees of Freedom (DoF) for the long bone reduction in vivo. In their research, the end-effector has been equipped with a pneumatic gripper for holding and manipulating fixator clamps. Another group from Germany, Westphal et al. [6] developed a telemanipulated robot using joystick control and integrated with an intra-operative 3D fracture image interface for assisting femoral fracture reduction. In this experiment, they also used a serial industrial manipulator model RX 90 from Stäubli Co. Ltd. In 2004, Seide et al. [7] from Hamburg, Germany developed a motorized hexapod external fixator which is based upon the Stewart Platform kinematics. It consists of two rings connected by six electrical linear actuators equipped with force sensors and spherical joints at both ends, called distractor in clinic terms. Hence it can provide 6-DoF spatial movement by

adjusting the length of distractors. Recently, in 2017, Mohammad et al. [8] proposed a new 6-DoF parallel robot with three legs for long-bone fracture reduction. Each leg is equipped with one prismatic actuator and one rotary actuator. In their publication, this architecture has a much larger dexterous and rotational workspace in comparison to the well-known six prismatic legs Stewart platform. They fabricated a prototype for verifying the performance of the robot in fracture reduction maneuvers. The results indicate this prototype was sufficient and potential for fracture alignment. In this study, a 3-RRPS parallel robot is proposed to use in longitudinal bones reduction. The paper is organized as followed: the next Section will explain the architecture of the mechanism as well as its kinematic analysis. Then, the third Section will present the velocity model of 3-RRPS parallel robot. In the fourth Section, kinematic simulations are carried out to validate the mechanism kinematic and velocity models. A bone reduction surgery simulation also is shown in this Section. The conclusion of the present study is provided in the last Section.

## 2 Mechanical Architecture and Kinematic Analysis

The 3-RRPS parallel robot presented in this paper has been defined by Alizade in 1994. A illustration is shown in Fig. 2(a). It is composed of two platforms: one is fixed that is considered as the base and one is a moving platform. The moving platform is connected to the base via three identical closed loop chains. Each chain is a classical RPS mechanism that is found on most tripod mechanism. The prismatic joint is active while the revolute and spherical joints remain passive. But unlike the standard tripod mechanism, the position of the revolute joint is not fixed as each RPS arm is here mounted on a slider that moves along a circular rail. It is kinematically represented as a virtual linkage that connects a virtual active revolute joint located at the fixed ring center to the slider. Each mechanism arm is therefore referred to as RRPS. The kinematic schematic of the 3-RRPS parallel robot is shown in Fig. 2(b). The reference frame attached to the base and the moving platform are respectively denotes as  $\{Oxyz\}$  and  $\{O_1x_1y_1z_1\}$ .

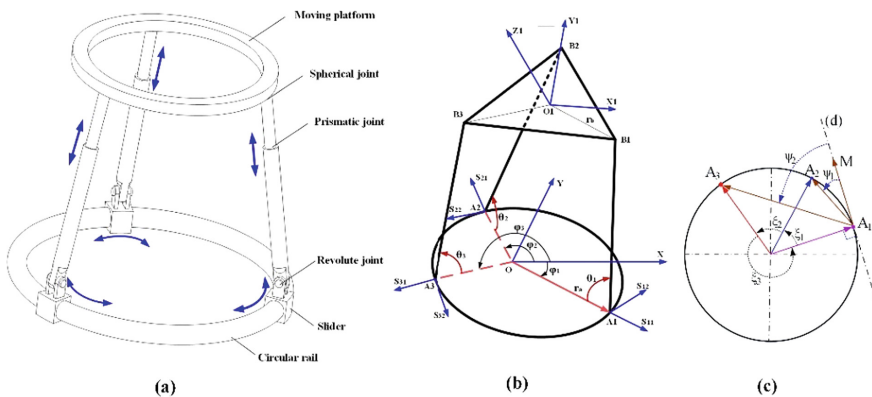


**Fig. 2.** (a) The 3-RRPS parallel robot; (b) The schematic representation of 3-RRPS parallel robot and (c) The schematic for determining the order of sliders.

The origin  $O$  of the fixed reference frame is located at the center of the circular rail and another origin  $O_1$  is located at the center of the circumcircle of the equilateral triangle  $B_1B_2B_3$  of moving platform. The motion of  $i^{\text{th}}$  sliders on the circular rail associated with the  $i^{\text{th}}$  revolute joints (for  $i = 1, 2, 3$ ) is defined by actuator variables  $\varphi_i$  that represents the relative angle between  $Ox$  and  $OA_i$  about the  $z$ -axis. The notation used to describe the length of the  $i^{\text{th}}$  active prismatic actuators, the distance between revolute joints  $A_i$  and spherical joints  $B_i$  is  $L_i$ . The linear position  $O_1$  of moving platform respect to the global reference frame  $\{Oxyz\}$  is defined by the vector  $O_1 = [x_I \ y_I \ z_I]^T$ . And the orientation of the moving platform can be expressed by three Euler angles  $\gamma, \beta, \alpha$  which are angles rotated about  $z, y, x$  axes of the fixed reference. This yields the following rotation matrix associated with the mobile circular ring:

$$\mathbf{R} = \begin{pmatrix} c\beta c\gamma & s\alpha s\beta c\gamma - c\alpha s\gamma & c\alpha s\beta c\gamma + s\alpha s\gamma \\ c\beta s\gamma & s\alpha s\beta s\gamma + c\alpha c\gamma & c\alpha s\beta s\gamma - s\alpha c\gamma \\ -s\beta & s\alpha c\beta & c\alpha c\beta \end{pmatrix}, \quad (1)$$

Where  $s(\cdot)$  and  $c(\cdot)$  are respectively equal to  $\sin(\cdot)$  and  $\cos(\cdot)$ .

Assuming that  $r_a, r_b$  are the radius of the base circular rail and the moving platform respectively, the position vector of the sliders  $A_1, A_2$ , and  $A_3$  are expressed in the global coordinate system  $\{Oxyz\}$  as followed:

$${}^O\mathbf{a}_i = [r_a c\varphi_i \quad r_a s\varphi_i \quad 0]^T \quad (i = 1, 2, 3) \quad (2)$$

The position vector of the active spherical joint  $B_i$  with respect to the reference frame  $\{O_1x_1y_1z_1\}$  can be computed as:

$${}^{O_1}\mathbf{b}_i = [r_b c\varphi_{bi} \quad r_b s\varphi_{bi} \quad 0]^T, \quad (3)$$

With  $\varphi_{bi} = -\frac{\pi}{6}, \frac{\pi}{2}, \frac{7\pi}{6}$ .

From the geometry, it is obvious that the position vector of the spherical joint  $B_i$  would be expressed in the global frame  $\{Oxyz\}$  as followed:

$${}^O\mathbf{b}_i = \mathbf{O}_1 + \mathbf{R} {}^{O_1}\mathbf{b}_i \quad (4)$$

Therefore, the length of the prismatic actuators could be determined by

$$L_i = \|A_i B_i\| = \|[x_{ABi} \quad y_{ABi} \quad z_{ABi}]^T\| = \|\mathbf{O}_1 + \mathbf{R} {}^{O_1}\mathbf{b}_i - {}^O\mathbf{a}_i\| \quad (5)$$

Let  $\mathbf{s}_{i1}$  and  $\mathbf{s}_{i2}$  be unit vectors of the reference frame at the passive revolute joints  $A_i$ , where  $\mathbf{s}_{i1}$  points in the same direction as vectors  $\mathbf{OA}_i$  and  $\mathbf{s}_{i2}$  is along the rotation axis of the revolute joints as shown in Fig. 2(b). This yields:

$$\mathbf{s}_{i1} = [\cos(\varphi_i) \quad \sin(\varphi_i) \quad 0]^T \quad (6)$$

$$\mathbf{s}_{i2} = [-\sin(\varphi_i) \quad \cos(\varphi_i) \quad 0]^T \quad (7)$$



The prismatic actuators are only able to rotate about the axis of revolute joints  $A_i$ . Hence the unit vectors  $\mathbf{s}_{i2}$  will be perpendicular to vector  $\mathbf{A}_i\mathbf{B}_i$  that can be expressed as the following constraint equations:

$$\mathbf{A}_i\mathbf{B}_i^T \cdot \mathbf{s}_{i2} = 0 \quad (8)$$

By substituting Eq. (5) into Eq. (8), the rotation angles  $\varphi_i$  of the active revolute joints could be obtained by:

$$\varphi_i = \arctan\left(\frac{y_{A_iB_i}}{x_{A_iB_i}}\right) \quad (9)$$

This result shows that each slider could have two positions. In other words, it is possible to find a total of eight configurations of the robot to achieve the desired position and orientation. All the mechanism configurations for a given position of the moving platform are illustrated in Fig. 3. In this example, the chosen coordinates are:  $x_I = -0.03$  m,  $y_I = 0.04$  m,  $z_I = 0.250$  m and  $\alpha = 10^\circ$ ,  $\beta = -5^\circ$ ,  $\gamma = -20^\circ$  where  $r_a = 0.175$  m and  $r_b = 0.125$  m. However, some solutions are not suitable the physical constraints such as prismatic joint motion range, the order of sliders, and allowable working angle of spherical joints.

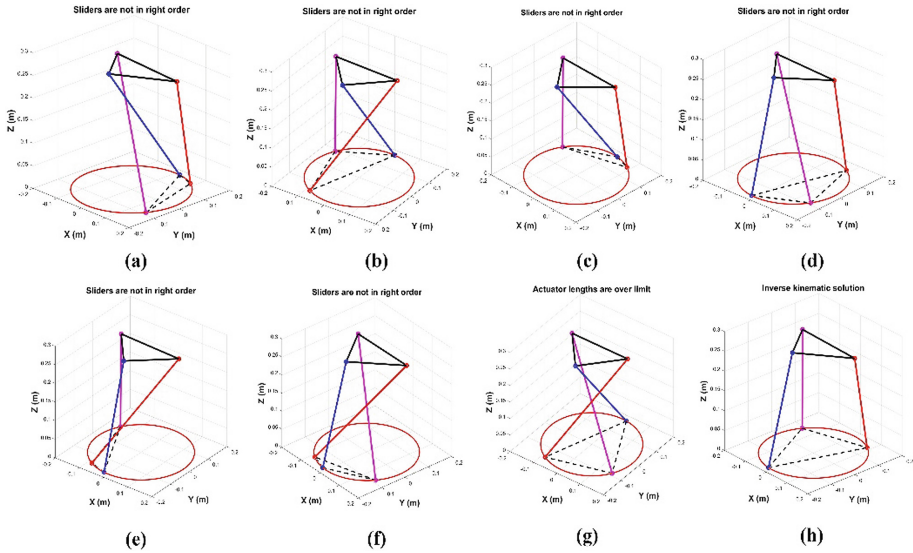


**Fig. 3.** Kinematic representation of the mechanism in eight different configuration corresponding to the same end effector position.



Therefore, the solution of inverse kinematic would be determined by checking the following constraints:

- The limited prismatic actuator lengths (1)
- The order of sliders (2)
- The collision of sliders (3)
- The limited spherical joints (4)

All these constraints shall be formulated.

(1) The length values of actuators calculated by Eq. (5) are checked to make sure that they remain within the stroke range limits that can be written as:

$$L_{imin} < L_i < L_{imax} \text{ for } i = 1, 2, 3, \quad (10)$$

Where  $L_{imin}$  and  $L_{imax}$  are respectively the maximum and minimum lengths of the  $i^{\text{th}}$  prismatic actuators.

(2) In order to determine the order of sliders, a vector  $A_1M$  is assumed to be on the tangent line ( $d_1$ ) at the point  $A_1$  of the circular rail so that the vector  $A_1M$  directs in the counter-clockwise as illustrated in Fig. 2(c). The angle between two vectors  $A_1M$  and  $A_1A_2$  and the angle between two vectors  $A_1M$  and  $A_1A_3$  could be determined by:

$$\psi_1 = \text{ATAN2}(\|A_1M \times A_1A_2\|, A_1M^T A_1A_2) \quad (11)$$

$$\psi_2 = \text{ATAN2}(\|A_1M \times A_1A_3\|, A_1M^T A_1A_3) \quad (12)$$

Then, the constraint equations related to the order of sliders can be expressed as:

$$\psi_1 < \psi_2 \quad (13)$$

(3) Let  $\xi_1$ ,  $\xi_2$  and  $\xi_3$  be respectively the angle between sliders ( $A_1, A_2$ ), ( $A_2, A_3$ ) and ( $A_3, A_1$ ) as shown in Fig. 3(c). They can be calculated as:

$$\xi_1 = \text{ATAN2}(\|{}^O a_1 \times {}^O a_2\|, {}^O a_1^T {}^O a_2) \quad (14)$$

$$\xi_2 = \text{ATAN2}(\|{}^O a_2 \times {}^O a_3\|, {}^O a_2^T {}^O a_3) \quad (15)$$

$$\xi_3 = \text{ATAN2}(\|{}^O a_3 \times {}^O a_1\|, {}^O a_3^T {}^O a_1) \quad (16)$$

Then, the constraint equations for the sliders do not collide:

$$\xi_{min} < |\xi_i|, \quad (17)$$

Where  $\xi_{min}$  is the minimum angle between the sliders.

(4) Let  $n_i$  be the unit vectors along the symmetrical axis of the spherical joints at  $B_i$ . Then, the constraint equations of the spherical joint can be formulated as

$$\vartheta_{min} < \text{ATAN2}(A_i B_i \times R n_i, A_i B_i^T R n_i) < \vartheta_{max}, \quad (18)$$

Where  $\vartheta_{min}$ ,  $\vartheta_{max}$  are respectively the maximum and minimum allowable angle of the  $i^{\text{th}}$  spherical joints.

### 3 Mechanism Velocity Model

In this section, the velocity analysis of the mechanism is described. The actuator velocity vector is denoted by a vector  $\dot{\mathbf{q}} = [\dot{L}_1 \ \dot{L}_2 \ \dot{L}_3 \ \dot{\phi}_1 \ \dot{\phi}_2 \ \dot{\phi}_3]$ . The end effector velocity with respect to the global frame  $\{\text{Oxyz}\}$  can be written as a vector  $\dot{\mathbf{v}} = [v_x \ v_y \ v_z \ \omega_x \ \omega_y \ \omega_z]^T$ . The relationship between the actuator velocity  $\dot{\mathbf{q}}$  and the end effector velocity  $\dot{\mathbf{v}}$  is derived as:

$$\mathbf{J}_A \dot{\mathbf{q}} = \mathbf{J}_B \dot{\mathbf{v}}, \quad (19)$$

Where  $\mathbf{J}_A$  and  $\mathbf{J}_B$  are two Jacobian matrices of the mechanism. In order to find the Jacobian matrices, the Eq. (5) can be rewritten as:

$$L_i^2 = \mathbf{A}_i \mathbf{B}_i^T \mathbf{A}_i \mathbf{B}_i \quad (20)$$

Then, differentiating the Eq. (20) with the time, yields:

$$L_i \dot{L}_i + \mathbf{A}_i \mathbf{B}_i^T {}^O \dot{\mathbf{A}}_i = \mathbf{A}_i \mathbf{B}_i^T \dot{\mathbf{O}}_1 + \{\mathbf{R}^{O1} \mathbf{B}_i \times \mathbf{A}_i \mathbf{B}_i\}^T \boldsymbol{\omega}, \quad (21)$$

Where  $\boldsymbol{\omega}$  is the angular velocity vectors of the moving platform,  $\dot{\mathbf{O}}_1$  is the linear velocity of the end effector  $\text{O}_1$ ,  $\dot{L}_i$  is the linear velocity of prismatic actuators and  ${}^O \dot{\mathbf{A}}_i$  is the linear velocity of sliders.

Similarly, differentiating the constraint Eq. (8), yields:

$$\mathbf{s}_{i2}^T {}^O \dot{\mathbf{A}}_i - \mathbf{A}_i \mathbf{B}_i^T \dot{\mathbf{s}}_{i2} = \mathbf{s}_{i2}^T \dot{\mathbf{O}}_1 + \{\mathbf{R}^{O1} \mathbf{B}_i \times \mathbf{s}_{i2}\}^T \boldsymbol{\omega} \quad (22)$$

The Jacobian matrices are determined by re-arranging Eqs. (21) and (22)

$$\mathbf{J}_A = \begin{pmatrix} \text{diag}(L_i) & \text{diag}(\mathbf{A}_i \mathbf{B}_i^T \cdot \frac{d\mathbf{A}_i}{d\phi_i}) \\ O & \text{diag}(\mathbf{s}_{i2}^T \cdot \frac{d\mathbf{A}_i}{d\phi_i} - \mathbf{A}_i \mathbf{B}_i^T \frac{d\mathbf{s}_{i2}}{d\phi_i}) \end{pmatrix}_{6 \times 6} \quad (23)$$

And

$$\mathbf{J}_B = \begin{pmatrix} \mathbf{A}_i \mathbf{B}_i^T & (\mathbf{R}^{O1} \mathbf{B}_i \times \mathbf{A}_i \mathbf{B}_i)^T \\ \mathbf{s}_{i2}^T & (\mathbf{R}^{O1} \mathbf{B}_i \times \mathbf{s}_{i2})^T \end{pmatrix}_{6 \times 6} \quad (24)$$

### 4 Simulation on the Mechanism and Bone Reduction

In order to verify the inverse kinematics and velocity models of the mechanism, a series of simulations have been carried out. The inverse kinematic and velocity models are verified by generating a 6 DoF motion of the mechanism end effector given by the

Eq. (25) and obtaining the corresponding evolution of the actuator variables  $q = [L_1 \ L_2 \ L_3 \ \varphi_1 \ \varphi_2 \ \varphi_3]^T$  and the actuator velocity  $\dot{q} = [\dot{L}_1 \ \dot{L}_2 \ \dot{L}_3 \ \dot{\varphi}_1 \ \dot{\varphi}_2 \ \dot{\varphi}_3]^T$ .

$$\begin{cases} x(t) = 0.02\sin\left(\frac{\pi}{45}t\right) \\ y(t) = -0.03\cos\left(\frac{\pi}{90}t\right) \\ z(t) = 0.05\sin\left(\frac{\pi}{180}t\right) \\ \alpha(t) = \frac{\pi}{18}\cos\left(\frac{\pi}{45}t\right) \\ \beta(t) = \frac{\pi}{12}\cos\left(\frac{\pi}{90}t\right) \\ \gamma(t) = \frac{\pi}{9}\cos\left(\frac{\pi}{180}t\right) \end{cases} \quad (25)$$

With  $t$ , the time variable in second.

The simulations are performed on two software: Matlab and Adams. On one hand, the evolution of the mechanism input variables are obtained by programming the mechanism kinematic and velocity models on the numerical simulation software Matlab. On the other hand a graphic model of the mechanism is implemented into the kinematic simulation software Adams. The input variables resulting from both software are then compared, as illustrated in Figs. 4 and 5. According the graphic, no error can be found. Indeed, in both studies (positions and velocities), the curves showing the mechanism joint positions and velocities issued from Matlab and Adams have the exact same evolutions.

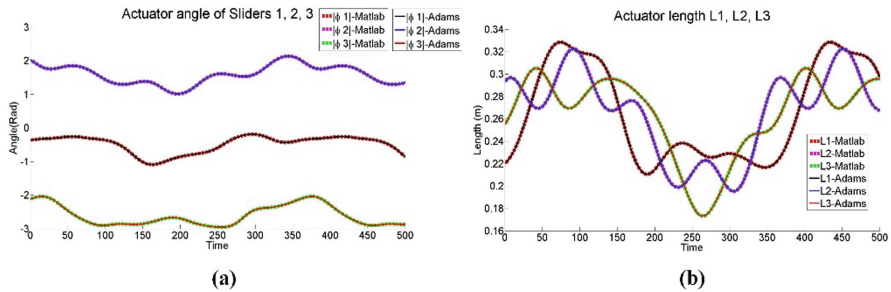


**Fig. 4.** Comparison of the mechanism input variables resulting from Adams and Matlab. (a) Input coordinates  $\varphi_1, \varphi_2, \varphi_3$ ; (b) Input coordinates  $L_1, L_2, L_3$ .

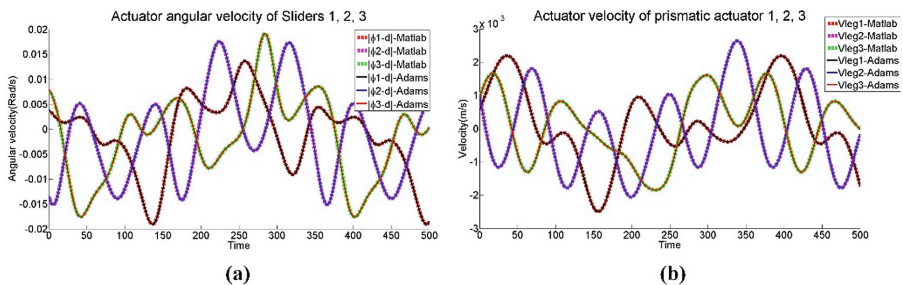


**Fig. 5.** Comparison of the mechanism input velocities resulting from Adams and Matlab. (a) Input velocities  $\dot{L}_1, \dot{L}_2, \dot{L}_3$  (b) Input velocities  $\dot{\varphi}_1, \dot{\varphi}_2, \dot{\varphi}_3$ .

To verify the feasibility of performing the fractured bone reduction using the mechanism introduced in Sect. 2, a simulated bone reduction has been conducted on Adams. A 3D model of two fragments is imported into the 3D simulation Adams. One fragment is fixed to the mechanism base and the other is attached to the mechanism moving platform. As results, the robotic bone reduction simulation on the 3D visualization tool has revealed that the mechanism can successfully reproduce the motion required to perform such a surgery. The different steps of motion performed by the mechanism to successfully reposition the two femur fragments are illustrated in Figs. 6 and 7.

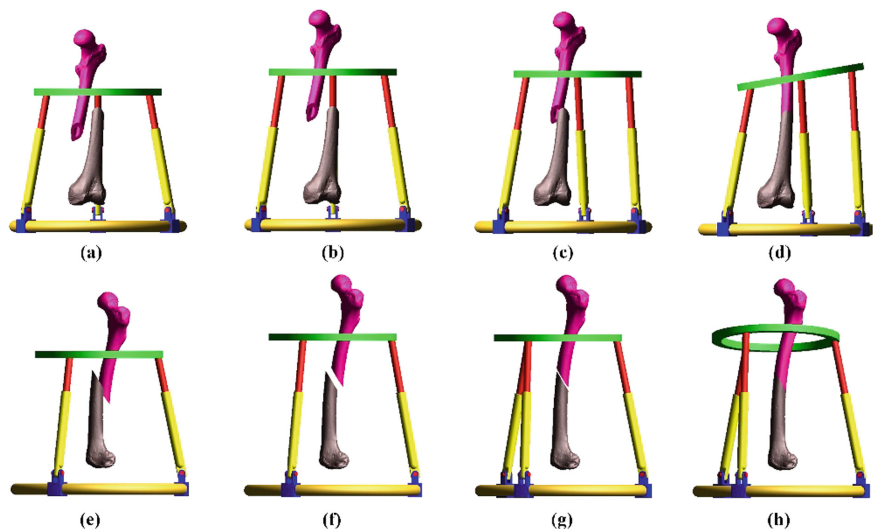


**Fig. 6.** Simulation of robotic-assisted bone reduction surgery. Repositioning in XZ view (a) to (d). YZ view (e) to (h).

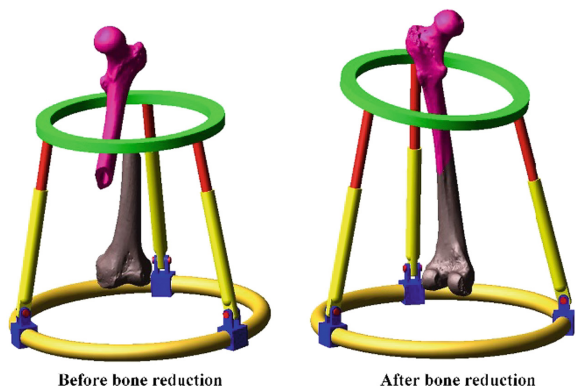


**Fig. 7.** Simulation of robotic-assisted bone reduction surgery in Iso view.

## 5 Conclusion

In the present study, the kinematic design of mechanical architecture is proposed for bone reduction surgery. It is based on a 3-RRPS parallel mechanism. The kinematic and velocity models of the mechanism is provided. A series of kinematic simulations has allowed the validation of the mechanism kinematic and velocity models. A successful bone reduction simulation using 3-RRPS robot has also been demonstrated on a 3D simulation software. Which shows that the mechanism is a good candidate for performing the bone reduction surgery.

## References

1. Chad, S., Megan, L.W., Byron, L.H.: Application of the distally pedicled peroneus brevis: technique, case study, and pearls. *Foot Ankle Online J.* **9**(3), 3 (2016)
2. Doron, K., Mark, E.: Clinical utility of the Taylor spatial frame for limb deformities. *Orthop. Res. Rev.* **9**, 51–61 (2017)
3. Kim, Y.H., Lee, S.-G.: Computer and robotic model of external fixation system for fracture treatment. In: *Computational Science - ICCS 2004, Part IV*, Kraków, Poland, 6–9 June 2004, pp. 1081–1087. Springer (2004)
4. Viceconti, M., Andrisano, A.O., Toni, A., Giunti, A.: Automatic fracture reduction with a computer-controlled external fixator. *Med. Eng. Phys.* **16**, 143–149 (1994)
5. Füchtmeier, B., Egersdoerfer, S., Mai, R., Hente, R., Dragoi, D., Monkman, G., Nerlich, M.: Reduction of femoral shaft fractures in vitro by a new developed reduction robot system ‘RepoRobo’. *Int. J. Care Inj.* **35**, S-A113–S-A119 (2004)
6. Westphal, R., Winkelbach, S., Gössling, T., Hüfner, T., Faulstich, J., Martin, P., Krettek, C., Wahl, F.M.: A surgical telemanipulator for femur shaft fracture reduction. *Int. J. Med. Robot. Comput. Assist. Surg.* **2**, 238–250 (2006)
7. Seide, K., Faschingbauer, M., Wenzl, M.E., Weinrich, N., Juergens, C.: A hexapod robot external fixator for computer-assisted fracture reduction and deformity correction. *Int. J. Med. Robot. Comput. Assist. Surg.* **1**(1), 64–69 (2004)
8. Abedinnasab, M.H., Gallardo-Alvarado, J., Farahmand F.: A Wide-open 3-legged parallel robot for long bone fracture reduction. *J. Mech. Robot.* **9**(1), 015001-1–015001-10 (2017)
9. Alizade, R.I., Tagiyev, N.R., Duffy, J.: A forward and reverse displacement analysis of a 6-DOF in-parallel manipulator. *Mech. Mach. Theory* **29**(1), 115–124 (1994)



# Multi-objective Optimization of a Reconfigurable Spherical Parallel Mechanism for Tele-Operated Craniotomy

Terence Essomba<sup>1</sup>(✉), Juan Sandoval<sup>2</sup>, Med Amine Laribi<sup>2</sup>,  
and Said Zeghloul<sup>2</sup>

<sup>1</sup> Department of Mechanical Engineering, National Central University,  
No. 300, Zhongda Road, Zhongli City, Taoyuan County 32001, Taiwan  
tessomba@cc.ncu.edu.tw

<sup>2</sup> Department of GMSC, Pprime Institute CNRS, ENSMA,  
University of Poitiers, UPR 3346, Poitiers, France

**Abstract.** The practice of neurosurgery sometime requires to open a large space through the skull. The drilling operation is called craniotomy. The neurosurgeon needs to use specific surgical drill to perform this task. The high dexterity required for this operation has justified the development of robotic system for the manipulation of craniotomy instruments. A series of motion capture and force experimentation on Human cadavers have been carried out to collect kinematic and force data for the definition of a mechanical architecture specification. A 3-RRR Spherical Parallel Mechanism is proposed for the manipulation of the neurosurgical drill. This mechanism is modified by adding a variable parameter that changes the configuration of its base. Three pantographic mechanisms are integrated to control this variable parameter. The mechanism is optimized to generate the highest kinematic performance and the lowest motor torque to generate the minimum required drilling force. A series of kinematic simulation reveals that the introduction of the new reconfiguration parameter can improve both the dexterity and the force transmission of the mechanism.

**Keywords:** Spherical parallel mechanism · Reconfigurable mechanism · Craniotomy · Motion capture · Optimization

## 1 Introduction

In open neurosurgery, a physical access to the patient's brain is required. However, it is protected by the most solid bone of Human anatomy, the skull. The neurosurgeon therefore need to provide an opening in order to insert specific neurosurgical instruments. A surgical technique called craniotomy can be performed to allow that physical access to the brain. It consists in using specific instruments to drill into the skull material [1]. For the most complicated cases, a very specific type of drill called “rosen burr” drill is required. The tip of this drill has the shape of a ball and it allows drilling both radially and axially as show in Fig. 1. Although this instrument provides more freedom of motion and flexibility than classical drills, only highly experienced neurosurgeons are allowed to operate it, due to the high level of dexterity that is required for to manipulate it.

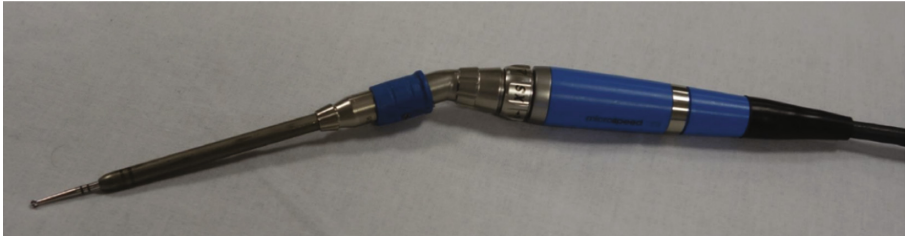


**Fig. 1.** “Rosen burr” type surgical drill for craniotomy.

The use of robotic manipulator for the control of the neurosurgical drill is justified by the high level of dexterity required for the manipulation of “rosen burr” drill. Robotics applications have been therefore continuously addressed since the end of the nineties. Indeed, the quality of craniotomy is significantly improved by the positioning accuracy provided by robots. Also, the use of robotic manipulators increases the stability of the motion. Due to the effort required to drill the skull, the neurosurgeon’s hand will have a brutal residual motion when the bone is completely drilled. Robotic manipulators do not suffer from such dangerous reactions. For these reasons, several cases of robotic assisted craniotomy have been reported. The first use of a robot to perform craniofacial surgery has been reported in 1998. It was an industrial manipulator PUMA 260 [3]. Since then, several anthropomorphic manipulators has been reprogrammed for craniotomy: “Neurobot” in 2001 [4], a Staubli RX-130 [5] and a CASPAR [5] both in 2003 [6], a PA-10 in 2006 [7]. Non-anthropomorphic architectures have then appeared in craniotomy: a Steward platform in 2007 [8], a mechanism that decouples position and orientation the same year [9], the “CRANIO” hexapod in 2010 [10], a reconfigurable hexapod in 2012 [11]. The recent literature highlights a new approach based on mechanism design, such as the optimization of a serial spherical mechanism in 2015 [12], the design of a decoupled hybrid mechanical architecture in 2016 [13] and the development of a parallel mechanism in 2018 [14].

The present work proposes to follow the recent tendency in robotic craniotomy by focusing on the mechanism design aspect. The multi-objective optimization of a spherical parallel mechanism adapted to craniotomy is proposed. The next Section presents the experiments that have permitted the kinematic and force specification analysis. The kinematic analysis of the mechanical architecture is studied in Sect. 3. The multi-objective optimization method and result are provided in Sect. 5. The last Section is dedicated to conclusion.

## 2 Specification Analysis

In order to collect the kinematic and force data associated to the practice of craniotomy, a series of medical experimentations have been carried out. The results will allow defining the specifications of a mechanism for this application.

## 2.1 Experimental Protocol

The development of robotic systems for craniotomy needs important design requirements: the motion and workspace of the surgical drill required to cut and remove the bone flap and the force interaction between the drill and the skull. Each aspect has been studied using to different experimental protocols. For the kinematic analysis, an experienced neurosurgeon was asked to perform this task on a training station (using 3D printed skull model) and in real situation (on cadaver), as shown in Fig. 1, in order to analyze the motion and the technique he uses. Meanwhile, a Qualysis optronic capture system was recording his motion of the drill. The system uses a set of high-resolution cameras to detect reflective markers placed on subject and the surgical drilling (Fig. 2).

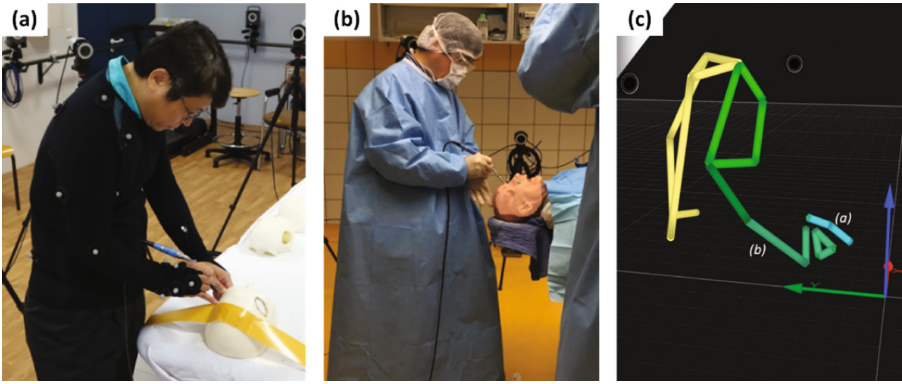


**Fig. 2.** Motion capture experimental setup: (a) Craniotomy training on 3D printed skull model - (b) Actual craniotomy on Human cadavers - (c) 3D reconstruction of the surgeon motion.

In order to record the efforts exerted by the drilling tool on the skull, a method based on a tele-operated robot has been used. It is composed of a 3-DoF control device (Novint Falcon) that can control a 7-DoF robot (Franka Emika). The surgeon controls the translational movements of the surgical drill held by the robot by operating the Novint Falcon. The control of angular motions is provided by pressing buttons on the device ball grip. Each joint of the Franka robot is equipped with a torque sensor that measures the external torques generated by the contact with the skull. These external torques  $\tau_{ext} \in \mathbb{R}^7$  are projected to the Cartesian space to obtain the contact forces/torques  $F_{ext} \in \mathbb{R}^6$  between the tool and the skull, through the following relationship:

$$F_{ext} = (\mathbf{J}^T)^+ \tau_{ext}, \quad (1)$$

Where  $\mathbf{J} \in \mathbb{R}^{6 \times 7}$  is the Jacobian matrix which denotes the relationship between the joint space and the end effector Cartesian space. A ROS-based framework is used to allow the data exchanges between the master and the slave system. Figure 3 shows the bloc diagram of the platform.



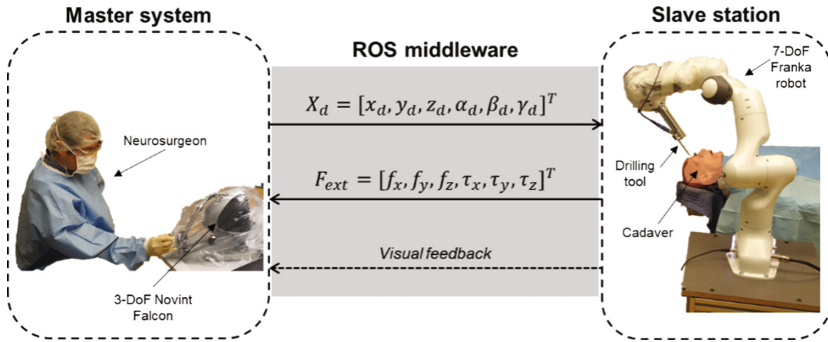


**Fig. 3.** Tele-operation platform with force feedback.

## 2.2 Motion and Force Data Analysis

The neurosurgeon has performed several craniotomy operations on in real situation (on Human cadaver) in the same conditions as in a surgical room. Several locations of the skull has been targeted: left frontal, hole frontal and temporal. During those operations, the software recorded the position of markers at frequency of 100 Hz. Then, the position of markers was used by the software in order to define the motion of different solids (drilling tool, segments of surgeon body). Marker coordinates are exported and processed under Matlab. The workspace swept by the surgical drill is described by a cone. This simple geometric form is given by a half-apex angle and tilt angle of the principal axis, namely  $\theta$  and  $\psi$  respectively. These angles are the Euler angles defined in Fig. 4. The maximal range obtained through motion capture computation are equal to  $\Delta\theta = 20^\circ$  and  $\Delta\psi = 18^\circ$ .

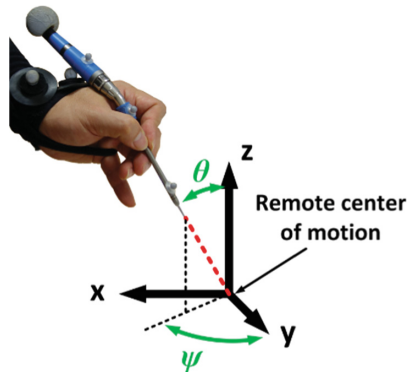


**Fig. 4.** Kinematic of the surgical drill in craniotomy.

In order to identify the order of magnitude of the interaction forces generated during a craniotomy, the neurosurgeon used the tele-operation platform presented in Fig. 3 to perform different craniotomy tasks on cadavers. The tele-operated robot has recorded forces for linear drilling trajectories executed on the frontal bone of the skull. Other similar trajectories were executed, obtaining the same order of magnitude for the tangential force, i.e. around 13 N as shown in one example illustrated in Fig. 5. The identification of this order of magnitude will be useful for the optimization of the mechanism to insure it is capable of supplying the same amount of force.

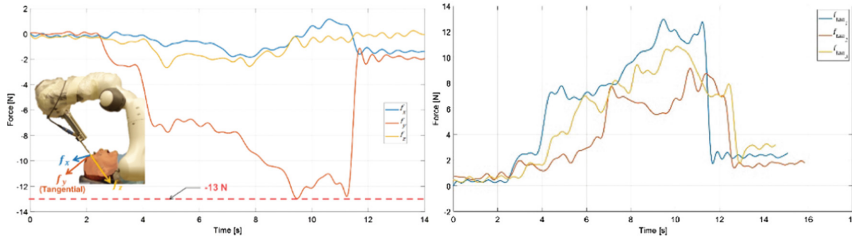


**Fig. 5.** Interaction forces recorded between the drilling tool and the skull during the execution of a tangential trajectory.

### 3 Reconfigurable Spherical Parallel Mechanism

A 3-RRR Spherical Parallel Mechanism (SPM) is proposed to manipulate the surgical drill. The kinematic and force aspect of this mechanism are studied.

#### 3.1 Mechanical Architecture

The 3-RRR SPM can be found in several references in the mechanism literature review [15, 16]. The choice of a spherical architecture is justified by the kinematic of the surgical drill that has been identified in the previous Section. It is also known that the use of a parallel architecture can increase the kinematic performance. In the present study, the SPM is improved by the integration of a variable parameter that modifies the mechanism behavior. The variable parameter changes the configuration of the mechanism base by re-orienting the first revolute joint axis of the legs  $\mathbf{z}_{IK}$  ( $K = A, B, C$ ). However, these axes must remain directed to the mechanism center of rotation. To insure that characteristic, three pantograph linkages are used to manipulate the  $\mathbf{z}_{IK}$  axes as shown on Fig. 5. The center of rotation of each pantographic linkage is located at the SPM center of rotation. Therefore, the value of the variable  $\omega$  is directly controlled by the configuration of the pantographic linkages. When  $\omega = 0$ , the base of the SPM will have a trihedral form (Fig. 6).

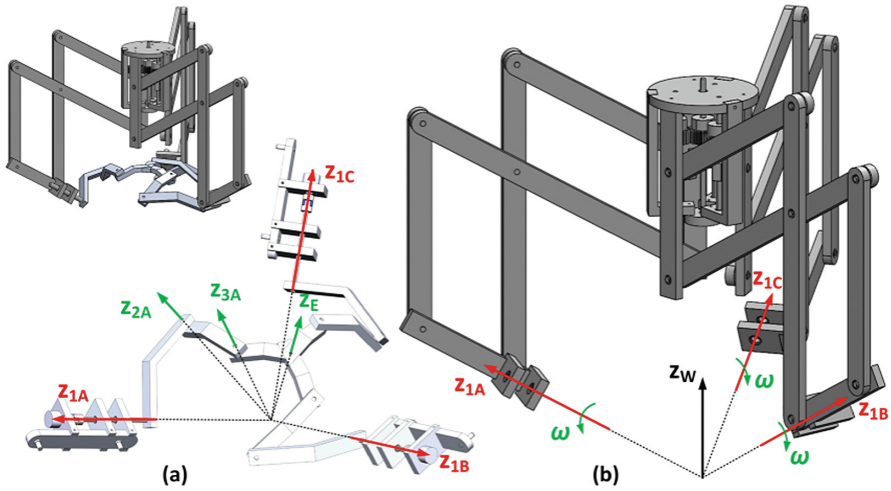


Fig. 6. Conceptual CAD of the 3-RRR reconfigurable spherical parallel mechanism.

### 3.2 Inverse Kinematic Model

The inverse kinematic model (IKM) of the 3-RRR SPM has been already addressed in [16]. The resolution method consists in finding, for each RRR leg, the input coordinate  $\theta_{1k}$  that places the second joint  $\mathbf{z}_{2k}$  at an angle of  $\beta$  from the third joint  $\mathbf{z}_{3k}$  which is located by the end effector. This can be described as followed:

$$\mathbf{z}_{2k} \cdot \mathbf{z}_{3k} = \cos \beta, \quad (2)$$

With  $k = A, B$  or  $C$ , referring to the mechanism RRR legs. For each leg, the input coordinate allowing the end effector to reach the orientation  $(\psi, \theta, \varphi)$  is given by the following equation:

$$\theta_{1k} = \cos^{-1} \left( N_k / \sqrt{L_k^2 + M_k^2} \right) + \text{atan2}(M_k, L_k), \quad (3)$$

With  $L_k, M_k$  and  $N_k$ , functions of the mechanism geometric parameters  $\alpha, \beta$  and  $\gamma$ , and the end effector orientation angles  $\psi, \theta$  and  $\varphi$ .

The IKM of the 3-RRR SPM can be resolved by finding the solution of Eq. (2). For each arm, the coordinates of the joint axes  $\mathbf{z}_{3k}$  are calculated using the rotation matrix  $\mathbf{R}_E$  and additional ones that include the angle  $\gamma$ . The axis  $\mathbf{z}_{2k}$  is calculated by the angle  $\alpha$ , the input coordinate  $\theta_{1K}$  and the angle  $\omega$  that gives the orientation of the base located by  $\mathbf{z}_{1k}$ . The SPM base axes coordinates are now obtained as follows:

$$\begin{cases} \mathbf{z}_{1A} = \mathbf{R}_x(\pi/4) \cdot \mathbf{R}_z(\omega) \cdot \mathbf{x} \\ \mathbf{z}_{1B} = \mathbf{R}_y(\pi/4) \cdot \mathbf{R}_x(\omega) \cdot \mathbf{y} \\ \mathbf{z}_{1C} = \mathbf{R}_z(\pi/4) \cdot \mathbf{R}_y(\omega) \cdot \mathbf{z} \end{cases} \quad (4)$$

Each base axis of the SPM is specifically oriented from one-unit vector of the origin reference frame ( $\mathbf{x}$ ,  $\mathbf{y}$  or  $\mathbf{z}$ ). The first rotation matrix allows the axis to spin so that of its  $\omega$ -inclination is oriented toward the center of the reference frame. The axis  $\mathbf{z}_{2K}$  of each arm is then calculated as shown below:

$$\begin{cases} \mathbf{z}_{2A} = \mathbf{R}_x(\theta_{1A}) \cdot \mathbf{R}_z(\alpha) \cdot \mathbf{z}_{1A} \\ \mathbf{z}_{2B} = \mathbf{R}_y(\theta_{1B}) \cdot \mathbf{R}_x(\alpha) \cdot \mathbf{z}_{1B} \\ \mathbf{z}_{2C} = \mathbf{R}_z(\theta_{1C}) \cdot \mathbf{R}_y(\alpha) \cdot \mathbf{z}_{1C} \end{cases} \quad (5)$$

For each arm, the IKM leads to the same solution as given by Eq. (3). The difference is that the parametric functions  $L_k$ ,  $M_k$  and  $N_k$  now include the variable  $\omega$ . It can be consequently anticipated that the variable has an impact on the SPM behavior (workspace, kinematic performance, etc.).

#### 4 Effort Model of the Mechanism

The velocity model of spherical parallel mechanism, that gives the relationship between the mechanism input velocities  $\dot{\mathbf{q}}$  and its end effector angular velocities  $\boldsymbol{\omega}$ , can be written in the following matrix form:

$$\mathbf{B}\dot{\mathbf{q}} = \mathbf{A}\boldsymbol{\omega}, \quad (6)$$

With  $\mathbf{A}$  and  $\mathbf{B}$  the parallel and serial Jacobian matrices. In the present case,  $\dot{\mathbf{q}} = [\dot{\theta}_{1A} \ \dot{\theta}_{1B} \ \dot{\theta}_{1C}]^T$ . When applied to the present 3-RRR SPM, the IKM given in Eq. (2), is differentiated with the time and written in a matrix form. The expression of the parallel and serial Jacobian matrices are found:

$$\mathbf{A} = \begin{bmatrix} (\mathbf{z}_{2A} \times \mathbf{z}_{3A})^T \\ (\mathbf{z}_{2B} \times \mathbf{z}_{3B})^T \\ (\mathbf{z}_{2C} \times \mathbf{z}_{3C})^T \end{bmatrix}, \mathbf{B} = \begin{bmatrix} \mathbf{z}_{1A} \times \mathbf{z}_{2A} \cdot \mathbf{z}_{3A} & 0 & 0 \\ 0 & \mathbf{z}_{1B} \times \mathbf{z}_{2B} \cdot \mathbf{z}_{3B} & 0 \\ 0 & 0 & \mathbf{z}_{1C} \times \mathbf{z}_{2C} \cdot \mathbf{z}_{3C} \end{bmatrix}. \quad (7)$$

Therefore, the Jacobian matrix  $\mathbf{J}$  of the SPM is given by:

$$\mathbf{J} = \mathbf{A}^{-1} \cdot \mathbf{B}. \quad (8)$$

As result, the relationship between the mechanism input torques  $\tau_A$ ,  $\tau_B$ ,  $\tau_C$  and the force applied by the end effector is written as:

$$\begin{bmatrix} \tau_A \\ \tau_B \\ \tau_C \end{bmatrix} = \mathbf{J}^{-1} \cdot \begin{bmatrix} f_x \\ f_y \\ f_z \end{bmatrix}, \quad (9)$$

With  $f_x$ ,  $f_y$  and  $f_z$  the components of the force exerted at the mechanism end effector.

## 5 Multi-objective Optimization

The 3-RRR RSPM is subject to an optimization for the practice of robotic craniotomy. The objective is to identify the dimensions that generates the highest performances.

### 5.1 Optimization Criteria and Formulation

A total of three indexes shall be calculated to process a population of RSPM individuals. An optimum mechanism must be able to cover the entire prescribed workspace identify in Sect. 2.2. A minimum prescribed workspace is therefore considered as a constraint. It is calculated by checking if the IKM has a non-complex solution all possible end effector orientations on that workspace. A solution to the IKM given by Eq. (3) can be written as followed:

$$\begin{cases} C_{k1}(\psi, \theta) = L_k^2 + M_k^2 - N_k^2 > 0 \\ C_{k2}(\psi, \theta) = L_k^2 + M_k^2 - 1 = 0 \end{cases} \quad (10)$$

With  $k = A, B$  or  $C$ . A function  $P_k$  is created to indicate if one RRR leg of the mechanism satisfies the conditions  $C_{k1}$  and  $C_{k2}$  for an orientation of its end effector:

$$P_k(\psi, \theta) = \begin{cases} 0 & \text{if } C_{k1} > 0 \text{ and } C_{k2} = 0 \\ 1 & \text{otherwise} \end{cases} \quad (11)$$

The minimum prescribed workspace index is then written and followed:

$$W(\mathbf{I}) = \sum_{\psi=0}^i \sum_{\theta=0}^j P(\psi, \theta), \quad (12)$$

Where  $P = P_A + P_B + P_C$  and  $\mathbf{I}$  is the design vector that contains the mechanism design parameters. The index  $W(\mathbf{I})$  counts the number of orientations that are not reachable by the mechanism. This index must be equal to zero for mechanism to be considered as a potential solution and to be evaluated with the optimization criteria.

Two criteria must be implemented in the present optimization: the global dexterity and the required motor torques. The mechanism local dexterity is calculated as the inverse of the Jacobian matrix conditioning number [17]. For each end effector orientation, this local index is calculated for several possible angle  $\omega$ . The maximum value given by the following equation is then considered as the local index.

$$\eta(\psi, \theta) = \max_{\omega} (1 - (1/\kappa(\mathbf{J}))). \quad (13)$$

The maximum local dexterity  $\eta$  is calculated for all orientation of the prescribed workspace and the mechanism global dexterity  $K(\mathbf{I})$  is the average value of these indexes:

$$K(\mathbf{I}) = \sum_{\psi=0}^i \sum_{\theta=0}^j \eta(\psi, \theta). \quad (14)$$

The implementation of the mechanism required torques as a criteria has two functions: (1) to insure that the mechanism is capable of supplying the minimum required drilling force identified in Sect. 2.2 and (2) to minimize the motor torques required to supply this force.

For a given set of force components  $[f_x, f_y, f_z]^T$ , the mechanism motor torques are found using Eq. (9). For each end effector orientation, these torques are calculated for all possible drilling tangential directions given by the angle  $\varphi$ . The force components are calculated as followed:

$$\begin{bmatrix} f_x \\ f_y \\ f_z \end{bmatrix} = R_z(\psi) \cdot R_x(\theta) \cdot R_z(\varphi) \cdot \begin{bmatrix} 0 \\ 0 \\ f_T \end{bmatrix}, \quad (15)$$

Where  $f_T$  is the value of the tangential force measured in Sect. 2.2 at 13 N. For an orientation of the end effector  $(\psi, \theta)$ , the mechanism motor torques  $\tau_A, \tau_B, \tau_C$  is calculated for all possible tangential directions and the maximum torque is collected.

$$\tau(\psi, \theta) = \max_{\varphi}(\tau_A(\varphi), \tau_B(\varphi), \tau_C(\varphi)), \quad (16)$$

The maximum value of the local index given by Eq. (16) over the workspace is collected as the global index.

$$T(\mathbf{I}) = \max_{(\psi, \theta)}(\tau(\psi, \theta)). \quad (17)$$

The optimization problem is formulated and implemented into a Genetic Algorithm (GA) to identify the most suitable mechanism design parameters. An optimization problem can be therefore written as followed:

$$\left\{ \begin{array}{l} \text{Minimize}(F(\mathbf{I})) \\ \text{Subject to } W(\mathbf{I}) = 0 \\ \mathbf{I} = [\alpha \quad \beta \quad \gamma] \\ x_i \in \mathbf{I}, \quad x_i \in [x_{i_{min}}; x_{i_{max}}] \end{array} \right\}, \quad (18)$$

Where  $F(\mathbf{I})$  is the fitness function calculated for the mechanism individual  $\mathbf{I}$ .

## 5.2 Results and Simulations

As a preliminary study, the GA has been executed to optimize the mechanism in term of kinematic performance and in term of force transmission using the fitness functions  $K(\mathbf{I})$  and  $T(\mathbf{I})$  by merging the two criteria in to a multi-objective fitness function. The algorithm now seeks to minimize the following function:

$$F(\mathbf{I}) = (1 - K(\mathbf{I})) * T(\mathbf{I}) \quad (20)$$

The GA has been executed with a population of 100 individuals and a termination convergence criterion of  $10^{-6}$ . At the XXth generation, an optimum population has

been identified. The kinematic optimization has resulted an optimum mechanism  $\mathbf{I}_{\text{opt}}$  that generates a global dexterity of 0.89 and its local dexterity goes from 0.74 to 0.99 for an angle  $\omega$  that varies from  $-78$  to  $-50$  as shown in Fig. 7-(a). Its design parameters are given as followed:

$$\mathbf{I}_{\text{opt}} = [85.72 \quad 85.72 \quad 35.27] \quad (21)$$

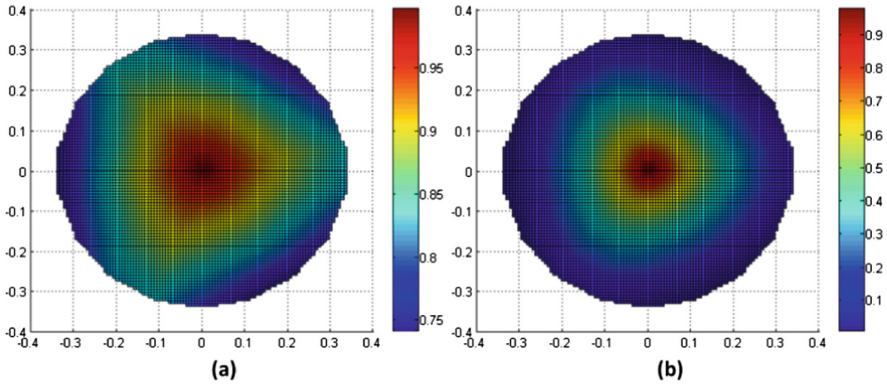


**Fig. 7.** Evolution of the dexterity over the prescribed workspace for the RSPM with variable base parameter (a) and for the classical SPM with fixe trihedral base (b).

Additional simulation have shown that if the parameter  $\omega$  was fixed to zero, the mechanism has dexterity that varies from 0.007 to 0.99. This shows that this parameter prevent the dexterity to drastically drop when the mechanism end effector moves away from its workspace center. It also revealed that by modifying the parameter  $\omega$  from  $-12$  to  $19$ , its motor torques vary from 0.07 to 4.44 Nm.

## 6 Conclusion

In the present study, a 3-RRR SPM has been proposed to perform craniotomy. A new parameter that can be used as to reconfiguration variable is used to optimize its dexterity and force transmission while manipulating the surgical drill. The mechanical method to control its value consists in using three pantographic linkages. A series of motion capture experiments have allowed to measure the motion of a surgical drill during craniotomy on Human cadavers. The data collected have allowed the kinematic optimization of the proposed RSPM. This represents an improvement in terms of safety would this mechanism be used for a robotic assisted craniotomy.

## References

1. Bast, P., Popovic, A., Wu, T., Heger, S., Engelhardt, M., Lauer, W., Radermacher, K., Schmieder, K.: Robot-and computer-assisted craniotomy: resection planning, implant modelling and robot safety. *Int. J. Med. Robot. Comput. Assist. Surg.* **2**, 168–178 (2006)
2. Hsiao, M.-H., Kuo, C.-H.: A review to the powered drilling devices for craniotomy. *J. Med. Dev.* **6**(1), 017557
3. Burghart, C., Raczkowski, J., Rembold, U., Wörn, H.: Robot cell for craniofacial surgery. In: *Proceedings of the 24th Annual Conference of the IEEE Industrial Electronics Society*, Aachen, Germany, pp. 2506–2511 (1998)
4. Sim, C., Ng, W.S., Teo, M.Y., Loh, Y.C., Yeo, T.T.: Image-guided manipulator compliant surgical planning methodology for robotic skull-base surgery. In: *International Workshop on Medical Imaging and Augmented Reality*, Shatin, Hong Kong, China, pp. 26–29 (2001)
5. Federspil, P.A., Geisthoff, U.W., Henrich, D., Plinkert, P.K.: Development of the first force-controlled robot for otoneurosurgery. *Laryngoscope* **113**(3), 465–471 (2003)
6. Korb, W., Engel, D., Boesecke, R., Eggers, G., Kotrikova, B., Marmulla, R., Raczkowski, J., Wörn, H., Mühling, J., Hassfeld, S.: Development and first patient trial of a surgical robot for complex trajectory milling. *Comput. Aided Surg.* **8**(5), 247–256 (2003)
7. Weimin, S., Jason, G., Yanjun, S.: Using tele-robotic skull drill for neurosurgical applications. In: *Proceedings of the IEEE International Conference on Mechatronics and Automation*, Luoyang, China, pp. 334–338 (2006)
8. Tsai, T.C., Hsu, Y.L.: Development of a parallel surgical robot with automatic bone drilling carriage for stereotactic neurosurgery. *Biomed. Eng.: Appl. Basis Commun.* **19**(4), 269–277 (2007)
9. Matinfar, M., Baird, C., Batouli, A., Clatterbuck, R., Kazanzides, P.: Robot-assisted skull base surgery. In: *Proceedings of the IEEE/RSJ International Conference on Intelligent Robots and Systems*, San Diego, CA, USA, pp. 865–870 (2007)
10. Cunha-Cruz, V., Follmann, A., Popovic, A., Bast, P., Wu, T., Heger, S., Engelhardt, M., Schmieder, K., Radermacher, K.: Robot- and computer-assisted craniotomy (CRANIO): from active systems to synergistic man-machine interaction. *Proc. Inst. Mech. Eng. Part H: J. Eng. Med.* **224**(3), 441–452 (2010)
11. Kobler, J.P., Kotlarski, J., Öltjen, J., Baron, S., Ortmaier, T.: Design and analysis of a head-mounted parallel kinematic device for skull surgery. *Int. J. Comput. Assist. Radiol. Surg.* **7**(1), 137–149 (2012)
12. Li, G.-K., Essomba, T., Wu, C.-T., Lee, S.-T.: Kinematic design and optimization of a novel dual-orthogonal remote center-of-motion mechanism for craniotomy. *Proc. Inst. Mech. Eng. Part C: J. Mech. Eng. Sci.* **231**(6), 1129–1145 (2016)
13. Essomba, T., Wu, C.-T., Lee, S.-T., Kuo, C.-H.: Mechanical design of a craniotomy robotic manipulator based on optimal kinematic and force performance. *Robot. Mechatron. Mech. Mach. Sci. Ser.* **37**, 191–198 (2016)
14. Dehghani, M., Moghadam, M.M., Torabi, P.: Analysis, optimization and prototyping of a parallel RCM mechanism of a surgical robot for craniotomy surgery. *Ind. Robot: Int. J.* **45**(1), 78–88 (2018)
15. Gosselin, C.M., Lavoie, E.: On the kinematic design of spherical three-degree-of-freedom parallel manipulators. *Int. J. Robot. Res.* **12**(4), 393–402 (1993)
16. Essomba, T., Laribi, M.A., Zeghloul, S., Poisson, G.: Optimal synthesis of a spherical parallel mechanism for medical application. *Robotica* **34**(3), 671–688 (2016)
17. Angeles, J., López-Cajún, C.S.: Kinematic isotropy and the conditioning index of serial robotic manipulators. *Int. J. Robot. Res.* **11**(6), 560–571 (1992)





# Autonomous Robot-Assistant Camera Holder for Minimally Invasive Surgery

Juan Sandoval<sup>(✉)</sup>, Med Amine Laribi, and Saïd Zeghloul

Department of GMSC, Pprime Institute,  
CNRS - University of Poitiers - ENSMA - UPR 3346, Poitiers, France  
{juan.sebastian.sandoval.arevalo,med.amine.laribi,  
said.zeghloul}@univ-poitiers.fr

**Abstract.** In this paper we present an autonomous camera holder robotic system for minimally invasive surgery (MIS). The proposed system is composed of a 7-DoF collaborative robot, i.e. Franka robot, holding the surgical camera and a motion capture system, i.e. Qualisys system, tracking online the surgical tools movements. The robot adapts its movements to continuously monitor the surgical gestures, based on the tools tips coordinates provided by the Qualisys system. The surgical camera is inserted into the patient's body through a surgical device, i.e. trocar, generating a kinematic constraint commonly known as Remote Center of Motion (RCM) constraint. In order to preserve the patient safety, the RCM constraint is guaranteed by the control approach. Moreover, a compliance control law is implemented to smooth the robot movements as well as to reduce the efforts generated by the human-robot interactions. Robot Operating System (ROS) framework has been used to establish the communication between the robot and Qualisys, using the UDP protocol for data exchange.

**Keywords:** Robot-assisted minimally-invasive surgery · Collaborative robot · Motion capture

## 1 Introduction

The use of robotized assistant systems for medical applications is growing rapidly in recent years [1]. In the context of minimally invasive surgery (MIS), researchers and companies are developing new robotic systems to join in the supply market, among others, the well-known Da Vinci surgical system [2].

Besides the functionalities provided by a fully teleoperated system, such as the Da Vinci system or other recently proposed systems [3], other different needs are evidenced by surgeons, where a robotic assistant could also provide a solution. For instance, in classical minimally invasive surgical procedures, the surgeon usually uses both hands to manipulate the surgical instruments (scissors, forceps, needle holders, ... etc.) during the task execution. These instruments are inserted into the patient's body through trocar devices placed at the desired incision points. In order to obtain a visual feedback of the surgical gestures, an endoscopy camera is also inserted into the patient's body and is held by a medical staff assistant or a medical student [4]. During the procedure, the surgeon continuously gives orders to the assistant to correctly move

the camera so that it correctly follows the surgical tips instruments. However, this method doesn't filter assistant hand's tremor, it generates a lack of precision, time delays in the surgical task execution as well as an increase of the stress suffered by the surgeon. Moreover, these difficulties can be significantly aggravated due to the lack of the assistant expertise. To overcome this problem, robotic solutions have been proposed over the past years. The Automated Endoscopic System for Optimal Positioning (AESOP) was a robotic camera holder developed by Computer Motion [5]. This robot provided different modes to be controlled, i.e. manual motion, joystick/foot pedal control, or voice control [6] and was tested in different laparoscopic surgeries [7]. Another proposed solution to replace the assistant is the EndoAssist camera holder robotic device, whose movements are directly controlled by the head movements of the surgeon, using an infrared device attached to his head [8]. It is worth mentioning that both the AESOP and the EndoAssist systems were discontinued due to a lack of commercial interest. Similarly, FreeHand is a lightweight robotic camera holder system, designed with ergonomic features. The direction of the camera movements is chosen by the surgeon through a head movement (using a headset) and the movement is activated using a footswitch [9]. More recently, EndoControl company produced ViKY, a 3-DoF robotized camera holder [10]. The robot is manually positioned over the trocar and fixed through a poly-articulated support. Surgeon can control the camera movements either by voice commands or through a footprint. In [11], a 7-DoF commercial robot is proposed as a camera holder, where gaze gestures of the surgeon are used to control the camera movements.

Although the solutions presented above replace the human assistant, surgeon is always requested to continuously send commands to the robot according to the desired camera movements. To cope with, an autonomous robot-assistant camera holder system for MIS is proposed in this paper, using a 7-DoF collaborative robot as the camera holder. Due to the kinematic constraint generated by the trocar device, creating a Remote Center of Motion (RCM) constraint [12], robot orientates the camera around the RCM point according to the instruments tips movements. Most of the studies carried out about the automatic instruments position identification concern the use of image recognition algorithms [13–16]. Unlike these methods, the presented work proposes to use a Motion Capture (MoCap) system composed of a set of 8 high resolution cameras, i.e. Qualisys system (<https://www.qualisys.com>), for the online pose instruments identification.

Several approaches have been proposed to consider the RCM constraint in the control approach of serial redundant robots, for instance, by exploiting the robot's null-space [17] or by defining the task-space coordinates in terms of the RCM coordinates [18]. In this work, a cartesian compliance control approach has been implemented [19], where the origin of the task-space coordinates is defined along the camera axis, so that it delimits the segment of the camera that will be inserted into the patient's body. Thus, a fixed desired position is defined in such a way that it coincides with the RCM constraint, whereas the desired orientation is automatically calculated to focus the camera towards the instrument tips. The zoom functionality is directly managed through the camera system. The main advantage of using a compliance control approach is to provide smooth robot movements, avoiding sudden changes of velocity, and to reduce the contact forces generated along the trocar.

This paper is organized as follows. The description of the robot-assistant platform is presented in Sect. 2. Then, the overall control approach allowing to determine the desired instrument tips position related to the robot reference frame as well as the torque control approach implemented in the robot are presented in Sect. 3. The last section presents the conclusions of the presented work.

## 2 Robot-Assistant Platform

The proposed robot-assistant platform is mainly composed of a 7-DoF Franka Emika robot and a MoCap Qualisys system. The proposed platform is presented in Fig. 1, in a surgical training environment. A potential surgeon executes training tasks with a pelvic trainer, whereas a 7-DoF collaborative robot, i.e. Franka Emika, holds and orientates the camera according to the instrument movements. During the task execution, the surgeon receives a visual feedback from the surgical camera, allowing him to keep visible his task execution.

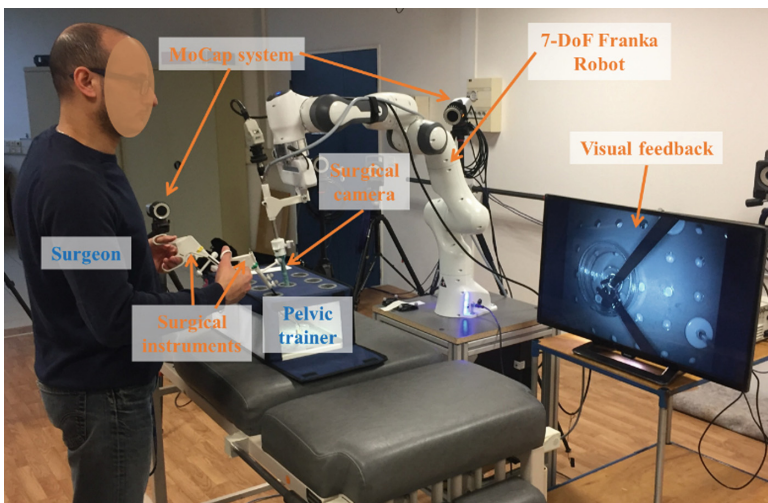


**Fig. 1.** Robot-assistant platform for camera holder assistant during MIS

The MoCap system is composed of 8 high resolution IR cameras allowing to identify the position of 4 markers fixed on each surgical instrument. The identification of these markers allowed to reconstruct the overall position and orientation of each instrument as a rigid-body, with respect to the Qualisys reference frame fixed to the base of the robot. Knowing the relative distances between the markers and the tip on each instrument, it is possible to identify in real time the position coordinates of each instrument tip. Figure 2 shows a screenshot of the instruments bodies reconstructed on real time by the MoCap system, where the relative reference frame for each instrument has been placed at its tip.

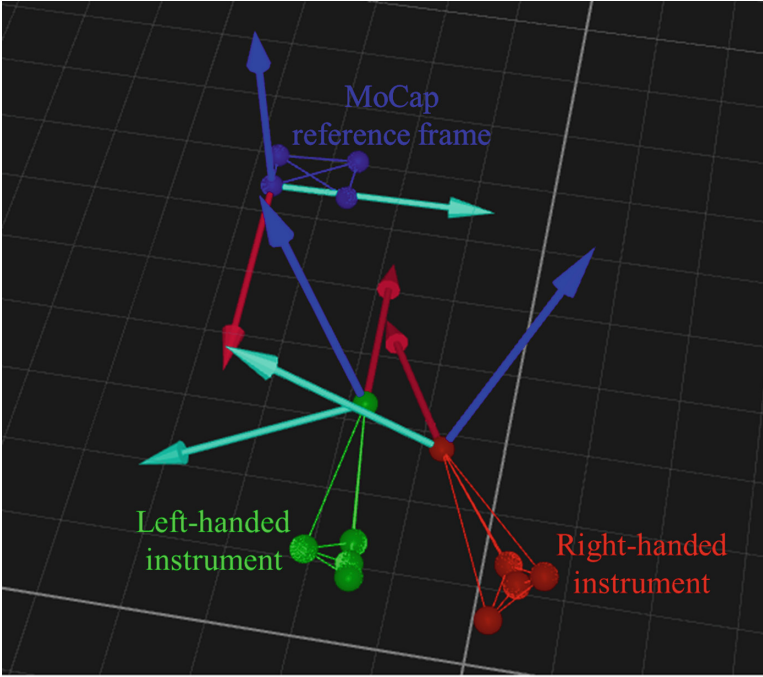


**Fig. 2.** Screenshot of the Qualisys system 3D reconstruction

### 3 Control Approach

Communication between the Qualisys system and the Franka robot has been established using the Robot Operating System (ROS) framework, using the User Datagram Protocol (UDP) for data exchange, where the Franka controller and the Qualisys laptop run at 1 kHz and 0.1 kHz, respectively.

In the following, the mapping between the MoCap and Franka coordinates is described. Then, the compliance control approach implemented to guarantee smooth movements is depicted.

#### 3.1 Coordinates Transformation

Figure 3 shows the reference frames fixed to each component of the platform. Concerning the camera holder robot,  $\{F\}$  has been defined as the fixed reference frame attached to the base of the robot. Reference frame  $\{C\}$  is fixed to the camera and its origin is located along the camera axis. Before starting the surgical procedure, a gravity compensation law is activated in the robot controller in order to allow a member of the medical staff to manually move the robot until the trocar and insert the camera into the patient's body (represented by the pelvic trainer in Fig. 1), ensuring that the origin of  $\{C\}$ , coincides with the RCM generated by the trocar. In the next section, a cartesian

control law for the robot is defined, where the task-space coordinates are related to the fixed reference frame  $\{F\}$ , and defined by the position coordinates of the origin of  $\{C\}$  and its orientation.

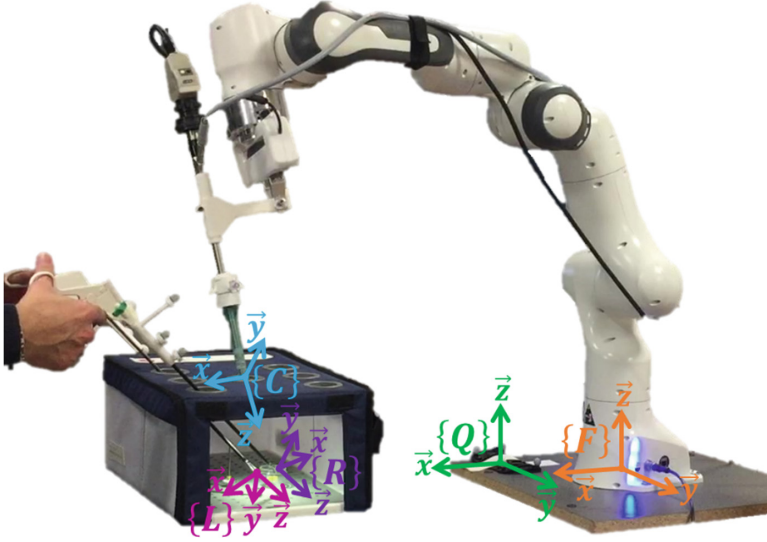


**Fig. 3.** Representation of the transformation between the reference frames defined for each element of the platform

The reference frame of the MoCap system, denoted by  $\{Q\}$ , has been fixed to the base of the robot. The homogeneous transformation matrix of  $\{Q\}$  with respect to  $\{F\}$  is defined as follows,

$$T_Q^F = \begin{bmatrix} I^{3 \times 3} & P_Q^F \\ 0^{1 \times 3} & 1 \end{bmatrix} \quad (1)$$

where  $P_Q^F$  is the constant position coordinates of the origin of  $\{Q\}$  with respect to  $\{F\}$ .

The reference frames  $\{R\}$  and  $\{L\}$  are attached to the right-handed and left-handed instruments, respectively, with the origin located at each instrument tip. In order to simultaneously focus the camera towards the two instruments tips, a virtual focus target point  $P_T^Q$  has been calculated as the middle coordinate point between the two tips with respect to  $\{Q\}$ ,

$$P_T^Q = \frac{P_R^Q + P_L^Q}{2} \quad (2)$$

where  $P_R^Q$  and  $P_L^Q$  are the position coordinates of the origin of  $\{R\}$  and  $\{L\}$  with respect to  $\{Q\}$ , respectively. Then, the target point can be mapped to the robot reference frame  $\{F\}$  through the transformation matrix  $T_Q^F$ ,

$$P_T^F = T_Q^F P_T^Q \quad (3)$$

The desired camera orientation is such that the z-axis of  $\{C\}$  is oriented towards the target point  $P_T^F$ . Defining the target unit vector  $\hat{V}_T^F = \frac{P_T^F - P_C^F}{\|P_T^F - P_C^F\|}$ , the error between the current and the actual camera orientation can be represented as an angle error  $\theta_e$  measured around an axis  $e_{axis}^F$ , based on the axis-angle representation. Thus, the orientation error  $e_o^F \in \mathbb{R}^3$  can be written as follows,

$$e_o^F = \theta_e \cdot e_{0_{axis}}^F = \cos^{-1}(\hat{V}_T^F \cdot \hat{Z}_C^F) \cdot (\hat{V}_T^F \times \hat{Z}_C^F) \quad (4)$$

where  $\hat{Z}_C^F$  is the unit vector of the z-axis in  $\{C\}$ , with respect to  $\{F\}$ .

Finally, the position error  $e_p^F \in \mathbb{R}^3$  can be defined as the difference between the origin position of  $\{C\}$  with respect to  $\{F\}$ ,  $P_C^F$ , and the RCM position  $P_{RCM}^F$  generated by the trocar,

$$e_p^F = P_C^F - P_{RCM}^F \quad (5)$$

### 3.2 Robot Control

The proposed camera holder robot, i.e. Franka Emika, is a 7-DoF ( $n = 7$ ) collaborative robot conceived to coexist and share a common workspace with human. Since the robot has torque-controlled features, a compliant control strategy [19] can be implemented. As explained before, the compliance feature allows to smooth robot movements, avoiding sudden gestures, as well as to reduce the intensity of the interaction forces at the insertion position of the camera into the patient's body, i.e. trocar position. Thus, it is possible to define the torque control input  $T_i$  as follows:

$$T_i = J^T [K_{p_x} e_x - K_{d_x} \dot{X}_c] + \hat{C}(q_c, \dot{q}_c) + \hat{g}(q_c) \quad (6)$$

The cartesian error  $e_x \in \mathbb{R}^6$  is composed of the orientation and position errors defined in (5) and (6), i.e.  $e_x = [e_p^F \ e_o^F]^T$ . The current cartesian velocity is represented by  $\dot{X}_c \in \mathbb{R}^6$ . The torque input compensates the inertial and dynamic effects by including an estimation of the Coriolis and Centrifugal torques  $\hat{C}(q_c, \dot{q}_c) \in \mathbb{R}^n$ , as well as the gravity compensation torques  $\hat{g}(q_c) \in \mathbb{R}^n$ , calculated according to the current joint position vector  $q_c \in \mathbb{R}^n$ .

The degree of compliance is regulated along each axis (in position and orientation) by the choice of the cartesian stiffness diagonal matrix  $K_{p_x}$  and the cartesian damping diagonal matrix  $K_{d_x}$ .

Preliminary experimentations have been achieved in a pelvic trainer during simple exercises of pick and place, where the practicing had to move and insert the objects into a metallic stem. Some screenshot of the proposed tasks are provided in Fig. 4. As it can be observed, robot continuously orientates the camera so that the two instrument tips could always be focused.

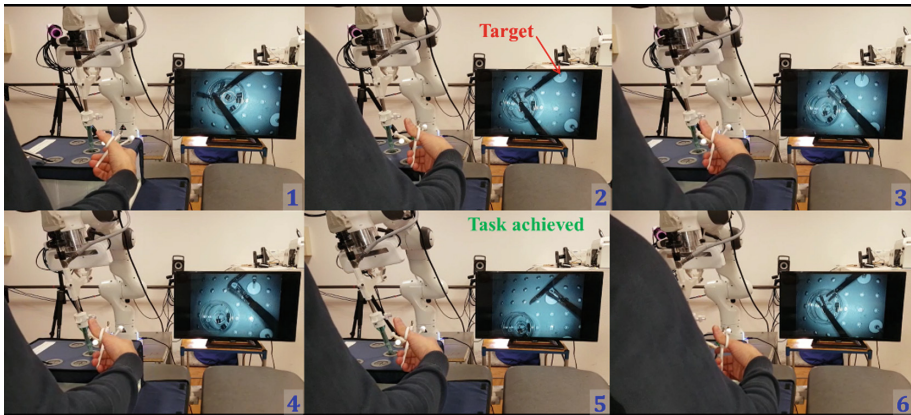


**Fig. 4.** Screenshots of a classical pick and place training task performed in a pelvic trainer

## 4 Conclusion

In this paper, an autonomous Robot-Assistant Camera Holder for Minimally Invasive Surgery was presented. The proposed system is based on real time tracking of the surgical tool movements avoiding the continuous request of surgeon instructions, contrary to existing systems. An additional advantage yields on the use of a collaborative robot allowing the smooth motion given by the implemented compliant control. The presented innovative solution has been preliminary validated through experimental tests performed under pelvic trainer during simple exercises of pick and place. Future work will be focused on the validation of autonomous robot-assistant camera holder during a real suturing tasks on cadavers.

**Acknowledgements.** This research was funded by the region “Nouvelle-Aquitaine” (program HABISAN 2015-2020) with the financial participation of the European Union (FEDER/ERDF, European Regional Development Fund). This work was also sponsored by the French government research program Investissements d’avenir through the Robotex Equipment of Excellence (ANR-10-EQPX-44).

## References

1. Hoeckelmann, M., Rudas, I.J., Fiorini, P., Kirchner, F., Haidegger, T.: Current capabilities and development potential in surgical robotics. *Int. J. Adv. Robot. Syst.* **12**, 16 (2015)



2. Intuitive Surgical Inc. History – da Vinci surgery is born August 2012. [http://www.intuitivesurgical.com/company/history/is\\_born.html](http://www.intuitivesurgical.com/company/history/is_born.html). Accessed 10 Oct 2014
3. Ateş, G., Majani, R., Dede, M.C.: Design of a teleoperation scheme with a wearable master for minimally invasive surgery. In: Carbone, G., Ceccarelli, M., Pisla, D. (eds.) *New Trends in Medical and Service Robotics: Advances in Theory and Practice*, pp. 45–53. Springer, Cham (2019)
4. Abbas, P., Holder-Haynes, J., Taylor, D.J., et al.: More than a camera holder: teaching surgical skills to medical students. *J. Surg. Res.* **195**(2), 385–389 (2015)
5. Taylor, R.H., Menciassi A., Fichtinger G., Dario, P.: Medical robotics in computer-integrated surgery. In: Siciliano, B., Khatib, O. (eds.) *Handbook of Robotics*, Ch. 66, 2nd edn., pp. 1199–1222. Springer Cambridge (2008)
6. Allaf, M.E., et al.: Laparoscopic visual field: Voice versus foot pedal interfaces for control of the aesop robot. *Surg. Endosc.* **12**, 1415–1418 (1998)
7. Kraft, B.M., Jäger, C., Kraft, K., Leibl, B.J., Bittner, R.: The AESOP robot system in laparoscopic surgery: Increased risk or advantage for surgeon and patient? *Surg. Endosc. Other Int. Tech.* **18**, 1216–1223 (2004)
8. Gilbert, J.M.: The endoassist robotic camera holder as an aid to the introduction of laparoscopic colorectal surgery. *Ann. Roy. Coll. Surg. Engl.* **91**(5), 389–393 (2009)
9. Stolzenburg, J., Franz, T., Kallidonis, P., Minh, D., Dietel, A., Hicks, J., Nicolaus, M., Al-Aown, A., Liatsikos, E.: Comparison of the FreeHand® robotic camera holder with human assistants during endoscopic extraperitoneal radical prostatectomy. *BJU Int.* **107**, 970–974 (2011)
10. Voros, S., Haber, G.P., Menudet, J.F., Long, J.A., Cinquin, P.: ViKY robotic scope holder: initial clinical experience and preliminary results using instrument tracking. *IEEE/ASME Trans. Mechatron.* **6**, 879–886 (2010)
11. Fujii, K., Salerno, A., Sriskandarajah, K., Kwok, K., Shetty, K., Yang, G.: Gaze contingent cartesian control of a robotic arm for laparoscopic surgery. In: 2013 IEEE/RSJ International Conference on Intelligent Robots and Systems, Tokyo, pp. 3582–3589 (2013)
12. Kuo, C.-H., Dai, J.S., Dasgupta, P.: Kinematic design considerations for minimally invasive surgical robots: an overview. *Int. J. Med. Rob. Comput. Assist. Surg.* **8**(2), 127–145 (2012)
13. Nageotte, F., Zanne, P., Doignon, C., De Mathelin, M.: Visual servoing-based endoscopic path following for robot-assisted laparoscopic surgery. In: 2006 IEEE/RSJ International Conference on Intelligent Robots and Systems, pp. 2364–2369 (2006)
14. Wei, G.-Q., Arbter, K., Hirzinger, G.: Real-time visual servoing for laparoscopic surgery. *IEEE Eng. Med. Biol. Mag.* **16**, 40–45 (1997)
15. Voros, S., Long, J., Cinquin, P.: Automatic localization of laparoscopic instruments for the visual servoing of an endoscopic camera holder. *Med. Image Comput. Comput. Assist. Interv.* **4190**, 535–542 (2006)
16. Krupa, A., Gangloff, J., Doignon, C., Mathelin, M., Morel, G., Leroy, J., Soler, L., Marescaux, J.: Autonomous 3D positioning of surgical instruments in robotized laparoscopic surgery using visual servoing. *IEEE Trans. Robot. Autom.* **19**(5), 842–853 (2003)
17. Sandoval, J., Poisson, G., Vieyres, P.: Improved dynamic formulation for decoupled cartesian admittance control and RCM constraint. In: 2016 IEEE International Conference on Robotics and Automation (ICRA), pp. 1124–1129. IEEE (2016)
18. Sandoval, J., Poisson, G., Vieyres, P.: A new kinematic formulation of the RCM constraint for redundant torque-controlled robots. In: 2017 IEEE/RSJ International Conference on Intelligent Robots and Systems (IROS). IEEE (2017)
19. Ott, C.: *Cartesian impedance control of redundant and flexible-joint robots*. Springer-Verlag, Heidelberg (2008)





# A Low-Cost 6-DoF Master Device for Robotic Teleoperation

Juan Sandoval<sup>(✉)</sup>, Med Amine Laribi, and Said Zeghloul

Department of GMSC, Pprime Institute CNRS, ENSMA, University of Poitiers,  
UPR 3346, Poitiers, France

{juan.sebastian.sandoval.arevalo,med.amine.laribi,  
said.zeghloul}@univ-poitiers.fr

**Abstract.** This paper deals with the design and application of a low-cost master device with six degrees of freedom (6-DoF), with haptic feedback along the three translational axes. The proposed device has been developed using the association of a Novint Falcon, a commercial 3-DoF translational haptic interface, and of a spherical wrist integrating an inertial measurement unit to fully control the orientation. The main focus of this paper is the practical issues related to the use of such a master device for robotic teleoperation and its capabilities to be used in medical applications, namely for robot-assisted Doppler sonography. Experimentations in a tele-operation platform using a slave collaborative robot demonstrate the usefulness of the proposed 6-DoF device.

**Keywords:** 6-DoF master device · Doppler sonography · Teleoperation · Haptic feedback

## 1 Introduction

Haptic technology has been applied in many different applications, in particular, virtual reality simulation, surgery, training, rehabilitation, manufacturing and design. In the medical field, haptics enhances skill acquisition [1] and interaction with tools [2]. As well, haptic sensation has been used in rehabilitation robots for enabling more efficient and effective training. In general, haptic devices are based on mechanical interfaces that relate tactile information between a human and the device.

Several haptic devices have been developed and built on serial, parallel or hybrid architectures. In general, serial devices, as the PHANTOM 6DoF [3] and the Freedom-7 [4], suffer from inertia, rigidity, and positioning accuracy issues. To cope with these drawbacks, devices with parallel architectures have been proposed with double-chain legs and a novel configurable platform [5], for instance. But parallel architectures in turn suffer from limited workspace and singular configurations inside the workspace. As a consequence and in order to take advantage from each architecture specifications, hybrid architectures have been explored by some researchers. For instance, one can cite the commercial devices Sigma.7 from Force Dimension, the compact 6-DOF device from Tsumaki et al. [6], or the Delta-R [7] combining a Delta robot [8] for translational motions and a serial wrist for rotational motions.

These hybrid devices present acceptable performances and are suitable for haptic applications. They benefit from additional improvements in rigidity and inertia due to the parallel architecture section as well as of an enlarged workspace given by the serial architecture section. In general, additional improvements are always needed.

In the context of teleoperation systems, several applications require a master device allowing to control a 6-DoF Cartesian task executed by the slave robot. Nevertheless, most of the 6-DoF commercial haptic interfaces are usually too expensive, such as the ones aforementioned. Otherwise, a few cheaper solutions can be found but against a loss of DoF and performance. In addition, it is common that commercial interfaces are not easily adapted to specific situations and applications. In some cases, such as in robot-assisted Doppler Sonography [9, 10] where a sonographer tele-operates a robot holding an ultrasound probe over the patient's body, the Cartesian task has to be fully controlled (6-DoF), whereas only force feedback along the translation coordinates (3-DoF) is required.

For a moderate investment, an optimal solution fulfilling the requirements of this type of applications is presented in this paper. The proposed device associates a 3-DoF commercial haptic device for the translational control and haptic feedback, i.e. Novint Falcon interface, and a spherical wrist coupled to its end-effector. In order to obtain the orientation of the spherical wrist, an inertial measurement unit (IMU) has been integrated. Although the Novint Falcon is an inexpensive haptic device, several studies have proved its excellent quality-price ratio for diverse applications [11–13]. Due to the parallel architecture of the Novint Falcon, the proposed device keeps all the mentioned advantages of a hybrid architecture, with position/orientation directions fully decoupled.

The paper is organized as follows. Section 2 depicts the architecture of the proposed 6-DoF master device. The master device is integrated in a teleoperation platform using a slave collaborative robot, as described in Sect. 3. Experimental results allowing to validate the usefulness of the master device in the teleoperation platform is presented in Sect. 4. Conclusions of the presented work are provided in the last section.

## 2 The 6-DoF Master Device

The Novint Falcon is a 3-DoF haptic device allowing only translational motions (see Fig. 1). Its kinematics is based on a 3-DoF variant of the parallel delta-robot configuration, similar to the one proposed by Tsai [14], whereby the spherical joints of Clavel's design [15] are replaced by single DoF rotary joints. The workspace is characterized by a 3D displacement of 10.16 cm along each direction, and a maximum force feedback of around 9 N.

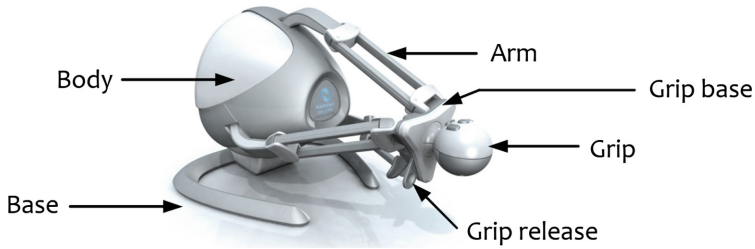


**Fig. 1.** 3-DoF Novint Falcon<sup>TM</sup> haptic device [taken from [www.vrs.org.uk](http://www.vrs.org.uk)].

The proposed device augments the available DoF of the Falcon interface by attaching a spherical wrist to its end-effector, as shown in Fig. 2. The remaining end-effector linked to the wrist has been designed in the form of a virtual probe, called holder, including an inertial measurement unit. This association allows to create a 6-DoF device with haptic feedback along the translational axes.

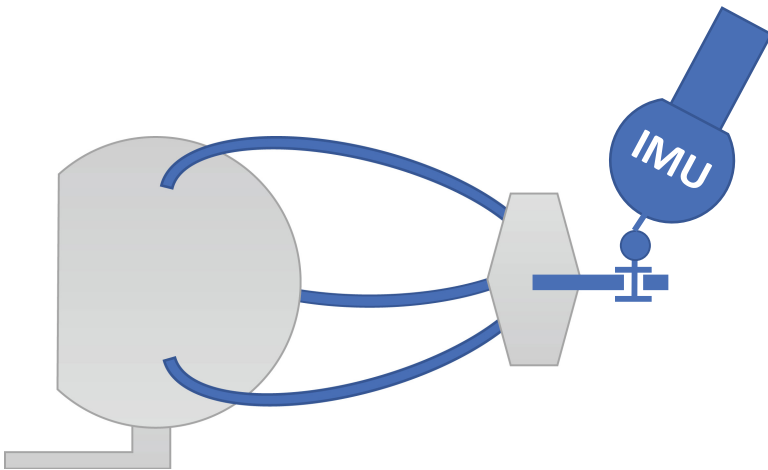


**Fig. 2.** Low cost 6-DoF master device architecture.

A first issue addressed in the design of this association was to obtain the largest orientation workspace. In the context of Doppler sonography, the required workspace was investigated in [9]. Furthermore, the same kinematics can also be used for robotized craniotomy applications [16]. The results of experimentations have highlighted that the tele-ultrasound system as well as the tele-craniotomy system are able to perform the requested motions. The probe as well as the drilling tool, respectively, are able to make a spherical wrist (three DoF of rotation) and translations along their three axes (for translational motion). The design of the holder has the same shape of real probe for the case of echo Doppler examination, and it can also be assimilated to a real drilling tool for craniotomy. This reduces the learning period.

The ADIS 16470 IMU sensor from Analog Devices has been used to measure the holder's attitude (Roll, Pitch and Yaw angles), through the given triaxial gyroscopes and accelerometers. These angles can be obtained from  $\varphi_1$ ,  $\varphi_2$  and  $\varphi_3$  which represent respectively the angles around the X, Y and Z-axis of the holder as illustrated in Fig. 3.

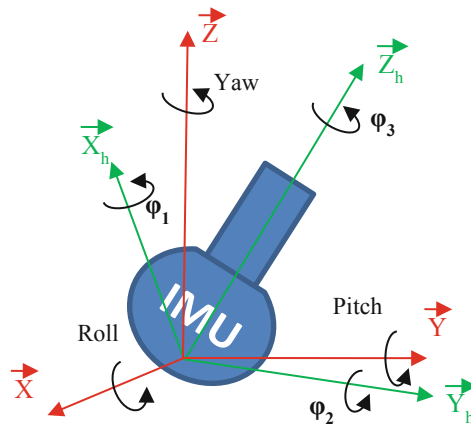


Fig. 3. Reference frame and axis of the holder

### 3 Control Architecture for Robotic Teleoperation

#### 3.1 Teleoperation Platform

The robotics team of Pprime Institute develops teleoperation platforms based on collaborative robots. These platforms are mainly developed for medical applications, such as Doppler sonography or surgery applications. On this context, we propose a new teleoperation platform using the master device with 6-DoF and a 7-DoF Franka Emika robot. ROS-based framework is used to establish the data exchanges between the master device and the robot. Figure 4 shows a bloc diagram of the proposed platform.

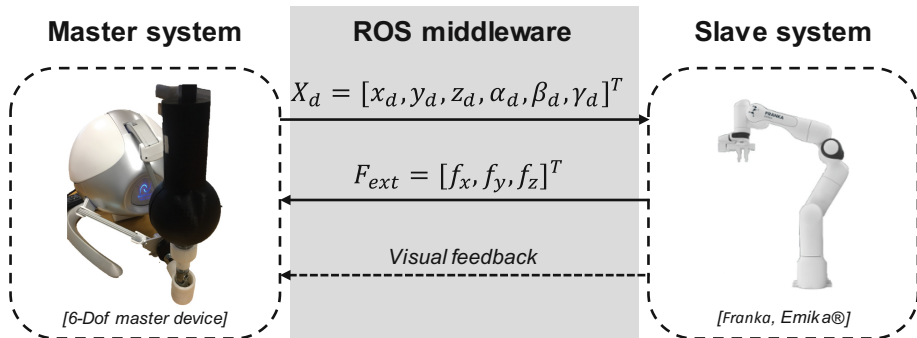


Fig. 4. Teleoperation platform using a 6 DoF master device and a collaborative robot.

Franka Emika is a 7-DoF ( $n = 7$ ) torque-controlled robot useful to coexist with human in a shared common workspace. We can then implement a compliant strategy to guarantee a safe physical human-robot interaction. Thus, the torque control input  $T$  is defined as follows:

$$T = J^T [K_{p_x}(X_d - X_c) - K_{d_x}\dot{X}_c] + N(q_c)\xi + \hat{C}(q_c, \dot{q}_c) + \hat{g}(q_c) \quad (1)$$

The master device provides the desired pose vector  $X_d \in \mathbb{R}^m$  of dimension  $m = 6$ , where  $X_d$  is composed of the desired position vector,  $X_{d_p}$ , and the desired orientation vector,  $X_{d_o}$ , i.e.  $X_d = [X_{d_p} \ X_{d_o}]^T$ . The current pose is represented by  $X_c \in \mathbb{R}^m$ . The torque input compensates the inertial and dynamic effects by including an estimation of the Coriolis  $\hat{C}(q_c, \dot{q}_c) \in \mathbb{R}^n$  and gravity  $\hat{g}(q_c) \in \mathbb{R}^n$  torques, calculated according to the current joint position vector  $q_c \in \mathbb{R}^n$ . The transpose of the Jacobian matrix  $J \in \mathbb{R}^{m \times n}$  allows a projection between the Cartesian and the joint space. Moreover, redundancy of the robot can be exploited by performing additional tasks through the vector  $\xi \in \mathbb{R}^n$  projected to the null-space by a projector  $N(q_c)$ . The compliance law is regulated by the constants  $K_{p_x}$  and  $K_{d_x}$ .

### 3.2 Kinematics and Translation/Orientation Relationships

The kinematics of the Novint Falcon, being equivalent to the general Delta robot, allows to tele-operate the translation of the Franka slave robot along the three axes. In order to synchronize the Franka and the falcon movements, the desired position vector  $X_{d_p}$  can be defined as follows,

$$X_{d_p} = X_{i_p} + \Delta X_{Falcon_p} \quad (2)$$

where  $X_{i_p}$  represents the initial position of the Franka's end-effector and  $\Delta X_{Falcon_p}$  is the falcon displacement. A button has been adapted in the device to allow largest movements, assigning  $X_{i_p}$  to the current position.

Let redefine the pose error  $e_X = X_d - X_c$  in (1), including both the position and orientation errors, i.e.  $e_X = [e_p \ e_o]^T$ . Concerning the position error, it can be calculated as,

$$e_p = X_{d_p} - X_{c_p} \quad (3)$$

with  $X_{c_p}$  as the current franka Cartesian position.

The orientation control has been developed based on quaternion representation. First, the current probe orientation can be represented through a quaternion, i.e.  $Q_{c_{probe}} = f(\varphi_1, \varphi_2, \varphi_3)$ . Once the tele-operation task is activated (through an user button), the initial difference between the probe orientation and the slave orientation is measured through the quaternion  $Q_{delta}$ . The desired tool orientation is the calculated as,

$$Q_d = Q_{delta} * Q_{c_{probe}} \quad (4)$$

The quaternion error between the current and desired orientation is given by,

$$Q_e = Q_c * Q_d^{-1} \quad (5)$$

This error can also be expressed in terms of the equivalent axis-angle representation, i.e.  $Q_e \equiv \{e_{o_{axis}}, e_{o_{angle}}\}$ , in order to obtain an available 3-dimension error to complete the pose error  $e_X$ ,

$$e_o = e_{o_{axis}} \cdot e_{o_{angle}} \quad (6)$$

## 4 Teleoperation Task and Experiments

In order to verify the effectiveness of the proposed master device, a simple teleoperation task has been performed, using the teleoperation platform presented in Sect. 3. The task consisted on execution translational and rotational movements along the three axis with the proposed device. The compliance parameters were chosen as:  $K_{p_x} = \text{diag}\{6000, 6000, 6000, 800, 800, 800\}$  N/m and  $K_{d_x} = \text{diag}\{300, 300, 300, 40, 40, 40\}$  Ns/m, respectively. The objective function (null-space) was used to stabilize the internal motion by minimizing the joint velocities, as follows:  $\xi = -0.1\dot{q}_i$ . Figures 5 and 6 show the obtained results, where a comparison between de desired pose given by the user through the master device and the trajectory executed by the Franka robot.

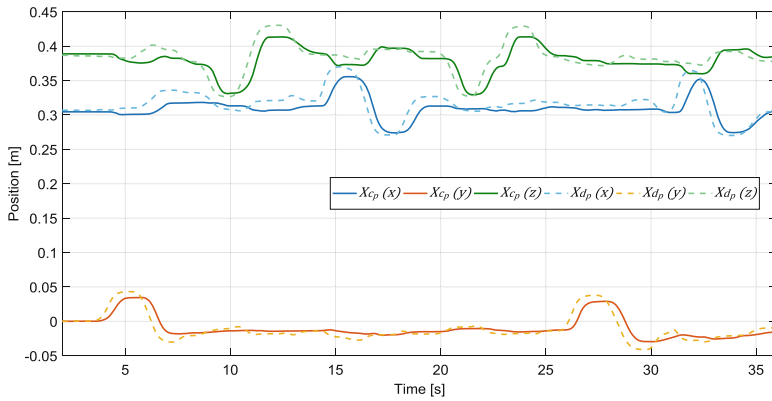


**Fig. 5.** Position trajectories of the master and slave devices.

It is worth mentioning that the time offset between the master and slave trajectories is not given by a communication delay, it is actually the natural effect of the compliance control law applied to the robot, where higher values of  $K_{p_x}$ , tuning the virtual stiffness, generate minor time offset values.

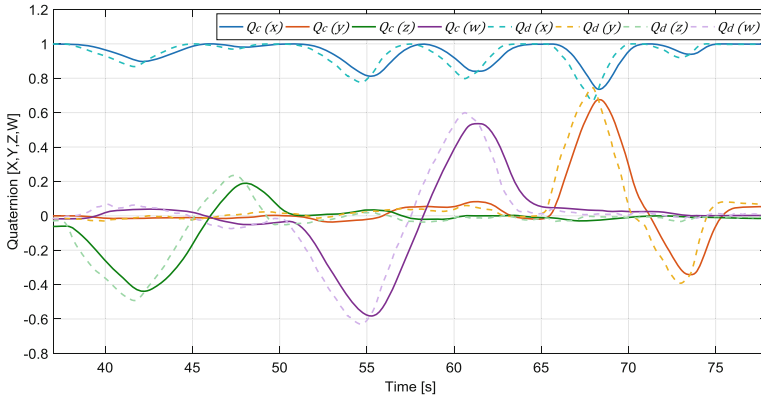


**Fig. 6.** Orientation trajectories of the master and slave devices.

## 5 Conclusion

The paper has described the design and implementation of a low-cost master device with six degrees of freedom (6-DoF). The aim of this work is not to provide the haptic community with a new interface but instead to demonstrate that it is possible to design and build a simple one, based on the association of one Novint Falcon and an inertial measurement unit. The proposed interface is validated through a teleoperation scheme of a collaborative robot and specifically during the Doppler sonography teleoperation.

**Acknowledgements.** This research was funded by the region “Nouvelle-Aquitaine” (program HABISAN 2015–2020) with the financial participation of the European Union (FEDER/ERDF, European Regional Development Fund). This work was also sponsored by the French government research program Investissements d’avenir through the Robotex Equipment of Excellence (ANR-10-EQPX-44).

## References

1. Su, E.L.M., Ganesh, G., Yeong, C.F., Teo, C.L., Ang, W.T., Burdet, E.: Effect of grip force and training in unstable dynamics on micromanipulation accuracy. *IEEE Trans. Haptics* **4**(3), 167–174 (2011)
2. Okamura, A.M.: Methods for haptic feedback in teleoperated robot-assisted surgery. *Ind. Robot.* **31**(6), 499–508 (2004)
3. Massie, T.H., Salisbury, J.K.: The phantom haptic interface: a device for probing virtual objects. In: *Proceedings of the ASME Winter Annual Meeting, Symposium on Haptic Interfaces for Virtual Environment and Teleoperator Systems*, vol. 55, pp. 295–300 (1994). <https://doi.org/10.1.1.361.4710>
4. Hayward, V., Gregorio, P., Astley, O., Greenish, S., Doyon, M., Lessard, L., McDougall, J., Sinclair, I., Boelen, S., Chen, X., et al.: Freedom-7: a high fidelity seven axis haptic device with application to surgical training. In: *Experimental Robotics V*, pp. 443–456 (1998)

5. Lee, J., Eom, K.: Design of a new 6-DOF parallel haptic device. In: IEEE International Conference on Robotics and Automation, ICRA 2001, vol. 1, pp. 886–891 (2001)
6. Lambert, P., Herder, J.: A novel parallel haptic device with 7 degrees of freedom. In: IEEE World Haptics Conference, WHC 2015, pp. 183–188 (2015)
7. Tsumaki, Y., Naruse, H., Nenchev, D.N., Uchiyama, M.: Design of a compact 6-DOF haptic interface. In: IEEE International Conference on Robotics and Automation, ICRA 1998, vol. 3, pp. 2580–2585 (1998)
8. Arata, J., Kondo, H., Ikedo, N., Fujimoto, H.: Haptic device using a newly developed redundant parallel mechanism. *IEEE Trans. Robot.* **27**(2), 201–214 (2011)
9. Préault, C., Laribi, M.A., Arsicault, M., Zeghloul, S.: Real time redundancy-based approach to robot-patient safe enhancement: application to Doppler sonography. In: Gasparetto, A., Ceccarelli, M. (eds.) *Mechanism Design for Robotics, MEDER 2018. Mechanisms and Machine Science*, vol. 66. Springer, Cham (2019)
10. Sandoval, J., Laribi, M.A., Zeghloul, S., Arsicault, M.: Towards a safe physical human-robot interaction for tele-operated system: application to doppler sonography. In: Gasparetto, A., Ceccarelli, M. (eds.) *Mechanism Design for Robotics, MEDER 2018. Mechanisms and Machine Science*, vol. 66. Springer, Cham (2019)
11. Vanacken, L., De Boeck, J., Coninx, K.: The phantom versus the falcon: force feedback magnitude effects on user's performance during target acquisition. In: Nordahl, R., Serafin, S., Fontana, F., Brewster, S. (eds.) *Haptic and Audio Interaction Design, HAID 2010. Lecture Notes in Computer Science*, vol. 6306. Springer, Heidelberg (2010)
12. Block, D., Michelotti, M., Sreenivas, R.: Application of the Novint Falcon haptic device as an actuator in real-time control. *Paladyn J. Behav. Robot.* **4**(3), 182–193 (2013)
13. Standen, P., Brown, D., Battersby, S., et al.: A study to evaluate a low cost virtual reality system for home based rehabilitation of the upper limb following stroke. *Int. J. Disabil. Hum. Dev.* **10**(4), 337–341 (2011)
14. Tsai, L.-W.: Multi-degree-of-freedom mechanisms for machine tools and the like. United States Patent, Patent Number: 5,656,905 (1997)
15. Clavel, R.: Delta, a fast robot with parallel geometry. In: 18th International Symposium on Industrial Robots, pp. 91–100 (1988)
16. Essomba, T., Sandoval, J., Laribi, M.A., Wu, C.T., Breque, C., Zeghloul, S., Richer, J.P.: Kinematic and force experiments on cadavers for the specification of a tele-operated craniotomy robot. In: *Mechanism Design for Robotics. In: 29th International Conference on Robotics in Alpe Adria Danube Region (RAAD 2019), Kaiserslautern, Germany, June 2019 (2019)*



# **Historical Development in Robotics and Mechatronics**



# The Exhibit of Industrial Robots Based on Concepts of Technology Education: Take “Smart Manufacturing Experience Zone” at National Science and Technology Museum as an Example

Jian-Liang Lin<sup>(✉)</sup> and Chieh-Ya Lin

National Science and Technology Museum, Kaohsiung 807, Taiwan (R.O.C.)  
jllin927@mail.nstm.gov.tw

**Abstract.** One of the museum’s missions is education. Based on the orientation of the National Science and Technology Museum, science and technology knowledge is essential. The exhibition of science and technology is the basis of the museum to promote the activity of science and technology education. In 2018, the National Science and Technology Museum built the exhibit of industrial robots at the smart manufacturing experience zone of power and machines gallery per the 4-year project of the Ministry of Education for achieving a smart museum. The purpose of the exhibit is to deliver the concepts of smart manufacturing and industry 4.0 and to promote innovative technology education. The design concept of the exhibition is an in-depth experience for the knowledge of industrial robots. Through techniques of digital media and interactive applications, the professional subject can be much enjoyable, attractive, and understandable for the public. The exhibit of industrial robots consists of five sections: the definition of robots, the historical development of industrial robots, the mechanical structure, and applications of industrial robots. In this exhibit, thirteen industrial robots, including the types of 6-DOF series robots, SCARA and wafer robot, are applied for the display of products and miniatures, demonstration for various processes as well as experience of interactive devices. In a word, the exhibit is not only the material of technology education but also a successful example for the cooperation between the museum and industrial companies.

**Keywords:** Industrial robots · Museum exhibition · Technology education

## 1 Introduction

Museums have different types of presentations according to different collections, and various kinds of museums follow their respective missions and objectives to perform diverse functions [1]. In terms of their tasks, museums can be generally divided into four essential services, including display, collection, research, and education. Further, the museums cover information dissemination and leisure recreation [2]. Since the 19th century, education gradually became one of the museums’ core functions. The educational concepts of museums are the inevitable results from history, culture, and society.

With the development of social history, many tendencies of social movements and thoughts have influenced the emergence and types of museums to promote the forming and change of their educational concepts [3, 4]. Therefore, it is necessary to understand museum education from the level of explaining human culture and its living environment. As time goes by, museum education has increasingly emphasized the negotiation of concept with the public. Through the active participation and feedback of the people, the museum shaped the narrative with mutual consensus and constructed a more meaningful interpretation of material culture [5]. Since museum education is non-formal education. There is no fixed form, teaching materials, regardless of age, grade, and free choice of educational opportunities. By the exhibition of the museum, visitors can understand the development of technology, human history, and digital information, and can stimulate their learning motivations, i.e., the exhibition has a profound educational function [6]. Therefore, the museum's display and educational activities can be used for planning teaching activities at all levels of schools. Regardless of any museum, the mission of education is based on its display and collection. Consequently, the exhibition of technology museum can deliver the knowledge of technology for the public to achieve the purpose of lifelong learning.

The "Twelve Construction Projects" approved by the Executive Yuan in 1979 listed museums as part of the central government's cultural infrastructure development policy. The National Science and Technology Museum (NSTM in short) was established to become the first museum for applied sciences in Taiwan and also the first national science education organization in southern Taiwan. The missions of the museum are to collect and study technological artifacts, host technology-related exhibits, promote technology education, and provide citizens with a place for leisure and lifelong learning. Now there are 16 exhibit halls in the museum. Since 2017, the Ministry of Education promoted a 4-year project (2017–2020) about the services of innovative technology on ten social education organizations (six national museums, three national libraries, and one educational radio), and NSTM is included. The project's objective of NSTM is to build a smart museum with innovative services and applications, cloud services for recording the visiting process, interdisciplinary content of exhibit, cultural and creative development, the cooperation of industrial companies as well as international communications. NSTM concluded six subjects in this project, consisting of the Internet of Things (IoT), driverless cars, industrial robots, smart agriculture, advanced materials for clothing, intelligent medical equipment and services, and food safety in turns. IoT is a special exhibition held in 2017, shown in Fig. 1. Since 2018, other subjects are the yearly update works corresponding to regular exhibition galleries. And, an experience zone called "Smart Manufacturing" involved various exhibition galleries that can be built for developing a smart museum.

"Driverless cars" and "industrial robots" are the update subjects at power and machines exhibition gallery and finished in 2018. The exhibit of industrial robots gets numerous resources of professional information, professional engineers, equipment and products from several companies, such as robots, actuators and motors from HIWIN, RV reducers from TSUNTIEN, and harmonic gearbox from HARMONIC DRIVE SYSTEMS. In general, it is believed that smart manufacturing exhibit is a successful example of technology exhibit connecting museum and industry. Therefore, we introduce the building process and design concepts of robots' exhibition based on the promotion of science education in this paper.



Fig. 1. A special exhibit “IoT” of NSTM in 2017

## 2 Design Concepts of Exhibit

Design concepts of an exhibit are critical points. The ideas can determine the direction and orientation of an exhibition, including its storyline, style of the technique of presentation, planning of content, application of digital media, and space design. Following the design concepts, the subject of the exhibit can be systematically displayed to transmit its knowledge with a much clear and understandable way for the public or the subjected targets.

“Industrial robot” is a professional subject with automatic control, mechatronic, mechanism design, etc., and is very difficult for the public. The targets for the exhibit of industrial robots include elementary school students. Therefore, the exhibition focused on introducing their basic knowledge, historical development, research results, and possible applications by simple descriptions, bright illustrations, and real objects. Numerous interactive experience devices with the technology of digital media are built to explain such a hard subject and to provide the feelings of wisdom and innovation for visitors. The exhibit of industrial robots is the display of situation, technology, and experience. It is conveyed that the process and achievements of industrial transformation and upgrading by applying big data and cloud technologies. The entire exhibit creates a situation of smart manufacturing.

An exhibition of the smart museum emphasized the in-depth experience. The exhibit of smart manufacturing experience zone customizes an APP to start the operation of interactive experience devices and record the experience process of visitors, as shown in Fig. 2. There are several nodes in the content of these devices. And, the nodes are designed to distinguish the learning levels of visitors. Collecting the learning

records of visitors are the application of big data. The museum can analyze the data to conclude the advantages, disadvantages, and learning effects of exhibit content as a reference for the update work in the future.

In summary, the exhibit of industrial robots uses multiple digital techniques to represent smart manufacturing. The advanced visiting method satisfies the requirement of intelligent museums. For audiences, the storyline of the exhibit is to describe the interaction of robots and humanity and to deliver the concept of industry 4.0. And, they can get an in-depth experience and learning by the method of playing games.



Fig. 2. APP interface for smart manufacturing

### 3 Industrial Robots of Smart Manufacturing Exhibit

“Power and Machines,” is one of the earliest exhibition galleries at NSTM, and is the most appropriate place for industrial robots. By the above design concepts of the exhibit, the topic of industrial robots has five sections: the definition of robots, the historical development of industrial robots, the mechanical structure, and applications of industrial robots [7–10]. Several emerging technologies like augmented reality (AR), virtual reality (VR) and motion-sensitive interactive devices are applied, except for the real objects from the cooperation of industry. In what follows, the exhibit content of the industrial robot unit is introduced in detail.

#### 3.1 Definition of Robot

In the traditional impressions of ordinary people, especially for primary school students, a robot is a machine that looks like a human being and performs various complex acts. This kind of device is a humanoid robot, and their ability of automatic control systems is not as deft as expected. In the viewpoint of engineering, an industrial robot is broadly defined that a mechanism or device can accomplish complicated and repeatable motions by automatic control systems. Some robots are classified based on their applications, like service robots and medical robots.

In this section, robots are clearly defined for ordinary people at first. The term “robot” has existed in several Slavic languages for a long time and originally meant repetitive, dull work or slave labor. In 1942, Russian Issac Asimov proposed the well-known four laws of robotics. The exhibit of this section is merely in words, but the essential elements of robots could be understood.

### 3.2 Historical Development of Industrial Robots

Robots developed numerous types for various applications. Here, the exhibit about the historical development of robots focused on industrial robots. We talk about the history of robots based on global trends and present the representative events and products of different ages. The world’s first industrial robot invented by George Devol, Unimate robots, Stanford arm in the 1960s, PUMA in 1970s, six-axis robot and SCARA robot in 1980s, the famous industrial robots companies in the world including Switzerland’s ABB, Germany’s KUKA as well as Japan’s FANUC and YASKAWA are introduced. The developments of industrial robots in Taiwan are presented further. Taiwan’s industrial robots were developed on the Industrial Technology Research Institute and academia before 1997. Until 2007, owing to the urgent demand for products with short life cycles, low costs, high efficiency, and high productivity, the manufacturing industry apply robots on the automated production line. It directly motivated Taiwan’s industrial robot manufacturers. Except for the descriptions in words, figures, and physical miniature models for representative types of industrial robots are displayed, as shown in Fig. 3. The visitors can know the necessary information about the internal and international historical development of industrial robots and the detailed image for representative robots.

### 3.3 Mechanical Structure

Following the visiting line of the exhibit, visitors should know the definition of robots, the historical development of industrial robots at home and abroad as well as the overall image for industrial robots in turns. Next, it is essential to understand the mechanical structure of industrial robots for visitors, including the classification of mechanisms and the mechanical elements. The section is to identify the robots based on Mechanisms and introduce what mechanical components or mechanisms are covered in the shell of machines. The professional information seems to be difficult and tedious for ordinary people without the background of mechanical engineering. The content much depends on the multiple designs and techniques of an exhibit to attract visitors’ attention to achieve the execution of science and technology education, such as the explosion version of a real industrial robot, a representation of dissembled mechanisms, a dynamic or static show of real objects, and figures.

The common forms of robotic arms are divided into two types: series and parallel. The information is presented at the beginning of the section “Mechanical structure.” Delta, Stewart platform, articulated robot, Cartesian coordinate robot, cylindrical robot, and SCARA are included in the exposition. Two simulation devices respectively for the production line of cookies by SCARA and wafer process by wafer robots are built, as shown in Fig. 4. It is necessary to present links and joints, two fundamental

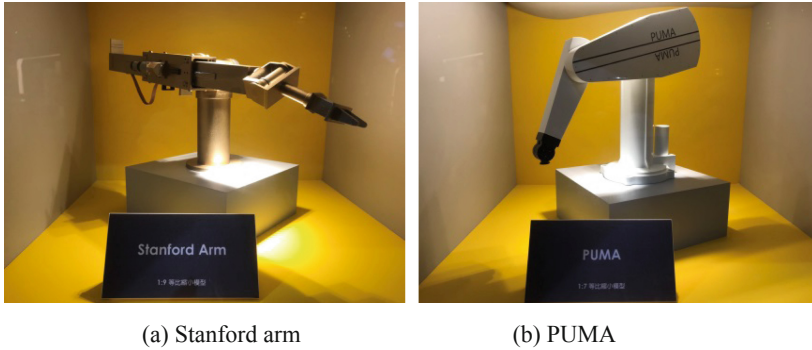


**Fig. 3.** Miniature models of industrial arms

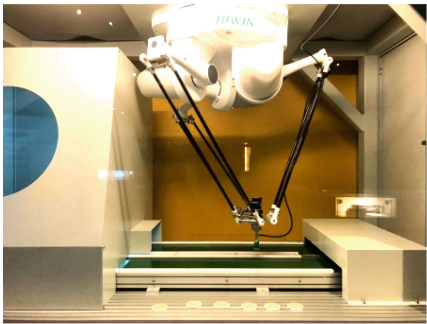
components for mechanisms, in the exposition. Except for large-sized operational models and illustrations, a six DOF robot is displayed by the explosion drawing style, as shown in Fig. 5, and the essential components, including motors and reducers are visible. Also, these critical components are disassembled in the exhibit. The visitors can understand the internal structure of RV reducers and harmonic reducers even though they cannot figure out the professional knowledge included in these devices. Furthermore, several end effectors and a screw spline device are exhibited by action simulations to explain the three action types based on the motor control for various applications, as shown in Fig. 6.

### 3.4 Applications of Industrial Robots

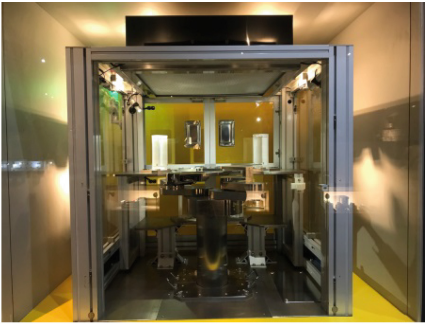
The most common tasks of industrial robots are picking up, placing, welding, spray coating, assembly, service, and the motions for a particular process. They are widely used in industry, but not constrained for the automation production lines. In order to deliver various applications of industrial robots with attractive methods, five interactive experience exhibit devices are built in the section, including drawing, chess playing, service of store seller, stamping and Jenga playing, as shown in Fig. 7.

These interactive experience devices are operated through the customized APP “smart manufacturing.” The robots are used in a wide variety of ways in entertainment. The apparatus of Jenga playing, the experimenter’s hand is synchronized with the robot to pick up the blocks. For the device of drawing, the picture of experiences is transmitted to the SCARA by a cloud server. The apparatus of “Tic Tac Toe” uses robot arms, combining image sensors, to discern the position of the pieces by a challenger against a robot on a chessboard. This device is to simulate the process of playing chess with a computer with artificial intelligence to present the image of AI robots. The apparatus of a robot seller is to introduce the concept of unmanned sales service including logistics, warehouse, and payment. In a word, these interactive experience devices deliver their technology knowledge and possible applications related to industrial robots. Also, they seem to be particular developments for the company of industrial robots (Fig. 7).





(a) Cookie factory (SCARA)



(b) Wafer process

**Fig. 4.** Simulation models of industrial arm



**Fig. 5.** Explosion display of 6-DOF industrial arm

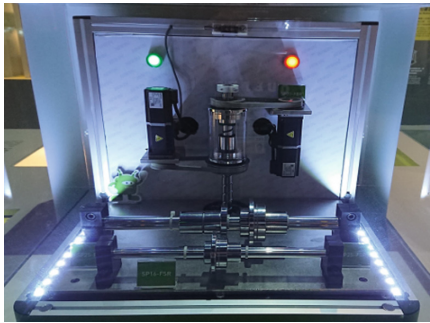
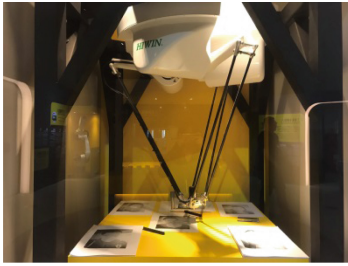


**Fig. 6.** Screw spline device (HIWIN)

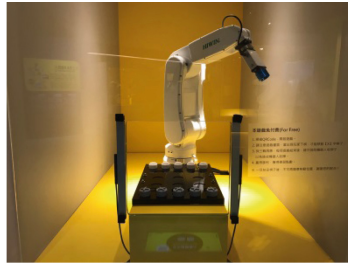
### 3.5 Robots in Industry 4.0

Indeed, industry 4.0 is the origin to build the industrial robots of smart manufacturing. Automated robots replaced human workers to perform high-risk, complex, and monotonous tasks for rapid production and labor-saving in the “industry 3.0” stage. As far as the next stage “industry 4.0” is concerned, robots integrating with the technologies of sensing and the Internet of Things achieve smart manufacturing models with high speed and high quality. Human-robot collaboration, mobile robots, smart robots, and collaboration of robots are the trends in the development of industry 4.0. And, these main concepts are presented next to the interactive experience devices that we introduced above. By the surrounding of the exhibition, visitors can have bright ideas related to the professional phrases and exposition to understand more natural further.

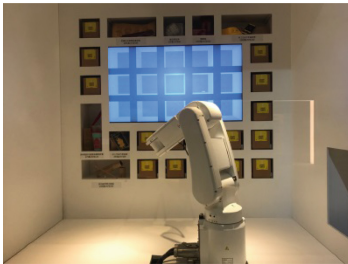




(a) drawing



(b) chess playing (Tic Tac Toe)



(c) store seller



(d) stamping



(d) Jenga playing

**Fig. 7.** Operational devices by the applications of industrial robots

## 4 Statistical Analysis of Learning Records

The exhibition applied the concept of the Internet of Things and database analysis. The customized APP is the key to experiencing the whole interactive devices in the show. Each user must register in the APP to get a QR code as the personal ID. And, the background system of the APP can record the experiencing process and results of the users as learning records. The collection of learning records formed a database by the background system for statistical analysis. The critical factors to affect the experience and the learning of the users can be concluded based on the distribution of quantitative visiting behaviors. By the learning trend of the display, we can investigate if the manner of presentation is appropriate to the display topic and content for the ordinary people.

For the qualitative and quantitative analysis of visiting records, the content of interactive devices is categorized four indexes, and each index sets three levels. The qualitative index contains reading, involvement, operation, and discussion. “Reading” means that whether the questions related to the exhibition were correctly answered. “Involvement” means the amount of time spent at each unit. “Operation” means that whether each mission is successfully completed. “Discussion” means that whether the experience at the exhibition was shared on Facebook or other social media. The learning records are quantitatively divided into three levels to describe the process and distinguish the performances of learning. In what follows, two interactive devices are introduced as examples.

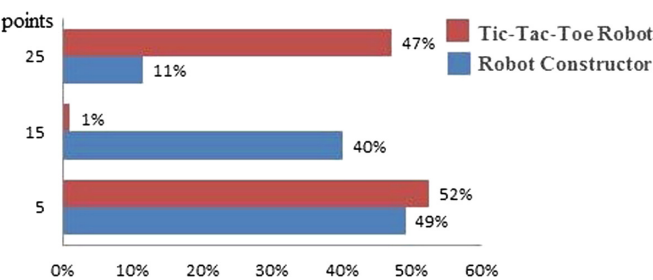


Fig. 8. Data of three interactive devices

**a. Tic Tac Toe Robot (red data)**

The device is the integration of the sensors and the 6-DOF series robot. The visitor plays chess with a robot. The data of the visiting records is discretely distributed. The visitors either give up quickly or finish the experience successfully. It is suggested that the ages of visitors and the errors of operations are the factors of the distribution. It is much easy for most of the people. But the visitors easily make errors to crash the robot during the operation process.

**b. Robot Constructor (blue data)**

The device is the integration of the visual identification technique and the 6-DOF series robot. The game mode of human-robot synchronization is applied. The grades of the visiting records are low. It is possible that the game mode is too hard to achieve the assignment. The visitors give up the experience quickly. It shows that the difficulty of experience should be considered for the device which the qualitative index is regarded as “Operation.”

**5 Conclusions**

An industrial robot is one of the essential elements of industry 4.0. The related knowledge should be emphasized as technology education for the public through the method of a museum exhibit. The advanced techniques and creative design concepts for museum exhibit and visiting are applied to promote the public to understand such

professional subjects and content. In this exhibit, people can be familiar with the intelligent and innovative technology, historical developments, mechanical structure, various applications, and developing trends of industrial robots. Industrial robots are clearly defined, the history of the international and internal development and the essential components of industrial robots are introduced. Five interactive experience devices, operated by a customized APP called “smart manufacturing,” are built to deliver various applications integrated with mechanical designs, control systems, visual identification, and artificial intelligence. By the content management system of APP, the learning and experience process of visitors is recorded to achieve the analysis of big data for the exhibit of the smart museum. The concept of industry 4.0 is presented by following the storyline of the exhibition. Indeed, the whole presentation can be regarded as the teaching material.

Further, the visitors can find out the impact and change of smart manufacturing on the industry and the way of life, and then explore the various aspects of technological applications emphasizing the relationship between technology and living. Except for technology learning, the interactions between industry and society are studied. And, it is found that the exhibit topic is close to the life of the public in the coming future. Furthermore, the exhibit topic is a good connection between the museum and industry. The museum can get precise and abundant resources from the industry to achieve a great exhibit. Also, the industry can have a platform to show their research results through the professional design of a museum exhibit.

**Acknowledgement.** The authors are grateful to the Ministry of Education for the financial support of exhibition building and *HIWIN* Company for the sponsorship of industrial robots.

## References

1. 高慧芬 (1992), 博物館之類型及其環境教育角色與作法, 博物館學季刊, 第3期, 第25-31頁。
2. Ho, C.J.: Museum education from the viewpoint of lifelong learning. *Museol. Q.* **2**, 7–14 (2000). (in Chinese).  
何青蓉 (2000), 從終身學習談博物館教育, 博物館學季刊, 第2季, 第 7-14頁。
3. Teng, Y.J.: Study into the School Children’s Learning Process and Learning Outcomes in the Children’s Cultural Workshop at the National Palace Museum. Thesis, National University of the Arts, Tainan, Taiwan, R.O.C. (2014).  
鄧淵仁 (2014), 探究國立故宮博物院兒童研習營中學童學習歷程與所得, 國立臺南藝術大學, 臺南。
4. Jia, C.M.: Some problems in museum education. *Museol. Q.* **3**, 67–83 (2000). (in Chinese).  
賈建明 (2000), 論博物館教育諸問題, 博物館學季刊, 第3季, 第67-83頁。
5. Liu, H.Y.: Prospects for museum education in the age of communities. *Museol. Q.* **2**, 97–123 (2008). (in Chinese).  
劉襄儀 (2008), 社群時代的博物館教育展望, 博物館學季刊, 第2期, 第97-123頁。

6. Tsai, H.L.: Visualizing recent development of museum education by bibliometric analysis. *J. Sci. Humanit.* **4**, 188–206 (2018). (in Chinese).  
蔡欣倫 (2018)，文獻計量法可視化分析：  
探索博物館教育之發展現況，科學與人文研究，第4期，第188-206頁。
7. Kuo, C.H., Huang, J.H.: Exhibition Content of Industrial Robots. Commissioned Research Report, National Science and Technology Museum (2017)
8. MacDougall, W.: INDUSTRIE 4.0 smart manufacturing for the future. Germany Trade and Invest, Berlin (2014)
9. Lin, H.I., Hsieh, M.F.: Intelligent robots in industry 4.0. *Instrum. Today* **205**, 12–20 (2015). (in Chinese).  
林顯易、謝名豐 (2015)，工業4.0中的智慧機器人，科儀新知，第205期，第12-20頁。
10. Chen, M.Y., Jhong, B.G.: The trend of intelligent robot development in industry 4.0. *Second. Educ.* **3**, 6–13 (2015). (in Chinese).  
陳美勇、鍾秉剛 (2015)，工業4.0計畫中智慧型機器人發展之趨勢，中等教育，3，6-13。



# Ancient Chinese Puzzle Locks

K. H. Hsiao<sup>1</sup>✉, Y. Zhang<sup>2</sup>, K. Shi<sup>3</sup>, Y. H. Chen<sup>4</sup>, and H. An<sup>5</sup>

<sup>1</sup> National Science and Technology Museum, Kaohsiung 80765, Taiwan  
khhsiao@mail.nstm.gov.tw

<sup>2</sup> Beijing University of Chemical Technology, Beijing 100096, China  
zhy@mail.buct.edu.cn

<sup>3</sup> Shandong University of Science and Technology, Qingdao 266510, China

<sup>4</sup> National Taiwan University of Science and Technology, Taipei 10607, Taiwan

<sup>5</sup> Shanxi Folk Arts Museum, Taiyuan 030001, China

**Abstract.** No matter whether it was the invention of China or other ancient countries, the lock has several thousand years of history. With the change of society and the progress in technology, locks' functions and security are becoming more and more improved. Their designs and making are promising. The barbed-springs lock is the typical one in ancient China and can be dated to 200 BC. The locks started to be used in large numbers in the later period of the Eastern Han Dynasty (about AD 200), and the materials were mainly bronze-based. In the Tang Dynasty (AD 618–907), the craftsmanship of lock manufacturing was quite advanced, and the types, shapes, and carvings were increasingly numerous. It was no later than the Ming Dynasty (AD 1368–1644) that locks which needed specific procedures and methods to open were widely manufactured and used. These kinds of locks can be named as puzzle locks. They were difficult to open within a short period of time even if the correct keys were in place. According to the opening methods and the types of keyholes, ancient Chinese puzzle locks can be divided into two classifications, including open-keyhole and hidden-keyhole puzzle locks. This paper introduces the developments of lock history in ancient China first. Then, the characteristics of two typical puzzle locks are provided as examples to illustrate the opening processes. Final section is the conclusions of the work.

**Keywords:** History of MMS · Barbed-spring lock · Puzzle lock

## 1 Introduction

The production of locks is highly related to the materials, tools, everyday life, society, economics, folklore, and culture. However, since ancient times, the design and making of locks have been conducted by specialized artisans, whose skills are never taught openly. As a result, it is rather difficult for common people to know more about the skills of locks. Moreover, it is rather difficult for us to trace locks back to its development and origin. From a modern perspective, with the functions of security, management, and even decoration, a lock is a security device released by a key, a touch pad, a dial, an electric circuit, or other devices to prevent objects from being opened or moved away [1].

China has a very long history but there are very few articles discussing the development and applications of locks. Needham delineated the brief history of the development of Chinese and Western locks and discussed their mutual influences. He also introduced the internal structures of a few typical locks. He lamented that there was a serious lack of literature exploring the development of locks in Asia, and it needed more concern and researches [2]. Yan collected and studied locks and introduced their development and features systematically to display the appearances and historical implications of ancient Chinese locks [1]. In addition, Yan et al. used the padlocks featured with spring leaf as examples to propose a systematic method of designing the structures of spring leaves. With the explorations of encyclopedias and dictionaries, they compared the linguistic meanings of locks in China and the West [3–5]. Shi et al. studied the characteristics of traditional Chinese maze padlocks during operation and discussed the process of the key's insertion into the keyhole [6]. Hsiao studied ancient Chinese open-keyhole and hidden-key puzzle locks and presented the variations in their topological structures [7, 8]. Ancient Chinese puzzle locks are saturated with images of craft and folklore of ancient artisans, and were a cultural treasure. However, there are very few literature described the puzzle locks. This paper provides two main types of ancient Chinese puzzle locks from existing ones to find out the structures and crafts of ancient Chinese locks to attract people's attention on puzzle locks.

## 2 History of Locks' Development

For thousands of years, locks have been used widely in daily life. It is a mechanical device derived from people's pursuit of security. Hence, it has been widely used to safeguard people's security and privacy. Even more, it has been closely related to people's everyday life, and death. As people demand for safety rose, various kinds of locks were invented and developed. In addition to promoting higher security, the convenience of locks had been taken into considerations during their production. Likewise, the design of locks keeps updating. Swinging back and forth between convenience and complexity, the origins of this object are hardly mentioned.

More simplified bronze locks began to appear around 200 BC. Inside the locks, they were installed spring leaves. Using the geometric relationship between the key and the spring leaf, it worked to lock and unlock. Starting from the second century, metal locks had been widely used. Made with bronze as the major material, there were engraved with animal or insect patterns on them. In the Tang Dynasty (AD 618–907), lock making craft was prospered, and the design of locks was becoming more complicated. Some were even equipped with traps. In addition to bronze locks, some were made with other metals, such as brass, iron, silver, or other metals. Figure 1(a) is a brass lock with people and flower patterns. Coming in various types, they were becoming more diverse in appearances. It was no later than the Ming Dynasty (AD 1368–1644) that locks which needed specific procedures and methods to open were widely manufactured and used. These kinds of locks can be named as puzzle locks. They were difficult to open within a short period of time even if the correct keys were in place. Figure 1(b) shows a lock that has an end plate to cover the keyhole well.

The first step of opening the lock is to find out the keyhole. It is belonged to one type of the hidden-keyhole puzzle lock. Starting from the Han Dynasty (206 BC–AD 220), locks with metal spring leaves were the major lock type used in China. For about two thousand years, although there had been changes in the appearance of ancient Chinese locks, there was very little improvement in their internal structures. It was not until the 1960s, with the general use of pin tumbler locks from the West, ancient Chinese locks began to fade away.

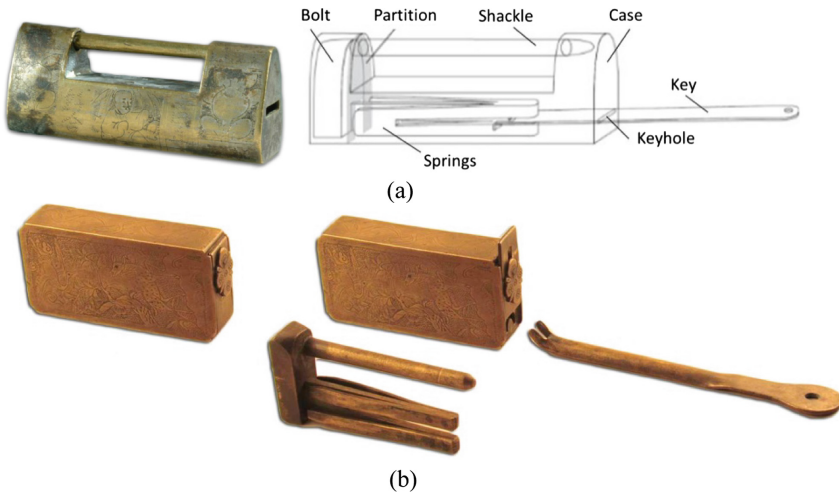


**Fig. 1.** Barbed-springs locks.

### 3 Mechanical Structure

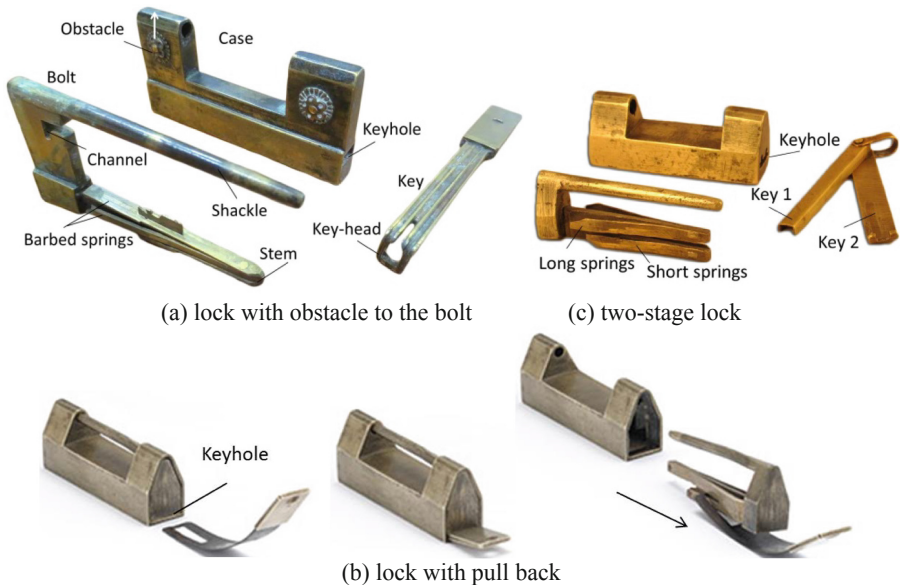
The open-keyhole lock means the keyhole is visible on the case straight. Figure 1(a) is a common open-keyhole lock that consists of four members including the case, the bolt, the barbed springs, and the key. When the lock is closed, the splayed ends of the springs are trapped against the partition inside the case, preventing the release of the bolt. Opening this lock only needs three steps including inserting the key-head into the keyhole directly, pushing the key to cause the key-head to press the barbed springs and the barbed springs are pushed through an opening in the partition, and sliding the bolt out of the case. It is a common lock without trap. According to the opening processes and the types of keyholes, ancient Chinese puzzle locks can be divided into two main classifications, including open-keyhole and hidden-keyhole puzzle locks. The mechanical structures of two main puzzle locks are described as follows:

#### 3.1 Open-Keyhole Puzzle Lock

There are three primary types of open-keyhole puzzle locks, including locks with extra obstacle, locks with indirect insertion, and multi-stage locks. Figure 2 shows the typical

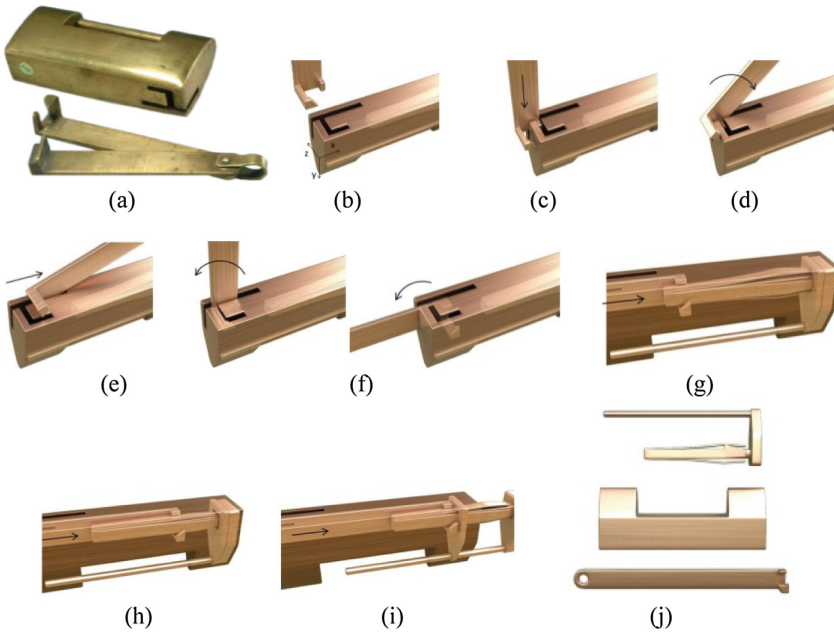
three open-keyhole puzzle locks. Each type of open-keyhole puzzle locks has many sub-types [7]. Figure 2(a) is a lock with extra obstacle. There is a channel on the bolt. The left button is the obstacle that is attached to the bolt. In order to open the lock, the left button must be pushed up first. Then, the bolt can be slid by the key. Figure 2(b) is a lock with indirect insertion. In generally, the key is pushed to slide the bolt to open the lock. However, opening the lock in Fig. 2(b) is to pull back the key to press the barbed springs. Figure 2(c) is a two-stage lock that has two sets of springs and two keys. Key 1 must be inserted into the keyhole first and slide the bolt a little bit. Then, key 2 is inserted into the keyhole and slide out the bolt from the case. Using two keys made it possible to require the presence of two people to open it. But which key must be used first and should the key-heads face up or down? Determining how to open the lock is akin to solving a simple puzzle.

Figure 3(a) is a maze lock that is provided as an example to illustrate the opening process. Since inserting the key-head into the keyhole needs four steps, it belongs to the lock with indirect insertion. There are totally seven steps in the opening process. The first step is to place the key-head vertically over the keyhole, Fig. 3(b), and translate the key to insert the keyhole a little bit, Fig. 3(c). The second step is to rotate the key clockwise about  $45^\circ$ , Fig. 3(d). Third, the key is translated to right, Fig. 3(e). The fourth step is to rotate the key counterclockwise and insert the key-head into the keyhole totally, Fig. 3(f). The fifth step is to push the key to connect to the barbed springs, Fig. 3(g). The sixth step is to press the barbed springs in order to allow them to pass the opening of the partition, Fig. 3(h). When the barbed springs enter the opening of the partition, the bolt is moved by the pressing of the key, Fig. 3(i). Finally, the bolt is slid out of the case completely, and the lock is opened, Fig. 3(j).



**Fig. 2.** Open-keyhole puzzle locks.





**Fig. 3.** A maze lock.

### 3.2 Hidden-Keyhole Puzzle Lock

According to the first step of opening the hidden-keyhole puzzle lock, they have four main types, such as locks with a sliding plate, locks with a rotating decoration, locks with a poke hole, and locks with a push button. Each type of hidden-keyhole puzzle locks also has many sub-types [8]. Figure 4(a) shows a lock with a sliding bottom plate. The keyhole is covered by the bottom plate. The bottom plate must be slid to left to find out the keyhole. When the key is inserted into the keyhole, the key must be turned left to press the long springs to slide the bolt a little bit. Then, the key is turned right to press the short springs to slide out the bolt. Figure 4(b) shows a lock with rotating decoration. The keyhole is covered by a decoration. The decoration must be rotated to find out the keyhole. When the key is inserted, the key must be pulled back to press the springs to open. Figure 4(c) shows a lock with poking hole. It consists of 10 members including the case, the bottom plate, the end plate, the bolt, spring 1, springs 2, springs 3, key1, key 2, and key 3. Key 1 is poked into the hole to press spring 1 to release the bottom plate. When the bottom plate took off, keyhole 1 is appeared. Then, key 2 is used to press springs 2 to release the end plate. And, keyhole 2 is appeared. Finally, key 3 is used to press springs 3 to slide out the bolt from the case to open the lock.

In order to increase the security, locksmiths employed two or more of these obstacles in the same lock. Figure 5(a) shows a lock that combines pushing a button and poking a hole. It consists of 9 members including the case, the bolt, the button, the bottom plate, the end plate, spring 1, spring 2, springs 3, and the key. The first step of

opening process is to push down the button to press spring 1, Fig. 5(b). Then, slide the bolt a little bit, Fig. 5(c). Since the sliding of the bolt, there is a space for sliding the bottom plate, Fig. 5(d). After sliding the bottom plate, there is a hole appeared on the bottom plate. Use the pin of the key to insert the hole to press spring 2, Fig. 5(e) and slide the bolt again, Fig. 5(f). Since the sliding of the bolt again, the end plate is parted from the shackle. Then, the end plate can be rotated and the keyhole can be found out, Fig. 5(g). Insert the key into the keyhole to press springs 3, Fig. 5(h). Finally, slide out the bolt from the case to open the lock, Fig. 5(i).

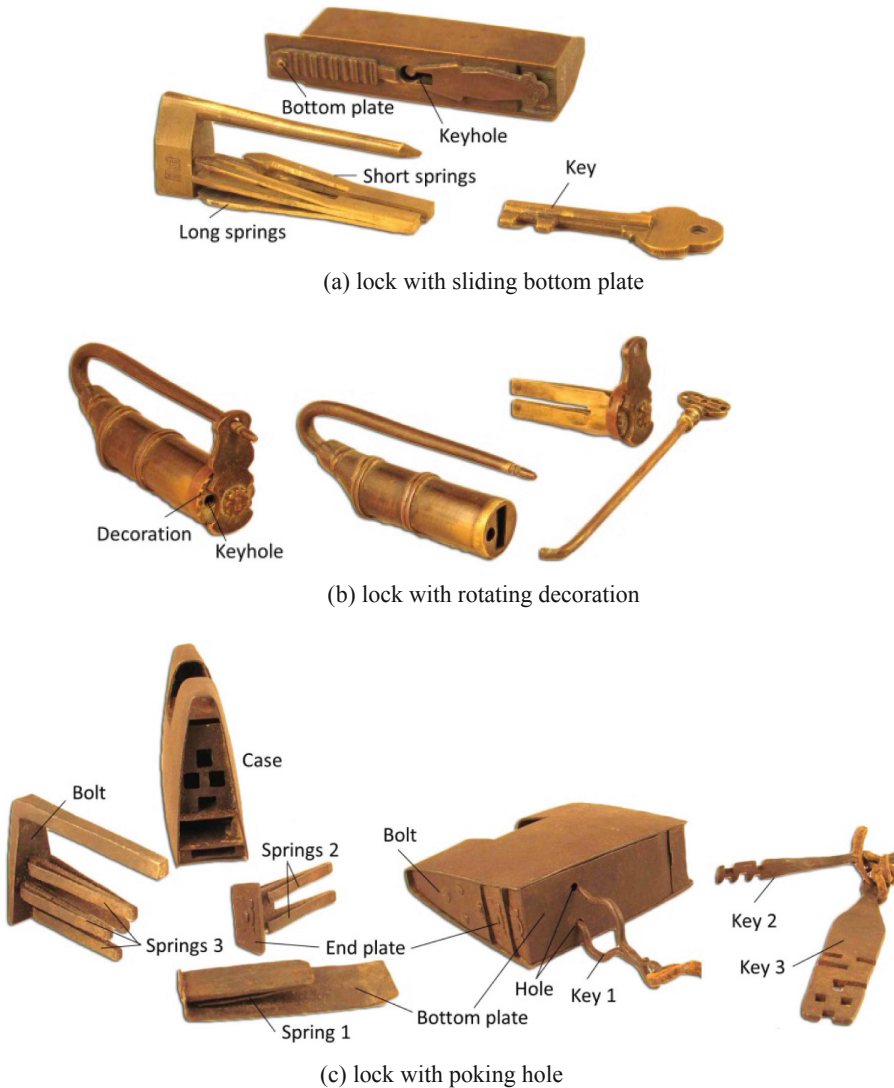


**Fig. 4.** Hidden-keyhole puzzle locks.

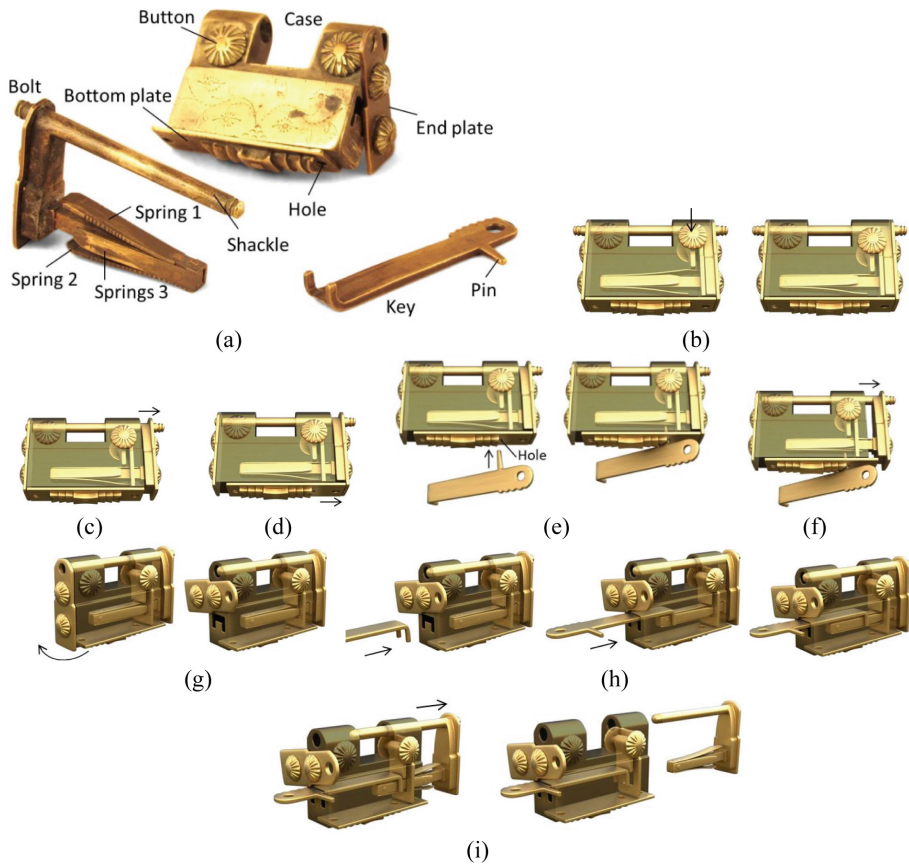


**Fig. 5.** A lock with a push button.

## 4 Conclusions

From ancient times till now, locksmiths around the world have used different kinds of materials and ideas to make locks securer and suitable to their times and environments. Since the puzzle lock is hard to open than the common lock, the security is better than the common one. Improved continuously, different types of ancient Chinese puzzle locks with different structures and different manners of opening were invented. According to the styles of the keyholes, there are two main types, such as open-keyhole and hidden-keyhole puzzle locks. Each type has many sub-types. Otherwise, their internal structures are neat, demonstrating that ancient artisans accumulated experience by testing and making them repeatedly to promote innovation. This work presents the types and the opening processes of the representative Chinese puzzle locks. It provides the sketch of puzzle locks for people realizing the characteristics of locks in China.

**Acknowledgements.** The authors are grateful to the Ministry of Science and Technology (Taipei, Taiwan) under grant MOST 108-2622-E-359-001-CC2 for the financial support of this work. Support from the Ancient Chinese Machinery Cultural Foundation (Tainan, Taiwan) and the Classical Chinese Puzzle Foundation (Berkeley, USA) are also greatly appreciated.

## References

1. Yan, H.S.: The Beauty of Ancient Chinese Locks. Ancient Chinese Machinery Cultural Foundation, Tainan, Taiwan (2004)
2. Needham, J.: Science and Civilization in China, vol. 4. Cambridge University Press, Cambridge (1965)
3. Yan, H.S., Huang, H.H.: On the spring configurations of ancient Chinese locks, In: Proceedings of 2000 HMM International Symposium on History of Machines and Mechanisms, pp. 87–92. Kluwer Academic Publishers, Casino, Italy (2000)
4. Yan, H.-S., Huang, H.-H.: Design consideration of ancient Chinese padlocks with spring mechanisms. *Mech. Mach. Theory* **39**, 797–810 (2004)
5. Yan, H.S., Huang, H.H.: A study on Western and Chinese locks based on encyclopedias and dictionaries, In: Proceedings of 2004 HMM International Symposium on History of Machines and Mechanisms, pp. 41–56. Kluwer Academic Publishers, Casino, Italy (2004)
6. Shi, K., Zhang, Y., Lin, J.L., Hsiao, K.H.: Ancient Chinese maze locks. *T. Can. Soc. Mech. Eng.* **41**(3), 433–441 (2017)
7. Hsiao, K.H.: On the structural analysis of open-keyhole puzzle locks in ancient China. *Mech. Mach. Theory* **118**, 168–179 (2017)
8. Hsiao, K.H.: Structural analysis of traditional Chinese hidden-keyhole padlocks. *Mech. Sci.* **118**, 168–179 (2018)



# A Historical Study of Rope Applications in Mechanical Devices in Three Eastern Countries

Yu-Hsun Chen<sup>(✉)</sup>

National Taiwan University of Science and Technology, Taipei 10607, Taiwan  
yhchen@mail.ntust.edu.tw

**Abstract.** Ropes have been widely used in mechanical devices for a long time as a unique component with characteristics of flexibility and rigidity. Many records in ancient books show the applications of rope in the machines to a variety of transmission purposes. From the viewpoint of mechanisms, 15 devices in Chinese, Arabian, and Japanese ancient books are analyzed and classified based on its mechanical characteristic of flexibility and rigidity.

**Keywords:** History of technology · Ancient machines · Rope components

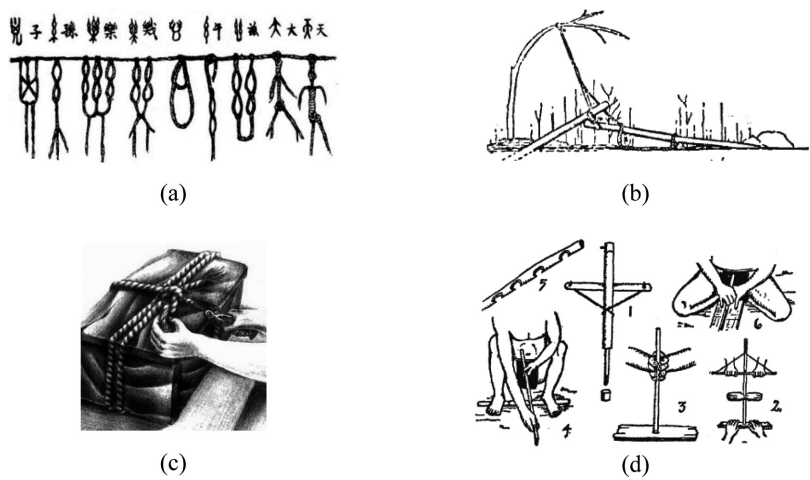
## 1 Introduction

A rope is a flexible component composed by the long strips of fiber material and widely used for connection or traction. Since the ancient time, people have developed various ways to apply ropes, such as the talking knots in ancient China and Peru, the traps in Africa, the fishing nets in North America, the knot locks in Greece and China, and the bow drills in Egypt [1–3], as shown in Fig. 1.

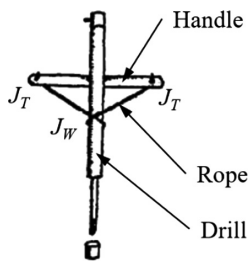
As a mechanical component, a rope is with good tensile strength but cannot transmit power until it is straightened. Due to its flexibility (when wrapping around something) and rigidity (when straightening by a tensile force), a rope is a special component in mechanical applications. In this study, the mechanical characteristics of the ropes are analyzed and classified, and the application examples in the ancient literature from three Eastern countries are introduced.

## 2 Classification

As one of the rope applications shown in Fig. 1(d), the bow drill is composed of a handle, a drill, and a rope, Fig. 2. The rope is wrapped around the drill in the middle, so the joint is defined as a wrapping pair ( $J_W$ ). The rope is also tied to the handle in both of the ends, and the joints are defined as the thread pairs ( $J_T$ ). The degrees of freedom (D.O.F.) of the joints are arranged in Table 1. Here, the thread joint works as a revolute joint in the planar mechanism and functions as a spherical joint in the spatial mechanism, therefore the thread joint has different D.O.F. in these two kinds of mechanisms.

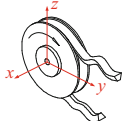
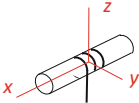


**Fig. 1.** Application examples of ropes in prehistoric times: (a) The talking knots [1], (b) A trap [2], (c) A knot lock [2], (d) A bow drill [2].



**Fig. 2.** A mechanism analysis of the bow drill

**Table 1.** Mechanism joints with ropes [4]

Type of joint	Symbol	Diagram	Degrees of freedom
Wrapping joint	$J_W$		1
Thread joint	$J_T$		1 (Planar mechanism) 3 (Spatial mechanism)

When a rope is used with a wrapping joint ( $J_W$ ), the characteristics of flexibility is observed, and it usually functions in a sheave mechanism for transmitting the motion of continuous rotation. On the other hand, when a rope is used with a thread joint ( $J_T$ ), the rope is usually tightened up to straighten by hanging other links or connecting to an elastic part such as a spring. The characteristic of rigidity is shown to work as a linkage in a mechanism.

### 3 Application Examples

The applications of rope in the ancient period are recorded with illustrations in many Eastern literature, especially in China [5–7], Arab [8], and Japan [9]. These records reflect the way of life and development of mechanical technology in the three countries.

#### 3.1 Ancient China

Ropes were used in a variety of working machines in ancient China for milling the grain, lifting water, pressing oil, furnace bellows, archery... etc. Figure 3 shows four devices with ropes, including the animal-powered mill, a water-driven wind box, a water lifting device with a string of bamboo, and a water-lifting winch. For the first three devices, the rope is connected to two wheels through two wrapping joints ( $J_W$ ),

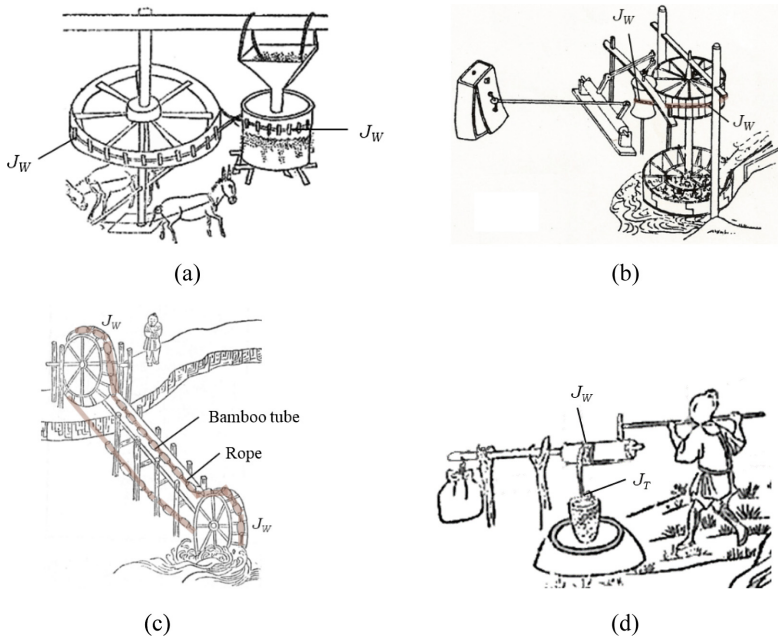


**Fig. 3.** The applications of rope with wrapping joints in China: (a) An animal-powered mill [5], (b) A water-driven wind box [10], (c) A water lifting device with a string of bamboo [5], (d) A water lifting winch [5].

and both the input and output motions of this sheave mechanism are continuous rotations. The winch device also uses the rope through a wrapping joint ( $J_W$ ) to lift up the filled bucket that transmits the revolute motion to a vertical reciprocated motion. In these four devices, the rope is used as a flexible component to achieve the functions.

Ropes are also used to hang or support the other components in the device, such as a handle of the mill, a sieve for grain, and an oil pressing rod, as shown in Fig. 4. In these applications, the rope is connected to the frame and the other link through two thread joints ( $J_T$ ), respectively. The ropes are straightened by the weight of the links, so they can be analyzed as a rigid link from the viewpoint of mechanisms. However, the flexibility of the rope provides more degrees of freedom to adjust the operation than the application of a real rigid link.

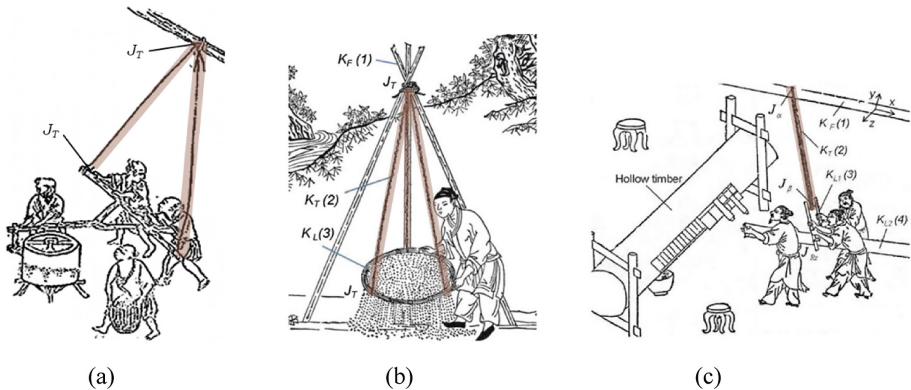


**Fig. 4.** The applications of rope with thread joints in China: (a) A mill with a handle [5], (b) A grain sieving device [5], (c) An oil pressing device [6].

In addition, some devices composed of a rope and an elastic component, such as the cotton loosening device, a water-driven wind box, and a repeating crossbow as Fig. 5. In these applications, a rope connects to the elastic wood or bamboo through a thread joint ( $J_T$ ) to restore the original position after moving by the elastic potential. Therefore, the ropes are analyzed as the rigid components in these devices.

### 3.2 Ancient Arab

Al-Jazari is one of the most important Arabian engineers in the 12<sup>th</sup> century with various mechanical inventions [8]. In this paper, a water-lifting device and an automaton puppet are introduced as examples of rope applications in ancient Arab. Figure 6(a) shows the animal-driven water lifting device with a frame, a scoop wheel, two pair of gears, a pulley, and a rope with buckets. The input motion is continuous rotation from the cattle that drives the shaft of the gears at the right side, and the motion is transmitted through the upper gears, the pulley, and the rope with buckets to drown and lift water from the pool. The rope is connected to the pulley through a wrapping joint ( $J_W$ ) that shows its flexibility characteristic. According to the descriptions in the book [8], this device can also be driven by the scoop wheel.



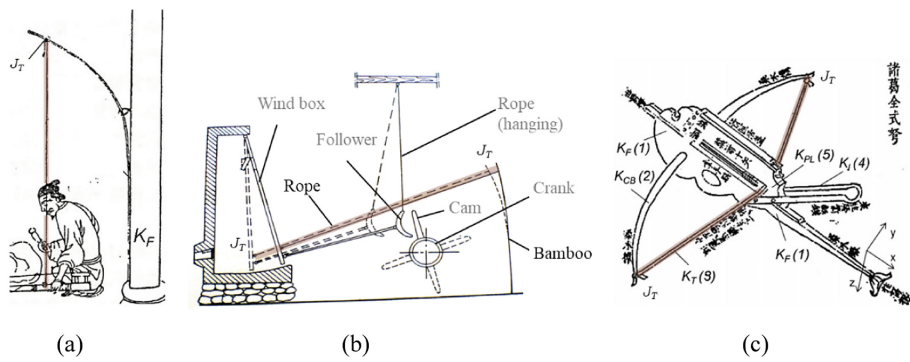


**Fig. 5.** The applications of rope with thread joints and elastic component in China: (a) A cotton loosening device [6], (b) A water-driven wind box [4], (c) A repeating crossbow [7].

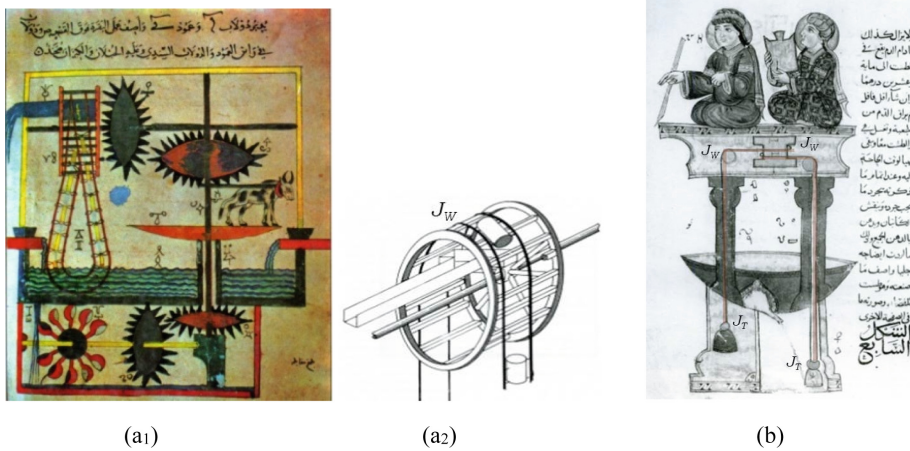


**Fig. 6.** The applications of rope in Arab: (a) An animal-powered water lifting device [8], (b) A mechanical puppets with pulley [8].

An Arabic automaton is shown in Fig. 6(b) composed of a frame, a pulley, and a rope. The rope is connected to the pulley through a wrapping joint ( $J_W$ ) and tied to the two weights at both ends to keep the tensile force. When water flows into the tank at the right side, the right weight floats and the left weight falls, therefore the pulley and the puppets are rotated through the transmission of rope. The flexibility characteristic of the rope is applied to this device.

### 3.3 Ancient Japan

According to the Japanese literature [9] of the 18<sup>th</sup> century, various elaborate automata were developed in Japan at that period. In this paper, three mechanical devices are introduced as examples to discuss the applications of rope in that time and area.

A man-powered wind box is shown in Fig. 7(a) composed of frame, an oscillating lever, two airbags, two sheaves, and a rope. The input is a reciprocated motion provided by the operator, and the motion transmits through the rope that changes the directions of motion through the sheaves to oscillating rotation of the lever. The two airbags are compressed and stretch respectively to make the air blowing out. In this device, the rope is connected to the two sheaves and both ends of the lever through two wrapping joints ( $J_W$ ) and two thread joints ( $J_T$ ), respectively.

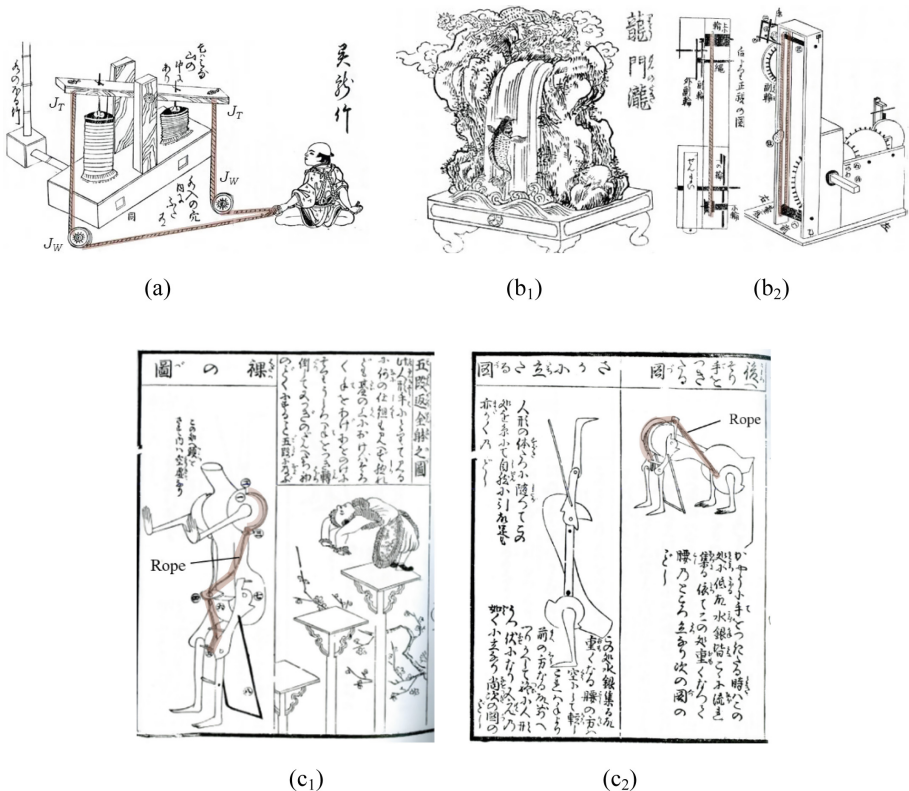


**Fig. 7.** The applications of rope in Japan: (a) Wind box with a lever [9], (b) A mechanical automaton with a countercurrent carp [9], (c) the five steps tumbling puppet [9].

A mechanical automaton, Fig. 7(b), presents a traditional Japanese legend. When a carp countercurrents and leaps to the top of the falls, it transforms into a dragon and raises into the sky. The main part of this automaton is composed of a frame, two sheaves, and a rope. The rope connecting to the sheaves through two wrapping joints ( $J_W$ ). By rotating the lower sheave, a carp attached to the rope raises up in the front side of the device.

Figure 7(c) shows a special application of rope. This automaton puppet tumbles down from the top of the five stairs that touches the ground with its hands and feet in

sequence. The internal mechanism is composed of a body as a frame, a link of hands, a link of legs, and a rope. The rope goes through a small hole of the body and is connected to the hand link and the leg link at the both ends by two thread joints ( $J_T$ ). When the puppet is in a standing posture, the rope is not straightened so the motion cannot transmit as Fig. 7(c<sub>1</sub>). However, when the puppet is in the waist posture, the center of gravity locates at its shoulder, and the rope is straightened that pulls the leg link rotates clockwise to tumble down the stairs as Fig. 7(c<sub>2</sub>). Both the flexibility and rigidity characteristics of rope are used in this automaton that reflects the creativity of designer.

An arrangement of the mechanical devices with rope in the presented ancient literature is shown in Fig. 8. A classification of rope components is made based on its mechanical characteristic of flexibility and rigidity, and the applications recorded in the literature are listed to the corresponding characteristics.

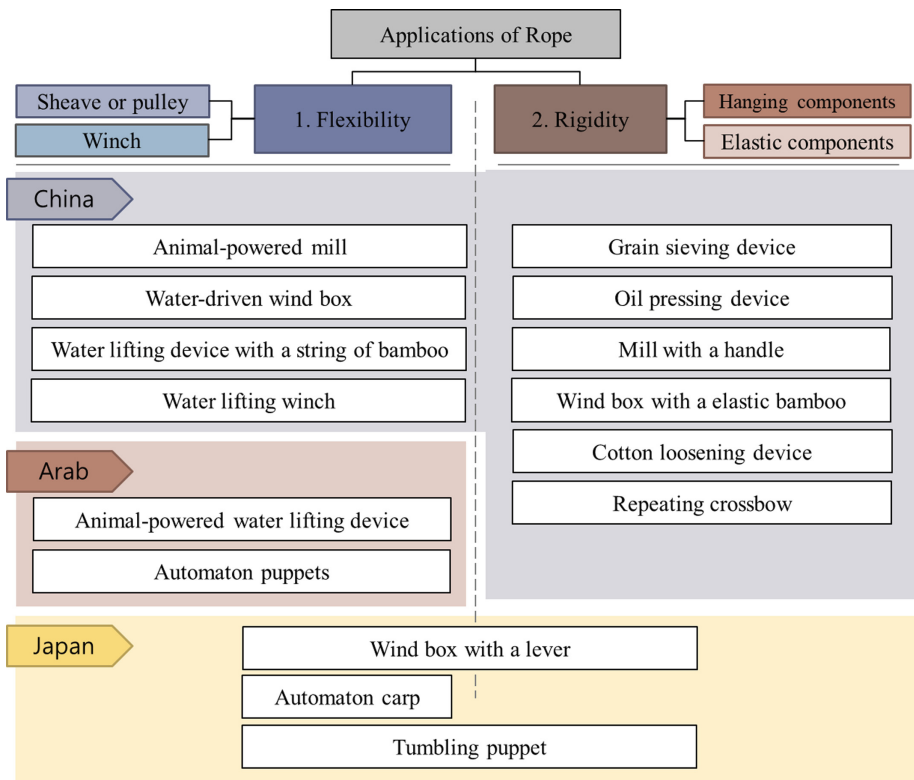


**Fig. 8.** A classification and applications of rope components in three ancient Eastern countries.

## 4 Conclusions

From a viewpoint of mechanisms, the records of rope applied to mechanical devices in the ancient literature from three Eastern countries are surveyed, classified, and analyzed, including ten Chinese devices, two Arabian devices, and three Japanese devices. When a rope is used as a flexible component, it is usually applied with sheaves, pulleys, or a winch with wrapping joints. When it is used as a rigid component, it must be tied to other rigid links or an elastic component with thread joints. With a rope, the motion of the mechanism can be transformed from rotation to linear motion and vice versa. A rope component can transmit motion only when it is straightened, and this characteristic makes it a special part in mechanical applications. In modern time, although ropes are almost replaced by wires, belts or chains in the industrial machines, these mechanical characteristics are still used. Moreover, the applications recorded in ancient literature provide historical evidence of technology development.

## References

1. Mou, Z.W.: The Origin of Ancient Chinese Characters. Shanghai People Publishing House, Shanghai (2000). (in Chinese)
2. Paz, E.B., Ceccarelli, M.: A Brief Illustrated History of Machines and Mechanisms. Springer, Madrid (2007)
3. Rope: Wikipedia. <https://zh.wikipedia.org/wiki/%E7%B9%A9>. Accessed 12 Mar 2019
4. Hsiao, K.H., Yan, H.S.: Mechanisms in Ancient Chinese Books with Illustrations. Springer, Cham (2014)
5. Wang, Z.: The Book of Agriculture. Modern republished: Zhonghua Book Company, Beijing (1991). (in Chinese, 1300s)
6. Pan, J.X.: Annotation of Tian Gong Kai Wu. Shanghai Ancient Books Publishing House, Shanghai (1993). (in Chinese)
7. Mao, Y.Y.: Wu Bei Zhi. Henan Education Press, Henan (2001). (in Chinese)
8. Al-Jazari, I.: A-R. Knowledge of Ingenious Mechanical Devices. Translated by Hill, D.R., Elite Publishers (Private) Ltd., Islamabad (1989). (in Arabian, the 11th century)
9. Tagaya, K., Hosokawa, H.: Karakuri Kinmō Kagami-Gusa/Karakuri Zui. Modern republished: Edo Kagaku Koten Series, Kouwa Publication, Tokyo (1976). (in Japanese, 1730s)
10. Lu, J.Y.: History of Chinese machinery. In: Ancient Chinese Machinery Cultural Foundation (Tainan, Taiwan). Yuen Yin Publishing House, Taipei (2003). (in Chinese)



# Current Research Topics in Robotics at IGMR

Burkhard Corves<sup>(✉)</sup>, Mathias Huesing, Nils Mandischer,  
Markus Schmitz, Amirreza Shahidi, Michael Lorenz,  
and Sami Charaf Eddine

Institute of Mechanism Theory, Machine Dynamics and Robotics,  
Aachen, Germany

corves@igmr.rwth-aachen.de  
<https://www.igmr.rwth-aachen.de>

**Abstract.** This paper gives an overview of current research topics at the Institute of Mechanism Theory, Machine Dynamics and Robotics of RWTH Aachen University. A variety of application areas is introduced, including robotic reconstruction, agile production, additive manufacturing and human-robot collaboration. Each topic offers novel and unique contributions to its field of robotics.

**Keywords:** Radar SLAM · Additive manufacturing · Agile production · Human-robot-collaboration · Internet of robotics

## 1 Introduction

The institute of Mechanism Theory, Machine Dynamics and Robotics (IGMR) is an established chair at RWTH Aachen University with many national and international partners in research and industry. Ever since, the focus of research has been the development and optimization of mechanisms of any kind. In 2018, the institute's name was visibly augmented by robotics, which has been a well-established research group within the institute for many years. In the early years, the robotics group has focused on classical stationary industrial robots only, while maintaining the link to mechanism development. In the last years, novel fields of application have given rise to mobile robotics at IGMR. Certain research projects are funded by either the European Union or the German Universities Excellence Initiative, in addition to industrial funding.

In this paper, first two approaches in the field of stationary robotics in the application areas of additive manufacturing (2) and human-robot-collaboration (Sect. 3) are described. Afterwards, two approaches to mobile manipulation in the application areas agile assembly systems (Sect. 4) and reconstruction robotics (Sect. 5) are introduced.

## 2 Multidirectional Additive Manufacturing

Additive manufacturing processes offer new possibilities to meet constantly growing requirements for product individualization and smaller batch sizes, since production is largely independent of complex component geometries and is possible for more and more materials. Solids are produced by the layered addition of material, which represents an added value compared to conventional processes, especially in the production of complex geometries with cavities and undercuts [1].

In Fused Layer Manufacturing (FLM), the material (usually thermoplastics) is successively deposited in a flat layer through a nozzle. This makes it possible to set up inexpensive manufacturing systems (3D printer, Fig. 1a). However, the component properties are limited by inhomogeneity due to the layer-by-layer structure [2]. In addition, there is the necessity for non-functional support structures for overhangs and inclined surfaces [3].

The aforementioned limitations of 3D printers can be reduced by adjusting the layer thicknesses and material quantities [4] or curved layers in near-surface areas [5], which not only improves the printing speed but also the mechanical properties of the component [6]. The radii of curvature are limited by the fixed orientation of the nozzle. The addition of further degrees of freedom is therefore a consistent further development in order to achieve a greater curvature of the layers. By using robot-guided nozzles, three rotational degrees of freedom can be realized in addition to three translational degrees [7], Fig. 1b. The combination of object rotation and translational movement [8] of the nozzle generates five degrees of freedom, Fig. 1c.

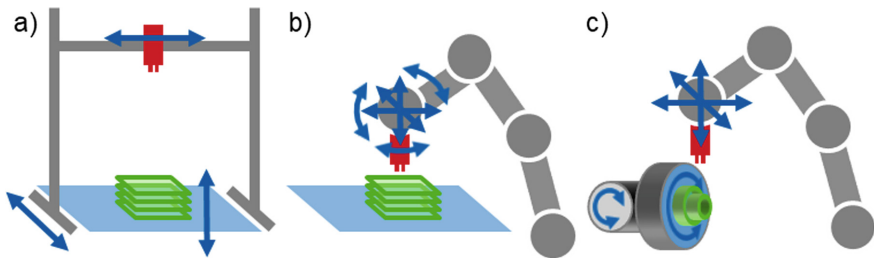


**Fig. 1.** (a) Classical 3D printer; (b) and (c) Concepts for the realization of additional degrees of freedom in additive manufacturing.

Within the scope of research at IGMR, a 5D printing technique is developed and implemented [9], in which the object to be printed is continuously moved by a robot under a stationary 3D print head (see Fig. 2). The addition of degrees of freedom to the shown component reduces the need for support structures. The strength of the components can also be increased, since the layers can be arranged according to the expected stresses and strains in the component.

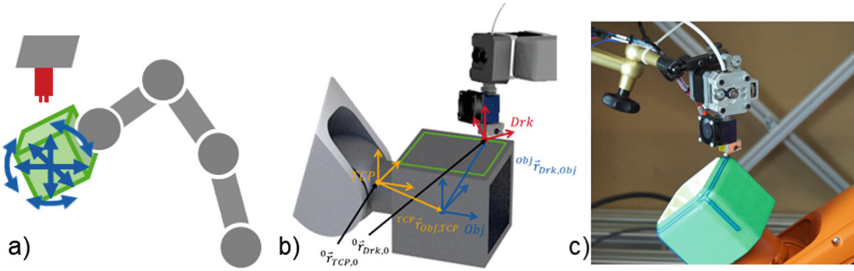


**Fig. 2.** 5D-Printing at IGMR

One focus is the optimization of the trajectory exploiting the kinematic redundancy. Here significant increases of the printing speed could be proven. Recently, research into the entire process of additive manufacturing from CAD models to the execution of an optimized trajectory has moved into focus. This is motivated by the use of multidirectional additive manufacturing for TIG welding with wire feed, Fig. 3a. Since the material is fed eccentrically, the freedom of movement of the welding head is strongly restricted. The pure manipulation of the component (with six degrees of freedom) can therefore avoid this problem and thus enable the above-mentioned advantages for this process as well. Without the previously mentioned redundancy, preprocessing will be used for optimization in the future.

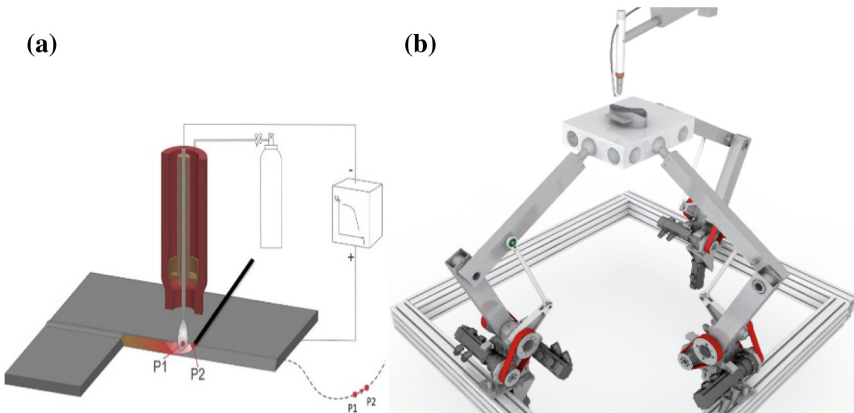


**Fig. 3.** (a) Schematic illustration of the TIG welding process [11], (b) Paragrip [12] used for multidirectional additional manufacturing

Generally, additive manufacturing is based on a sequence of points (path) in the object coordinate system, which allows the calculation of a sequence of joint states for a manipulator (3D printer). Input data for the preprocessing of additive manufacturing are 3D data sets, for example, from a CAD environment. The component information (CAD data) is transferred to a so-called slicer, which cuts the component into a finite



number of slices depending on the printing direction [10]. Then, within each layer, a path is planned that can be executed almost directly on the printer.

With the extension to multidirectional additive manufacturing, the process is no longer constrained to a single printing-direction. Furthermore, the solution of sectioned construction of the component is also conceivable and the path planning can vary depending on the manipulator kinematics and dynamics (e.g. for the Paragrip structure, Fig. 3b). The essential difference of multidirectional additive manufacturing of TIG welding at this point is the possible conversion of a single object element into multiple possible robot end effector poses but just one possible robot configuration to move to a neighbored object element. The various extensions therefore open up space for optimization already during the path planning. Therefore, further research at IGMR will study the possibility of manipulator-based path planning for multidirectional additive manufacturing.

### 3 Human-Robot Collaboration

Research on human-robot collaboration (HRC) provides a wide range of applications in the context of Industry 4.0. By combining human capabilities, such as experience, improvisation and learning skills, with the precision and high payload capacity of robot manipulators, HRC systems prove particularly suitable as an assistance medium and for automating risky or monotonous activities. However, the future scenario of an optimal, collaborative work sharing compete with conventional automation, despite its safety restrictions and reduced performance.

The continuous development of robot manipulators, sensor systems and safety devices enables a rising use of industrial robots within HRC. In this context, humans and robots work interactively and without separating safety fences in a common workspace. The classification of human-robot collaboration into different forms of interaction between humans and technology is illustrated in Fig. 4. Whereas other forms of interaction tend to spatially or temporally separate manual and automated activities, human-robot collaboration ensures the simultaneous work of human and robot on the same object [13].

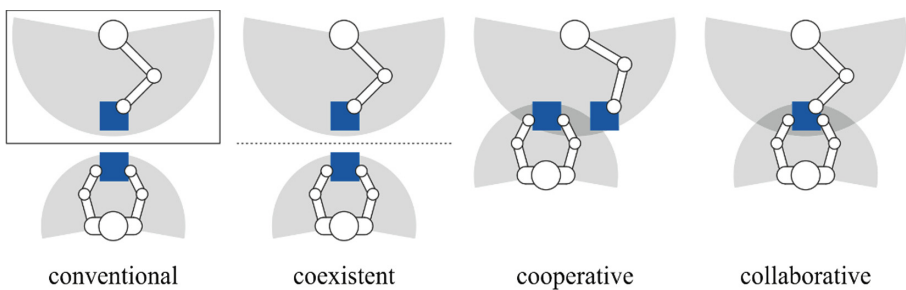


**Fig. 4.** Types of human-robot interaction



The physical integrity of humans is guaranteed by sensor-based safety devices and intelligent control systems, which minimize the risk potential of robots by active collision avoidance or force and power limitation. Accordingly, the physical contact between humans and robots is accompanied by significantly reduced velocities, as well as force and torque monitoring, in order to minimize technical risks and prevent injuries to humans in accordance with standardized biomechanical limits [14].

Collaborative operation of industrial robots requires compliance with specified velocity and force/torque limits and the use of an appropriate protective equipment [15]. In this context, practical applications distinguish between velocity and proximity monitoring systems, preventing physical contact between humans and robots, and systems with power and force limitation, limiting the contact forces occurring during collisions.

In the first case, the robot is exemplarily equipped with a capacitive sensor skin or the entire working area is monitored using visual sensors. Force and power limitation can be actively controlled by torque sensors or a tactile skin. In addition, such robots provide smooth surfaces and rounded edges and can be equipped with further passive safety mechanisms, such as flexible drives or a padded covering.

In this context, Industry 4.0 provides outstanding opportunities for the generation of new jobs - especially through the development of new technologies and efficient communication between people and innovative machines and plants. Within the project “Inclusive workplaces of the next generation” this idea will be addressed at IGMR by upgrading the private sector workplaces with robotic support systems (see Fig. 5). Thus, innovative and inclusion-promoting jobs are to be created, especially for physically and cognitively disabled people, often receiving little attention on the general labor market.

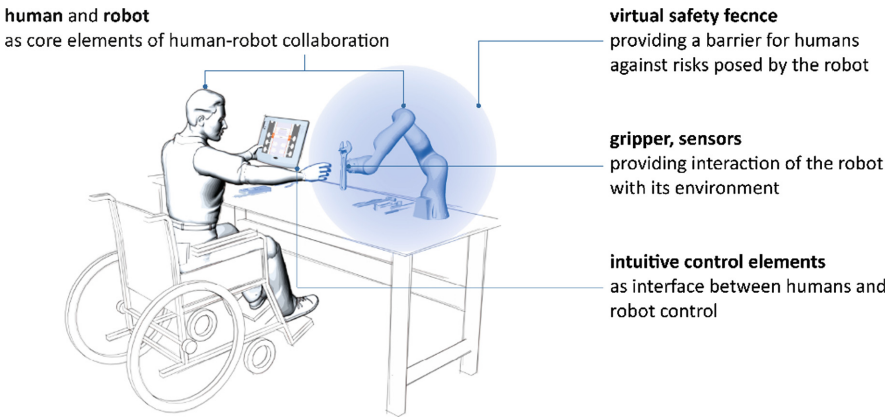


**Fig. 5.** Inclusive workplaces based on human-robot collaboration

The core element of the project is the use of lightweight robots as flexible support systems for the individual expansion of physical and cognitive abilities of disabled people. In this way, the conflict between economic productivity and the inclusion of

disabled people can be resolved: On the one hand, companies develop a new group of employees for technically supported, demanding fields of activity. On the other hand, disabled people are given the opportunity of equal participation in working life - and a satisfied and more independent life based on work.

#### 4 Agile Assembly Systems via Consensus of Robotic and Sensoric Networks

Agile and freely networked assembly systems, which are characterized by the collaboration between several mobile and stationary robots in a sensoric network, can be represented as a part of the Internet of Production (IoP) [16]. To realize such a system the robotic and global sensoric systems should be networked with each other. The information flow from other domains of production can also be integrated in this network to gain the advantages of big data for machine learning. A corresponding modelling approach and the application to exemplary individual processes provide insights into the necessary data provision (sensor network), data structuring (perception) and data feedback (information network) (see Fig. 6).

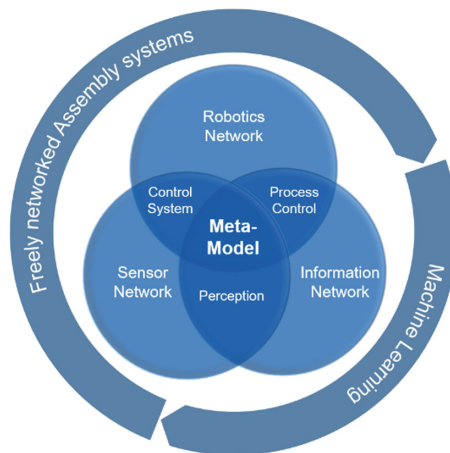


**Fig. 6.** Robotic, sensoric and information networks

At IGMR an assembly system consisting of such a combination of robotic and sensoric systems is available. To smoothen the integration in the infrastructure of the Internet of Production, a framework consisting of four scopes is established. A cloud computation structure is responsible for the up-level comprehensive control of the system (see Fig. 7) [17]. Different robotic systems collaborate in the process. The robotic agents can be divided in three main types: (mobile) manipulators, mobile robots and stationary robots as stationary reconfigurable workstation (e.g. gantry robot).

The local referencing and metrology between these agents is realized by an indoor GPS (iGPS). The environment of the process is monitored via depth cameras. The communication takes place via a common information network. A metamodeling structure implemented in a cloud structure supports communication between these scopes.

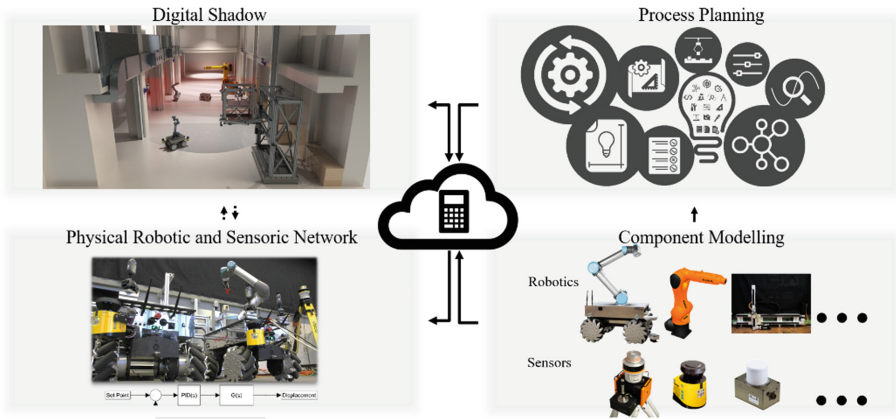


**Fig. 7.** Framework for an agile robotic assembly network

In the applications of Industry 4.0, robots are used in very diverse scenarios, in which they collaborate and interact with humans or other robots. The topics of robotic artificial intelligence, machine learning and autonomous robotics are of particular interest. Before such an application is realized, they can be tested and examined in a virtual environment. Not only the robots, but also the environment with machines, humans and sensors are modelled and their interactions simulated. Furthermore, the knowledge from the real world (such as quality management, maintenance, user feedback circle, etc.) is integrated in the models. A corresponding modelling approach provides insights into the necessary data provision, data structuring and data feedback, which enables the generation of a so-called digital shadow. The Digital Shadow brings a dual capability to the system: On the one hand, prefabricated data in the simulation can facilitate the data mining capabilities (adaptive systems, artificial intelligence, etc.) on the other hand, the real-time data flow from the physical environment will generate an adaptable and self-optimizing system based on the simulation of reality [18]. Following, the scopes of the Fig. 7 are detailed:

### Digital Shadow

This section concerns the modelling and simulation of the whole system and its scopes. These system scopes enable the development of comprehensive communication and adaptive control systems. The common application of extended Augmented Reality (AR) or Virtual Reality (VR) in the physical environment of the robot network can also be integrated in the process.

### **Process Planning**

The process planning scope is responsible for the optimal task planning and scheduling of the overall system. The system-specific information from component modelling (e.g. robot workstation, payload, gripper information and internal sensor network information) is collected and comprehensive process specific parameters are determined.

### **Component Modelling**

The independent modelling of all system components is part of the component modelling scope. Within, the kinematics and dynamics model of the robots its internal sensors are carried out and model reduction and sensor data integration are realized.

### **Physical Robotic and Sensoric Network**

Local control systems (e.g. adaptive regulation for failure compensation) as a complement to the higher-level control system in the cloud is implemented within the physical robotic and sensoric network scope. Real-time exchange of information with the cloud enables possible re-planning of the process.

The further research focus at IGMR in this context is set on the optimization of a meta-model, integrated in the cloud structure and the development and evaluation of a simulation environment for robot and sensor systems, which constitutes a basis to the “Digital Shadow”.

## **5 Cognition in Low Visibility Environments**

Despite the high degree of industrial automation, robotic solutions are not yet widely used for reconstruction. Manual Asbestos-removal in particular is a cost-intensive process, which also requires complex security measures to protect the human workers from possible health hazards. This can lead to delays or the complete cancellation of the removal process. In order to counteract the challenges of Asbestos-removal, a semi-autonomous robotic system is being developed within the EU project “Robots to Reconstruction” (Bots2ReC) [19]. A central challenge of this project is the localization of the mobile unit in the infested building using a Simultaneous Localization and Mapping (SLAM) approach. Although the original SLAM problem has been extensively addressed in literature [20], the low visibility environment, constituted by dust and debris from the removal process, requires unique and novel cognition approaches.

Parts of this article were already published in [21] in German language.

### **5.1 Radar Technology: Benefits and Challenges**

In common SLAM approaches, laser or vision sensors are used to generate a map of the environment. In this map, the robot can localize itself using the current sensor readings and an optimization approach. In low visibility environments, operating vision or laser sensors is prone to high errors. Laser beams offer a short wavelength, which leads to reflections from even the smallest particles. In opposition, radar sensors with their longer wavelengths are able to penetrate dust and thin walls (see Fig. 8) [22]. This property makes radar a perfect fit for Bots2ReC.



**Fig. 8.** Foggy environment (left) and the corresponding sensor readings (red: laser is limited by fog particles, rainbow: radar penetrates fog)

Still, the differences in wavelength and carrier energy introduce special properties, which have to be addressed in the SLAM approach. For once, radar offers multiple detections per beam, which inflate the size of each data set on a non-constant base (laser: 720, radar:  $\sim 15k$  points/scan). Secondly, in comparison to laser ranging, radar offers less accuracy, while being more prone to noise. Furthermore, radar offers intensity values for each detection, which relate to the presence of objects and their density.

## 5.2 Radar-SLAM for Low Visibility Environments

The proposed radar SLAM is based on the Probabilistic Iterative Correspondence (pIC) approach, which uses the Mahalanobis distance metric in order to counteract uncertainties in the sensor readings [23]. Mahalanobis uses a statistical approach, which assigns a shorter distance to points along the main axis of a point set. Based on this metric, pIC uses simple Least Squares to align a scan with the generated map. The proposed approach augments pIC with three main aspects, enabling the algorithm for online computation:

### Radar Filter

The first step is to reduce the size of the data set. Therefore, a radar filter is developed with the aim to erase those points, which offer no value to cognition. As objects are depicted as a cluster of points, it is sufficient to use only the one point per beam, which correlates with the face of the object. Therefore, the data set is filtered with an intensity/range threshold and clustered. Afterwards, on each beam and cluster the most intense point is selected. This reduces the size of the point set to about 360 points.

### Efficient Optimization

As the Least Squares approach in pIC uses multiple 1000 iterations, the algorithm cannot be executed online. While using a similar cost function to pIC, the proposed algorithm uses the Nelder-Mead optimization approach instead [24]. This algorithm is able to optimize all three components of the robot's pose ( $x$ ,  $y$ ,  $\theta$ ) simultaneously, while only needing up to 150 iterations. Each iteration is more costly than in Least Squares, but overall the optimization is accelerated significantly.

### Storage Architecture

Many operations in optimization and distance metric computation are searches for nearest neighbors. In literature, Quadtrees are used to accelerate such actions [25]. However, trees have the drawback that if a point and its neighbor are part of different branches, the computational effort rises significantly. Therefore, a simple storage architecture is developed, which assigns points to quadrants of fixed size. In this structure, indexation is very simple and cost-efficient. Therefore, nearest neighbor search is faster than in Quadtrees, which is validated by benchmark testing.

Tests are performed in an empty, large-scale office. The tiles floor is very rough and results in bad odometric data, which has to be compensated by the algorithm. The test result is depicted in Fig. 9.

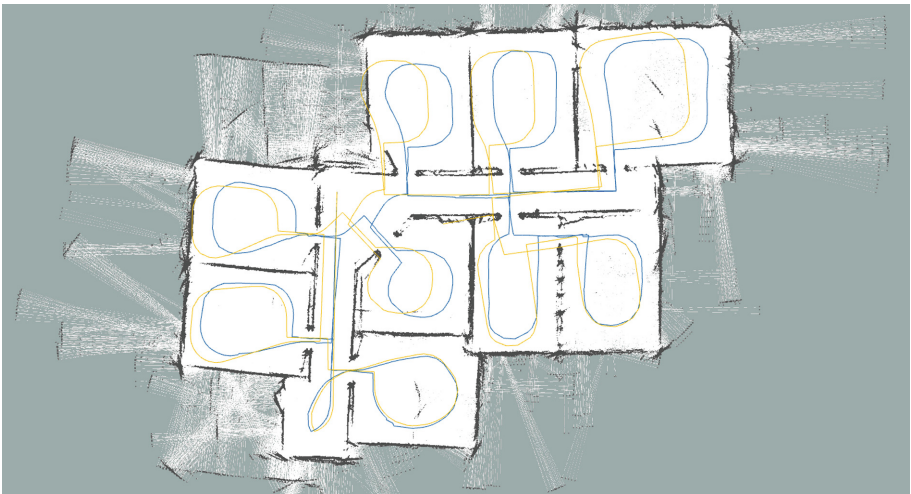


Fig. 9. Radar SLAM results in an office building (o.: robot odometry, b.: SLAM path)

## 6 Summary

This paper summarizes the current research topics at IGMR in the field of robotics, which span from classical robotics approaches, like additive manufacturing (Sect. 2), to IT-heavy research, like computer vision and cognition (Sect. 5). Most research is

performed in the field of collaborative tasks and work sharing between robots and humans. Human-robot-collaboration in particular will be an important topic in future casual life and research.

**Acknowledgement.** The authors would like to thank:

The German Research Foundation DFG for the kind support within the Cluster of Excellence “Internet of Production” - Project-ID: 390621612.

The European Union for the kind support within the project “Robots to Re-Construction” - Project-ID: 687593.

## References

1. Huang, S.H., Liu, P., Mokasdar, A., et al.: Additive manufacturing and its societal impact: a literature review. *Int. J. Adv. Manuf. Technol.* **67**(5–8), 1191–1203 (2013). <https://doi.org/10.1007/s00170-012-4558-5>
2. Siebrecht, J., Jacobs, G., Beckers, A., et al.: Einfluss von Prozessparametern auf die Funktionserfüllung von Bauteilen beim Fused Deposition Modeling. In: Krause, D., Paetzold, K., Wartzack, S. (eds.) *Design for X: Beiträge zum 27. DfX-Symposium*. TuTech Verlag, Hamburg, pp. 123–134 (2016)
3. Allen, R.J.A., Trask, R.S.: An experimental demonstration of effective Curved Layer Fused Filament Fabrication utilising a parallel deposition robot. *Addit. Manuf.* **8**, 78–87 (2015)
4. Hope, R.L., Roth, R.N., Jacobs, P.A.: Adaptive slicing with sloping layer surfaces. *Rapid Prototyp. J.* **3**(3), 89–98 (1997). <https://doi.org/10.1108/13552549710185662>
5. Jin, Y., Du, J., He, Y., et al.: Modeling and process planning for curved layer fused deposition. *Int. J. Adv. Manuf. Technol.* **91**(1–4), 273–285 (2017). <https://doi.org/10.1007/s00170-016-9743-5>
6. Spoerk, M., Arbeiter, F., Cajner, H., et al.: Parametric optimization of intra- and inter-layer strengths in parts produced by extrusion-based additive manufacturing of poly(lactic acid). *J. Appl. Polym. Sci.* **134**(41), 1 (2017). <https://doi.org/10.1002/app.45401>
7. Fraunhofer IPA: 3D-gedruckte Leichtbauteile für den Mittelstand (Endlosfaserdrucken) (2016). [https://www.ipa.fraunhofer.de/de/presse/presseinformationen/2016-07-21\\_3d-gedruckte-leichtbauteile-fuer-den-mittelstand.html](https://www.ipa.fraunhofer.de/de/presse/presseinformationen/2016-07-21_3d-gedruckte-leichtbauteile-fuer-den-mittelstand.html). Accessed 09 Apr 2018
8. Stratasys Ltd.: 8-Axis Freedom for Strong Composites: Get better-performing composite parts faster with the Robotic Composite 3D Demonstrator (2019). <https://www.stratasys.com/demonstrators>. Accessed 25 Mar 2019
9. Detert, T., Lorenz, M., Schmitz, M., et al.: Robotergeführte Objektmanipulation für die generative Fertigung. In: Beitel Schmidt, M. (ed.) *Tagungsband 12. Kolloquium Getriebetechnik: Technische Universität Dresden*, 20–22 September 2017. TUD Press, Dresden (2017)
10. Livesu, M., Ellero, S., Martínez, J., et al.: From 3D models to 3D prints: an overview of the processing pipeline. *Comput. Graph. Forum* **36**(2), 537–564 (2017). <https://doi.org/10.1111/cgf.13147>
11. Reisgen, U., Stein, L.: *Grundlagen der Fügetechnik: Schweißen, Löten und Kleben*. Fachbuchreihe Schweißtechnik, Band 161. DVS Media GmbH, Düsseldorf (2016)
12. Mannheim, T., Riedel, M., Hüsing, M., et al.: A new way of grasping: PARAGRIP—the fusion of gripper and robot. In: Carbone, G. (ed.) *Grasping in Robotics*, pp. 433–464. Springer, London (2013)



13. Thomas, C.: Entwicklung einer Bewertungssystematik für die Mensch-Roboter-Kollaboration. Dissertation, Shaker Verlag GmbH (2017)
14. ISO International Organization for Standardization (2016-02-00) Robots and robotic devices - Collaborative robots 25.040.30 (15066)
15. DIN German Institute for Standardization: Industrieroboter – Sicherheitsanforderungen – Teil 1: Roboter (DIN 10218-1) (2016)
16. Lu, Y.: Industry 4.0: a survey on technologies, applications and open research issues. *J. Ind. Inf. Integr.* **6**, 1–10 (2017). <https://doi.org/10.1016/j.jii.2017.04.005>
17. Shahidi, A., Detert, T., Hüsing, M., et al.: Agile assembly system by consensus of robot and sensor network – an introduction to industry 4.0: Fünfte IFToMM D-A-CH Konferenz 2019 (2019)
18. CoE IoP: RWTH AACHEN UNIVERSITY Cluster of Excellence Internet of Production - English (2019). <http://www.iop.rwth-aachen.de/cms/~gpfz/Produktionstechnik/lidx/1/>. Accessed 19 Mar 2019
19. Detert, T., Charaf Eddine, S., Fauroux, J.-C., et al.: Bots2ReC: introducing mobile robotic units on construction sites for asbestos rehabilitation. *Constr. Robot.* **1**(1–4), 29–37 (2017). <https://doi.org/10.1007/s41693-017-0007-1>
20. Cadena, C., Carlone, L., Carrillo, H., et al.: Past, present, and future of simultaneous localization and mapping: toward the robust-perception age. *IEEE Trans. Robot.* **32**(6), 1309–1332 (2016). <https://doi.org/10.1109/TRO.2016.2624754>
21. Charaf Eddine, S., Mandischer, N., Huesing, M., et al.: Bots2ReC: Radar-SLAM für die teilautonome Asbestsanierung. In: VDI Mechatroniktagung, Paderborn (2019)
22. Adams, M., Jose, E.: *Robotic Navigation and Mapping with Radar*. Artech House, Norwood (2012)
23. Montesano, L., Minguéz, J., Montano, L.: Probabilistic scan matching for motion estimation in unstructured environments. In: 2005 IEEE/RSJ International Conference on Intelligent Robots and Systems, Edmonton, AB, Canada, 2–6 August 2005. IEEE Operations Center, Piscataway pp. 3499–3504 (2005)
24. Singer, S., Nelder, J.: Nelder-Mead algorithm. *Scholarpedia* **4**(7), 2928 (2009). <https://doi.org/10.4249/scholarpedia.2928>
25. Samet, H.: The quadtree and related hierarchical data structures. *ACM Comput. Surv.* **16**(2), 187–260 (1984). <https://doi.org/10.1145/356924.356930>